TEAM tAO

3 December 2004

Science

Vol. 306 No. 5702
Pages 1633–1844 $10

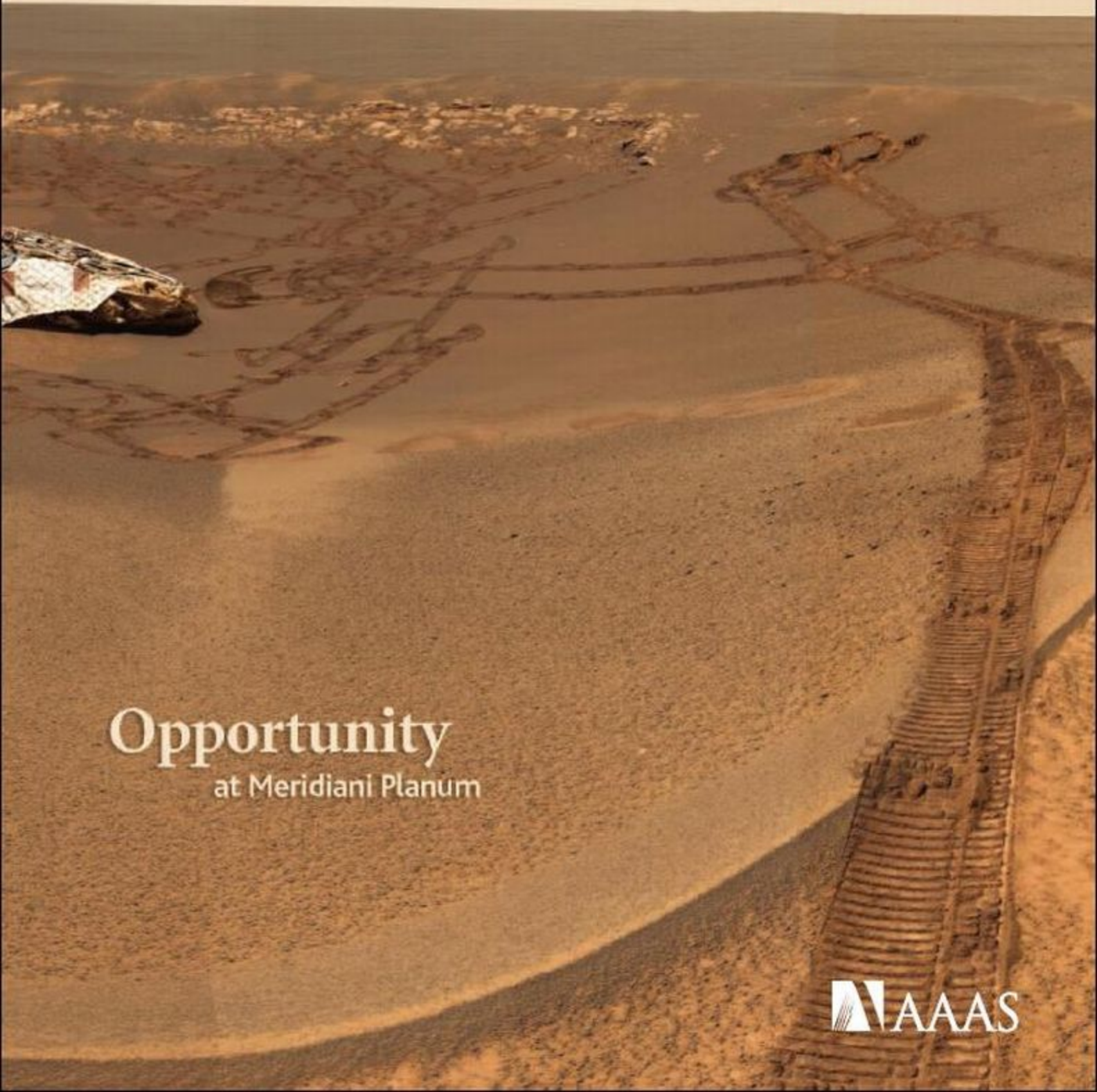

Opportunity
at Meridiani Planum

AAAS

Science

Special Issue

Opportunity at Meridiani Planum

A portion of the "Lion King" panorama acquired by the Pancam instrument onboard the Mars Exploration Rover Opportunity, 23 to 25 March 2004. The view is toward the northwest, overlooking Eagle crater (diameter 20 m) in which Opportunity landed; the lander can be seen at the center left. The bright outcrop along the crater's far wall consists of sedimentary, water-formed rocks. This is an approximate true-color rendering of the scene generated from Pancam's 750-, 530-, and 480-nm filters. [Photo: SA/JPL/Cornell]

Volume 306
3 December 2004
Number 5702

Introduction

Research Articles and Reports

related Perspective page 1689; Report page 1758

Departments

1670

News of the Week

1672

News Focus

Letters

Contents continued

Science

1693

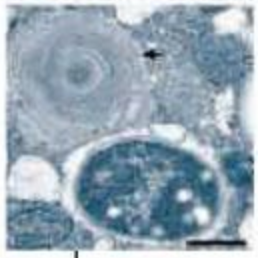

SCIENCE EXPRESS www.sciencexpress.org

MICROBIOLOGY: **Escape of Intracellular *Shigella* from Autophagy**
M. Ogawa, T. Yoshimori, T. Suzuki, H. Sagara, N. Mizushima, C. Sasakawa
Harmful bacteria disguise their identity by coating telltale surface proteins with other proteins, thereby escaping digestion by the cells they invade.

CLIMATE CHANGE
Asynchronous Terrestrial and Marine Signals of Climate Change During Heinrich Events
T. C. Jennerjahn, V. Ittekkot, H. W. Arz, H. Behling, J. Pätzold, G. Wefer

The Duration of Forest Stages in Southern Europe and Interglacial Climate Variability
P. C. Tzedakis, K. H. Roucoux, L. de Abreu, N. J. Shackleton

PERSPECTIVE: **Ecological Versus Climatic Thresholds**
M. Maslin
Climate and pollen records from the same deep sea cores show that some forest ecosystems responded slowly to glacial climate swings, whereas others declined irreversibly even during relatively stable periods.

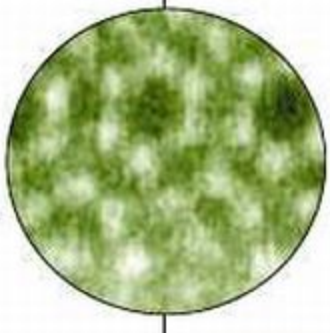

1768

Contents continued

Science

REPORTS CONTINUED

1694 & 1780

1796

AAAS
ADVANCING SCIENCE, SERVING SOCIETY

SCIENCE (ISSN 0036-8075) is published weekly on Friday, except the last week in December, by the American Association for the Advancement of Science, 1200 New York Avenue, NW, Washington, DC 20005. Periodicals Mail postage (publication No. 484900) paid at Washington, DC, and additional mailing offices. Copyright © 2004 by the American Association for the Advancement of Science. The title SCIENCE is a registered trademark of the AAAS. Domestic individual membership and subscription (51 issues): $130 ($74 allocated to subscription). Domestic institutional subscription (51 issues): $500. Foreign postage extra: Mexico, Caribbean (surface mail) $55; other countries (air assist delivery) $85. First class, airmail, student, and retired rates on request. Canadian rates with GST available upon request, GST # 125488122. Publications Mail Agreement Number 1069624. Printed in the U.S.A.

Change of address: allow 4 weeks, giving old and new addresses and 8-digit account number. Postmaster: Send change of address to Science, P.O. Box 1811, Danbury, CT 06813–1811. Single copy sales: $10.00 per issue prepaid includes surface postage; bulk rates on request. Authorization to photocopy material for internal or personal use under circumstances not falling within the fair use provisions of the Copyright Act is granted by AAAS to libraries and other users registered with the Copyright Clearance Center (CCC) Transactional Reporting Service, provided that $15.00 per article is paid directly to CCC, 222 Rosewood Drive, Danvers, MA 01923. The identification code for Science is 0036-8075/03 $15.00. Science is indexed in the Reader's Guide to Periodical Literature and in several specialized indexes.

Contents continued

sciencenow www.sciencenow.org Daily News Coverage

Not-So-Cosmic Microwaves?
Subtleties in the big bang's afterglow suggests a more local origin for some radiation.

Arrested Development Keeps Bees on Task
Pheromone that prevents young bees from maturing ensures they do what's best for the hive.

Protein Mends Broken Hearts
A key player in heart development may prevent damage from heart attacks.

Science and entertainment converge.

science's next wave www.nextwave.org Career Resources for Young Scientists

Global: Science Careers in Arts and Entertainment—Feature Index *E. Pain*
Next Wave's December feature focuses on science careers in the entertainment field.

Global/Europe: A Mathematical Model for Lyrical Singing *I. Arroabarren*
A telecommunications engineer relates the physiology and acoustics of singing.

Global/Canada: Attack of the Dinobots *A. Fazekas*
Space-robotics engineers in Canada design animatronic dinosaurs for a Florida-based amusement park.

Postdoc Network: Workshop on the Postdoc Experience Calls for "Culture Change" *B. Benderly*
Correcting the inequities that bedevil postdocs requires a culture change at labs and universities nationwide.

MiSciNet: The Quantum Ripples of Life *C. Choi*
A researcher at the Stanford Linear Accelerator Center credits science with helping him escape the stresses of inner city life.

MiSciNet: Bridging the Cultural Divide in Medicine *E. Francisco*
The dean at Dartmouth Medical School talks about her experiences as a female Navajo in science.

science's sage ke www.sageke.org Science of Aging Knowledge Environment

Perspective: Mitochondrial Injury—A Hot Spot for Parkinsonism and Parkinson's Disease? *B. I. Giasson*
Mutations in distinct genes might lead to Parkinson's disease through a common mechanism.

News Focus: Paying the Price *R. J. Davenport*
Long-lived worms can't compete.

News Focus: Partners in Death *M. Leslie*
Alzheimer's protein rouses cell-suicide enzyme.

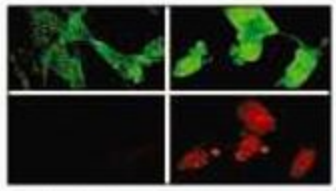

Lighting up suicidal cells.

science's stke www.stke.org Signal Transduction Knowledge Environment

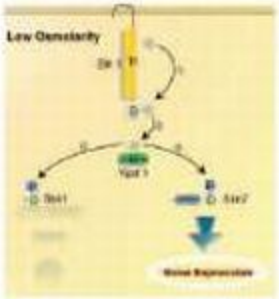

Phosphorelay signaling in *S. cerevisiae*.

Teaching Resource: Nuclear Receptor and Transcriptional Complex Cycles *A. M. Fowler and E. T. Alarid*
The animation demonstrates the cycles involved in estrogen receptor–regulated gene expression.

Teaching Resource: Phosphorelay Signaling in Yeast in Response to Changes in Osmolarity *J. L. Santos and K. Shiozaki*
The animation shows signaling through the high osmolarity glycerol (HOG) pathway.

Separate individual or institutional subscriptions to these products may be required for full-text access.

Nano-Motion Pictures

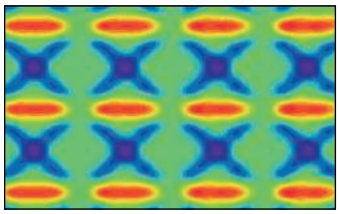

One goal of ultrafast x-ray structural studies is to image atomic motions in materials in a nondestructive manner. **Bargheer *et al.*** (p. 1771; see the Perspective by **Bucksbaum**) imaged coherent atomic motions in a GaAs/AlGaAs superlattice that were induced by exciting electron-hole pairs in the GaAs subband. This excitation process weakens the bonding in the GaAs layers, which causes them to expand and the AlGaAs layers to contract. From their analysis of the small changes they observed in weak reflections, the authors argue that the layers cycle between expansion and contraction every 3.5 picoseconds and launch coherent acoustic standing waves.

Gas Leak on Mars

Spectra obtained by the Planetary Fourier Spectrometer onboard the Mars Express spacecraft show a detection of methane in the martian atmosphere. **Formisano *et al.*** (p. 1758, published online 28 October 2004; see the Perspective by **Kargel** and the Special Section on Mars Opportunity beginning on p. 1697) found that the amount of methane detected varies with space and time, and they suggest that there might be some localized sources. The possible sources of this methane are diverse and include microorganisms, hydrothermal activity, cometary impacts, and dissociation of hydrated clathrates.

Amphibians in Decline

The IUCN Global Amphibian Assessment (GAA), which commenced in 2001, has just been completed, and **Stuart *et al.*** (p. 1783, published online 14 October 2004) present the key findings. The data set covers 5743 species, and confirms that the current conservation status of amphibians is alarming, with 1856 species (32.5% of the total) being globally threatened, 2468 (43.2%) in decline, 435 (7.6%) in rapid decline, and 129 (2.2%) having disappeared since 1980 (many of which are probably extinct). These numbers indicate a much worse situation than seen so far for any other taxonomic group. Of the rapidly declining species, 50 are subject to overharvesting, and 183 are facing severe habitat loss. A third group of 207 species has declined catastrophically, even in situations where there are no obvious threats.

A Day at the Beach

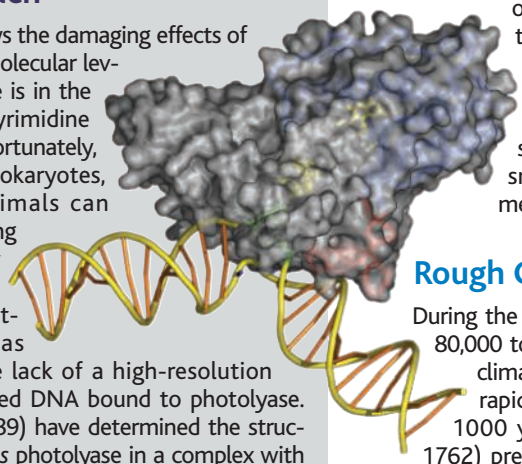

Any Sun worshiper knows the damaging effects of ultraviolet rays. At the molecular level, much of this damage is in the form of cyclobutane pyrimidine dimers (CPD) in DNA. Fortunately, DNA photolyases in prokaryotes, plants, and many animals can repair these lesions using blue light as an energy source. Understanding the mechanism of light-driven DNA repair has been hampered by the lack of a high-resolution structure of UV-damaged DNA bound to photolyase. Now **Mees *et al.*** (p. 1789) have determined the structure of *Anacystis nidulans* photolyase in a complex with duplex DNA containing a CPD-like lesion at 1.8 Å resolution. Apparently synchrotron radiation triggered repair of the CPD so that the structure represents a cryo-trapped cleavage intermediate in which the thymine dimer is flipped into the active site of the photolyase. The structure explains much existing biochemical data and provides a basis for future studies of mechanism.

CREDITS: (TOP TO BOTTOM) BARGHEER *ET AL.*; MEES *ET AL.*

Giving a Self-Antigen Its Natural Identity

Natural killer (NK) T cells recognize lipids, rather than protein-derived antigens, that are presented by major histocompatibility class 1–like CD1 molecules. Although certain artificial lipids and a handful derived from bacteria have been shown to stimulate NKT cells, the identity of naturally occurring endogenous lipid ligands has been elusive. **Zhou *et al.*** (p. 1786, published online 11 November 2004; see the Perspective **by Godfrey *et al.***) now reveal that a single mammalian lysosomal glycosphingolipid, isoglobotrihexosylceramide, or iGb3, can stimulate large numbers of human and mouse NKT cells, and found that mice lacking a subunit of an enzyme responsible for generating iGb3 have a profound deficiency in NKT cell development in the thymus. This lipid antigen may thus play a role in directing NKT cell development and function and may contribute to a variety of disease states, from infection to cancer.

A Daily Measure

How can we measure in a rigorous and cost-effective way how people spend their time and how they experience the various activities and settings of their lives? **Kahneman *et al.*** (p. 1776) propose a technique to help people reconstruct their daily activities and to report on their daily psychological experiences in the process. Using this technique, about 1000 full-time employed women in urban Texas reported on their activities for the previous day and on their feelings related to these activities in a personal interview. Particular life circumstances (such as income and marital status) had a surprisingly small effect on the enjoyment of life.

Rough Glacial Times

During the last glacial period, roughly 80,000 to 20,000 years ago, Earth's climate changed frequently and rapidly, often within less than 1000 years. **Martrat *et al.*** (p. 1762) present a 250,000-year-long record of sea surface temperature from the western Mediterranean Sea which shows that such variations were during the previous glacial interval, between 230,000 and 130,000 years ago, as well. Abrupt warming was more common than abrupt cooling, and protracted cold periods were less numerous than extended warmer ones. Rates of warming or cooling were generally 2.5° to 5°C per thousand years, but in some cases, the climate warmed by as much as 10°C per thousand years.

The Best of Both Worlds

Nearly all animal species use sexual reproduction despite that fact that each individual transmits only half of its genome to any progeny.

CONTINUED ON PAGE 1647

Published by AAAS

Pearcy *et al.* (p. 1780; see the Perspective by **Gadagkar**) report an unusual system of reproduction in the ant *Catagylphis cursor*, whereby it circumvents this cost. The queens use alternative modes of reproduction for the production of nonreproductive and reproductive offspring: Only the workers are produced by sexual reproduction, while new queens are almost exclusively produced by parthenogenesis. *C. cursor* has been able to capitalize on the ant caste system to minimize the costs and maximize the benefits associated with sexual reproduction, because queens increase the transmission rate of their genes to their reproductive female offspring while maintaining genetic diversity in the worker force.

Hydrogen-Bond Sunscreen

Life on Earth began before enough ozone built up in the atmosphere to screen out intense ultraviolet (UV) solar irradiation. Thus, DNA had to be exceptionally resistant to photo-induced structural damage. Because of the complexity of DNA structure, the origin of its resilience is difficult to probe. **Schultz *et al.*** (p. 1765) have thus studied gas-phase 2-aminopyridine clusters, which model isolated hydrogen bonded DNA base pairs. Using time-resolved photoionization, they found that the planar H-bonded dimer dissipates UV excitation energy within 65 picoseconds, more than 20 times faster than the monomer or larger clusters. Ab initio calculations implicated an intermediate state, formed by transient charge and proton transfer through the H-bond, to account for the rapid relaxation.

Rare Attachment

Silicon nitride is a high-performance ceramic whose mechanical properties can be enhanced with the addition of rare earth atoms. However, it is not clear why this enhancement occurs, or why some rare earth species work better than others. Using high-resolution transmission electron microscopy and electron-energy loss spectroscopy, **Ziegler *et al.*** (p. 1768) show that the atoms are located at the sharp interfaces between the silicon nitride grains and the thin intergranular phase. The silicon nitride grains end in dangling bonds to which the rare earth atoms attach; the attachment position depends on the size of the particular rare earth atom, its electronic configuration, and the presence or absence of oxygen at the interface.

The Good News, or the Bad News?

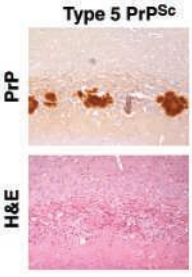

Clinical cases of variant Creutzfeldt-Jakob disease (vCJD), the human counterpart of bovine spongiform encephalopathy (BSE, or mad cow disease), has only been found in individuals homozygous for methionine at polymorphic residue 129 of the prion protein. Primary transmission of BSE or vCJD prions to transgenic mice expressing human PrP valine 129 exhibits a substantial transmission barrier, with a low rate of both clinical prion disease and subclinical prion infection. **Wadsworth *et al.*** (p. 1793, published online 11 November 2004; see the Perspective by **Carrell**) now report that this transmission barrier is not reduced upon second passage in these mice. A valine residue at position 129 of human PrP severely restricts the propagation of both BSE and vCJD prions, and this result suggests that humans of this genotype will be relatively resistant to BSE prion infection. If they do become infected, it will probably be as a result of propagation of a distinct prion strain that results in a disease phenotype distinct from that of vCJD.

A Little Is Still Too Much

Benzene poses a significant health risk through environmental exposure. **Lan *et al.*** (p. 1774; see the news story by **Stokstad**) undertook a cross-sectional study of factory workers in China, who were either routinely exposed to benzene, ranging to below 1 part per million (the current permitted occupational standard in the United States), or who worked in benzene-free environments. The benzene-exposed workers showed significant hematopoietic defects, most notably in progenitor cells, although mature cells of the immune system were also affected. The defects were greatest among individuals carrying alleles for a variant of the gene for myeloperoxidase, an enzyme implicated in benzene hematoxicity. A re-examination of standard occupational levels of benzene exposure in the workplace may thus be required.

CREDIT: WADSWORTH *ET AL.*

Clinical Trials and Public Trust

In July, hope was expressed on this page about new developments in the accessibility of clinical trial data. Several leading medical journals had pressed for a requirement that all clinical trials be placed in a public registry, a proposal endorsed by the American Medical Association (AMA) and the Association of American Medical Colleges. The AMA had urged the institutional review boards (IRBs) that review trial protocols to require such registration before approval of a drug. The World Health Organization further supports an international registry.

That good news has proved transitory, as subsequent events have damaged the public's faith in a process that is, after all, vital to its health. The alleged failure of Merck and Co. to release damaging data about cardiac risks associated with its blockbuster pain drug Vioxx (a COX-2 inhibitor) has prompted congressional hearings, with charges that the company knew of the risks earlier but didn't say so. That scandal followed another: a year-long delay by the U.S. Food and Drug Administration (FDA) to warn about the suicide risks of certain antidepressants given to children.

What's needed to restore confidence in the system that brings us new medicines? It is natural to focus blame on the drug companies. After all, they're rich, and people are mad about their prices. Although clinical trials can be well run, the companies that sponsor and organize them want the "right" result, and opportunities for influence abound. An important trial may involve many centers, each with an IRB of tired and overstretched members. One resistant IRB can be pressed for approval because "all the others have approved." Many trials are outsourced for management by clinical research organizations (CROs), which are motivated to please the employer (after all, doesn't the wedding coordinator want to please the bride's mother?).

But the FDA's end of the process is a natural target, too. The agency has had good external advisory committees in the past. But the recent history of administrative removals, particularly that of COX-2 critic Curt Furberg from a panel considering those drugs, has invited public suspicion. This and other questions about other already-marketed drugs have raised concern about the FDA's susceptibility to drug company influence. These have now led to several actions: a request by the agency for a comprehensive review by the Institute of Medicine; a system of internal appeals, in which an employee concerned about a drug safety issue can be heard by a panel with participation from outside the agency; and a renewed search for a director of the Office of Drug Safety.

Some critics have urged that the situation is so bad that we need a new government agency charged with the conduct of all clinical trials, using funds supplied by the manufacturers. That might be a solution, but political enthusiasm for it will be low for a while. Meanwhile, there are possible short-term fixes. Regional or national IRBs might do a better job, but institutions are reluctant to use them because of the added liability they could take on. Better, perhaps, to provide resources to beef up existing IRBs. Second, require that all late-stage clinical trials, including those testing for unapproved uses of already-marketed drugs, be entered into a registry that would make all results, including the negative ones, available publicly, which is a step beyond the proposals contained in legislation now under Senate consideration.

The most important task is to provide one essential tool. Through no fault of the FDA, the United States has lacked a system than can detect things that go wrong with an already-marketed drug. Physicians are asked to make voluntary reports and manufacturers are required to tell the FDA when they spot a problem, but there's little incentive for either. Moreover, there is no centralized way of knowing how much of a given drug is being used, so there is no denominator and no adverse reaction rate can be calculated. That's not to say that it can't be done right. Kaiser Permanente, the health plan giant, maintains electronic patient records and its doctors do report problems, allowing them to conduct adverse reaction epidemiology (a Kaiser study spotted the Vioxx problem early). The absence of an effective national adverse event reporting and analysis capacity is an embarrassment. Instead of complaining about the FDA, Congress should fund it to support an effective Office of Drug Safety, with the authority needed to encourage physician reporting and a way to audit prescriptions.

Donald Kennedy
Editor-in-Chief

10.1126/science.1107657

Published by AAAS

EDITORS' CHOICE

edited by Gilbert Chin

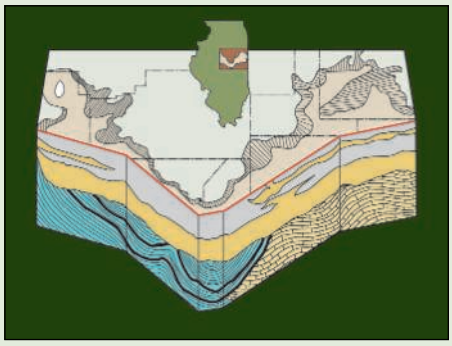

The Mahomet aquifer.

GEOCHEMISTRY

Reducing Arsenic

Dangerously high concentrations of arsenic can be found in groundwater drawn from unconsolidated sediments around the world. Previous studies have shown that bacteria, particularly those that reduce arsenate, can release arsenic from sediments and, in essence, add it to the groundwater.

Kirk *et al*. have studied the Mahomet glacial aquifer in central Illinois and found that high arsenic concentrations correlate with low sulfate concentrations. The authors suggest that in regions where sulfate-reducing bacteria are active, they produce sulfides that precipitate arsenic and remove it from the water. In contrast, where methanogenic bacteria are active, little sulfide is produced and arsenic is not precipitated. If arsenic concentrations are indeed affected by bacteria in this fashion, then a low sulfate concentration, which is much easier to measure, can be used as a sign of potentially unsafe water. Furthermore, adding sulfate to arsenic-rich aquifers may stimulate sulfate-reducing bacteria and thus reduce arsenic concentrations. — LR

Geology **32**, 953 (2004).

CLIMATE SCIENCE

Uniformly Productive

Moist tropical forests of the Amazon basin experience a seasonal variation of rain, in which the radiation available for photosynthesis is much more abundant during the dry season. In spite of this fluctuation, these forests maintain high rates of primary production throughout the 5-to-6 month dry season. Two non-exclusive explanations have been proposed: the first is that many plants in the tropical forest have deep roots, which would allow them access to water during the dry season; the second is that they have developed patterns of leaf phenology (the cycle of leaf fall and emergence) that facilitate an even growth rate.

Xiao *et al*. have combined analyses of satellite images and field data from a CO_2 flux tower site in a Brazilian forest in order to develop and validate a new satellite-based vegetation photosynthesis model for estimating the dynamics of production in seasonally moist tropical evergreen forest. They find that this forest displays subtle changes in the seasonal dynamics of leaf phenology and that the forest experienced no water stress in the dry seasons of 1998–2002. They use these data as input to a model that successfully predicts high productivity in the late dry season, consistent with observation. — HJS

Remote Sensing Environ. **94**, 105 (2005).

ECOLOGY/EVOLUTION

Balls of String

The two great lineages of flowering plants—the monocots and dicots—diverged early in flowering plant evolutionary history more than 100 million years ago (Ma). Fossils from the Early Cretaceous have provided evidence of the range of form in early dicots, but the relationships and appearance of the early monocots have remained more mysterious.

Friis *et al*. have unearthed a new fossil monocot from deposits in Portugal, dating to approximately 120 Ma. The fossil, named *Mayoa*, mostly consists of pollen and associated structural fragments and is clearly allied to the family Araceae, whose modern representatives include arum lilies and cheeseplants. *Mayoa* pollen shows highly distinctive narrow ribs separated by grooves, giving the pollen grains the appearance of neat balls of string—a morphology that is most similar to that of the modern aroid genus *Holochlamys*, which occurs in tropical Southeast Asia. *Mayoa* provides the best fossil evidence to date of a recognizable monocot family soon after the dawn of the angiosperms. — AMS

Proc. Natl. Acad. Sci. U.S.A. **101**, 16565 (2004).

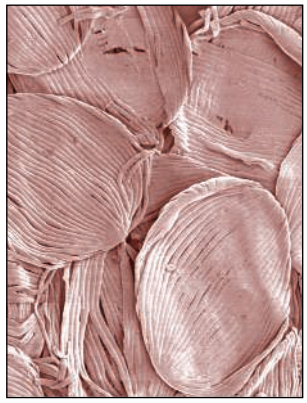

Scanning electron micrograph of *Mayoa* pollen.

CHEMISTRY

Give and Take

Alkene binding to low-valent transition metals is common. The strong interaction involves electron donation from olefin to metal, as well as back-bonding from metal d-orbitals to the olefin. For s-block metals such as the alkaline earths, however, there are no d electrons to give back, and examples of alkene coordination have been elusive. Beyond fundamental interest, such compounds would model intermediates involved in metal-catalyzed alkene polymerization. By tethering a butenyl chain to a cyclopentadienyl (Cp) ligand, Schumann *et al*. have succeeded in preparing compounds of the three heavy alkaline earth metals (Ca, Sr, and Ba) that show evidence of alkene interaction. The metal is sandwiched between two Cp rings, and x-ray diffraction reveals close contact in the solid state between the metal center and the C=C bonds dangling from each ring, whereas in the Mg compound, the butenyl chains face away from the metal and do not interact with it. — JSY

Angew. Chem. Int. Ed. **43**, 6208 (2004).

PSYCHOLOGY

Crunch Time

All of us have had to perform under pressure, either during an athletic contest or an academic examination, and sometimes we miss the penalty kick or choose the antonym instead of the synonym. A great deal of research, some of it under the contemporary guise of sports psychology, has indicated that pressure elicits suboptimal performance of oft-rehearsed sensorimotor tasks by disrupting automated

CONTINUED ON PAGE 1653

Published by AAAS

execution; in other words, pressure engages explicit monitoring and results in our having to learn how to perform the task all over again.

Beilock *et al*. have shifted the spotlight from the pitch into the classroom and assessed the performance of college students on easy and hard modular arithmetic problems in the absence or presence of social and monetary inducements to select the right answer quickly. The hard problems demanded lots of working memory, and the results suggest that the effect of pressure is to distract some portion of working memory, leaving less available to support problem-solving. In another analysis, Beilock and Carr find that when comparing a group of individuals with high working memory capacity to one with less, the performance (on difficult problems) of the former group under pressure declines to the point where their advantage over the other group (measured on easy problems) actually disappears. The implication, as they note, is that the high-achieving students (see Garman, Book Reviews, p. 1685) may be more likely to stumble under pressure. — GJC

France v. England, Euro 2004.

CREDITS: SHAUN BOTTERILL/GETTY IMAGES (2004)

J. Exp. Psych: Gen. **133**, in press (2004); *Psychol. Sci.* **16**, in press (2005).

BIOMEDICINE

Profiling Bystanders

Remarkable progress has been made in identifying the molecular features of tumor cells that mediate their survival and uncontrolled growth. Tumor cells do not grow in isolation, however, and recently there has been heightened interest in exploring the extent to which their behavior is influenced by nonmalignant cells in the tumor microenvironment.

A new study shows that, at least for one tumor type, the cells in the tumor microenvironment may determine the clinical course of the disease. Dave *et al*. carried out gene expression profiling analyses on tumor biopsy samples obtained at diagnosis from patients with follicular lymphoma, a cancer for which survival ranges from less than 12 months to more than 20 years. Surprisingly, the genes that served as the best predictors of patient survival were not expressed by the tumor cells themselves but rather by the nonmalignant immune cells infiltrating the tumors (T cells, macrophages, and follicular dendritic cells). These results not only underscore the critical interplay between tumor cells and their environment, but they provide an important starting point for identifying the immune cell–derived signals that influence the growth of follicular lymphoma cells—information that could lead to new therapies. — PAK

N. Engl. J. Med. **351**, 2159 (2004).

HIGHLIGHTED IN *SCIENCE*'S SIGNAL TRANSDUCTION KNOWLEDGE ENVIRONMENT

Science's stke www.stke.org

More Than a Scaffold

Yotiao is an anchoring protein that, in the heart, mediates the formation of a complex consisting of the I_{Ks} channel (a subunit KCNQ1 and regulatory subunit KCNE1), protein kinase A (PKA), and protein phosphatase 1 (PP1). Mutations that disrupt this complex interfere with the cardiac response to stress and can cause death. The effect of PKA on the channel can be mimicked by a mutation (S97D) in the KCNQ1 subunit. Using cells transfected with this mutant channel, Kurokawa *et al*. demonstrated that interaction with Yotiao increased channel current by slowing channel deactivation in the absence of cAMP. This effect was not blocked by inhibitors of PKA or protein kinase C, indicating that Yotiao was not promoting phosphorylation. Conversely, Yotiao did not alter wild-type channel kinetics in the absence of cAMP, which suggests that Yotiao not only promotes PKA phosphorylation of the channel but may also exert subsequent phosphorylation-dependent effects on channel deactivation kinetics. — NG

Proc. Natl. Acad. Sci. U.S.A. **101**, 16374 (2004).

NetWatch

edited by Mitch Leslie

IMAGES

Rock-Art Festival

Getting lost in the outback was a trial for rancher Joseph Bradshaw and his brother, but it was a boon for rock-art enthusiasts. Wandering remote northwest Australia in 1891, the pair stumbled across stunning paintings, some of which are at least 17,000 years old. The works, along with many other examples of ancient creativity, are on display at this site from the Bradshaw Foundation, based in Geneva, Switzerland.

The site's many educational features include photo surveys to a host of rock-art sites around the world. For example, a gallery showcases 32 of the so-called Bradshaw paintings. Who painted these statuesque, 73-centimeter-tall figures (above) and what they signify remains a mystery. Other locales range from Easter Island to Twyfelfontein in Namibia, where beginning 6000 years ago, unknown artists engraved a menagerie of animals and speckled the rocks with golf ball–sized indentations. Be sure to check out the site's interactive map that traces the expansion of our species throughout the world.

www.bradshawfoundation.com

DATABASE

To Build a Fly

An inert egg can't morph into a flitting fruit fly without *tinman* and *Mothers against dpp*, *klumpfuss* and *knirps*, *legless*, *heartless*, *tailless*, and *hairless*. Find out how these and more than 600 other genes mold *Drosophila* development at the Interactive Fly, created 9 years ago by neurogeneticist Thomas Brody of the National Institute of Neurological Disorders and Stroke and hosted by the Society for Developmental Biology.

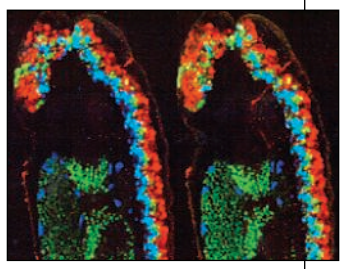

The genetic encyclopedia includes detailed accounts of each gene's role in shaping the insect. *tinman*, for instance, is vital for heart formation, and *knirps* helps with construction of a wing vein. You can browse the genes alphabetically, by pathway, or by function. The site also brims with background information on fly formation, including a developmental atlas. A gallery links to Fly*Move* from the University of Münster in Germany, where you can screen videos and animations of the stages from egg to grub. Above, the head of an embryonic fly stained to show the activity of three genes.

www.sdbonline.org/fly/aimain/1aahome.htm

NET NEWS

A Google for Academia

As if you weren't spending enough time Googling, now the search engine offers another reason to loiter there: a bibliographic tool aimed at scientists and other researchers. Google Scholar, a beta version of which launched last month, trolls for articles, reports, and other documents from publishers, universities, professional societies, and abstract databases such as PubMed. Almost all top scholarly publishers have agreed to let Google index their sites, says principal engineer Anurag Acharya, including the publishers of *Science* and *Nature*.

Instead of the list of Web sites, an author search for Francis Crick returns a roster of his works, beginning with a citation for the 1953 paper on DNA structure. To rank the results, Google Scholar applies the same criteria that scientists use when deciding which papers to read, says Acharya, including the importance of the journal and how often the work has been cited. Although you can obtain abstracts for most articles, you or your library will need a subscription to download the full text of some publications. Acharya says upcoming features will include limiting searches by date.

scholar.google.com

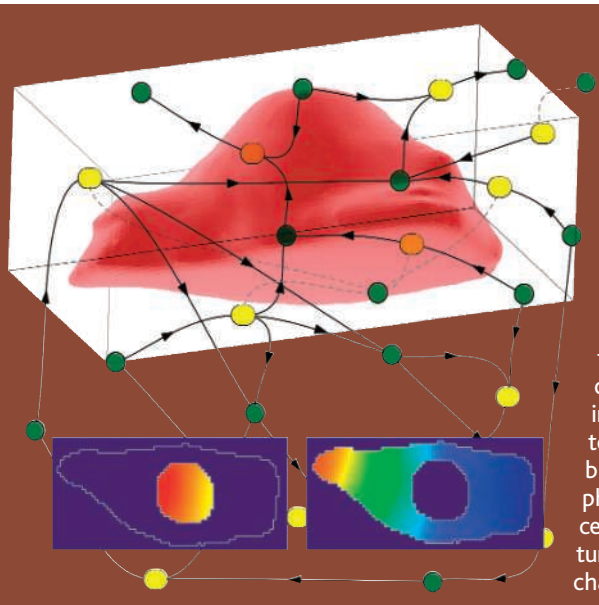

TOOLS

Silicon Cell Biology

Forget petri dishes and incubators; the cells at this site never need food or clean glassware, and they can't die if you neglect them. The Virtual Cell from the University of Connecticut Health Center in Farmington lets researchers customize models to simulate biochemical and electrophysiological activities of cells. You can install structures such as organelles and channels through the cell membrane, stock the cytoplasm with various molecules, and specify what biochemical reactions can occur. What sets the Virtual Cell apart from most modeling software, says project director Leslie Loew, is that it allows users to incorporate processes involving cell structure, such as diffusion and membrane transport. Visitors can share their creations through a central database. Other models have tackled everything from calcium balance in pancreatic cells to the breakdown of the nuclear membrane during mitosis.

www.nrcam.uchc.edu

Send site suggestions to netwatch@aaas.org. Archive: www.sciencemag.org/netwatch

CREDITS (TOP TO BOTTOM): BRADSHAW FOUNDATION; WARD ODENWALD/NIH; LESLIE LOEW/NRCAM

Published by AAAS

This Week

PAGE 1665
Benzene toxicity

1666
India-China moon race

U.S. SCIENCE BUDGET

Science Agencies Caught in Postelection Spending Squeeze

An Administration determined to hold down spending in all but a handful of priority areas imposed its will on a lame-duck Congress shortly before the Thanksgiving holiday (*Science*, 26 November, p. 1453). The result was a turkey of a 2005 science budget for the majority of researchers—and the odds are that next year's menu will feature more of the same.

Homeland security and defense research came away the big winners in the budget for the 2005 fiscal year, which began on 1 October, with NASA getting a last-minute boost and the Department of Energy's (DOE's) science programs doing surprisingly well. The National Science Foundation (NSF), on the other hand, took a cut despite promises of lofty growth, while the formerly high-flying National Institutes of Health (NIH) eked out a small increase for the second year in a row. Those spending decisions by Congress, wrapped into a massive omnibus appropriations bill (H.R. 4818), met the Bush Administration's goal of holding discretionary spending not related to defense and homeland security to a mere 1% rise over 2004. That squeezed most domestic programs, including nearly all basic research (see table; more details at aaas.org/spp/rd/approp05.htm). And it left individual legislators feeling powerless.

"While I understand the need to make hard choices in the face of fiscal constraint, I do not see the wisdom in putting science funding far behind other priorities," complained Representative Vernon Ehlers (R–MI), a former physicist and senior member of the House Science Committee, shortly before the House acted on 20 November. "Under protest I will vote for the bill. But my vote does not in any way represent my approval for the funding cuts to the NSF."

SELECTED RESEARCH AGENCIES (IN $ MILLIONS)

Agency	2004	2005 Request	2005	% Change
National Institutes of Health	27,800	28,527	28,371	+2.0%
National Science Foundation	5,578	5,745	5,472	–1.9%
NASA	15,378	16,244	16,070	+4.5%
Department of Defense, basic research	1,404	1,330	1,490	+6.1%
Department of Energy, Office of Science	3,500	3,431	3,600	+2.8%
Department of Homeland Security R&D	1,037	1,141	1,243	+19.9%
National Institute of Standards and Technology labs	331	417	373	+12.4%
Environmental Protection Agency	782	689	744	–5.0%
U.S. Geological Survey	938	920	935	–0.3%
USDA National Research Initiative	164	180	180	+10.0%
Total Defense/Security R&D	**70,187**	**73,499**	**74,976**	**+6.8%**
Total Civilian R&D	**55,989**	**57,218**	**57,224**	**+2.2%**

The Administration's support for national security was never in doubt. But its commitment to the moon-Mars exploration vision that the president outlined last winter (*Science*, 23 January, p. 444)—and ignored during the campaign—was a surprising twist to the budget finale. The White House pushed strongly for a significant budget boost for such exploration, according to congressional and Administration aides, and persuaded legislators to impose a 0.8% tax on all agencies to raise the extra money for NASA and a few other priorities. "We are really excited about it," said Alphonso Diaz, the agency's new science chief, promising that the appropriation will lead to a "very robust science program."

That optimism glosses over the hidden costs NASA has accumulated since the beginning of the year, leaving the agency $1.4 billion in the hole for the current fiscal year. Congress directed NASA to spend $291 million of its $16.1 billion budget on servicing the Hubble Space Telescope, a cost not anticipated by the Administration. The cost of returning the space shuttle to orbit has risen by $762 million. Lawmakers also added more than $200 million for projects not requested by the president that benefit specific districts and states. "Somebody isn't going to get what they need," says Lennard Fisk, an astrophysicist at the University of Michigan, Ann Arbor, who chairs the National Academies' Space Studies Board.

The spending bill gives NASA Administrator Sean O'Keefe unprecedented power to move money between the agency's science and aeronautics accounts and the exploration portfolio, although Congress must approve his operating plan early next year. Many researchers fear that NASA's science program will bear the brunt of the inevitable cuts. That view is shared by the American Physical Society (APS), which released a report on 22 November warning that NASA's exploration plan could eat science's lunch. Congress is also worried and has asked NASA to have the National Academies conduct a thorough study of the plan's implications for science.

Sitting at the other end of this year's spending seesaw is NSF, facing the biggest cut in its research budget in 35 years as part of a record $106 million reduction. The new budget is probably the death knell for a 2001 law that authorizes a 5-year doubling of NSF's budget, and it's already triggering some serious soul-searching at the agency. "This budget won't give us what we need, so we will have to figure out a way to live within our means," says newly confirmed NSF Director Arden Bement, whose 9-month stint as acting director was converted into a full 6-year term by the Senate just before it left town on 21 November. Warren Washington, chair of NSF's oversight body the National Science Board, worries that "we may be reaching the point where some very good scien- ▶

CREDIT: PHOTOS.COM; SOURCE: CONGRESS AND AAAS

Published by AAAS

The Omnibus Bill Isn't Only About Dollars

The massive spending bill that each house of Congress adopted last month wasn't just a budget bill. It addressed many controversial issues, including the following science-related items:

• **H-1B visas:** The omnibus bill allows the State Department to grant 20,000 additional H-1B visas every year to foreign nationals with a master's or a Ph.D. from a U.S. university. Business and academic organizations lobbied for the legislation after this year's quota of 65,000 H-1B visas—open to skilled foreign workers regardless of educational qualification—was reached on 1 October, the first day of the fiscal year. A previous cap of 195,000 expired in 2003. **–Y.B.**

• **Census:** The American Community Survey, a streamlined form designed to provide continuously updated, neighborhood-level census data, has finally gotten the green light for the 2010 census. The survey is getting its 2005 request of $146 million, reversing a Senate vote to allocate only $65 million. "This was a do-or-die year," says Census Bureau spokesperson Jefferson Taylor. "Without the money we would have had to begin preparations to go back to the long form." **–C.H.**

• **Nuclear weapons:** For the Department of Energy and the National Nuclear Security Agency, the big news is that there is no money for the so-called bunker buster warhead. Congress rejected the Administration's request for $27.6 million to design a weapon that could burrow meters into the ground—and told the White House that a $9 million bid for research on other new weapons should be used to make existing designs safer and more reliable. **–C.S.**

• **NIH management:** The omnibus bill drops provisions added by the House of Representatives that would have barred funds for two psychology research grants opposed by conservatives and imposed a 50-person limit on NIH attendance at foreign meetings. The bill also tells NIH officials to consider all the comments on its proposal to increase public access to NIH-funded research papers and to provide Congress with a cost estimate. **–J.K.**

tists are discouraged from even applying."

The legislators left Bement with some hard choices. One is whether to fund a new, $30 million round of science and technology centers now undergoing final review. Bement says he's inclined to support as many of the six planned centers as he can afford. At the same time, Bement says a $20 million workforce initiative that Congress has rejected 2 years running will be reworked to make its goals clearer, and a $10 million innovation fund that legislators nixed will be scrapped because NSF has other ways to support high-risk research.

Two proposed starts—a high-energy physics experiment at Brookhaven National Laboratory in Upton, New York, and a renovated ocean drilling vessel—survived the budget squeeze, although at 50% and 40% of their requested amounts. "It's a dream come true," says Michael Marx of Columbia University about Brookhaven's Rare Symmetry Violating Processes project. But a proposed ecological network received only planning and design money. The slowdown promises to clog NSF's pipeline of planned major construction. At the same time, legislators told the agency to spend $5 million to begin designing a $700 million, 30-meter segmented telescope that is still undergoing NSF review.

At NIH, the success rate for individual investigators is expected to dip in 2005 because the agency received only a 2% hike and needs more money to sustain existing research projects. Institute officials "had already expressed it would be a very difficult year, and [the final number] certainly doesn't help," says David Moore, head of governmental relations for the Association of American Medical Colleges.

The boost to DOE's Office of Science budget comes courtesy of the people heading the agency's two spending panels, Representative David Hobson (R–OH) and Senator Pete Domenici (R–NM). "They are very strong proponents of science, and there was a meeting of the minds on this bill," says APS's Michael Lubell. Highlights include $10 million to start designing a facility for characterizing proteins and molecular tags at a site not yet chosen and $30 million more for the office of Advanced Scientific Computing Research. Legislators also encouraged DOE to proceed with a dark energy mission, a joint DOE-NASA project that could fall victim to impending cuts at NASA.

Lighter load. Arden Bement has left NIST after the Senate confirmed him as NSF director—just in time for a budget cut.

Work on inertial confinement fusion—inducing a small pellet of heavy hydrogen to fuse by slamming it with lasers—received a $50 million boost, but lawmakers cut $25 million from the $4 billion National Ignition Facility at Lawrence Livermore National Laboratory in California, the prime U.S. inertial confinement lab, and asked for an outside study to determine whether the project is on the right track.

The president's budget request for 2006, which he will submit to Congress in early February, is expected to continue this year's emphasis on science aimed at strengthening national security. The Administration is also expected to support continued planning for a Hubble rescue mission, which Congress said "should be one of NASA's highest priorities." Conversely, NSF and NIH officials are bracing for tiny increases, at best. That won't be a new experience for Bement. For the past 3 years he's also been director of the National Institute of Standards and Technology (NIST), whose in-house research budget took a sharp hit in 2004 before rebounding this year. So he's diplomatic when asked about prospects for 2006. "We had hoped for better [in 2005]. And so did most people. But we'll keep trying."

–Andrew Lawler and Jeffrey Mervis

With reporting by Charles Seife, Jocelyn Kaiser, Constance Holden, and Yudhijit Bhattacharjee.

CREDIT: RICK KOZAK

Published by AAAS

TOXICOLOGY

Factory Study Shows Low Levels of Benzene Reduce Blood Cell Counts

There's no doubt that benzene, a widely used industrial chemical, can be harmful. Workers highly exposed to benzene fumes, for example, run an increased risk of leukemia and bone-marrow toxicity. But the risk from smaller exposures is unclear. Now a tightly controlled study in Chinese factories, reported on page 1774, provides reason for concern: Workers who inhaled less than 1 part per million (ppm) of benzene—an exposure considered safe under U.S. occupational guidelines—had fewer white blood cells than did unexposed workers.

Although the workers weren't sick, the results hint that low doses of benzene may alter the bone marrow and could lead to health problems, some experts say. The study also provides the first direct evidence in humans that benzene harms the progenitor cells that give rise to blood cells. "It really breaks new ground on the potential effects of low levels," says toxicologist Bernard Goldstein of the University of Pittsburgh's School of Public Health.

Hazard? A study of shoe workers in China suggests that even low doses of benzene affect blood cells.

CREDIT: MICHAEL S. YAMASHITA/CORBIS

Benzene is ubiquitous. People are commonly exposed to it from secondhand cigarette smoke, gasoline vapors, and air pollution, although typically only on the order of parts per billion. Studies of the chemical's health effects in industrial settings, where benzene is used as a solvent and in chemical manufacturing, led the United States in 1987 to regulate the maximum allowable workplace exposure at 1 ppm of benzene averaged over 8 hours.

To determine whether blood cells are affected at even smaller exposures, a group of researchers from the U.S. National Cancer Institute (NCI) in Bethesda, Maryland, the Chinese Center for Disease Control and Prevention in Beijing, the University of California, Berkeley, and other institutions compared 250 workers exposed to benzene-laden glues in two shoe factories in China to 140 unexposed workers who sew clothes in other Chinese factories. The researchers carefully gauged benzene exposure by taking urine samples and testing air in the factories, as well as at each worker's home. After 16 months, they took blood samples from the workers.

As expected, workers exposed to benzene at levels of 1 ppm and higher had fewer white blood cells, such as granulocytes and B cells, than did unexposed workers. But this also held true for the 109 workers exposed to less than 1 ppm benzene, even after controlling for smoking and other potential confounding factors. These workers had on average 15% to 18% fewer granulocytes and B cells than did unexposed workers—raising concerns about bone-marrow health, says Qing Lan of NCI.

Luoping Zhang of the University of California, Berkeley, and others in the research team also studied the effect of benzene on the progenitor cells that give rise to blood cells. They found that the ability of progenitor cells to grow and multiply declined with higher exposures. "The key point is that high levels of benzene had a more toxic effect on the progenitor cells than on mature cells," says study co-author Nathaniel Rothman of NCI. "That may suggest we're underestimating the effects of benzene by just studying mature cells."

But Richard Irons of the University of Colorado Health Sciences Center in Denver and Fudan University in Shanghai suggests that counting progenitor cells from blood samples probably does not accurately reflect what's happening to such cells in bone marrow. Irons, who leads a $20 million industry-funded study of benzene effects in Shanghai, also says it's possible that the low-dose changes seen in the *Science* paper stem from exposure to other chemicals or factors such as nutrition. "Because the magnitude of the changes are so small, it becomes difficult to discriminate between transient effects and benzene toxicity," he says.

Still, the findings may lead to demands for lowering the benzene exposure standard, says geneticist Gilbert Omenn of the University of Michigan Medical School in Ann Arbor: "This paper should cause a stir in occupational and environmental health circles." **–ERIK STOKSTAD**

ScienceScope

No Meeting of Minds on NIH Honoraria Ban

Intramural scientists at the National Institutes of Health (NIH) remain upset about a proposed ban on university honoraria after meeting this week with NIH Director Elias Zerhouni. "This meeting did not really explain what the rules are," says Alexander Wlodawer, a cancer institute lab chief.

Zerhouni and his deputy Raynard Kington held a closed-door meeting with lab chiefs and many institute directors after more than 170 senior scientists endorsed a letter protesting a proposed ban on honoraria from institutions receiving NIH grants (*Science*, 19 November, p. 1276). Participants said that NIH has yet to clarify its policies on matters such as teaching and whether speaking, even on official duty, could pose a conflict. But some were encouraged by Zerhouni's promise to carve out "exceptions" for some activities, such as bona fide awards, and to set up a "mechanism" for collecting staff input. **–JOCELYN KAISER**

Salmon Plan Raises Hackles

PORTLAND, OREGON—The Bush Administration's plan to protect salmon on the Columbia and Snake rivers is a "step backwards," according to 250 fisheries scientists who have signed a last-ditch petition seeking changes in the court-ordered plan. A draft of that document became final on 30 November.

An earlier plan was dismissed by Federal District Judge James Redden, who will also review the new plan, for relying on questionable recovery actions. Critics say the current version sidesteps the problem by reinterpreting provisions of the Endangered Species Act, arguing that fisheries managers need only ensure the survival of species rather than their recovery. "The new analysis is an alarming sea change in approach with no supporting scientific justification," the petition concludes. **–ROBERT SERVICE**

Swiss Endorse Stem Cell Law

BASEL—In the first-ever national referendum on the issue, Swiss voters have overwhelmingly approved the use of human stem cells for research. On 28 November, two out of three voters endorsed a law passed last December that allows scientists to use stem cells harvested from embryos no older than 7 days. The law bans therapeutic cloning and research on the embryos themselves and requires several layers of approval, including the consent of the donors. "This is incredibly encouraging for us," says Patrick Aebischer, president of the Swiss Federal Institute of Technology in Lausanne. **–GISELLE WEISS**

Published by AAAS

LUNAR EXPLORATION

India, China Vie for Best Look at the Moon

UDAIPUR, INDIA—The new kids on the space block are having their own race to the moon. Last week, at an international meeting here* on lunar exploration, Chinese scientists presented details of the country's planned lunar orbiter mission, named Chang'e, to be launched sometime in 2007. Not to be outdone, Indian space officials revealed at the same time that they have added an impactor probe to the suite of instruments aboard Chandrayaan-1, which is headed to the moon the same year. The increased attention to Earth's closest neighbor is not lost on space scientists from other countries.

"It has all the makings of a new race," says German high-energy physicist Horst Uwe Keller of the Max Planck Institute for Solar System Research in Katlenburg-Lindau, which hopes to build a payload for the Indian spacecraft. "And that's good. Healthy competition has never killed anybody."

The Chinese mission, the country's first outside Earth's orbit, hopes to put a 2-ton satellite into a 200-kilometer circular polar orbit for a year's worth of exploration. Its 150-kg scientific payload will include a stereo camera to map the terrain of the moon and a gamma and x-ray spectrometer to study its elemental and mineral composition, as well as instruments to measure solar winds and spot high-energy particles from deep space. The Chang'e mission will also carry a microwave radiometer to analyze the density, depth, and composition of the lunar soil, the first time such an instrument has been trained on the moon.

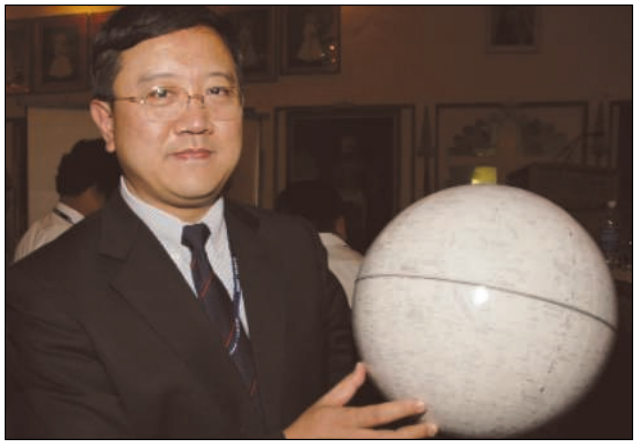

Moonstruck. Wu Ji leads China's team that is building a 2007 lunar orbiter.

There are no international partners on the Chang'e mission, which the Chinese government approved last year on an accelerated timetable. "We are in a real hurry and don't have time to get any foreign payloads," says Wu Ji, executive director of the Center for Space Science and Applied Research in Beijing. China hopes to send a lander and a rover to the moon in 2012, adds Wu, who emphasized that there are no plans to place humans there. "It is out of the question," he says.

India has no plans for a human mission either, Madhavan Nair, chair of the Indian Space Research Organization in Bangalore, told *Science*. But it is expanding its robotic observations. Nair announced that Chandrayaan-1 will now include a 30-kg probe to penetrate the lunar surface. He called the probe a necessary step in preparing for a proposed soft landing and lunar rover mission by 2015. "We do not want to lag behind," he says.

–PALLAVA BAGLA

*International Conference on Exploration and Utilization of the Moon, Udaipur, Rajastan, 22–26 November.

CELL BIOLOGY

Long-Term Stress May Chip Away at the Ends of Chromosomes

We all know stress makes you haggard and causes you to lose your hair. Now comes even more depressing news: Stress may also rob you of DNA. In a report published online this week in the *Proceedings of the National Academy of Sciences*, investigators conclude that the harried mothers of chronically ill children show more cellular aging, as evidenced by shortened chromosomal tips, than do mothers of healthy children.

There is already abundant evidence that long-term stress leads to poor health and reduced immune activity. To delve further into this connection, researchers led by Elissa Epel of the University of California, San Francisco, compared the stress levels and telomeres of 39 mothers of chronically ill children with those of 19 mothers with healthy children. Telomeres, complexes of DNA and protein that cap the ends of chromosomes like the tips of shoelaces, typically shorten with every cell replication and thus can serve as markers of the biological age of most cells.

The scientists gave each mother a questionnaire to assess her level of psychological stress over the preceding month and examined blood samples to determine telomere lengths and measure the activity of telomerase, the enzyme that maintains the telomeres. To assess oxidative stress, a process destructive to cells that is caused by unstable free-radical molecules, the researchers also took urine samples from each mom and measured levels of compounds associated with oxidation.

When divided into groups based on their questionnaire answers, the women with the highest perceived stress, which included some with healthy children, had shorter telomeres than less-stressed women. And within the caregiving group, the older the ill child—and therefore the longer the period of high-stress mothering—the lower the telomerase activity, the greater the oxidative stress, and the shorter the mothers' telomeres. This result persisted independent of age and body mass index. In the highest-stress group, this meant a loss of about 550 base pairs from the mothers' telomeres. Based on the telomere clock, the researchers estimate that the white blood cells of the high-stress mothers had aged 9 to 17 years more than the cells of the low-stress group of the same chronological age.

The scientists say oxidative stress is the most likely mechanism for translating a harried life into shortened telomeres. It has already been demonstrated that chronic activation of stress hormones generates oxidative stress, and that such stress can shorten telomeres in vitro.

Stress researcher Janice Kiecolt-Glaser of Ohio State University in Columbus notes that the study shows that stress, which has already been shown to prematurely weaken the immune response, contributes to "cellular aging more broadly … [and] suggests that major deleterious effects of stress may in fact be far worse for younger adults than previously thought." Cell biologist Jerry Shay of the University of Texas Southwestern Medical Center in Dallas adds that it would be interesting to see if telomere lengths "bounce back" when the stressful situation ends.

–CONSTANCE HOLDEN

CREDIT: PALLAVA BAGLA

Published by AAAS

GENETIC DIVERSITY

Consortium Hopes to Map Human History in Asia

TOKYO—Researchers from 11 Asian countries and regions have forged a landmark agreement to study genetic diversity throughout Asia. Describing their goal as a "genetic map of human history in Asia," they intend to collect blood samples from their populations and analyze them for single nucleotide polymorphisms (SNPs)—sites where a single nucleotide in the genome sequence varies from one individual to another. In addition to hinting at the patterns of migration and settlement throughout the continent, the map could be a step toward identifying genetic characteristics associated with certain diseases.

"We are aware that scientifically, the impact of this work may be considered by some as incremental. But we are convinced that this heralds the rise of Asian biosciences," says Edison Liu, executive director of the Genome Institute of Singapore and one of the key organizers of the effort.

The Pacific Pan-Asian SNP Initiative was formally adopted on 18 November by scientists from institutions based in China, India, Indonesia, Japan, Korea, Malaysia, Nepal, Philippines, Singapore, Thailand, and Taiwan. "This is very much a grassroots effort," says Yoshiyuki Sakaki, director of the RIKEN Genomic Sciences Center in Yokohama, Japan, and president of the Pacific branch of the Human Genome Organization, which sponsored the meeting in Singapore. Organizers estimate the project could take more than 2 years and cost up to $3 million.

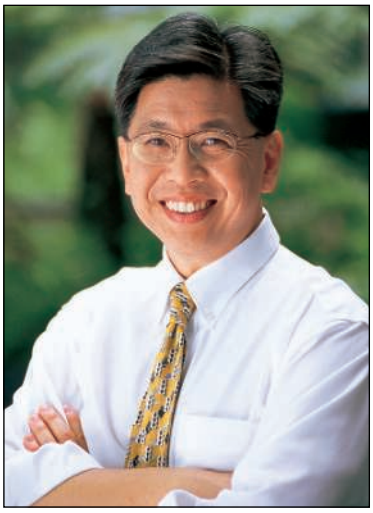

On track. Singapore's Edison Liu hopes that SNPs will explain Asian migration patterns.

CREDIT: GENOME INSTITUTE OF SINGAPORE

Scientists in the consortium hope to collect a total of 2600 samples, including between 20 and 100 samples from each ethnic group. Liu says one challenge will be defining "ethnic group." China has 50 recognized minorities, and Indonesia and India claim to have hundreds. Sakaki says the total should be enough to outline the extent of genetic diversity and similarity throughout Asia, data that should clarify relationships among ethnic groups and suggest how and when successive waves of human ancestors populated the region. Future genomic medicine studies, he says, could answer questions about why some populations seem predisposed to certain diseases or react differently to certain drugs.

All data will be put in an open database, and Liu says the group is amenable to cooperating with other efforts such as the International HapMap Project, which is developing a database of genes associated with diseases and drug responses, although there have been no official contacts as yet. Affymetrix Inc. in Santa Clara, California, will be providing at reduced cost new microarrays that allow researchers to probe 50,000 SNPs in each sample. The initiative will rely on a set of previously defined SNPs whose frequencies are already known to be highly divergent among populations.

Institutions in Japan, Singapore, China, and Korea are likely to provide technical and scientific training for scientists in less-developed countries if sufficient funding can be found. "For us in Indonesia, the benefit is that we can access state-of-the-art technology which is currently out of reach," says Sangkot Marzuki, head of the Eijkman Institute for Molecular Biology in Jakarta. Liu says the group is still looking for collaborators from Laos, Burma, Cambodia, and Mongolia.

Researchers at institutes without the capacity to prepare and analyze the microarrays may have to reconcile their work with local regulations prohibiting the export of DNA materials. One possibility may be to prepare the DNA for chip hybridization while rendering the sample unusable for further research before shipping. Another is that participating scientists may be able to hand deliver samples to one of the technology centers, collaborate in the typing, and then bring the remaining materials back home. Liu says they are still investigating whether these approaches will be accepted by authorities.

Despite these obstacles, and a modest budget, Liu hopes the SNPs consortium is a forerunner of larger collaborations. "It's a good time for us in Asia to take the first steps toward working together as colleagues," he says.

–DENNIS NORMILE

ScienceScope

China Tightens Biolab Rules

BEIJING—China has adopted new biosafety rules that could include criminal penalties for lab managers who violate them. The regulations follow World Health Organization (WHO) biosafety guidelines by specifying four levels of laboratories and defining which pathogens can be handled only at level-3 and -4 labs.

In the past, say Chinese officials, lab safety was up to individual ministries, practices were not standardized, and enforcement was lax. Song Ruilin, an official with the State Council's Legislative Affairs Office, says that work on the new rules began last year and was accelerated after sloppy lab practices at the Center for Disease Control and Prevention in Beijing killed one scientist and spread the SARS virus.

Julie Hall, the WHO coordinator for communicable disease surveillance and response in Beijing, says the new regulations are "a very positive move" and that lab biosafety management "was one of the failings" of the previous system. The rules went into effect on 27 November, but Hall predicts that "changing the research culture" will take time. –DENNIS NORMILE AND XIONG LEI

The Cost of Science Advice

The Federation of American Scientists (FAS) is offering the government some free advice for improving scientific decision-making. But it comes with a hefty price tag.

This week, the Washington, D.C.–based organization, best known for its work on arms control, proposed ways for the Bush Administration and Congress to receive more input on policy issues from gasoline additives to stem cells. It recommends a $20-million-plus-a-year replacement for the Office of Technology Assessment, which Congress killed in 1995, as well as boosting the budget of the White House Office of Science and Technology Policy to better coordinate the work of federal agencies. The FAS report also suggests strengthening the presidentially appointed body of advisers to the White House by giving its members fixed terms and a budget to commission rapid-fire studies. Although the National Academies play an important role in advising the government, the report notes, some topics require a quicker turnaround time than the academies' bureaucracy can deliver.

"Now that the election is over, we're offering nonpartisan, practical solutions to meet the government's need for the best technical advice," says FAS president Henry Kelly. "You can't force the government to base its policies on science. But you can improve the chances that it will."

–JEFFREY MERVIS

Published by AAAS

ITER

Cadarache: More Than Just a Candidate Site

CAMBRIDGE, U.K.—Government ministers from the 25 European Union (E.U.) countries declared last week that they want to keep negotiating with the other five partners in the international effort to build a $6 billion fusion reactor. But the one thing that is not up for negotiation, they say, is the site.

Here we stand. E.U. ministers expect ITER to be built at this site in Cadarache, France.

That message was contained in the new instructions they gave to the European Commission, the E.U.'s executive arm: It declared that the southern French town of Cadarache is no longer Europe's *candidate* site for the International Thermonuclear Experimental Reactor (ITER), but instead it is *the* site. The six ITER partners have been arguing for a year over whether to locate the reactor in Japan or France. All that remains to be decided, E.U. leaders say, is how many of the six partners will remain on board.

Scientists hope ITER will show that fusing deuterium and tritium in a sustained reaction can produce more power than the reactor consumes and so form a viable new source of energy. An international consortium spent nearly 15 years designing ITER, but the current partners—China, the E.U., Japan, Korea, Russia, and the United States—are divided on whether to build at Cadarache or at the Japanese site at Rokkasho.

The statement that came out of last week's council of ministers seemed less confrontational than other recent comments. After a council meeting in September, observers hinted that the E.U. was ready to press ahead without an agreement (*Science*, 1 October, p. 26). And when E.U. officials suggested that Japan was ready to concede before a meeting of ITER partners last month, Japanese negotiators were furious (*Science*, 19 November, p. 1271). E.U. officials "misread the signs coming from Japan," says a senior European fusion researcher. As a result, last week's statement did not mention ultimatums or deadlines but instead called for a project involving "all six parties currently negotiating."

This more diplomatic stance won praise from the Japanese. "We appreciate that [the E.U.] now reaffirmed the importance of the six-party framework. There is no mention of unilateral action; that is quite good," says Satoru Ohtake, head of the Office of Fusion Energy at Japan's Ministry of Education, Culture, Sports, Science, and Technology.

The ministers showed no flexibility, however, on the site. In return for Cadarache, they offered Japan the role of "privileged partner," meaning that Japan would receive more than its share of industrial contracts for ITER components and could choose the ITER director general and have its pick of the extra facilities that have been bolted onto the project to speed the transition to commercial power generation. This could include a materials testing center, a supercomputer lab for fusion simulations, or a beefing up of Japan's own JT-60 fusion reactor.

Members of the European fusion community argue that Cadarache has a clear advantage on scientific grounds. They note that Europe is home to the world's largest fusion reactor, the Joint European Torus near Oxford, U.K., and that it has the largest fusion research program in the world, equal to that of the United States and Japan put together. The decision may be overdue, but for the sake of decorum, the E.U. ministers seem prepared to wait a little while longer. **–DANIEL CLERY**

With reporting from Dennis Normile in Tokyo.

CREDIT: © CEA CADARACHE

SCIENCE POLICY

Europe Advances a Plan for Merit-Based Funding

PARIS—The European Research Council (ERC)—a new funding agency that would support basic research based solely on quality—inched closer to reality at a meeting of the European Union's (E.U.'s) science, education, and industry ministers in Brussels last week. All but two of the E.U.'s 25 member countries support the idea and have asked the European Commission to work out a proposal.

The ERC, a brainchild of Europe's scientific organizations, has quickly gained popularity over the past 2 years among researchers and politicians alike. It would be created as part of Framework Programme 7, the E.U.'s science funding round for the period 2007–10. In early November, it got a new high-level nod of approval from an expert group led by former Dutch prime minister Wim Kok; his panel backed the ERC in a report about the lack of progress on the Lisbon strategy, Europe's plan to reinvigorate its economy.

The Dutch government, which currently holds the rotating presidency of the E.U., had hoped that last week's meeting of the council of ministers would result in a formal invitation to the European Commission to come up with a plan. But Italy and Poland refused to go along. The Italian government objected to the ERC, as it explained in an earlier statement, in part because the agency's merit reviews might lead to some grants being awarded to groups from just one country, which Italy says violates E.U. principles. Poland, for its part, is worried that it may lose out in the competition for ERC funds. The lack of unanimity was "quite disappointing," says Peter Nijkamp, head of the Netherlands Organisation for Scientific Research, who, along with the Dutch government, had invested a lot of time trying to win over the Italian government.

But Jose Mariano Gago, who chairs the Initiative for Science in Europe, a lobby group created to promote the ERC, says unanimity at this point would be too much to expect; he says he's very pleased with the outcome. The meeting's conclusions, although not shared by all, send a "strong positive message," he says, adding that European Commissioner Janez Potočnik now knows he has the backing of the vast majority of countries to come up with a plan.

Meanwhile, the Italian government has come under attack from its own scientists for opposing the ERC. The Italian Academy of Sciences issued a position paper supporting the ERC last month, pointing out that it had not been consulted on the matter and calling the government's position "dangerous for the prestige of the Italian scientists in Europe." In addition, more than 2200 scientists have signed an online petition in favor of the ERC launched by an association of young researchers. **–MARTIN ENSERINK**

Twenty years after the event, researchers are returning to the site of the world's worst chemical spill to pick up health studies that some believe were set aside too soon

Revisiting the Bhopal Tragedy

BHOPAL, INDIA—Ashraf lies on a corner bed in the ophthalmology ward of the Bhopal Memorial Hospital and Research Centre (BMHRC), a thick, white bandage covering his left eye. For the second time in 3 years, the 38-year-old is recuperating from cataract surgery. His sight has not been the same since the night 20 years ago when water entered a storage tank filled with methyl isocyanate (MIC) at a pesticide factory here, triggering a runaway reaction that sent a lethal cloud of chemicals wafting through his neighborhood. The vapors attacked his eyes, which led to a severe infection that gave way to chronic tearing and gradually, cataract-clouded vision. The gases also ravaged Ashraf's lungs, and today he suffers from chronic breathlessness and fatigue.

Like thousands of survivors, Ashraf has turned to the BMHRC medical staff for help with the injuries he received in the world's worst chemical accident. More than half a million people claim to have been exposed to the MIC-derived cloud on the night of 2 to 3 December 1984. At least 3000 men, women, and children died from breathing the lethal gases. And now at least 5000 survivors line up every day outside clinics and hospitals here to be treated for gas-related illnesses.

Despite a flurry of studies in the 1980s documenting the initial effects of MIC exposure, scientific follow-up has waned. An ambitious long-term monitoring effort led by the New Delhi–based Indian Council of Medical Research (ICMR) ended in 1994 when the council abruptly pulled the plug. ICMR handed oversight of its cohort of 80,021 gas victims and 15,931 nonaffected Bhopal residents to the Madhya Pradesh state government, which still keeps tabs on the original ICMR cohort, now numbering about 50,000 people, through the Centre for Rehabilitation Studies (CRS).

ICMR has never fully discussed why it removed itself from the gas tragedy. But some scientists speculate that the government, eager to modernize India's economy, was concerned that tallying up the health consequences too aggressively would scare away foreign investment. Many still bemoan ICMR's decision. It was "ridiculous," says Nalok Banerjee, research officer at CRS. "The state government has no specific expertise in designing studies."

Aftermath. Protests mark the 20th anniversary of a gas leak that has been blamed for chronic ailments such as lung disease.

Confounding matters, the Indian government in 1985 filed a civil suit against the Union Carbide Corp. in the United States—parent of the firm that owned and ran the plant—and imposed restrictions on publishing data on the Bhopal incident, deeming some details too sensitive to be released. The legal wrangling dragged on for 6 years, and subsequent disaster-related lawsuits are still in the courts. "Unfortunately, a lot of research never got published because the scientists retired, or moved on, or lost interest," says Indraneel Mittra, director general of BMHRC.

In May, ICMR published the first of three promised technical reports on the investigations it carried out through 1994. Checking the data was slow and difficult work, says immunologist Nirmal Kumar Ganguly, director general of ICMR, who adds, "It took a long time for the government to give clearance for publication."

The 117-page document describes the findings of some 20 epidemiological studies, noting that death, miscarriage, and general morbidity rates were higher in exposed areas in the decade following the gas leak. Most long-term complications involved the eyes and lungs, but the report gives few specifics. "After 20 years they should have come out with some complete results," says Bhopal oncologist Shyam Agrawal, a member of a new Indian Supreme Court–appointed advisory panel for the gas victims. More details may be elucidated in the next several months when the technical reports on ICMR's toxicological and clinical studies are published.

Researchers in India and North America are poised to conduct a handful of studies that could shed new light on the Bhopal tragedy and its health consequences. Although not lavishly funded, they cover topics from the biology of lung surfactants to the MIC gas cloud.

Picking up the pieces

BMHRC in a perverse way owes its very existence to the gas leak. The medical complex opened 4 years ago and is operated with interest accrued from about $20 million from the sale of Union Carbide's 50.9% stake in the Indian subsidiary that ran the infamous pesticide plant. Recently, the hospital trust's board members earmarked $1 million to develop research facilities, and in August, they okayed the start-up next year of an epidemiology and biostatistics department. The department will study the 270,000 gas vic-

CREDITS: PALLAVA BAGLA

Published by AAAS

tims registered at the hospital and its eight outreach clinics. Because each patient is issued a memory chip–equipped "smart card," the potential new cohort is fully enumerated, identified, and easy to track—a situation found nowhere else in India or any other developing country, says Mittra: "It gives us a unique opportunity to do first-class epidemiological studies, whether gas-related or not."

Other BMHRC research teams set up shop earlier this year. One group plans to delve into the anomalies in lung surfactants of gas victims. Pulmonary surfactant is a lubricant packed with proteins and phospholipids that fights off respiratory pathogens and aids breathing by keeping a low surface tension in the lungs' tiny air sacs, or alveoli. The researchers will compare the levels of various phospholipids and proteins in exposed and nonexposed patients suffering from chronic obstructive pulmonary disease, pulmonary fibrosis, bronchial asthma, and pulmonary tuberculosis. Once an internal board approves the $45,000 project, BMHRC will provide start-up funds.

Another BMHRC research group aims to use new molecular technology to look for genetic mutations that MIC, a suspected mutagen, or other chemicals in the gas cloud may have triggered in gas victims and their children. Studies conducted in the 1980s detected alterations in the chromosomes of some gas victims. More recently, cytogeneticist Narayanan Ganesh of the Jawaharlal Nehru Cancer Hospital and Research Centre, has noted birth defects such as syndactyly—fused or webbed fingers or toes—and pigeon chest among the offspring of people who were exposed to the lethal cloud. The new research team is awaiting approval to revisit these findings.

The health of young adults who were exposed in utero to the gas is the focus of a $75,000 study getting under way at the comparatively cramped offices of the Sambhavna Trust Clinic, just west of the derelict pesticide factory. Community health workers are tracking down almost 400 children born to women who were pregnant at the time of the gas leak and participated in a 1985 study led by Daya Varma of McGill University in Montreal, Canada. That study, published 2 years later in *Environmental Health Perspectives*, found that 43.8% of 865 pregnancies in 3270 families ended in miscarriages. The current project, which Varma is also heading and which is being funded by the Canadian Institutes of Health Research, will analyze the health problems of the young people and measure various physical parameters. It builds on work, reported by the team last October in the *Journal of the American Medical Association*, which found growth retardation in young boys, but not young girls, who were exposed to the gas in the womb or as toddlers.

Ramana Dhara, a specialist in occupational and environmental medicine at Emory University in Atlanta, Georgia, hopes to determine what toxins were unleashed that night by recreating the runaway reaction at the U.S. Department of Energy's (DOE's) hazardous materials test site in Nevada. If that study gets funded—it's couched in terms of emergency preparedness for a terrorist attack—scientists

Heavy toll. Researchers are planning health studies of those living near the ruins of the pesticide plant.

at DOE's Frenchman Flats facility will add water to a tank of MIC and monitor the resultant gas cloud. Early autopsy studies as well as analyses of the gooey residue left in the Bhopal storage tank found about two dozen chemical constituents. "But we still don't know exactly what compounds were in the cloud itself," Dhara says.

By determining the cloud's contents, Dhara and his colleagues could answer one of the more acrimonious debates that raged for months after the tragedy: whether victims should have been treated with sodium thiosulfate, an antidote for cyanide poisoning. In the days immediately after the leak, there was no information about the toxicity of MIC nor what chemicals could result from its pyrolysis and their toxicities. Doctors suspected that the color of the lungs—"cherry red"—was due to hydrogen cyanide, which binds to hemoglobin and blocks its ability to transport oxygen. A study of 20 gas victims given the antidote found a reduction in symptoms and an increased excretion of thiocyanate in urine, evidence to some that cyanide was present and that the treatment was helping people. But the medical community soon split over the efficacy of administering sodium thiosulfate, saying there was not enough evidence to back up its use, and abandoned it as an antidote for the majority of gas victims when the issue was moot.

The potential findings of the experiment in the Nevada desert will have no direct impact on the treatment of gas survivors today because "the chemicals have long since left the bodies of the victims," Dhara says. "But at least the information should be out there, if only to say to the victims that we've finally got some answers."

Although the recent ICMR report notes that it would be "desirable" to extend the long-term observation of the Bhopal cohort to monitor for "cancer and long-term involvement of other organs," that hasn't happened. Banerjee says CRS has little money to do comprehensive epidemiological studies on the cohort of gas victims. "How can you cook food," he says, "without fire." ICMR did set up an outpost of its population-based registries in Bhopal in 1986 to monitor for various cancers that experts thought would ensue after the chemical exposure. Surprisingly, the expected rise in cancers of the blood, bone marrow, and lung never materialized. "There are slight differences between the exposed and nonexposed population, but they are not significant," says Biswajit Sanyal, director of the Jawaharlal Nehru Cancer Hospital and Research Centre.

Sanyal and other Bhopal doctors nonetheless are bracing for cancers to begin popping up in the gas-affected population in the next 5 years. "A person can get lung cancer 30 years after smoking," says BMHRC's Mittra. "In the same way, it is still possible that the rise in cancer incidence is yet to be."

Another source of cancer risk is pollution from the derelict pesticide plant, which looms as a general threat to Bhopal's future. Abandoned shortly after the gas leak, the site was never properly cleaned up. Its remediation is the subject of an ongoing civil suit in U.S. courts by gas victims who claim that chemicals, including some carcinogens, are leaching into the drinking water of some of the city's poorest neighborhoods, where more than 20,000 people live. In May, the Indian Supreme Court directed the state government to supply clean drinking water to the residents. Plans for a pipeline to bring potable water to the affected communities have yet to be drawn up.

In the meantime, gas victims are marking the 20th anniversary of the tragedy with demonstrations in Bhopal and New Delhi. "They are thought of as second-class citizens," says Agrawal. "But the gas victims are a scientific treasure. The opportunity to study them should not be wasted."

—CHARLENE CRABB

Charlene Crabb is a science writer in Paris.
With reporting by Pallava Bagla.

CREDITS: PALLAVA BAGLA

Plant Pathologists Gear Up for Battle With Dread Fungus

No soybean can resist a rust that has finally arrived in the United States, spurring a search for new varieties, predictive models, and monitoring techniques

On 6 November, plant pathologist Ray Schneider of Louisiana State University AgCenter gave a routine tour of the research fields near Baton Rouge to a visiting soybean farmer. "I offered to show him diseases he probably didn't have in Illinois," Schneider recalls saying. Both got a shock. In the course of the tour, Schneider came across signs of a disease never seen before in North American fields: the devastating fungal disease called soybean rust.

Schneider alerted the U.S. Department of Agriculture's Animal and Plant Health Inspection Service (APHIS) and FedEx'ed samples to a USDA lab in Beltsville, Maryland. When DNA tests came back positive on 9 November, APHIS sent in its soybean rust SWAT team the next day. Four groups of plant pathologists then fanned out across the state, surveying fields in 14 counties. Samples from four came back positive. Within days, APHIS had detected soybean rust in Arkansas, Mississippi, Alabama, and Florida.

The arrival of this fungus, although expected, could be very bad news for U.S. soybean growers, who raised more than $18 billion worth last year. Soybean rust spreads rapidly and hits plants hard, defoliating fields in less than 2 weeks. "It's an aggressive, hungry beast," says Martin Draper, a plant pathologist at South Dakota State University in Brookings. All commercially planted soybeans are susceptible to the fungus. If applied quickly, fungicides help, but USDA has estimated that losses could still range from $240 million to $2 billion a year, depending on the severity of outbreaks.

Unfortunately, the invader is the most aggressive kind of soybean rust, *Phakopsora pachyrhizi*. The spores are thought to have blown in with September hurricanes from South America, where farmers have incurred huge costs from fighting the disease. "In my country, we have two eras," says Alvaro Almeida, a plant pathologist at the Brazilian Ministry of Agriculture, EMBRAPA Soja, in Londrina, "before the arrival of soybean rust and after." The good news for the United States is that almost all soybeans had already been harvested this year, and researchers have a few months to refine their plans. This week, top experts are gathering at a USDA conference in Baltimore, Maryland.

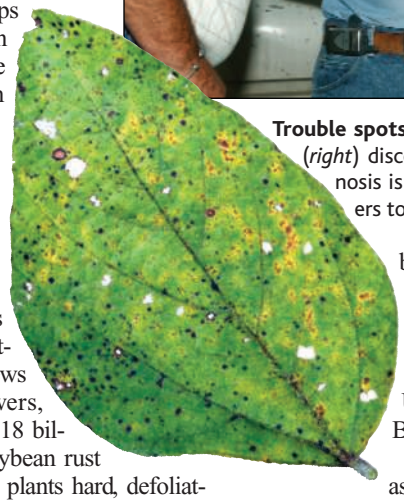

Trouble spots. Leaf lesions (*inset*) helped Ray Schneider (*right*) discover soybean rust in Louisiana. Early diagnosis is crucial, so pathologists are teaching farmers to identify signs of the pathogen.

Work is already under way, as infection has long been seen as inevitable: Every major soybean-producing area of the world except North America has the fungus. Over the past few years, plant epidemiologists have created computer models to predict its arrival and spread. Others have been working out ways to track the disease from airplanes and satellites. USDA researchers have been testing the efficacy of various fungicides in countries already infested and screening germ plasm for signs of resistance that could be bred or genetically engineered into commercial varieties. "We're throwing everything we can at this," says molecular biologist Reid Frederick of USDA's Agricultural Research Service (ARS) in Fort Detrick, Maryland.

Searching for resistance

Soybean rust is a formidable foe. Unlike most rusts, *P. pachyrhizi* has a broad range of hosts—more than 95 species including other crops and common weeds such as kudzu—so it's impossible to eradicate. It releases massive numbers of wind-blown spores that have been reported to hang like haze over infected fields. "There's just no way to contain it," Schneider says. First reported in Japan in 1902, soybean rust was later found in China and other Asian countries, where it sometimes slashes yields by as much as 80%. The fungus jumped to Africa in 1996, with alarming effects. Worries among USDA scientists heightened when the fungus arrived in South America in 2001, spreading north from Paraguay. In Brazil last year it cost farmers $2 billion. The United States is likely to be spared such huge losses; the rust cannot survive freezes, so it will live year-round only in the southern states. From there it could spread north each spring.

About 2 years ago, USDA researchers set up field experiments in Zimbabwe and Paraguay to test the efficacy of 15 kinds of fungicides. All seem to work well, including the two that are currently approved for use in the United States. Concerned that supplies might be inadequate, 25 states have applied to the Environmental Protection Agency for emergency exemptions that would allow farmers to spray other fungicides. Researchers also want a variety of fungicides at farmers' disposal to lessen the chances of the fungus evolving resistance. "It's a recipe for disaster if you use the same thing over and over," says Kent Smith of USDA's Office of Pest Management Policy in Washington, D.C.

The best defense, however, would be a soybean variety that resists rust. That has been a challenge to researchers. For starters, the pathogen can't be cultured. A sequencing effort launched in 2002 hit snags when the genome turned out to contain at least 700 million base pairs—14 times larger and much more difficult to assemble than expected. And because APHIS considers soybean rust a bioterrorism "select agent," it must be studied at biosafety level-3 greenhouses, located only at Fort Detrick, Maryland.

Frederick and others there have been evaluating the most commonly planted varieties and their ancestral stock. All of the roughly 1000 lines tested so far have proved highly susceptible to soybean rust. But there is reason to hope. In the 1970s, researchers

CREDITS: RAYMOND W. SCHNEIDER/LOUISIANA STATE UNIVERSITY AGCENTER

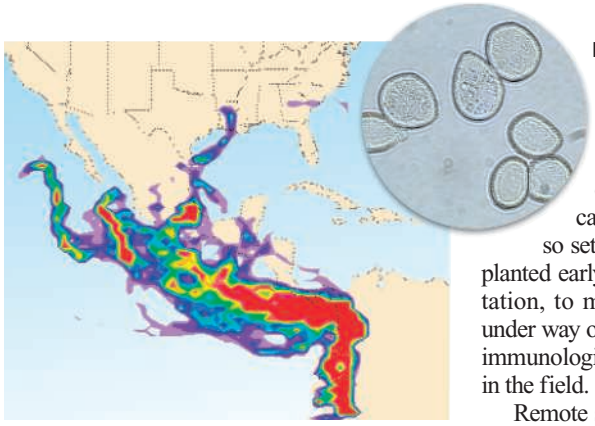

Rust belt. A model predicted the path of soybean rust spores (*inset*) and will forecast their spread.

found four varieties that each exhibited resistance to a single strain of *P. pachyrhizi*. These varieties didn't succeed in the field, however, succumbing to other strains of the pathogen. Plant breeders are now trying to broaden crop resistance by combining the genes from these varieties.

Researchers are also racing to find other sources of resistance. In the last 18 months, Frederick and Glen Hartman of the ARS in Urbana, Illinois, have tested all 17,000 types of soybean in the USDA germ plasm collection. Nothing has shown exceptional resistance, but the team is now examining 500 candidates that suffered lesser symptoms, such as fewer lesions or delayed onset of spores. To get a better feel for how these traits might fare in the field, USDA researchers have sent 180 varieties to collaborators in South Africa, Zimbabwe, China, Thailand, Brazil, and Paraguay. Progress has been bumpy so far, with comparisons hindered by differences in experimental conditions.

Resistance traits could also come from other plants. This year Frederick and Marcial Pastor-Corrales of ARS tested 16 varieties of common beans (*Phaseolus vulgaris*), such as pinto and black beans, and found that five were much more resistant to the pathogens than were soybeans. If those resistance genes can be cloned, they could potentially be genetically engineered into soybean.

In another approach, plant physiologist Bret Cooper of the ARS in Beltsville is using mass spectrometry to search through thousands of plant proteins for those that play a role in disease resistance. They've also begun working on dry bean rust, which can be studied outside the biosecure greenhouse, and plan to expand the search to *P. pachyrhizi*. In collaboration with James English of the University of Missouri, Columbia, Cooper will be looking for peptides that would interfere with infection or block spore germination. Such peptides might eventually be turned into sprays or engineered into soybean.

Early warning?

In the meantime, plant pathologists and extension agents are gearing up to educate farmers. Rust is easily confused with other diseases, and early identification is crucial. Researchers are also setting up a system of sentinel plots, planted early with prime conditions for infestation, to monitor for the disease. Work is under way on a hand-held sensor, based on an immunological assay, to detect the pathogen in the field.

Remote sensing could provide early detection, too. Forrest Nutter, a plant disease epidemiologist at Iowa State University (ISU) in Ames, has been working in Brazil and elsewhere on satellite detection of soybean rust. The spectral signature of leaf loss, although not unique to rust, can pinpoint outbreaks on the scale of meters. The same approach may work from airplanes, a cheaper and faster way of getting images, he says. Nutter plans to try tracking the disease this way next spring. "There's no doubt that rust is going to be established in the United States. The question is how it's going to spread," he says.

Farmers may also eventually get even earlier warning from a model developed by plant pathologist X. B. Yang of ISU and atmospheric modeler Zaitao Pan of St. Louis University in Missouri. They use a short-term climate model to project likely trajectories of spores over the next 120 days. In August, they predicted that spores would be more likely to enter because of the hurricane season and highlighted Louisiana as a probable beachhead.

Now the model can be adapted to predict the spread of spores from southern states north each spring. If it works, Pan says, a 3-month prediction could help farmers decide whether to stock up on fungicides, reserve spraying equipment—or even whether to plant soybeans at all. **–ERIK STOKSTAD**

CREDITS (TOP TO BOTTOM): Z. PAN AND X. B. YANG; (INSET) REID D. FREDERICK/USDA; MARY ALTAFFER/ASSOCIATED PRESS

Clinical Trials

Nail-Biting Time for Trials of COX-2 Drugs

Preliminary studies suggest that the COX-2 inhibitor Celebrex may stem cancer and Alzheimer's disease, but testing these possibilities has just gotten tougher

Psychiatrist John Breitner was in a hotel room in Sun City, Arizona, when he heard the news on television. It was 30 September, and CNBC was reporting that the COX-2 inhibitor Vioxx would be yanked off the market by its maker, Merck, after experts saw a frightening increase in cardiovascular side effects. Breitner's own heart skipped a beat. In an instant, he realized that his effort to stop Alzheimer's disease using Celebrex, a Vioxx competitor, had just gotten trickier.

Breitner, an expert on aging based at the University of Washington, Seattle, is one of dozens of researchers exploring whether COX-2 inhibitors can do more than they were designed to do—ease the painful inflammation of arthritis. Over the years, animal studies have suggested that these medications, along with more traditional nonsteroidal anti-inflammatory drugs (NSAIDs), may be able to lower the risk of cancer and reduce inflammation suspected in Alzheimer's.

In the past few years, scientists have launched one study after another to put these hopeful ideas to the test. The pace picked up after the U.S. Food and Drug Administration (FDA) confirmed data in 1999 showing that Celebrex reduces intestinal polyps in patients with familial adenomatous polyposis, a hereditary condition that leads to colon cancer. Excitement has focused on COX-2 inhibitors because they are believed to be less likely than NSAIDs to cause stomach problems, a big drawback in long-term prevention trials.

Similar but different. The withdrawal of Vioxx has put Celebrex in the spotlight.

Few Vioxx prevention studies have been conducted or were planned, researchers say, partly because Merck was less willing than

Pfizer, the maker of Celebrex, to donate a COX-2 inhibitor to such trials. The result is that about 10,000 volunteers are participating in or being recruited for Celebrex studies, but scientists can't say for certain whether the drug shares Vioxx's hazards. Now trial managers are debating the risks, reassuring study participants, and keeping a hand on the emergency brake just in case.

The last 2 months have been nail-biters for these researchers and their funders. The concern is heightened because in most of these trials, volunteers are healthy, and although many are at risk, not all will develop disease. "This is not fun for anybody," says Curtis Meinert, chair of the steering committee for the Alzheimer's Celebrex trial and a clinical trials expert at Johns Hopkins University in Baltimore.

"Obviously, I was concerned" about the Vioxx announcement, says Jenny Mao, a pulmonologist at the University of California, Los Angeles, who's enrolling 180 former smokers in a lung cancer prevention trial that's testing Celebrex. Her biggest fear, she says, is that Celebrex, too, will be pulled, and that "all this work over all these years would go down the drain."

Like most researchers, Mao believes that Celebrex doesn't induce the heart attacks and strokes seen with Vioxx. Although both drugs are COX-2 inhibitors, Vioxx is a more potent blocker of the COX-2 enzyme—a potential source of its problems—and also has a longer half-life. In addition, some cardiologists had warned for years of Vioxx's cardiovascular risks.

But a heightened level of scrutiny brought down Vioxx: The trial that persuaded Merck to withdraw its drug lasted 18 months and included 2600 people—longer than any single large, published Celebrex study. The purpose was to test whether Vioxx could prevent colon polyps—a precursor of cancer—in those at risk for developing them. Among volunteers on Vioxx, 3.5% suffered heart attacks or strokes, compared to 1.9% on placebo.

So far, "the data that are available … don't show the same" risks for Celebrex, says Meinert. "That," he hastens to add, "isn't proof they don't exist."

If there are cardiac problems, they might be hard to detect; researchers are straining to catch warning signs. The largest and longest running Celebrex prevention trial, a 2000-person study looking at the reappearance of colon polyps in patients with a history of them, has added a cardiovascular expert to its data safety and monitoring board (DSMB). In a meeting after Vioxx was withdrawn, DSMB members pored over trial data and agreed that the trial should continue, says Ernest Hawk, a chemoprevention expert at the U.S. National Cancer Institute who is program manager for the NCI-funded trial. NCI has also created a "cardiovascular adjudication process," essentially asking a group of cardiologists to review and classify every potential cardiovascular event. Although DSMBs overseeing Celebrex prevention trials have been on heightened alert, and many have added a cardiac expert to their ranks, they "have not halted the trials or demanded changes to them based on cardiovascular risk," says Hawk. (A Pfizer spokesperson confirmed that the company is not running any prevention trials with Bextra, its other COX-2 inhibitor.)

Alzheimer's prevention trials face challenges, too. Breitner's 2500-person study, the Alzheimer's Disease Anti-Inflammatory Prevention Trial (ADAPT), funded by the U.S. National Institute on Aging (NIA), uses Celebrex. All subjects must be at least 70 years old, putting them at a high risk of heart disease to begin with. Susan Molchan, NIA's program director for Alzheimer's disease clinical trials, contacted FDA after Vioxx was pulled off the market "to see if they had information" about Celebrex "that they could share," she says. "They confirmed we weren't missing any information."

NCI is trying to improve monitoring of Celebrex studies, according to Hawk. Meinert has urged agency officials to meld safety data from all the trials, making small signals easier to detect. "Trials are fairly weak instruments at finding adverse events," he says, especially if they occur infrequently. "We need to have a better model, in my opinion, with regard to the harvest of safety data" among different trials studying the same drug. NCI's Hawk confirmed that the institute is speaking to Celebrex investigators about better ways to evaluate cardiac safety.

As scientists probe the Vioxx-Celebrex relation, they find that study participants are often primed with questions. "I've conducted town hall meetings for patients," says Peter Lance, a gastroenterologist at the University of Arizona in Tucson, who's heading a 1600-person colorectal adenoma prevention trial involving Celebrex and the mineral selenium. Several dozen attended recent meetings in Tucson and Phoenix, where Lance explained that, thus far, there has not been an "imbalance" in cardiac problems among those taking Celebrex. "We're taking otherwise healthy people and asking them to take a medication or an intervention for which we don't have scientific evidence" of a clinical benefit, he says. "Our thoughts about safety are very intense."

In the ADAPT trial, says Breitner, "we have people who are being advised to drop out by their physicians" and patients "who say they were going to enroll but aren't. We're definitely taking a hit from this." Between 20 and 50 participants have refused to continue taking study medications (Celebrex, naproxen, or placebo), Breitner adds. To keep enrollment steady, ADAPT's coordinators have sent information about Celebrex, in lay language, to field sites. Although Breitner agrees that more information about Celebrex's long-term cardiac effects are needed, he doesn't think it poses anything like the risk of Vioxx: "I don't think that I'm running a trial where we're poisoning people."

Many other trials haven't suffered much. UCLA's Mao says her staff was far more concerned with how the Vioxx withdrawal might influence their study than were participants. Other trials, moreover, include patients with such a high chance of cancer that cardiac risks pale in significance. For example, the 360 patients to be enrolled in the oral cancer prevention study headed by Scott Lippman of M. D. Anderson Cancer Center in Houston, Texas, will have a 60% chance of developing cancer in the next 3 years.

Celebrex researchers are hopeful that regardless of whether these trials show any effect on cancer or Alzheimer's risks, they will answer once and for all the question that's lingered since boxes of Vioxx were shipped back to Merck: whether Celebrex shares Vioxx's downside, and to what degree. Says Mao: "We'll keep our fingers crossed."

—JENNIFER COUZIN

Selected Prevention Studies Using Celebrex

Condition	Start Date	# of participants	Lead Center
Colon cancer	2000	2000	Brigham and Women's Hospital, Boston
Alzheimer's disease	2001	2500	University of Washington, Seattle
Colorectal polyps	2001	1600	University of Arizona, Tucson
Breast cancer	2003	110	University of Kansas, Lawrence
Lung cancer	2003	180	University of California, Los Angeles
Colon polyps	2004	1200	University of North Carolina, Chapel Hill
Oral cancer	2005	360	M. D. Anderson Cancer Center, Houston

Did Jupiter and Saturn Team Up to Pummel the Inner Solar System?

LOUISVILLE, KENTUCKY—With time off to catch a couple of races at nearby Churchill Downs, about 700 solar system researchers met here 8 to 12 November at the annual meeting of the Division for Planetary Sciences.

The solar system may have passed through a violent youth before it came of age. More than a half-billion years after the inner solar system's molten beginnings, a barrage of impacters slammed into Earth and the moon, according to some dating studies of the impact craters left behind on the moon (*Science*, 1 December 2000, p. 1677). That bombardment would have formed the huge, lava-filled basins that shape "the man in the moon." It would also have snuffed out any but the most deeply buried life struggling to get a start on Earth.

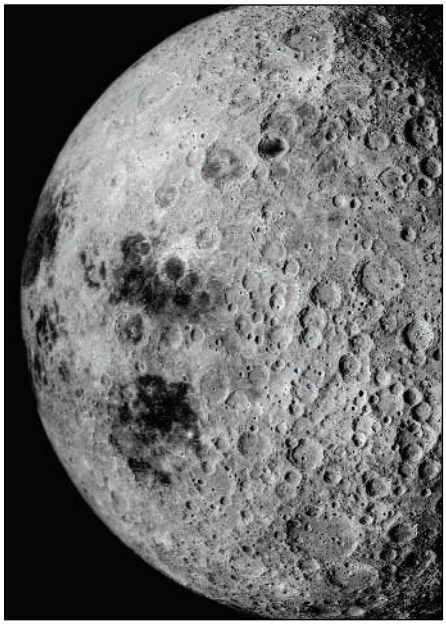

Battered. An outer planet pairing may have led to the late cratering of the moon.

But where could those impacting bodies have been lurking all that time, and what could have prompted the delayed onslaught? At the meeting, planetary dynamicists showed how Jupiter and Saturn could have joined forces to fling debris toward Earth from a reservoir in the outer reaches of the solar system.

The key to creating a late heavy bombardment is the orbital migration of Jupiter and Saturn, according to an international team of planetary dynamicists including Rodney Gomes of the National Observatory in Rio de Janeiro and Kleomenis Tsiganis of the Observatory of the Côte d'Azur in Nice, France. When chunks of planet-building debris wander too close to one of the growing giant planets, the big guys can catch them in a net of gravity and fling them away.

But hurling planetesimals one way inevitably sends the hurler the other. Although Jupiter was too massive to move much by tossing planetesimals, the far less hefty Saturn would have spiraled outward as it cleared its neighborhood of planetesimals. Gomes and his colleagues used a computer model to study this migration process. Their innovation was to start all four of the outer planets in the simulations bunched together and well inward of their present orbital distances.

That planetary placement means that as Saturn migrated outward, it would eventually be orbiting the sun once each time Jupiter orbited twice. At that point, the two planets would be in their so-called 1:2 resonance—in which every second jovian orbit, they would be closest together at the same point in their orbits. Whenever that occurred, the larger planet could give Saturn repeated gravitational nudges whose effects could accumulate, the way repeatedly pushing a swing at the same point in its arc sends it higher.

The resonant interactions of the two largest planets would have stirred the outer solar system into a chaotic frenzy. In the group's simulations, Jupiter pumps up the orbital energy of Saturn, which in turn destabilizes the orbits of the far smaller and more distant Uranus and Neptune. That scatters the two smaller planets outward, where they encounter an undisturbed disk of planetesimals. Then, as many as a billion years after planet formation, enough of the planetesimals rain toward the inner solar system to produce more than 10^{15} hits on the moon in a bombardment lasting less than 100 million years. Thus, the modeled late heavy bombardment triggered by a resonance passage matches the one often inferred from dating of craters, Tsiganis noted. It's as late, as intense, and as brief.

Once the model's planetesimals are cleared out, migration ceases, and the restless outer planets lock into slightly elongated, tilted orbits, much like the planets' actual orbits. This is the first time, said Tsiganis, that an orbital simulation has gotten anything but circular, flat orbits for the four outer planets. Likewise, the Trojans, minor planets that share Jupiter's orbital space, have hard-to-explain large orbital inclinations in the present-day solar system that also show up in simulations as Jupiter and Saturn pass out of their 1:2 resonance.

Planetary dynamicists find passage through a resonance promising as a trigger for a late heavy bombardment. "It does tie together several things," says Martin Duncan of Queen's University in Kingston, Ontario. "It definitely deserves attention." It should also prompt the crater daters to prove once and for all that there was indeed a late heavy bombardment.

Hydrocarbon Seas of Titan Gone Missing

Like the dog that didn't bark in the night, the sunlight that didn't glint off the surface of Saturn's big moon Titan spoke volumes. When the Cassini spacecraft flew by for a close look late last month, scientists expected to see sunlight reflected from liquid surfaces, but none of Cassini's cameras picked up the anticipated telltale glint (*Science*, 5 November, p. 952). That was a surprise because Titan's thick haze was thought to hide a network of "rain"-fed hydrocarbon seas—perhaps the dark areas spied telescopically in recent years at haze-piercing infrared wavelengths. At the meeting, Cassini scientists reported that these dark areas appear to be as dry as the "seas" that Galileo spotted on Earth's moon. Liquids on Titan seem to be confined to scattered lakes or even underground, if they exist at all.

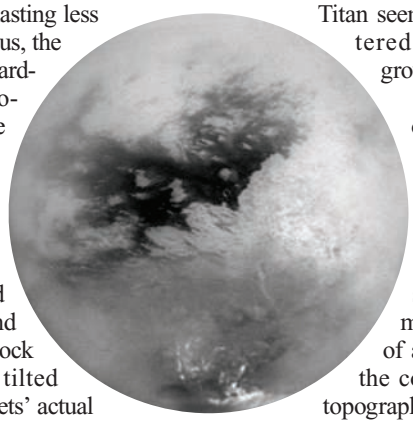

Mystery shadings. From Earth, Titan's dark regions looked like seas, and even more so from Cassini (above), but the details of how light reflects from them are wrong for liquid.

The way light reflects off a surface can provide a wealth of information. If sunlight glints off, the surface must be very smooth, almost mirror smooth. The only natural surface that approaches mirror smoothness is that of a liquid. But variations in the composition, texture, and topography of a nonliquid surface

CREDITS (TOP TO BOTTOM): NASA; NASA/JPL/SPACE SCIENCE INSTITUTE

Published by AAAS

can produce subtle but revealing variations in the intensity of reflected sunlight. Cassini scientist Robert M. Nelson of NASA's Jet Propulsion Laboratory (JPL) in Pasadena, California, and other members of the Visible and Infrared Mapping Spectrometer team reported their analyses of light reflected at various angles from two dark, circular features that looked like possible impact craters 1000 kilometers across and from a similarly sized but irregularly shaped dark feature.

The three dark regions seemed likely places for hypothesized methane rains to collect, but Nelson's analysis found nothing that indicated pools of liquid. Brightness variations across the three features were too large to be coming from liquid surfaces or even varying topography. They only made sense as variations in surface reflectivity. Apparently, the two circular features are not depressions but perhaps ancient impact scars that are now filled in. There's "no evidence whatsoever to suggest there are accumulations of liquid of any form," says Nelson.

The search for liquids on Titan is not over, however. Their nondetection has "certainly been a surprise," said Cassini project scientist Dennis Matson of JPL, but "we've only seen a part of Titan to this stage." Nelson allows that small lakes might yet be found. The liquid methane might even be hiding beneath the surface like groundwater. If so, the Huygens probe scheduled to parachute to the Titan surface on 15 January would arrive with a thudding jolt rather than a splash.

Snapshots From the Meeting

Ring hits. Planetary scientists knew that any solar system body continually sweeps up bits and pieces of debris, but they never expected to hear the impacts. So space physicist Donald Gurnett of the University of Iowa, Iowa City, drew applause for "the music of the rings," a plasma-wave signal from Saturn's rings, stepped down to audible frequencies. Gurnett's plasma-wave instrument onboard the Cassini spacecraft recorded the signal as it flew over the rings last July. The music resembled the sound of crickets: short, 1- to 2-second tones every second or so, each with a narrow frequency range. Gurnett decided that marble-size, 200,000-kilometer-per-hour ring impacters were producing the tones. Ring specialists will want to use his recorded impact tempo in their studies of how impacts age and erode the rings.

A dark mystery. Saturn's two-faced moon Iapetus is not giving up its secrets easily. Spectroscopist Bonnie Buratti of the Jet Propulsion Laboratory in Pasadena, California, reported that the Visible and Infrared Mapping Spectrometer on the Cassini spacecraft managed to get the first clean spectrum of the side of this moon that always points forward as it orbits Saturn. It is dark, while the trailing side is icy bright. In the infrared, the spectral signature of the dark side resembles that of Saturn's distant moon Phoebe and smaller moons beyond it. The similarity supports the "It Came From Outer Space" theory of Iapetus's dark side, said Buratti. According to that scenario, small meteorite impacts knock dark material off the outer satellites, and Iapetus sweeps it up on its leading side. But the new spectrum also shows that at visible wavelengths Phoebe and the Iapetus dark stuff look quite different. That prompted hallway chatter about the alternative: dark goo oozing from the interior. A much closer look by Cassini scheduled for New Year's Day may help.

Amazing Shrinking Kuiper Belt Objects

They aren't actually shrinking, of course, but the icy leftovers from the solar system's formation that orbit out beyond Neptune are getting smaller in the eyes of astronomers. Thanks to two independent means of determining the true reflectivity of subplanetary-size bodies, the so-called Kuiper belt objects (KBOs) now look to be 40% smaller than had been assumed. That's good news for Pluto supporters. They've been holding their breath as new discoveries drove up the apparent size of the largest known KBO, threatening to knock Pluto from its status as a bona fide planet. Now a usurper seems much less likely.

KBOs are "shrinking" because until recently astronomers could only guess what fraction of sunlight they reflect. When a solar system object is so small and far away that even the largest telescope shows only a point of light, the only way astronomers can calculate the object's size is from its brightness. To do that, they must assume a reflectivity. KBOs were discovered in 1992 after planetary dynamicists suggested they had to be there to supply icy comet nuclei to the inner solar system. Because comets are pitch black—they reflect just 4% of the sunlight hitting them—planetary scientists reasoned that KBOs were in all likelihood inky black, too, and therefore large.

Now that picture is changing. At the meeting, astronomers reported how improving technology is allowing them to determine KBOs' reflectivities. The more reflective the objects actually are, the smaller they must be for a given brightness. Astronomer John Stansberry of the University of Arizona, Tucson, and his colleagues reported results from infrared observations of eight KBOs using the Spitzer Space Telescope, which has been in Earth orbit since August 2003. By measuring the brightness of a KBO at both a short wavelength, at which the light is entirely reflected, and a long wavelength, where it is emitted, they could calculate a reflectivity because both reflected and emitted brightness depend on the size of the object. The reflectivity of the eight KBOs ranged from 7.5% to 18% and averaged 12%, three times the assumed KBO reflectivity.

In an entirely different approach, two groups, respectively led by Jean-Luc Margot of Cornell University and by Keith Noll of the Space Telescope Science Institute in Baltimore, Maryland, watched KBOs orbit about each other in binary pairs, in essence a system of a miniplanet and its minimoon. From a binary's orbital dynamics, they could calculate a total mass for the pair. Assuming a density of 1 (a reasonable assumption), they could calculate a reflectivity. Of the dozen binary KBOs known, Margot found estimated reflectivities for four of them ranging from 8% to 41%, averaging 22%. Noll has observed eight binaries that average 12% reflectivity.

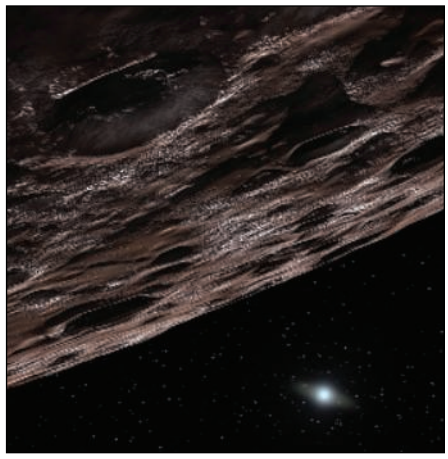

CREDIT: NASA/JPL

No longer coal black. Kuiper belt objects are brighter and therefore larger than thought.

KBOs averaging 12% reflectivity would be 60% of the size estimated on the basis of low cometary reflectivities and just 20% of the mass. Presumably, astronomers were misled by comet nuclei that start out as relatively reflective KBOs—"dirty snowballs"—but darken as the sun's heat drives off their bright ices. KBO hunters are far less likely to turn up a rival the size of Pluto anytime soon, notes Noll. Long live planet Pluto.

–RICHARD A. KERR

Published by AAAS

Random Samples

Edited by Constance Holden

Flipping Over a New Tail

Fuji, a 34-year-old bottlenose dolphin at Japan's Okinawa Churaumi Aquarium, was crippled by necrosis, which destroyed most of her tail. But now she's doing swimmingly thanks to a custom-designed prosthesis developed by aquarium vets and Bridgestone, Japan's largest tiremaker. Masaya Koami, Fuji's trainer, says the dolphin was initially leery of the flexible carbon-fiber–reinforced plastic prosthesis, which clamps around the tail stump. But after months of rehab, "she was jumping out of the water." Bridgestone says it has spent close to $100,000 on the new tail and is hoping to improve the prosthesis by experimenting with more exotic materials.

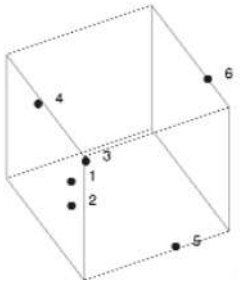

Data points of three faces (1–3) cluster, but the other three appear to have been painted by three other artists.

Verifying Art With Math

Scientists claim they can teach a computer to recognize the works of particular artists using a technique that requires only a digitized image of a drawing or painting.

Three mathematicians at Dartmouth College in Hanover, New Hampshire, speculated that they could identify individual styles by analyzing the frequency of certain types of lines—just as writers have been identified through context-free word counts. Team member Hany Farid says that to test the idea, they used "wavelet decomposition," a method that digitally encodes an image as a rough version followed by successive refinements. The researchers report in the 24 November online edition of the *Proceedings of the National Academy of Sciences* that they tried it out on eight drawings by 16th century artist Pieter Breugel and five known-to-be-fake Breugels. The computer was able to tell which ones were authentic. They also analyzed "Madonna With Child" by the 16th century Italian painter Perugino and found that the six faces in the painting were the work of four sets of hands, presumably the artist and three apprentices—a result that supports the more intuitive judgment of art experts. Ellen Handy, chair of the art department at The City College of New York, says if the technique works, and if historians and curators can figure out how to use it, "it can start to make art history ... a science."

Sardines to the Rescue?

For more than a century, people living along Namibia's Atlantic coast have reported frequent sulfurous submarine emanations, often accompanied by mass die-offs of fish and lobsters. Many scientists believe that these eruptions of methane and hydrogen sulfide, which are potent contributors to the greenhouse effect, are released by decaying blooms of phytoplankton that blanket the sea floor in meters-deep ooze.

Two years ago, researchers Andrew Bakun of the University of Miami, Florida, and Scarla Weeks of the University of Cape Town, South Africa, noticed that a respite from the eruptions coincided with a resurgence in local sardine stocks. Now, in the November *Ecology Letters*, they speculate that sardines were eating phytoplankton that might otherwise have drifted to the sea floor. If the link is proven, Bakun says Namibia's experience could serve as a warning to other areas with similar offshore conditions, such as Morocco and California.

Toxic plume off Namibia.

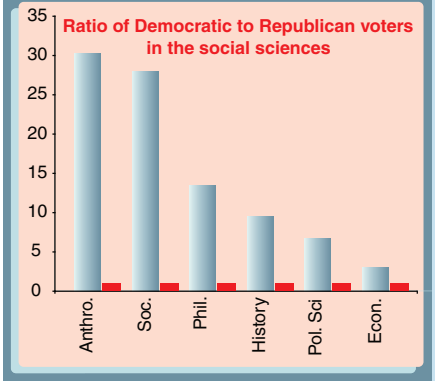

Academia as "One-Party" System

Universities in the United States are very keen on fostering "diversity" as long as it's not ideological diversity, according to the National Association of Scholars (NAS), a conservative group of academics. Last year NAS surveyed members of scholarly societies in six fields in the social sciences, asking which political party they identified with. About 30% of the 5486 people polled responded; of these, 80% were Democrats. Economist Daniel B. Klein of Santa Clara University in California and Charlotta Stern of the Institute for Social Research in Stockholm, Sweden, conclude that because the prevalence of Democrats was even higher among younger academics, it appears that "lopsidedness has become more extreme over the past decades, and ... unless we believe that current professors occasionally mature into Republicans, it will become even more extreme in the future."

"The 'one-party campus' is a problem irrespective of what one's own views happen to be," the authors warn. (Klein says Stern is a liberal and he himself is a libertarian.) They suggest that measures could be taken—such as "proportional voting on curriculum and hiring decisions"—to enable political minority voices to be heard.

CREDITS (TOP TO BOTTOM): COURTESY OF OKINAWA CHURAUMI AQUARIUM; *PNAS*; NASA

Published by AAAS

PEOPLE

Edited by Yudhijit Bhattacharjee

JOBS

New Fermi chief. Peruvian-born particle physicist Pier Oddone is hoping to sell Congress and the public on the value of delayed gratification. As the next director

of Fermi National Accelerator Laboratory, the Department of Energy's high-energy physics facility in Batavia, Illinois, Oddone will be an advocate for the first new U.S. accelerator in decades. But he admits that it's tough "generating support for science that doesn't provide immediate applications, like a gadget or eternal life."

The 60-year-old Oddone, now deputy director at Lawrence Berkeley National Laboratory in California, succeeds Michael Witherell, who is stepping down in June to become vice chancellor of research at the University of California, Santa Barbara.

MONEY MATTERS

Shot in the arm. Information technology pioneer Bill Brehm and his wife Dee have waged a personal battle against diabetes since Dee was diagnosed in 1949. Last week they gave $44 million to their alma mater, the University of Michigan (UM), Ann Arbor, to help researchers conquer the disease.

The gift—the second largest in UM's history—will be used to build a new $30 million center for type I diabetes research, establish a cross-disciplinary network to share diabetes information, and endow eight new faculty positions. "This could have an enormous impact on diabetes research," says medical school dean Allen Lichter.

Brehm, 75, hopes the center's computer network will foster collaboration by making it easier for researchers to share their results. "The goal is to create a new kind of scientific framework for discovery," says Lichter.

DATAPOINT

Watchful eye. More institutions are reporting instances of falsification, plagiarism, fabrication, and other scientific fraud than ever before, according to the latest numbers from the Office of Research Integrity (ORI) in the Department of Health and Human Services. Universities and other organizations opened 105 new research misconduct cases in 2003—20% more than the previous year's figure of 83 and 52% more than the 10-year average of 69.

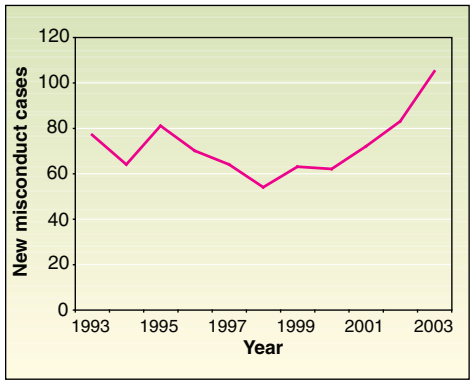

The increase may be a reflection that "institutions are getting better at recognizing scientific misconduct," says ORI Director Christopher Pascal. "Until a decade ago, many institutions were unsure about how to handle allegations of misconduct," he says. "Now they're a lot less shy about investigating them."

Nerves of steel. A metallurgical engineer is in line to be the first woman president of the University of Alberta in Edmonton, Canada. The 52-year-old Indira Samarasekera, who is currently vice president of research at the University of British Columbia in Vancouver, will begin her 5-year term on 1 July, succeeding Rod Fraser.

Samarasekera says she plans to promote a "creative climate where risk-taking and creative research are not only supported but fostered." Samarasekera was born in Colombo, Sri Lanka, and moved to Canada in 1977 for graduate studies.

PIONEERS

An idea revisited. Nobelist Harold Varmus wanted to start a graduate school when he directed the U.S. National Institutes of Health (NIH) but was talked out of it by advisers who argued that it wasn't needed. Now he's gotten his wish. The Memorial Sloan-Kettering Cancer Center (MSKCC) in New York City, which Varmus has headed since he left NIH 5 years ago, is launching a new graduate school that will give students earning a Ph.D. in cancer biology a taste of clinical research.

The idea follows a trend—translational research—promoted by his successor at NIH, Elias Zerhouni. But whereas that phrase can mean developing new drugs, Varmus wants to produce bench scientists who "know what cancer is like as a disease" but who don't want to spend extra years earning a medical degree, too.

Named for the former IBM CEO who helped bring in $30 million in philanthropic support, the Louis V. Gerstner Jr. Graduate School of Biomedical Sciences will enroll a dozen students in July 2006 and build up to 60. (MSKCC has about 100 graduate students already, but their degrees are awarded by Cornell or Rockefeller universities.) Molecular biologist Kenneth J. Marians will serve as the school's dean.

Got any tips for this page? E-mail people@aaas.org

CREDITS (TOP TO BOTTOM): UNIVERSITY OF MICHIGAN; FERMILAB; UNIVERSITY OF ALBERTA; OFFICE OF RESEARCH INTEGRITY

Published by AAAS

LETTERS

Prescribed Fire and Natural Disturbance

THE RECENT COVERAGE OF OUR WORK ON THE relationship between fire history and an emerging forest epidemic called sudden oak death highlights landscape-level aspects of disease spread, which are often overlooked ("Fighting sudden oak death with fire?", J. Withgott, News Focus, 20 Aug., p. 1101). Although we are interested in the possible role of prescribed fire in managing this disease, subsequent reports in the popular press have claimed that we advocate such an approach as treatment. A cautionary note is therefore required at this point. We have not found a direct connection between fire suppression and this disease, and there is reason to suspect that the effects of past wildfires could be very different than those of the typical controlled burn. The decision to use prescribed fire in an ecosystem should be guided by location- and case-specific considerations (*1*).

Skeletons of federally listed (threatened) Morro Manzanita shrubs (*Arctostaphylos morroensis*) immediately after a prescribed burn, which led to its local extirpation (*2*).

As Lindenmayer *et al.* note in their Policy Forum "Salvage harvesting policies after natural disturbance" (27 Feb., p. 1303), natural disturbances such as fire are integral to the healthy functioning of most ecosystems and are often poorly understood in policy and management arenas. The emphasis here is on "natural" disturbances and the important role they play. Most prescribed burns, however, are attempted during conditions when fire is not likely to escape control (e.g., outside the normal fire season). Burning under these conditions will not necessarily produce the natural range of fire severities and subsequent fire effects that could result from past wildfires.

Restoring fire regimes is of great importance, but prescribed fires must ultimately mimic natural events to fulfill their role in disturbance-mediated ecosystems. Prescribed fires that do not attain this goal can have harmful ecological effects, even if successful for goals of fuel reduction and fire reintroduction. Populations of fire-dependent native species can be decimated (*2*) if timing or heating requirements for regeneration are not met. Invasive species may also be promoted, which can lead to near-permanent alteration of fire regimes and ecosystem functioning (*3*). Whether for ecosystem health in general, or management of forest pathogens in particular, prescribed fire will need to be tailored to the societal goals and ecological requirements of the situation at hand.

MAX A. MORITZ[1] AND DENNIS C. ODION[2]
[1]Ecosystem Sciences Division, Department of Environmental Science, Policy, and Management, University of California at Berkeley, Berkeley, CA 94720, USA. [2]Institute for Computational Earth Systems Science, University of California at Santa Barbara, Santa Barbara, CA 93106, USA.

References
1. S. Pyne, *Science* **294**, 1005 (2001).
2. D. Odion, C. Tyler, *Conserv. Ecol.* **6**, 4 (2002).
3. M. Brooks *et al.*, *BioScience* **54**, 677 (2004).

The Origins of Afroasiatic

IN THEIR REVIEW "FARMERS AND THEIR languages: the first expansions" (25 Apr. 2003, p. 597), J. Diamond and P. Bellwood suggest that food production and the Afroasiatic language family were brought simultaneously from the Near East to Africa by demic diffusion, in other words, by a migration of food-producing peoples. In resurrecting this generally abandoned view, the authors misrepresent the views of the late I. M. Diakonoff (*1*), rely on linguistic reconstructions inapplicable to their claims (*2*), and fail to engage the five decades of Afroasiatic scholarship that rebutted this idea in the first place. This extensive, well-grounded linguistic research places the Afroasiatic homeland in the southeastern Sahara or adjacent Horn of Africa (*3*–*8*) and, when all of Afroasiatic's branches are included, strongly indicates a pre–food-producing proto-Afroasiatic economy (*1, 7, 8*).

Letters to the Editor

Letters (~300 words) discuss material published in *Science* in the previous 6 months or issues of general interest. They can be submitted through the Web (www.submit2science.org) or by regular mail (1200 New York Ave., NW, Washington, DC 20005, USA). Letters are not acknowledged upon receipt, nor are authors generally consulted before publication. Whether published in full or in part, letters are subject to editing for clarity and space.

A careful reading of Diakonoff (*1*) shows his continuing adherence to his long-held position of an exclusively African origin (*4, 5*) for the family. He explicitly describes proto-Afroasiatic vocabulary as consistent with non–food-producing vocabulary and links it to pre-Neolithic cultures in the Levant and in Africa south of Egypt, noting the latter to be older. Diakonoff does revise his location for the Common Semitic homeland, moving it from entirely within northeast Africa to areas straddling the Nile Delta and Sinai, but continues to place the origins of the five other branches of the Afroasiatic language family wholly in Africa (*1*). One interpretation of the archaeological data supports a pre–food-producing population movement from Africa into the Levant (*9*), consistent with the linguistic arguments for a pre-Neolithic migration of pre–proto-Semitic speakers out of Africa via Sinai (*8*).

The proto-language of each Afroasiatic branch developed its own distinct vocabulary of food production, further supporting the view that herding and cultivation emerged separately in each branch after the proto-Afroasiatic period (*7*, *8*). Diamond and Bellwood adopt Militarev's (*2*) solitary counterclaim of proto-Afroasiatic cultivation. However, not one of Militarev's proposed 32 agricultural roots can be considered diagnostic of cultivation. Fifteen are reconstructed as names of plants or loose categories of plants. Such evidence may reveal plants known to early Afroasiatic speakers, but it does not indicate whether they were cultivated or wild. Militarev's remaining roots are each semantically mixed, i.e., they have food-production–related meanings in some languages, but in other languages have meanings applicable to foraging or equally applicable to foraging or cultivating.

Furthermore, the archaeology of northern Africa does not support demic diffusion of farming populations from the Near East. The evidence presented by Wetterstrom (*10*) indicates that early African farmers in the Fayum initially incorporated Near Eastern domesticates into an indigenous foraging strategy, and

only over time developed a dependence on horticulture. This is inconsistent with in-migrating farming settlers, who would have brought a more abrupt change in subsistence strategy. The same archaeological pattern occurs west of Egypt, where domestic animals and, later, grains were gradually adopted after 8000 yr B.P. into the established pre-agricultural Capsian culture, present across the northern Sahara since 10,000 yr B.P. (*11*). From this continuity, it has been argued that the pre–food-production Capsian peoples spoke languages ancestral to the Berber and/or Chadic branches of Afroasiatic, placing the proto-Afroasiatic period distinctly before 10,000 yr B.P. (*8*). Furthermore, there is evidence that cattle domestication occurred independently in the early Holocene eastern Sahara, earlier than in the Near East (*12*), casting doubt on the idea of a single origin of food production in the Levant.

A critical reading of genetic data analyses, specifically those of Y chromosome phylogeography and TaqI 49a,f haplotypes, supports the hypothesis of populations moving from the Horn or southeastern Sahara northward to the Nile Valley, northwest Africa, the Levant, and Aegean (*13*–*15*). The geography of the M35/215 (or 215/M35) lineage, which is of Horn/East African origin, is largely concordant with the range of Afroasiatic languages. Underhill *et al.* state that this lineage was carried from Africa during the "Mesolithic" (*13*). The distributions of the Afroasiatic branches and this lineage can best be explained by invoking movements that originated in Africa and occurred before the emergence of food production, as well as after.

CHRISTOPHER EHRET,[1] S. O. Y. KEITA,[2] PAUL NEWMAN[3]

[1]Department of History, University of California at Los Angeles, Los Angeles, CA 90095, USA. [2]National Human Genome Center at Howard University, Howard University Hospital, Washington, DC 20060, USA, and Department of Anthropology, Smithsonian Institution, National Museum of Natural History, Washington, DC 20560, USA. [3]Department of Linguistics, Indiana University, Bloomington, IN 47405, USA.

References
1. I. M. Diakonoff, *J. Semit. Stud.* **43**, 209 (1998).
2. A. Militarev, in *Examining the Farming/Language Dispersal Hypothesis*, P. Bellwood, C. Renfrew, Eds. (McDonald Institute for Archaeological Research, Cambridge, 2003), chap. 12.
3. J. H. Greenberg, *Studies in African Linguistic Classification* (Compass Publishing, New Haven, CT, 1955).
4. I. M. Diakonoff, *Altorientalische Forschung.* **8**, 23 (1981).
5. I. M. Diakonoff, *Afrasian Languages* (Nauka Publishing House, Moscow, 1988).
6. H. L. Fleming, in *The Non-Semitic Languages of Ethiopia*, M. L. Bender, Ed. (Michigan State University, African Studies Center, East Lansing, MI, 1976), pp. 298–323.
7. C. Ehret, *J. Afr. Hist.* **20**, 161 (1979).
8. C. Ehret, in *Symposium 13d: Rock Art and the Sahara*, in *Proceedings of the International Rock Art and Cognitive Archaeology Congress*, A. Muzzolini, J.-L. Le Quellec, Eds. (Centro Studie Museo d'Arte Prehistorica, Turin, Italy, 1999) (HTML-CD Rom edition, ehlist1.jpg).
9. O. Bar Yosef, *Afr. Archaeol. Rev.* **5**, 29 (1987).
10. W. Wetterstrom, in *Archaeology of Africa*, T. Shaw *et al.*, Eds. (Routledge, London, 1993), pp. 165–226.
11. N. Rahmani, *Le Capsien typique et le Capsien supérieur*, Cambridge Monographs in Archaeology 57 (Cambridge Univ. Press, Cambridge, 2003).
12. F. Wendorf *et al.*, Eds., *Holocene Settlement of the Egyptian Sahara*, vol. 1, *The Archaeology of Nabta Playa* (Kluwer Academic/Plenum Publishers, New York, 2001).
13. P. Underhill *et al.*, *Am. J. Hum. Genet.* **65**, 43 (2001).
14. G. Lucotte, G. Mercier, *Am. J. Phys. Anthropol.* **121**, 63 (2003).
15. O. Semino *et al.*, *Am. J. Hum. Genet.* **74**, 1023 (2004).

Response

EHRET *ET AL.* SUGGEST THAT EARLY Afroasiatic languages were spread by Mesolithic foragers from Africa into the Levant. In our Review, we did not positively favor either the African or the Levant origin hypothesis (p. 601). But in the map (Fig. 2), I chose the Levant hypothesis, because I believe, on balance, that it provides the best explanation for the evidence that has survived through 12,000 years of prehistory.

In linguistic terms, Ehret (*1*) has presented a phylogenetic history for Afroasiatic languages, based on shared phonological innovations, that contains a primary division between the Omotic languages of Ethiopia and an Erythraean subgroup that includes all other Afroasiatic languages (including Semitic and Ancient Egyptian). This ordering, if correct, suggests an African origin for the family. But is it correct? Diakonoff (*2*, *3*) has offered a completely different grammatical subgrouping structure for Afroasiatic, in the process, casting doubt on Omotic as a member of the family and suggesting [(*2*), p. 218] that the predomestication [but probably early cultivating (*4*)] Natufian archaeological complex of Palestine matches well with proto-Afrasian (Afroasiatic) cultural and environmental vocabulary reconstructions. Militarev's reconstructed proto-Afroasiatic vocabulary (*5*), whether "agricultural" or not, is also peopled with animals and plants of Levant, not African, origin and matches a Natufian cultural landscape. Ehret *et al.* point out that Militarev's semantic reflexes are mixed, but perhaps this is to be expected given that plants of Levant (winter rainfall) origin did not spread prehistorically into the desert or summer rainfall belts of northern Africa beyond the Mediterranean coast, Egypt, and highland Ethiopia.

In archaeological terms, I agree that early Saharans managed cattle, and Ehret himself convincingly relates the earliest appearance of this tradition to Nilo-Saharan–speaking populations (*6*). The Egyptian Neolithic economy, however, was manifestly of Levant and not African origin. Domesticated sheep and goats were probably introduced via Arabia into the Horn of Africa at a similar time, circa sixth millennium B.C.

My assumption is that the spread of Afroasiatic occurred as a result of actual human movement, not language diffusion alone. There is no significant archaeological evidence for a population movement from Africa into the Levant, whether Mesolithic or Neolithic, at the time in question. The genetics papers quoted by Ehret *et al.* do not settle this matter. The Y chromosome evidence appears to signal complex two-way population movements, with very uncertain chronologies. My working assumption, therefore, is that early Afroasiatic languages spread from the Levant into Africa between 7000 and 12,000 years ago, probably in more than one movement. Subsequent history has seen an enormous spread of Semitic languages, including Ethiopian Semitic and, of course, Arabic, on such a scale that the original phylogenetic geography of the Afroasiatic language family must have been considerably erased. Because of this, the geographical source of this family will not reveal itself easily. I have just published a detailed discussion of Afroasiatic prehistory from archaeological and linguistic perspectives (*4*), and the above points are made in more detail there.

PETER BELLWOOD

Department of Archaeology & Anthropology, Australian National University, Canberra, ACT 0200, Australia.

References
1. C. Ehret, *Reconstructing Proto-Afro-Asiatic* (Univ. of California Press, Berkeley, CA, 1995).
2. I. M. Diakonoff, *J. Semit. Stud.* **43**, 209 (1998).
3. I. M. Diakonoff, *J. Near Eastern Stud.* **55**, 293 (1996).
4. P. Bellwood, *First Farmers* (Blackwell, Oxford, 2004), pp. 97–106, 207–210.
5. A. Militarev, in *Examining the Farming/Language Dispersal Hypothesis*, P. Bellwood, C. Renfrew, Eds. (McDonald Institute for Archaeological Research, Cambridge, 2003), chap. 12.
6. C. Ehret, in *Examining the Farming/Language Dispersal Hypothesis*, P. Bellwood, C. Renfrew, Eds. (McDonald Institute for Archaeological Research, Cambridge, 2003), chap. 14.

Earth's Entropy

RALPH LORENZ'S PERSPECTIVE "FULL STEAM ahead—probably" (7 Feb. 2003, p. 837) on the recent groundbreaking work of Roderick Dewar (*1*) mentions the puzzle that "All else being equal, MEP [maximum entropy production] would predict a planet's meridional temperature contrast to be independent of its rotation rate. This disagrees with some rudimentary GCM [general circulation model] experiments, and with meteorologists' intuition."

It is well known that tidal and atmospheric motions exert torque on the solid Earth, which detectably affects its rotation rate (*2*, *3*). Hadley-cell–driven trade winds, for example, exert torque on Earth's surface in a direction that promotes continued rotation. This could conceivably amount to ordered work that acts as an additional mode of entropy production. Perhaps climate modelers should investigate whether one consequence of maximum entropy production on Earth may be partial regulation of planetary rotation rate.

NATHAN G. PHILLIPS
Geography Department, Boston University, 675 Commonwealth Avenue, Boston, MA 02215, USA.

References
1. R. L. Dewar, *J. Phys. A. Math. Gen.* **36**, 631 (2003).
2. See http://badc.nerc.ac.uk/data/aam/.
3. See http://tycho.usno.navy.mil/leapsec.990505.html.

Response

PHILLIPS SUGGESTS THAT THERMODYNAMICS may guide planetary rotations. For Earth, at least, this is unlikely to be so. The usefulness of maximum entropy production (MEP) is only as a selection guideline among dynamically permitted steady states, and the rotation state of the planet may control which states are dynamically possible. The system must first comply with the rigid laws of physics, notably the conservation of mass, energy, and angular momentum: These factors are imposed as constraints on the system before MEP applies.

Even if Earth's whole atmosphere were to spin up to the speed of sound (an extreme case!), angular momentum balance means the rotation period of the solid Earth (where much of the solar heat is absorbed and reradiated) changes by only about one part in one million—a level unlikely to affect heat transfer. Thus, even if the dynamics allowed such a spin-up, it seems the system would gain little from the effort.

However, Phillips' basic suggestion, that optimality in heat transport may guide rotation rates, may have merit for the atmospheres of extrasolar giant planets (*1*) where atmospheric motions at the relatively high altitudes where starlight is absorbed and thermal radiation emitted are largely decoupled from the motion of the planet's interior. If the motions are guided by an MEP heat transport criterion, close-in extrasolar planets, even if tidally locked to their parent star, may nonetheless have only modest day:night temperature contrasts.

RALPH D. LORENZ
Lunar and Planetary Laboratory, University of Arizona, Tucson, AZ 85721, USA.

Reference
1. J. I. Lunine, R. D. Lorenz, "A simple prescription for calculating day-night temperature contrasts on synchronously rotating planets," 33rd Annual Lunar and Planetary Science Conference, 11 to 15 March 2002, Houston, TX, abstr. no.1429.

The Brain, Neurons, and Behavior

I OPENED THE SPECIAL ISSUE ON COGNITION and Behavior (15 Oct., pp. 431–452) with a "there we go again" feeling. So it was a relief to read Donald Kennedy's Editorial "Neuroscience and neuroethics" (p. 373). It has become fashionable to equate the brain with the mind, which in turn controls behavior. Presumably it's hard science, because neurons are involved. But it isn't. It's just a confusion of the necessary with the sufficient, a point made in the Editorial. Altogether too often, sight is lost of the fact that any particular brain can evolve into any particular mind, depending on the experiences encountered.

JOSEPH M. NOTTERMAN
Department of Psychology, Princeton University, Princeton, NJ 08544, USA.

CORRECTIONS AND CLARIFICATIONS

News Focus: "RNAi shows cracks in its armor" by J. Couzin (12 Nov., p. 1124). On page 1125, in the second column, second paragraph, the sentence, "At a meeting last week in Titisee, Germany, Sharp presented preliminary data from his lab showing a 10-fold change in protein levels with only a twofold microRNA difference, the level commonly seen from an off-target effect," the term "microRNA" should have read "mRNA."

Random Samples: "Good as new" (5 Nov., p. 971). This item incorrectly reported that a new laser technique for cleaning ancient coins was developed by Italian archaeologists. It was devised by physicists at IFAC-CNR in Florence, Italy. The accompanying photo credit should have read S. Siano.

Reports: "Requirement for caspase-2 in stress-induced apoptosis before mitochondrial permeabilization" by P. Lassus *et al.* (23 Aug. 2002, p. 1352). This paper reported that silencing expression of caspase-2 with an siRNA prevented apoptosis. Since the time of publication, the authors have identified an siRNA that silences expression of the caspase-2 protein but fails to prevent apoptosis. The authors are investigating three possibilities to explain their results: (i) These siRNAs differentially silence caspase-2 isoforms, which alters the outcome of drug-induced apoptosis; (ii) one of the two siRNAs silences an unidentified gene(s), whose product is involved in apoptosis; and (iii) one of the two siRNAs has some effect unrelated to RNAi.

NEUROPSYCHOLOGY

Getting Things Right

Ralph Adolphs and James Woodward

The human brain in some sense models the world for each individual, and our culture in some sense offers such a model for society. But how do we know that we are not mistaken—that what we believe about the world is in fact true? One way of beginning to answer this difficult epistemological question is by examining the underlying mechanisms that give rise to our beliefs. In *The Physiology of Truth*, a translation of his *L'Homme de vérité* (Odile Jacob, Paris, 2002), Jean-Pierre Changeux provides an account whereby selection among an initial plethora of possibilities yields those that are true, a process evident both in brain development and in knowledge acquisition. Along the way, he espouses a hopeful naturalism: evolution ensures that our nervous systems aim at representing the truth, and aspects of our culture—notably freedom, communication, and pursuit of the scientific method—can ensure that we as a society have true beliefs.

Defending these claims requires some work, making the book a dense 260 pages (supplemented by 40 pages of citation notes) that range widely over computational models, genes, synapses, anthropology, cognitive science, language, and epistemology and that require stamina to digest fully. Nonetheless, the book is intended for a general audience. Changeux, a neurobiologist at the Institut Pasteur in Paris, begins by reviewing the philosophical problems and their recalcitrance. He then considers the neurobiology and its complexity and lastly extends his discussion to culture and society. Although Changeux offers numerous examples from science to illustrate the points he wishes to make and repeats conceptual points in various places, the book occasionally suffers from references that are too cryptic to be illuminating, at least for the nonexpert. This sometimes results in comical prose, as when the role of glutamatergic neurotransmission in cell death and "Chinese restaurant syndrome" are mentioned in the same sentence without further explanation, leading the naïve reader to imagine how Chinese food and death might be related.

The Physiology of Truth
Neuroscience and Human Knowledge
by Jean-Pierre Changeux, translated by M. B. DeBevoise

Harvard University Press, Cambridge, MA, 2004. 324 pp. $45, £29.95. ISBN 0-674-01283-6.

Changeux's view of progress—evolutionary, developmental, and cultural—includes both constructivist and nativist forces. However, he emphasizes largely random initial variation (in genes, in the brain's synaptic and functional architecture, and in the ideas individuals and societies generate) as providing the basis for subsequent selection, similar in spirit to Gerald Edelman's "neural Darwinism." His examples range from the spontaneous electrical activity of immature nervous systems to pretend play and the babbling of infants acquiring language. Experience thus does not directly instruct, as in associationist accounts, but rather selects from among a preexisting set of alternatives. Knowledge grows the same way, through cycles of hypothesis proliferation and elimination via confrontation with experience, an idea that was originally defended by the philosopher Karl Popper.

As Darwin realized, this model fits the evolution of biologically heritable traits very well. But anyone proposing to extend it to neural development, the growth of scientific knowledge, and social change more generally must answer several questions. If the process that generates alternatives is really "blind," what ensures that these alternatives will include any possibility that is close enough to being correct or advantageous? How exactly are the alternatives evaluated? Changeux himself notes that in the case of the brain, an obvious worry is that the absence of constraints on endogenous activity means too many possibilities will be generated to be efficiently tested in a limited time. Similarly, in the case of scientific ideas, the generation of too many unconstrained alternatives may simply foster confusion, undermining progress rather than promoting it.

Changeux is aware of these problems, and he suggests that the concept of "relevance" (first made explicit by Dan Sperber and Deirdre Wilson) can come to the rescue. He argues that relevance is provided by context—the relations among many brain states or among people within a society. Changeux also assigns a crucial role to consciousness, a function he elaborates in terms of the workspace model that he and Stan Dehaene have proposed. A key ingredient in their model is the widespread accessibility of information within neural networks, which permits the evaluation of hypotheses by reference to coherence with other available information (activity that Changeux locates in the prefrontal cortex).

The persuasiveness of Popper's model for generating true hypotheses is predicated on the assumption that we are essentially rational in how we select among alternatives. But a glance at the daily newspaper quickly casts doubt on that assumption. Humans are perfectly capable of believing in the entirely irrational, wrong, and nonsensical—so much so that they are willing to give their lives for such beliefs. Indeed, a more pessimistic view might be that evolution has been too shortsighted to help us cope with the global, complex problems we face today. In response, Changeux argues that our plasticity and ability to learn as individuals—cultural evolution—might prevail where biological evolution fails. At the level of society, he sees us as generating hypotheses in culturally consensual interaction. But why think that this process necessarily generates beliefs that are true? Again, we see a multitude of "truths" held by different cultures, which undermine hope for the integrated global culture Changeux proposes at the end of the book.

Although Changeux does not resolve these difficulties, he has at least suggested a path by which they might be surmounted. His vision is at once that of the detached scientist and the deeply caring humanist—for him, the two go hand in hand. He believes that applying the standards of the scientific method to society will promote freedom of ideas and individual rights, and that from this a stable consensual agreement on truth can emerge. Let us hope that this attractive vision prevails.

DOI: 10.1126/science.1105394

CREDIT: JOE SUTLIFF

The reviewers are in the Division of Humanities and Social Sciences, California Institute of Technology, Pasadena, CA 91125, USA. E-mail: radolphs@hss.caltech.edu and jfw@hss.caltech.edu

EDUCATION

Stressed for Success

Bryan Garman

Since the Soviet Union launched Sputnik in 1957, American schools have been among the most maligned of public institutions, criticized for graduating underachievers who are ill-equipped for college and unprepared for employment. Recently, policymakers have placed the blame squarely on teachers and have suggested that a culture of accountability, based largely on the establishment of national standards, will cure the woes. In *School of Dreams*, Pulitzer Prize–winner Edward Humes recognizes that neither the diagnosis nor the treatment is so simple. After spending a year teaching essay writing at Whitney High, a top-ranked school in suburban Los Angeles, Humes understands that a school "is like an organism, living, breathing, complex, impossible to know in its entirety. A thousand dramas unfold daily, endless storylines, alliances, jockeying, heartbreaks, victories, and secrets."

School of Dreams
Making the Grade at a Top American High School
by Edward Humes

Harcourt, New York, 2004. 400 pp. $25. ISBN 0-15-100703-9. Paper, $14. ISBN 0-15-603007-1.

Humes examines this organism carefully, weaving anecdotes and student essays into a sometimes untidy but always moving account. Although the author generally eschews analysis, he identifies key components of a successful education and looks critically at the toll that competitive college admissions and standardized testing take on life and learning. The vastness of the subject prevents Humes from exploring certain topics as fully as he might, but his narrative is evocative, insightful, and sensitive.

When Whitney opened in 1976, few would have predicted that within 11 years the U.S. Department of Education would recognize it as a Blue Ribbon School of Excellence. Bob Beall, the founding principal, transformed Whitney from a vocational learning center into a top-flight college preparation power. Undeterred by limited funding, Beall hired teachers who built a rigorous but supportive environment. Whitney has its share of the usual conflicts—rifts between administrators and teachers, union politics, and budget cuts—but a commitment to students transcends such challenges.

Heart-wrenching scenes are staged in the offices of counselors and grade-level advisors, where Humes captures the sense of urgency and the practice of triage that characterize a school: Students on probation weep. Angry parents dispute low grades. A drug-addicted student pleads for help. Teachers learn that a colleague's son has been killed in a drive-by shooting. Each day is replete with reward and disappointment, drama and trauma. Both counselors and students are stretched emotionally and intellectually, shouldering more than they should bear and together negotiating the vagaries of adolescence.

Careful not to idealize his subject, Humes presents professionals who are both triumphant and fallible. He does, however, have a soft spot for teachers who go beyond textbooks and promote critical thought. In one example, he applauds a teacher who launches an Alka-Seltzer–propelled rocket and challenges his students to explain the physics behind its flight. Students calculate velocity, derive equations, and present results to a panel of engineers. Humes thoughtfully enumerates the project's challenges, chronicling student battles with self-doubt and celebrating a teacher who remains supportive while demanding excellence.

Humes appreciates good teaching, but his deepest sympathies rest with students, whose sincerity and talents move him. Anecdotes and student essays, however, reveal unsettling trends. To improve college admission odds, students stockpile advanced placement courses and SAT prep programs, complete four hours of homework nightly, participate in extracurricular activities (Humes fails to appreciate the import of these), and expend spare moments thinking about college. The pressure, Humes suggests, produces sleepless nights, young Starbucks customers, and students who care more about grades than they do about learning. Such unfortunate developments are hastened by the expectations of parents, many of whom seek primarily to channel their children into high-status colleges. The traditions of immigrant families often complicate matters with Whitney's diverse population. In an especially poignant essay, a Korean-American struggles to map her way between old ways and new. Humes's portrait of student life is rich, but surprisingly the topic of teenage depression, an increasingly common condition, is not present.

Skirting policy debates, Humes offers rare but forceful analysis, notably when he assails Neil and George Bush. A founder of a company that seeks to use technology to make learning "fun," Neil Bush visited Whitney to promote software that packages the Seminole War as a football game between Native Americans and (Andrew) "Jacksons." Humes expresses contempt for such gimmicks by relating the response of a student, who informs an incredulous Bush that she prefers textbooks. In addition, Humes bemoans the president's No Child Left Behind Act. Skeptical of standardized tests, he argues that teaching and learning subside when test prep quickens.

Whitney's students post high scores and matriculate to desirable colleges. But great schools enable more; they meet the emotional and spiritual needs of students. In the midst of frenzy, the people at Whitney sustain one another. According to one grateful student, Whitney "showed me that I wasn't worthless because I was a girl…they were there for me when my home life was rough.…They showed me that it's possible to trust someone unconditionally.…Whitney gave me something that really nowhere else has truly given me: acceptance." When it comes to building authentic relationships and appreciating their presence in successful schools, both Whitney and Humes do more than make the grade.

DOI: 10.1126/science.1106680

The reviewer is at Sidwell Friends School, 3825 Wisconsin Avenue, NW, Washington, DC 20016, USA. E-mail: garmanb@sidwell.edu

BROWSINGS

CREDIT: INSTITUTE OF VERTEBRATE PALEONTOLOGY AND PALEOANTHROPOLOGY, CHINESE ACADEMY OF SCIENCES

The Jehol Biota. The Emergence of Feathered Dinosaurs, Beaked Birds and Flowering Plants. *Mee-mann Chang et al., Eds.* Shanghai Scientific and Technical Publishers, Shanghai, 2004. 210 pp. 350 Yuan. ISBN 7-5323-7318-5.

Exquisitely preserved fossils from Early Cretaceous lake deposits have made the Liaoning region of China a paleontological Mecca. The contributors outline the geologic and evolutionary contexts of the biota and survey its major taxonomic components. The volume's lavish illustrations present many spectacular specimens (such as the pterosaur *Sinopterus dongi*, above) and colored life reconstructions.

This year's essay series highlights the benefits that scientists, science, and technology have brought to society throughout history.

The Scientific Consensus on Climate Change

Naomi Oreskes

Policy-makers and the media, particularly in the United States, frequently assert that climate science is highly uncertain. Some have used this as an argument against adopting strong measures to reduce greenhouse gas emissions. For example, while discussing a major U.S. Environmental Protection Agency report on the risks of climate change, then–EPA administrator Christine Whitman argued, "As [the report] went through review, there was less consensus on the science and conclusions on climate change" (*1*). Some corporations whose revenues might be adversely affected by controls on carbon dioxide emissions have also alleged major uncertainties in the science (*2*). Such statements suggest that there might be substantive disagreement in the scientific community about the reality of anthropogenic climate change. This is not the case.

Without substantial disagreement, scientists find human activities are heating the Earth's surface.

The scientific consensus is clearly expressed in the reports of the Intergovernmental Panel on Climate Change (IPCC). Created in 1988 by the World Meteorological Organization and the United Nations Environmental Programme, IPCC's purpose is to evaluate the state of climate science as a basis for informed policy action, primarily on the basis of peer-reviewed and published scientific literature (*3*). In its most recent assessment, IPCC states unequivocally that the consensus of scientific opinion is that Earth's climate is being affected by human activities: "Human activities … are modifying the concentration of atmospheric constituents … that absorb or scatter radiant energy. … [M]ost of the observed warming over the last 50 years is likely to have been due to the increase in greenhouse gas concentrations" [p. 21 in (*4*)].

IPCC is not alone in its conclusions. In recent years, all major scientific bodies in the United States whose members' expertise bears directly on the matter have issued similar statements. For example, the National Academy of Sciences report, *Climate Change Science: An Analysis of Some Key Questions*, begins: "Greenhouse gases are accumulating in Earth's atmosphere as a result of human activities, causing surface air temperatures and subsurface ocean temperatures to rise" [p. 1 in (*5*)]. The report explicitly asks whether the IPCC assessment is a fair summary of professional scientific thinking, and answers yes: "The IPCC's conclusion that most of the observed warming of the last 50 years is likely to have been due to the increase in greenhouse gas concentrations accurately reflects the current thinking of the scientific community on this issue" [p. 3 in (*5*)].

Others agree. The American Meteorological Society (*6*), the American Geophysical Union (*7*), and the American Association for the Advancement of Science (AAAS) all have issued statements in recent years concluding that the evidence for human modification of climate is compelling (*8*).

The drafting of such reports and statements involves many opportunities for comment, criticism, and revision, and it is not likely that they would diverge greatly from the opinions of the societies' members. Nevertheless, they might downplay legitimate dissenting opinions. That hypothesis was tested by analyzing 928 abstracts, published in refereed scientific journals between 1993 and 2003, and listed in the ISI database with the keywords "climate change" (*9*).

The 928 papers were divided into six categories: explicit endorsement of the consensus position, evaluation of impacts, mitigation proposals, methods, paleoclimate analysis, and rejection of the consensus position. Of all the papers, 75% fell into the first three categories, either explicitly or implicitly accepting the consensus view; 25% dealt with methods or paleoclimate, taking no position on current anthropogenic climate change. Remarkably, none of the papers disagreed with the consensus position.

Admittedly, authors evaluating impacts, developing methods, or studying paleoclimatic change might believe that current climate change is natural. However, none of these papers argued that point.

This analysis shows that scientists publishing in the peer-reviewed literature agree with IPCC, the National Academy of Sciences, and the public statements of their professional societies. Politicians, economists, journalists, and others may have the impression of confusion, disagreement, or discord among climate scientists, but that impression is incorrect.

The scientific consensus might, of course, be wrong. If the history of science teaches anything, it is humility, and no one can be faulted for failing to act on what is not known. But our grandchildren will surely blame us if they find that we understood the reality of anthropogenic climate change and failed to do anything about it.

Many details about climate interactions are not well understood, and there are ample grounds for continued research to provide a better basis for understanding climate dynamics. The question of what to do about climate change is also still open. But there is a scientific consensus on the reality of anthropogenic climate change. Climate scientists have repeatedly tried to make this clear. It is time for the rest of us to listen.

The author is in the Department of History and Science Studies Program, University of California at San Diego, La Jolla, CA 92093, USA. E-mail: noreskes@ucsd.edu

References and Notes

1. A. C. Revkin, K. Q. Seelye, *New York Times*, 19 June 2003, A1.
2. S. van den Hove, M. Le Menestrel, H.-C. de Bettignies, *Climate Policy* **2** (1), 3 (2003).
3. See www.ipcc.ch/about/about.htm.
4. J. J. McCarthy *et al.*, Eds., *Climate Change 2001: Impacts, Adaptation, and Vulnerability* (Cambridge Univ. Press, Cambridge, 2001).
5. National Academy of Sciences Committee on the Science of Climate Change, *Climate Change Science: An Analysis of Some Key Questions* (National Academy Press, Washington, DC, 2001).
6. American Meteorological Society, *Bull. Am. Meteorol. Soc.* **84**, 508 (2003).
7. American Geophysical Union, *Eos* **84** (51), 574 (2003).
8. See www.ourplanet.com/aaas/pages/atmos02.html.
9. The first year for which the database consistently published abstracts was 1993. Some abstracts were deleted from our analysis because, although the authors had put "climate change" in their key words, the paper was not about climate change.
10. This essay is excerpted from the 2004 George Sarton Memorial Lecture, "Consensus in science: How do we know we're not wrong," presented at the AAAS meeting on 13 February 2004. I am grateful to AAAS and the History of Science Society for their support of this lectureship; to my research assistants S. Luis and G. Law; and to D. C. Agnew, K. Belitz, J. R. Fleming, M. T. Greene, H. Leifert, and R. C. J. Somerville for helpful discussions.

10.1126/science.1103618

IMMUNOLOGY

The Elusive NKT Cell Antigen—Is the Search Over?

Dale I. Godfrey, Daniel G. Pellicci, Mark J. Smyth

Conventional CD4$^+$ and CD8$^+$ T cells of the immune system recognize specific peptide antigens bound to major histocompatibility complex (MHC) class II or MHC class I molecules, respectively. In contrast, a specialized subpopulation of T cells called NKT cells recognizes glycolipid antigens presented by the MHC class I–like molecule, CD1d (*1*). NKT cells express both a conserved αβ T cell receptor (TCR) and natural killer (NK) cell receptors. These cells are important for suppressing autoimmunity and graft rejection, enabling resistance to infection, and promoting tumor immunity (*2*, *3*). Yet surprisingly little is known about the specific endogenous antigens that NKT cells recognize. This is set to change with the report by Zhou *et al.* (*4*) on page 1786 of this issue. Through a combination of deduction and experimentation that unfolds like a detective story, these investigators identify the glycosphingolipid, isoglobotrihexosylceramide (iGb3), as a key endogenous NKT cell antigen.

Enhanced online at www.sciencemag.org/cgi/content/full/306/5702/1687

During development in the thymus, NKT cells branch from the mainstream T cell precursor pool when they randomly generate a TCR that interacts with CD1d. CD1d presents endogenous glycolipid antigens that have been processed in lysosomes to NKT cells, and this presentation is necessary for efficient NKT cell development (see the figure) (*5*). Mature NKT cells display a perpetually activated/memory phenotype and low-level autoreactivity, which suggests the presence of endogenous CD1d-restricted antigens on the surface of antigen-presenting cells in the periphery (see the figure) (*3*, *5*). In most studies of NKT cell function, these cells are stimulated with a synthetic glycosphingolipid called α-galactosylceramide, originally derived from a marine sponge (*6*). This molecule potently stimulates NKT cells in both mice and humans in a CD1d-dependent manner. In addition to providing valuable insights into the possible function of NKT cells, α-galactosylceramide is currently being tested in cancer patients (*2*, *3*). However, because α-galactosylceramide is not a normal product of mammalian cells, a key question is whether equivalent mammalian glycolipid antigens exist, and if they do, whether they are involved in NKT cell development and activation.

In their study, Zhou and colleagues (*4*) demonstrate that mice deficient in the enzymes β-hexosaminidase A and B, which degrade glycosphingolipids in lysosomes, exhibit defective NKT cell development. Subsequent experiments narrowed down the possible causative abnormalities in these mice to an apparent deficiency in the production of lysosomal iGb3. Their data show that iGb3 is a broadly reactive agonist ligand for mature NKT cells that induces robust stimulation of these cells that is comparable to stimulation by α-galactosylceramide. Although these data suggest that iGb3 is a primary ligand for NKT cells, the authors do not exclude the possibility that other CD1d-restricted antigens (possibly mammalian, tumor, or microbial-derived) also activate NKT cells in the periphery (*5*). Indeed, partial diversity in the β chain of the TCR of NKT cells implies that peripheral NKT cells may have multiple antigen specificities. This possibility is supported by the clonal expansion of an NKT cell subset in response to the disialoganglioside GD3 (*7*).

The Zhou *et al.* study (*4*) provides multiple lines of evidence to suggest that iGb3 is an (possibly the) endogenous ligand for NKT cells. Yet the presence of this glycolipid in the thymus and peripheral lymphoid organs of mice and humans remains to be formally demonstrated. Probably the most contentious issue is whether iGb3 is an endogenous ligand for human NKT cells. This molecule contains a Galα1,3Gal carbohydrate linkage considered foreign to human immune cells as hu-

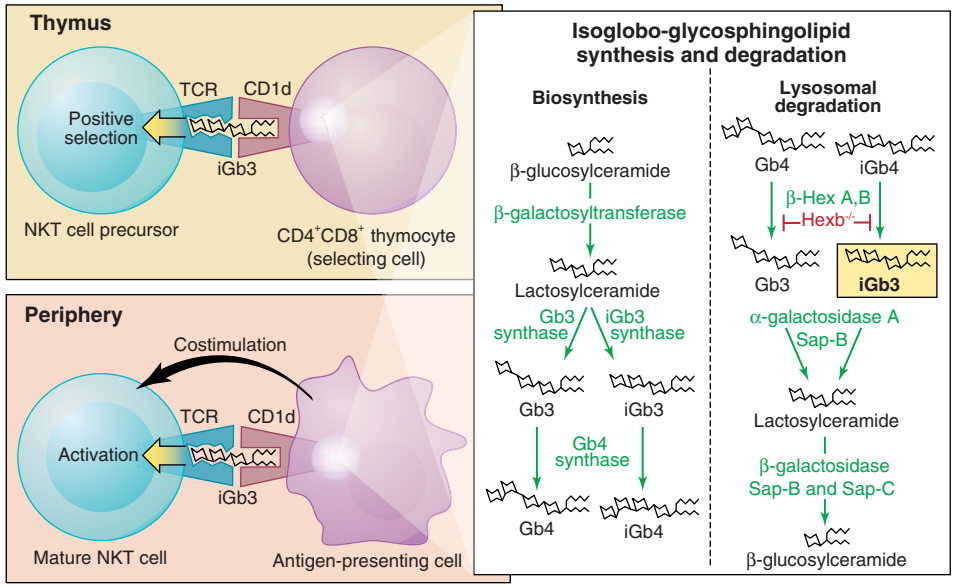

An antigen for NKT cells. The TCR of NKT cells has been shown to specifically recognize the glycosphingolipid iGb3 presented in the context of CD1d (*4*). This study suggests that recognition of iGb3 occurs during NKT cell selection in the thymus (**top**) and activation in the periphery (**bottom**) (*4*). Loading of iGb3 into CD1d first requires biosynthesis of the isoglobo-series glycosphingolipids and the subsequent degradation of these molecules in lysosomes by the enzymes β-hexosaminidase A and B (**box**). This process presumably needs to take place in immature CD4$^+$ and CD8$^+$ thymocytes that are responsible for NKT cell selection in the thymus, and in peripheral antigen-presenting cells that are responsible for NKT cell activation in the periphery. Costimulatory factors produced by antigen-presenting cells may be required for full NKT cell activation (*3*). Although other glycosphingolipids, such as Gb3 and iGb4, may bind to CD1d, their distinct oligosaccharide structures might prevent binding to the TCR of NKT cells.

D. I. Godfrey and D. G. Pellicci are in the Department of Microbiology and Immunology, University of Melbourne, Melbourne, Victoria, Australia. M. J. Smyth is in the Cancer Immunology Program, Peter MacCallum Cancer Institute, Melbourne, Victoria, Australia. E-mail: godfrey@unimelb.edu.au

Published by AAAS

mans lack a functional α1,3Galactosyltransferase enzyme (*8*). Indeed, ~1% of human immunoglobulin G (IgG) reacts with Galα1,3Gal moieties, providing a major barrier to xenotransplantation (*9*, *10*). However, the observation that human IgG does not react with iGb3 (*4*) suggests that this, or a closely related, glycolipid may not be considered foreign by human immune cells. Theoretically, this could result in the selective clonal deletion of human B cells with specificity for the Galα1,3Gal moiety in the context of iGb3. In further support of this possibility, formation of the Galα1,3Gal linkage in iGb3 is specifically controlled by the enzyme iGb3 synthase rather than by α1,3Galactosyltransferase (see the figure) (*11*). Furthermore, NKT cell autoreactivity against human dendritic cells can be blocked with the Galα1,3Gal-specific lectin, isolectin-B4 (*4*). These observations are at least consistent with the possibility that iGb3 is an endogenous ligand for NKT cells in humans as well as mice.

If iGb3 is an endogenous ligand for NKT cells, important questions and exciting possibilities emerge. From the standpoint of developmental biology: How do NKT cells undergo positive selection in the thymus in response to a ligand that activates them in the periphery? It is possible that iGb3 levels vary among tissues or among different cell types, or that costimulatory factors like interleukin-12 determine the extent to which NKT cells respond to this self antigen (*5*). Are the residual NKT cells in β-hexosaminidase–deficient mice selected by different glycolipid ligands, or might a few iGb3 molecules be loaded into CD1d independently of the lysosomal degradation pathway? An intriguing possibility is that variable levels of iGb3 may be responsible for determining the wide range in numbers of NKT cells observed between humans and distinct mouse strains (*2, 3*). In this context, it will be interesting to discover whether patients with Sandhoff disease, who lack β-hexosaminidase A and B (*12*), are deficient in NKT cells.

Regarding the development of potential therapeutics, it will be important to know whether iGb3 is involved in NKT cell–mediated immune suppression of autoimmune disease and tissue grafts, and whether this molecule, or related agonist compounds, could be used to enhance immunological tolerance. Conversely, if iGb3 contributes to destructive NKT cell activities such as the promotion of atherosclerosis or airway hypersensitivity (*2*), it may be possible to ameliorate these diseases by specifically blocking this ligand. It also will be important to discern whether levels of iGb3 in tumor cells correlate with NKT cell–dependent tumor rejection, and whether transfecting tumor cells with the gene encoding iGb3 synthase would generate more effective tumor vaccines.

As more is learned about the factors that determine NKT cell development and activity, we will improve our ability to manipulate these cells therapeutically. The identification of iGb3 as a mammalian NKT cell ligand is an important step in the right direction. Whether iGb3 is unique or just one of many other ligands that activate NKT cells is the next burning question to be answered.

References and Notes

1. D. I. Godfrey *et al.*, *Nat. Rev. Immunol.* **4**, 231 (2004).
2. D. I. Godfrey, M. Kronenberg, *J. Clin. Invest.* **114**, 1379 (2004).
3. M. Kronenberg, L. Gapin, *Nat. Rev. Immunol.* **2**, 557 (2002).
4. D. Zhou *et al.*, *Science* **306**, 1786 (2004); published online 11 November 2004 (10.1126/science.1103440).
5. M. Brigl, M. B. Brenner, *Annu. Rev. Immunol.* **22**, 817 (2004).
6. T. Kawano *et al.*, *Science* **278**, 1626 (1997).
7. D. Y. Wu *et al.*, *J. Exp. Med.* **198**, 173 (2003).
8. U. Galili *et al.*, *J. Biol. Chem.* **263**, 17755 (1988).
9. M. S. Sandrin, I. F. McKenzie, *Curr. Opin. Immunol.* **11**, 527 (1999).
10. U. Galili *et al.*, *Blood* **82**, 2485 (1993).
11. J. J. Keusch *et al.*, *J. Biol. Chem.* **275**, 25308 (2000).
12. M. Jeyakumar *et al.*, *Neuropathol. Appl. Neurobiol.* **28**, 343 (2002).

13. We thank M. McConville, M. Sandrin, and S. Berzins for helpful discussions. D.I.G., D.G.P., and M.J.S. are supported by research grants from the National Health and Medical Research Council of Australia, the Association for International Cancer Research, and the NIH.

10.1126/science.1106932

PLANETARY SCIENCE

Proof for Water, Hints of Life?

Jeffrey S. Kargel

On 25 January of this year, NASA's Opportunity rover landed on Mars' Meridiani Planum, a smooth, flat plain unlike any feature studied by earlier martian landers. Eleven papers in this issue characterize Opportunity's landing site in detail (*1*–*11*). The analyzed rocks mainly consist of iron oxides and hydrated magnesium, calcium, and iron sulfates; they were deposited in or altered by salty, acidic water, perhaps a sea (*1*, *2*). Together with orbital observations (*12*), the reports for the first time document the geology and geochemistry of a martian hydrological event. The results indicate aqueous sedimentation or aqueous alteration and are consistent with models of a warmer, wetter martian past (*12*–*15*).

Opportunity was the last of a recent international armada of space probes to reach Mars. Just a few weeks before it touched down, its twin rover, Spirit, landed in Gusev crater, halfway around the planet. But previous landers, including Spirit, found only volcanic rock rubble and inorganic soils. Opportunity was the first to sample bedrock (see the figure). Sediments appear to have accumulated layer-by-layer and experienced episodic drying (*2*). The regular fine lamination (see figure, panels C, D, and G), bundled sets of laminae (panel G), thicker bedding on the meter scale (panels B and F), and much thicker layers (panel A) indicate several frequencies of cyclic deposition. If the fine-scale rhythm (panels C and D) is annual, and if it constitutes much of the 600-m-thick sedimentary rock record in Meridiani Planum, then this sequence could have formed in about 250,000 Mars years. Annual laminae would imply a seasonal response of the water mass, thin or no ice cover, and a much warmer climate than today's or else ultracold concentrated acid solutions. Polygonal cracks (panels D, E, H, and I) suggest that hydrous deposition or alteration also played a role (*2*). It remains unclear whether the polygons formed in drying, salty mud or whether they resulted from subsequent salt dehydration or from repetitive freezing and thawing of ice.

The strata contain large fractions of magnesium, calcium, and iron sulfates, traces of chlorine, bromine, and phosphorus, and insoluble or weakly soluble iron oxides and aluminosilicate impurities (*3*–*7*). The salty outcrops are generally much softer than volcanic rocks examined by the Spirit rover in Gusev crater (*8*). They are softer than many terrestrial sedimentary rocks and are similar to highly hydrated salts in Earth's ephemeral desert lakes. The outcrops have a spongy texture like that caused by dissolution or dehydration.

The mineral jarosite detected at Meridiani Planum (*6*) requires highly acidic conditions (*16*–*21*). Other minerals that have been observed or modeled at the site are consistent with acid brine, as is the absence of calcium carbonate (which reacts to gypsum in acid sulfate solution). High sulfur-to-chlorine ratios and high iron contents of the nine salty rocks analyzed by Opportunity (*5*) suggest a relatively warm (>265 K) acid sulfate solution (*18*). The mineral assemblage and chemistry is typical of acid mine drainage systems affected by sulfide oxidation (*19*–*21*). To explain the huge amounts of sulfur, sulfate salts had to be in-

The author is with the U.S. Geological Survey, Flagstaff, AZ 86001, USA. E-mail: jkargel@usgs.gov

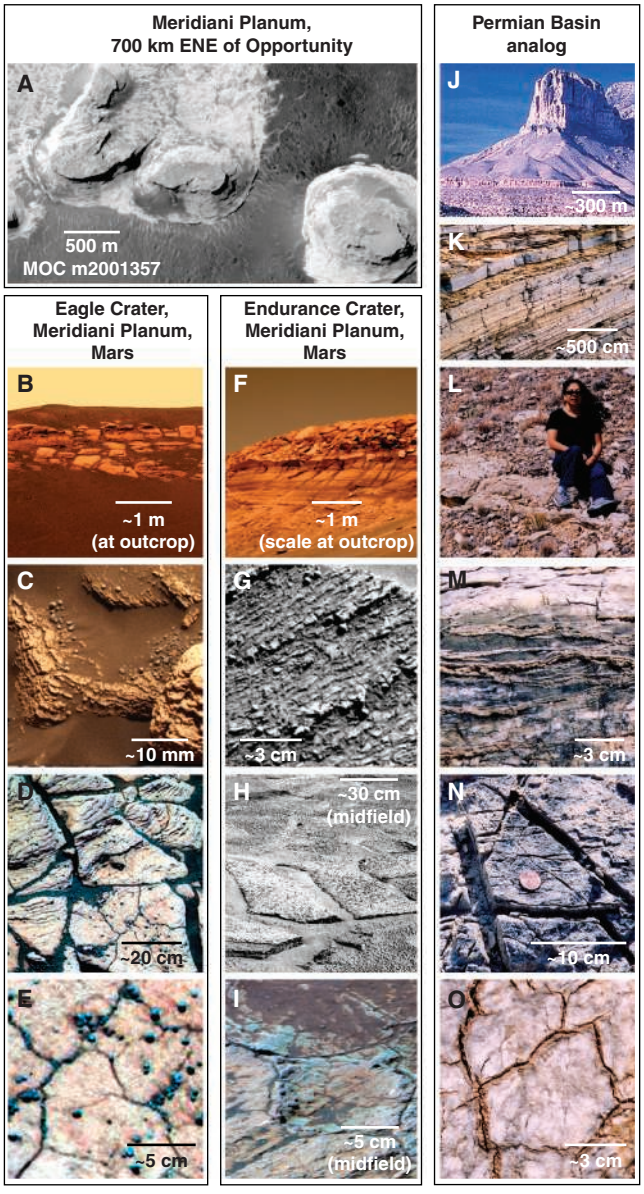

Similar yet different. The Opportunity rover and orbiting spacecraft have imaged physical indicators of changing aqueous conditions in Meridiani Planum (*2*, *12*), including a hierarchy of layers spanning five orders of magnitude in thickness. The layers probably represent distinct rock types and shifts in depositional environments and processes. (**A**) Mars Orbital Camera image shows eroded rock layers in eastern Meridiani Planum forming cliffs and flat-topped mountains hundreds of meters high. (**B** to **E**) Opportunity images of a finely laminated and polygonally fractured outcrop in Eagle crater. (**F** to **I**) Opportunity images of a rock sequence in Endurance crater. (**J** to **O**) Rock strata in the Permian Basin marine deposits of Texas and New Mexico (USA) exhibit a hierarchy of coarse and fine layers, including salt beds. There are key differences from Meridiani Planum, but some aspects are similar. Sedimentary layers of El Capitan loom in (J). Rhythmic deep-water carbonates and submarine landslides (K) are unlike what has been seen so far in Meridiani Planum, where only 1% of the rock sequence has been explored. The evaporitic gypsum bed in L is of comparable thickness to Eagle crater's sulfate bed. Fine laminae in dolomite (M) are related to biological activity. Polygonal fractures in gypsum caused by dewatering and dissolution are seen in (N and O).

troduced, perhaps as groundwater, acid aerosols, dust, or by acid digestion of volcanic rocks. When sulfur oxide is removed from the salty rocks, the residue is similar (except for calcium depletion) to the martian shergottite meteorites (*1*) and a unique rock, Bounce, analyzed by Opportunity (*1*, *5*).

Bounce, a partly altered volcanic rock apparently tossed into (or excavated from) Meridiani Planum by an impact (*1*), might be integral to the story. Bounce and the salty rocks (*5*) seem to comprise a mixing or chemical fractionation series. Chemical fractionation by freezing or drying and precipitation of first sulfates and then chlorides (*17*) is suggested by sulfur and chlorine trends in the salty rocks. All measured elements except potassium, sodium, and chlorine are correlated among the salty rocks and Bounce. Curiously, potassium, sodium, and chlorine correlate positively with the insoluble aluminosilicate material in the salty rocks but are decoupled from Bounce, indicating that these elements had a separate history from the other elements.

The observed chemical fractionation in the top few meters of Meridiani Planum's rock record may be explained by two brines. Although this scenario is not unique, it is consistent with Squyres *et al.* (*1*). First, an acid sulfate brine permeated a laminated volcanic tuff or, more likely, digested Bounce-like rocks and then reprecipitated a laminated sequence of impure magnesium, calcium, and iron sulfates. Next, a chloride brine (possibly a modified remnant of the first brine) oxidized iron, selectively redissolved and removed some sulfates (especially magnesium sulfate), and generated porosity. The brine's dregs precipitated sodium and potassium chlorides in the pores as the sediment dried and cracked. The aqueous epoch was followed by a long, cold, dry period of small impacts and continuing wind activity.

Meridiani Planum is unusual; that is why Opportunity was sent there. However, its iron oxides and magnesium, calcium, and iron sulfate hydrates have long been a staple of Mars geochemical models (*22*) and may occur widely (*23*); smaller amounts of these compounds were found at Spirit's site in Gusev crater (*24*). Does martian geochemistry resemble a global acid mine pollution site of ochre and sulfate mineralization? The source of Mars' sulfate may be crustal sulfide mineral oxidation (common in acid-mine pollution sites on Earth) or thermal metamorphism of buried sulfate layers; presumably those minerals trace back even further to venting of primordial mantle gases.

As Opportunity has continued its traverse, the European Space Agency's Mars Express orbiter has detected martian atmospheric methane at up to 30 parts per billion (*25*). Although the column abundance of methane in the martian atmosphere is less than 0.01% of its column abundance in Earth's atmosphere, this trace gas is crucially important. Questions remain regarding the mixing of the martian atmosphere and the causes of methane's uneven distribution. It may require a patchy subsurface methane reservoir or patchy release of methane. Ancient methane perhaps was long stored in martian permafrost (*25*, *26*). An important greenhouse gas, methane might help to explain geologic evidence of massive environmental change on Mars.

Could martian methane be formed by life? Might Meridiani Planum's salts be linked through life and water to regional concentrations of methane? Life exists on Earth at acidities and salinities comparable to those inferred for Meridiani Planum (*18*, *19*). A cold acid-sulfate geochemical model of Meridiani Planum overlaps with some models of the ocean on Europa, one of Jupiter's moons where life could exist (*27*). Such "extreme environments" are rare on Earth, but may be common elsewhere. Few terrestrial species tolerate conditions that are simultaneously supercold, salty, and acidic; none of those that can survive such extremes also generate methane, but maybe on Mars they do, or maybe martian methanogens live in more alkaline and reducing regions.

No location on Earth closely resembles Meridiani Planum, but many sites share aspects with it. Chemical analogs include the acid mine drainage of Rio Tinto in Spain, where microbial activity exists in a mineral assemblage resembling that of Meridiani Planum (*19*). Another new Mars model is based on the hypersaline Permian Basin in

North America (*28*). In that classic salt sea, repetitive cycles of evaporation and flooding produced a layered, salty rock sequence (panels J to O). One can speculate that the Permian Basin's biogenesis, salt-trapping, and slow release of hydrocarbons may also serve as an analog for methane-involving processes on Mars.

Despite appearances, Mars may never have been very Earth-like. Less water-rich alternatives lacking the appeal of life will be explored. Martian methane and salts might be unconnected, with neither relating closely to what geologists see on Earth. Although Meridiani Planum provides a record of aqueous processes, it might be a poor astrobiological site. Might methane be generated in mantle or crustal systems isolated from sulfate and sulfur dioxide? Might sulfates be related more to Io's sulfur dioxide volcanism or Venus' sulfur dioxide–driven dry weathering than to Earth's evaporative seas?

Given what we now know about Mars, planetary protection considerations require the assumption that martian life exists, until we learn otherwise. All possible care must be taken to avoid cross-contamination between Earth and Mars. Before proceeding with sample returns or human missions to Mars, we must review measures for planetary biological protection. The possible future discovery of life (or fossil life) beyond Earth, anticipated for millennia, would complete the Galilean revolution that removed Earth and its life from the center of the universe. Alternatively, if we search martian aqueous deposits and find them barren, then Earth might be seen as the only land of the living for light-years around. Methane and salts may then provide humans with raw materials for building a new civilization on Mars (*28*) and with an increased respect for life on our own planet.

References

1. S. W. Squyres *et al.*, *Science* **306**, 1698 (2004).
2. S. W. Squyres *et al.*, *Science* **306**, 1709 (2004).
3. J. F. Bell III *et al.*, *Science* **306**, 1703 (2004).
4. K. E. Herkenhoff *et al.*, *Science* **306**, 1727 (2004).
5. R. Rieder *et al.*, *Science* **306**, 1746 (2004).
6. G. Klingelhöfer *et al.*, *Science* **306**, 1740 (2004).
7. P. R. Christensen *et al.*, *Science* **306**, 1733 (2004).
8. R. E. Arvidson *et al.*, *Science* **306**, 1730 (2004).
9. L. A. Soderblom *et al.*, *Science* **306**, 1723 (2004).
10. M. T. Lemmon *et al.*, *Science* **306**, 1753 (2004).
11. M. D. Smith *et al.*, *Science* **306**, 1750 (2004).
12. B. M. Hynek *et al.*, *J. Geophys. Res.* **107**, 10.1029/2002JE001891 (2002).
13. T. J. Parker *et al.*, *Icarus* **82**, 111 (1989).
14. V. R. Baker *et al.*, *Nature* **352**, 589 (1991).
15. M. C. Malin, K. S. Edgett, *Science* **302**, 1931 (2003).
16. D. C. Catling, *Nature* **429**, 707 (2004).
17. G. M. Marion *et al.*, *Geochim. Cosmochim. Acta* **67**, 4251 (2003).
18. K. C. Benison, D. A. Laclair, *Astrobiology* **3**, 609 (2003).
19. D. C. Fernández-Remolar *et al.*, *J. Geophys. Res.* **108**, 10.1029/2002JE001918 (2003).
20. J. L. Jambor, D. K. Nordstrom, C. N. Alpers, in *Sulfate Minerals, Crystallography, Geochemistry, and Environmental Significance,* vol. 40 of *Reviews in Mineralology & Geochemisry,* C. N. Alpers *et al.*, Eds. (Mineralogical Society of America, Washington, DC, 2000), pp. 303–350.
21. J. E. Dutrizac, J. L. Jambor, in *Sulfate Minerals, Crystallography, Geochemistry, and Environmental Significance*, vol. 40 of *Reviews in Mineralogy & Geochemisry,* C. N. Alpers *et al.*, Eds. (Mineralogical Society of America, Washington, DC, 2000), pp. 405–452.
22. R. G. Burns, *Proc. Lunar Planet. Sci. Conf.* **18**, 713 (1988).
23. W. C. Feldman *et al.*, *Geophys. Res. Lett.* **31**, L18701 (2004).
24. M. D. Lane *et al.*, *Geophys. Res. Lett.* **31**, 10.1029/2004GL021231 (2004).
25. V. Formisano *et al.*, *Science* **306**, 1758 (2004); published online 28 October 2004 (10.1126/science.1101732).
26. R. E. Pellenbarg *et al.*, *J. Geophys. Res.* **108**, 10.1029/2002JE001901 (2003).
27. J. S. Kargel *et al.*, *Icarus* **148**, 226 (2000).
28. J. S. Kargel, *Mars: A Warmer Wetter Planet* (Praxis, Chichester, UK, 2004).

10.1126/science.1105533

APPLIED PHYSICS

X-ray Movies of Wiggling Crystals

Philip H. Bucksbaum

When a solid absorbs a short pulse of laser light, it moves—if only a little. The light drives vibrations, much like ringing a bell. The oscillations are called "coherent phonons," a name which suggests sound; but unlike a bell chime, we cannot hear or see this motion. It is too fast, usually around a trillion oscillations per second, and too faint, with crystal lattice planes moving much less than a hundredth of the distance between the atoms in the solid.

Laser-induced coherent phonons have been detected indirectly, usually through their effect on the optical index of the material. This approach allows the motion to be detected, but does not reveal how bonds stretch and atoms move. On page 1771 of this issue, Bargheer *et al.* (*1*) use subpicosecond x-ray diffraction to image the atomic motion directly. The authors study oscillations of laser-excited semiconductor composites composed of alternating layers of two crystalline semiconductors. Because such "multiple quantum wells" are the basis for the semiconductor lasers used in optical communication, it is particularly important to understand how they interact with laser light.

Bargheer *et al.* use multiple quantum wells composed of 8-nm-thick layers of gallium arsenide (GaAs) interleaved with layers of aluminum gallium arsenide ($Al_{0.4}Ga_{0.6}As$) of a similar thickness. When laser light with a wavelength of 800 nm shines on these multiple quantum wells, it induces an oscillating mode known as a zone-folded longitudinal acoustic phonon (ZFLAP), in which the GaAs layers expand when the AlGaAs layers contract, and contract when the AlGaAs layers expand. The thickness of GaAs-AlGaAs layer pairs (which make up the smallest repeating unit, or unit cell, in the structure) does not change, because the motion in neighboring well elements is opposite.

Such a unit cell–preserving motion is called an optical phonon mode, whereas an expansion, compression, or other distortion of the whole unit cell is called an acoustic phonon mode. As its name implies, a ZFLAP is an acoustic mode with respect to the atoms in the GaAs, because these layers expand and contract. But it is an optical mode with respect to the overall structure.

Why does the light excite such oscillating modes? More than one mechanism has been proposed. In one mechanism, called impulsive Raman scattering, a very short pulse of light literally kicks the lattice, sending it into motion. The momentum transferred in this kick depends on the strength of the light pulse, but it is typically tiny. Nevertheless, impulsive Raman scattering can be the dominant excitation mechanism for optical phonons, particularly in transparent materials.

Other mechanisms require optical absorption. At 800 nm, the GaAs layers are opaque, whereas the AlGaAs layers are transparent. In the opaque GaAs, absorption of light excites electron-hole pairs. This excitation can change the equilibrium distances between atoms, essentially creating instantaneous strain that relaxes via expansion or contraction of the material. This is called displacive excitation.

Impulsive and displacive excitations cause different types of oscillation. The difference can be easily demonstrated with a simple pendulum (see the figure). You can see this for yourself with a pencil lightly held by its eraser or by a string, hanging straight down. You can also make a pendulum by holding your computer mouse by its cord. Starting with your pendulum at rest, give it a tap to set it in motion. This is impulsive excitation. Observe that the distance away from equilibrium oscillates in time as $\sin(\omega t)$, where ω is the angular frequency of oscillation. Now start with the pendulum at rest

The author is at the Department of Physics, University of Michigan, Ann Arbor, MI 48109 and the Stanford Synchrotron Radiation Laboratory, Menlo Park, CA 94025, USA. E-mail: phb@umich.edu

again, and this time suddenly displace the top of the pendulum sideways, and watch how the bottom end catches up. It oscillates about its new equilibrium position according to cos(ωt). This is displacive excitation.

Naturally, there are many other effects and details to consider, such as heating, diffusion of electrons, and the specifics of the Raman impulse. To a first approximation, however, the ZFLAP excitation mechanism is revealed by the phase of the resulting oscillation—sine or cosine. To find out which mechanism dominates, one therefore needs to take snapshots of the atomic motion at precise intervals after excitation has taken place.

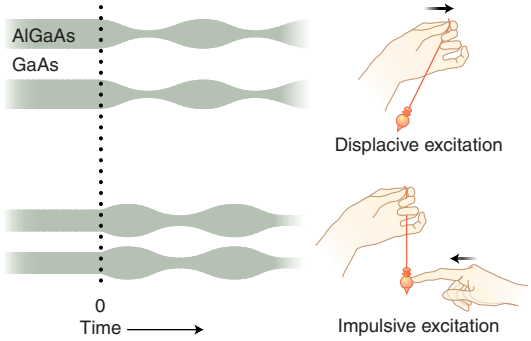

How crystals oscillate. (Left) Displacive and impulsive excitations can be distinguished by the phase of the oscillations. The distortions are greatly exaggerated in these drawings to show that displacive excitations oscillate as cos(ωt), whereas impulsive excitations oscillate as sin(ωt). **(Right)** A pendulum can be used to demonstrate the two excitation mechanisms.

X-ray diffraction from the planes of atoms in the crystal can be used to take such snapshots if the x-ray pulse is short enough, just as a flashbulb freezes motion. The structural question is very simple: What is the spacing between atomic layers? On the other hand, the timing is very difficult. To capture the motion, the x-ray pulses must be much less than 1 ps in duration. Such pulses can be created with a laser-induced plasma, which generates a burst of x-rays from a tiny metal target, timed precisely to the laser that excites the ZFLAP's. With this method, Bargheer *et al.* show that cosine oscillations dominate in their multiple quantum wells, and that the excitation must therefore be displacive.

This is not the first time that ultrafast x-rays have been used to probe optical phonons. Other groups have pioneered the production of subpicosecond x-ray pulses (*2, 3*) and their use in resolving optical phonons and revealing their structural dynamics (*4*). Bargheer *et al.* built on these previous results and also implemented substantial improvements in the average x-ray flux and the laser repetition rate.

As the authors point out, such advances pave the way for many future studies of chemical and solid-state dynamics using ultrafast x-rays. Many laboratories around the world are developing similar sources using plasmas or electron accelerators (*5*), and x-ray free-electron lasers will soon provide much brighter ultrafast x-rays (*6*). Ultrafast x-rays from these new sources will reveal with ever greater clarity the atomic motion in molecules and crystals.

References

1. M. Bargheer *et al.*, *Science* **306**, 1771 (2004).
2. C. Rischel *et al.*, *Nature* **390**, 490 (1997).
3. C. W. Siders *et al.*, *Science* **286**, 1340 (1999).
4. K. Sokolowski-Tinten *et al.*, *Nature* **422**, 287 (2003).
5. L. Bentson *et al.*, *Nuclear Instrum. Methods* **507**, 205 (2003).
6. J. Andruszkow *et al.*, *Phys. Rev. Lett.* **85**, 3825 (2000).

10.1126/science.1106755

BIOMEDICINE

Prion Dormancy and Disease

Robin W. Carrell

There has been concern that the outbreak of mad cow disease (bovine spongiform encephalopathy, or BSE) in the United Kingdom would result in a large-scale spread of the infection to humans. Public worries, however, appear to have been allayed by the fading of the current epidemic (*1*) of the human form of mad cow disease, variant Creutzfeldt-Jacob disease (vCJD). Yet recent survey findings (*2*) and blood transfusion studies (*3*, *4*) raise deep concerns among prion researchers that many more cases of undetected prion protein infection may underlie the overt epidemic. It is crucial to know whether such apparently dormant carriers are themselves infective and whether they are at risk of eventually developing clinical disease. The need for more extensive clinical surveys in the UK is a priority, but the urgency for these and other follow-up studies has been dampened by the disparate nature of recent findings, which are readily dismissed by some as "atypical" or of "uncertain significance." These reasons for inaction are rebutted by the experimental studies of Wadsworth *et al.* (*5*) reported on page 1793 of this issue. Using transgenic mice expressing the normal human prion protein, they show that an amino acid sequence variation (polymorphism) at position 129 of this protein drastically affects the infectivity and clinical consequences of BSE and vCJD infection.

The normal human prion protein expressed by brain neurons can undergo an aberrant change in conformation, resulting in misfolded forms that self-propagate. These aberrant prion proteins produce characteristic neurodegenerative changes in brain tissue resulting in a progressive and fatal encephalopathy (*6*, *7*). This disease process occurs sporadically in humans: Each year one in a million deaths worldwide is attributed to the spontaneous development of Creutzfeldt-Jakob disease (CJD). Consequently, based on a life expectancy of 70 years, one in 15,000 people will die from CJD, with the likelihood that rather more than that number are infected but die from other causes. Thus, humans have always been exposed to CJD, but because the spread of the disease requires either the direct ingestion or injection of infected tissues, CJD has remained a sporadic disease confined to a few individuals. Historically, the great risk to our species from prion protein infection has come from cannibalism, as evidenced by the devastating kuru epidemic among the Fore tribe of Papua New Guinea. Evolution has provided some protection against this threat: Variations at critical amino acids in the normal human prion protein se-

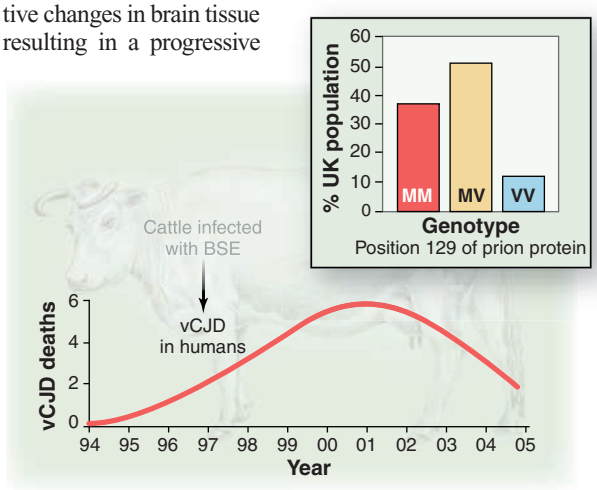

A waning epidemic? Projected incidence in the UK of vCJD (deaths per 3 months), the human form of mad cow disease (*1*). A total of 150 people have been affected, all of whom carry one genotype (129MM), which is present in just 37% of the population (**Inset**).

CREDIT: (TOP) PRESTON HUEY/*SCIENCE*; (BOTTOM) KATHARINE SUTLIFF/*SCIENCE*

The author is at the Cambridge Institute for Medical Research, University of Cambridge, Cambridge CB2 2XY, UK. E-mail: rwc1000@cam.ac.uk

quence limit susceptibility to infective propagation of aberrant forms of the prion protein (*8*). Notably, a polymorphism at position 129 of the normal human prion protein—either a valine (V) or a methionine (M)—provides some protection against kuru among 129MV heterozygous individuals. In contrast, 129MM homozygotes are particularly susceptible to prion infection (*9*).

The protective effect of a valine rather than a methionine at position 129 is evident in the current vCJD epidemic in the UK. This epidemic is a consequence of widespread infection of cattle with BSE from the early 1980s to 1996. During this period, hundreds of thousands of infected cattle entered the food chain (*10*). The consequent cross-species infection of humans with BSE resulted in the new variant form of prion encephalopathy called vCJD. This disease differs from sporadic human CJD in both brain tissue pathology and in the electrophoretic pattern that classifies each of the aberrant forms of prion protein. The UK vCJD epidemic, which now appears to be fading at 150 cases (*1*), has two striking features (see the figure). All of the affected individuals are 129MM homozygotes, and most are young, less than 30 years old. The tailing-off of this epidemic has been assumed by many to be the end of the vCJD threat, but to those involved in prion research it seems unlikely that infection would be confined to just one age group or to a single genotype. These fears are supported by recent findings.

In a UK survey of 12,700 surgically removed appendices, three stained positively for prion protein accumulation, indicating an unexpectedly high rate of infection, equivalent at a national level to thousands of infected individuals (*2*). Doubts as to the significance of the appendix survey findings have been answered by later studies of two recipients of blood transfusions from a donor who subsequently developed vCJD. The first recipient, who had a 129MM genotype, developed vCJD with typical clinical and histological changes 6 years after transfusion (*3*). But the critical findings came from autopsy of the second recipient, of genotype 129MV, who remained in good neurological health but died 5 years after the transfusion from a ruptured aortic aneurysm (*4*). Autopsy showed no evidence of brain involvement, but a pattern of prion protein accumulation was observed in lymphoid tissue similar to the diffuse deposition seen in the positive specimens in the appendix survey. The overall conclusion from these studies is that there are two levels of infection: one that results in overt vCJD, as in the genotype 129MM transfusion recipient, and another that results in a subclinical or dormant carrier state, as in the 129MV recipient.

These conclusions are strongly supported by the new study of Wadsworth *et al*. (*5*). These investigators analyzed transgenic mice expressing the 129MM or 129VV variant of the normal human prion protein for susceptibility to infection with BSE or vCJD. Exposure of 129MM mice to vCJD resulted in the consistent development of clinical disease, whereas 129VV mice were relatively resistant to infection. The infection that did occur in 129VV mice resulted in the atypical diffuse deposition of prion protein that was also observed in the human appendix and transfusion studies. Moreover, subpassage of brain tissue from infected 129VV mice resulted in typical vCJD infection among 129MM mouse recipients, but only in subclinical and atypical infection among 129VV mice.

These findings underscore the quandary faced by public health officials in the UK. Are the thousands of dormant carriers of vCJD indicated by the appendix survey at risk of developing clinical disease? Are they infective to others, or only to 129MM individuals, or not at all? Or are the survey findings just a manifestation of dormant sporadic CJD present in all populations? These questions need to be addressed with priority and urgency. The answers are vital to the future practice of blood transfusion, surgery, and dentistry in the UK and for health services in other countries. Progress is frustratingly slow. Essential follow-up studies and access to data are being hindered or even prevented by demands for patient anonymity (*2*) or by medico-legal concerns (*4*). Such reservations are out of proportion to the potential threats posed by a resurgence of vCJD infection in the UK. Progress will require political will. Meanwhile, prion researchers watch the inaction with dismay.

References

1. N. J. Andrews, The UK Creutzfeldt-Jakob Disease Surveillance Unit, www.cjd.ed.ac.uk/vcjdqshort.htm (accessed 6 November 2004).
2. D. A. Hilton *et al., J. Pathol.* **203**, 733 (2004).
3. C. A. Llewelyn *et al., Lancet* **363**, 417 (2004).
4. A. H. Peden *et al., Lancet* **364**, 527 (2004).
5. J. D. F. Wadsworth *et al., Science* **306**, 1793 (2004); published online 11 November 2004 (10.1126/science.1103932).
6. S. B. Prusiner, *Science* **278,** 245 (1997).
7. S. J. Collins, V. A. Lawson, C. L. Masters, *Lancet* **363**, 51 (2004).
8. S. Mead *et al., Science* **300**, 640 (2003).
9. H. S. Lee *et al., J. Infect. Dis.* **183**, 192 (2001).
10. R. M. Anderson *et al., Nature* **382**, 779 (1996).

10.1126/science.1106679

DEVELOPMENTAL BIOLOGY

Bits and Pieces

Alessandro Minelli

The body architecture of vertebrates, arthropods, and annelids is composed of segments. The segmentation of individual organs—epithelial, muscular, neural, excretory, reproductive—often arises independently of body segmentation. To obtain "true" segments (integrated modules repeated along the main body axis), these two developmental processes must be integrated. Sometimes, however, independent segmentation patterns survive within the same animal. A good example is the independent seriation of gill arches and vertebrae in vertebrates (*1*). Thus, segments are often permanent and functionally relevant features of body organization, although in terms of development, they may be little more than a way to distribute clumps of precursor cells in regular patterns (*2*, *3*).

Recent interest in the molecular mechanisms of segmentation, and the popular but questionable view that Urbilateria (the last common ancestor of all bilaterally symmetrical metazoans) could have been segmented, have stimulated debate about the nature of this conspicuous feature of animal architecture. For example, are the somites of vertebrate mesoderm equivalent to the serially repeated units of fruit fly ectoderm? Is a tapeworm segmented, or should its chain of body units be viewed as a linear colony of autonomous individuals?

Segmentation anomalies are not limited to comparisons among distantly related phyla, but are sometimes found at lower taxonomic scales, even within the same animal (*4*). Take the millipede. Next to the head, whose segmental composition is a problem in itself, there is an elongated trunk subdivided into units whose segmental nature is far from obvious. In most arthropods there is close correspondence between segments and appendages: Some segments are limbless, but whenever limbs are present, there is exactly one limb pair on each body segment. It is different for millipedes: The first trunk unit is limbless and is followed by three seemingly conventional segments plus a longer series of units, each with two pairs of legs and other lateral and ventral "double" features. This mismatch between dorsal and ventral aspect has prompted several explanations, the most fashionable of which pos-

The author is in the Department of Biology, University of Padova, I 35131 Padova, Italy. E-mail: alessandro.minelli@unipd.it

tulates that sets of two "true" segments are incompletely fused to form "diplosegments." In pill millipedes—short-body arthropods that roll up like armadillos—there is another complication due to the putative fusion of anterior dorsal plates (see the figure).

Developmental genetics had been completely silent about the mechanisms of millipede segmentation, until Janssen *et al*. analzyed segmentation in the pill millipede

Glomeris marginata (*5*). They report that segmentation genes in the dorsal and ventral sides of the embryo are expressed independently. They argue that the dorsal and ventral segments are independent units and not dorsal and ventral aspects of trunk segments or diplosegments. They discovered that the *wingless* gene is expressed in ventral segments only, whereas *engrailed*, *hedgehog*, and *cubitus interruptus* are expressed both dorsally and ventrally but in different expression patterns.

The major divergence from the developmental gene expression patterns of the fruit fly *Drosophila* and other arthropods is the dorsal expression of these genes, which is shifted by half a segmental unit that is delimited by intersegmental grooves in the growing embryo. In the pill millipede, gene expression seems to mark the posterior borders of the millipede's dorsal plates. As these plates are mineralized (*6*), they may be analogous to the shell of mollusks, the margin of which is demarcated by expression of the *engrailed* gene (*7*). Dorsal expression of *engrailed* in the pill millipede could be related to biomineralization rather than to segmentation. This does not imply conservation of biomineralization from mollusks to arthropods, but rather provides evidence of repeated independent cooption of the *engrailed* gene among different phyla. Later in development, the dorsal and ventral segments of the pill millipede become aligned, giving rise to the serial organization of the animal's trunk. In terms of function, the result is no different than if the trunk had been built out of a series of "true" segments. It is clear that the millipede body is not formed by serially adding complete segmental units one after the other. "True" segments simply do not exist, at least in this arthropod.

The Janssen *et al.* findings raise two interesting phylogenetic questions. First, are the independent expression patterns of segmentation genes found in the pill millipede shared by other members of this group, including those with a more typical cylindrical shape (*5*)? The basal position of pill millipedes among the Diplopoda (*8*) supports this prediction.

Second, within arthropods, is segmentation in the pill millipede a primitive or derived event? I suspect that the mismatch in gene expression between dorsal and ventral segments is an ancient feature, particularly given the morphology of several long-extinct groups. It is possible that those Paleozoic arthropods with different serially repeated structures may eventually be grouped with millipedes in a clade that excludes other modern arthropods. Recent advances in arthropod molecular phylogeny make this a hypothesis worth testing (*9*, *10*). A better understanding of segmentation mechanisms will enable the validity of the recently defined subphylum Myriochelata (the Chelicerata plus the Myriapoda) (*9*) to be tested. In members of this putative group, both extinct and extant, there is nothing comparable to the "textbook" segments regarded as the true building blocks of arthropod bodies. All of these animals share a series of individual features that are serially repeated along the main body axis. These features are not integrated into anatomically and functionally individual segments, as is usually the case in the insect thorax and abdomen. Far from being a primitive feature of arthropods, these units may be the product of historical changes in the genetic mechanisms of segmentation that have been fostered by the adaptive value gained from the different resulting morphologies (*11*, *12*).

References

1. P. H. W. Holland, *Semin. Dev. Biol.* **1**, 135 (1990).
2. P. A. Lawrence, *The Making of a Fly* (Blackwell, Oxford, 1992).
3. V. Braun *et al.*, *Bioinformatics* **19**, 851 (2003).
4. A. Minelli, *The Development of Animal Form* (Cambridge Univ. Press, Cambridge, 2003).
5. R. Janssen *et al.*, *Dev. Biol.* **268**, 89 (2004).
6. A. Ansenne, P. Compere, G. Goffinet, in *Proceedings of the 7th International Congress of Myriapodology*, A. Minelli, Ed. (Brill, Leiden, Netherlands, 1990), pp. 125–134.
7. D. K. Jacobs *et al.*, *Evol. Dev.* **2**, 340 (2000).
8. P. Sierwald *et al.*, *J. Zool. Syst. Evol. Res.* **41**, 87 (2003).
9. D. Pisani *et al.*, *BMC Biol.* **2**, 1 (2004).
10. E. Negrisolo *et al.*, *Mol. Biol. Evol.* **21**, 770 (2004).
11. G. E. Budd, *Evol. Dev.* **3**, 332 (2001).
12. A. Minelli, G. Fusco, *Trends Ecol. Evol.* **19**, 423 (2004).

10.1126/science.1098138

EVOLUTION

Sex...Only If Really Necessary in a Feminine Monarchy

Raghavendra Gadagkar

The honey bee society was famously described as "The Feminine Monarchy" by the cleric Charles Butler in 1634. Honey bees and their relatives—including all hymenopteran societies—qualify for this label because their colonies are headed by one or a small number of fertile queens. These queens produce a large number of sterile or nearly sterile daughter workers and, later, with their assistance, produce a smaller number of fertile sons and daughter queens (*1*). The complex and diverse life cycles and social organization of the feminine monarchies are matched by their equally complex and diverse strategies for sexual and asexual reproduction (*2*). On page 1780 of this issue, Pearcy *et al*. (*3*) uncover a new dimension in the complexity of hymenopteran reproduction.

In the Hymenoptera, males are typically haploid and females are diploid (see the figure). It has been shown that sex is determined by a highly variable sex determination locus such that homozygosity (a very rare possibility, given the low probability of a female mating with a male having the same allele as herself) or hemizygosity (expected in all haploid individuals) results in male development, whereas heterozygosity results in female development (*4*). In social Hymenoptera, virgin queens make nuptial flights during which they acquire sperm from one or more males and store and nurture the sperm in their spermatheca—a tiny gland that opens into the oviduct. Queens have perfect control over the sex of their offspring. To produce daughters, a queen lets sperm flow from the spermatheca into her oviduct and then lays fertilized diploid eggs. Whether the diploid eggs develop into sterile workers or fertile queens depends on the nutritional environment of the young larvae. To produce sons, however, a queen prevents the flow of sperm into the oviduct and lays unfertilized haploid eggs. Such parthenogenetic development of males—known as arrhenotoky—is a universal and well-known feature of the Hymenoptera. Less widely known (and apparently rather infrequent) is another form of

The author is in the Centre for Ecological Sciences, Indian Institute of Science, 560 012 Bangalore, India, and the Evolutionary and Organismal Biology Unit, Jawaharlal Nehru Centre for Advanced Scientific Research, Jakkur, 560 064 Bangalore, India. E-mail: ragh@ces.iisc.ernet.in

CREDIT: MARCO ULIANA

parthenogenesis known as thelytoky, which permits the production of diploid daughters without the need for a paternal genome (*1*).

Thelytoky (of the kind referred to as automictic) involves the secondary fusion of two nonsister haploid nuclei after the meiotic second division. Automictic thelytoky restores diploidy and yet has the potential for maintaining heterozygosity at the sex determination locus, so that the sex of the resulting adult is female. Although thelytoky has been suspected as a minor form of reproduction in many species, it has been unequivocally demonstrated in one honey bee species (*Apis mellifera capensis*) and five phylogenetically distant species of ants. In all of these six cases, workers use thelytoky to produce diploid female offspring, even though they cannot mate. Thelytoky thus gives workers a degree of freedom from their queens, inasmuch as they themselves can produce both male and female offspring. For this reason, thelytoky may also be interpreted as an attempt by the workers to revolt against the hegemony of the queen, and as a potential early step in the eventual loss of sociality (*5*).

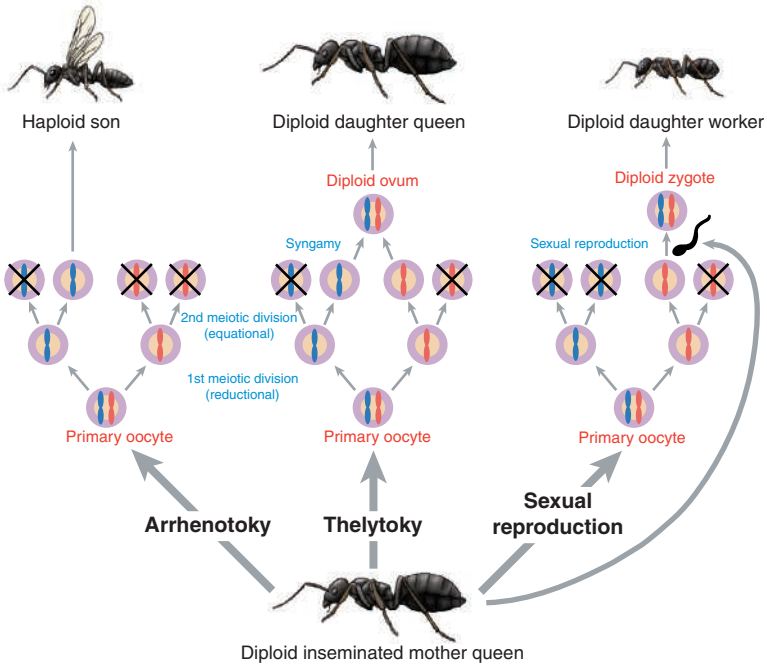

Diversity of reproductive strategies. The European ant *C. cursor* uses arrhenotoky to produce haploid sons, thelytoky to produce diploid daughter queens, and normal sexual reproduction to produce diploid daughter workers (*3*). The process of oogenesis results in one egg pronucleus and four polar bodies at the end of the meiotic second division. The polar bodies degenerate (indicated by an X). During arrhenotoky, the cell bearing the egg pronucleus develops parthenogenetically into a haploid adult male. During sexual reproduction, the cell bearing the egg pronucleus is fertilized by a sperm from the queen's spermatheca to produce a diploid zygote that develops into a female offspring, a daughter worker. In thelytoky, two nonsister haploid nuclei produced during the second meiotic division fuse secondarily to restore diploidy without the need for a paternal genome. The resulting diploid ovum develops into a viable female offspring, a daughter queen.

But what Pearcy *et al*. (*3*) have found in the European formicine ant, *Cataglyphis cursor*, is radically different. In this species, workers in orphaned colonies were already known to produce diploid female offspring (both workers and queens). Now it appears that queens themselves use thelytoky to produce daughter queens. The authors genotyped workers and queens collected from field colonies as well as laboratory-raised workers and gynes (queens) at four highly polymorphic microsatellite loci. Their results provide unambiguous evidence that perhaps a small fraction of the workers but certainly the large majority of laboratory-raised gynes (54 of 56 gynes studied) were produced by the queens through thelytoky. Confidence in thelytoky as the mode of production of the gynes arises from the fact that all of them only carried alleles that could be attributed to the mother queen. The probability that this could be the result of a chance mating of the queens with males carrying alleles identical to their own is estimated at less than 10^{-28}!

Apparently, then, *C. cursor* queens use arrhenotoky to produce male offspring, normal sexual reproduction to produce worker progeny, and thelytoky to produce daughter queens (see the figure). The most striking consequence of this complex strategy, which the authors emphasize, is in the context of the cost of sex. Sexual reproduction involves a twofold cost because, relative to a parthenogenetic mother, a sexually reproducing mother transmits only half the number of her genes to each offspring (*6*). This genetic cost is thought (more precisely, hoped!) to be offset by the advantages of sexual reproduction in terms of enhanced genetic variability of the offspring. Such genetic variability is expected to be useful in dealing with variable environments—the physical environment to some extent, but biological environments such as rapidly adapting parasites in particular (*7*). *C. cursor* queens appear to forgo this benefit and save on the cost of sex while producing daughter queens, but reap the benefits of sex while producing daughter workers. Because workers are generally sterile and do not constitute a way for the queens to transmit their genes to future generations, the twofold cost of sex is irrelevant during their production. On the other hand, the benefits of sexual reproduction are expected to be profound. Workers are much more exposed than queens to different physical and biological environments. More important, genetic diversity among workers is known to facilitate efficient division of labor, driven by a genetic predisposition for task specialization (*8*). Daughter queens, by contrast, are the mode for transmitting genes to future generations, making the twofold cost of sex entirely relevant during their production. Pearcy *et al*. (*3*) make the reasonable argument that queens are relatively protected from the environment, so that the lack of genetic variability may not be as serious a problem for them. In short, *C. cursor* queens seem to have the best of both worlds—they reap the benefit of sex where it is most needed and the benefit of thelytoky where it is most affordable.

If *C. cursor* uses such a wonderful strategy, why don't other social Hymenoptera do so? One possibility is that too few species have been studied in sufficient detail to conclude that this strategy is not more widespread (*1*). Alternatively, this may be an artifact of gyne production in the laboratory—an unlikely possibility but one that has not yet been ruled out. Perhaps the most interesting possibility is that the luxury of mixing sex and nonsex in this way is not available to all. What then is special about *C. cursor*? Do their queens not need genetic variability, or do they mix sex and nonsex even while producing queens in nature? Genetic variability may, of course, be more important in some environments than others and more important for some species than others. There is also the intriguing possibility that the advantage of thelytoky for queens may be offset by the danger of such a powerful tool falling into the clutches of the workers, who could then use it for subversive purposes. Clearly, the time is ripe for theoretical and empirical investigations of a new paradigm: sex versus nonsex in the service of queens and workers.

References

1. E. O. Wilson, *The Insect Societies* (Belknap/Harvard, Cambridge, MA, 1971).
2. R. H. Crozier, P. Pamilo, *Evolution of Social Insect Colonies—Sex Allocation and Kin Selection* (Oxford Univ. Press, Oxford, 1996).
3. M. Pearcy, S. Aron, C. Doums, L. Keller, *Science* **306**, 1780 (2004).
4. M. Beye *et al*., *Cell* **114**, 419 (2003).
5. R. Gadagkar, *Curr. Sci.* **72**, 950 (1997).
6. J. Maynard Smith, *The Evolution of Sex* (Cambridge Univ. Press, Cambridge, 1978).
7. W. D. Hamilton, *Oikos* **35**, 282 (1980).
8. R. E. Page Jr. *et al*., *Nature* **338**, 576 (1989).

10.1126/science.1106673

INTRODUCTION

Opportunity Runneth Over

Actually, the Opportunity rover never did run across the martian surface; it was more like a stop-and-go boogie at an average crawl of 3.6 meters per hour. Nor did the mobile rover go very far in its first 56 sols and 56 nights, spending most of its sunlit working hours in the 20-meter-diameter Eagle crater that it serendipitously bounced into. Still, it was the hottest rover on six wheels, on this cold and desolate planet, from the moment that it put up its mast and scanned the broken but distinct outcrop that rimmed part of its landing site. Never before had a slab of martian bedrock been seen or touched by robotic inquisitiveness, including NASA's successful predecessors: Spirit from the Mars Exploration Rovers (MER) mission, Sojourner rover from the Pathfinder mission, and the landers from the Viking 1 and 2 missions. Here within Meridiani Planum, just meters from the landing pod, was a layered rock, bent and fractured by impact events, but still partially intact and providing a history of environmental changes.

Opportunity turned a trickle of in situ evidence for liquid water on Mars into a flood. After the overview of the first 90 sols of the mission by Squyres *et al*. (p. 1698), the next eight papers describe in some detail the fine-scale layering, the hydrated minerals, the enrichment of sulfur, and the salty surfaces that suggest that the layered rock formed by repeated cycles of flooding, evaporation, and desiccation or erosion. Opportunity also found the source of the hematite (Fe_2O_3) that was remotely sensed over hundreds of kilometers by the Thermal Emission Spectrometer (TES) on the Mars Global Surveyor orbiter. The hematite is mostly concentrated in millimeter-sized spherules, initially called blueberries by the MER team. The spherules are embedded in the layered rocks and distributed as loose particles on the plains. These plains probably represent a lag deposit: a thin layer of larger particles left over after disaggregation of the rocks and removal of smaller particles by the wind. The embedded spherules are randomly oriented relative to the layering, which suggests that they formed later by secondary alteration. The last two papers describe the composition, opacity, and dynamics of the martian atmosphere measured with the instruments on Spirit and Opportunity.

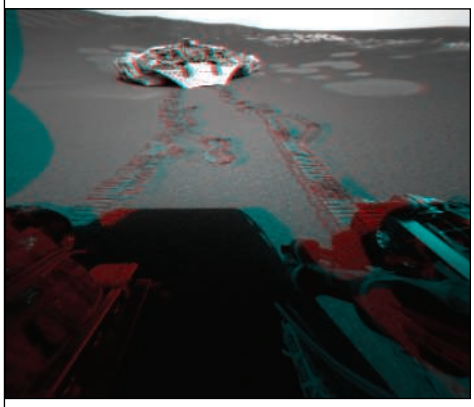

In his Perspective (p. 1689), Kargel offers one scenario to explain the bedrock. There are other possible scenarios; however, they all require liquid water and acidic conditions. Both MER rovers are still collecting data almost a year later, and Spirit has recently found some bedrock too. The flood of new in situ evidence for liquid water allows for the possibility of microbial organisms living, perhaps transiently, when the acidic brines were active, like terrestrial acidophiles. Opportunity's run is definitely not over yet.

–LINDA ROWAN

CONTENTS

RESEARCH ARTICLES AND REPORTS

See also Perspective on page 1689 and Report on page 1758.

CREDIT: JPL/NASA

Science

Published by AAAS

RESEARCH ARTICLE

The Opportunity Rover's Athena Science Investigation at Meridiani Planum, Mars

S. W. Squyres,[1]* R. E. Arvidson,[2] J. F. Bell III,[1] J. Brückner,[3] N. A. Cabrol,[4] W. Calvin,[5] M. H. Carr,[6] P. R. Christensen,[7] B. C. Clark,[8] L. Crumpler,[9] D. J. Des Marais,[10] C. d'Uston,[11] T. Economou,[12] J. Farmer,[7] W. Farrand,[13] W. Folkner,[14] M. Golombek,[14] S. Gorevan,[15] J. A. Grant,[16] R. Greeley,[7] J. Grotzinger,[17] L. Haskin,[2] K. E. Herkenhoff,[18] S. Hviid,[19] J. Johnson,[18] G. Klingelhöfer,[20] A. H. Knoll,[21] G. Landis,[22] M. Lemmon,[23] R. Li,[24] M. B. Madsen,[25] M. C. Malin,[26] S. M. McLennan,[27] H. Y. McSween,[28] D. W. Ming,[29] J. Moersch,[28] R. V. Morris,[29] T. Parker,[14] J. W. Rice Jr.,[7] L. Richter,[30] R. Rieder,[3] M. Sims,[10] M. Smith,[31] P. Smith,[32] L. A. Soderblom,[18] R. Sullivan,[1] H. Wänke,[3] T. Wdowiak,[33] M. Wolff,[34] A. Yen[14]

The Mars Exploration Rover Opportunity has investigated the landing site in Eagle crater and the nearby plains within Meridiani Planum. The soils consist of fine-grained basaltic sand and a surface lag of hematite-rich spherules, spherule fragments, and other granules. Wind ripples are common. Underlying the thin soil layer, and exposed within small impact craters and troughs, are flat-lying sedimentary rocks. These rocks are finely laminated, are rich in sulfur, and contain abundant sulfate salts. Small-scale cross-lamination in some locations provides evidence for deposition in flowing liquid water. We interpret the rocks to be a mixture of chemical and siliciclastic sediments formed by episodic inundation by shallow surface water, followed by evaporation, exposure, and desiccation. Hematite-rich spherules are embedded in the rock and eroding from them. We interpret these spherules to be concretions formed by postdepositional diagenesis, again involving liquid water.

The Mars Exploration Rover Opportunity landed in Eagle crater on Meridiani Planum on 24 January 2004 UTC, 21 days after the landing of Spirit at Gusev crater (*1*). Both vehicles landed using a variant of the airbag landing system that was developed for Mars Pathfinder, deploying the rovers after the landers had come to rest on the surface (*2*). The primary scientific objective of their mission is to explore two sites on the martian surface where water may once have been present, and to assess past environmental conditions at those sites, including their suitability for life. Here we provide an overview of the results from the 90-sol (*3*) nominal mission of Opportunity.

Like Spirit, Opportunity carries the Athena science payload (*4*). The topography, morphology, and mineralogy of the scene around the rover are revealed by a panoramic camera [Pancam (*5*)] and a miniature thermal emission spectrometer [Mini-TES (*6*)]. Both instruments view the scene using a mast (*4*) at a height of about 1.5 m above the ground. The payload also includes a 5-degree-of-freedom robotic arm (*4*). The arm carries an Alpha Particle X-ray Spectrometer [APXS (*7*)] that measures elemental abundances of rocks and soils and a Mössbauer Spectrometer (*8*) that determines the mineralogy and oxidation state of Fe-bearing phases. It also carries a Microscopic Imager [MI (*9*)] that is used to obtain high-resolution (30 μm per pixel) images of rock and soil surfaces (*10*) and a Rock Abrasion Tool [RAT (*11*)] that can remove up to ~5 mm of material over a circular area 45 mm in diameter. Finally, the payload includes seven magnets that attract fine-grained magnetic materials and can be viewed by payload instruments (*12*).

The rover itself uses a six-wheel rocker-bogie suspension system and onboard autonomous navigation and hazard avoidance capability, allowing traverse distances of tens of meters per sol (*2*). Navigation and hazard avoidance are aided by two monochromatic navigation cameras (Navcams) mounted on the mast and by four hazard avoidance cameras (Hazcams) mounted in fore- and aft-facing stereo pairs on the rover body (*13*).

The Meridiani Planum landing site (*14*) was chosen for Opportunity because its smooth flat topography would favor a safe landing and because Mars Global Surveyor TES data showed it to contain ~15 to 20% (by fractional area) of the mineral hematite (*15*). Hematite can form by a number of processes, many of which involve the action of liquid water. Orbital images showed that the hematite-bearing unit is the top stratum of a layered sequence about 600 m thick that overlies Noachian cratered terrain (*16–18*). We landed on this sequence with the hope that the hematite was an indicator that aqueous processes had been involved in its formation.

The Rover traverse. Opportunity touched down in the eastern portion of the Meridiani Planum landing ellipse (Plate 5) in an impact crater 20 m in diameter that we named Eagle crater (*19*). The landing site is named the Challenger Memorial Station (*20*). Its location in inertial coordinates was determined by fitting direct-to-Earth two-way

[1]Department of Astronomy, Space Sciences Building, Cornell University, Ithaca, NY 14853, USA. [2]Department of Earth and Planetary Sciences, Washington University, St. Louis, MO 63130, USA. [3]Max Planck Institut für Chemie, Kosmochemie, Mainz, Germany. [4]NASA Ames Research Center/SETI Institute, Moffett Field, CA 94035, USA. [5]Department of Geological Sciences, University of Nevada, Reno, NV 89557, USA. [6]U.S. Geological Survey, Menlo Park, CA 94025, USA. [7]Department of Geological Sciences, Arizona State University, Tempe, AZ 85287, USA. [8]Lockheed Martin Corporation, Littleton, CO 80127, USA. [9]New Mexico Museum of Natural History and Science, Albuquerque, NM 87104, USA. [10]NASA Ames Research Center, Moffett Field, CA 94035, USA. [11]Centre d'Etude Spatiale des Rayonnements, Toulouse, France. [12]Enrico Fermi Institute, University of Chicago, Chicago, IL 60637, USA. [13]Space Science Institute, Boulder, CO 80301, USA. [14]Jet Propulsion Laboratory, California Institute of Technology, Pasadena, CA 91109, USA. [15]Honeybee Robotics, New York, NY 10012, USA. [16]Center for Earth and Planetary Studies, Smithsonian Institution, Washington, DC 20560, USA. [17]Department of Earth, Atmospheric, and Planetary Sciences, Massachusetts Institute of Technology, Cambridge, MA 02139, USA. [18]U.S. Geological Survey, Flagstaff, AZ 86001, USA. [19]Max Planck Institut für Aeronomie, Katlenburg-Lindau, Germany. [20]Johannes Gutenberg-University, Mainz, Germany. [21]Botanical Museum, Harvard University, Cambridge MA 02138, USA. [22]NASA Glenn Research Center, Cleveland, OH 44135, USA. [23]Department of Atmospheric Sciences, Texas A&M University, College Station, TX 77843, USA. [24]Department of Civil and Environmental Engineering and Geodetic Science, Ohio State University, Columbus, OH 43210, USA. [25]Niels Bohr Institute, Ørsted Laboratory, Copenhagen, Denmark. [26]Malin Space Science Systems, San Diego, CA 92191, USA. [27]Department of Geosciences, State University of New York, Stony Brook, NY 11794, USA. [28]Department of Earth and Planetary Sciences, University of Tennessee, Knoxville, TN 37996, USA. [29]NASA Johnson Space Center, Houston, TX 77058, USA. [30]DLR Institute of Space Simulation, Cologne, Germany. [31]NASA Goddard Space Flight Center, Greenbelt, MD 20771, USA. [32]Lunar and Planetary Laboratory, University of Arizona, Tucson, AZ 85721, USA. [33]Department of Physics, University of Alabama at Birmingham, Birmingham, AL 35294, USA. [34]Space Science Institute, Martinez, GA 30907, USA.

*To whom correspondence should be addressed. E-mail: squyres@astro.cornell.edu

X-band Doppler radio transmissions and two passes of UHF two-way Doppler between Opportunity and Mars Odyssey. The lander location is 1.9483°S, 354.47417°E based on analyses of these data, translated to Mars Orbiter Laser Altimeter (MOLA)–based International Astronomical Union 2000 coordinates. The lander is located at 1.9462°S, 354.4734°E based on analyses of horizon features seen in panoramas and also observed in Mars Global Surveyor Mars Orbiter Camera (MOC) images.

Early Navcam images of the site (Fig. 1) revealed that the surface around the lander consisted of dark, fine-grained soil. Less than 10 m away from the lander was an exposure of layered bedrock in the slope of the crater wall. Egress from the lander took place on sol 7. Post-egress investigation of the soil adjacent to the lander showed it to be sprinkled with small spherules, typically 4 to 6 mm in diameter. (These spherules have become known informally as "blueberries" although their color is gray rather than blue.) On sol 14, we approached the outcrop at its closest point to the lander, a location we named Stone Mountain. Pancam and MI images showed that the spherules were weathering out of the outcrop, and APXS measurements revealed that the sulfur content of the outcrop was high. Mössbauer results suggested that the sulfate mineral jarosite was present, and Mini-TES results indicated the presence of Mg and Ca sulfates. Sols 16 to 19 were spent driving along the exposed outcrop, acquiring Pancam images for use in planning future activities. This was followed on sol 23 by use of the rover wheels to excavate a trench in soil on the crater floor and subsequent investigation of the interior of the trench. On sol 26, we drove the rover to a portion of the rock outcrop called El Capitan that we had identified in the images acquired during sols 16 to 19. Sols 27 to 36 were spent on detailed investigation of the targets Guadalupe and McKittrick on El Capitan and yielded compositional and textural evidence that liquid water had been involved in the formation and diagenesis of the outcrop rock.

On sols 37 and 38, we drove the rover to another portion of the outcrop called Last Chance that we had also identified in the images from sols 16 to 19. Detailed MI imaging of Last Chance on sols 39 and 40 and of another nearby rock called The Dells on sol 41 revealed small-scale ripple cross-lamination that provided evidence that these rocks had been deposited in flowing liquid water. The remaining sols in Eagle crater were spent investigating spherules and soil and showed that the spherules are the primary carriers of hematite at the site.

We drove Opportunity out of Eagle crater on sol 57 to begin a traverse to a much larger nearby crater named Endurance. On sols 64 to 69, we investigated an unusual basaltic rock called Bounce Rock just beyond the rim of the crater. The traverse to Endurance included a stop at a shallow trough called Anatolia (sols 70 to 72), excavation of another trench that cut through an eolian ripple (sol 73), and a stop at a 9-m impact crater called Fram (sols 85 to 88). The longest single-sol traverse, on sol 82, was 140 m. The 90-sol nominal mission ended with Opportunity ~200 m from the rim of Endurance crater and in excellent health. The total traverse distance over the nominal mission was 812 m.

Engineering data from the rover's mobility system were used to characterize materials along the traverse. Slippage during upslope traverses of soil slopes gentler than 10° in Eagle crater was less than 20% but increased rapidly with increasing slope angles (*21*), reaching a maximum of 100% on the first attempt to exit Eagle crater. Slip values are consistent with engineering testbed experience for a rover traveling over dry, loose, poorly sorted sand. Profiles retrieved from engineering data for the long traverse across the plains on sol 82 show standard deviations of the measured elevations of only 3.2 cm over the first 55 m and 40.3 cm over the total traverse distance of 140 m, which is consistent with standard deviations in elevation for Meridiani Planum determined using data from the Mars Global Surveyor MOLA instrument.

Soils. Soils at the landing site (*22*) are dominated by fine-grained basaltic sands, mixed with minor amounts of dust that is derived locally from sulfate-rich outcrops as well as globally from airfall. The first soil analyzed in Eagle crater, called Tarmac, is typical, composed of dark fine-grained olivine basalt sand with ~10% of the Fe present as hematite (*23*, *24*). MI images show the sand to be well sorted, with a mean grain size in the range of 50 to 150 μm (*25*), the size most easily moved by saltation on Mars.

Hematite in the soil is concentrated in spherules and their fragments, which are abundant on nearly all soil surfaces (Fig. 2). The abundance of hematite in Mini-TES data shows significant lateral variability (Plate 3), and the hematite abundance correlates with the abundance of spherules on the surface (*26*). Several trenches excavated using the rover wheels (Plates 14 and 15) showed that the subsurface is dominated by basaltic sand,

Fig. 1. The first image of the martian surface acquired by Opportunity. It is a Navcam image acquired on sol 1, reduced in resolution to 512 × 512 pixels and obtained before deployment of the Pancam Mast Assembly. (Image ID = 1N128285132.)

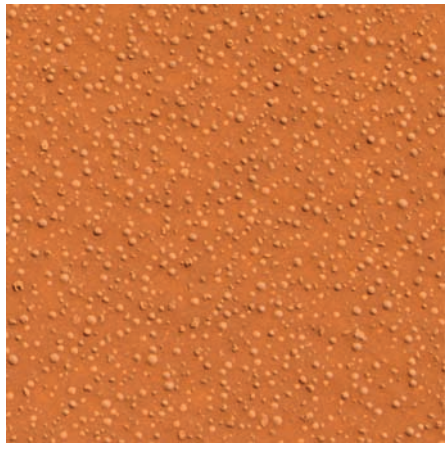

Fig. 2. Pancam image of Meridiani soil, showing a typical concentration of spherules and spherule fragments. Scale across the image is about 25 cm. This is an approximate true-color image, assembled using all of Pancam's left-eye filters. It is a 512 × 512–pixel subframe, acquired at 13:30 local solar time on sol 54.

with a much lower abundance of spherules than at the surface (*21*). The surface concentration of spherules and spherule fragments therefore constitutes a thin lag deposit or pavement. Irregular and in some cases vesicular lithic fragments, which may be basaltic, also occur in these surface concentrations.

Pancam multispectral images of soil clasts at the Opportunity landing site exhibit greater variability in reflectance spectral properties (0.4 to 1.0 μm) than previously observed in data collected from the martian surface, whether from orbit or from Earth (*27*). Spherules in particular exhibit a range of spectral properties. As spherules are exhumed from the soil by wind, some emerge with coatings that have distinct spectral characteristics. These coatings may have formed while the spherules resided in the uppermost few millimeters of the soil, where sulfates and/or other salts became cemented onto their surfaces.

Images of wheel tracks and impressions made by the Mössbauer spectrometer contact plate indicate that the soils are cohesive, with the fine-grained component filling voids between larger grains during remolding of the soils. Motor currents associated with soil trenching operations show that soils are more easily excavated at Meridiani Planum than at the Spirit landing site in Gusev crater (*21*).

At several locations along the rover's traverse, sulfate-rich bedrock outcrops are covered by no more than a meter or so of soil. Examples include immediately outside Eagle crater, near the troughs at Anatolia, and at Fram crater. In other places, the soil is thinly draped over underlying blocks of sulfate-rich rock. These observations suggest that the soils that blanket the plains are typically no more than 1 or 2 m thick, underlain everywhere by sulfate-rich rock. Because spherules are sparsely distributed in the soil, concentrated primarily at the surface, the total inventory of spherules in the soil may be the equivalent of a region-wide layer of spherules no more than a centimeter thick. The observed concentration of spherules in the underlying rock is about 1 to 2% by volume (*28*), so only about 1 m of rock needs to have been eroded away to produce all of the spherules observed in the soil.

Eolian processes. Wind at the Opportunity landing site has eroded rock, sorted soil particles during transport, formed and changed ubiquitous ripples on the plains as well as ripples and dunes in craters and troughs, and formed wind streaks seen from orbit in MOC images. Saltation of fine-grained basaltic sand has been a particularly important eolian process, abrading clasts and outcrop rock and generating impact ripples.

The plains are dominated by low ripples extending to the horizon in all directions (Fig. 3). Ripples are typically ~1 cm high, although slightly larger examples are found rimming depressions such as Eagle crater and the Anatolia trough system. The surfaces of the ripples are dominated by fragments of hematite-rich spherules. Trenching through a ripple (Plate 15) revealed induration and a substantial fraction of sand in the ripple interior (*21*) but no internal stratification. Surfaces between ripples are relatively flat, with a mixture of sand, partly buried spherule fragments, and a scattering of generally well-perched spherules. Ripple formation probably involved transport of millimeter-sized grains, either driven across the surface by saltation-induced creep or rolled directly by the wind. Individual plains ripples are oriented about 26° east of north but commonly are grouped en echelon into alignments along a secondary orientation of about 4° east of north, preserving evidence for reorientation from a clockwise change in wind direction.

Fig. 3. En echelon wind ripples on the Meridiani plains, with rover tracks (each 16 cm wide) for scale. Navcam image acquired on sol 70. (Image ID = 1N134401857.)

Ripples similar to those on the plains are seen on the southwest interior wall of Eagle crater, but otherwise the bedforms inside depressions are different. Immediately adjacent to the Challenger Memorial Station within Eagle crater is a patch of ripples composed of very fine dark sand (Plate 16). Similar ripples are seen in patches within the Anatolia troughs and Fram crater. The ripples on the floor of Eagle crater are oriented about 38° east of north. This direction is consistent with transverse motion driven by the same winds that are responsible for a bright wind streak, visible in MOC images, that extends southeast downwind from Eagle crater, supporting the notion that these sands were mobilized by the same winds that produced the streak. APXS and Mössbauer measurements on soils outside the crater that lie within the wind streak indicate that the composition of the bright material is consistent with airfall dust (*23*, *24*), preserved in protected areas immediately downwind from the crater.

Small tails of sculpted rock extend from some spherules that lie partially embedded within and protruding from some rocks and indicate erosion of these rocks due to saltating particles driven by strong unidirectional winds. No dunes were observed during the 90-sol nominal mission, but dunes were subsequently discovered on the floor of Endurance crater.

Bedrock outcrops. The bedrock outcrop in Eagle crater (Plate 13) is 30 to 50 cm high and is exposed in an arc that subtends nearly 180 degrees of the crater wall, centered on its northwest quadrant. Brecciation associated with the impact crater has disrupted the stratigraphy. The dominant physical characteristic of the rock is fine lamination on scales of a few millimeters (Fig. 4). The outcrop can be subdivided and mapped into several distinct units based on its color, morphology, texture, and structural attitude (*28*).

The rock composing the outcrop is physically weak compared to some other rocks on Mars. The energy required to grind it with the RAT is 30 to 50 times lower per unit of volume than for the basaltic rocks investigated at Gusev crater by Spirit (*21*). The greatest resistance to grinding within the outcrop is found on the steepest slopes: The more resistant target Guadalupe is located on a 36° slope whereas the less resistant target McKittrick is located on a 7° slope, consistent with the idea that harder rocks retain steeper slopes because they are more resistant to erosion.

At a microscopic scale (*25*), four primary physical constituents are seen in the rock. The dominant one is medium to coarse sand grains, which tend to be well sorted within individual laminae. The second is the gray spherules, typically 4 to 6 mm in diameter, that are embedded within the rock (Plates 7, 9, and 10) with a spatial distribution that is more uniform than random. The third is fine-grained cement that binds the sand grains, and the fourth is small tabular vugs (Plate 9) that crosscut the laminations at random orientations.

The rock has a high concentration of sulfur, with up to about 25 weight percent SO_3 found in some locations (*23*). Much of the sulfur may be present in sulfate salts. The Mössbauer spectrometer has detected the Fe sulfate jarosite in all exposures of the outcrop that we have investigated (*24*). Mini-TES spectra of the outcrop also indicate that Mg and Ca sulfates are present at levels of a few tens of percent (*26*), although jarosite is below the Mini-TES detection limit. Chlorine and bromine are also detected by the APXS, and the Cl/Br ratio of the rock varies by more than an order of magnitude over small length scales (*23*).

The spherules are different in chemistry from the rock in which they are embedded. Based on Mössbauer and APXS data (*24*, *23*), we estimate that the spherules are more than 50% hematite by mass. Because of this composition, their spatial distribution, and several distinctive aspects of their morphology (*28*), we interpret the spherules to be concretions that formed by precipitation from aqueous fluids within the rock sometime after the sediments were deposited. The vugs are interpreted to represent crystal molds (*29*) formed by dissolution of one or more soluble mineral phases, possibly sulfates.

At several locations, the laminations within the rock exhibit cross-stratification (*28*). Some cross-bed sets may have resulted from eolian processes, but others show a small-scale festoon geometry indicating transport in subaqueous ripples (Plates 6 and 7). The three-dimensional geometry required by such cross-stratification implies that the ripples had highly sinuous crestlines with characteristic length scales of a few centimeters, a geometry that is indicative of transport by gently flowing water (*30*–*32*).

Rocks with these characteristics are not limited to Eagle crater. Rocks with similar properties were also observed within the Anatolia troughs (Fig. 5), although the rover was unable to approach the rocks there because of safety concerns, and the origin of the troughs remains enigmatic. Similar rocks were also observed at Fram crater (Plate 4), and there we made measurements with all the in situ instruments that confirmed that the rocks are virtually identical in composition, texture, and spherule content to ones observed at Eagle crater. We can therefore infer that sulfate-dominated sedimentary rocks extend laterally over a length scale of at least half a kilometer at the Opportunity landing site.

Bounce Rock. About 20 m beyond the rim of Eagle crater, we encountered a solitary rock about 40 cm across that we named Bounce Rock because of its proximity to an airbag bounce mark (Plate 12). The composition of Bounce Rock is unique at the Meridiani site and is also distinct from any material observed at Gusev crater by Spirit. The Mössbauer spectrum of Bounce Rock shows only pyroxene, with no other Fe-bearing minerals present in detectable quantities (*24*). The APXS chemistry is basaltic, with a normative mineralogy dominated by pyroxene and plagioclase and lacking in olivine (*23*). In both its mineralogy and chemistry, Bounce Rock is similar to Lithology B of the shergottite meteorite EETA79001 (*33*). In MI images it exhibits a rough and largely aphanitic texture, with some features suggestive of brecciation (*25*). Despite the basaltic composition, grinding with the RAT shows that it is weak and friable, with a grinding energy per unit of volume of 3.7 J/mm^3, almost an order of magnitude lower than is typical of fresh basalts at Gusev crater (*21*).

These distinct characteristics of Bounce Rock, together with its isolated occurrence, suggest that it may not be locally derived. A possible source for this enigmatic rock is a relatively fresh 25-km crater located 75 km southwest of Eagle crater, whose continuous ejecta lies atop the hematite-bearing plains (*34*). Rays of blocky material from this crater are observed within 10 km of Eagle crater in Mars Odyssey Thermal Emission Imaging System nighttime images (*35*), indicating that material from this crater was deposited on the current surface of Meridiani Planum in the vicinity of Eagle crater. The weak friable nature of Bounce Rock is consistent with a history involving impact shock and ballistic transport. A 25-km crater samples to depths of several kilometers, suggesting that Bounce Rock may represent materials from the older volcanic plains that have been interpreted to underlie the layered unit of the Meridiani Formation (*17*, *18*, *34*, *35*). In this case, these lower units are compositionally distinct from the basaltic sands that cover the plains around Eagle crater.

Atmospheric science. In addition to our geologic investigations, the remote sensing instruments on the payload have been used to observe the martian atmosphere. Upward-looking Mini-TES spectra are diagnostic of the vertical thermal structure of the atmosphere between about 20 m and 2 km above the surface, column-integrated infrared aerosol optical depth and water vapor abundance, and aerosol particle size. In particular, temperature profiles retrieved from Mini-TES observations of the 15-μm absorption band of CO_2 provide systematic characterization of the martian boundary layer (*36*). These observations show the development of a near-surface superadiabatic layer during the afternoon and a deep inversion layer at night. Upward-looking Mini-TES "stares," in which spectra are collected every 2 s for up to an hour, show warm and cool parcels of air moving through the Mini-TES field of view on a time scale of 30 s. Dust properties are consistent with previous measurements; spe-

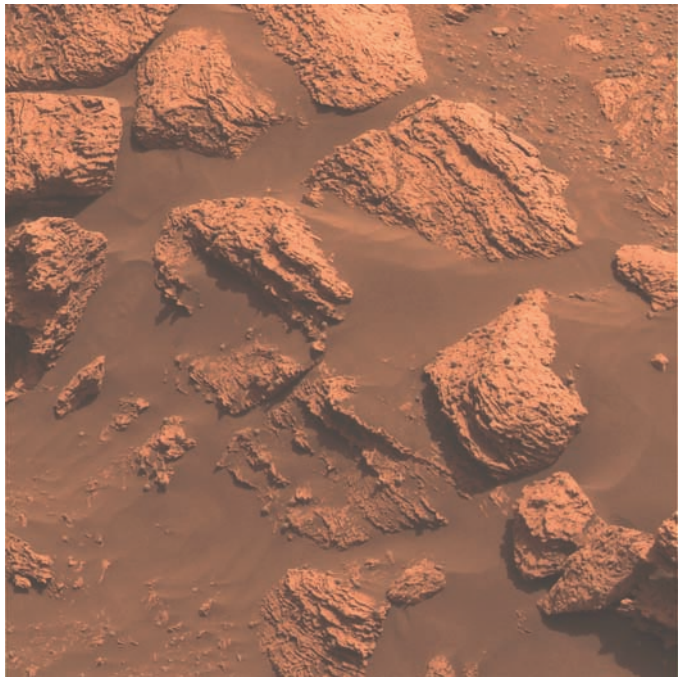

Fig. 4. Pancam image showing fine-scale laminations in the Eagle crater outcrop. Scale across the image is about 60 cm. This is an approximate true-color image, assembled using images from the 480-, 540-, and 600-nm filters. It was acquired at about 11:00 local solar time on sol 14.

cifically, cross-section mean radius is 1.5 ± 0.2 μm.

Pancam and Mini-TES observations of aerosols have been used to monitor the fallout of dust after a large regional dust storm that occurred in December 2003 and the further clearing associated with the transition into the southern hemisphere fall season (*37*). Direct solar imaging using Pancam with the 440/880-nm neutral density filters provides an accurate measurement of visible-wavelength aerosol optical depth. Visible-wavelength dust optical depth at the Meridiani Planum landing site dropped from a value of 0.90 soon after landing to about 0.6 on sol 91 (*38*).

Atmospheric dust transport can also be investigated by study of dust buildup rates on rover surfaces, particularly solar cells (*21*). Analyses of short-circuit current monitor solar cell data show a decrease in current of 0.29% per sol (corrected for seasonal variations in Mars-Sun distance and solar elevation angle) during the first 25 sols of the mission, slowing to 0.13% per sol by sol 90. Given the low surface albedo, high winds must remove dust deposits on a frequent basis, thereby keeping the surface relatively free of dust.

Evolution of Meridiani Planum. The Opportunity landing site is underlain by flat-lying sedimentary rocks. We interpret these rocks to be a mixture of chemical and siliciclastic sediments with a complex diagenetic history (*28*). The environmental conditions that they record are episodic inundation by shallow surface water, followed by evaporation, exposure, and desiccation. Our data suggest that the sediments are, by weight, ~50% fine-grained siliciclastic materials derived from weathering of basaltic parent rocks, ~40% sulfate minerals, and ~10% hematite. After deposition, hematite-rich concretions grew by precipitation from groundwater, and tabular mineral grains, probably sulfates, grew and were subsequently removed to produce the vugs. Some concretions were later eroded from the rock by eolian processes and are now concentrated in near-surface soils, producing the strong hematite signal seen from orbit.

The aqueous history recorded in these rocks may be characteristic of a large geographic region. MOC images show that a relatively high-albedo unit that correlates with the outcrop exposures near the Opportunity landing site is at least discontinuously present across most of Meridiani Planum. It seems likely, then, that the area over which these aqueous processes operated was at least tens of thousands of square kilometers in size.

The timing of the sedimentation is more difficult to determine. An upper bound on the age can be derived from analyses of orbital images that show that the Meridiani plains materials disconformably overlie dissected Middle to Late Noachian cratered terrains (*39*), suggesting that the sedimentary rocks at the Opportunity site could be as much as several billion years old.

Sometime after the end of aqueous activity at Meridiani, a thin layer of fine-grained basaltic sand was deposited atop the sedimentary rocks. The source of this sand cannot be determined from our data. One possibility is that it was excavated by impacts from units that underlie the sulfate-rich sediments, but we have been unable to identify such units in our traverse to date. Ejecta of Eagle, Fram, and Endurance craters do not show obvious strewn fields of basaltic rock fragments, so we presently have no good evidence for any basaltic rock immediately beneath the sulfate-rich sediments. And although Bounce Rock is a basalt, its pyroxene-dominated composition differs from that of the sand.

Another possible origin for the sand is that it is the erosional remnant of some overlying unit that has now been mostly removed. To the extent that superjacent, poorly consolidated strata were stripped away by erosion, the upper surface of the sulfate-rich sediments would seem to have created a barrier to continuing sediment removal. However, no evidence of former overlying units has emerged in the traverse to date either. Indeed, the flat surface of Meridiani Planum and the lack of erosional remnants of stratigraphically higher units suggest that the current plains surface may effectively represent the original depositional top of the entire sedimentary sequence. If the basaltic sand is neither excavated from below the sulfate-rich sediments nor the remnants of a former overlying unit, then perhaps it was transported by saltation from adjacent regions.

Regardless of the origin of the thin surface layer of sand, the underlying sulfate-rich sedimentary rocks at Meridiani Planum clearly preserve a record of environmental conditions different from any on Mars today. Liquid water was once present intermittently at the martian surface at Meridiani, and at times it saturated the subsurface. Because liquid water is a key prerequisite for life, we infer that conditions at Meridiani may have been habitable for some period of time in martian history.

Fig. 5. The Anatolia trough system. Portion of a Navcam mosaic obtained at about 12:30 local solar time on sol 74.

References and Notes

1. S. Squyres *et al.*, *Science* **305**, 794 (2004).
2. J. A. Crisp *et al.*, *J. Geophys. Res.* **108**, 8061 (2003).
3. A martian solar day has a mean period of 24 hours 39 min 35.244 s and is referred to as a sol to distinguish it from a ~3% shorter solar day on Earth.
4. S. W. Squyres *et al.*, *J. Geophys. Res.* **108**, 8062 (2003).
5. J. F. Bell III *et al.*, *J. Geophys. Res.* **108**, 8063 (2003).
6. P. R. Christensen *et al.*, *J. Geophys. Res.* **108**, 8064 (2003).
7. R. Rieder *et al.*, *J. Geophys. Res.* **108**, 8066 (2003).
8. G. Klingelhöfer *et al.*, *J. Geophys. Res.* **108**, 8067 (2003).
9. K. E. Herkenhoff *et al.*, *J. Geophys. Res.* **108**, 8065 (2003).
10. The term martian soil is used here to denote any loose, unconsolidated materials that can be distinguished from rocks, bedrock, or strongly cohesive sediments. No implication of the presence or absence of organic materials or living matter is intended.
11. S. Gorevan *et al.*, *J. Geophys. Res.* **108**, 8068 (2003).
12. M. B. Madsen *et al.*, *J. Geophys. Res.* **108**, 8069 (2003).
13. J. Maki *et al.*, *J. Geophys. Res.* **108**, 8071 (2003).
14. M. P. Golombek *et al.*, *J. Geophys. Res.* **108**, 8072 (2003).
15. P. R. Christensen *et al.*, *J. Geophys. Res.* **105**, 9632 (2000).
16. B. M. Hynek and R. J. Phillips, *Geology* **29**, 407 (2001).
17. R. E. Arvidson *et al.*, *J. Geophys. Res.* **108**, 8073 (2003).
18. B. M. Hynek, R. E. Arvidson, R. J. Phillips, *J. Geophys. Res.* **107**, 5088 (2002).

19. Names have been assigned to geographic features by the Mars Exploration Rover (MER) team for planning and operations purposes. They are not formally recognized by the International Astronomical Union.
20. The Challenger Memorial Station was named to honor the crew of the Space Shuttle *Challenger*, who perished on 28 January 1986. The name Challenger Memorial Station refers both to the lander itself and to the martian terrain that it occupies.
21. R. E. Arvidson *et al.*, *Science* **306**, 1730 (2004).
22. L. A. Soderblom *et al.*, *Science* **306**, 1723 (2004).
23. R. Rieder *et al.*, *Science* **306**, 1746 (2004).
24. G. Klingelhöfer *et al.*, *Science* **306**, 1740 (2004).
25. K. E. Herkenhoff *et al.*, *Science* **306**, 1727 (2004).
26. P. R. Christensen *et al.*, *Science* **306**, 1733 (2004).
27. J. F. Bell III *et al.*, *Science* **306**, 1703 (2004).
28. S. W. Squyres *et al.*, *Science* **306**, 1709 (2004).
29. P. W. Choquette, L. C. Pray, *Am. Assoc. Petrol. Geol. Bull.* **54**, 207 (1970).
30. J. C. Harms, J. B. Southard, R. G. Walker, *Structures and Sequences in Clastic Rocks* (Society of Economic Paleontologists and Mineralogists, Tulsa, OK, 1982).
31. G. V. Middleton, J. B. Southard, *Mechanics of Sediment Movement* (Society of Economic Paleontologists and Mineralogists, Providence, RI, 1984).
32. J. B. Southard, J. A. Boguchwal, *J. Sed. Petrol.* **66**, 680 (1990).
33. A. Banin, B. C. Clark, H. Wänke, in *Mars*, H. H. Kieffer, B. M. Jakosky, C. W. Snyder, M. S. Matthews, Eds. (Univ. of Arizona Press, Tucson, AZ, 1992), pp. 584–625.
34. P. R. Christensen, R. V. Morris, M. D. Lane, J. L. Bandfield, M. C. Malin, *J. Geophys. Res.* **106**, 23 (2001).
35. P. R. Christensen, S. W. Ruff, *J. Geophys. Res.* **109**, E08003 (2004).
36. M. D. Smith *et al.*, *Science* **306**, 1750 (2004).
37. M. D. Smith, *Icarus* **167**, 148 (2004).
38. M. T. Lemmon *et al.*, *Science* **306**, 1753 (2004).
39. R. E. Arvidson *et al.*, *J. Geophys. Res.* **108**, 8073 (2003).
40. We are deeply indebted to the many hundreds of engineers and scientists—far too numerous to name here—who made the MER Project and the Athena Science Investigation possible. Funding for the MER Project, including most of the Athena Payload, was provided by NASA. The APXS and Mössbauer instruments were funded by the German space agency (DLR), and the magnet array was funded by the Danish government. A portion of the research described in this paper was carried out at the Jet Propulsion Laboratory, California Institute of Technology, under a contract with NASA. The MER Project was led with skill and dedication by P. Theisinger, and the development of the MER flight system was led with equal skill and dedication by R. Cook and B. Goldstein. J. Rademacher managed the development of the Mini-TES, APXS, and Mössbauer payload elements, M. Schwochert led the engineering teams for Pancam and the Microscopic Imager, and S. Kondos and M. Johnson managed the development of the RAT. To all of them, and to the hundreds of members of the MER family who have made this adventure such a joy and privilege to be part of, we express our heartfelt and lasting thanks.

Plates Referenced in Article

www.sciencemag.org/cgi/content/full/306/5702/1698/DC1

Plates 3 to 7, 9, 10, and 12 to 16

7 October 2004; accepted 2 November 2004

RESEARCH ARTICLE

Pancam Multispectral Imaging Results from the Opportunity Rover at Meridiani Planum

J. F. Bell III,[1]* S. W. Squyres,[1] R. E. Arvidson,[2] H. M. Arneson,[1] D. Bass,[3] W. Calvin,[4] W. H. Farrand,[5] W. Goetz,[6] M. Golombek,[3] R. Greeley,[7] J. Grotzinger,[8] E. Guinness,[2] A. G. Hayes,[1] M. Y. H. Hubbard,[1] K. E. Herkenhoff,[9] M. J. Johnson,[1] J. R. Johnson,[9] J. Joseph,[1] K. M. Kinch,[10] M. T. Lemmon,[11] R. Li,[12] M. B. Madsen,[6] J. N. Maki,[3] M. Malin,[13] E. McCartney,[1] S. McLennan,[14] H. Y. McSween Jr.,[15] D. W. Ming,[16] R. V. Morris,[16] E. Z. Noe Dobrea,[1] T. J. Parker,[3] J. Proton,[1] J. W. Rice Jr.,[7] F. Seelos,[2] J. M. Soderblom,[1] L. A. Soderblom,[9] J. N. Sohl-Dickstein,[1] R. J. Sullivan,[1] C. M. Weitz,[17] M. J. Wolff[5]

Panoramic Camera (Pancam) images from Meridiani Planum reveal a low-albedo, generally flat, and relatively rock-free surface. Within and around impact craters and fractures, laminated outcrop rocks with higher albedo are observed. Fine-grained materials include dark sand, bright ferric iron–rich dust, angular rock clasts, and millimeter-size spheroidal granules that are eroding out of the laminated rocks. Spectra of sand, clasts, and one dark plains rock are consistent with mafic silicates such as pyroxene and olivine. Spectra of both the spherules and the laminated outcrop materials indicate the presence of crystalline ferric oxides or oxyhydroxides. Atmospheric observations show a steady decline in dust opacity during the mission. Astronomical observations captured solar transits by Phobos and Deimos and time-lapse observations of sunsets.

On 24 January 2004 UTC, the Mars Exploration Rover Opportunity landed on Mars within the classical low-albedo Noachian terrain of Meridiani Planum. The landing region was previously identified in orbital remote sensing data as being flat-lying layered and/or etched materials characterized by an unusual surficial concentration of coarse-grained gray hematite at the 15 to 20% areal abundance level (*1*–*3*). The lander and encapsulated rover came to rest inside an impact crater, 3 m deep and 20 m in diameter, informally known as Eagle crater (*4*). Using the Pancam charge-coupled device (CCD) imaging system (*5*, *6*), we acquired high spatial resolution multispectral panoramic images of the landing site and its environs to characterize the morphology, composition, and physical and atmospheric properties of the region.

Pancam images were calibrated using preflight laboratory measurements and then converted to *I/F* (where I = measured scene radiance and πF = the solar irradiance at the top of the martian atmosphere), which is reflectance relative to the onboard Pancam calibration target, corrected for solar incidence angle and dust deposition effects (*5*–*7*). During Opportunity's 90-sol primary mission, more than 8900 Pancam images were acquired and downlinked. These images include two 360° 5- and 6-color stereo panoramas from inside Eagle crater and on the plains just outside the crater, four 7-color stereo mosaics covering the Eagle crater outcrop at high resolution, more than 100 11-color multispectral spot observations of trenches, Rock Abrasion Tool (RAT) drill holes and other rock and soil (*8*, *9*) regions of interest within Eagle crater and during the traverse across the plains, and photometric imaging sequences designed to

[1]Department of Astronomy, Cornell University, Ithaca NY 14853, USA. [2]Department of Earth and Planetary Sciences, Washington University, St. Louis, MO 63130, USA. [3]Jet Propulsion Laboratory, California Institute of Technology, Pasadena, CA 91109, USA. [4]Department of Geological Sciences, University of Nevada, Reno, NV 89501, USA. [5]Space Science Institute, Boulder, CO 80301, USA. [6]University of Copenhagen, DK-2100 Copenhagen Ø, Denmark. [7]Department of Geological Sciences, Arizona State University, Tempe, AZ 85287, USA. [8]Department of Earth, Atmospheric, and Planetary Sciences, Massachusetts Institute of Technology, Cambridge, MA 02139, USA. [9]U.S. Geological Survey, Flagstaff, AZ 86001, USA. [10]Aarhus University, DK-8000 Aarhus C, Denmark. [11]Department of Atmospheric Sciences, Texas A&M University, College Station, TX 77843, USA. [12]Department of Civil and Environmental Engineering and Geodetic Science, Ohio State University, Columbus, OH 43210, USA. [13]Malin Space Science Systems Inc., San Diego, CA 92191, USA. [14]Department of Geosciences, State University of New York, Stony Brook, NY 11794, USA. [15]Department of Earth and Planetary Sciences, University of Tennessee, Knoxville, TN 37996, USA. [16]NASA Johnson Space Center, Houston, TX 77058, USA. [17]Planetary Science Institute, Tucson, AZ 85719, USA.

*To whom correspondence should be addressed. E-mail: jfb8@cornell.edu

provide information on surface physical properties and albedo and to facilitate comparisons between orbital remote sensing observations and ground truth.

Physiographic observations. The initial panoramic views of the Opportunity landing site concentrated on the interior of Eagle crater (Plate 1). The interior of Eagle crater has a surface area of ~350 m^2 and is dominated by dark reddish-brown, fine-grained, unconsolidated debris. Preserved indentation and disturbance patterns generated by the impact and retraction of the lander airbags (Fig. 1) and observations of wheel tracks and trench wall slopes (*10*) (Plates 14 to 16) indicate that this debris is weakly cohesive.

Two new classes of martian surface materials were discovered inside the crater. One class consists of high-albedo, yellowish-red outcrop about halfway up the inside of the crater wall (Plates 1 and 13, the latter of which shows a ~10-m-long section of the northern part of the outcrop) in the western and northern half of the crater. Outcrop exposures are ~50 cm high by 30 m wide; some are flush with the crater wall, and others protrude ~30 cm above the fine-grained debris that covers the floor and wall of the crater. The outcrop consists of indurated or lithified materials, some of which exhibit subcentimeter-scale laminations (*11*) (Fig. 2) (Plates 6 and 7). Some of the large-scale bedding exhibits juxtaposed strike and dip angles, suggesting that the outcrop may have been faulted or disrupted by the impact process (*11*). The second class consists of a population of millimeter- to subcentimeter-sized dark, spherical granules (spherules) found heterogeneously distributed within the crater. Some of the spherules are embedded in or eroding from the outcrop (*12*) (Fig. 3), which suggests that the origin of the spherules is intimately tied to the origin of the outcrop material.

Observations of the plains made immediately after Opportunity left Eagle crater on sol 57 (*13*) show a flat (~10 cm relief or less), dark terrain with only one large rock and a few small pebbles visible out to the horizon (Plate 2). A pattern of brighter, redder streaks on the plains is interpreted as wind ripples (*12*) that follow a dominantly northwest-southeast trend throughout the region in orbital images (*2*, *3*, *14*). Shallow linear depressions and other small, roughly circular craters and depressions, similar to features observed throughout the region from Mars Global Surveyor (MGS) high-resolution orbital images, are also visible in Pancam

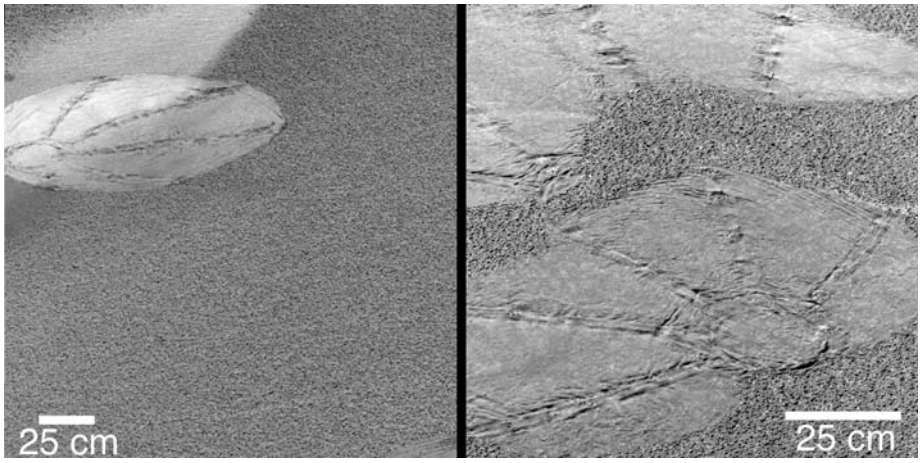

Fig. 1. Pancam images of imprint marks left in the soil as the airbag-shrouded lander came to a rest within Eagle crater. Left: Pancam 750-nm filter image from sol 3, sequence P2213, acquired at 11:22 LTST (*13*). Right: Pancam 750-nm filter image from sol 2, sequence P2217, acquired at 13:41 LTST.

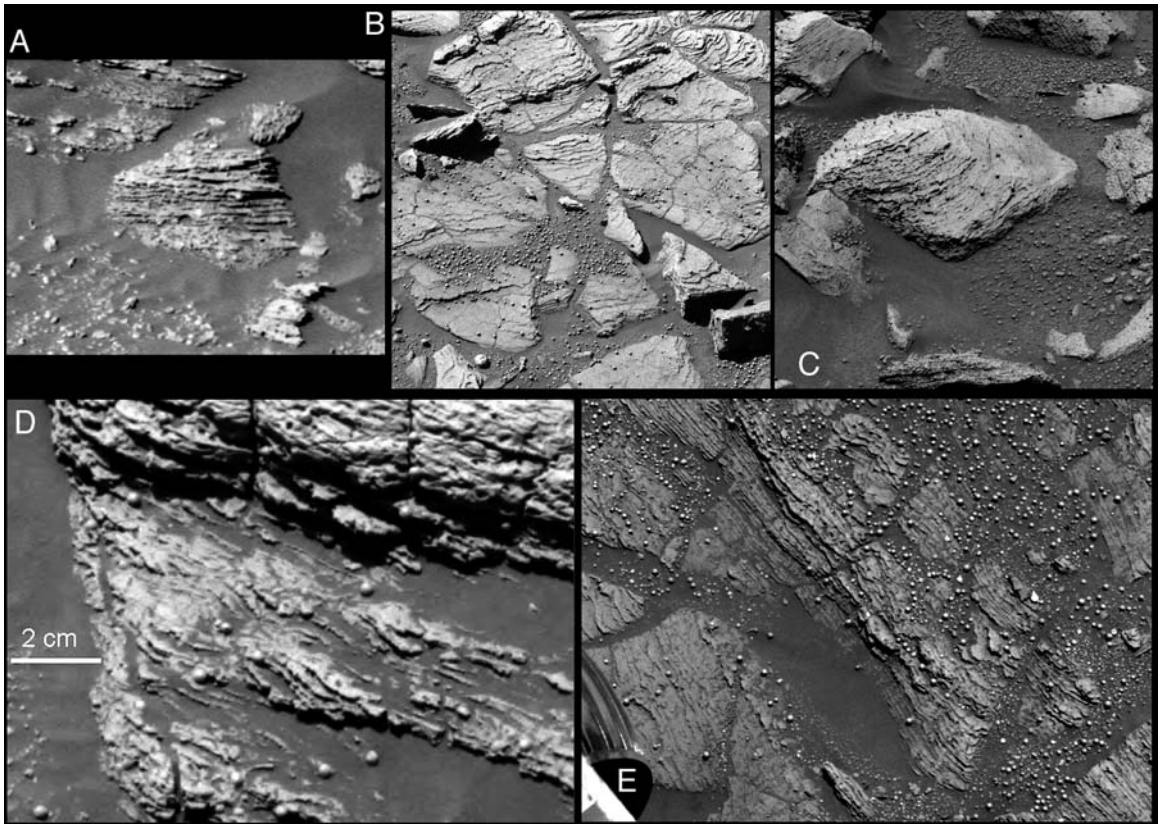

Fig. 2. Examples of laminated, spherule-bearing outcrop deposits in Pancam images, from 430-nm filter images. (**A**) Unnamed 12-cm-wide rock from sol 16, sequence P2260, in Eagle crater. (**B**) An 80-cm-wide part of Shoemaker's Patio from sol 49, sequence P2400, in Eagle crater. (**C**) The 20-cm-wide rock Pilbara from sol 85, sequence P2532, near Fram crater. (**D**) Part of the rock Last Chance from sol 38, sequence P2538, in Eagle crater. (**E**) An 80-cm-wide part of the rock Slickrock from sol 43, sequence P2555, in Eagle crater. Opportunity's front left wheel can be seen at lower left.

images of the plains. During the traverse to Endurance crater (Plate 5), the rover obtained images of one of the linear depressions, called Anatolia, showing outcrop similar in color and texture to the outcrop in Eagle crater (Fig. 4). The shallow impact crater called Fram, 8 m in diameter, also contains outcrop similar to that in Eagle crater (Plate 4).

The color properties, the ubiquitous presence of fine lamination and spherules within bright outcrop at Eagle, Anatolia, Fram, and Endurance, and the independent compositional evidence for uniformly high sulfur and jarosite [$(K,Na)Fe_3(SO_4)_2(OH)_6$] in the outcrop (*15*, *16*) all suggest that the substrate materials are laterally continuous and support the interpretation that the outcrop is a widespread deposit formed in liquid water (*11*). In this region of Meridiani Planum, this ancient sedimentary unit is buried beneath relatively thin (~1 m) deposits of darker sand, spherules, and dust.

Rocks and fine-grained materials. High-resolution Pancam images of clastic materials within Eagle crater and in the plains of Meridiani reveal distinct populations of materials based on morphology, color, and other properties (Fig. 5). Fine-grained materials include dark sand and brighter dust deposits. Where disturbed by airbags or the rover's wheels, these materials are observed to darken in brighter regions and to redden in darker regions. The darkening is probably a result of excavation of slightly coarser grains that underlie a thin, fine-grained ferric iron–rich surface layer, similar to disturbed surfaces at the Viking and Mars Pathfinder landing sites. The reddening is probably the result of burial and/or dispersal of coarse-grained ferric iron–rich materials such as the spherules. Clastic grains include bright and dark granules; some are spherical and range in size from ~1 to 5 mm, whereas others are angular and range in size from ~1 mm to 10 cm (*17*). There is a bimodal distribution of fine-grained materials, consisting of the 1- to 5-mm granules visible to Pancam and very fine sand (<100 μm) visible to the Microscopic Imager (MI) (*12*), and a lack of fine, medium, and coarse sand (~125 to 800 μm).

Larger rocky materials at the site are limited to the outcrop deposits seen at Eagle (Fig. 2), Anatolia (Fig. 4), Fram (Plate 4), Endurance, and (rarely) rocks seen elsewhere in the plains (Plate 12) (*12*). The outcrop remained intact after being scuffed and driven over by the rover wheels (Fig. 5, C and D), which supports the interpretation that it is a lithified unit rather than weakly indurated soil deposits (*10*).

Photometric observations. Calibrated Pancam images acquired on sol 22 with the broadband filter (L1, 739 ± 338 nm bandpass) were used to estimate the albedo (*18*) of the dark deposits within Eagle crater to be 0.14 ± 0.01. This is comparable to the average albedo of the plains outside of Eagle crater, estimated to be 0.12 ± 0.01 on the basis of L1 imaging measurements on sol 68. These albedos are comparable to the Viking Orbiter Infrared Thermal Mapper bolometric albedo (0.14 ± 0.06) and to the MGS Thermal Emission Spectrometer (TES) bolometric albedo (0.12 ± 0.03) of the Opportunity landing site pixel, which is in a lower-than-average albedo portion of the landing ellipse (*2*). The bright outcrop materials within Eagle crater exhibit an average albedo of 0.25 ± 0.06, and brighter wind streak deposits within and surrounding Eagle crater exhibit albedo values between 0.19 and 0.29, consistent with the albedo of bright dust.

We acquired images of surface features within Eagle crater and the plains at different times of day to document reflectance variations related to physical properties such as texture, grain size, and porosity (*19*, *20*). Examples include images targeted along the photometric equator, both within Eagle crater and in the plains east of Fram crater, and images targeted to monitor variations within specific regions of spherules and rock clasts (Fig. 6). Although much of the surface exhibits approximately Lambertian photometric behavior, the spherules and some clasts exhibit strong specular glints that suggest smooth and/or indurated surfaces. Several of these photometric sequences were timed to coordinate with down-looking observations

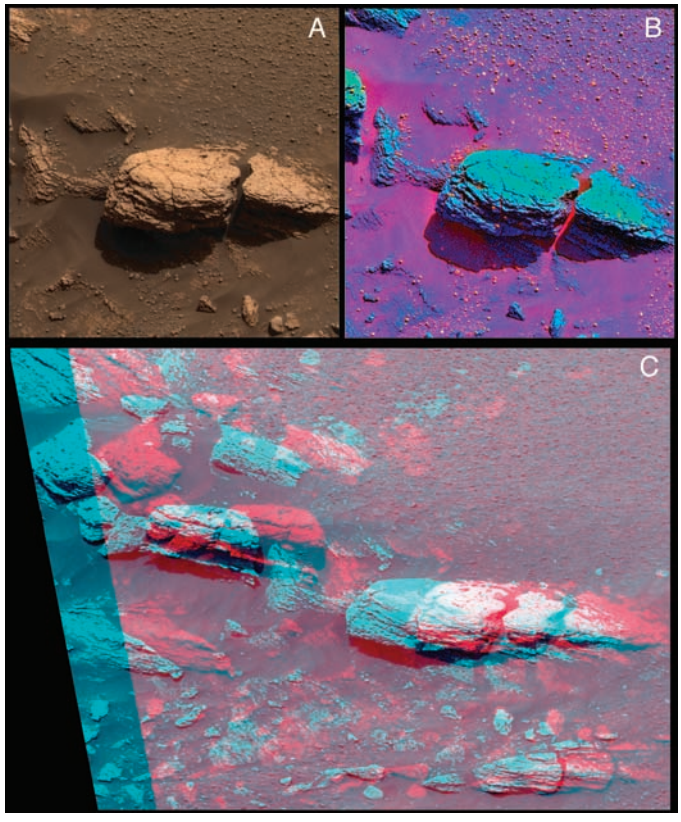

Fig. 3. Sol 13 and 14 Pancam images of the northeast end of the Eagle crater outcrop. (**A**) Approximate true-color rendering of the rock Stone Mountain, 16 cm high by 35 cm wide, acquired on sol 14 from sequence P2550 and generated with Pancam's left eye 600-, 530-, and 480-nm filters. (**B**) False-color composite from the same sequence as in (A) but generated with Pancam's right eye filters, with red = the 430- to 750-nm color ratio, green = *I*/*F* at 430 nm, and blue = the 900- to 1030-nm color ratio. (**C**) Stereo anaglyph image of this region of the Eagle crater outcrop, for viewing with red/blue stereo glasses. Images were acquired on sol 13 as part of sequence P2376.

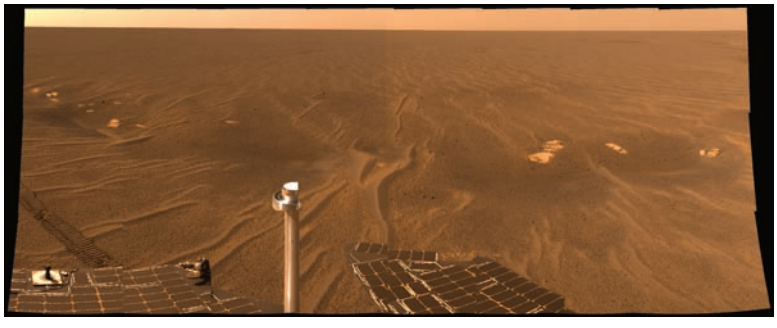

Fig. 4. Pancam color mosaic of the linear depression known as Anatolia, from sol 71, sequences P2281 and P2282. The part of the feature seen here is ~12 m wide. This is an approximate true-color rendering generated with Pancam's 750-nm filter for red, 480-nm filter for blue, and an average of those two filters as a synthesized green channel.

of the landing site during spacecraft overflights by the Mars Odyssey, Mars Express, and MGS orbiters [e.g., (*21*)].

Multispectral observations. Multispectral images were frequently used to identify potentially distinct compositional and mineralogic units and trends within outcrop and plains materials and to help guide the choice of specific targets for detailed in situ investigation with the rover's arm instruments. Targeted 11-color Pancam multispectral observations identified unique visible to near-infrared (IR) spectral units within Eagle crater and during the plains traverse to Endurance crater (Figs. 7 and 8). These units include bright and dark versions of soils, granules, rock clasts, and outcrop materials; larger dark rocks; regions of soil and rock disturbed by airbag, rover wheel, or RAT actions; and the sky.

The spectra provide constraints on the iron-bearing mineralogy of the materials exposed at the site. For example, outcrop materials in Eagle crater and elsewhere (Fig. 7; Fig. 8, A and E) exhibit a strong and relatively smooth near-ultraviolet to visible reflectance increase that is consistent with the presence of ubiquitous, fine-grained, perhaps nanophase (*22*) ferric iron–bearing iron oxide. Physical properties experiments (*10*) (Fig. 5, C and D) indicate that the fine-grained ferric iron material is not eolian dust covering the outcrop rocks. Spectra of the outcrop in Eagle crater were used to search for and identify other outcrop deposits in observations of the plains and distant drive targets (e.g., Figs. 4, 7E, and 8E) (Plate 4).

Most dark sand and other dark Eagle crater floor and Meridiani plains materials also exhibit a ferric iron spectral signature, but in contrast to the outcrop, their spectra show stronger evidence of crystalline ferrous or ferric iron–bearing phases (Fig. 7; Fig. 8, A, B, and E). Specifically, a stronger kink in the spectra near 530 nm and a shallow absorption band centered near 900 to 950 nm are consistent with ferric iron–bearing phases such as schwertmannite, ferrihydrite, and disordered goethite [e.g., (*23*, *24*)]. Although the 900- to 950-nm band is not consistent with the presence of fine-grained, crystalline ("red") hematite alone, the presence of that band and the kink at 530 nm may indicate a mixture of red hematite and (i) a ferric iron–bearing phase such as the hydroxide sulfate phase jarosite, (ii) a ferric oxyhydroxide such as goethite, or (iii) a ferrous iron–bearing volcanic phase such as pyroxene (*25*–*27*). The dark Eagle crater floor and Meridiani plains materials are observed to brighten and redden where compacted by the lander's airbags (e.g., Figs. 7B and 8B); such spectral behavior is consistent with either the creation of finer grained ferric iron phases from crushing and/or disaggregation of coarser phases, or the preferential burial of the coarser grained ferric iron materials during the compaction event. The latter interpretation is supported by MI imaging (*12*).

Small granules, rock clasts, and rare dark rocks exhibit a range of spectral diversity in the visible to near-IR range (e.g., Figs. 6, 7C, and 8C). Spectra of individual dark spherules

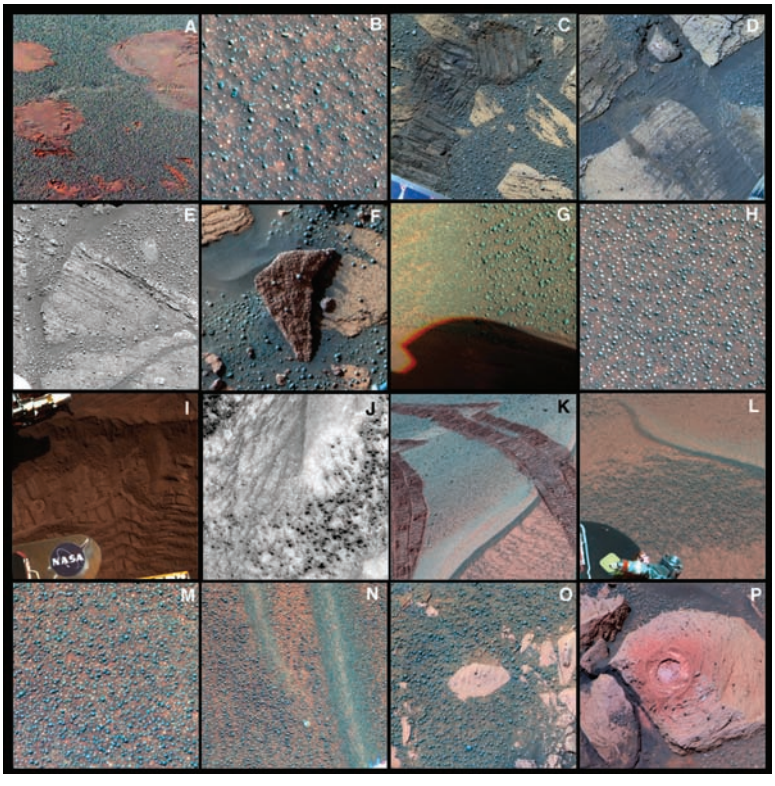

Fig. 5. Examples of color and morphologic diversity observed at Pancam's highest spatial resolution during Opportunity's first 90 sols. The features are ~1.6 m from the camera; each image is ~40 to 50 cm across. The smallest features visible in the images are ~0.8 to 1.0 mm across. (**A**) Sol 2, sequence P2218. (**B**) Sol 17, sequence P2555. (**C**) Sol 37, sequence P2534. (**D**) Sol 37, sequence P2535. (**E**) Sol 43, sequence P2554. (**F**) Sol 49, sequence P2571. (**G**) Sol 53, sequence P2599. (**H**) Sol 54, sequence P2530. (**I**) Sol 55, sequence P2403. (**J**) Sol 59, sequence P2558. (**K**) Sol 60, sequence P2211. (**L**) Sol 60, sequence P2217. (**M**) Sol 63, sequence P2572. (**N**) Sol 73, sequence P2589. (**O**) Sol 85, sequence P2533. (**P**) Sol 88, sequence P2542, post-RAT drilling. Images were generated with the 430-nm filter alone (E) or the 750-nm filter alone (J), or are false-color composites generated with the 750-, 530-, and 480-nm filters [(A), (K), and (L)], 750-, 530-, and 430-nm filters [(B), (F) to (H), and (M) to (P)], or 600-, 530-, and 430-nm filters [(C) and (D)]. (I) is an approximate true-color composite generated with the 600-, 530-, and 480-nm filters.

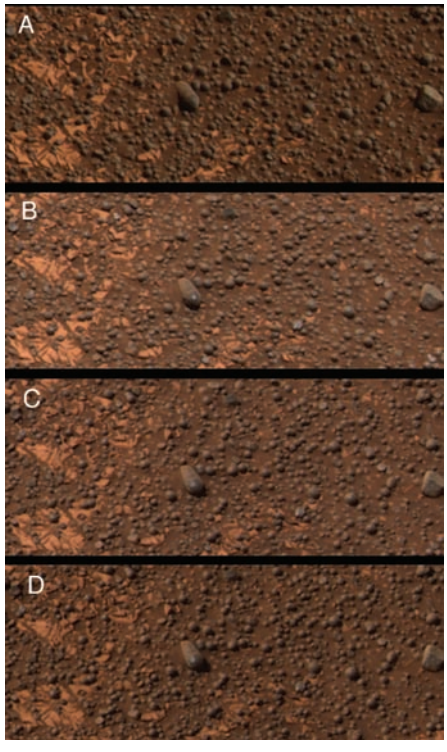

Fig. 6. Example of Pancam images from four times of day, showing differences in brightness and color of a patch of dark soil, spherules, rock clasts, and pieces of bright outcrop in Eagle crater. Each image is an approximate true-color rendering generated from Pancam's 600-, 530-, and 480-nm filters, and all are stretched to the same contrast and color level. The scene is ~50 cm across; the smallest grains visible in the images are ~1 mm in size. (**A**) Sol 32, sequence P2581, 09:20 LTST; illumination from upper right. (**B**) Sol 30, sequence P2579, 11:51 LTST; illumination from just right of center. (**C**) Sol 29, sequence P2575, 13:19 LTST; illumination from just left of center. (**D**) Sol 32, sequence P2587, 14:01 LTST; illumination from upper left.

from Eagle crater (Figs. 6 and 8F) (Plate 11) exhibit crystalline ferric iron spectral signatures similar to those seen in the dark Eagle crater soils and Meridiani plains. Color ratio images of Pancam filters R7 and R6 (1009 nm/934 nm) and other similar parameterizations (*9*) provide a quick way to map the distribution of spherules and indicate that they are ubiquitous across the part of the Meridiani plains imaged by Pancam. Some areas within Eagle crater have partially buried spherules that have a higher albedo of 0.20 to 0.25. Spectra of these higher albedo spherules are consistent with low-albedo spherules covered or coated by high-albedo nanocrystalline ferric iron–rich dust. In areas where the RAT ground into spherules embedded in the outcrop (e.g., Plates 9 to 11, which show examples of the 4.5-cm-diameter RAT holes), the RAT cuttings are redder than the unabraded rock surfaces and exhibit 11-color spectra consistent with the presence of fine-grained ferric iron oxides. These observations, combined with Miniature Thermal Emission Spectrometer (Mini-TES) and Mössbauer spectrometer identification of hematite signatures within spherule-rich regions (*16*, *28*), indicate that the spherules and their fragments are a carrier of the crystalline gray hematite observed from orbit in this region of Mars (*1*). However, similar crystalline ferric iron spectral signatures are also seen in Pancam spectra of some dark rock clasts and soil deposits (Fig. 7; Fig. 8, A, C, and F), implying that the spherules may not be the only carrier of the hematite in this region (*17*).

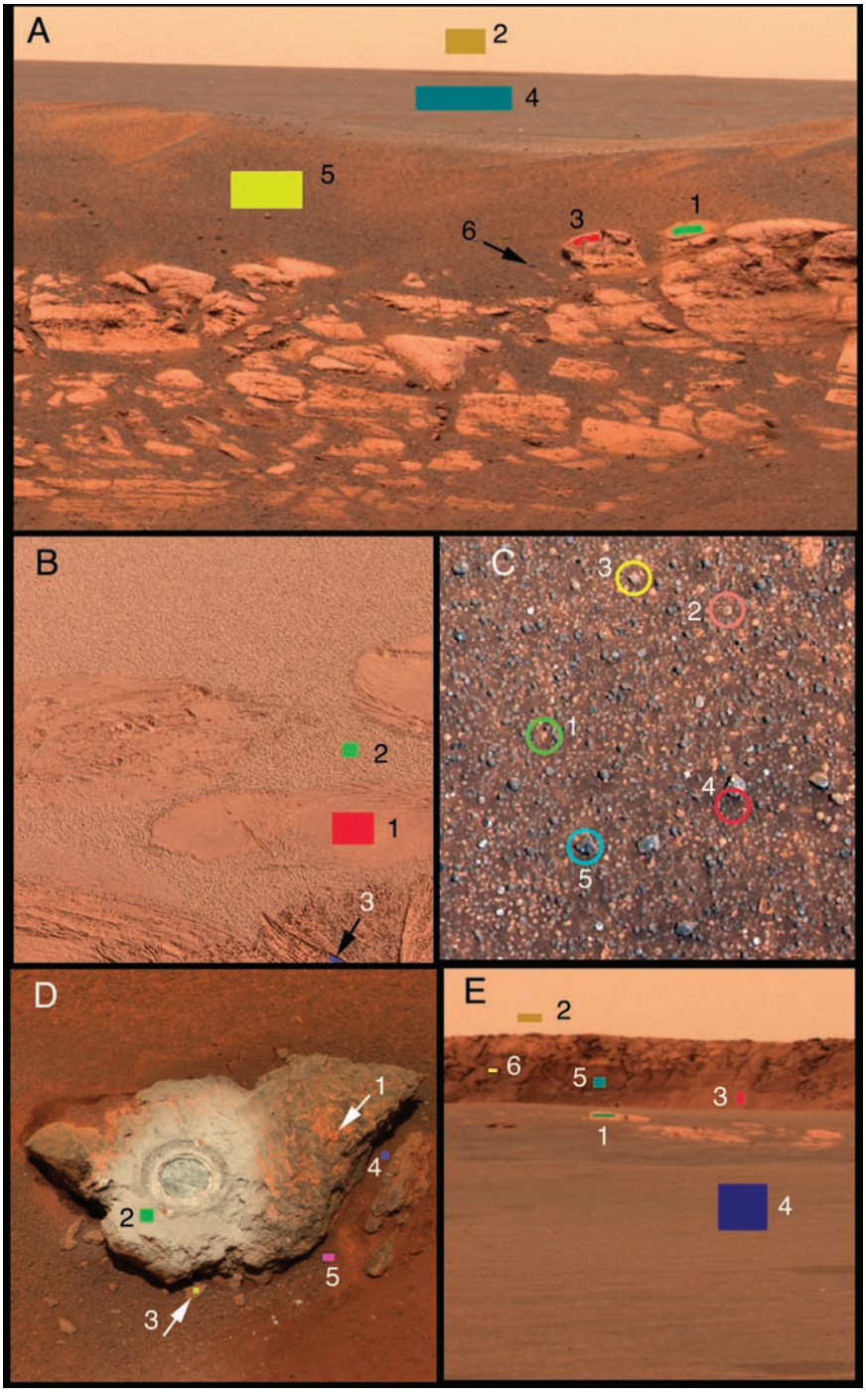

Fig. 7. Examples of regions chosen for detailed Pancam multispectral observations. Spectra extracted from the colored boxes are shown in Fig. 8. (**A**) A 3-m-wide region of the outcrop in Eagle crater: sol 4, sequence P2353. (**B**) Airbag bounce and drag marks within a 1.6-m-wide region of Eagle crater: sol 3, sequence P2530. (**C**) A 50-cm-wide region of soil and rock clast deposits in Eagle crater: sol 20, sequence P2564. (**D**) A 40-cm-wide Bounce rock in the plains outside of Eagle crater: sol 68, sequence P2581. (**E**) View across the plains at the eastern wall of Endurance crater: sol 94, sequence P2556. The rock at point 1 is ~75 cm wide and ~70 m away. All images are approximate true-color renderings generated using Pancam's 600-, 530-, and 480-nm filters.

Some small dark rock clasts within Eagle crater, as well as dust-free surfaces of Bounce rock exposed by grinding, exhibit a negative spectral slope from 750 to 1000 nm and/or a strong near-IR absorption band centered near 1000 nm or at a longer wavelength (Fig. 7; Fig. 8, C and D). These features are consistent with the presence of ferrous iron–bearing silicate phases such as pyroxene or olivine (*29*–*32*). In situ analysis by the Mössbauer spectrometer showed the presence of one or more pyroxene phases in Bounce rock, and also showed that olivine was negligible (*16*). Abundant pyroxene but only minor amounts of olivine were also identified in this rock on the basis of Mini-TES measurements (*28*).

Trenches ~16 cm wide by ~150 cm long by 5 to 10 cm deep were dug by the rover wheels in Eagle crater and in the plains near Anatolia (Plates 14 to 16). Multispectral images of these trenches show that the shallow subsurface has fewer spherules and rock clasts than the surface. Trench walls and excavated piles are slightly redder than surrounding untrenched materials. These observations support the interpretation of these surfaces as a deflationary lag or pavement deposit (*10*).

Atmospheric and astronomical observations. Generally similar atmospheric and astronomical imaging campaigns were conducted by both rovers during their 90-sol primary missions (*6*), except that nighttime imaging observations on Opportunity were precluded because of power limitations. Atmospheric observations include direct solar imaging, using 440- and 880-nm neutral-density filters, to derive and monitor the visible and near-IR dust opacity (*33*); time-lapse observations of sunsets to constrain the vertical distribution of atmospheric dust (Fig. 9); and

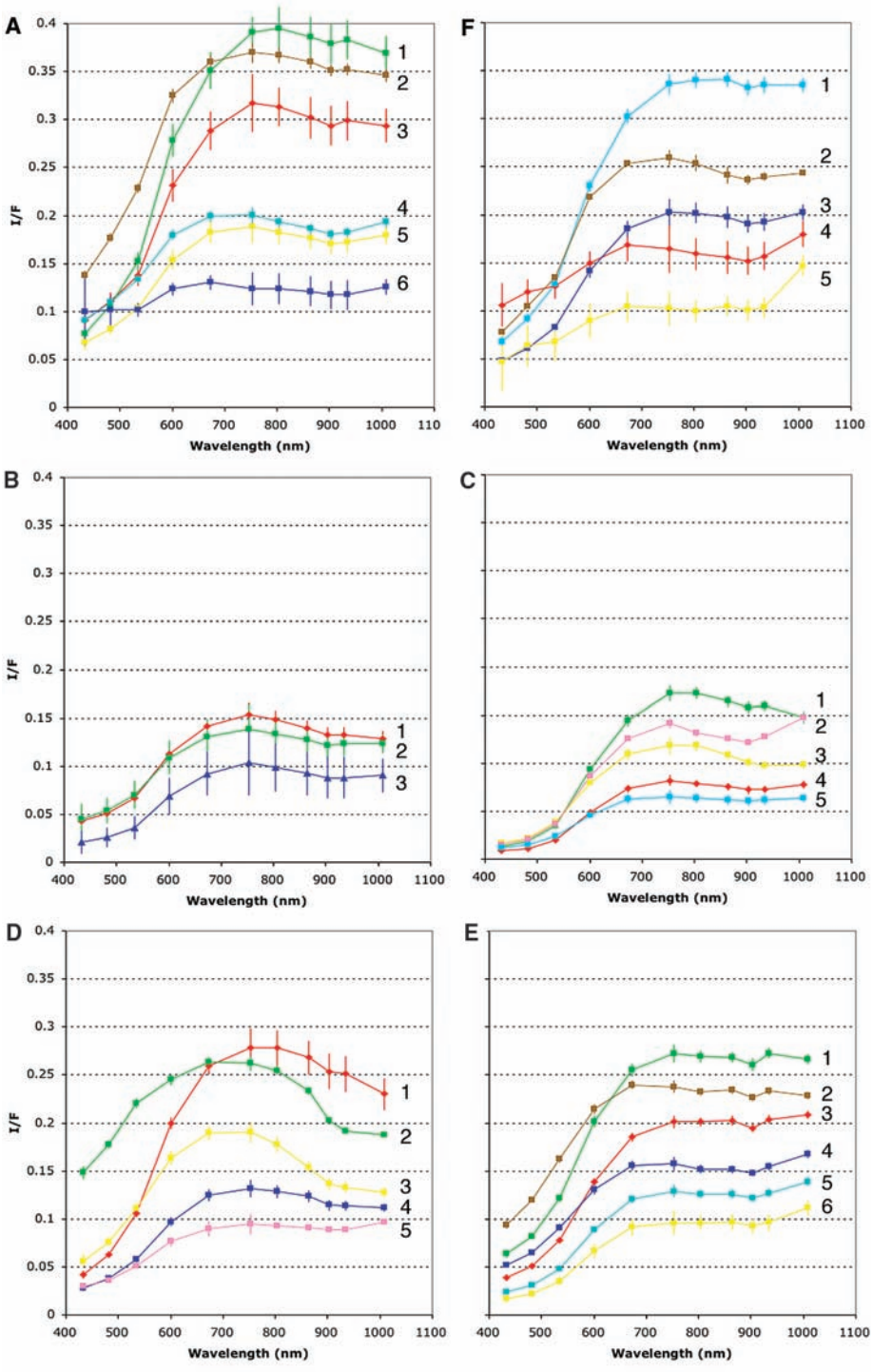

Fig. 8. Representative visible to near-IR Pancam spectra of units identified during Opportunity's primary mission. (**A**) to (**E**) correspond to locations shown in Fig. 7, A to E; (**F**) corresponds to spectra extracted from the following features in Plate 11A: (1) bright outcrop materials, (2) bright rock fragments, (3) dark outcrop material, (4) average of bright parts of spherules within the Berry Bowl, and (5) average of darker parts of spherules within the Berry Bowl.

special imaging campaigns designed to characterize the sky's diffuse illumination radiance field and to search for atmospheric water ice clouds. As of the end of the primary mission (areocentric longitude of the Sun ~24°, corresponding to early southern hemisphere autumn), no clouds were detected at the landing site in Meridiani, nor were any dust devils detected in targeted or serendipitous horizon imaging. Astronomical observations consisted of imaging of three solar transits by Phobos and one by Deimos to better constrain their orbital characteristics and orbital evolution histories (Fig. 10) (*34*).

Fig. 9. Sunset image acquired on sol 20 near 17:55 LTST with the Sun ~1° above the horizon. This is an enhanced color composite generated with Pancam's 750-, 530-, and 430-nm filters.

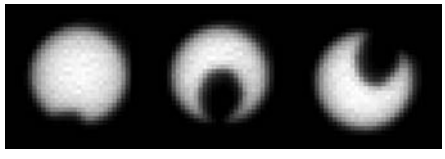

Fig. 10. Solar transit of Phobos observed on sol 47. Images taken through the Pancam right eye solar filter are shown at 10-s intervals, starting on the left, at 12 March 2004, 13:41:00 UTC.

References and Notes

1. P. R. Christensen *et al.*, *J. Geophys. Res.* **105**, 9623 (2000).
2. M. P. Golombek *et al.*, *J. Geophys. Res.* **108**, 10.1029/2003JE002074 (2003).
3. R. E. Arvidson *et al.*, *J. Geophys. Res.* **108**, 10.1029/2003JE001982 (2003).
4. Names have been assigned to aerographic features by the Mars Exploration Rover (MER) team for planning and operations purposes. The names are not formally recognized by the International Astronomical Union.
5. J. F. Bell III *et al.*, *J. Geophys. Res.* **108**, 10.1029/2003JE002070 (2003).
6. J. F. Bell III *et al.*, *Science* **305**, 800 (2004).
7. R. J. Reid *et al.*, *J. Geophys. Res.* **104**, 8907 (1999).
8. The term martian soil is used here to denote any loose unconsolidated materials that can be distinguished from rocks, bedrock, or strongly cohesive sediments. No implication of the presence or absence of organic materials or living matter is intended [e.g., (9)].
9. J. F. Bell III *et al.*, *J. Geophys. Res.* **105**, 1721 (2000).
10. R. E. Arvidson *et al.*, *Science* **306**, 1730 (2004).
11. S. W. Squyres *et al.*, *Science* **306**, 1709 (2004).
12. K. E. Herkenhoff *et al.*, *Science* **306**, 1727 (2004).
13. A martian solar day has a mean period of 24 hours 39 min 35.244 s and is referred to as a sol to distinguish this from a roughly 3% shorter solar day on Earth. A martian sidereal day, as measured with respect to the fixed stars, is 24 hours 37 min 22.663 s, as compared with 23 hours 56 min 04.0905 s for Earth. Local true solar time (LTST) on Mars is measured with respect to 24 "hours," with noon defined as the time when the Sun reaches its zenith in the sky. See www.giss.nasa.gov/tools/mars24 for more information.
14. R. Greeley, S. D. Thompson, *J. Geophys. Res.* **108**, 10.1029/2003JE002110 (2003).
15. R. Rieder *et al.*, *Science* **306**, 1746 (2004).
16. G. Klingelhöfer *et al.*, *Science* **306**, 1740 (2004).
17. L. A. Soderblom *et al.*, *Science* **306**, 1723 (2004).

18. An estimated albedo is derived by dividing *I/F* (determined from observations calibrated with the onboard calibration target) by the cosine of the solar elevation angle at the time of each observation. This albedo estimate should be comparable to the bolometric Lambert albedo values derived from orbital observations.
19. B. Hapke, *Theory of Reflectance and Emittance Spectroscopy* (Cambridge Univ. Press, New York, 1993).
20. J. R. Johnson *et al.*, *J. Geophys. Res.* **104**, 8809 (1999).
21. R. Greeley *et al.*, *Lunar Planet. Sci. Conf. XXXV*, abstr. 2162 (Lunar and Planetary Institute, Houston, TX, 2004) [CD].
22. R. V. Morris *et al.*, *Geochim. Cosmochim. Acta* **57**, 4597 (1993).
23. R. V. Morris *et al.*, *J. Geophys. Res.* **105**, 1757 (2000).
24. J. L. Bishop *et al.*, *J. Geophys. Res.* **103**, 31457 (1998).
25. R. V. Morris *et al.*, in *Mineral Spectroscopy: A Tribute to Roger G. Burns*, M. D. Dyar, C. McCammon, M. W. Schaefer, Eds. (Geochemical Society, Houston, TX, 1996), pp. 327–336.
26. R. V. Morris *et al.*, *J. Geophys. Res.* **100**, 5319 (1995).
27. R. V. Morris, D. C. Golden, *Icarus* **134**, 1 (1998).
28. P. R. Christensen *et al.*, *Science* **306**, 1733 (2004).
29. Both pyroxene and olivine exhibit broad Fe^{2+} absorption bands centered near 900 to 1100 nm [e.g., (*30*, *31*)], but because the long-wavelength sides of these bands are typically beyond the spectral range of silicon CCD detectors, it is usually not possible to uniquely identify the specific Fe^{2+}-bearing phases responsible for reflectance decreases observed in the longest wavelength filters of instruments such as Pancam (*32*).
30. J. B. Adams, *J. Geophys. Res.* **79**, 4829 (1974).
31. E. A. Cloutis *et al.*, *J. Geophys. Res.* **91**, 11641 (1986).
32. E. A. Cloutis, J. F. Bell III, *Icarus* **172**, 233 (2004).
33. M. T. Lemmon *et al.*, *Science* **306**, 1753 (2004).
34. J. F. Bell III *et al.*, in preparation.
35. We extend our sincere gratitude to the many hundreds of people who have contributed to the success of the Pancam investigation. These include the many MER engineers, managers, and support staffers at JPL; engineers and researchers at many vendor organizations; students and support staff at Cornell University, USGS/Flagstaff, Washington University, and other institutions; image processing and visualization experts at JPL and NASA/Ames Research Center; and many of the co-investigators, collaborators, and associates on the Athena Science Team. We also extend special thanks to our families and loved ones for their patience and support during mission operations and throughout the many years leading up to our spectacular travels on Mars.

Plates Referenced in Article
www.sciencemag.org/cgi/content/full/306/5702/1703/DC1
Plates 1, 2, 4 to 7, and 9 to 16

15 September 2004; accepted 15 October 2004

RESEARCH ARTICLE

In Situ Evidence for an Ancient Aqueous Environment at Meridiani Planum, Mars

S. W. Squyres,[1]* J. P. Grotzinger,[2] R. E. Arvidson,[3] J. F. Bell III,[1] W. Calvin,[4] P. R. Christensen,[5] B. C. Clark,[6] J. A. Crisp,[7] W. H. Farrand,[8] K. E. Herkenhoff,[9] J. R. Johnson,[9] G. Klingelhöfer,[10] A. H. Knoll,[11] S. M. McLennan,[12] H. Y. McSween Jr.,[13] R. V. Morris,[14] J. W. Rice Jr.,[5] R. Rieder,[15] L. A. Soderblom[9]

Sedimentary rocks at Eagle crater in Meridiani Planum are composed of fine-grained siliciclastic materials derived from weathering of basaltic rocks, sulfate minerals (including magnesium sulfate and jarosite) that constitute several tens of percent of the rock by weight, and hematite. Cross-stratification observed in rock outcrops indicates eolian and aqueous transport. Diagenetic features include hematite-rich concretions and crystal-mold vugs. We interpret the rocks to be a mixture of chemical and siliciclastic sediments with a complex diagenetic history. The environmental conditions that they record include episodic inundation by shallow surface water, evaporation, and desiccation. The geologic record at Meridiani Planum suggests that conditions were suitable for biological activity for a period of time in martian history.

The primary objective of the Mars Exploration Rover mission is to search for evidence in the martian geologic record of environmental conditions that might once have been suitable for life. Elsewhere in this issue (*1*) we describe the geologic setting in and around Eagle crater (*2*), the small impact crater in Meridiani Planum where the rover Opportunity landed. Here, we describe rocks exposed in the wall of Eagle crater in more detail and consider their implications for past aqueous processes and habitability.

Stratigraphy and sedimentology. The outcrop at Eagle crater can be mapped (Fig. 1) on the basis of color, morphology, texture, and structural attitude revealed in Pancam images (*3*). The maximum stratigraphic thickness exposed at any location within the outcrop is about 30 to 50 cm. Although the units we have mapped reveal a complex stratigraphy, intense brecciation associated with the impact event hinders reconstruction of the relative ages. Postdepositional surface weathering and collapse may also have contributed to brecciation.

The western part of the outcrop forms map unit A and includes an area called Shoemaker's Patio up to the point marked by the Slickrock fault. This unit is characterized by large breccia blocks and by the highest albedo (~0.30) within the outcrop when viewed in bulk. Bedding within blocks shows dips of 0° to 15°, defined by fine planar lamination, low-angle cross-stratification, and cross-bed sets as thick as 7 cm (Fig. 2A). Embedded spherules are present, but vugs are rare to absent. The margins of some breccia blocks show rims with raised relief and redder colors (*3*).

Map unit B, extending from the Slickrock fault northeastward toward the rock called El Capitan, is characterized by large blocks that are lower in albedo than those in map unit A. Bedding within the blocks is steep on the east side of the fault, with dips up to 60° as observed at Slickrock and a rock called the Dells. Bedding within unit B is characterized by planar lamination to low-angle cross-stratification (Fig. 2B), ripple cross-lamination (Plate 7), and crinkly to undulatory lamination (Fig. 2C). Embedded spherules and vugs are abundant.

Map unit C includes El Capitan and other rocks along the northern and outer margin of Eagle crater. Bedding planes are nearly horizontal, and bedding is more poorly expressed than elsewhere. In the upper part of El Capitan (Guadalupe), the bedding is only faintly visible. Embedded spherules are present and vugs are abundant. The upper part of

[1]Department of Astronomy, Cornell University, Ithaca, NY 14853, USA. [2]Department of Earth, Atmospheric, and Planetary Sciences, Massachusetts Institute of Technology, Cambridge, MA 02139, USA. [3]Department of Earth and Planetary Sciences, Washington University, St. Louis, MO 63031, USA. [4]Department of Geological Sciences, University of Nevada, Reno, NV 89557, USA. [5]Department of Geological Sciences, Arizona State University, Tempe, AZ 85287, USA. [6]Lockheed Martin Corporation, Littleton, CO 80127, USA. [7]Jet Propulsion Laboratory, California Institute of Technology, Pasadena, CA 91109, USA. [8]Space Science Institute, Boulder, CO 80301, USA. [9]U.S. Geological Survey, Flagstaff, AZ 86001, USA. [10]Johannes Gutenberg University, D-55128 Mainz, Germany. [11]Botanical Museum, Harvard University, Cambridge, MA 02138, USA. [12]Department of Geosciences, State University of New York, Stony Brook, NY 11794, USA. [13]Department of Earth and Planetary Sciences, University of Tennessee, Knoxville, TN 37996, USA. [14]NASA Johnson Space Center, Houston, TX 77058, USA. [15]Max-Planck-Institut für Chemie, Kosmochemie, D-55128 Mainz, Germany.

*To whom correspondence should be addressed. E-mail: squyres@astrosun.tn.cornell.edu

unit C has greater relief than the lower part, a more massive appearance, a redder and more mottled color, and possibly a greater amount of intergranular cement. It is also the strongest material found in Eagle crater, as revealed by Rock Abrasion Tool (RAT) grinding energy (*4*).

Map unit D includes the eastern part of the outcrop, named Big Bend. This unit is characterized by relatively intact stratigraphy, with dips of 20° to 30° that define a northeast-plunging open fold. The outcrop here exhibits strong eolian etching parallel to bedding, giving it a ribbed appearance. Sedimentary structures include ripple cross-lamination (Plate 6) and crinkly bedding. Spherules are present, but vugs are rare to absent.

Map unit E represents zones within the outcrop consisting of brecciated blocks with or without visible bedding, but for which no other attributes can be assigned, in some areas because the rover did not examine them in sufficient detail.

Microscale texture. Microscopic Imager (MI) images (*5*) reveal four physical constituents in the outcrop. The primary component consists of moderately rounded medium to coarse sand-sized grains; these grains are well sorted within laminae but show some variations in grain size among layers. Especially in the well-laminated rocks of unit B, individual laminations are a single grain thick, with lamina thickness varying from 0.3 mm to nearly 1 mm (Fig. 2D). The second component is the gray spherules that are embedded in all units of the outcrop (Fig. 3). Spherule diameters are typically 4 to 6 mm. The third component is cement, which is fine-grained through much of the unit. Locally, coarser millimeter-scale cement crystals are observed to form sockets around some spherules (*5*). Finally, vugs are common in some units (Fig. 4). The vugs have tabular prismatic shapes and random orientations that cut across lamination, and they intersect the surface to form openings with typical widths of 1 to 2 mm and lengths of ~1 cm. Sharp angles are common for vugs not rounded by weathering; in particular, many vugs are thickest in the middle and taper toward both ends.

Chemistry and mineralogy. The elemental composition of the Eagle crater outcrop, as measured with the Alpha Particle–X-Ray Spectrometer (APXS), is most noteworthy for high concentrations of sulfur, with nearly 25 weight percent SO_3 found in some locations (*6*). This proportion of S is greater than that in typical Meridiani soils (*7*) by a factor of ~5 and greater than in the basaltic rocks at the Gusev crater landing site investigated by Spirit (*8*) by a factor of nearly 20. Although S is strongly enriched in the Eagle crater outcrop, Cl is not; hence, if both are present in salts, fractionation by differential solubility may have occurred.

Overall, the high concentrations of S in the outcrop are most readily explained by high abundances of sulfate salts. Mineralogic observations from the Mössbauer spectrometer and the Miniature Thermal Emission Spectrometer (Mini-TES) confirm this interpretation. The Mössbauer spectrometer has detected the ferric sulfate mineral jarosite $[(K,Na,H_3O,X^{+1})Fe_3(SO_4)_2(OH)_6]$ in all exposures of the outcrop (*9*), and Mini-TES spectra of the outcrop indicate ~20 to 40% by weight of Mg and Ca sulfates (*10*).

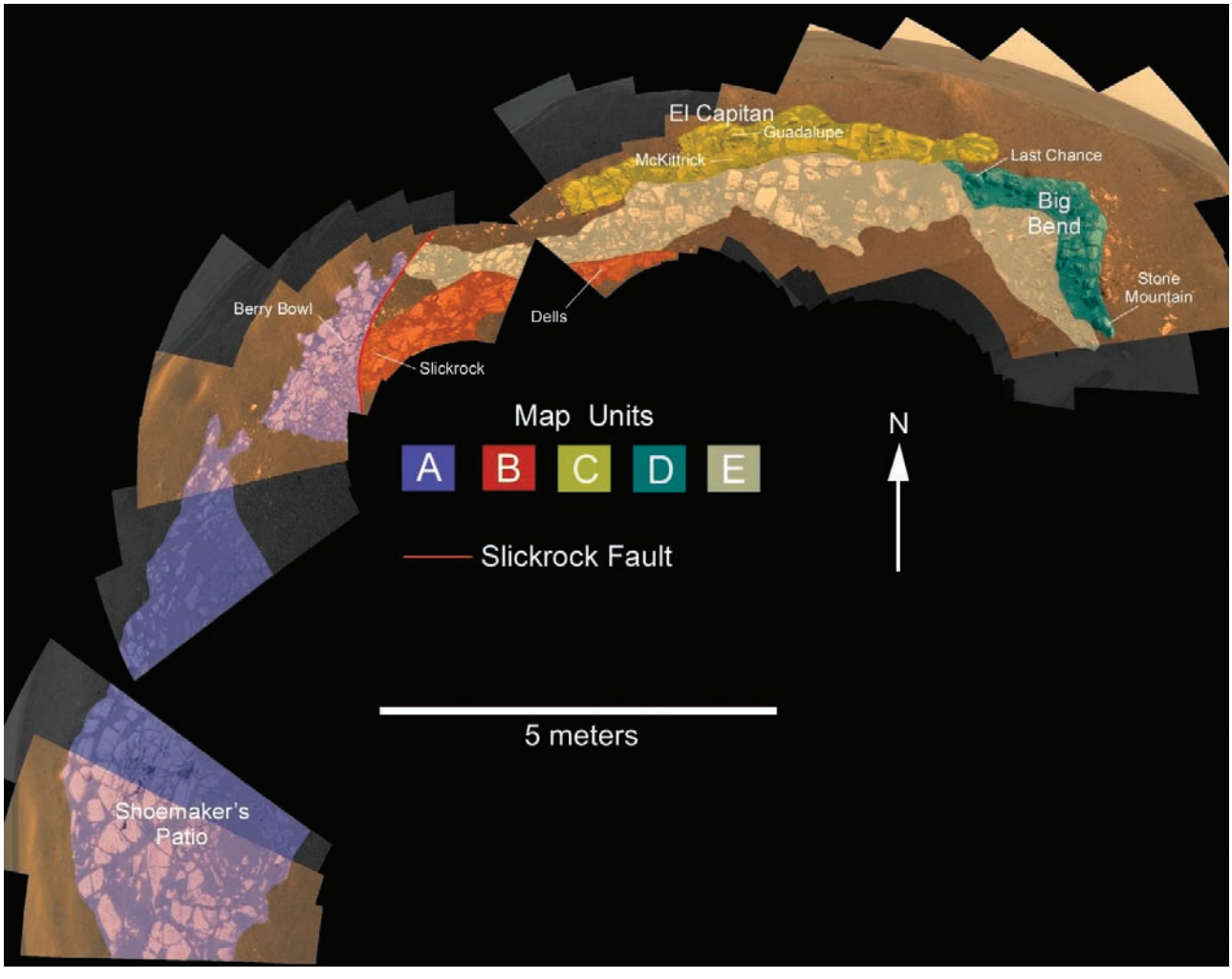

Fig. 1. Pancam images of the outcrop in Eagle crater, in a vertical projection overlain with map units.

Another noteworthy characteristic of the outcrop rocks is that the concentration of bromine is highly variable, ranging from 30 ppm or less to as much as 440 ppm (*6*). These variations are found over small length scales; Br concentrations in two RAT holes in El Capitan (Guadalupe and McKittrick) differ by more than an order of magnitude, even though their locations differ by only 20 cm in elevation. The lowest Br concentrations in the outcrop yield Cl/Br ratios comparable to the chondritic Cl/Br ratio, whereas the highest are substantially enhanced in Br. Bromides are generally more soluble than chlorides of the same cations, and large local enhancements in Br relative to Cl are sometimes found in terrestrial evaporite deposits (*11*, *12*).

On Earth, the most common +1 cation in jarosite is K^+, but K is impoverished in the outcrop and Na^+ or H_3O^+ must compensate. The most abundant available cation by far is Mg^{2+}. One or more hydrated Mg sulfate salts, such as kieserite, hexahydrite, and/or epsomite, may be present. Adequate Na is available for halite, although bischofite [$MgCl_2 \cdot 6(H_2O)$] or antarcticite [$CaCl_2 \cdot 6(H_2O)$] could be present. Ca sulfates (anhydrite, bassanite, gypsum) may also be found in the outcrop, as well as various double salts with Na^+, such as bloedite, vanthoffite, or glauberite. These geochemical inferences are supported by the Mini-TES data that indicate substantial quantities of Mg and Ca sulfates. If all the Mg and two-thirds of the Ca are in the form of sulfates, the balance of the S can be accounted for by jarosite. Most of these candidate salts, including the jarosite detected by the Mössbauer spectrometer, are hydrated compounds, probably providing at least some of the hydrogen atoms that have been detected from orbit over Meridiani Planum by the Mars Odyssey Gamma-Ray Spectrometer experiment (*13*).

Along with sulfate salts, the outcrop rock must contain a substantial fraction of siliciclastic materials. APXS data show that the elemental composition of this component is basaltic in character (*6*), but evidence for primary igneous minerals is weak. Mini-TES detections of small amounts of olivine, pyroxene, and feldspar in outcrop exposures are best explained as surface contamination by the abundant wind-blown basaltic sand (*10*). The Mössbauer spectrometer detected no olivine in outcrop rock exposed by the RAT, and only a weak feature that is provisionally

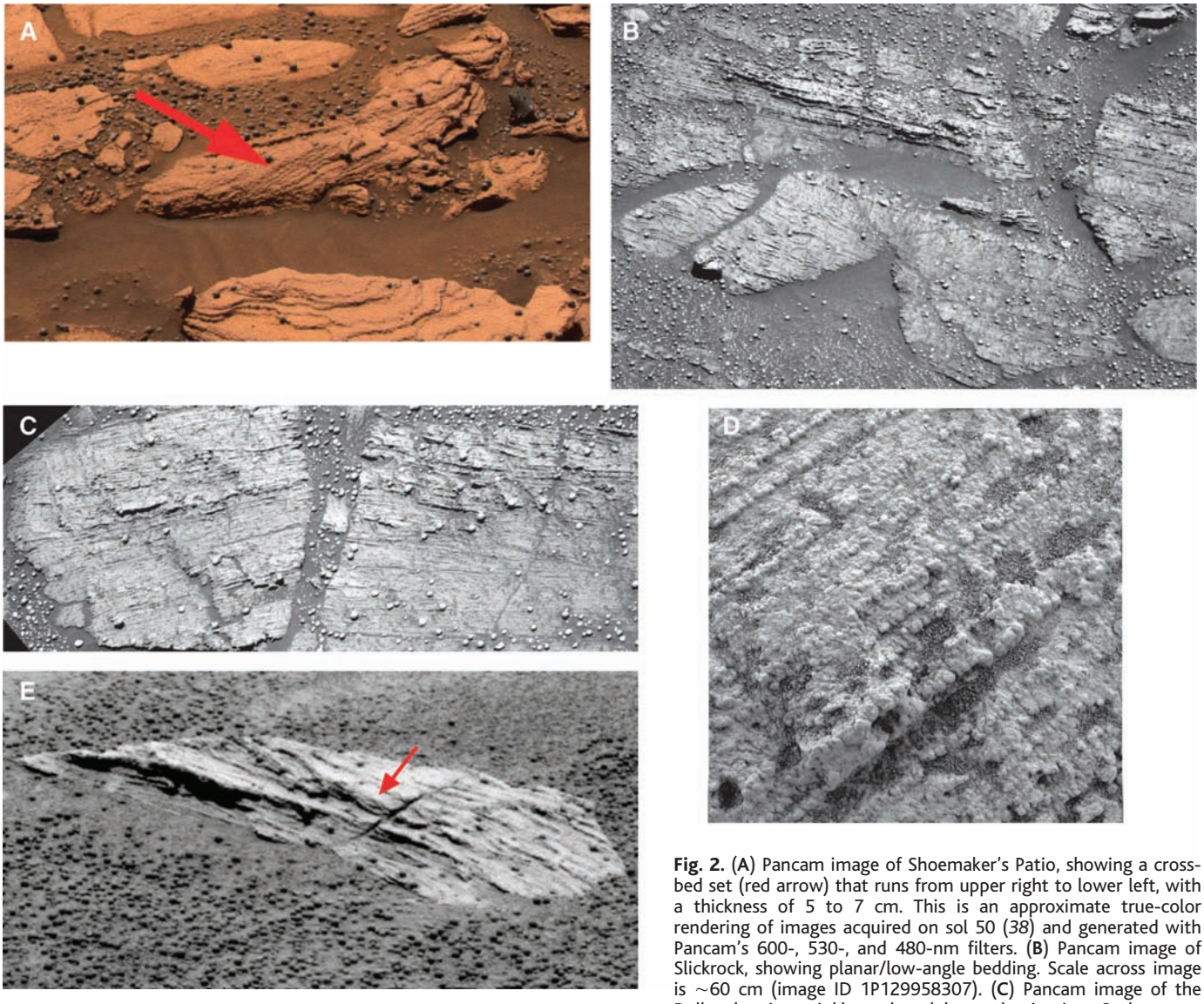

Fig. 2. (**A**) Pancam image of Shoemaker's Patio, showing a cross-bed set (red arrow) that runs from upper right to lower left, with a thickness of 5 to 7 cm. This is an approximate true-color rendering of images acquired on sol 50 (*38*) and generated with Pancam's 600-, 530-, and 480-nm filters. (**B**) Pancam image of Slickrock, showing planar/low-angle bedding. Scale across image is ~60 cm (image ID 1P129958307). (**C**) Pancam image of the Dells, showing crinkly and undulatory lamination. Scale across image is ~55 cm (image ID 1P131822391). (**D**) MI image of laminations that are a single grain thick. Scale across image is ~30 mm (image ID 1M131912465). (**E**) Pancam image of Scoop, a rock just outside Eagle crater, showing small-scale ripple cross-lamination with festoon geometry (red arrow). Scale across image is ~40 cm. Sum of six left-eye images obtained on sol 52.

assigned to pyroxene but that could be some other Fe^{2+} phase (*9*).

The spherules differ in composition from the rock in which they are embedded. Pancam images show that the spherules have distinctly different visible and near-infrared spectral properties than the rock (*3*). Because the spherules are much smaller than the fields of view of the APXS and Mössbauer instruments, it is not possible to isolate individual spherules for detailed compositional analysis by these instruments. However, two independent observations demonstrate that their composition is dominated by hematite. First, Mini-TES observations of spherules that lie atop Meridiani soil show that the concentration of hematite as detected by Mini-TES correlates with the fraction of the Mini-TES field of view filled by spherules (*10*). Second, a Mössbauer measurement was made on an accumulation of loose spherules that are fortuitously concentrated together in a local topographic depression in the outcrop named the Berry Bowl. This measurement shows a strong hematite signal relative to a measurement made on spherule-free outcrop immediately adjacent to the Berry Bowl (*9*).

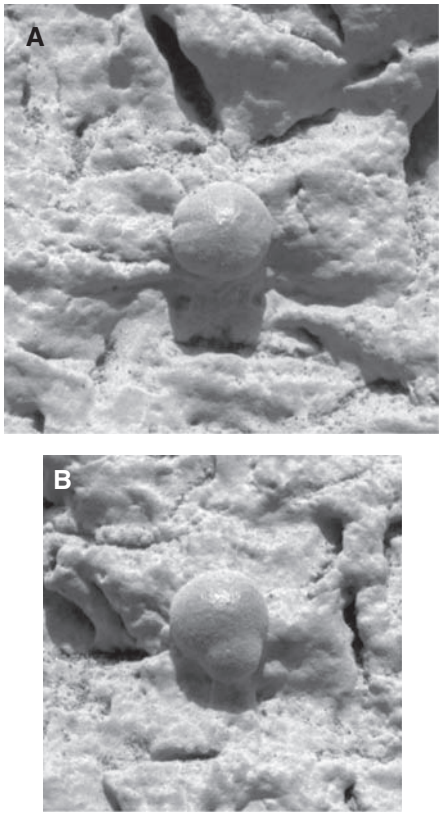

Fig. 3. (**A**) MI image of a spherule showing banding across it, aligned with local lamination in the surrounding sediments. Scale across image is ~15 mm (image ID 1M130760791). (**B**) A "doublet" spherule formed by two interpenetrating spherules. Scale across image is ~13 mm (image ID 1M130672582).

Other observations also point to a strong hematite concentration in the spherules. APXS measurements of the Berry Bowl show anomalously high Fe and a high Fe/Mn ratio (*6*). Pancam spectra of spherules are also indicative of hematite (*3*), and spherules sectioned with the RAT show consistent Pancam spectral properties throughout their interiors, indicating that the hematite is not simply present in coatings. Indeed, the spherules, which are strewn across most soils at the Opportunity landing site (*14*), both inside Eagle crater and on the surrounding plains, appear to be the primary carriers of the coarse-grained gray hematite that was detected from orbit by the Mars Global Surveyor TES instrument (*15*). Not all hematite is in spherules, however, because the Mössbauer spectrometer also detects hematite in spherule-free outcrops (*6*), albeit at lower concentrations than in the spherules. Grinding of the outcrop with the RAT consistently produces a pronounced brick-red stain in the RAT cuttings (*3*). This color differs from that of the outcrop and is consistent with production of fine-grained hematite, perhaps from both the rock and the spherules, during the grinding process.

Cross-stratification. Stratification styles observed in the rocks of Eagle crater include planar lamination, low-angle cross-stratification, cross-bedding, ripple cross-lamination, and crinkly and undulatory lamination.

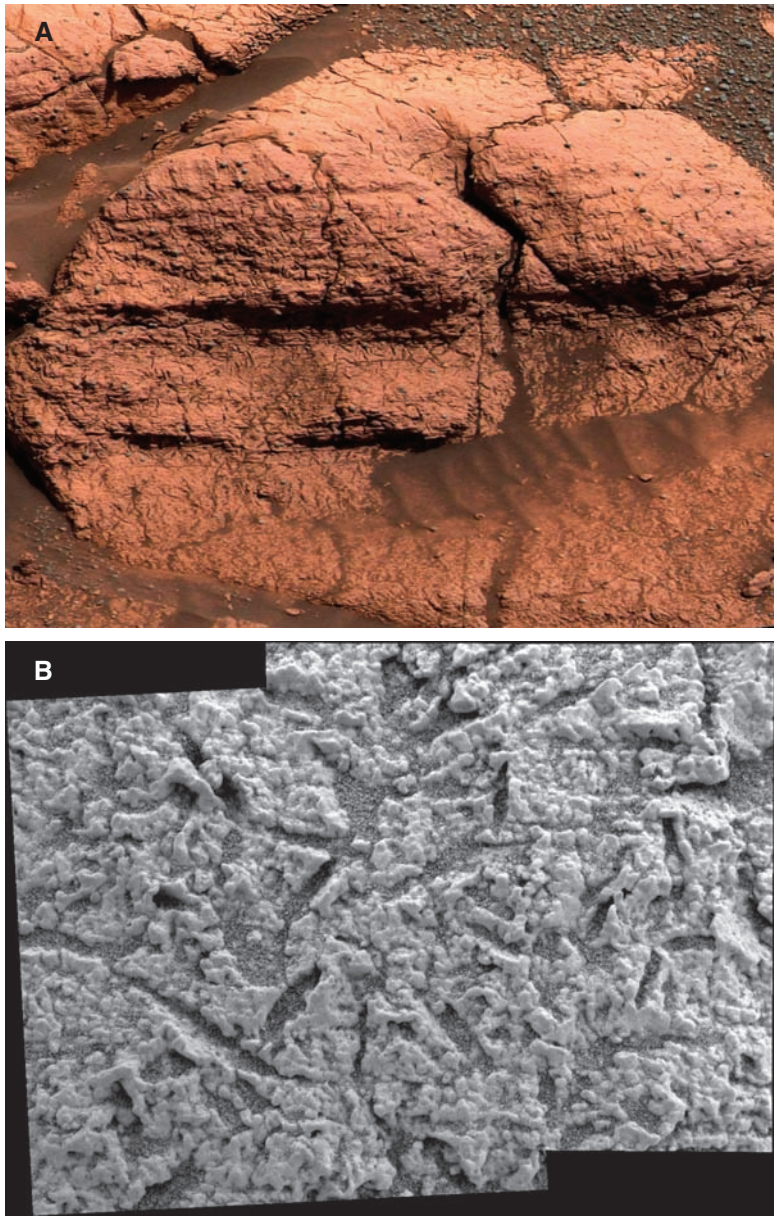

Fig. 4. (**A**) Pancam image of vugs in El Capitan, acquired on sol 27 and generated with Pancam's 750-, 530-, and 480-nm filters. Scale across image is ~43 cm (image ID 1M130670922). (**B**) MI mosaic of vugs in El Capitan. Scale across each individual image frame is 30 mm (image IDs 1M130670922 and 1M130671284).

Planar lamination and low-angle cross-stratification are well developed in several locations, particularly at Slickrock and Shoemaker's Patio. MI images at Slickrock show laminations of single-grain thick layers (Fig. 2D) suggestive of eolian sediment transport (*16*). At Shoemaker's Patio, a single cross-bed set with thickness of 5 to 7 cm is preserved (Fig. 2A). The set is truncated at either end because of brecciation, so bed set geometry is unconstrained, but cross-strata lap downward tangentially against the lower bounding surface. This geometry represents deposition of either subaerial or subaqueous dunes (*17*). The presence of adjacent breccia blocks with planar lamination and low-angle cross-lamination suggests that eolian processes may have been dominant here, perhaps forming in response to the passage of adhesion ripples on an aggrading and moist depositional surface.

In contrast, ripple cross-lamination with festoon geometry is present at the rock called Last Chance (Big Bend area; Plate 6), at the Dells (Plate 7), and in an isolated rock called Scoop (Fig. 2E) on the southwest rim of the crater. Ripple cross-laminae sets are 0.8 to 1.7 cm thick. The sets at Scoop may be climbing. These geometries indicate sediment transport in subaqueous ripples. The reconstructed former bedforms are inferred to be only a few centimeters in size and are therefore too small to be eolian dunes (*17*, *18*). But they are also too large (and of the wrong geometry) to be the climbing translatent cross-strata produced by eolian wind ripples (*16*, *19*). Their size is, however, consistent with subaqueous formation. Also, their festoon geometry requires that the reconstructed ripples have three-dimensional geometry defined by highly sinuous crestlines. Such bedforms are known only to develop in subaqueous, subcritical flows, with velocities as fast as a few tens of centimeters per second (*17*, *18*, *20*). Mars' lower gravity has only a small effect on the initiation of sediment transport and bedform size (*20*, *21*), posing no challenge to the subaqueous interpretation.

Diagenetic features. The rocks exposed in Eagle crater exhibit a complex diagenetic history. Observed diagenetic features are consistent with formation within the fluid-saturated (phreatic) zone of a groundwater system (*22*, *23*). There is minimal disruption of primary sedimentary features, which suggests that diagenetic processes involved little bulk volume change.

The most conspicuous diagenetic features are the hematitic spherules (Fig. 3). These are found in all rock exposures in Eagle crater and represent ~2% of the rock by volume. They exhibit a narrow size range, and their shapes deviate only slightly from spherical. Spherules sectioned by the RAT lack internal structure at scales visible to the MI (*5*). The spatial distribution of spherules within outcrop rock is more uniform than a spatially random (i.e., Poisson) distribution; in particular, they are not concentrated along bedding planes. Spherules generally do not disturb surrounding laminations, but some show banding or grooves that parallel the lamination in the rock that immediately surrounds them (Fig. 3A). Most spherules occur as single bodies, but occasionally they are found as doublets or triplets (Fig. 3B). Their resistance to weathering and to grinding with the RAT (*4*) indicates that spherules are harder than the surrounding rock.

On the basis of these characteristics and their hematite-dominated composition, we interpret the spherules as concretions that formed during early burial diagenesis, after the primary phase of compaction and under near-isotropic permeability and near-static fluid conditions (*24*, *25*). Their formation may have involved replacement of preexisting sulfate minerals and filling of primary porosity. The fact that the concretions formed within sandy sediments but do not preserve sandy textures in their interiors suggests that dissolution was involved and that the siliciclastic grains within the rock are much smaller than sand size. The exact chemical reactions involved in spherule formation are not well constrained, but breakdown of jarosite to form hematite during a period of fluid recharge is thermodynamically plausible.

The vugs (Fig. 4) are unevenly distributed at Eagle crater, but in the rocks where they are present, they typically cover about 5% of the surface. When abraded by the RAT (providing a deeper view into the rock), the apparent size of vugs can expand; this suggests that they are related to chemical dissolution rather than physical erosion. Because of this characteristic, and especially because of their tabular shape, we interpret the vugs to represent a crystal-mold porosity (*26*) formed by dissolution of a relatively soluble mineral phase (or phases), likely sulfates.

Crosscutting relationships suggest that the concretions postdated the formation of the primary vug-filling minerals, and that the development of secondary porosity that yielded the vugs postdated the formation of concretions (Fig. 5). Because spherules crosscut and truncate vugs, the vug-filling minerals presumably were present first. But there is no perturbation of the spherical shape of concretions where vugs abut against them or where concretions impinge into vug space; this finding implies that the secondary porosity was not present when the concretions formed.

In addition to spherule and vug formation, one or more episodes of cementation may have taken place in the outcrop rock. Lithification is likely related to pore-filling cement consisting of sulfate minerals and possibly hematite. Parts of the outcrop (e.g., Guadalupe) are much more resistant to the RAT and have a more massive appearance where freshly exposed, perhaps because of a locally higher degree of cementation and/or an episode of recrystallization. In places, exposed concretions are surrounded by a socket that could represent another generation of recrystallization.

History. We interpret the rocks of the Eagle crater outcrop to be a mixture of chemical and siliciclastic sediments with a complex diagenetic history. The environmental conditions that they record are episodic inundation by surface water to shallow depths, followed by evaporation, exposure, and desiccation. The festoon cross-lamination provides evidence for inundation by water, the mineralogy and geochemistry indicate precipitation of dissolved salts, and the planar to low-angle lamination and larger scale cross-bedding are consistent with sediment transport across a dry surface. Terrestrial analogs for such a suite of facies and surface processes include interdune depressions

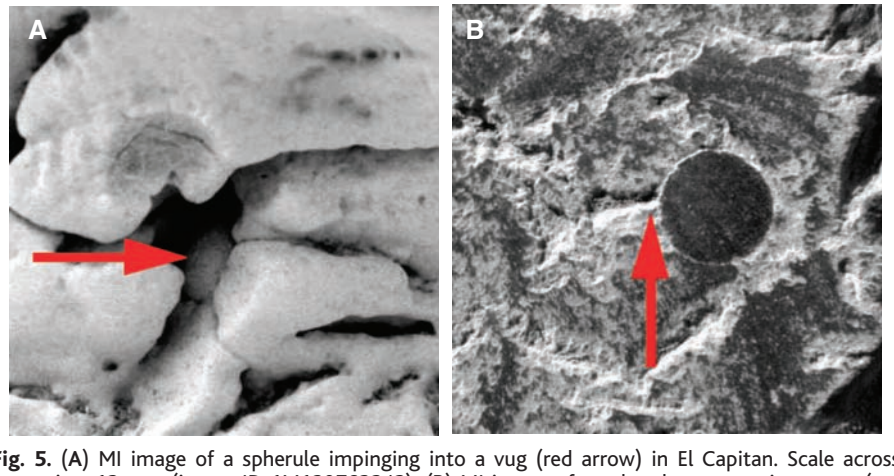

Fig. 5. (**A**) MI image of a spherule impinging into a vug (red arrow) in El Capitan. Scale across image is ~12 mm (image ID 1M130762242). (**B**) MI image of a spherule crosscutting a vug (red arrow) in a portion of El Capitan that was exposed by the RAT. Scale across image is ~12 mm (image ID 1M131212783).

(*27*), playa lakes (*28*), and sabkhas adjacent to marginal seaways (*29*).

Our elemental and mineralogic data suggest that the sedimentary rocks are, by weight, ~50% fine-grained siliciclastic materials derived from basaltic rocks, ~40% sulfate minerals (including Mg sulfate and jarosite), and ~10% hematite. Primary igneous minerals are not readily identified in the siliciclastic fraction, suggesting a substantial degree of chemical alteration. The sulfate minerals may have formed via direct precipitation from water or within the sediment during early burial. In the intervals when surface water was present, it may have been open to the martian atmosphere, but in the absence of unambiguous wave ripples we cannot rule out the possibility of an ice cover.

Aqueous and eolian transport of sulfate-rich sand grains was followed by cementation by fine-grained material, probably mostly sulfates and perhaps also hematite. Concretions formed via precipitation of hematite from groundwater, and tabular mineral grains (probably sulfates) grew. Subsequent diagenetic events included local recrystallization of cements and dissolution of the soluble mineral grains to form vugs. All of these processes were followed after an unknown time interval by the formation of Eagle crater itself, exposing the sedimentary rocks and causing much of the observed brecciation.

It is noteworthy that the environmental conditions recorded at Eagle crater may have prevailed over a large area. All of the bedrock observed during Opportunity's traverse to Endurance crater, more than half a kilometer from the landing site, showed the same characteristics as the outcrop in Eagle crater (*1*). More important, orbital data from the Mars Orbiter Camera show that a relatively high-albedo unit that correlates with the outcrop exposures near the Opportunity landing site is at least discontinuously present across most of Meridiani Planum. It seems likely, then, that the area over which these aqueous sedimentary and diagenetic processes operated was at least tens of thousands of square kilometers in size.

The timing and duration of aqueous processes at Meridiani are more difficult to determine. The crater size frequency distributions for the Meridiani plains suggest a complex history of crater production and removal (*30*), compromising our ability to extract useful ages from crater abundances. An upper bound on the age can be derived from analyses of orbital images showing that the Meridiani plains materials disconformably overlie dissected Middle to Late Noachian cratered terrains (*31*), which suggests that the rocks in Eagle crater could be as much as several billion years old. Nothing in our observations at Eagle crater places useful bounds on the duration of aqueous activity at Meridiani.

Implications. Liquid water, which our results show was once abundant at Meridiani Planum, is widely viewed as a key prerequisite for life. Therefore, we infer that surface conditions at Meridiani may have been habitable for some period of time in martian history.

The recorded environmental conditions, however, would have posed at least two kinds of challenges to development of martian biology. One set of challenges deals with water chemistry. Mineral assemblages similar to those in Eagle crater are found on Earth. Commonly these are associated with mine drainage, but in some cases, notably the Rio Tinto basin in Spain (*32*), mineral deposition predates mining activity. Precipitating waters tend to be acidic, sometimes strongly so. In addition, in the saline waters suggested by Meridiani geology, water activity could have been at least episodically prohibitive.

High acidity and salinity do not pose insurmountable challenges to microbial life on Earth. Acidic waters can support a phylogenetically wide array of bacteria and microscopic eukaryotes (*33*, *34*); microorganisms can also accommodate to both short-term desiccation and (within limits) persistent hypersalinity (*35*). Such organisms, however, belong to specialized populations that have evolved to survive in highly acidic or saline environments. It is less clear that such conditions are suitable for the kinds of prebiotic chemical reactions commonly invoked to explain the origin of life.

A second class of challenges to biology at Meridiani deals with the persistence of water. The rocks at Eagle crater expose tens of centimeters of sulfate-rich stratigraphy. At nearby Endurance crater, the exposed thickness of similar rocks approaches 10 m. Despite this substantial thickness, the apparent prevalence of sulfate-cemented eolian sands suggest that water on Meridiani Planum may have been regionally extensive but temporally discontinuous, increasing the difficulty of biological persistence over long time intervals.

We cannot determine whether life was present or even possible in the waters at Meridiani, but it is clear that by the time the sedimentary rocks in Eagle crater were deposited, Mars and Earth had already gone down different environmental paths. Sample return of Meridiani rocks might well provide more certainty regarding whether life developed on Mars. Sulfate deposits are known to preserve both chemical and morphological fossils (*36*), and iron oxide precipitates at Rio Tinto contain beautifully preserved fossils, including minute fossils of coccoid and filamentous microorganisms (*37*). Meridiani Planum therefore can be considered an attractive candidate for further study, both by landed missions and by sample return.

References and Notes

1. S. W. Squyres *et al.*, *Science* **306**, 1698 (2004).
2. Names have been assigned to aerographic features by the Mars Exploration Rover (MER) team for planning and operations purposes. The names are not formally recognized by the International Astronomical Union.
3. J. F. Bell III *et al.*, *Science* **306**, 1703 (2004).
4. R. E. Arvidson *et al.*, *Science* **306**, 1730 (2004).
5. K. E. Herkenhoff *et al.*, *Science* **306**, 1727 (2004).
6. R. Rieder *et al.*, *Science* **306**, 1746 (2004).
7. The term martian soil is used here to denote any loose unconsolidated materials that can be distinguished from rocks, bedrock, or strongly cohesive sediments. No implication of the presence or absence of organic materials or living matter is intended.
8. R. Gellert *et al.*, *Science* **305**, 829 (2004).
9. G. Klingelhöfer *et al.*, *Science* **306**, 1740 (2004).
10. P. R. Christensen *et al.*, *Science* **306**, 1733 (2004).
11. L. A. Hardie, *Am. J. Sci.* **284**, 193 (1984).
12. L. A. Hardie, *Annu. Rev. Earth Planet. Sci.* **19**, 131 (1991).
13. W. V. Boynton *et al.*, *Science* **297**, 81 (2002).
14. L. A. Soderblom *et al.*, *Science* **306**, 1723 (2004).
15. P. R. Christensen *et al.*, *J. Geophys. Res.* **105**, 9623 (2000).
16. R. E. Hunter, D. M. Rubin, in *Eolian Sediments and Processes*, M. E. Brookfield, T. S. Ahlbrandt, Eds. (Elsevier, Amsterdam, 1983), pp. 429–454.
17. J. C. Harms *et al.*, *Structures and Sequences in Clastic Rocks* (Society of Economic Paleontologists and Mineralogists, Tulsa, OK, 1982).
18. G. V. Middleton, J. B. Southard, *Mechanics of Sediment Movement* (Society of Economic Paleontologists and Mineralogists, Providence, RI, 1984).
19. D. M. Rubin, R. E. Hunter, *Sedimentology* **29**, 121 (1982).
20. J. B. Southard, J. A. Boguchwal, *J. Sediment. Petrol.* **66**, 680 (1990).
21. P. L. Wiberg, J. D. Smith, *Water Resour. Res.* **23**, 1471 (1987).
22. L. A. Hardie *et al.*, in *Sixth Symposium on Salt* (Northern Ohio Geological Society, Cleveland, 1983), pp. 11–39.
23. J. P. Smoot, T. K. Lowenstein, in *Evaporites, Petroleum, and Mineral Resources*, J. L. Melvin, Ed. (Elsevier, Amsterdam, 1991), pp. 189–347.
24. J. Sellés-Martínez, *Earth Sci. Rev.* **41**, 177 (1996).
25. A. Seilacher, *Sediment. Geol.* **143**, 41 (2001).
26. P. W. Choquette, L. C. Pray, *Am. Assoc. Petrol. Geol. Bull.* **54**, 207 (1970).
27. N. P. Mountney, D. B. Thompson, *Sedimentology* **49**, 805 (2002).
28. R. W. Renault, W. M. Last, *Sedimentology and Geochemistry of Modern and Ancient Saline Lakes* (Society of Economic Paleontologists and Mineralogists, Tulsa, OK, 1994).
29. D. J. Kinsman, *Am. Assoc. Petrol. Geol. Bull.* **53**, 830 (1969).
30. M. D. Lane *et al.*, *Geophys. Res. Lett.* **30**, 10.1029/2003GLO17183 (2003).
31. R. E. Arvidson *et al.*, *J. Geophys. Res.* **108**, 10.1029/2002JE002041 (2003).
32. D. C. Fernández-Remolar, N. Rodriguez, F. Gómez, R. Amils, *J. Geophys. Res.* **108**, 10.1029/2002JE001918 (2003).
33. L. Ameral Zettler *et al.*, *Nature* **417**, 137 (2002).
34. B. J. Baker, J. F. Banfield, *FEMS Microbiol. Ecol.* **44**, 139 (2003).
35. D. Billi, M. Potts, *Res. Microbiol.* **153**, 7 (2002).
36. S. Bonny, B. Jones, *Can. J. Earth Sci.* **40**, 1483 (2003).
37. D. Fernández-Remolar, R. Amils, R. V. Morris, A. H. Knoll, *Proceedings of the 33rd Lunar and Planetary Science Conference* (Houston, TX, March 2002), abstr. 1226.
38. A martian solar day has a mean period of 24 hours 39 min 35.244 s and is referred to as a sol to distinguish this from a roughly 3% shorter solar day on Earth.
39. This research was carried out for the Jet Propulsion Laboratory, California Institute of Technology, under a contract with NASA.

Plates Referenced in Article

www.sciencemag.org/cgi/content/full/306/5702/1709/DC1
Plates 6 and 7

26 August 2004; accepted 19 October 2004

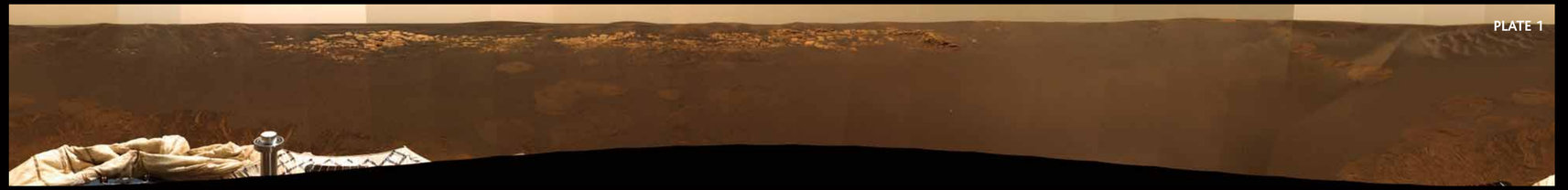

PLATE 1

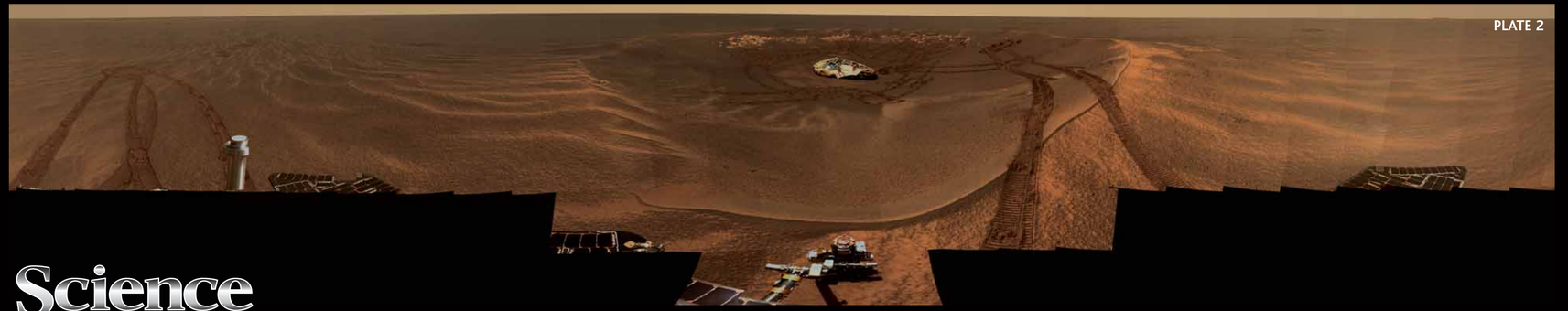

PLATE 2

Science

PLATE 4

PLATE 1. Pancam pre-standup Mission Success 360° panorama color composite (red, 750 nm; green, 530 nm; blue, 480 nm) of the Opportunity landing site within Eagle crater. The panorama was generated from imaging sequences P2211 to P2218 acquired on sols 2 and 3. Colors were processed to match the spectral properties of the Pancam calibration target, as observed on Mars, to its properties as measured during prelaunch laboratory calibrations, and thus they represent only an approximate rendering of true color.

PLATE 2. Pancam Lion King 360° panorama color composite (red, 750 nm; green, 530 nm; blue, 480 nm) acquired from a point just outside the southern rim of Eagle crater. The panorama was generated from imaging sequences P2211 to P2218 acquired on sols 58 and 60. Colors were processed to represent only an approximate rendering of true color.

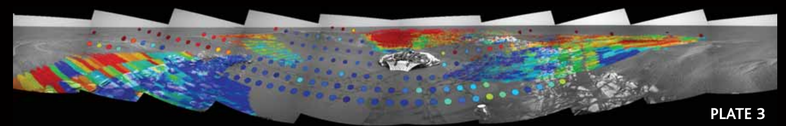

PLATE 3

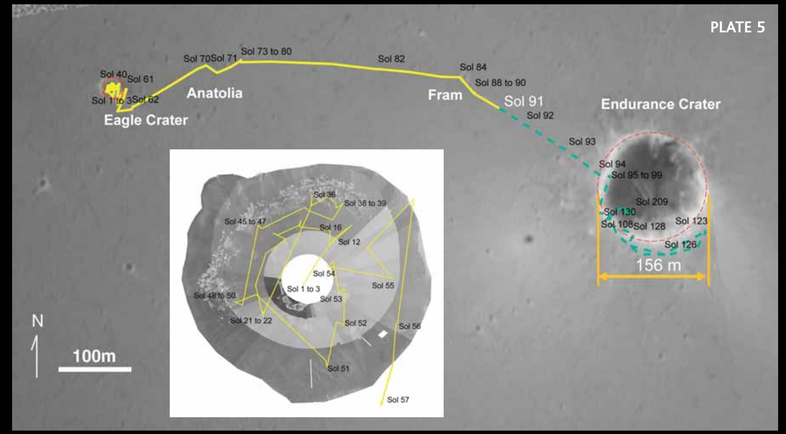

PLATE 3. Miniature thermal emission spectrometer (Mini-TES) gray hematite abundance map of Eagle crater, superimposed on a Navcam 360° panorama (red, high hematite abundance; blue, low hematite abundance).

PLATE 4. Pancam color composite mosaic (red, 750 nm; green, 530 nm; blue, 430 nm) of Fram crater, generated from imaging sequence P2285 acquired on sol 88 during the Opportunity traverse across the plains to Endurance crater. Colors were processed to represent only an approximate rendering of true color.

PLATE 5. Opportunity traverse path graphic, showing the rover's route during the primary mission from the landing site within Eagle crater (inset; diameter, ~22 m) east across the plains to Anatolia fracture, Fram crater, and eventually to the rim of Endurance crater. The base map is from the rover's Descent Image Motion Compensation imager. The inset, generated from Navcam images, covers an area 25 m east-west by 24 m north-south.

CREDITS: (PLATES 1,2 & 4) NASA/JPL/CORNELL; (PLATE 3) NASA/JPL/ASU; (PLATE 5) NASA/JPL/OSU

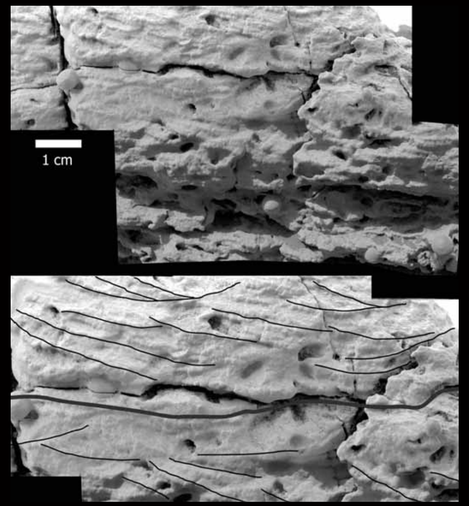

PLATE 6

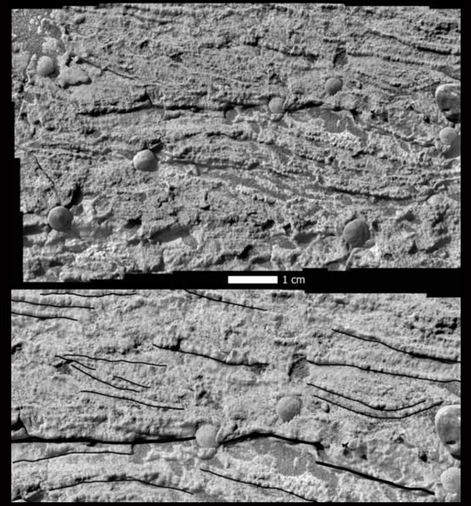

PLATE 7

PLATE 6. **(Top)** Microscopic Imager (MI) mosaic of Last Chance, taken on sols 39 and 40; upper part of the mosaic taken in shadow, lower part of the mosaic taken in full sunlight. **(Bottom)** Detail of upper part of the mosaic, annotated to show interpretation of festoon cross-lamination. Scale bar applies only to top panel.

PLATE 7. MI mosaic of East Dells, taken on sol 41. Illumination is from the upper left. **(Top)** Full mosaic showing millimeter-scale laminations that are not draped over spherules. **(Bottom)** Detail of upper part of the mosaic, annotated to show the interpretation of festoon cross-lamination. Scale bar applies only to top panel.

PLATE 8. **(A)** Pre- and **(B)** post-RAT (Rock Abrasion Tool) color images of the Eagle crater outcrop rock known as McKittrick. Pre-RAT image is from sol 29, imaging sequence P2578; post-RAT image is from sol 36, imaging sequence P2531. These are enhanced color composites generated with Pancam's 600-, 530-, and 480-nm filters.

PLATE 9. **(A)** Pre- and **(B)** post-RAT color images of the Eagle crater outcrop rock Guadalupe. Pre-RAT image is from sol 27, imaging sequence P2387; post-RAT image is from sol 35, imaging sequence P2598. These are enhanced color composites generated with Pancam's 600-, 530-, and 480-nm filters.

PLATE 10. **(A)** Pre- and **(B)** post-RAT color images of the Eagle crater outcrop rock Flat Rock. Pre-RAT image is from sol 42, imaging sequence P2547; post-RAT image is from sol 45, imaging sequence P2560. These are enhanced color composites generated with Pancam's 600-, 530-, and 480-nm filters.

PLATE 11. **(A)** Pre- and **(B)** post-RAT color images of the Eagle crater outcrop rock Berry Bowl. Pre-RAT image is from sol 45, imaging sequence P2556; post-RAT image is from sol 48, imaging sequence P2568. These are enhanced color composites generated with Pancam's 600-, 530-, and 480-nm filters.

PLATE 8A

PLATE 8B

PLATE 9A

PLATE 9B

PLATE 10A

PLATE 10B

PLATE 11A

PLATE 11B

Science

PLATE 12A

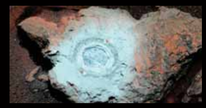

PLATE 12B

PLATE 13

PLATE 12. **(A)** Pre- and **(B)** post-RAT color images of the Meridiani plains rock Bounce rock. Pre-RAT image is from sol 65, imaging sequence P2574; post-RAT image is from sol 68, imaging sequence P2581. These are enhanced color composites generated with Pancam's 600-, 530-, and 480-nm filters.

PLATE 13. Pancam vertical projection color composite mosaic of the Eagle crater outcrop from two adjacent rover positions along the outcrop, generated from imaging sequences P2261, P2263, and P2265 acquired on sols 17 to 19. This is an approximate true-color rendering generated with Pancam's 600-, 530-, and 480-nm filters.

PLATE 14. Pancam color composite image of the first Eagle crater trench excavated on sol 23, generated from imaging sequence P2385 acquired on sol 26. This is an approximate true-color rendering generated with Pancam's 600-, 530-, and 480-nm filters.

PLATE 15. Pancam color composite image of the trench excavated within the plains outside of Eagle crater on sol 73, generated from imaging sequence P2421 acquired on sol 81. This is an approximate true-color rendering generated with Pancam's 600-, 530-, and 480-nm filters.

PLATE 16. Pancam color composite image of the trench excavated near the center of Eagle crater next to the lander on sol 54, generated from imaging sequence P2404 acquired on sol 55. This is an approximate true-color rendering generated with Pancam's 600-, 530-, and 480-nm filters.

PLATE 14

PLATE 15

PLATE 16

CREDITS: (PLATES 6 & 7) NASA/JPL/USGS; (PLATES 8–16) NASA/JPL/CORNELL

Soils of Eagle Crater and Meridiani Planum at the Opportunity Rover Landing Site

L. A. Soderblom,[1]* R. C. Anderson,[2] R. E. Arvidson,[3] J. F. Bell III,[4] N. A. Cabrol,[5] W. Calvin,[6] P. R. Christensen,[7] B. C. Clark,[8] T. Economou,[9] B. L. Ehlmann,[3] W. H. Farrand,[10] D. Fike,[11] R. Gellert,[12] T. D. Glotch,[7] M. P. Golombek,[2] R. Greeley,[7] J. P. Grotzinger,[11] K. E. Herkenhoff,[1] D. J. Jerolmack,[11] J. R. Johnson,[1] B. Jolliff,[3] G. Klingelhöfer,[13] A. H. Knoll,[14] Z. A. Learner,[4] R. Li,[15] M. C. Malin,[16] S. M. McLennan,[17] H. Y. McSween,[18] D. W. Ming,[19] R. V. Morris,[19] J. W. Rice Jr.,[7] L. Richter,[20] R. Rieder,[12] D. Rodionov,[13] C. Schröder,[13] F. P. Seelos IV,[3] J. M. Soderblom,[4] S. W. Squyres,[4] R. Sullivan,[4] W. A. Watters,[11] C. M. Weitz,[21] M. B. Wyatt,[7] A. Yen,[2] J. Zipfel[12]

The soils at the Opportunity site are fine-grained basaltic sands mixed with dust and sulfate-rich outcrop debris. Hematite is concentrated in spherules eroded from the strata. Ongoing saltation exhumes the spherules and their fragments, concentrating them at the surface. Spherules emerge from soils coated, perhaps from subsurface cementation, by salts. Two types of vesicular clasts may represent basaltic sand sources. Eolian ripples, armored by well-sorted hematite-rich grains, pervade Meridiani Planum. The thickness of the soil on the plain is estimated to be about a meter. The flatness and thin cover suggest that the plain may represent the original sedimentary surface.

Martian soils (*1*) are remnants of their source rocks and thus provide insight into geologic processes and history on local, regional, and global scales. Whether soils are actively changing or represent static records of past climates is a key question for Mars. The soils of Meridiani Planum, where Opportunity landed, contrast with soils at sites visited by the Viking Landers, Mars Pathfinder, and Spirit. The regional albedo of Meridiani Planum is ~0.12, among the lowest on Mars (*2*, *3*). Mars Global Surveyor (MGS) Mars Orbiter Camera (MOC) images (*4*) show that the floors of the sparse impact craters, such as Eagle and Endurance (*5*), are slightly darker than the surrounding plains. Some observers have suspected that these dark crater floors represent active, saltating dark sand deposits (*6*, *7*). Meridiani Planum is also unique in its orbital signature; the MGS Thermal Emission Spectrometer showed the strongest, most extensive signature for coarsely crystalline hematite of any region on the planet (*8*). Because most modes of hematite formation involve liquid water, Meridiani Planum is a prime site for exploration. Understanding the nature of its unusual soils, confirming the existence and understanding the nature of occurrence of hematite, and relating these to the regional geologic history are key objectives of Opportunity's mission and are the subject of this report.

During landing, Opportunity bounced ~26 times, traveled ~300 m across Meridiani Planum, and finally came to rest inside 20-m-diameter Eagle crater. The airbags remained clean (Plate 1), unlike those of Pathfinder and Spirit, which were stained with reddish dust (*9*, *10*). Evidently the Meridiani surface is less dusty, presumably because of ongoing deflation by wind, stripping away dust left by annual global storms. Airbag bounce marks on the crater floor indicate that deflation leaves a thin, dark lag deposit that is easily depressed into the brighter, redder subsurface soil. Two crater-floor trenches show brighter materials just below the surface (Plates 14 and 16). Panoramic Camera (Pancam) images show the 750-nm albedo of the surface to be ~30% darker than that of the trench floor (Plate 14). Other landing sites usually show the reverse; in general, the surface is brighter than the subsurface when exposed by tracks and trenches (*9*, *11*).

Pancam images, Miniature Thermal Emission Spectrometer (Mini-TES), Mössbauer Spectrometer (MB), and Alpha Particle X-Ray Spectrometer (APXS) data for the relatively dust-free, dark sand surface at Tarmac, a soil site reached soon after Opportunity's egress, show that the composition and mineralogy of an olivine-bearing basalt with ~10% of the Fe is in the form of hematite (*3*, *12–14*). Microscopic Imager (MI) images show that this dark surface sand is finer than ~150 μm (*15*). The grain size expected to be most easily moved by saltation on Mars is ~100 μm (*16*). Pancam images show well-developed eolian saltation impact ripples of varying wavelengths across the crater floor. The lower limit of the sand grain size is unknown, owing to the MI resolution (pixel size ~30 μm). However, we suspect the sand to be well sorted roughly in the size range 50 to 150 μm, because the bulk of the grains are resolvable in the MI images (2 to 5 pixels) and most of the sparse sand grains lying silhouetted on the brighter outcrop are resolvable (*15*).

The low albedo of the surface soils in Eagle crater shows it to be relatively dust-free. Further, when pressed into the Tarmac sand, the MB footprint exhibited poorly defined margins, as would be expected for cohesionless sand-sized particles. No compaction was apparent; the fine-grained sand simply flowed around coarser clasts (*15*). By contrast, when the MB was pressed into the bright, reddish floors of the trenches, the materials were compacted with well-preserved imprints, as expected for cohesive silt- to clay-sized particles (*15*, *17*). It is our interpretation that the surface of the crater floor is covered by a deposit of actively moving, fine-grained dark sand that is least dusty and darkest at its surface and increases in dust content below the surface. Trench walls in the Eagle crater floor exhibit some clods and clumps, suggesting very weak cohesion, although any cementation is

[1]U.S. Geological Survey, Flagstaff, AZ 86001, USA. [2]Jet Propulsion Laboratory, Caltech, Pasadena, CA 91109, USA. [3]Department of Earth and Planetary Sciences, Washington University, St. Louis, MO 63130, USA. [4]Department of Astronomy, Cornell University, Ithaca, NY 14853, USA. [5]NASA Ames/SETI Institute, Moffett Field, CA 94035, USA. [6]University of Nevada, Reno, Geological Sciences, Reno, NV 89557, USA. [7]Department of Geological Sciences, Arizona State University, Tempe, AZ 85287–1404, USA. [8]Lockheed Martin Corporation, Littleton, CO 80127, USA. [9]Enrico Fermi Institute, University of Chicago, Chicago, IL 60637, USA. [10]Space Science Institute, Boulder, CO 80301, USA. [11]Massachusetts Institute of Technology, Earth, Atmospheric and Planetary Sciences, Cambridge, MA 02139, USA. [12]Max Planck Institut für Chemie, Kosmochemie, Mainz, Germany. [13]Johannes Gutenberg–University, Mainz, Germany. [14]Botanical Museum, Harvard University, Cambridge, MA 02138, USA. [15]Department of Civil and Environmental Engineering and Geodetic Science, Ohio State University, Columbus, OH 43210, USA. [16]Malin Space Science Systems, San Diego, CA 92191, USA. [17]Department of Geosciences, State University of New York at Stony Brook, Stony Brook, NY 11794, USA. [18]Department of Earth and Planetary Sciences, University of Tennessee, Knoxville, TN 37996, USA. [19]NASA Johnson Space Center, Houston, TX 77058, USA. [20]DLR Institute of Space Simulation, D-51147, Cologne, Germany. [21]Planetary Science Institute, Tucson, AZ 85719, USA.

*To whom correspondence should be addressed. E-mail: lsoderblom@usgs.gov

weaker than that found at other landing sites and on Meridiani Planum (*11*, *17*, *18*).

Before Opportunity drove off the lander, Mini-TES mapped the abundance of hematite across the floor and rim of Eagle crater and out onto the Meridiani plain (Plate 3 and Fig. 1) (*12*). The hematite abundance decreases from northwest to southeast across the crater floor, increases toward the crater rim and out onto the plain, and is lowest in the bounce marks. The visible–near-infrared reflectance spectrum of fine-grained hematite (as well as many Fe^{3+} minerals) shows a broad absorption feature with a minimum near 0.9 μm and a rapid increase in reflectance toward 1.0 μm (*3*). A ratio of Pancam images at 1.00 μm and 0.93 μm shows a pattern consistent with Mini-TES measurements between the hematite-poor bounce marks and undisturbed soil (Fig. 1B). Evidently the hematite occurs in a thin surface lag that is easily pushed into the hematite-poor soils. Ultimately the Mini-TES hematite signature was traced by MB and APXS (*12*–*14*) to the ubiquitous spherules on Meridiani Planum believed to be have been formed as concretions in the outcrop during diagenesis (*19*).

Global circulation models (*20*) and bright wind streaks seen in MOC and descent images indicate that the current prevailing wind direction is to the southeast. The Opportunity Ledge outcrop is centered in the northwest wall of Eagle crater (*19*); we infer that it is being exposed by wind deflation, the fine-grained basaltic sand that buries the outcrop being stripped off and deposited on the crater floor and opposite wall. This sand deposit terminates on the downwind crater rim in a large sinuous crested eolian bedform (Plate 2). Its sharp crest and steep outward slope (~30°) suggest a dune slip face. Also visible in Plate 2 are bright dust deposits in the lee of the crest. These represent the thickest local accumulations of bright dust found at the Meridiani site.

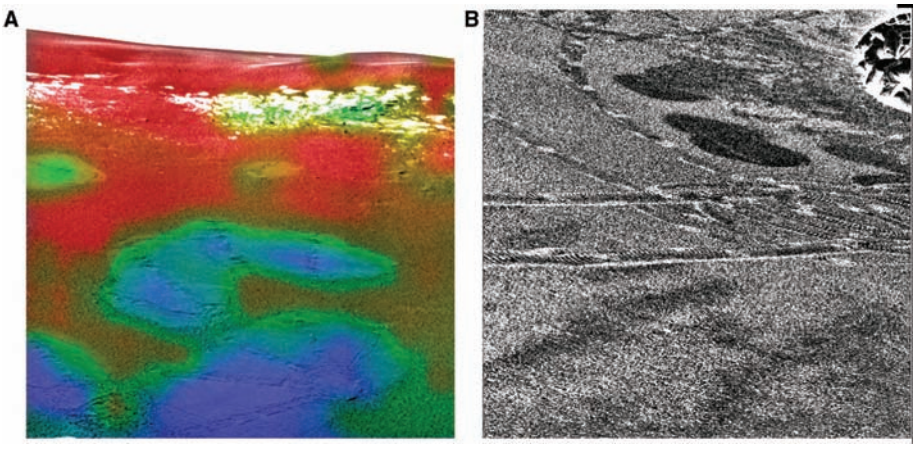

Fig. 1. (**A**) Mini-TES map of hematite abundance for a section of the floor of Eagle crater near the lander acquired before egress (red, high; blue, low). (**B**) Pancam ratio image of bounce marks acquired from the south rim of Eagle crater (sol 60) using images acquired for two near-infrared bands (R7/R6; central λ: 1001 nm and 933 nm). Bounce marks are roughly a meter in diameter.

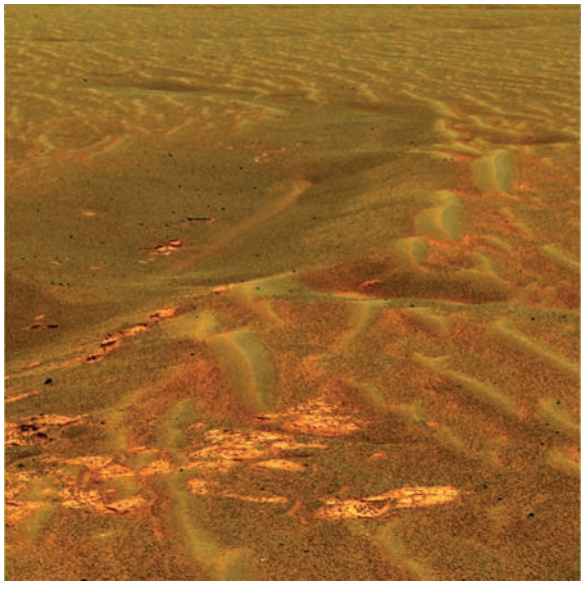

Fig. 2. Pancam-enhanced natural color image (RGB: L2, L5, L7; central λ: 753 nm, 535 nm, and 440 nm) of ubiquitous small crested bedforms of Meridiani Planum at Anatolia (sol 71). The foreground width of the image is ~2 m.

During sols 60 to 90 (*21*), Opportunity drove ~570 m to the east across Meridiani Planum toward Endurance crater (*22*). In contrast to the floor of Eagle crater, the flat plain is characterized by ubiquitous small sinuous crested eolian bedforms (Plate 2 and Fig. 2) and intervening troughs. These crested forms are ~10 cm wide, meters long, and 1 to 2 cm high; the spacing between ripple crests is tens of centimeters. Such forms also occur on the northern and western inner walls of Eagle crater where they lap over the rim from the plains (Plates 1 and 2). Using its front wheels, Opportunity dug a trench through one of these bedforms on sol 73 (*17*). MI and Pancam images of the Ripple-X trench wall cut through the crest (*17*) show none of the internal stratification that might be expected for small active dunes. The bedforms are similar to granule-armored eolian ripples studied by Spirit in Gusev crater (*11*, *23*, *24*). In both cases, the crests are armored with well-sorted millimeter-sized rounded granules that overlie fine-grained sand and dust. These granules appear to form as millimeter-sized grains, driven across the surface by creep induced by the impact of saltating sand-sized particles or rolled directly by the wind, pile up, and migrate in sinuous swaths. The resulting armor impedes removal of the subjacent sand. Thus, as saltating sands move through the system, fine-grained particles are continuously removed from adjacent troughs, leaving elevated, armored ripple crests.

Pancam images of the MI-accessible targets can be acquired from as close as ~1.5 m with pixel spacing of ~0.4 mm. Although the limiting Pancam optical resolution is ~1 mm (*3*), these oversampled images provide high signal-to-noise for multispectral analysis of the clasts. By merging the Pancam spectral cubes with the higher resolution (30 μm/pixel) MI images, composite image cubes are made that permit correlation of spectral classes with the morphologies of individual clasts (Fig. 3). Even with some exaggeration of the natural color (Fig. 3B), variation among the clasts is difficult to distinguish. By including the near-infrared bands (0.8 to 1.0 μm), the spectral variations are more apparent (Fig. 3C).

Several types of soil clasts can be identified at the Chocolate Chip soil site near the center of the Eagle crater floor (Fig. 3). In addition to the spherules that are yellow, orange, and purple in the near-infrared color composites, two other types of lithic fragments, most likely basalt clasts, are also evident (blue and green in Fig. 3C). They exhibit vesicles, are irregular in shape, and have rounded edges, presumably owing

to abrasion by basaltic sand. There may be two different basaltic sources. Although most are 3 to 5 mm in diameter, spherule diameters are 0.6 to 6 mm (*15*). Most lithic fragments are 1 to 3 mm in size, although cm-sized cobbles, possibly of basaltic composition, are scattered in Eagle crater.

At the Chocolate Chip site, the spherules exhibit a correlation between their spectral reflectance and their depth of burial in the soil (Fig. 3). Our interpretation is as follows. As they are exposed by wind deflation, spherules emerge coated with brighter material. The coatings have been abraded from the spherules that have fully emerged and are now perched on the surface. These are darkest and least red in their overall spectra (their actual color would be gray) (*3*) and exhibit the strongest broad Fe^{3+} absorption band centered at 0.9 μm (Fig. 3D). A few that are broken exhibit the same spectra in their interiors, leading to the conclusion that the darker, perched spherules are uncoated. Spherules that are still about half buried show this absorption band weakly in their centers, where the path length through a thin coating would be minimized. The most deeply buried and heavily coated spherules (bright yellow in Fig. 3, A and C) show a rougher texture; in most cases, dark grains (presumably basalt) are visible in or on the coatings. The spectral reflectance of these thick coatings is similar to that of bright martian dust and to the Eagle crater sulfate-rich outcrop materials. Some bright granules probably are outcrop fragments.

A possible explanation for the origin of the coatings involves formation while spherules reside in the uppermost few millimeters of the soil, where salts interact with low-level moisture that interchanges diurnally between the surface and atmosphere (*25*). Alternatively, the coatings may be remnants of sulfate-rich outcrop material still adhering to spherules. Most spherules found at the base of the outcrop are uncoated. However, these may not have been derived from local outcrop but rather may have been transported from the adjacent plains down-slope into the crater (*12*).

Pancam multispectral images of the Eagle crater soil clasts (e.g., Fig. 3) exhibit greater variability in reflectance (0.4 to 1.0 μm) of lithologic materials than previously observed in data collected from the surface, from orbit, or from Earth (*3*). Abrasion of the surfaces in Eagle crater by actively saltating, fine-grained sand, coupled with the diverse collection of materials, both derived locally and carried into the crater by wind and impact, accounts for the observed spectral diversity. This abrasion may enhance the TES orbital hematite signature (*8*). Many spherules show pitted surfaces; others are smooth, suggesting variable exposure to the abrasive eolian environment.

MI images of the troughs between the pervasive ripples on the Meridiani plains (Fig. 2) reveal that most of the clasts are spherules (Fig. 4A) whose Pancam spectra are the same as those of the uncoated spherules found in Eagle crater. Compared to the crater floor, the plains exhibit a greater abundance of bright red material, likely silt-sized or finer dust and sulfate-rich outcrop material. MB imprints in the ripple crests show that the grains are cemented by a surface crust of this bright red material (*15*). Vesicular fragments like those on Eagle crater floor are rare. Mixed with the hematitic spherules in the troughs are smaller fragments that exhibit the same Pancam spectrum as the spherules (*3*). This, coupled with the arcuate edges of a few of the fragments, suggests that they are broken spherules. Figure 4B shows the densely packed population of rounded and sorted spherule fragments that armor the ripples in Meridiani Planum. A combination of Mini-TES, MB, and APXS data confirms that these rounded granules are hematitic (*12–14*). Indeed, because of the small contribution of basaltic sand on the crests, MB data for these armors or pavements show the highest measured concentration of hematite (*14*). The grains are well sorted with a mean diameter of ~1 mm (SD ~0.3 mm). The coarse basaltic sand grains that armor the ripples on the Gusev plains have mean diameters of ~1.8 mm (*24*). The smaller mean diameter at Meridiani could be related to higher specific gravity of the hematitic grains or to higher threshold wind speeds.

Trends in compositional variations can help to elucidate the sources of the soils. The elemental composition of Meridiani soils, as measured by APXS, is quite close to the results for previous sites (*13*), although soil compositions from the different sites differ in detail (Fig. 5) (*26–30*). Whereas Meridiani soils lie atop a sulfate-rich evaporite deposit, they exhibit the lowest average S concentrations of all sites. Fe enrichment trends toward the

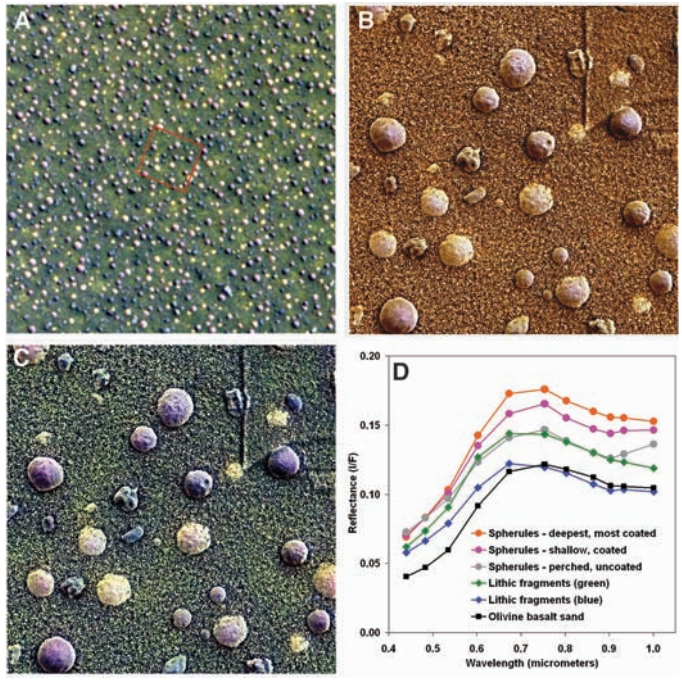

Fig. 3. Merge of MI and 13-filter Pancam images of Chocolate Chip soil target on the floor of Eagle crater from sol 54. (**A**) Pancam visible–near-infrared false-color image (RGB: filters R7, R2, R1; central λ: 1001 nm, 750 nm, and 440 nm). MI footprint shown in red is 3 cm wide. (**B**) Enhanced natural-color MI-Pancam merged image (RGB: filters L2, L5, L7; central λ: 750 nm, 535 nm, and 440 nm; image width 3 cm). (**C**) Visible–near-infrared false-color MI-Pancam merged image (RGB: filters R7, R2, R1; image width 3 cm). (**D**) Spectral reflectance of selected clasts.

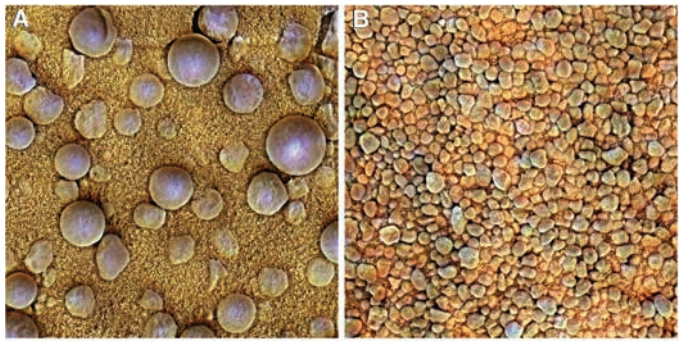

Fig. 4. Merge of MI and 13-filter Pancam images of typical Meridiani Planum ripple and trough acquired on sol 73. (**A**) Enhanced natural-color MI-Pancam merged image of inter-ripple trough (RGB: filters L2, L5, L7; central λ: 753 nm, 535 nm, and 440 nm; image width 3 cm). (**B**) Same MI-Pancam image version of ripple crest [color filters and processing as in (A); image width 3 cm].

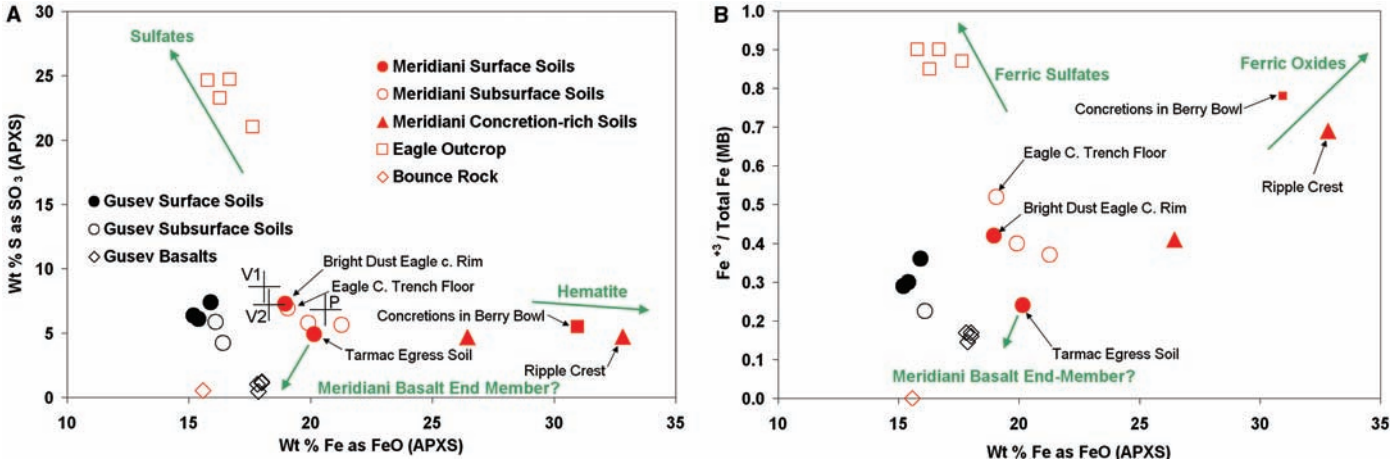

Fig. 5. Trends in sulfate (**A**) and iron-oxidation state (**B**) among Meridiani soils and local sources materials. Shown for comparison are Gusev soils and rocks and average soil from the Viking 1 and 2 and Pathfinder sites. Green arrows are schematic and denote compositional end members that constitute the Meridiani soils.

hematite-rich soils, consistent with the occurrence and abundance of ferric-iron–rich spherules as components in the soils. Apart from those that exhibit Fe^{3+} enrichment, Meridiani soil compositions cluster near Pathfinder and Viking soils. Two of the Meridiani soils with highest SO_3 content (Fig. 5A) are among the most oxidized of the spherule-poor soils (Fig. 5B). These may be the best candidates for airborne dust. The higher Fe in Meridiani soils cannot be explained by igneous rocks of the class of Bounce rock (*22*) nor of the bulk matrix in the outcrop. However, admixture of weathered-out hematite spherules and their fragments could increase the Fe in this soil to the observed composition. Abundances of sulfates in Meridiani soils are lower than those found in outcrop materials by a factor of 4 to 5, consistent with erosion of these weak rocks with near complete removal of the outcrop debris by active eolian activity.

Soils must dominate Meridiani Planum's regional signatures of basalt and hematite observed from orbit. The hematite signature is imparted by hematitic spherules and their fragments eroded from sulfate-rich evaporite rocks. The source of the basalt sand remains unknown. Although Eagle crater sand is dominantly olivine-bearing basalt, MB data show that ~10% of the Fe in the Tarmac soil is in the form of hematite (*14*). A model composition for the Meridiani basalt suggests a slightly higher FeO concentration than for the Gusev basalts. The Fe-poor Bounce rock pyroxene-rich basalt (*3*, *12*–*14*, *22*) is not the source of the basaltic sand. One or both of the vesicular clasts (blue and green in Fig. 3) could be examples of the source lithology. If so, the vesicular grains suggest that the source may have been a coherent basaltic rock rather than volcanic ash. The ejecta of Eagle, Fram, and 170-m-diameter Endurance craters (Opportunity was ~200 m from Endurance on sol 90) do not show strewn fields of basalt that should have been excavated from depth if there were a competent basaltic unit in the near subsurface. The many dark cobbles on the plain and in Eagle crater could, like Bounce rock (*22*), be impact erratics and may not represent the local source. If basaltic sand is not locally derived, it could have been transported by saltation from adjacent regions. Grains from a coherent basaltic rock could survive transport over hundreds of kilometers (*20*).

On the traverse to Endurance crater, outcrops were observed at shallow depths: outside the rim of Eagle crater, near the linear troughs [possibly a fracture system (*22*)] at Anatolia (Fig. 2), and at Fram crater (Plate 4) located on a regional rise (*17*). Soil often is thinly draped over underlying blocks of outcrop. Thus, the soils on the plains are probably only on the order of a meter thick. The concentration of spherules in the Eagle crater outcrop is roughly 1 to 2% by volume (*19*). Given that the spherules are concentrated at the surface, being sparse in trenches, the spherules may comprise a layer no more than a centimeter thick. This would suggest that the amount of eroded sulfate-rich strata needed to generate the observed spherules would be a few meters at most. The flat nature of the Meridiani Planum is striking; nowhere do we see erosional remnants (mesas or hillocks) of stratigraphically higher units. It also seems unlikely that most of the spherules have been transported out of the region or destroyed by mechanical erosion. Taken together, these observations suggest that the current plains surface is approximately at the top of the original evaporite stratigraphic sequence.

References and Notes

1. The term "soil" is used here to denote any loose, unconsolidated materials that can be distinguished from rocks, bedrock, or strongly cohesive sediments. No implication for the presence or absence of organic materials or living matter is intended.
2. M. P. Golombek *et al.*, *J. Geophys. Res.* **108**, 8072 (2003).
3. J. E. Bell III *et al.*, *Science* **306**, 1703 (2004).
4. MOC image R0802184 was radiometrically calibrated using the ISIS (Integrated Software for Imagers and Spectrometers) available from the Astrogeology Team (http://isis.astrogeology.usgs.gov/Isis2/isis-bin/isis.cgi) of the U.S. Geological Survey in Flagstaff, AZ.
5. Names have been assigned to geographic features by the Mars Exploration Rover (MER) team for planning and operations purposes. The names are not formally recognized by the International Astronomical Union.
6. P. R. Christensen, *J. Geophys. Res.* **93**, 7611 (1988).
7. M. C. Malin, K. S. Edgett, *J. Geophys. Res.* **106**, 23429 (1988).
8. P. R. Christensen, *et al.*, *J. Geophys. Res.* **105**, 9623 (2000).
9. M. P. Golombek, *et al.*, *J. Geophys. Res.* **104**, 8523 (2000).
10. S. W. Squyres *et al.*, *Science* **305**, 794 (2004).
11. R. E. Arvidson *et al.*, *Science* **305**, 821 (2004).
12. P. R. Christensen *et al.*, *Science* **306**, 1733 (2004).
13. R. Rieder *et al.*, *Science* **306**, 1746 (2004).
14. G. Klingelhöfer *et al.*, *Science* **306**, 1740 (2004).
15. K. E. Herkenhoff *et al.*, *Science* **306**, 1727 (2004).
16. R. Greeley *et al.*, *Geophys. Res. Lett.* **7**, 121 (1980).
17. R. E. Arvidson *et al.*, *Science* **306**, 1730 (2004).
18. H. J. Moore *et al.*, *J. Geophys. Res.* **82**, 4497 (1977).
19. S. W. Squyres *et al.*, *Science* **306**, 1709 (2004).
20. R. Greeley, S. Thompson, *J. Geophys. Res.* **108**, 8093 (2003).
21. A martian solar day has a mean period of 24 hours 39 min 35.244 s and is referred to as a sol to distinguish this from a roughly 3% shorter solar day on Earth.
22. S. W. Squyres *et al.*, *Science* **306**, 1698 (2004).
23. R. P. Sharp, *J. Geol.* **71**, 617 (1963).
24. R. Greeley *et al.*, *Science* **305**, 810 (2004).
25. B. C. Clark, D. C. Van Hart, *Icarus* **45**, 370 (1981).
26. R. V. Morris *et al.*, *Science* **305**, 833 (2004).
27. R. Gellert *et al.*, *Science* **305**, 829 (2004).
28. B. C. Clark *et al.*, *J. Geophys. Res.* **87**, 10059 (1982).
29. H. Wänke *et al.*, *Space Sci. Rev.* **96**, 317 (2001).
30. J. Brückner *et al.*, *J. Geophys. Res.* **108**, 8094 (2003).
31. The research described in this paper was partially carried out at the Jet Propulsion Laboratory, California Institute of Technology, under a contract with NASA.

Plates Referenced in Article

www.sciencemag.org/cgi/content/full/306/5702/1723/DC1
Plates 1, 2, 3, 4, 14, 16

10 September 2004; accepted 28 October 2004

Evidence from Opportunity's Microscopic Imager for Water on Meridiani Planum

K. E. Herkenhoff,[1]* S. W. Squyres,[2] R. Arvidson,[3] D. S. Bass,[4] J. F. Bell III,[2] P. Bertelsen,[5] B. L. Ehlmann,[3] W. Farrand,[6] L. Gaddis,[1] R. Greeley,[7] J. Grotzinger,[8] A. G. Hayes,[2] S. F. Hviid,[9] J. R. Johnson,[1] B. Jolliff,[3] K. M. Kinch,[10] A. H. Knoll,[11] M. B. Madsen,[5] J. N. Maki,[4] S. M. McLennan,[12] H. Y. McSween,[13] D. W. Ming,[14] J. W. Rice Jr.,[7] L. Richter,[15] M. Sims,[16] P. H. Smith,[17] L. A. Soderblom,[1] N. Spanovich,[17] R. Sullivan,[2] S. Thompson,[7] T. Wdowiak,[18] C. Weitz,[19] P. Whelley[7]

The Microscopic Imager on the Opportunity rover analyzed textures of soils and rocks at Meridiani Planum at a scale of 31 micrometers per pixel. The uppermost millimeter of some soils is weakly cemented, whereas other soils show little evidence of cohesion. Rock outcrops are laminated on a millimeter scale; image mosaics of cross-stratification suggest that some sediments were deposited by flowing water. Vugs in some outcrop faces are probably molds formed by dissolution of relatively soluble minerals during diagenesis. Microscopic images support the hypothesis that hematite-rich spherules observed in outcrops and soils also formed diagenetically as concretions.

The Athena science payload on the Mars Exploration Rover (MER) mission includes the Microscopic Imager (MI), a camera designed to provide views that are similar to that seen through a geologist's hand lens (*1*, *2*). MI data are acquired in order to place other MER instrument data in context and to aid in petrologic and geologic interpretations of rocks and soils on Mars. The MI on Opportunity is essentially identical to the MI on Spirit and is used in a similar manner (*3*).

During the first 90 sols (*4*) of its surface mission (*5*), the Opportunity rover acquired and returned 870 MI images (including subframes) of rocks, soil/bedform targets, and the martian sky (for calibration). Tracks and trenches created by the rover wheels were also imaged (*6*), as were the filter and capture magnets on the front of the rover (*7*).

MI observations of soil-like materials (*8*) within Eagle crater (*9*) and on the surrounding plains have been used to assess cohesion and cementation of very fine-grained (<125 μm) material, based on soil morphology after disturbances caused by the rover wheels and by the Mössbauer spectrometer (MB) contact plate (*10*). Granules on the surface typically are pressed into the underlying very fine sand by MB contact; cohesion between grains is indicated where this results in very short, near-vertical walls in the surrounding soil (Fig. 1). Some MI observations of soils disturbed by the MB contact plate show apparent fractures, suggesting that cementation of surface particles has formed a crust. The thickness of this crust is estimated to be at least 1 mm (the penetration depth of the MB contact plate) based on images taken after the surface was disrupted (e.g., Fig. 1). Plausibly, and consistent with Alpha Particle X-Ray Spectrometer (APXS) spectra of soil-like deposits at the Meridiani site (*11*), the cementation is caused by precipitation of various salts (e.g., Cl- and SO_4-bearing) that bridge soil particles. Salts in the dust (unresolved by the MI) may dissolve and migrate into voids between soil particles in thin films of water (*12*) adsorbed onto soil particles. Thin liquid films may occur in soils when the spin axis obliquity and atmospheric relative humidity are high enough to cause precipitation or condensation of water. During warming events, salts precipitate on soil particles as thin liquid films evaporate (*13*), weakly cementing the upper soil surface.

In many places, Meridiani soils contain a major, distinctive component in the form of 0.6- to 6-mm-diameter spherules (*14*). These

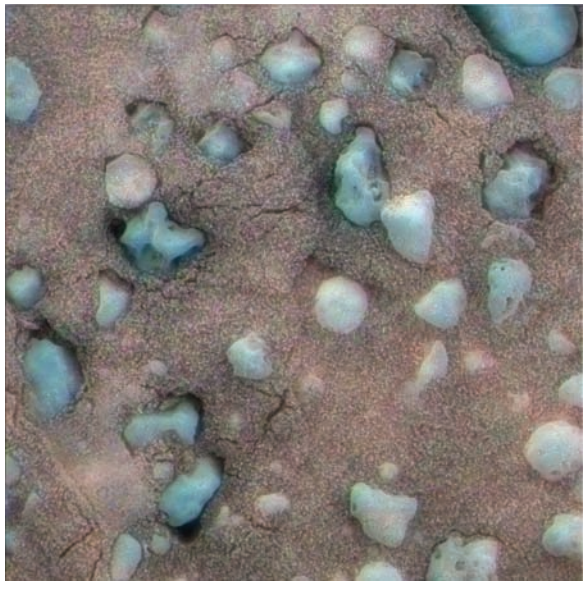

Fig. 1. False-color merge of MI image of target Munter (1M133692453), taken on sol 62, with Pancam multispectral data (effective wavelengths of 602, 535, and 483 nm). The MI image was acquired after MB contact, when the target was in complete shadow. The area shown is 3 cm across.

[1]U.S. Geological Survey Astrogeology Team, Flagstaff, AZ 86001, USA. [2]Department of Astronomy, Space Sciences Building, Cornell University, Ithaca, NY 14853, USA. [3]Department of Earth and Space Sciences, Washington University, St. Louis, MO 63130, USA. [4]Jet Propulsion Laboratory, California Institute of Technology, Pasadena, CA 91109, USA. [5]Center for Planetary Science, Danish Space Research Institute and Niels Bohr Institute for Astronomy, Physics and Geophysics, University of Copenhagen, Denmark. [6]Space Science Institute, Boulder, CO 80301, USA. [7]Department of Geological Sciences, Arizona State University, Tempe, AZ 85287, USA. [8]Department of Earth, Atmospheric and Planetary Sciences, Massachusetts Institute of Technology, Cambridge, MA 02139, USA. [9]Max Planck Institut für Aeronomie, Katlenburg-Lindau, D-37191, Germany. [10]Institute of Physics and Astronomy, Aarhus University, Aarhus, Denmark. [11]Department of Organismic and Evolutionary Biology, Harvard University, Cambridge, MA 02138, USA. [12]State University of New York, Department of Geosciences, Stony Brook, NY 11794, USA. [13]Department of Earth and Planetary Sciences, University of Tennessee, Knoxville, TN 37996, USA. [14]Astromaterials Research and Exploration Science Office, NASA Johnson Space Center, Houston, TX 77058, USA. [15]DLR Institut fur Raumsimulation, Linder Hoehe, Koln, Germany. [16]NASA Ames Research Center, Moffett Field, CA 94035, USA. [17]Lunar and Planetary Laboratory, University of Arizona, Tucson, AZ 85721, USA. [18]Department of Physics, University of Alabama, Birmingham, AL 35294, USA. [19]Planetary Science Institute, Tucson, AZ 85719, USA.

*To whom correspondence should be addressed. E-mail: kherkenhoff@usgs.gov

spherules, interpreted to be hematitic concretions (*5*), are also found as a relatively resistant component of the outcrops exposed in the walls of Eagle and Fram craters. These observations indicate that the spherules are more resistant to physical and/or chemical erosion than the supporting outcrop matrix. Two other classes of coarse particles are usually present: (i) subangular, irregular particles 1.5 to 5.0 mm in maximum dimension, some with submillimeter circular voids; and (ii) rounded particles 0.5 to 2.0 mm in diameter that are not derived from the spherules or spherule fragments. The irregular particles are probably vesicular basalt fragments, based on their morphology and color (*14*). The rounded particles are often found, along with spherule fragments, within or emerging from a matrix of fine-grained sand and armor ripple bedforms (*6*).

MI images of the soil taken soon after egress show a soil dominated by dark, very fine-grained (<125 μm) particles. Closer to the outcrop, soils contain a greater proportional abundance of spherules. Soils on the opposite side of Eagle crater have more diverse grain populations than those adjacent to the outcrop. The size and shape of the larger grains contained within these soils change considerably over small areas. The cause of these variations is unknown, but wind activity has influenced the distribution of grains within Eagle crater (*14*). MI images taken outside of Eagle crater do not show as much diversity in grain types; spherules, spherule fragments, and dark, very fine sands dominate the soils of the Meridiani plains. There is also a higher fraction of bright material, interpreted to be windblown dust, outside of Eagle crater (*14*).

Surface soil particles imaged by the MI have a generally bimodal size distribution, with grains larger than 1 to 3 mm (very coarse sand to granules) set in a matrix of very fine (<125 μm) sand (*15*, *16*). Whereas the shape of the spherules is primary, other large grains are generally rounded, suggesting abrasion during transport. The bimodal size distribution is inferred to represent wind transport and size sorting, in which the larger grains are moved by surface creep to form a lag, whereas the very fine sands move in saltation (*17*). The paucity of grains intermediate in size between the granules and very fine sand implies either extensive saltation and sorting or a lack of medium-to-coarse sand grains in the source region. The very fine sand grains are more easily moved by wind than the granules, so the coarser grains probably have more local sources than the very fine sand. In contrast to Gusev soils imaged by the MI (*3*), most large grains imaged in Meridiani Planum are relatively free of adhering dust. This observation suggests that very fine sand grains in Meridiani have recently been moved by winds, causing dust removal from grain surfaces. MI images (Fig. 1) suggest that at the surface the fine-grained material is well sorted with a mean grain size in the range of 60 to 150 μm. The lower bound on the size range is uncertain because it is at the MI resolution limit, but the existence of a well-sorted deposit of ~100-μm grains is consistent with predictions of saltation threshold on Mars, because grains of this size are expected to be most easily moved by winds (*18*). However, subsurface soils contain a significant fraction of silt- or clay-size (dust) particles along with a few granules; they are more poorly sorted than the surface materials. Two trenches with maximum depth of ~10 cm were excavated within Eagle crater (*6*). No stratification was observed in the walls of these trenches below the surface layer of well-sorted, very fine sand. When the MB was pressed into the trench bottoms, they were compacted to smooth surfaces (*6*), as would be expected if the soil contained a high proportion of silt- or clay-size particles. In contrast, when the MB was pressed into the dark, fine-grained sand on the surface of the crater floor, much less compaction was apparent (e.g., Fig. 1). These observations suggest that dust particles have been removed from the near-surface layer by winds, concentrating coarser grains that cannot be suspended in the atmosphere (*6*, *14*).

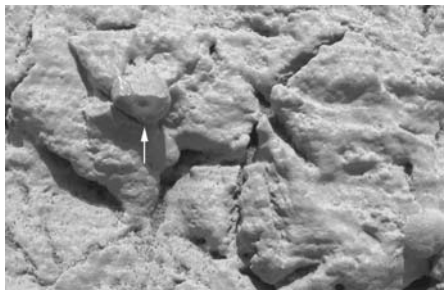

Fig. 2. Part of merge of five MI images of outcrop feature McKittrick (1M130672440 to 1M130672724), taken on sol 28. Illumination is from the top, and the area shown is 2.8 cm across. Concentric banding in the shaded face of a broken spherule is indicated by the arrow. Vugs cut across subhorizontal bedding and are partly filled by dark, very fine sand grains.

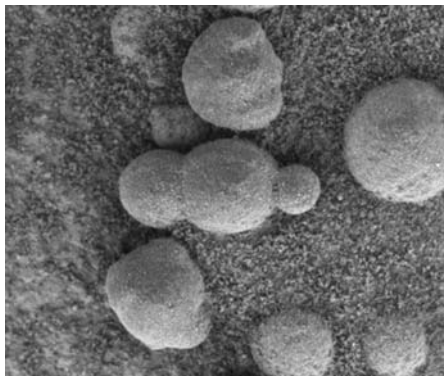

Fig. 3. Part of MI image 1M132444583 of target Tripleberry in the Berry Bowl, taken on sol 48 when the target was in full shadow. The area shown is 1.4 cm across.

In the investigation of sedimentary rocks exposed in and near Eagle crater, the MI has provided key data that help to integrate observations made by the Panoramic Camera (Pancam) (*19*) with chemical analyses made by the APXS (*11*), MB (*10*), and Miniature Thermal Emission Spectrometer (Mini-TES) (*20*). MI images indicate that outcrop rocks have four principal components: (i) moderately rounded medium to coarse (0.2 to 1 mm) sand grains (probably reworked heterogeneous evaporites—mixtures of sulfates and very fine-grained siliciclastic material) that form mm-scale laminations; (ii) fine-grained and coarser crystalline textures of subsequently precipitated cements and areas of recrystallization; (iii) centimeter-size vugs that record the early diagenetic growth and subsequent dissolution of crystals similar to sulfate crystals in terrestrial evaporites; and (iv) mostly 3- to 5-mm spherules distributed throughout the outcrops. MI images document spatial relationships among these constituents, recording a complex history of deposition and diagenesis. Sandy laminae have been cemented, probably by sulfate minerals, during earliest diagenesis. The large vugs cut across bedding, indicating that the minerals that once filled them also formed diagenetically within the sediments (Fig. 2). Where present, the vugs are found to continue into the rock for at least as deep as the Rock Abrasion Tool (RAT) (*21*) was able to grind (~5 mm) and usually are seen to increase in size with increasing abrasion depth. Accordingly, they are interpreted to represent an intrinsic feature of the outcrops. Vugs exhibit prismatic to discoidal geometry, characteristically with maximum width (1 to 2 mm) near their midpoints and tapering toward their ends. This morphology is consistent with precipitation of certain evaporite minerals within the rock matrix, either displacing or replacing the matrix grains during growth. Vug geometry is most consistent with a monoclinic precursor mineral, analogous to some terrestrial sulfate minerals such as gypsum or kieserite. Subsequently, these minerals were either dissolved by percolating fluid or abraded by wind activity to produce the vugs.

Textural, mineralogical, and compositional features are consistent with the spherules being secondary hematite-cemented concretions formed in a sedimentary sequence, rather than volcanic lapilli or impact glass (*14*, *22*). In particular, MI and Pancam (*19*) images of outcrops show that spherules are not concentrated along depositional bedding planes and thus show no evidence for transport or reworking by physical sedimentary processes

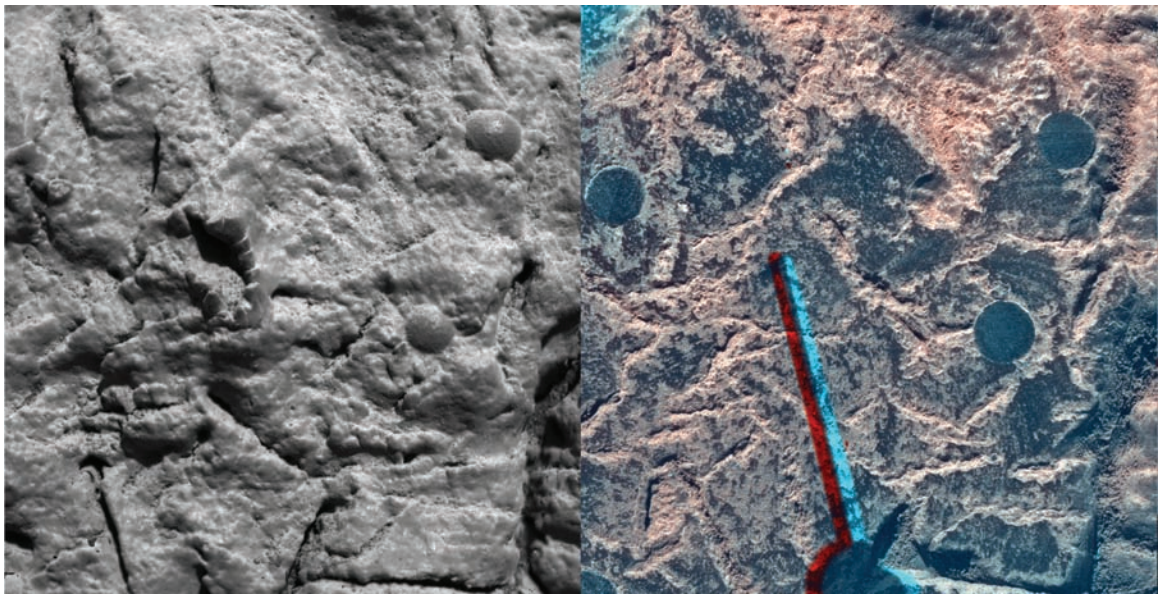

Fig. 4. (**Left**) Merge of three MI images (1M131201538 to 1M131201699) of target King2 on Guadalupe, taken on sol 34 before RAT abrasion. Illumination is from the top, and the area shown is 3 cm across. (**Right**) False-color composite of MI images of the same target on Guadalupe, taken on sol 35 after RAT abrasion. The image taken through the dust cover (1M131296470) is displayed in red, the image taken with the dust cover open (1M131296281) is displayed in green, and the difference (open-closed) is displayed in blue. Red and blue bars are artifacts caused by motion of the shadow of the MI contact sensor between images. Illumination is from the upper left, and the area shown is 3 cm across. Note the lack of internal structure in three abraded spherules (lineations caused by RAT).

(Plates 6 to 10). Bedding is not displaced by spherules, nor are laminae draped over spherules. In rare instances, the spherules form doublets or even triplets aligned along a single axis (Fig. 3). Also, in some cases, in situ spherules have surface grooves parallel to bedding that may reflect minor variations in porosity and permeability among encompassing laminae (*22*). Concretions that impinge into vugs (Fig. 4) and accretionary grooves on concretions that line up with adjacent vugs rather than bedding support the hypothesis that concretionary growth postdated the precipitation of vug precursor crystals. Many spherules show evidence for an increase in the granularity of the matrix immediately adjacent to their margins (Fig. 5), with grains up to a few mm in size sometimes showing radial symmetry around the spherule. This change in granularity might represent a reaction rim, produced as a result of fluid interaction within the adjacent matrix during growth of the spherule. Within the resolving power of the MI (*15*), spherules that are broken or have been cut by the RAT are massive with no internal structure (Fig. 4), except for one broken spherule (Fig. 2) that shows concentric banding (*23*). Spherules are typically polished smooth by the RAT and are harder than the host rock (*6*). The absence of sand textures in the spherules despite formation within a sandy matrix suggests that the primary outcrop grains were soluble and were therefore diagenetically unstable and easily dissolved or recrystallized during concretion growth.

MI images and mosaics provide evidence for the presence of small-scale cross bedding with festoon geometry at Meridiani Planum. An MI mosaic (Plate 6) of part of the outcrop target called Last Chance shows festoon cross-lamination, expressed by lines that dip dominantly to the right, at variable, concave-up angles. Projected into the rock, these lines are contained within dipping planes, which once formed the down-current surfaces of migrating ripples (*22*). The dominance of right over left dips suggests that the outcrop face was oriented at an oblique angle to the current flow direction. In the lower part of Last Chance, the MI mosaic (Plate 6) illustrates several sets of ripple cross-lamination. Cross-laminae dip to the right, indicating that the current that created the cross-lamination was flowing from left to right. A third MI mosaic of a rock called East Dells (Plate 7) reveals abundant small-scale discordant laminae and truncations, including ripple cross-laminae. In a manner similar to that at Last Chance, this rock preserves evidence for festoon ripple cross-lamination, in a view that is largely transverse to current paleoflow. The MI images confirm two key features that lead to the interpretation of water having flowed at times across the surface at the landing site: centimeter-scale cross-stratification and festoon geometry of cross-lamination (*22*).

Bounce rock is an isolated basaltic rock found on the plains of Meridiani southeast of

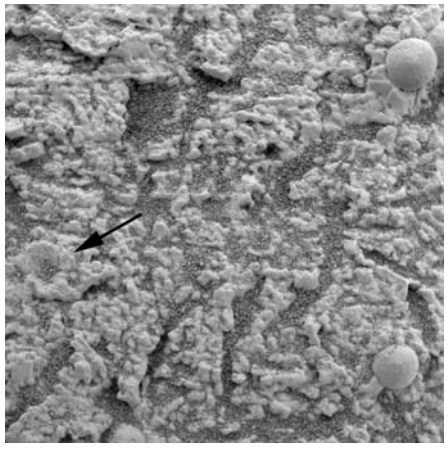

Fig. 5. Merge of five MI images (1M130671710 to 1M130672029) of Algerita outcrop, taken on sol 28 in complete shadow. The area shown is 3 cm across. The arrow indicates a depression, possibly representing the former location of a spherule. Coarser grains (up to ~2 mm) surrounding a spherule can be seen at upper right. The nodular appearance of this outcrop is common in terrestrial evaporites. Dark, very fine sand grains partly fill vugs and other depressions in the outcrop.

Fig. 6. MI image 1M133955069 of target Achsel on Bounce rock, taken on sol 65. Target was in shadow when the image was acquired. Area shown is 3 cm across.

Eagle crater. It may have been ejected by a large, distant impact event. Bounce rock displays an unusual surface texture dominated by polished, parallel striations, ostensibly similar to slickensides formed by differential motion under pressure in terrestrial rocks. The striated surfaces also resemble those found in shatter cones, fracture surfaces commonly found in terrestrial impact structures (*24*). MI images show lineations down to a sub-mm scale and irregular flat surfaces that may be responsible for the rock's specular reflectance (Fig. 6). The MI images further show that these features are limited to a 2- to 3-mm-thick surface that may be differentially resistant to erosion by sandblasting on Meridiani Planum. The rock interior has a rough but predominantly aphanitic texture, with some dark grains that may be phenocrysts. The rock contains mm-scale rounded clasts in exposed fractures and eroded recesses and has been fractured in a pattern that suggests compressional deformation.

References and Notes

1. S. W. Squyres *et al.*, *J. Geophys. Res.* **108**, 8062 10.1029/2003JE002121 (2003).
2. K. E. Herkenhoff *et al.*, *J. Geophys. Res.* **108**, 8065 10.1029/2003JE002076 (2003).
3. K. E. Herkenhoff *et al.*, *Science* **305**, 824 (2004).
4. A martian solar day has a mean period of 24 hours 39 min 35.244 s and is referred to as a sol to distinguish this from a ~3% shorter solar day on Earth.
5. S. W. Squyres *et al.*, *Science* **306**, 1698 (2004).
6. R. E. Arvidson *et al.*, *Science* **306**, 1730 (2004).
7. M. Madsen *et al.*, *J. Geophys. Res.* **108**, 8069, 10.1029/2002JE002029 (2003).
8. The term martian soil is used here to denote any loose, unconsolidated materials that can be distinguished from rocks, bedrock, or strongly cohesive sediments. No implication of the presence or absence of organic materials or living matter is intended.
9. Names have been assigned to geographic features by the MER team for planning and operations purposes. The names are not formally recognized by the International Astronomical Union.
10. G. Klingelhöfer *et al.*, *Science* **306**, 1740 (2004).
11. R. Rieder *et al.*, *Science* **306**, 1746 (2004). Note the abundance of salt-forming elements in soils.
12. G. M. Marion, Special Report 95-12, Cold Regions Research and Engineering Laboratory, U.S. Army Corps of Engineers (1995).
13. W. W. Dickinson, M. R. Rosen, *Geology* **31**, 199 (2003).
14. L. A. Soderblom *et al.*, *Science* **306**, 1723 (2004).
15. The ability to resolve individual grains with the MI depends on the illumination of the scene and the contrast between the grain and its surroundings. Typically, an object must subtend at least 3 pixels to be recognized in an image (about 100 μm for the MI).
16. Grain-size classifications use the Wentworth scale (*25*).
17. An example of a terrestrial eolian lag is shown in figure 6 of Greeley *et al*. (*26*).
18. J. D. Iversen, B. R. White, *Sedimentology* **29**, 111 (1982).
19. J. Bell III *et al.*, *Science* **306**, 1703 (2004).
20. P. R. Christensen *et al.*, *Science* **306**, 1733 (2004).
21. S. Gorevan *et al.*, *J. Geophys. Res.* **108**, 8068, 10.1029/2003JE002061 (2003).
22. S. W. Squyres *et al.*, *Science* **306**, 1709 (2004).
23. Although terrestrial concretions commonly contain internal structures that parallel bedding, this is by no means a ubiquitous or diagnostic feature of concretions; see (*27*).
24. R. S. Dietz, in *Shock Metamorphism of Natural Materials*, B. M. French, N. M. Short, Eds. (Mono-Books, San Francisco, CA, 1968), pp. 267–285.
25. C. K. Wentworth, *J. Geol.* **30**, 377 (1922).
26. R. Greeley *et al.*, *J. Geophys. Res.* **104**, 8573 (1999).
27. J. Sellés-Martínez, *Earth Sci. Rev.* **41**, 177 (1996).
28. The U.S. Geological Survey MER Team developed MI software and created various data products, including some of those displayed in this issue: B. Archinal, J. Barrett, K. Becker, T. Becker, D. Burr, D. Cook, D. Galuszka, T. Hare, A. Howington-Kraus, R. Kirk, E. Lee, B. Redding, M. Rosiek, D. Soltesz, B. Sucharski, T. Sucharski, and J. Torson (project engineer). The Ames MER team and M. Lemmon developed software to merge focal sections and generate anaglyphs from them. The MER Rover Planners provided excellent support of the MI investigation by commanding the instrument arm and MI dust cover. Reviews of this manuscript by J. Bishop, M. Chapman, J. Kargel, and an anonymous referee are much appreciated. This research was carried out for the Jet Propulsion Laboratory, California Institute of Technology, under a contract with the National Aeronautics and Space Administration.

Plates Referenced in Article

www.sciencemag.org/cgi/content/full/306/5702/1727/DC1
Plates 6 to 10

15 September 2004; accepted 9 November 2004

REPORT

Localization and Physical Property Experiments Conducted by Opportunity at Meridiani Planum

R. E. Arvidson,[1]* R. C. Anderson,[2] P. Bartlett,[3] J. F. Bell III,[4] P. R. Christensen,[5] P. Chu,[3] K. Davis,[3] B. L. Ehlmann,[1] M. P. Golombek,[2] S. Gorevan,[3] E. A. Guinness,[1] A. F. C. Haldemann,[2] K. E. Herkenhoff,[6] G. Landis,[7] R. Li,[8] R. Lindemann,[2] D. W. Ming,[9] T. Myrick,[3] T. Parker,[2] L. Richter,[10] F. P. Seelos IV,[1] L. A. Soderblom,[6] S. W. Squyres,[4] R. J. Sullivan,[4] J. Wilson[3]

The location of the Opportunity landing site was determined to better than 10-m absolute accuracy from analyses of radio tracking data. We determined Rover locations during traverses with an error as small as several centimeters using engineering telemetry and overlapping images. Topographic profiles generated from rover data show that the plains are very smooth from meter- to centimeter-length scales, consistent with analyses of orbital observations. Solar cell output decreased because of the deposition of airborne dust on the panels. The lack of dust-covered surfaces on Meridiani Planum indicates that high velocity winds must remove this material on a continuing basis. The low mechanical strength of the evaporitic rocks as determined from grinding experiments, and the abundance of coarse-grained surface particles argue for differential erosion of Meridiani Planum.

The Mars Exploration Rover (MER) Mission required accurate tracking of the location of Opportunity to ensure efficient drives and to place measurements in proper geological context, e.g., associating a rock target with a particular terrain or geologic unit (*1*–*3*). The location of the lander in inertial coordinates was determined by fitting direct-to-Earth, two-way, X-band Doppler radio transmissions and two passes of two-way Ultra High Frequency (UHF) Doppler transmissions between Opportunity and the Mars Odyssey Orbiter. Based on analyses of these observations, the landed location is 1.9483°S (with an accuracy of ~10 m) and 354.47417°E (with an accuracy of ~10 cm), translated to International Astronomical Union (IAU) 2000 areocentric coordinates. The landed location was also tied to Mars Global Surveyor (MGS) Mars Orbital Camera and MER descent image data to within ~10-m accuracy, by triangulation to three craters observed in the far field [through breaks in the local Eagle crater rim (*4*)] in Pancam images. These triangulation results, mapped to the cartographic network–derived MGS Mars Orbital Laser (MOLA) data (*5*), imply that the lander is located at 1.9462°S, 354.4734°E in IAU 2000 areocentric coordinates.

Opportunity stopped on the plains for a software upload on sols 75 to 78 (*6*), and its location (1.94752°S, 354.47716°E) was determined by analysis of two passes of UHF two-way Doppler tracking. The location was also determined by image-based triangulation to common features, with resultant values of 1.9453°S, 354.4766°E. For both landing and software-upload locations, the Doppler-based location was displaced 135 m

at an azimuth of 176° clockwise from north from the location derived from image-based analyses. This displacement is consistent with expected offset errors between inertially derived locations and positions estimated from the MOLA-based global cartographic network (*5*). These offsets provide a quantitative description of map errors expected for Mars in the equatorial regions when the current cartographic framework is used.

The first 57 sols of operations were conducted within Eagle crater (*6*), taking advantage of extensive rock outcrops exposed on the northwestern side of the crater. Slopes from the crater floor to the outcrops ranged up to 20° from horizontal and were covered by soils (*7*). The soil-covered slopes caused wheel slip and forced the MER team to plan novel approaches to rock targets. To traverse from one portion of the outcrop to another, Opportunity traveled across the crater floor and then turned directly upslope to approach a given rock target. In some cases, the rover used visual odometry to update positional information by acquiring stereo image data during traverses and using the range information to update positional knowledge. Observed slippage during upslope traverses of soil slopes of <10° was <20% in all cases, with more slip encountered at higher slopes. For example, 100% slip was encountered during the vehicle's initial attempt on sol 56 to egress from the crater on soil-covered slopes tilted at ~17°. The rover successfully completed egress on sol 57 by traversing at an oblique angle to the crater wall's topographic contours. These slip values are similar to those found during experiments in which the MER test rover traversed over dry, loose, poorly sorted, sand-sized materials.

For localization in Cartesian coordinates, we used forward- and backward-looking overlapping images of the surface, images of the sun, on-board inertial measurement unit (IMU) observations of rover tilt vectors, and tracking wheel turns in a least squares bundle-adjustment procedure to derive detailed positional estimates (Fig. 1). The magnitude of wheel slip within Eagle crater is evident, in that use of the bundle-adjustment technique and comparisons to positional estimates based on wheel turns alone demonstrate an accumulated error of 20 m over a total traverse distance of 183 m. For typical traverses of several meters, the rover position was delineated with an accuracy of several centimeters with the bundle-adjustment techniques.

Measurements of suspension system angles, together with rover tilt as inferred from IMU data, were used to reconstruct the elevation of each wheel at a 2- to 8-Hz sampling rate, relative to the start of each traverse (Fig. 1). Profile data retrieved for the sol 82 traverse across the plains show a height standard deviation of only 3.2 cm over the first 55 m and 40.3 cm over the total traverse distance of 141 m. These values are comparable to the small height standard deviations (<2 m over a 75-m-long scale) derived from pulse spreading observed in MOLA data (*8*), confirming the very smooth and flat nature of Meridiani Planum and the landing site. The smooth nature of the plains is occasionally interrupted by troughs and hollows that are typically several meters across or narrower, with depths less than several tens of centimeters (Fig. 1). Low-amplitude ripples (only several centimeters high) with wavelengths of less than a meter are ubiquitous on the plains.

Dust accumulation at the Meridiani Planum landing site is evident from analyses of Pancam data that show gradual reddening over 90 sols of the Pancam calibration target

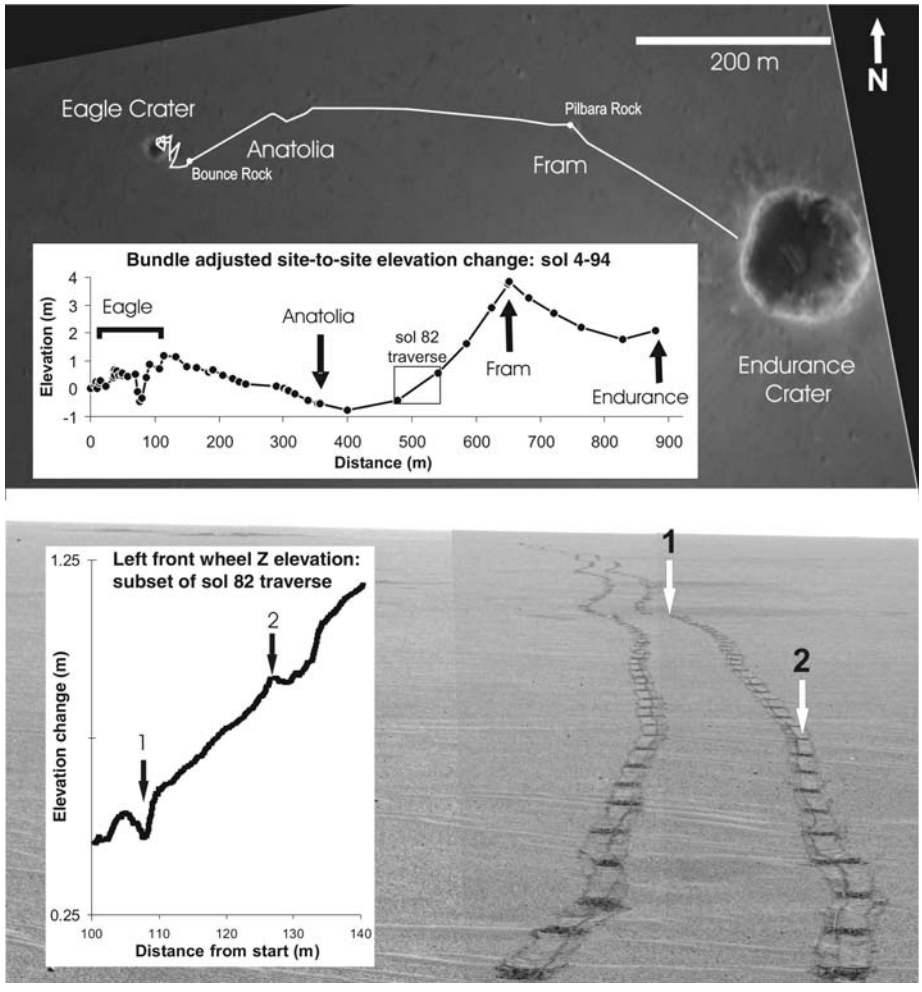

Fig. 1. (**Top**) MER Descent Image Motion Estimation System image showing traverses from the Eagle to Endurance craters, with stops at the Anatolia trough and Fram crater (image no. 1E128278513EDN0000F0006N0M1). (**Inset**) An elevation profile extracted from bundle-adjustments along the traverses. The dots on the profile correspond to localization stations for which backward- and forward-looking images were acquired. The relatively high elevation at the Fram location is interpreted to be due to a regional-scale but gentle rise and not due to the presence of the crater. The locations of the Bounce rock and Pilbara rock targets for the RAT are also shown. (**Bottom**) Pair of Pancam sol 82 images and vertical topographic profiles for traverses retrieved from rover tilt and wheel suspension data (Pancam frame nos. 1P135559477EFF1200P2431L7M1 and 1P135559499EFF1200P2431L7M1). Dark marks on the wheel tracks are associated with tie-down wheel cleats and are ~80 cm apart. Two shallow troughs are delineated by arrows at positions 1 and 2, and the low-amplitude ripples are evident in the foreground.

[1]Department of Earth and Planetary Sciences, Washington University, St. Louis, MO 63130, USA. [2]Jet Propulsion Laboratory, California Institute of Technology, Pasadena, CA 91109, USA. [3]Honeybee Robotics, 204 Elizabeth Street, New York, NY 10012, USA. [4]Department of Astronomy, Space Sciences Building, Cornell University, Ithaca, NY 14853, USA. [5]Department of Geological Sciences, Arizona State University, Tempe, AZ 85287, USA. [6]U.S. Geological Survey, Flagstaff, AZ 86001, USA. [7]NASA Glenn Research Center, Cleveland, OH 44135, USA. [8]Department of Civil and Environmental Engineering and Geodetic Science, The Ohio State University, Columbus, OH 43210, USA. [9]NASA Johnson Space Center, Houston, TX 77058, USA. [10]Deutsches Zentrum für Luft und Raumfahrt, Institut für Raumsimulation, Linder Höhe, Köln, D-51170, Germany.

*To whom correspondence should be addressed. E-mail: arvidson@wunder.wustl.edu

(*9*). Furthermore, analyses of short-circuit current-monitor solar cell data show a decrease in current of 0.29% per sol (corrected for seasonal variations in the Mars-sun distance and solar elevation angle) during the first 25 sols of operations, slowing to 0.13% per sol by sol 90. These values are comparable to those seen by Spirit at Gusev crater (*10*). Yet the MGS Thermal Emission Spectrometer–based bolometric albedo at the Meridiani site is only ~0.15 (*11*), consistent with Opportunity's observations that show that dust is a minor surface component in Eagle crater and on the plains (*9*, *12*). High-velocity winds must periodically scour the surface and remove surface dust accumulations from Meridiani Planum on a frequent basis.

The soils exposed at the Meridiani Planum landing site are dominated by dark, sand-sized and finer grained (<0.125 μm) basaltic materials overlain by sparsely to densely arrayed spherules and irregular particles with grain sizes that range up to a few millimeters across (*13*). Trenches excavated to 8- to 10-cm depths in soils on sols 23, 54 (both in Eagle crater), and 73 [adjacent to the Anatolia trough (Fig. 1)] show that these coarser grains are also found within the soils but at lower concentrations than on the surface (*14*). The spherules have a hematitic signature and have been found in outcrops observed by the rover (*9*, *12*, *15*, *16*). The high concentration of spherules and irregular particles at the surface is interpreted to be due to differential aeolian erosion of the evaporitic sedimentary rocks found by Opportunity (*16*), leaving behind a lag or pavement of relatively large and thus immobile materials. In addition, coarse-grained sand deposits have been reworked by wind to cover the ripples that are ubiquitous on the plains. The cores of the ripples are dominated by sand-sized and finer grained basaltic materials (*13*) (Fig. 2).

The physical nature of the soils within Eagle crater and on the plains can be inferred from a number of lines of evidence. Examination of wheel tracks shows that these deposits form high-fidelity casts of outer wheel surfaces, including cleat impressions with slopes greater than the angles of repose expected for most cohesionless materials. Impressions made by the Mössbauer contact plate (switch-activated when 1-N force was applied to soil surfaces) (Fig. 2), together with airbag bounce marks, show that spherules and irregular particles have been pressed into and partially covered by the finer grained soils (*13*), indicating that the uppermost fine-grained particles are easily displaced. In other cases, the spherules and irregular particles pressed into soils displace and expose millimeter-thick surface crusts. Furthermore, airbag seams are preserved well in bounce marks, and drag marks show complex curvilinear shapes with little indication of surface crumbling. All of these observations suggest that soils are only weakly cohesive (cohesive strength, ~1 to 3 kPa) and consist of sand-sized and smaller grain sizes, allowing the fine-grained component to fill voids between the larger grains during remolding of the soils.

With regard to standard soil mechanical properties, the estimated bearing strength of the Eagle crater floor soils, based on wheel track sinkage values (*17*) and on the depth of depressions made by the Mössbauer contact plate, average ~80 kPa with ~5 kPa of cohesive strength and an angle of internal friction of ~20°. The soils on the crater walls adjacent to the outcrops have an estimated bearing strength of ~8 kPa cohesion of ~0.5 kPa, and an angle of internal friction of ~20°. Motor currents associated with soil trenching operations show that soils are more easily excavated at Meridiani Planum, as opposed to the Spirit landing site in Gusev crater (*10*), and that excavation into a ripple on the floor of Eagle crater required the least amount of trenching energy. This result suggests that the soil deposits on the floor of the crater were modified relatively recently by winds and have not yet had the time to become cohesive.

Rock outcrops within Eagle crater ground by the Rock Abrasion Tool (RAT) (*18*, *19*) are of sedimentary origins (*13*) and include McKittrick (sol 30), Guadalupe (sol 34), and Flatrock (sol 44). Pilbara, another sedimentary rock located on the rim of Fram crater (Fig. 1), was ground on sol 86. Bounce rock, an igneous rock located on the plains near Eagle crater (Fig. 1), was ground on sol 66. Grinding of the McKittrick outcrop is illustrative of the multicomponent nature of the rocks exposed in Meridiani Planum. Two spherules were

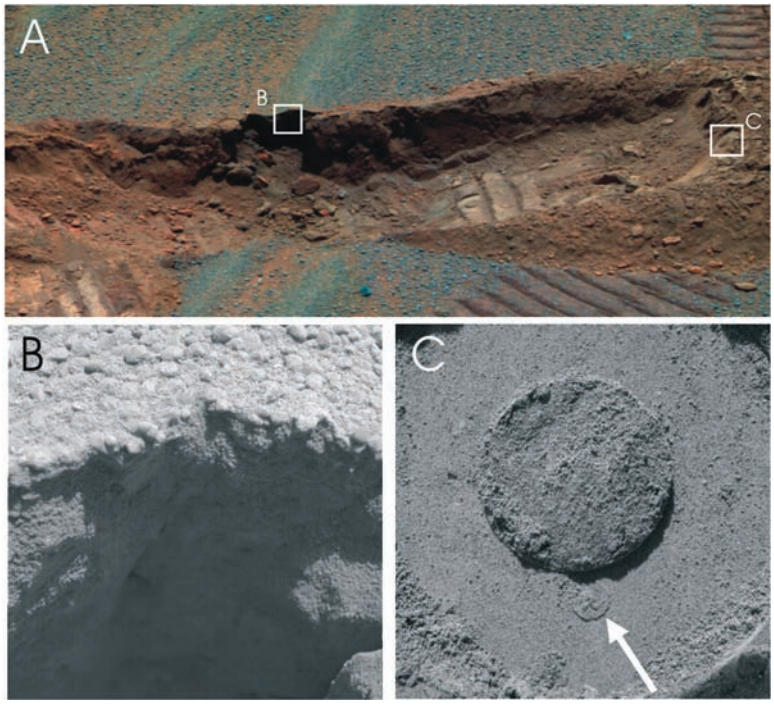

Fig. 2. (**A**) Pancam color mosaic of the Dog Track trench (image no. 1PP081EFF10CYL-CIP2421L256C1_full) excavated into soils at the Anatolia trough and acquired on sol 80. The trench is 8 to 10 cm deep. Boxes B and C show the locations of the Microscopic Imager (MI) images shown in (**B**) and (**C**). (**B**) MI frame (no. 1M135284929EFF10CGP2956M2M1) showing a monolayer or pavement of coarse sand on a ripple surface whose volume is dominated by sand and finer grained soils. (**C**) MI frame (no. 1M135284013EFF10CGP2956M2M1) showing the Mössbauer faceplate impression in soil, including the well-defined cast of a screw head on the faceplate.

Table 1. Rock energy/volume for RAT grinding for targets for the Gusev crater and Meridiani Planum (bold text) sites and selected rocks ground in the laboratory. Descriptions of terrestrial rock samples and targets ground by the Spirit rover at the Gusev site are given in (*10*). The table provides updated values for the Spirit rocks. Opportunity rock values are from (*19*).

Rock target	Grindability (J/mm^3)
Terrestrial non-vesicular basalt	66–133
Terrestrial dolomite	85
Gusev Humphrey rock	83
Gusev Mazatzal rock	65
Gusev Adirondack rock	51
Terrestrial limestone	17–21
Guadalupe	**7.3**
Terrestrial shale	5.2
Bounce rock	**3.7**
Pilbara	**1.0**
McKittrick	**0.92**
Flatrock	**0.45**

encountered during grinding, and their high grinding resistance relative to the weaker rock matrix caused the RAT to stop operations (Plate 8). One spherule was slightly rotated during the grinding, and an irregular clast was plucked from the rock and thrown downhill during grinding. The estimated grinding energies for the rock targets at Meridiani Planum are relatively low, as compared to rocks at Gusev crater and most samples ground in the laboratory (Table 1). The grind energy correlates with the slope angles for the outcrop, in that the more resistant Guadalupe target ground by the RAT is located on a 36 ± 5° slope, whereas the less resistant McKittrick target is located on a 6.7 ± 2° slope. The higher slope for the Guadalupe outcrop is interpreted to be due to higher resistance to weathering than the McKittrick outcrop. Finally, even Bounce rock is weaker than rocks ground at Gusev crater, consistent with the densely fractured appearance of this rock (Plate 12). Bounce rock is an isolated target on the plains and was probably transported to its current location as impact ejecta (*12*). The fractures may have been introduced during ejection and impact of this rock.

The hematite-bearing plains that Opportunity landed on are at the top of a section of layered strata that is ~300 m thick and that disconformably overlies the Noachian-aged cratered terrain (*11*). We interpret the smooth, flat nature of Meridiani Planum to be due to differential stripping of horizontally layered strata, combined with continuing diffusion-driven mobilization of loose material to fill local depressions; i.e., soil fills in the craters, hollows, and troughs. Spherules, irregular particles, coarse sand covers, and basaltic soils represent the net result of concentration of these particles as the spherules were eroded from the weak evaporitic rocks in former and current aeolian environments. The hematite signature observed from orbit (*20*) that led us to land Opportunity in Meridiani Planum is due to a concentration of hematite-rich spherules that occurred as they were eroded from the evaporitic rocks. The lack of evaporite deposits in the soils on Meridiani Planum is due to relatively rapid aeolian erosion and removal as dust in suspension of these mechanically weak deposits. The amount of erosion is not well constrained, but it could range from meters to many meters.

References and Notes

1. S. W. Squyres *et al.*, *J. Geophys. Res.* **108**, 8062 (2003).
2. R. E. Arvidson *et al.*, *J. Geophys. Res.* **108**, 8070 (2003).
3. R. Li *et al.*, *J. Geophys. Res.* **107**, 8005 (2002).
4. Names have been assigned to areographic features by the Mars Exploration Rover (MER) Team for planning and operations purposes. The names are not formally recognized by the International Astronomical Union.
5. M. P. Golombek *et al.*, *J. Geophys. Res.* **108**, 8072 (2003).
6. A martian solar day has a mean period of 24 hours 39 min 35.244 s and is referred to as a sol to distinguish this from a roughly 3% shorter solar day on Earth.
7. The term martian soil is used here to denote any unconsolidated materials that can be distinguished from rocks, bedrock, or strongly cohesive sediment. No implication of the presence or absence of organic materials or living matter is intended.
8. G. A. Neumann *et al.*, *Geophys. Res. Lett.* **30**, 1561 (2003).
9. J. F. Bell III *et al.*, *Science* **306**, 1703 (2004).
10. R. E. Arvidson *et al.*, *Science* **305**, 5685 (2004).
11. R. E. Arvidson *et al.*, *J. Geophys. Res.* **108**, 8073 (2003).
12. P. R. Christensen *et al.*, *Science* **306**, 1733 (2004).
13. L. A. Soderblom *et al.*, *Science* **306**, 1723 (2004).
14. K. E. Herkenhoff *et al.*, *Science* **306**, 1727 (2004).
15. G. Klingelhöfer *et al.*, *Science* **306**, 1740 (2004).
16. S. W. Squyres *et al.*, *Science* **306**, 1698 (2004).
17. L. Richter, P. Hamacher, paper presented at the 13th Conference of the International Society for Terrain-Vehicle Systems, Munich, 14 to 19 September 1999.
18. S. P. Gorevan *et al.*, *J. Geophys. Res.* **108**, 8068 (2003).
19. T. M. Mynck *et al.*, paper 2004-6096 presented at the American Institute of Aeronautics and Astronautics (AIAA) Space 2004 Conference and Exhibit, San Diego, CA, 28 to 30 September 2004.
20. T. M. Christensen *et al.*, *J. Geophys. Res.* **105**, 9623 (2000).

21. We thank the MER Team and the scientists and engineers who made the landing, traverses, and science observations a reality. Work funded by NASA through the MER Project.

Plates Referenced in Article

www.sciencemag.org/cgi/content/full/306/5702/1727/DC1
Plates 8 and 12

18 August 2004; accepted 13 October 2004

RESEARCH ARTICLE

Mineralogy at Meridiani Planum from the Mini-TES Experiment on the Opportunity Rover

P. R. Christensen,[1]* M. B. Wyatt,[1] T. D. Glotch,[1] A. D. Rogers,[1] S. Anwar,[1] R. E. Arvidson,[2] J. L. Bandfield,[1] D. L. Blaney,[3] C. Budney,[3] W. M. Calvin,[4] A. Fallacaro,[4] R. L. Fergason,[1] N. Gorelick,[1] T. G. Graff,[1] V. E. Hamilton,[5] A. G. Hayes,[6] J. R. Johnson,[7] A. T. Knudson,[1] H. Y. McSween Jr.,[8] G. L. Mehall,[1] L. K. Mehall,[1] J. E. Moersch,[8] R. V. Morris,[9] M. D. Smith,[10] S. W. Squyres,[6] S. W. Ruff,[1] M. J. Wolff[11]

The Miniature Thermal Emission Spectrometer (Mini-TES) on Opportunity investigated the mineral abundances and compositions of outcrops, rocks, and soils at Meridiani Planum. Coarse crystalline hematite and olivine-rich basaltic sands were observed as predicted from orbital TES spectroscopy. Outcrops of aqueous origin are composed of 15 to 35% by volume magnesium and calcium sulfates [a high-silica component modeled as a combination of glass, feldspar, and sheet silicates (~20 to 30%)], and hematite; only minor jarosite is identified in Mini-TES spectra. Mini-TES spectra show only a hematite signature in the millimeter-sized spherules. Basaltic materials have more plagioclase than pyroxene, contain olivine, and are similar in inferred mineral composition to basalt mapped from orbit. Bounce rock is dominated by clinopyroxene and is close in inferred mineral composition to the basaltic martian meteorites. Bright wind streak material matches global dust. Waterlain rocks covered by unaltered basaltic sands suggest a change from an aqueous environment to one dominated by physical weathering.

The Mini-TES has provided remote measurements of mineral abundances and compositions, thermophysical properties, atmospheric temperature profiles, and atmospheric dust and ice opacities at the Opportunity rover landing site in Meridiani Planum. Mini-TES is a Michelson interferometer that collects infrared spectra from 5 to 29 μm (339 to 1997 cm^{-1}) at a spectral sampling of 10.0 cm^{-1} (*1*–*3*). Mini-TES observations of varying raster size and dwell lengths were acquired during rover operations within Eagle crater and during the traverse across the plains between Eagle and Endurance craters (*4*, *5*). Coregistered panoramic camera (Pancam) observations (*6*) provide context and additional multispectral visible and near-infrared observations. Reflected downwelling atmospheric radiance has been removed from all spectra presented here with the use of Mini-TES sky observations to directly measure the atmospheric radiance (*7*, *8*).

Mg and Ca sulfate–rich outcrops. Among the most exciting discoveries at Meridiani is the occurrence of bedrock with high

Table 1. Numerical deconvolution results for Mini-TES outcrop spectra. The volume abundances listed have been rounded to the nearest 5% from the values from the deconvolution model.

Mineral group	Guadalupe	Gills	Last Chance Lower	Last Chance Left	Hippo	Pilbara	Tamanend Park	Chantry Flats	Tres Creek	Rhino Horn	Bunny Slope	Dolphin	Hamersley
Sulfate	25	25	10	15	25	30	35	30	35	30	25	25	15
Hematite	25	25	0	20	35	0	35	30	45	45	10	40	5
Sheet silicate	0	0	0	0	0	0	10	20	0	0	0	5	0
Glass	25	15	15	20	10	20	10	10	5	5	20	15	20
Oxide/hyroxide	0	5	20	20	5	10	0	0	5	5	5	0	0
Feldspar	10	15	25	10	15	20	0	0	0	5	15	0	45
Olivine	10	10	20	10	5	10	10	10	5	10	15	5	0
Pyroxene	5	5	10	5	5	5	0	5	0	5	15	5	15
Total	100	100	100	100	100	95	100	105	95	105	105	95	100

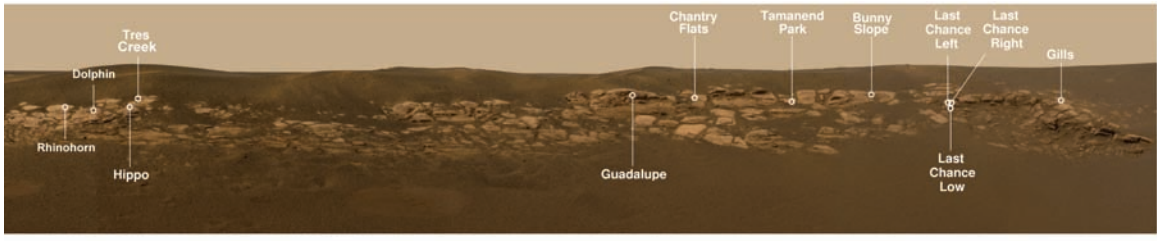

Fig. 1. Index map acquired from the lander showing the locations of the Mini-TES spectra of rocks within Eagle crater. The image is a mosaic 11.8 m in length made from Pancam images P2211, P2217, and P2218 acquired on sol 2.

sulfur abundances and preserved sedimentary structures (*4*, *9*). Mini-TES spectra were acquired in long-integration single-point stares at 14 locations along the outcrops at Eagle and other craters (Figs. 1 and 2). These spectra have varying amounts of a surface dust component (*3*, *10*), which was removed by first deconvolving each spectrum with an endmember library of 47 laboratory minerals and four scene spectra (Fig. 3) (*11*–*15*) and then subtracting the derived dust component to produce a dust-free spectrum (Fig. 4). Once dust has been removed, the resulting spectra still have subtle differences in shape and derived mineral abundances, but all spectra show (i) a pronounced absorption beginning at ~1250 cm^{-1}, (ii) a relatively flat shape between 900 and 1200 cm^{-1}, (iii) an absorption shoulder at ~780 cm^{-1}, and (iv) deep absorptions near 450 and 550 cm^{-1} (Fig. 4). The absorption edge at 1250 cm^{-1} is consistent with the sulfate mineral group. The broad mid-wavelength absorption is fit by a mixture of glass, silicates, and sulfates. The long wavelength absorptions coincide with coarsely crystalline hematite (Fig. 3).

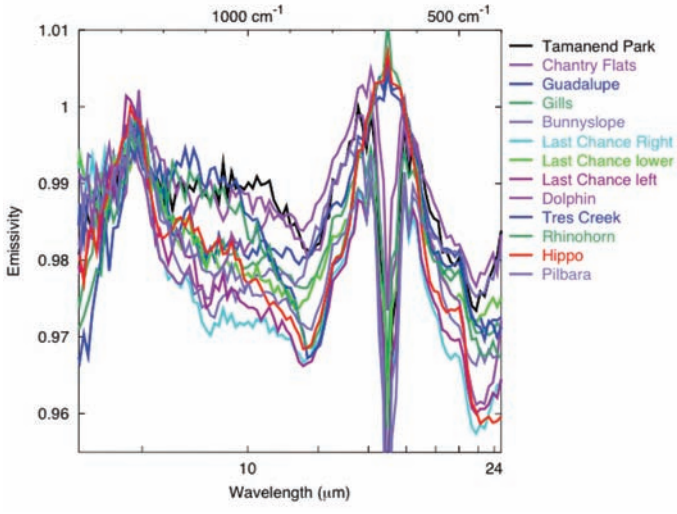

Fig. 2. Original Mini-TES spectra of the 13 outcrop locations. Variations in surface dust component and hematite spherules produce much of the variation in spectral character. All spectra presented here have been corrected to remove the effects of downwelling atmospheric radiance (*8*). Pilbara is located in Fram crater.

Sulfates are present in all of the outcrops we observed, with volume abundances, normalized to remove airfall dust, of 15 to 35% (Table 1) (*16*). The spectral library used to deconvolve the samples contained representative hydrous and anhydrous sulfates, including gypsum [$CaSO_4$-2(H_2O)], bassanite [2$CaSO_4$-(H_2O)], epsomite [$MgSO_4$-7(H_2O)], kieserite ($MgSO_4$-H_2O), glauberite [$Na_2Ca(SO_4)_2$], and jarosite [$KFe_3(SO_4)$-2$(OH)_6$] species. The best fit to the Mini-TES spectra was consistently provided by the Mg and Ca sulfates.

Jarosite, the Fe-bearing sulfate that was identified by the Mössbauer spectrometer (*17*), was detected in deconvolutions of several Mini-TES outcrop spectra but never in concentrations >5%. The outcrop has 17 weight % (wt %) FeO (*9*), with 28% of this Fe as jarosite (*17*). Together, these data indicate that ~10 wt % of the outcrop is jarosite. The average density of the outcrop derived with the Mini-TES mineral abundances (~3.3 g cm^{-3}; Table 1) is similar to the density of jarosite (3.1 to 3.3 g cm^{-3}),

[1]Department of Geological Sciences, Arizona State University, Tempe, AZ 85287, USA. [2]Department of Earth and Planetary Sciences, Washington University, St. Louis, MO 63130, USA. [3]Jet Propulsion Laboratory, California Institute of Technology, Pasadena, CA 91109, USA. [4]Department of Geological Science, Reno, NV 89557, USA. [5]Institute of Geophysics and Planetology, University of Hawaii, Honolulu, HI 96822, USA. [6]Department of Astronomy, Space Sciences Building, Cornell University, Ithaca, NY 14853, USA. [7]U.S. Geological Survey, Flagstaff, AZ 86001, USA. [8]Department of Earth and Planetary Sciences, University of Tennessee, Knoxville, TN 37996, USA. [9]National Aeronautics and Space Administration (NASA) Johnson Space Center, Houston, TX 77058, USA. [10]NASA Goddard Space Flight Center, Greenbelt, MD 20771, USA. [11]Space Science Institute, Martinez, GA 30907, USA.

*To whom correspondence should be addressed. E-mail: phil.christensen@asu.edu

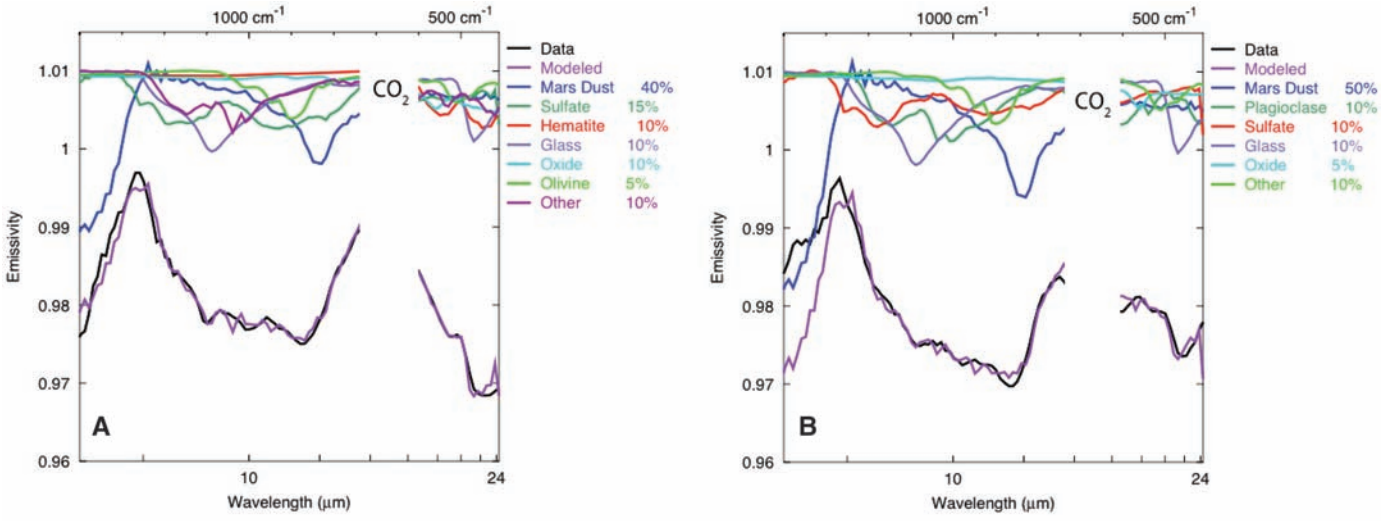

Fig. 3. (**A**) Spectral deconvolution of the Mini-TES spectrum of the outcrop at Gills in Eagle crater. The Mars dust component is subtracted from all of the measured spectra shown in Fig. 2 to produce the dust-removed spectra shown in Fig. 4. The individual minerals that fit to the spectra have been summed into mineral groups. The mineral abundances shown are best-fit values from the linear least squares deconvolution model; the endmember spectra are shown scaled by these abundances to show how each contributes to the measured spectrum. Derived abundances have accuracies of ±5 to 10%. Abundances shown in all figures have been rounded to the nearest 5%. Spectrum is average of 200 spectra acquired on sol 39. (**B**) Spectral deconvolution of the Mini-TES spectrum of the outcrop at Pilbara in Fram crater. The oxide component includes all oxides, typically modeled as magnetite and goethite, except hematite. Spectrum is the average of 100 spectra acquired on sol 85.

Fig. 4. Selected dust-removed spectra from outcrops in Eagle crater at locations Guadalupe, Gills, Last Chance Lower, Last Chance Left, and Hippo, and Fram crater at Pilbara. The spectrum of Pilbara is similar to the Eagle crater samples, suggesting that this rock is part of the same rock unit.

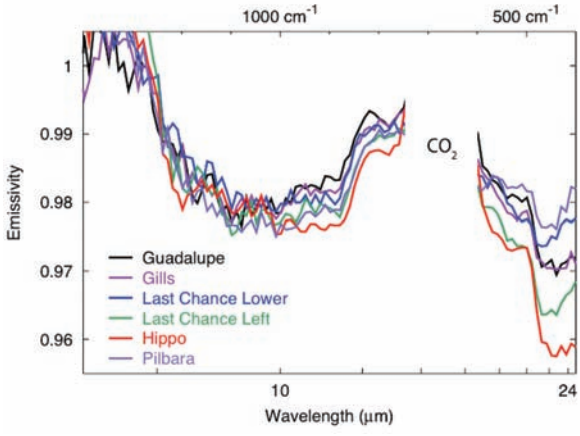

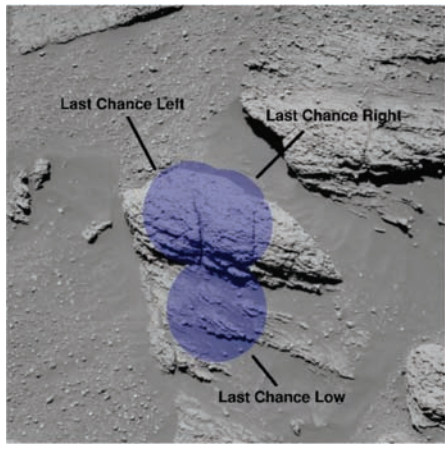

Fig. 5. Location of Mini-TES spectra for Last Chance outcrop location showing the mixture of outcrop, sand, and spherules that are present in the Mini-TES field of view. Each circle represents the Mini-TES field of view, which is ~15 cm in diameter.

indicating that the jarosite volume abundance is also ~10%. Given the low spectral contrast of this outcrop, this value is consistent with the marginal detection of jarosite by Mini-TES. The finding that Mg and Ca sulfates dominate is consistent with the Alpha Particle X-ray Spectrometer (APXS) results, which show that Mg and Ca are present, and that there is substantially more S and too little Fe for the sulfates to be jarosite alone (*9*, *18*).

Hematite is detected at volume abundances >10% in all but three outcrop locations (Table 1). Basaltic minerals are detected in all spectra. Loose, dark-toned sands and spherules that are likely wind transported from the overlying plains are common in cracks and ledges on the outcrop (Fig. 5) (*6*). Given the presence of these materials and the 12- to 15-cm diameter of the Mini-TES field of view (*19*), most of the Mini-TES observations are likely contaminated by these wind-blown materials and overestimate the hematite and basalt components (pyroxene and olivine) actually present in the outcrop. However, samples with the lowest basalt component (5 to 10%) still have hematite abundances of >30%. This Mini-TES–derived hematite abundance is higher than the abundance determined from the Mössbauer and APXS Fe results for the outcrop (*9*, *17*). However, it is likely that the larger Mini-TES fields of view (Fig. 5) included loose hematite-rich spherules observed in the Microscopic Imager (MI) (*20*) and Pancam images in the surrounding soils (*6*) in addition to the outcrop matrix and embedded spherules.

The areas of outcrop named Guadalupe, Gills, Last Chance Lower, Last Chance Left, Hippo, and Pilbara have the deepest absorption bands and provide the best Mini-TES measurement of the outcrop composition (Fig. 4). The reduced spectral contrast in other samples is likely due to multiple complicating effects, including blackbody cavity and temperature difference effects resulting from millimeter-scale pits (*21*). Intermediate- to high-silica components, modeled as high-silica glasses and feldspar, are fit to these six samples at abundances of ~10 to 25% (Table 1) (*13*, *14*, *16*, *22*–*25*). The derived abundance of the mafic igneous phases (olivine and pyroxene) varies from ~10 to 30%, with some of this component likely due to draping wind-blown sands (*6*). The derived abundance of oxides and hydroxides other than crystalline hematite, typically modeled as magnetite with minor goethite, is 5 to 20%. Taking the aver-

age of these best six outcrop spectra and deconvolving gives dust-removed abundances of 25% sulfate, 20% hematite, 30% high-silica component, 20% igneous phases, and 5% oxides other than hematite.

Light-toned outcrop is exposed in the ~10-m-diameter Fram crater, which is located 450 m from Eagle crater (*4*, *6*). Mini-TES spectra obtained from a sample of this outcrop at Pilbara (Fig. 4 and Table 1) are similar in spectral shape and derived mineral abundances to the outcrops at Eagle crater, suggesting that the process that formed these rocks was relatively uniform over a lateral distance of at least 450 m.

Mini-TES observations have demonstrated that crystalline silica minerals, such as quartz and chert, and carbonate phases are not present in these outcrops at abundances >~5%. The low olivine and pyroxene abundances in these rocks indicate that either they did not form from basaltic material or alteration of pyroxene and olivine in a basaltic parent rock has been nearly complete. The exact mineral phase of the high-silica component has not yet been determined, but the presence of these phases is consistent with the bulk APXS chemistry for the outcrop (*9*, *18*). The low abundance of other oxides and hydroxides in all but two samples (Table 1) is consistent with the results from the Mössbauer (*17*) and indicates that hematite is the dominant oxide and hydroxide in this outcrop.

Hematite spherules. The presence of coarsely crystalline hematite exposed on the surface has been predicted from orbital TES data (*26*, *27*) and was confirmed in the Mission Success panorama acquired beginning on sol 3 (*28*). The Mini-TES spectral signature of hematite is associated with spherules 0.6 to 6 mm in diameter (*20*). Mini-TES vertical scans of the plains were acquired from the near field to the horizon. These observations show a systematic increase in the depth of the diagnostic 450 and 550 cm^{-1} hematite absorption bands with decreasing elevation angle (Fig. 6), and a corresponding decrease in the depth of the basalt and dust component in the 700- to 1200-cm^{-1} region. The spectral shape of the hematite bands does not vary with elevation angle (*e*, measured downward from the horizontal), indicating that viewing geometry does not affect the spectral character of the spherules up to elevation angles of ~5° (*29*). With an average diameter (*d*) of 3 mm for the hematite spherules and only ~0.1 to 0.2 mm for the intervening sand (*30*), the spacing (*x*) of spherules only needs to be $x \leq d/\tan(90 - e)$, or ~25 mm, on the flat plains for the spherules to dominate the observed emission. This spacing is consistent with typical spherule spacing observed for plains soils (*30*, *31*).

Differencing the spectra from the highest and lowest elevation angles effectively isolates the spherule component of the soil. This derived spectrum matches a laboratory hematite sample (Fig. 7A) (*32*), which indicates that the spherules are dominated by hematite. No other components, including silica, carbonates, sulfates, silicates, or other oxides, are detected in the derived Mini-TES spherule spectra at a total abundance for non-hematite components of 5 to 10%. Whereas Mini-TES only directly samples the outermost 50 to 100 μm of the spherules (*33*), many of the spherules are eroded or broken (*30*), suggesting that the interiors of these particles are also dominated by hematite.

We tried to determine the spherule composition with the use of the entire instrument suite by comparing the hematite-rich Berry Bowl and nearby hematite-poor outcrop surfaces. However, the Mini-TES difference spectrum (Fig. 7B) shows the presence of hematite and basaltic sand, and Pancam images show the presence of dark-toned sand and spherules in the Berry Bowl (Plate 11) (*6*). This experiment demonstrates that the spectral differencing technique identifies all of the components that differ between the two observations, and provides support for the hematite-dominated spherule composition derived from the plains emission angle experiment.

The lateral distribution of hematite within Eagle crater was mapped by deconvolving high-resolution Mini-TES rasters acquired during the crater traverse to obtain mineral abundances (Plate 3). Hematite spherules occur nonuniformly around Eagle crater, with the highest abundance occurring on the western inner wall and decreasing on the northern wall (Plate 3). The crater floor has a low-hematite spectral signature over much of its surface. The trend of decreasing hematite abundance from the surrounding plains, along troughs and cracks in the outcrop, and onto the crater floor (Plate 3), suggests that these troughs are pathways of hematite transport from the plains into the crater. Thus, the primary source of hematite within the crater appears to be from the overlying plains, rather than from erosion of spherules present in the outcrop exposed in the crater wall.

The vertical distribution of hematite within the soils was investigated by comparing Mini-TES spectra of soils within and adjacent to

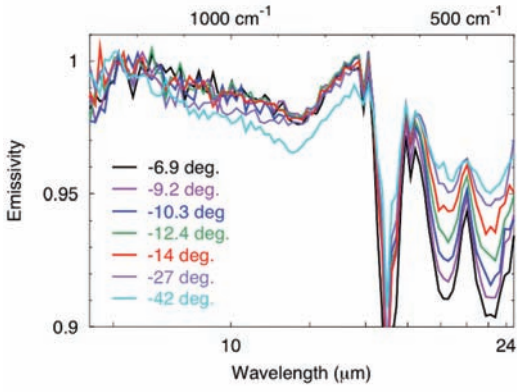

Fig. 6. Spectra of the plains surrounding Eagle crater at a range of elevation angles. The spectral bands at 450 and 550 cm^{-1}, where hematite has strong absorptions, deepen with decreasing elevation angle, corresponding to increasing emission angle. The basalt and dust silicate absorptions in the 750- to 1200-cm^{-1} region show a corresponding decrease, consistent with a reduction in basalt and an increase in hematite-rich spherules within the field of view at high emission angles. The deep absorptions centered near 667 cm^{-1} are due to atmospheric CO_2. Spectra were acquired on sol 72.

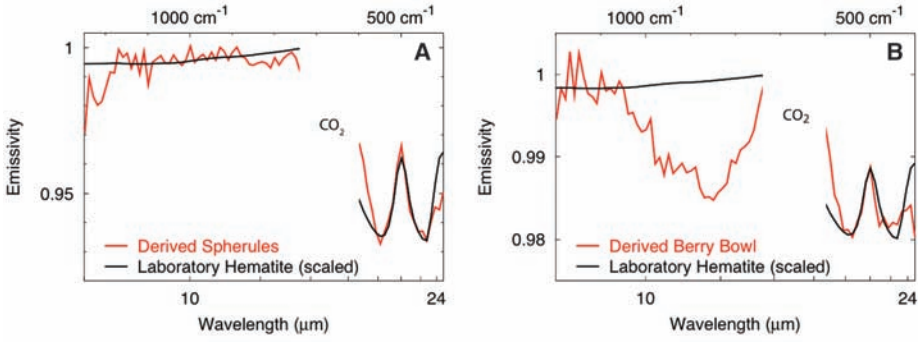

Fig. 7. (**A**) Derived Mini-TES spectra of spherules isolated by subtracting the high emission angle observation from the low emission angle observation shown in Fig. 6. The resulting spectrum matches a laboratory hematite sample (*32*). No other components are detectable in the derived Mini-TES spectrum, indicating that the spherules are dominated by hematite. (**B**) Derived spectrum of spherules and basalt sand within the Berry Bowl (*6*) determined by differencing a spectrum of the Berry Bowl from a spectrum from a nearby surface with low spherule and sand abundance. The derived Mini-TES spectrum is consistent with a mixture of hematite spherules (400 to 600 cm^{-1}) and basalt sand (750 to 1050 cm^{-1}), indicating that this differencing technique is sensitive to all components that were in the sample.

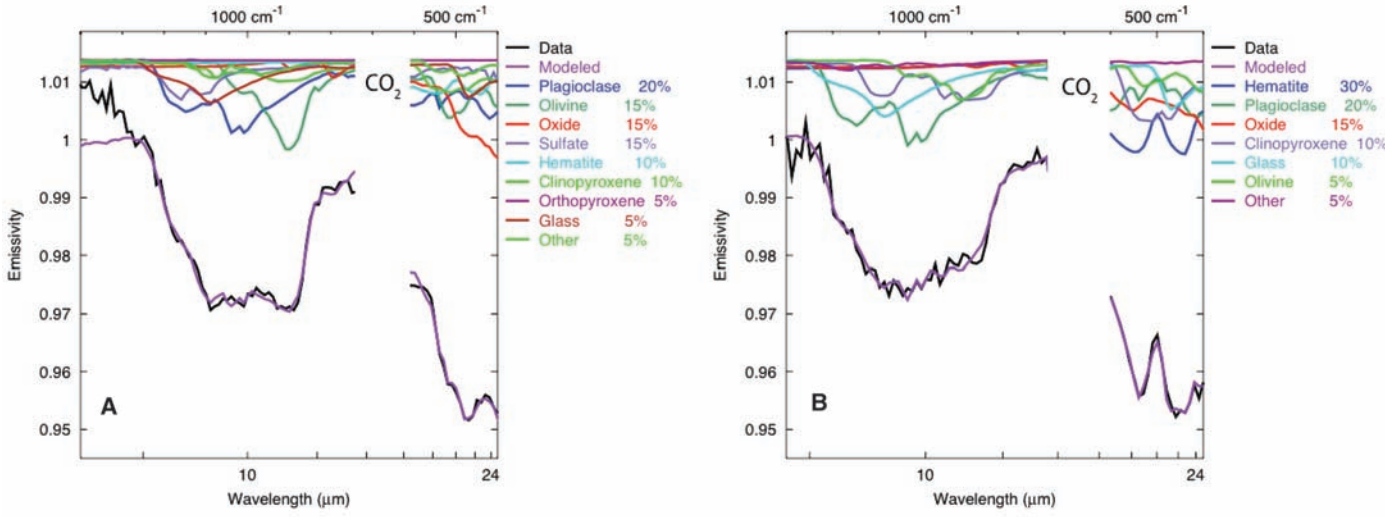

Fig. 8. (**A**) The mineral composition and abundance of basaltic sands on the floor of Eagle crater as derived from the deconvolution of dust-removed Mini-TES spectra. These sands are derived from a plagioclase, pyroxene, and olivine basalt with hematite and sulfate contaminants from the Eagle crater outcrop. Oxide includes all oxides except hematite. Spectrum is the average of 225 spectra acquired on sol 8. (**B**) The mineral composition and abundance of basalt and hematite spherule sands on the plains between Fram and Endurance craters derived from the deconvolution of dust-removed Mini-TES spectra. These sands appear to be derived from a plagioclase, pyroxene, and olivine basalt with more hematite and fewer sulfate contaminants than in the sands inside Eagle crater. Oxide component includes all oxides except hematite. Spectrum is the average of 90 spectra acquired on sol 90.

Fig. 9. Comparison of the spectral properties of the major components observed at the Meridiani landing site. The outcrop spectrum is the average of spectra of Guadalupe, Gills, Last Chance Lower, Last Chance Left, Hippo, and Pilbara; the olivine basalt sand spectrum is from Fig. 8A; the Bounce rock spectrum is from Fig. 10A; the hematite spherule spectrum is from Fig. 7A.

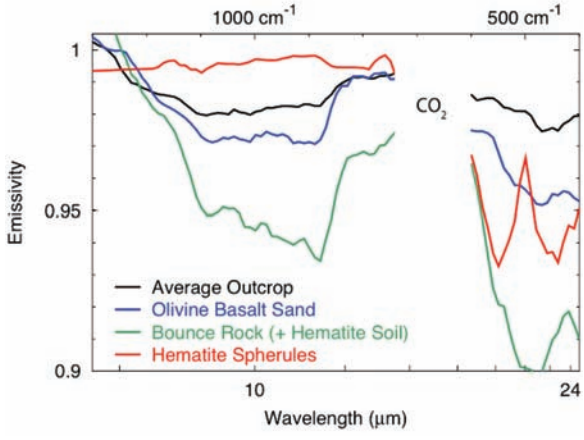

airbag bounce marks (*4*, *30*). The undisturbed soils show hematite absorptions at 450 and 550 cm^{-1} that are due to hematite spherules on the surface. The depths of these spectral bands are reduced in the spectra from bounce marks, indicating that the surficial hematite spherules were pushed beneath the surface by the airbag impact. MI observations support this by showing spherules pushed beneath the surface by placement of the Mössbauer instrument (*20*). These observations suggest that the spherules are a surficial lag, with a lower concentration in the subsurface fine-grained materials. This interpretation is supported by observations of vertical walls produced in trenching activities that show few spherules exposed in the trench walls (*30*, *34*). A possible scenario for the formation of this lag and the higher hematite spherule abundance on the plains is the erosion of an overlying spherule-bearing layer.

Olivine basalt soils. Soils with low hematite abundance all have similar mineralogies and are composed of basaltic minerals plagioclase, high-Ca clinopyroxene, olivine [~Fo60 (*35*)], oxides, orthopyroxene, and glass (Fig. 8). The sands on the floor of Eagle crater have derived mineral abundances, normalized to remove the dust, hematite, and sulfate components, of more intermediate plagioclase (~30%) than pyroxene (~20%), with ~20% olivine (~Fo60), ~10% glass, and ~15% oxides other than hematite, which are typically modeled as magnetite and lesser goethite (Fig. 8A). The sands on the plains between Eagle and Endurance craters typically have higher hematite abundance (Fig. 8B), but when these spectra are normalized to remove the dust, hematite, and sulfate components, they are also dominated by intermediate plagioclase (~35%), with 15% clinopyroxene, 10% ~Fo60 olivine, 15% glass, and 20% other oxides (Fig. 8B). Overall, these sands have a higher abundance of plagioclase relative to pyroxene and are close to the mineral compositions and abundances derived from orbital TES data for typical martian basaltic units found in the ancient cratered terrains of Mars (*23*, *24*, *36*).

These olivine basalt sands are not derived from any rock observed to date at Meridiani. It is possible that the sands at this site were transported from outside the layered terrain of Meridiani. However, the distance that a 500-μm basalt grain can be transported by aeolian saltation before it is reduced to a size that can be carried off in suspension is only ~300 km (*37*, *38*). Alternatively, these sands may have been derived from the mechanical breakdown of an overlying layer or from underlying material brought to the surface by impact cratering. The variability in olivine abundance may be due to transport sorting processes or may reflect real variations in the composition of source rocks that produced these sands.

Bounce rock. Bounce rock, the largest and darkest rock present on the exterior rim of Eagle crater, was selected for detailed investigation (*4*). The Mini-TES–derived mineral composition of Bounce rock, after the removal of airfall dust and the small amount of fine dust contaminant produced by the Rock Abrasion Tool (RAT) during abrasion of this rock, shows that Bounce rock is unique

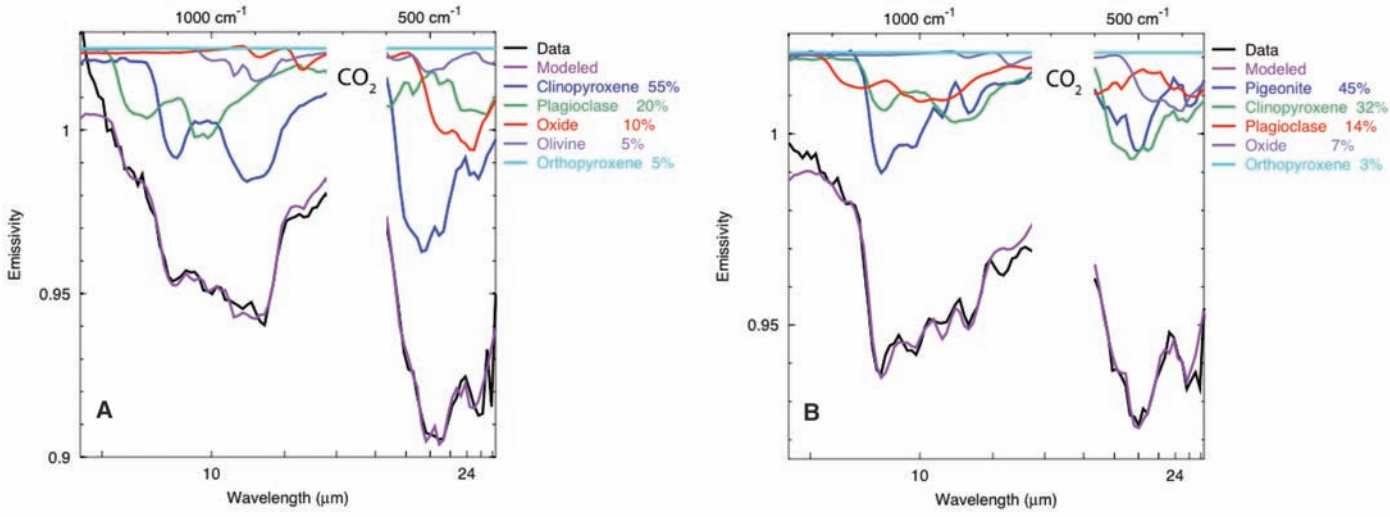

Fig. 10. (**A**) The mineral composition and abundance of Bounce rock as determined from the deconvolution of the average of 100 dust-removed Mini-TES spectra acquired on sol 68. This rock has much more clinopyroxene compared to plagioclase than seen in the basaltic sands. Oxide includes all oxides except hematite. Spectrum is the average of 100 spectra collected on sol 68. (**B**) The mineral composition of EETA#79001B from a laboratory spectrum (*41*). The spectrally derived composition of this rock matches its measured modal mineralogy (*43*). The spectrum of this meteorite differs from that of Bounce rock in the 9- to 12-μm region, suggesting that although the elemental abundance of Bounce rock matches that of EETA#79001B (*9*), the nature or composition of the pyroxenes may be somewhat different.

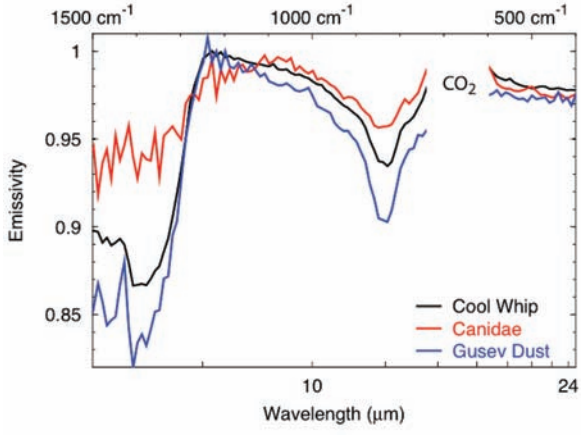

Fig. 11. The mineral composition and abundance of the bright material in soil and rocks. The surface at location Cool Whip is in the bright wind streak trending southeast from Eagle crater. This surface is essentially pure dust as determined from comparison with a dust spectrum from Gusev crater (*3*), suggesting formation from airfall dust. Canidae is a bright, dust-covered rock on the rim of Endurance crater.

among rocks investigated at either the Meridiani or Gusev sites (Fig. 9) (*3*, *39*).

Bounce rock has much higher pyroxene abundance than the basaltic sands and rocks observed here and at Gusev crater (*3*, *39*), with clinopyroxene accounting for ~55% of the rock and orthopyroxene ~5%, followed by ~20% plagioclase, ~5% olivine, and ~10% oxides (Fig. 10A). This composition is much closer to that of the martian basaltic shergottite meteorites (*40*) than the basaltic components observed at either Mars Exploration Rover (MER) site.

The elemental abundance of Bounce rock is similar to that of EETA#79001 lithology B (*9*); however, the infrared spectra of EETA#79001B (Fig. 10B) (*41*, *42*) and Bounce rock differ in the 9- to 12-μm region. Deconvolution of the laboratory spectrum of EETA#79001B (Fig. 10B) gives mineral abundances that closely match its measured modal mineralogy of 30 to 50% pigeonite, 10 to 25% high-Ca clinopyroxene, ~30% maskelynite (shocked plagioclase), and 5% opaque minerals (*43*). The best fit to the Bounce rock spectrum (Fig. 10B) gives high-Ca clinopyroxene instead of the low-Ca clinopyroxene pigeonite, although the four emissivity minima between 850 and 1100 cm^{-1} suggest that pigeonite is present in Bounce rock but poorly modeled with our current collection of pigeonite samples.

The TES-derived basalt compositions differ from those of the martian meteorites (*24*, *44*, *45*), and both lithologies have now been positively identified in situ on Mars. The ability of Mini-TES spectra to distinguish them and the similarity of Meridiani spectra to the TES orbital spectra strengthens previous interpretations that use TES data to determine the composition of basalt globally (*23*, *24*, *36*, *44*).

The distinct mineral composition and chemistry of Bounce rock, together with its isolated occurrence (*4*), suggest that this rock may not be locally derived. A possible source region is a relatively unmodified 25-km crater located 75 km southwest of Eagle crater, the continuous ejecta of which lie atop the hematite-bearing plains (*4*, *27*). In this case, Bounce rock may have been derived from materials that are compositionally distinct from the basaltic sands that cover the plains around Eagle crater (*4*).

Hamersley rock in Fram crater. A rock called Hamersley observed on the inner wall of the ~10-m-diameter crater Fram has a derived mineral abundance and composition that may be another endmember among the samples observed to date. Hamersley has the highest abundance of high-silica components (modeled as glass, feldspar, and sheet silicate) observed, although Bunny Slope and Dolphin at Eagle crater have similar spectral shapes.

Dust accumulation: Eagle crater bright streak. Upon exiting Eagle crater, Opportunity examined the composition and texture of the bright material seen from orbit to form a wind streak oriented downwind from Eagle crater (*4*, *30*). Mini-TES spectra of the surface within this streak match the spectra of typical bright low-inertia dust seen globally from orbit (*46*) and in situ at Gusev crater (*3*) (Fig. 11). The spectral match between this wind streak and regional dust deposits provides support for the model of bright wind streaks forming by deposition of airborne dust in the stagnant air created downwind of topographic obstacles during periods of high atmospheric stability (*47*).

Dust accumulation occurs on all of the outcrop rocks to some degree (Fig. 2). On some rocks, such as Canidae observed on the

rim of Endurance crater, dust accumulates to sufficient thickness (>~50 μm) (*48*, *49*) to mask the spectrum of the underlying rock (Fig. 11). Dust may accumulate more readily on rock surfaces than on the soil, because occasional saltation of sand-sized grains may entrain and remove the dust, resulting in surfaces that are dark and have a small dust component in Mini-TES spectra.

Global context. Analysis of orbital data has suggested that the extensive (500 × 250 km), ancient (*50*–*52*), layered, hematite-bearing units in Meridiani Planum formed by (i) chemical precipitation of a hematite precursor (*32*) from Fe-rich aqueous fluids under ambient conditions (*26*, *27*, *53*); (ii) precipitation from Fe-rich hydrothermal fluids (*26*, *27*, *51*, *54*); (iii) thermal oxidation of volcanic ash during eruption (*26*, *27*, *51*, *55*); or (iv) precipitation of Fe-oxides that were metamorphosed by burial to platy hematite (*56*).

These units were deposited in a standing body of liquid water on the basis of the morphology, composition, and vertical distribution of the hematite-bearing units seen from orbit (*53*). The discovery of sulfate-rich outcrops and hematite in concretions has provided conclusive evidence for deposition in an ancient aqueous system (*18*). However, the presence of extensive olivine, pyroxene, and feldspar in basaltic sands at this site and throughout Meridiani (*53*) suggests that physical weathering has dominated over chemical weathering during the time that these sands have been exposed on the surface. On a broader scale, the occurrence of basalts and olivine basalts throughout much of the equatorial and mid-latitude regions (*3*, *25*, *57*) suggests that chemical weathering may have been a relatively minor process, at least in low to mid-latitudes (*58*), throughout much of martian history. Thus, the presence of a body of water may represent a relatively brief, localized phenomenon early in Mars history.

References and Notes

1. P. R. Christensen *et al.*, *J. Geophys. Res.* **108**, 8064, 10.1029/2003JE002117 (2003).
2. Two-point radiometric calibration was intended to use two V-groove blackbody targets. However, as with the Spirit rover, the temperature sensors attached to the rover deck failed at extremely low temperatures (~–90°C) on the first night after landing. The calibration was modified to use prelaunch measurements of the instrument response function taken over temperature, with the instrument radiance determined from observations of the target mounted in the Pancam Mast Assembly. On the basis of comparison with orbiting Mars Global Surveyor (MGS) TES data and modeling of the atmospheric observations, the response function has not changed from prelaunch values and the calibration approach is providing the required accuracy. The 1σ radiometric precision for two-spectra summing is $\pm 1.8 \times 10^{-8}$ W cm^{-2} sr^{-1}/cm^{-1} between 450 and 1300 cm^{-1}, increasing to $\sim 7 \times 10^{-8}$ W cm^{-2} sr^{-1}/cm^{-1} at shorter (300 cm^{-1}) and longer (1800 cm^{-1}) wave numbers. The absolute radiance error is $< 5 \times 10^{-8}$ W cm^{-2} sr^{-1}/cm^{-1}, decreasing to $\sim 1 \times 10^{-8}$ W cm^{-2} sr^{-1}/cm^{-1}.
3. P. R. Christensen *et al.*, *Science* **305**, 837 (2004).
4. S. W. Squyres *et al.*, *Science* **306**, 1698 (2004).
5. Names have been assigned to aerographic features by the MER team for planning and operations purposes. The names are not formally recognized by the International Astronomical Union.
6. J. F. Bell III *et al.*, *Science* **306**, 1703 (2004).
7. M. D. Smith *et al.*, *Science* **306**, 1750 (2004).
8. The downwelling radiance is removed by solving for ε in the equation: radiance = $B(T_{surface} \times \varepsilon_{surface}) + (R_{atmosphere} \times R_{surface})$, where radiance is the measured total radiance from the surface, B is the Planck function, $T_{surface}$ is the surface temperature, $\varepsilon_{surface}$ is the surface emissivity, $R_{atmosphere}$ is the downwelling atmospheric radiance, and $R_{surface}$ is the surface infrared reflectivity that is equal to $(1 - \varepsilon_{surface})$. The surface temperature is derived from the measured Mini-TES spectrum (*1*, *3*). $R_{atmosphere}$ is the hemispherically integrated downwelling from the atmosphere and is approximated with Mini-TES observations taken at an emission angle of 60° from the zenith. The spectral radiance of the atmospheric path between Mini-TES and the target is assumed to be negligible, and the atmospheric transmissivity in this path is assumed to be 1.0. Removing the downwelling radiance deepens the absorption bands (*1*), but given the relatively high surface temperatures (typically >265 K) and the relatively low atmospheric opacity, the effect of the atmosphere on the spectra presented here is relatively small; the derived mineral abundances typically vary by less than 5% for any mineral for deconvolutions done with and without an atmospheric correction. Calculations based on the Discrete Ordinate Radiative Transfer code and including emitted, absorbed, and scattered surface and atmospheric radiative terms support the above conclusions.
9. R. Rieder *et al.*, *Science* **306**, 1746 (2004).
10. "Dust" is used throughout to indicate the fine-grained component of surface materials with similar spectral character to regional dust deposits observed by MGS TES and interpreted to be air fallout from regional and global dust storms.
11. The mineral suite used for deconvolution included a broad range of sulfate, carbonate, sheet silicates, oxides, pyroxene, feldspar, olivine, and surface dust compositions.
12. J. B. Adams, M. O. Smith, P. E. Johnson, *J. Geophys. Res.* **91**, 8098 (1986).
13. M. S. Ramsey, P. R. Christensen, *J. Geophys. Res.* **103**, 577 (1998).
14. K. C. Feely, P. R. Christensen, *J. Geophys. Res.* **104**, 24195 (1999).
15. V. E. Hamilton, P. R. Christensen, *J. Geophys. Res.* **105**, 9717 (2000).
16. The Mini-TES–derived volume abundances are estimated to have accuracies of ±5 to 10% on the basis of similar analyses of laboratory and MGS TES rock and mineral mixtures. The abundances listed in the figures and tables are the numerical best fit values derived from the linear least squares deconvolution model and are reported at the precision determined from the deconvolution model.
17. G. Klingelhöfer *et al.*, *Science* **306**, 1740 (2004).
18. S. W. Squyres *et al.*, *Science* **306**, 1709 (2004).
19. The Mini-TES nominal field of view is 20 mrad at infinity. For near-field observations, the field of view is the aperture diameter (6.35 cm) plus the 20-mrad divergence from the location of the telescope to the point being observed. Targets in the arm work volume are ~1.5 m in front of the rover, giving a total path length of ~3 m from the Mini-TES telescope. The resulting Mini-TES field of view is ~12 cm at the end of the rover arm.
20. K. E. Herkenhoff *et al.*, *Science* **306**, 1727 (2004).
21. J. Ondrusek, P. R. Christensen, J. H. Fink, *J. Geophys. Res.* **98**, 15903 (1993).
22. M. B. Wyatt, V. E. Hamilton, J. H. Y. McSween, P. R. Christensen, L. A. Taylor, *J. Geophys. Res.* **106**, 14711 (2001).
23. V. E. Hamilton, M. B. Wyatt, J. McSween, *J. Geophys. Res.* **106**, 14733 (2001).
24. P. R. Christensen, J. L. Bandfield, M. D. Smith, R. N. Clark, *J. Geophys. Res.* **105**, 9609 (2000).
25. J. L. Bandfield, *J. Geophys. Res.* **107**, 10.1029/2001JE001510 (2002).
26. P. R. Christensen *et al.*, *J. Geophys. Res.* **105**, 9623 (2000).
27. P. R. Christensen, R. V. Morris, M. D. Lane, J. L. Bandfield, M. C. Malin, *J. Geophys. Res.* **106**, 23873 (2001).
28. A martian solar day has a mean period of 24 hours 39 min 35.244 s and is referred to as a sol to distinguish this from a roughly 3% shorter day on Earth.
29. The millimeter-sized spherules are substantially larger than the wavelength of the emitted radiance. In this case, emission from the spherules should not exhibit angle-dependent emission because of Fresnel effects, which would be expected for a specular surface composed of particles comparable in size to the wavelength measured.
30. L. A. Soderblom *et al.*, *Science* **306**, 1723 (2004).
31. The term martian soil is used here to denote any loose unconsolidated materials that can be distinguished from rocks, bedrock, or strongly cohesive sediments. No implication of the presence or absence of organic materials or living matter is intended.
32. T. D. Glotch, R. V. Morris, P. R. Christensen, T. G. Sharp, *J. Geophys. Res.* **109**, EO7003, 10.1029/2003JE002224 (2004).
33. P. R. Christensen, S. T. Harrison, *J. Geophys. Res.* **98**, 19819 (1993).
34. R. E. Arvidson *et al.*, *Science* **306**, 1730 (2004).
35. The Fo (forsterite) value is the amount of FeO in the olivine, where forsterite is the Mg endmember and fayalite is the Fe endmember.
36. J. L. Bandfield, V. E. Hamilton, P. R. Christensen, *Science* **287**, 1626 (2000).
37. R. Greeley, M. D. Kraft, *Lunar and Planet. Sci. XXXII*, CD-ROM (abstr. 1839) (2001).
38. D. Rogers, P. R. Christensen, *J. Geophys. Res.* **108**, 5030, 10.1029/2002JE001913 (2003).
39. H. Y. McSween Jr. *et al.*, *Science* **305**, 842 (2004).
40. H. Y. McSween Jr., *Meteoritics* **29**, 757 (1994).
41. J. L. Bishop, V. E. Hamilton, *64th Annual Meteoritical Society Meeting* **36**, 21 (abstr. 5217) (2001).
42. V. E. Hamilton, P. R. Christensen, H. Y. McSween Jr., *J. Geophys. Res.* **102**, 25593 (1997).
43. H. Y. McSween Jr., E. Jarosewich, *Geochim. Cosmochim. Acta* **47**, 1501 (1983).
44. H. Y. McSween Jr., T. L. Grove, W. B. Wyatt, *J. Geophys. Res.* **108**, 5135, 10.1029/2003JE002175 (2003).
45. V. E. Hamilton, P. R. Christensen, J. H. Y. McSween, J. L. Bandfield, *Meteor. Planet. Sci.* **38**, 871 (2003).
46. J. L. Bandfield, T. D. Glotch, P. R. Christensen, *Science* **301**, 1084 (2003).
47. J. Veverka, P. Gierasch, P. Thomas, *Icarus* **45**, 154 (1981).
48. J. R. Johnson, P. R. Christensen, P. G. Lucey, *J. Geophys. Res.* **107**, 10.1029/2000JE001405 (2002).
49. T. G. Graff, thesis, Arizona State University (2003).
50. B. M. Hynek, R. J. Phillips, *Geology* **29**, 407 (2001).
51. B. M. Hynek, R. E. Arvidson, R. J. Phillips, *J. Geophys. Res.* **107**, 5088, 10.1029/2002JE001891 (2002).
52. M. D. Lane, P. R. Christensen, W. K. Hartmann, *Geophys. Res. Lett.* **30**, 1770, 10.1029/2003GL017183 (2003).
53. P. R. Christensen, S. W. Ruff, *J. Geophys. Res.* **109**, EO8003, 10.1029/2003JE002233 (2004).
54. D. C. Catling, J. M. Moore, *Icarus* **165**, 277 (2003).
55. R. E. Arvidson *et al.*, *J. Geophys. Res.* **108**, 8073, 10.1029/2002JE001982 (2003).
56. M. D. Lane, R. V. Morris, S. A. Mertzman, P. R. Christensen, *J. Geophys. Res.* **107**, 5126, 10.1029/2001JE001832 (2002).
57. T. Hoefen *et al.*, *Science* **302**, 627 (2003).
58. M. B. Wyatt, *Geology* **32**, 645 (2004).

59. We thank all of the individuals at Raytheon Santa Barbara Remote Sensing, led by S. Silverman, and at the Jet Propulsion Lab, whose effort and dedication have led to the successful acquisition of Mini-TES data from the surface at Meridiani Planum. We thank J. Bishop for providing the spectrum of EET A79001B. A. Watson provided assistance with data processing analysis. Funding was provided by the MER Project Science Office.

Plates Referenced in Article

www.sciencemag.org/cgi/content/full/306/5702/1733/DC1
Plates 3 and 11

7 September 2004; accepted 3 November 2004

RESEARCH ARTICLE

Jarosite and Hematite at Meridiani Planum from Opportunity's Mössbauer Spectrometer

G. Klingelhöfer,[1]* R. V. Morris,[2] B. Bernhardt,[1] C. Schröder,[1] D. S. Rodionov,[1,3] P. A. de Souza Jr.,[1,4] A. Yen,[5] R. Gellert,[1,6] E. N. Evlanov,[3] B. Zubkov,[3] J. Foh,[1,7] U. Bonnes,[7] E. Kankeleit,[7] P. Gütlich,[1] D. W. Ming,[2] F. Renz,[1] T. Wdowiak,[8] S. W. Squyres,[9] R. E. Arvidson[10]

Mössbauer spectra measured by the Opportunity rover revealed four mineralogical components in Meridiani Planum at Eagle crater: jarosite- and hematite-rich outcrop, hematite-rich soil, olivine-bearing basaltic soil, and a pyroxene-bearing basaltic rock (Bounce rock). Spherules, interpreted to be concretions, are hematite-rich and dispersed throughout the outcrop. Hematitic soils both within and outside Eagle crater are dominated by spherules and their fragments. Olivine-bearing basaltic soil is present throughout the region. Bounce rock is probably an impact erratic. Because jarosite is a hydroxide sulfate mineral, its presence at Meridiani Planum is mineralogical evidence for aqueous processes on Mars, probably under acid-sulfate conditions.

Mössbauer spectrometers provide quantitative information about the distribution of iron among its oxidation states, the identification of iron-bearing phases, and the distribution of iron among those phases. Characterizing the speciation and distribution of iron in martian rock and soil (*1*) constrains primary rock types; the conditions under which primary minerals crystallize; and the mineralogical composition, process, and extent of alteration and weathering. Hematite (α-Fe_2O_3) was detected in Meridiani Planum from orbital observations before the Mars Exploration Rover (MER) missions (*2*, *3*), and the region was selected as a MER landing site on a scientific basis, because the mineral is a beacon for aqueous processes, and on an engineering basis, because the terrain was considered safe for landing (*4*). The first Mössbauer spectrum from Meridiani Planum was obtained by the Opportunity rover on 4 February 2004, on soil near the lander at Eagle crater.

The MIMOS II (Miniaturized Mössbauer spectrometer) instrument (*5*) on the Opportunity rover is nearly equivalent to the one on the Spirit rover and is operated in the same manner (*6*–*8*). It is mounted on the robotic arm, which positions the instrument onto surface targets. Physical contact is confirmed by a contact plate. The instrument has backscatter geometry, a drive frequency of ~24 Hz, a triangular waveform divided into 512 data channels, and a selectable maximum drive velocity range up to about ±20 mm/s (*7*). Because of the diurnal temperature variation on Mars, the instrument settings were selected to store spectra in 13 separate memory areas that correspond to 11 temperature intervals 10-K wide between 180 and 290 K, plus <180 K and >290 K windows. The target area and sampling depth of the illuminating 14.4-keV ^{57}Co gamma radiation (~150 mCi at landing) are ~1.5 cm in diameter and ~0.2 mm (coherent rock) to ~3 mm (air-fall dust) deep, respectively. The Mössbauer contact plate assembly that comes into physical contact with the surface during data acquisition contains a sensor for temperature measurement. We report results for the resonantly scattered 14.4-keV γ rays.

We followed the data analysis procedures outlined by (*6*) for Mössbauer spectra from Gusev crater. Briefly, we optimized counting statistics by summing spectra for all temperature intervals for the same target and by summing the same temperature window for different targets whose spectra appear equivalent. Peak parameters (center, width, and area) were calculated by least squares fitting procedures with Lorentzian line shapes. The Mössbauer parameters δ (isomer shift relative to metallic iron), ΔE_Q (quadrupole splitting), and B_{hf} (strength of the internal magnetic hyperfine field) were calculated from peak centers. To correct peak areas for differences in recoil-free fractions (the f factor), we used the ratio $f(Fe^{3+})/f(Fe^{2+}) = 1.21$ independent of mineralogical composition (*9*, *10*). The centers and widths of low-intensity subspectra (both doublets and sextets) were constrained to the values measured in spectra where their intensities were high. Because we did not observe obvious textural effects, doublet peak areas and widths were always constrained to be equal. For sufficiently intense sextets, two different approaches were used to fit the data: (i) Peak areas were constrained in the proportion 3:x:1:1:x:3, and the widths were unconstrained except for the inner two peaks (which strongly overlap with the doublet peaks), whose widths were constrained to be equal. (ii) Peak areas were constrained in the proportion 3:x:1:1:x:3, and the widths were unconstrained but equal for all six lines.

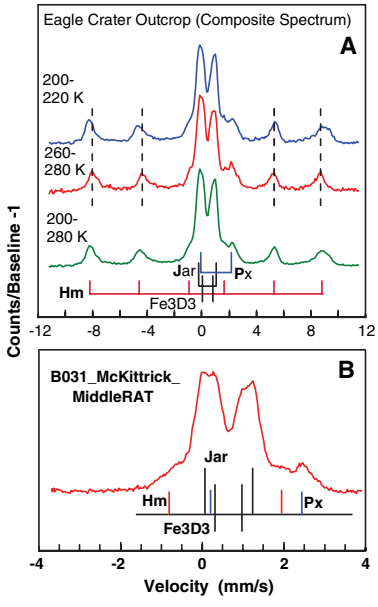

Fig. 1. Mössbauer spectra of jarosite-rich outcrop rock in Meridiani Planum for (**A**) wide and (**B**) reduced maximum velocities. The spectra in (A) are a composite spectrum obtained by summing all outcrop spectra from Eagle and Fram craters. The spectrum in (B) was obtained on target B031_McKittrick_MiddleRAT (postgrind). Outcrop spectra are characterized by two Fe^{3+} doublets [jarosite (Jar) and an unidentified oct-Fe^{3+} phase (Fe3D3)], a Fe^{2+} doublet [pyroxene (Px)], and a Fe^{3+} magnetic sextet [hematite (Hm)]. The dashed vertical lines are centered on the hematite peaks in the 260 to 280 K spectrum. The change in their positions in the 200 to 220 K is a result of the Morin transition.

[1]Institut für Anorganische und Analytische Chemie, Johannes Gutenberg-Universität, Staudinger Weg 9, D-55128 Mainz, Germany. [2]National Aeronautics and Space Administration (NASA) Johnson Space Center, Houston, TX 77058, USA. [3]Space Research Institute IKI, 117997 Moscow, Russia. [4]Companhia Vale do Rio Doce (CVRD) Group, Vitoria, Brazil. [5]Jet Propulsion Laboratory, California Institute of Technology, Pasadena, CA 91109, USA. [6]Max Planck Institut für Chemie, Becher-Weg 27, D-55128 Mainz, Germany. [7]Darmstadt University of Technology, D-64289 Darmstadt, Germany. [8]University of Alabama, Birmingham, AL 35294, USA. [9]Cornell University, Ithaca, NY 14853, USA. [10]Washington University, St. Louis, MO 63130, USA.

*To whom correspondence should be addressed. E-mail: klingel@mail.uni-mainz.de

Both approaches gave nearly the same results. For weaker sextets, the areas were constrained to 3:2:1:1:2:3.

Mineralogical assignments. Mössbauer spectra from Meridiani Planum are diverse and can be divided into four categories: (i) outcrop spectra (Fig. 1) that are dominated by doublets and magnetic sextets from octahedrally coordinated Fe^{3+} (oct-Fe^{3+}), (ii) soil spectra (Fig. 2A) that are dominated by a sextet from oct-Fe^{3+}, (iii) soil spectra (Fig. 2B) that are dominated by two oct-Fe^{2+} doublets with variable proportions of an oct-Fe^{3+} doublet and a usually weak oct-Fe^{3+} sextet, and (iv) a single rock [Bounce rock (*11*) (Fig. 2B)] with oct-Fe^{2+} doublets. Examples of the fitting procedures for representative spectra are shown (Fig. 3). Mössbauer parameters δ, ΔE_Q, and B_{hf} for component subspectra were calculated from spectra summed over temperature intervals for individual and combined targets (Table 1). Although the outcrop consists of spheroidal granules (spherules) dispersed throughout a matrix (*12*–*14*), our outcrop spectra, as determined from examination of images obtained by the Microscopic Imager (MI) (*15*), sampled only outcrop matrix. MI images showed that whole spherules are included in the spectrum for target B048_BerryBowl_Moessberry and that spherules and their fragmented equivalents are included in the spectra for soils (*14*) whose spectra are dominated by the oct-Fe^{3+} sextet.

Starting with outcrop spectra, a value of $\Delta E_Q \sim 1.22$ mm/s (temperature $T = 240 \pm 40$ K) is unusually high for oct-Fe^{3+} (*16*–*19*), even after extrapolation to 1.15 mm/s at 295 K (Fig. 4A). Because of the high value of ΔE_Q, the only viable assignment is the iron hydroxide sulfate mineral jarosite, whose generalized formula can be written $(K, Na, H_3O)(Fe_{3-x}Al_x)(SO_4)_2(OH)_6$, where $x < 1$. The endmembers $KFe_3(SO_4)_2(OH)_6$, $NaFe_3(SO_4)_2(OH)_6$, and $(H_3O)Fe_3(SO_4)_2(OH)_6$ are jarosite, natrojarosite, and hydronium jarosite, respectively. For jarosites, ΔE_Q increases in the order K > Na > H_3O and with Al^{3+} substitution for Fe^{3+} (*20*, *21*). The ΔE_Q for martian jarosite is most consistent with $(K, Na)(Fe, Al)_3(SO_4)_2(OH)_6$ that is Na^+- or K-rich jarosite with possible Al substitution. The mineral assignment is consistent with the elemental abundances of K plus Na, Al, Fe, and S for the outcrop (*22*) and the proportion of total iron associated with jarosite (Table 2). The jarosite is Na-rich, because there is insufficient K (*22*) by itself to account for all the jarosite. Sulfate minerals were also detected by the Miniature Thermal Emission Spectrometer (Mini-TES) (*23*), although jarosite was not detected by spectral deconvolution at levels above ~5%. Thus, the abundance of jarosite is well above the Mössbauer detection limit but, in the presence of other sulfates, at the detection limit of mini-TES. The presence of sulfate minerals, including jarosite, on Mars was advocated in a series of papers by the late Roger Burns (*24*–*28*). Jarosite formation in basaltic and andesitic environments on Earth has been reported (*20*, *29*–*31*).

The temperature dependence of the Mössbauer spectra of terrestrial jarosite samples (Fig. 4A) was measured by using a spare flight-model MIMOS II spectrometer (i.e., in backscatter measurement geometry). Room-temperature data from transmission Mössbauer measurements and documentation of the presence of jarosite for these samples are reported by (*29*). Considering

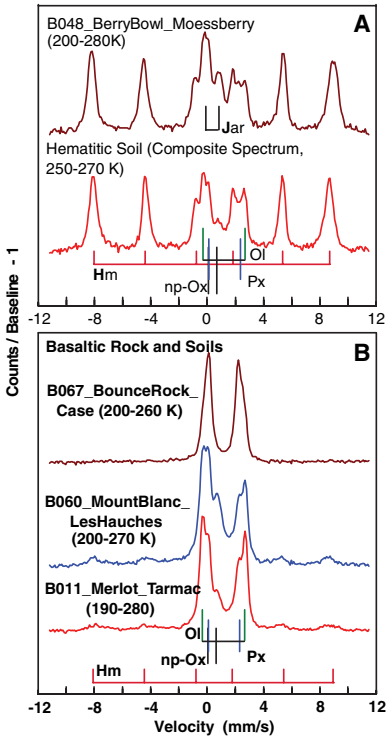

Fig. 2. Representative Mössbauer spectra of basaltic and hematite-rich materials. (**A**) Spectra of spherules and hematitic soils are dominated by the hematite sextet with minor Fe^{2+} doublets (olivine and minor pyroxene) and sometimes a Fe^{3+} doublet (jarosite). (**B**) Spectra of basaltic soils are characterized by two Fe^{2+} doublets (olivine and pyroxene), a Fe^{3+} doublet (np-Ox), and a magnetic sextet (hematite), and the spectrum of Bounce rock is characterized by Fe^{2+} doublets.

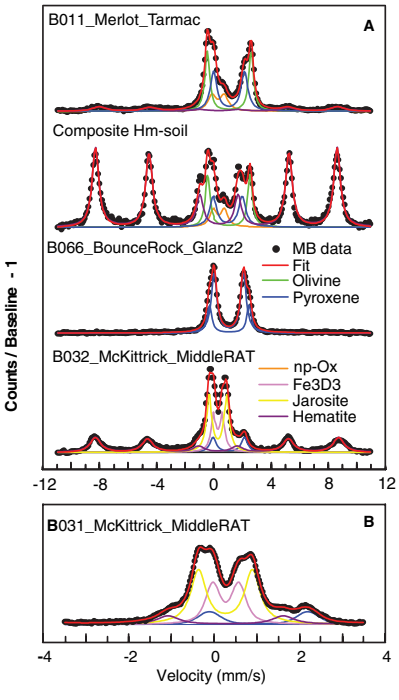

Fig. 3. Results of the fitting procedure for representative Mössbauer spectra from Meridiani Planum. (**A**) Full-velocity spectra for basaltic soil B011_Merlot_Tarmac, sum of hematitic soils, B066_BounceRock_Glanz2, and B032_McKittrick_MiddleRAT. (**B**) Reduced-velocity spectrum for B031_McKittrick_MiddleRAT.

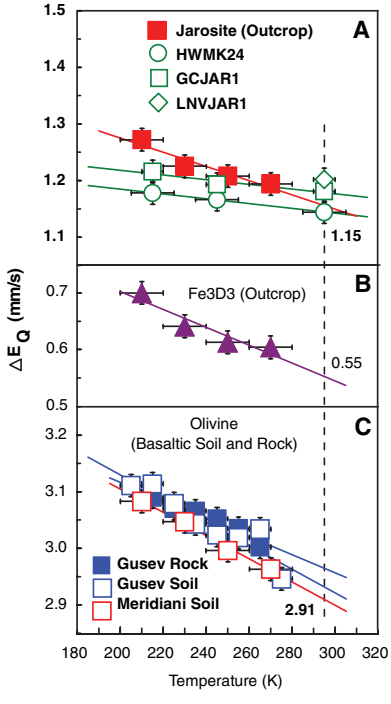

Fig. 4. Quadrupole splitting ΔE_Q with temperature for (**A**) jarosite from the outcrop; (**B**) unidentified Fe^{3+} phase (Fe3D3) from the Eagle crater outcrop; and (**C**) olivine from basaltic soil, rock from Gusev crater (*6*), and basaltic soil from Eagle crater. To maximize counting statistics, we summed spectra from corresponding temperature intervals of equivalent spectra before calculating ΔE_Q. Shown for comparison in (A) are results for naturally occurring jarosite samples (*29*, *31*) that were obtained with a flight-spare MIMOS II spectrometer. The solid lines are linear least squares fits, and the numbers are the values of ΔE_Q at room temperature. Preliminary results indicate both Meridiani and Gusev olivine have an intermediate composition (~Fo_{60}).

that the chemical composition of martian jarosite is not known (such as the relative distribution of K and Na and the degree of Al substitution and possibly other impurities), the agreement between martian and terrestrial data is good.

Outcrop Mössbauer spectra are characterized by four additional components (Table 1). One is a second doublet from oct-Fe^{3+} that has a lower quadrupole splitting (ΔE_Q ~ 0.64 mm/s) compared with that of jarosite (Fig. 1B). Doublets having this magnitude of splitting are not mineral-specific and could result, either singly or in combination, from a variety of phases including superparamagnetic hematite and goethite (α-FeOOH), lepidocrocite (γ-FeOOH), akaganeite (β-FeOOH), schwertmannite [~$Fe_{16}O_{16}(OH)_{12}(SO_4)_2 \cdot nH_2O$], ferrihydrite (~$Fe_2O_3 \cdot 9/5H_2O$), and certain phyllosilicates (*32*–*36*). This doublet, which we refer to as Fe3D3, is distinct from the nanophase ferric oxide (np-Ox) doublet (ΔE_Q ~ 0.88 mm/s) that we observed in basaltic Gusev crater soils (*6*) and basaltic Meridiani soils. Two other components are oct-Fe^{2+} doublets. In undisturbed targets like B029_McKittrick_MiddleRAT, these doublets are attributed to olivine and pyroxene in basaltic sand that contaminate outcrop surfaces. Because their intensity is low and their overlap with other peaks is substantial, the peak centers and widths for the two oct-Fe^{2+} doublets were constrained to the values for pyroxene and olivine in the basaltic soils. For other outcrop targets, in particular those where surface contamination was removed by grinding, the oct-Fe^{2+} doublet associated with olivine was not detected (Table 2). This implies that the remaining oct-Fe^{2+} doublet may be intrinsic to the outcrop matrix. Its Mössbauer parameters (Table 1), calculated from a spectrum obtained by summing all outcrop spectra that have no detectable olivine over all temperatures, are within the range for pyroxene, and we provisionally make this assignment. The parameters are the same within error as those for pyroxene in Bounce rock (Table 1). Because pyroxene is a common rock-forming mineral, the correspondence may be a coincidence and is therefore at best a weak constraint for the presence of a Bounce rock component in the outcrop. The fourth component is hematite.

The sextet observed in the spectra of all outcrop matrix targets, the spherule-rich target (B048_BerryBowl_MoessBerry), and the spherule-rich soil targets (Figs. 1 and 2A) is assigned to hematite. The assignment is consistent with the values of the Mössbauer parameters (Table 1) and their variation with temperature. The pattern of change in peak positions with temperature for spectra of outcrop hematite (Fig. 1A) is similar to that for spectra from all hematite-bearing targets. The vertical dashed lines are drawn through the peak maxima for hematite sextet peaks 1, 2, 5, and 6 in the outcrop spectrum from the 260 to 280 K temperature interval. Except for peak 5, whose maximum is at the same velocity, the maxima in the low-temperature spectra (200 to 220 K) are located at lower (peaks 1 and 2) and higher (peak 6) velocities relative to their positions in the

Table 1. Mössbauer parameters for individual and combined target spectra of rock and soil from Meridiani Planum. Jar, Jarosite; Fe3D3, unidentified Fe^{3+} phase; Hm, hematite; Ol, olivine; Px, pyroxene; np-Ox, nanophase ferric oxide. Numbers in parenthesis are the larger of the experimental uncertainty or the standard deviation of the average. Phase Px2 calculated from outcrop spectra that contain no detectable olivine. Numbers in brackets were used as constraints in fitting procedures.

Phase	Coordination	Temperature range (K)	δ (mm/s)	ΔE_Q (mm/s)	B_{hf} (T)
		Average outcrop matrix			
Jar	oct-Fe^{3+}	200–280	0.39(2)	1.22(2)	
Fe3D3	oct-Fe^{3+}	200–280	0.39(2)	0.64(4)	
Hm	oct-Fe^{3+}	200–220	0.36(2)	–0.01(2)	53.4(2)
Hm	oct-Fe^{3+}	200–280	0.37(2)	–0.06(4)	52.5(5)
Hm	oct-Fe^{3+}	260–280	0.39(2)	–0.11(2)	51.7(2)
Px2	oct-Fe^{2+}	200–280	1.18(2)	2.21(2)	
Px	oct-Fe^{2+}	200–280	[1.18]	[2.15]	
Ol	oct-Fe^{2+}	200–280	[1.18]	[3.02]	
		B048_BerryBowl_Moessberry			
Jar	oct-Fe^{3+}	200–280	[0.39]	[1.22]	
Fe3D3	oct-Fe^{3+}	200–280	[0.39]	[0.64]	
Px	oct-Fe^{2+}	200–280	[1.18]	[2.15]	
Ol	oct-Fe^{2+}	200–280	[1.18]	[3.02]	
Hm	oct-Fe^{3+}	200–220	0.39(2)	0.00(2)	54.0(2)
Hm	oct-Fe^{3+}	200–280	0.40(2)	–0.07(2)	53.4(2)
Hm	oct-Fe^{3+}	260–280	0.41(2)	–0.12(2)	52.4(2)
		Average hematitic soil			
np-Ox	oct-Fe^{3+}	250–270	[0.40]	[0.85]	
Px	oct-Fe^{2+}	250–270	1.14(2)	2.07(6)	
Ol	oct-Fe^{2+}	250–270	1.17(2)	2.95(6)	
Hm	oct-Fe^{3+}	250–270	0.39(2)	−0.16(2)	52.3(2)
		Average basaltic soil			
np-Ox	oct-Fe^{3+}	200–280	0.40(2)	0.85(4)	
Px	oct-Fe^{2+}	200–280	1.18(2)	2.15(5)	
Ol	oct-Fe^{2+}	200–280	1.18(2)	3.02(5)	
Hm	oct-Fe^{3+}	200–220	[0.39]	[–0.16]	[53.9]
Hm	oct-Fe^{3+}	200–280	[0.38]	[–0.19]	[53.1]
Hm	oct-Fe^{3+}	260–280	[0.38]	[–0.25]	[52.2]
		B023_HematiteSlope_Hema2			
np-Ox	oct-Fe^{3+}	200–280	[0.40]	[0.85]	
Px	oct-Fe^{2+}	200–280	1.16(2)	2.15(2)	
Ol	oct-Fe^{2+}	200–280	1.18(2)	3.01(2)	
Hm	oct-Fe^{3+}	200–220	0.39(2)	–0.16(2)	53.9(2)
Hm	oct-Fe^{3+}	200–280	0.38(2)	–0.19(2)	53.1(2)
Hm	oct-Fe^{3+}	260–280	0.38(2)	–0.25(2)	52.2(2)
		Bounce rock			
Px	oct-Fe^{2+}	200–280	1.18(2)	2.24(3)	
Px(Site-2)	oct-Fe^{2+}	200–280	1.17(2)	2.08(2)	
Px(Site-1)	oct-Fe^{2+}	200–280	1.20(2)	2.79(5)	

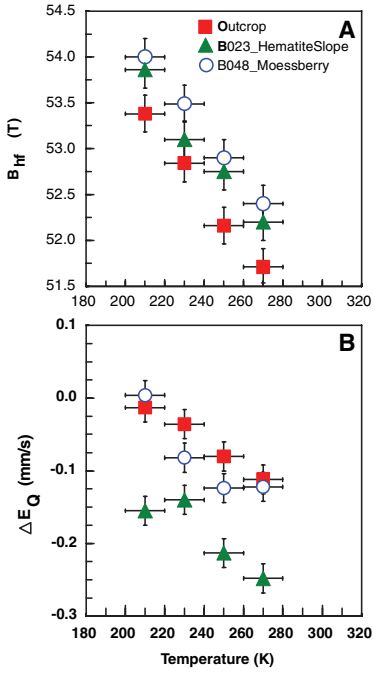

Fig. 5. Plot of (**A**) B_{hf} and (**B**) ΔE_Q as a function of temperature for hematite in the Eagle outcrop composite spectrum and targets B023_HematiteSlope_Hema2 and B048_BerryBowl_Moessberry. The temperature variations are consistent with the hematite Morin transition, which occurs near 260 K in chemically pure, well-crystallized, bulk hematite.

high-temperature spectrum. In particular, peak 6 in the 200 to 220 K spectrum is broader and maximum flatter relative to the same peak in the 260 to 280 K spectrum. This behavior implies that an additional sextet component is present in the low-temperature spectrum that is not apparent in the high-temperature spectrum. This behavior is consistent with the Morin transition of hematite, which occurs near 260 K for chemically pure, well-crystallized, bulk hematite (*37–39*). Many substitutional impurities including Al, poor crystallinity, and small particle diameters lower the temperature of the Morin transition and widen the temperature interval over which it occurs (*37–39*). Qualitatively, comparison of high- and low-temperature spectra implies that the low-temperature spectrum results from a population of hematite particles that includes members that are both above and below the Morin transition at 200 to 220 K. The temperature dependences of ΔE_Q and B_{hf} (Fig. 5), which were calculated from a one-sextet model, are consistent with the variation expected for the Morin transition (i.e., values of ΔE_Q and B_{hf} being more positive with decreasing temperature). The absence of overlap of the temperature dependence of ΔE_Q and B_{hf} for outcrop matrix, spherule, and B023_HematiteSlope targets (Fig. 5) implies that differences are present in the populations of hematite particles for the three targets with respect to hematite purity, crystallinity, and/or particle size.

In addition to hematite, the Mössbauer spectra of the hematitic soils have oct-Fe^{2+} doublets resulting from olivine (ΔE_Q ~ 2.95 mm/s and T = 240 ± 40 K) and pyroxene (ΔE_Q ~ 2.07 mm/s and T = 240 ± 40 K).

The basaltic soils at Meridiani Planum are dominated by two doublets from oct-Fe^{2+} with variable proportions of an oct-Fe^{3+} doublet (Fig. 2B). The spectra for the Meridiani Planum basaltic soils (Fig. 2B) are similar to the spectra for Gusev crater basaltic soils (*6*), and accordingly the doublets with ΔE_Q ~ 3.02, 2.15, and 0.85 mm/s [T = 240 ± 40 K (Table 1)] are assigned to olivine, pyroxene, and np-Ox, respectively. The values and temperature dependence of ΔE_Q for olivine from basaltic soil at Gusev crater and Meridiani Planum are the same within error (Fig. 4C), implying that the olivine at both sites has the same mineralogical composition (~Fo_{60}) (*40*, *41*). In general, the basaltic soils are also characterized by a weak magnetic sextet whose Mössbauer parameters imply hematite. However, because of the width of the sextet lines, we cannot exclude a substantial contribution from nonstoichiometric magnetite as detected at Gusev crater (*6*). Exceptions that have strong hematite sextets are targets B023_HematiteSlope_Hema2 and B062_BlackPatch_Munter; their unusually high hematite content may result from contributions of spherules and/or their fragments.

The spectrum of Bounce rock is the only one of its kind measured to date. The rock has a basaltic chemical composition (*22*), and its Mössbauer spectrum (Fig. 2B) is characterized by two strongly overlapping oct-Fe^{2+} doublets, a pattern characteristic of pyroxene as the only detectable iron-bearing phase (*16–19*). The spectrum is so clean with respect to other iron-bearing components and the counting statistic so good that we were able to obtain Mössbauer parameters for two oct-Fe^{2+} pyroxene sites (Table 1) and measure their temperature dependence (Fig. 6). We also include the parameters for a statistically poorer one-doublet fit for comparison to all other samples, where the pyroxene was modeled with one doublet. The value of ΔE_Q for the basaltic soils [~2.15 ± 0.05 mm/s over the temperature range from 200 to 280 K] is smaller than that for Bounce rock [~2.24 ± 0.03 mm/s over the temperature range from 200 to 280 K], implying that Bounce rock is not an important mineralogical component in Meridiani Planum basaltic soil. The Mössbauer spectrum and parameters and bulk composition (*22*) of Bounce rock are similar to corresponding data for basaltic martian meteorites (*42–45*).

Distribution of iron-bearing rock and soil at Meridiani Planum. The relative component areas for outcrop and Bounce rock targets (Table 2), for basaltic and hematitic soil targets (Table 3), and for targets that are mixtures of those components (Table 3) are used to characterize the spatial distribution of iron-bearing phases and provide constraints on the origin and genesis of those targets. In discussing these data, it is important to remember, for example, that A_{Ol} is the relative concentration of iron associated with olivine and not the actual abundance of olivine. If all the olivine in a target were

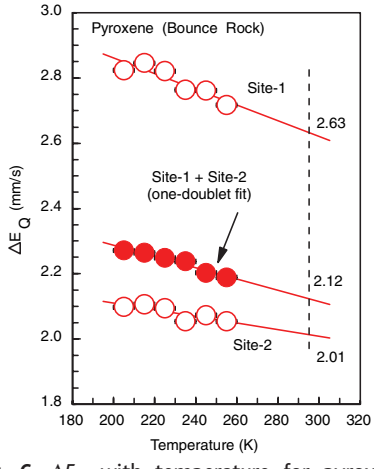

Fig. 6. ΔE_Q with temperature for pyroxene observed in targets on the basaltic rock Bounce rock. Results for both one-doublet and two-doublet models are shown. The two-doublet model gives a statistically better fit. The one-doublet results are used to compare to the results for all other spectra, where pyroxene is modeled with one doublet.

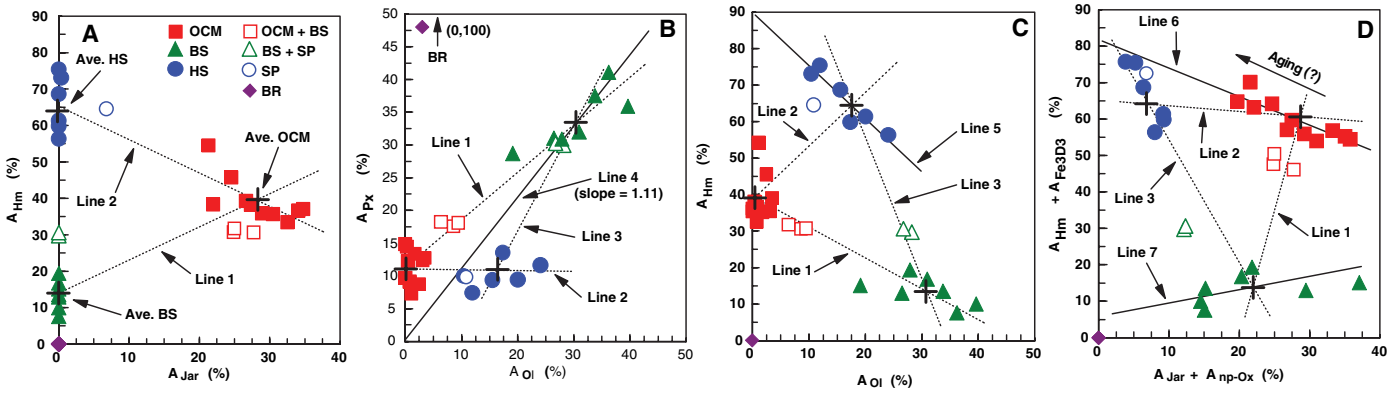

Fig. 7. Plots of (**A**) A_{Hm} versus A_{Jar}, (**B**) A_{Px} versus A_{Ol}, (**C**) A_{Hm} versus A_{Ol}, and (**D**) A_{Hm} plus A_{Fe3D3} versus A_{Jar} plus $A_{np\text{-}Ox}$ for Meridiani Planum rock and soil. Dotted lines 1, 2, and 3 are mixing lines between the average values for mineralogical endmembers. Solid line 4 is the A_{Px}/A_{Ol} ratio for basaltic soil. Solid lines 5, 6, and 7 are linear least squares fits to hematitic soil, outcrop matrix, and basaltic soil, respectively. OCM, outcrop matrix; BS, basaltic soil; SP, spherule; HS, hematitic soil; and BR, Bounce rock.

pure forsterite (iron-free olivine Mg_2SiO_4), the Mössbauer spectrometer would not detect olivine.

The Opportunity Mössbauer analyses suggest four endmember mineralogical groups within Eagle crater, at the rim of Fram crater, and on the intervening plains (Fig. 7): (i) outcrop (matrix plus spherules), (ii) basaltic soil, (iii) hematitic soil, and (iv) Bounce rock. Bounce rock, which is located on the plains between Eagle and Fram craters, is monomineralic pyroxene with respect to iron-bearing phases and is a single-member group. Because pyroxene in the basaltic soils has different Mössbauer parameters, basaltic soil developed from Bounce rock basalt has not been sampled and is presumably not volumetrically important. Bounce rock may be an impact erratic.

Lines 1, 2, and 3 (Fig. 7) are drawn between the average parameter values for the remaining three mineralogical groups. Data for any target that always plot near these mixing lines and between the same two mineralogical endmembers can be considered as mixtures of those two endmembers. Targets that meet these criteria are plotted with open symbols (Fig. 7), and some are known from independent observations by Panoramic Cam-

Table 2. Relative component areas (*A*) and Fe^{3+}/Fe_{total} for iron associated with specific iron-bearing phases for the Eagle crater and Fram crater outcrop and Bounce rock at Meridiani Planum. Example of naming convention: B016_StoneMtn_RobertE refers to the Opportunity sol (*47*) that the Mössbauer experiment ended, feature name, and target name. Undisturbed refers to targets that were not modified before measurement by rover wheels or by brushing or grinding. *A* values include the *f*-factor correction $f(Fe^{3+})/f(Fe^{2+}) = 1.21$. Ol, olivine; Px, pyroxene; np-Ox, nanophase ferric oxide; Jar, jarosite; Fe3D3, unidentified Fe^{3+} component; Hm, hematite. Uncertainty equals ±2% absolute for *A* and ±0.04 for Fe^{3+}/Fe_{total}. Numbers in parenthesis are the standard deviation of the average. Dash entries indicate not applicable.

Target name	Target descriptor	Locale	A_{Ol} (%)	A_{Px} (%)	$A_{np\text{-}Ox}$ (%)	A_{Jar} (%)	A_{Fe3D3} (%)	A_{Hm} (%)	A_{total} (%)	Fe^{3+}/Fe_{total} (%)
					Outcrop matrix					
B016_StoneMtn_RobertE	Undisturbed	Eagle crater	3	13	0	27	18	39	100	0.84
B030_Guadalupe_RATLower	Undisturbed	Eagle crater	2	9	0	25	19	46	100	0.89
B032_McKittrick_MiddleRAT	Post grind	Eagle crater	1	12	0	27	22	38	100	0.87
B035_Guadalupe_King3	Post grind	Eagle crater	1	9	0	36	18	37	100	0.90
B039_LastChance_Makar	Undisturbed	Eagle crater	0	15	0	29	21	35	100	0.85
B045_FlatRock_Mojo2	Post grind	Eagle crater	0	14	0	22	25	38	100	0.85
B046_BerryBowl_Empty	Undisturbed	Eagle crater	2	13	0	31	19	35	100	0.85
B049_RasberryNewton_Filling	Undisturbed	Eagle crater	3	12	0	20	29	35	100	0.84
B051_RealSharksTooth_Enamel1	Undisturbed	Eagle crater	1	7	0	22	16	54	100	0.92
B085_Baseball_Infield	Undisturbed	Fram crater	1	9	0	33	24	33	100	0.90
B088_Pilbara_Golf	Post grind	Fram crater	0	10	0	35	19	36	100	0.90
Average outcrop matrix	–	–	1(1)	11(2)	0	28(5)	21(4)	39(6)	100	0.88(2)
					Bounce rock					
B066_BounceRock_Glanz2	Undisturbed	Plains	0	100	0	0	0	0	100	0.00
B067_BounceRock_Case	Post grind	Plains	0	100	0	0	0	0	100	0.00
B068_BounceRock_Fips2	Undisturbed	Plains	0	100	0	0	0	0	100	0.00
B070_RedHerring_Maggie	Undisturbed	Plains	0	100	0	0	0	0	100	0.00

Table 3. *A* values and Fe^{3+}/Fe_{total} for iron associated with specific iron-bearing phases for basaltic and hematitic soil at Meridiani Planum. See Table 2 caption for more information.

Target name	Target descriptor	Locale	A_{Ol} (%)	A_{Px} (%)	$A_{np\text{-}Ox}$ (%)	A_{Jar} (%)	A_{Fe3D3} (%)	A_{Hm} (%)	A_{total} (%)	Fe^{3+}/Fe_{total} (%)
					Basaltic soil					
B011_Merlot_Tarmac	Undisturbed	Eagle crater	40	36	14	0	0	10	100	0.25
B025_BigDig_HemaTrench1	Trench	Eagle crater	19	29	37	0	0	15	100	0.52
B026_BigDig_HemaTrenchWall2	Trench	Eagle crater	31	32	20	0	0	17	100	0.37
B038_FineSoil_Paydirt	Undisturbed	Eagle crater	36	41	15	0	0	8	100	0.23
B060_MontBlanc_LesHauches	Undisturbed	Eagle crater	26	31	29	0	0	13	100	0.42
B078_DogPark_JeffsChoice	Trench	Plains	34	37	15	0	0	14	100	0.29
B090_PhotoTIDD_Nougat	Disturbed	Plains	28	31	22	0	0	19	100	0.41
Average basaltic soil	–	–	30(6)	33(4)	20(9)	0	0	17(8)	100	0.37(9)
					Hematitic soil					
B052_Goal5WorkVolume_Panaluu	Undisturbed	Eagle crater	10	10	7	0	0	73	100	0.80
B063_WhiteStreak_Cleo3	Undisturbed	Plains	17	14	9	0	0	60	100	0.69
B073_Seas_AegeanCrest	Undisturbed	Plains	12	7	5	0	0	75	100	0.81
B080_DogPark_JackRussell	Undisturbed	Plains	24	12	8	0	0	56	100	0.64
B084_Nullarbor_GreatSandy	Undisturbed	Plains	16	9	6	0	0	69	100	0.75
B091_PhotoTIDD_FredRipple	Undisturbed	Plains	20	9	9	0	0	61	100	0.71
Average hematitic soil	–	–	17(5)	10(2)	7(2)	0	0	66(8)	100	0.73(6)
					Mixtures					
B029_McKittrick_MiddleRAT	Undisturbed	Eagle crater	9	18	0	25	17	31	100	0.72
B041_Dells_HiHo	Undisturbed	Eagle crater	9	18	0	28	16	31	100	0.74
B043_FlatRock_Mojo2	Undisturbed	Eagle crater	6	18	0	25	19	32	100	0.75
B048_BerryBowl_MoessBerry§	Undisturbed	Eagle crater	10	11	0	6	8	64	100	0.79
B023_HematiteSlope_Hema2	Undisturbed	Eagle crater	28	30	12	0	0	30	100	0.42
B062_BlackPatch_Munter	Undisturbed	Plains	27	30	12	0	0	31	100	0.43

era and/or MI to be mixtures. The three targets B029_McKittrick_MiddleRAT, B041_Dells_HiHo, and B043_FlatRock_Mojo2 (labeled as "OCM + BS" in Fig. 7) are outcrop with thin or discontinuous surface coatings of basaltic soil and dust and plot near line 1. Similarly, the target B048_Berry-Bowl_Moessberry is whole spherules on top of outcrop matrix and basaltic sand (line 2). The two soils B023_HematiteSlope_Hema2 and B062_BlackPatch_Munter are mixtures of basaltic and hematitic soils (line 3).

The basaltic soils, which are distributed throughout the landing site, contain olivine and pyroxene in the ratio $A_{Ol}/(A_{Ol} + A_{Px}) = 0.45 \pm 0.03$ (line 4, $A_{Px}/A_{Ol} = 1.11$, in Fig. 7B), which is comparable to the value of that ratio (0.5) reported for basaltic soil at Gusev crater (*6*). The outcrop matrix, hematitic soils, and spherules (B048_Berrybowl_MoessBerry) all have $A_{Px} \sim 10\%$ (Fig. 7B). The spherules and hematitic soil, which is composed mainly of whole and fragmented spherules (*14*), are enriched in olivine [average hematitic soil $A_{Ol} = 17 \pm 5\%$] relative to outcrop matrix [average $A_{Ol} = 1 \pm 1\%$]. Our data cannot distinguish whether the olivine and hematite physically occur together in the same particle or whether there are separate populations of hematite-rich and olivine-rich particles. The latter is more reasonable if the spherules are interpreted as concretions (*13*). The hematitic soils are not binary mixtures of hematite and the basaltic soils, because the value of $A_{Ol}/(A_{Ol} + A_{Px})$ for hematitic soils is 0.61 ± 0.07 compared with 0.45 ± 0.03 for basaltic soils.

Line 5 (Fig. 7C) is a linear least squares fit for the hematitic soils. Extrapolation to $A_{Ol} = 0$ suggests that there may be hematitic soils where ~90% of the total iron is present as hematite. The hematitic soils [average $A_{Hm} = 66 \pm 8\%$ compared with $17 \pm 8\%$ for basaltic soils], which occur at ripple crests (*14*), are probably the origin of the hematite spectral signature observed from martian orbit by the Mars Global Surveyor TES (*2*, *3*).

The data shown in Fig. 7C suggest that the outcrop matrix has a lower proportion of its iron present as hematite compared to the hematitic soils. The difference is greatly reduced if the unidentified doublet in the Mössbauer spectrum of the outcrop (Fe3D3) is superparamagnetic (nanophase) hematite (Fig. 7D). Line 6 (Fig. 7D), which is a linear least squares fit of outcrop data, suggests either that natural variations in outcrop formation processes produced different hematite-to-jarosite ratios in the outcrop matrix or that the outcrop has undergone postformational neomineralization (aging) to form hematite.

Line 1 (Fig. 7, B and C) could imply that the mineralogical variation within the group of basaltic soils results from physical mixtures in different proportions of average outcrop matrix. This is not the case, because jarosite is not detected in the basaltic soils (Table 3) and because the mineralogical variation within the basaltic soil group (Fig. 7D, line 7) is not on a mixing line with average outcrop matrix. Mineralogical variations within the basaltic soil group result from variable proportions of np-Ox (Table 3). The two basaltic soils B025_BigDig_HemaTrench1 and B060_Mont-Blanc_LesHauches may be deposits of aeolian dust, because they are fine-grained and contain the highest proportion of the ferric alteration product np-Ox (*6*, *14*).

Implication for aqueous processes on Mars. Jarosite, which was identified by the Mössbauer instrument on the MER Opportunity rover and whose presence is consistent with the observations of the other MER instruments, has the equivalent of ~10 weight % (wt %) H_2O present in its structure as the OH anion. The mineral is thus mineralogical evidence for the presence of water on Mars and for aqueous acid sulfate processes under oxidizing conditions that lead to jarosite precipitation in the distant past. With use of average outcrop values of $A_{Jar} = 28\%$ (Table 2) and $[Fe_2O_3] = 18.3$ wt % (*22*), we calculate that average outcrop matrix has ~2 wt % H_2O contained within the jarosite alone. The alteration of basaltic material under acid sulfate and oxidizing conditions to form jarosite and other phases could have occurred under a wide range of aqueous conditions provided by, for example, shallow seas (*13*), groundwater (*26*, *27*), and condensation of volcanic emanations (*46*).

References and Notes

1. The term "soil" is used here to denote any loose, unconsolidated materials that can be distinguished from rocks, bedrock, or strongly cohesive sediments. No implication of the presence or absence of organic materials or living matter is intended.
2. P. R. Christensen *et al.*, *J. Geophys. Res* **105**, 9623 (2000).
3. P. R. Christensen, R. V. Morris, M. D. Lane, J. L. Bandfield, M. C. Malin, *J. Geophys. Res.* **106**, 23873 (2001).
4. Golombek *et al.*, *J. Geophys. Res.* **108**, 10.1029/2003JE002074 (2003).
5. Members of the MIMOS II consortium are G. Klingelhöfer, B. Bernhardt, P. A. de Souza Jr., J. Foh, R. Gellert, P. Gütlich, E. Kankeleit, R. V. Morris, F. Renz, D. S. Rodionov, C. Schröder, T. Wdowiak, and A. Yen.
6. R. V. Morris *et al.*, *Science* **305**, 833 (2004).
7. G. Klingelhöfer *et al.*, *J. Geophys. Res.* **108**, 10.1029/2003JE002138 (2003).
8. Velocity calibration was done by using a spectrum of an absorber of metallic iron and hematite that was acquired in transmission geometry simultaneously with surface measurements. The drive error signal (difference between theoretical and actual velocity curves) was measured before and after every integration and was used to correct velocity scale.
9. E. De Grave, A. Van Alboom, *Phys. Chem. Miner.* **18**, 337 (1991).
10. R. V. Morris, D. C. Golden, J. F. Bell III, H. V. Lauer Jr., *J. Geophys. Res.* **100**, 5319 (1995).
11. Names were assigned to areographic features by the MER team for planning and operations purposes. The names are not formally recognized by the International Astronomical Union.
12. S. W. Squyres *et al.*, *Science* **306**, 1698 (2004).
13. S. W. Squyres *et al.*, *Science* **306**, 1709 (2004).
14. L. Soderblom *et al.*, *Science* **306**, 1723 (2004).
15. K. Herkenhoff *et al.*, *Science* **306**, 1727 (2004).
16. R. G. Burns, T. C. Solberg, in *Spectroscopic Characterization of Minerals and Their Surfaces*, L. M. Coyne, S. W. S. McKeever, D. F. Blake, Eds. [American Chemical Society (ACS) Symposium Series no. 415, ACS, Houston, TX, 1990], p. 262.
17. C. McCammon, in *Mineral Physics and Crystallography: A Handbook of Physical Constants*, T. J. Ahrens, Ed., vol. 2 of *AGU Reference Shelf* [American Geophysical Union (AGU), Washington, DC, 1995], p. 332.
18. J. G. Stevens, A. M. Khasanov, J. W. Miller, H. Pollak, Z. Li, *Mössbauer Mineral Handbook* (Biltmore Press, Asheville, NC, 1998).
19. P. A. de Souza Jr., *Lab. Robotics Autom.* **11**, 3 (1999).
20. J. H. Johnson, *Geochim. Cosmochim. Acta* **41**, 539 (1977).
21. A. Z. Hrynkiewicz, J. Kubisz, D. S. Kulgawczuk, *J. Inorg. Nucl. Chem.* **27**, 2513 (1965).
22. R. Rieder *et al.*, *Science* **306**, 1746 (2004).
23. P. R. Christensen *et al.*, *Science* **306**, 1733 (2004).
24. R. G. Burns, *Nature* **320**, 55 (1986).
25. R. G. Burns, *J. Geophys. Res.* **92**, E570 (1987).
26. R. G. Burns, *Proc. Lunar Planet. Sci. Conf.* **18**, 713 (1988).
27. R. G. Burns, D. S. Fisher, *J. Geophys. Res.* **95**, 14415 (1990).
28. R. G. Burns, *Geochim. Cosmochim. Acta* **57**, 4555 (1993).
29. R. V. Morris, D. W. Ming, D. C. Golden, J. F. Bell III, in *Mineral Spectroscopy: A Tribute to Roger G. Burns*, M. D. Dyar, C. McCammon, M. W. Schaefer, Eds. (Special Publication No. 5, Geochemical Society, Houston, TX, 1996), p. 327.
30. J. L. Bishop, H. Froschl, R. L. Mancinelli, *J. Geophys. Res.* **103**, 31457 (1998).
31. R. V. Morris *et al.*, *J. Geophys. Res.* **105**, 1757 (2000).
32. R. V. Morris *et al.*, *J. Geophys. Res.* **94**, 2760 (1989).
33. J. L. Bishop, E. Murad, in *Mineral Spectroscopy: A Tribute to Roger G. Burns*, M. D. Dyar, C. McCammon, M. W. Schaefer, Eds. (Special Publication No. 5, Geochemical Society, Houston, TX, 1996), p. 337.
34. R. V. Morris *et al.*, *J. Geophys. Res.* **105**, 1757 (2000).
35. D. M. Sherman, N. Vero, *Am. Mineral.* **73**, 1346 (1988).
36. E. Murad, U. Wagner, *Clay Miner.* **29**, 1 (1994).
37. E. Murad, J. H. Johnson, in *Mössbauer Spectroscopy Applied to Inorganic Chemistry*, G. J. Long, Ed. (Plenum, New York, 1987), p. 507.
38. E. De Grave, R. E. Vandenberghe, *Phys. Chem. Miner.* **17**, 344 (1990).
39. M.-Z. Dang, D. G. Rancourt, J. E. Dutrizak, G. Lamarche, P. Provencher, *Hyperfine Interactions* **117**, 271 (1998).
40. Percentage molar ratio of Mg/(Mg + Fe) in the forsterite (Fo_{100})-fayalite (Fo_{00}) series.
41. O. N. Menzies, P. A. Bland, F. J. Berry, *Lunar and Planet. Sci.* **XXXII**, abstr. 1622 (2001).
42. M. D. Dyar, *Meteorit. Planet. Sci.* **38**, 1 (2003).
43. D. Rodionov *et al.*, *Meteorit. Planet. Sci.* **39** (suppl.), A91 (2004).
44. J. Zipfel *et al.*, *Meteorit. Planet. Sci.* **39** (suppl.), A118 (2004).
45. L. Vistisen, D. Petersen, M. B. Madsen, *Phys. Scr.* **46**, 94 (1992).
46. M. Settle, *J. Geophys. Res.* **84**, 8343 (1979).
47. A martian solar day has a mean period of 24 hours 39 min 35.244 s and is referred to as a sol to distinguish this from a ~3% shorter solar day on Earth.

48. Development and realization for MIMOS II was funded by the German Space Agency under contract 50QM 99022. The project has been supported by the Technical University of Darmstadt and the University of Mainz. P.A.deS. acknowledges support of Coordenação de Aperfeiçoamento de Pessoal de Nível Superior (CAPES) (contract PASJ 142/1999) and CVRD from Brazil. R.V.M. and D.W.M. acknowledge support of the NASA MER Project and NASA Johnson Space Center. The support of the Russian space agency is acknowledged. We acknowledge the unwavering support of Jet Propulsion Laboratory engineering and operations staff.

30 August 2004; accepted 25 October 2004

REPORT

Chemistry of Rocks and Soils at Meridiani Planum from the Alpha Particle X-ray Spectrometer

R. Rieder,[1]* R. Gellert,[1,2] R. C. Anderson,[3] J. Brückner,[1] B. C. Clark,[4] G. Dreibus,[1] T. Economou,[5] G. Klingelhöfer,[2] G. W. Lugmair,[1] D. W. Ming,[6] S. W. Squyres,[7] C. d'Uston,[8] H. Wänke,[1] A. Yen,[3] J. Zipfel[1]

The Alpha Particle X-ray Spectrometer on the Opportunity rover determined major and minor elements of soils and rocks in Meridiani Planum. Chemical compositions differentiate between basaltic rocks, evaporite-rich rocks, basaltic soils, and hematite-rich soils. Although soils are compositionally similar to those at previous landing sites, differences in iron and some minor element concentrations signify the addition of local components. Rocky outcrops are rich in sulfur and variably enriched in bromine relative to chlorine. The interaction with water in the past is indicated by the chemical features in rocks and soils at this site.

Opportunity landed on Mars at Meridiani Planum on 25 January 2004 coordinated universal time (UTC). The landing site was selected because in this region orbital instruments had identified hematite (*1*), a mineral possibly indicative of the past presence of water on Mars. Opportunity came to rest within a small crater, named Eagle crater (*2*), surrounded by intriguing outcrops (*3*).

The Alpha Particle X-ray Spectrometer (APXS) (*4*) measured the composition of soils (*5*) and rocks. Results obtained during the first 90 sols (*6*) are presented in Tables 1 and 2. These data were obtained under low-temperature conditions, yielding a resolution of <165 eV at 5.9 keV, and were collected when measurement times were adequate for good counting statistics. As a rule, these data were taken during the early morning hours, typically between 4:00 and 9:00 local solar time. Several sites have only been measured in the so-called "touch-and-go" mode (*3*) at elevated temperatures and with short measurement durations. Because of the low quality of these data, only two of these outcrop surfaces are included in the tables.

The first measurement with the APXS was performed on a stretch of soil named Tarmac within the base of Eagle crater. Its composition (Table 1) is similar to soils measured by the Spirit rover at Gusev crater and to soils analyzed by Pathfinder at the mouth of Ares Vallis (*7*). Except for Fe, major elements in Meridiani soils differ only slightly from soils at other landing sites. Larger differences exist for some minor elements—such as Na, Ti, Cr, Mn, and Ni—suggesting that there has been some admixture of debris from local rocks at Meridiani Planum to an otherwise globally homogenized soil (Fig. 1). Specifically, Fe, Ni, and Cr concentrations are higher in Meridiani soils than in Gusev soil. Larger variations of Fe are likely due to variable amounts of hematite-rich spherules, also found at Meridiani Planum.

On sol 15, without any brushing or grinding (surface as is), the APXS was placed against a rocky outcrop called Stone Mountain, located near the base of the Eagle crater wall. The analysis of this area showed a sulfur concentration of 7.7 weight % (wt %) (or 19.2 wt % SO_3) (Fig. 2), much higher than observed on Mars before. However, a corresponding increase in Cl, which is typical for all soils (*7*–*9*), was not observed in this outcrop. During the next weeks, several measurements were per-

[1]Max-Planck-Institut für Chemie, J. J. Becher-Weg 27, D-55128 Mainz, Germany. [2]Institut für Anorganische und Analytische Chemie, J. Gutenberg-Universität, D-55128 Mainz, Germany. [3]Jet Propulsion Laboratory, Pasadena, CA 911091, USA. [4]Lockheed Martin Corporation, Littleton, CO 80127, USA. [5]Laboratory for Astrophysics and Space Research, Enrico Fermi Institute, Chicago, IL 60637, USA. [6]Johnson Space Center, Houston, TX 77058, USA. [7]Center for Radiophysics and Space Research, Cornell University, Ithaca, NY 14853, USA. [8]Centre d'Etude Spatiale des Rayonnements, F-31028 Toulouse, France.

*To whom correspondence should be addressed. E-mail: rieder@mpch-mainz.mpg.de

Table 1. Chemical composition of soils at Meridiani Planum, in weight percent (*21*). Abs. stat. error, absolute statistical error, which is a 2σ error for a typical measurement of 4 hours duration. This number can also be considered as detection limit.

Feature		First soil	Hematite slope	Big Dig		Mont Blanc	DogPark		PHOTIDO Plains
Target	Abs. stat. error	Tarmac	Hema2	Hema trench1	Hema trenchwall2	Les Hauches	Jack Russell	Beagle Burrow	Nougat
Note		Surface	Surface	Floor	Side wall	Surface	Surface	Floor	Plains, scuff disturbed
Na_2O	0.3	1.4	1.6	1.5	1.5	1.7	1.6	1.7	1.8
MgO	0.2	7.2	7.0	7.0	7.0	7.2	6.4	7.2	7.4
Al_2O_3	0.2	8.8	8.1	8.7	8.6	8.8	7.2	9.4	8.8
SiO_2	0.4	45.5	41.9	45.0	44.3	44.7	37.8	46.3	45.0
P_2O_5	0.04	0.82	0.83	0.83	0.78	0.94	0.75	0.79	0.89
SO_3	0.05	4.93	4.68	6.92	5.62	7.29	4.79	4.52	5.77
Cl	0.03	0.43	0.46	0.47	0.40	0.54	0.46	0.33	0.41
K_2O	0.1	0.48	0.43	0.49	0.45	0.48	0.37	0.40	0.45
CaO	0.05	7.52	6.27	6.90	6.88	6.82	5.15	6.94	6.90
TiO_2	0.05	1.09	0.83	1.17	1.30	1.07	0.70	1.29	1.15
Cr_2O_3	0.02	0.52	0.37	0.45	0.52	0.37	0.36	0.54	0.51
MnO	0.02	0.40	0.32	0.38	0.38	0.37	0.28	0.38	0.40
FeO	0.2	20.1	26.5	19.1	21.3	19.0	33.4	19.3	19.9
Ni ppm	40	640	820	800	840	640	1090	750	590
Zn ppm	40	280	350	490	400	470	340	290	370
Br ppm	30	30	30	190	160	20	30	40	290

formed on various outcrops. Typically, the same spot was analyzed before (surface as is) and after application of the Rock Abrasion Tool (RAT) (*10*). At a location referred to as McKittrick on the outcrop El Capitan, the observed S concentration increased from 5.1 wt % in the as-is analysis to 8.4 wt % (or 21 wt % SO_3) in the RAT analysis (Fig. 2 and Table 2). An increase in S after surface removal was a common observation on these outcrops.

Analyses before and after abrading of McKittrick showed Br concentrations of 270 and 430 parts per million (ppm), respectively. When compared with the observed Cl concentrations, these concentrations are unusually high, because in most martian meteorites the Cl/Br ratio is close to the ratio in carbonaceous chondrite type 1 (CI) of 270 (*11*) (Fig. 3). Thus, the ratio of 9.1 in the McKittrick RAT measurement corresponds to an enrichment of Br over Cl relative to CI chondrite by a factor of 30. Another analysis area, called Guadalupe, about 20 cm higher on the El Capitan outcrop, was even richer in S than McKittrick but did not exhibit any detectable enrichment of Br relative to Cl (Figs. 2 and 3).

The wheels of Opportunity were used to excavate a trench in the soil. A difference in chemical composition, especially of Fe and Br, was observed between a location on undisturbed soil (Hematite Slope) and two locations inside the trench Big Dig, one on the wall and one on the floor (Table 1 and Fig. 2). Although the concentration of Br in the undisturbed soil was at the detection limit of the APXS (about 30 ppm), it was detectable on the wall and the floor of the trench Big Dig (Fig. 3) with Br enrichment factors of about 11 relative to the Cl/Br ratio of CI chondrites.

The landing site is covered with spherical grains nicknamed blueberries. APXS analyses were made on an outcrop called Berry Bowl. One half of this rock had a flat surface (Berry Bowl empty), and the other showed a depression filled with a large number of spherules (Berry Bowl full, see Table 2 and Fig. 2). Berry Bowl empty revealed concentrations similar to the outcrop McKittrick before grinding (McKittrick as is in Fig. 2) with a high SO_3 content of 14.0 wt %. The APXS analysis of Berry Bowl full shows an unusually high Fe content of 24.1 wt % (31.0 wt % FeO equivalent) and a low SO_3 content of 5.5 wt %, which is similar to the soil on Hematite Slope (Fig. 2). However, part of the spectrum originated from the Berry Bowl outcrop material and a detritus of dark sand (possibly basaltic grains) because the spherules do not completely fill the area of the bowl. The Fe/Mn ratios of Berry Bowl full (Fe/Mn = 107) and of the soil on Hematite Slope (Fe/Mn = 82) are higher than the ratios measured in

Table 2. Chemical composition of rocks at Meridiani Planum, in weight percent (*21*). Abs. stat. error, absolute statistical error, which is a 2σ error for a typical measurement of 4 hours duration. ND, not detected.

Feature		Stone Mountain	McKittrick		Guadalupe		Last Chance	Dells	Flat rock		Berry Bowl		Real Sharks Tooth	Bounce rock				Pilbara
Target	Abs. stat. error	Robert E.	middleRAT		Guadalupe RAT	King3	Makar	Hi-Ho	Mojo2		Rubel	Empty	Enamel 1	Glanz 2	Case	RedHerring Maggie		Golf
Note		As is*	As is	RAT	As is	RAT	As is	As is*	As is	RAT	As is, full	As is, empty	As is	As is	RAT	As is	RAT	
Na_2O	0.3	1.1	1.7	1.1	1.3	1.0	1.5	1.8	1.7	1.2	1.7	1.6	1.6	1.5	1.3	1.7	1.1	
MgO	0.2	7.9	7.7	7.4	7.4	7.8	7.1	7.6	7.3	7.8	6.4	7.4	7.6	6.1	6.4	7.2	8.0	
Al_2O_3	0.2	7.2	8.1	6.0	7.0	5.7	6.8	8.4	8.1	6.0	7.6	7.8	6.7	9.3	10.1	10.3	5.6	
SiO_2	0.4	39.5	42.7	38.1	40.1	36.3	38.1	43.5	42.7	36.2	38.9	42.4	38.1	47.7	50.8	47.0	34.7	
P_2O_5	0.04	0.99	1.01	1.00	1.04	0.99	1.03	1.04	1.02	1.03	0.78	1.00	1.02	1.00	0.95	0.92	0.98	
SO_3	0.3	19.2	12.7	21.0	18.6	24.6	18.7	11.4	12.9	23.3	5.50	14.0	18.5	3.59	0.52	4.61	24.7	
Cl	0.03	0.54	0.60	0.39	0.59	0.33	0.61	0.59	0.59	0.36	0.49	0.68	0.57	0.38	0.06	0.66	0.44	
K_2O	0.1	0.58	0.54	0.56	0.58	0.54	0.56	0.56	0.57	0.59	0.38	0.57	0.52	0.26	0.10	0.29	0.50	
CaO	0.05	5.11	5.92	4.49	5.02	5.02	4.95	5.87	6.17	5.28	5.34	5.65	4.46	11.3	12.5	10.2	4.90	
TiO_2	0.05	0.75	0.91	0.85	0.88	0.67	0.72	0.94	0.92	0.77	0.73	0.88	0.71	0.89	0.78	0.74	0.78	
Cr_2O_3	0.02	0.20	0.29	0.22	0.20	0.19	0.19	0.36	0.26	0.23	0.32	0.22	0.19	0.14	0.12	0.14	0.23	
MnO	0.02	0.26	0.32	0.32	0.31	0.32	0.30	0.35	0.31	0.27	0.29	0.36	0.25	0.46	0.43	0.40	0.37	
FeO	0.2	16.0	16.9	17.6	16.2	15.8	18.6	16.9	16.8	16.3	31.0	16.8	19.0	16.7	15.6	15.4	16.7	
Ni ppm	40	780	710	880	810	690	800	720	760	790	950	730	770	350	180	260	750	
Zn ppm	40	670	340	320	430	370	440	330	480	490	380	490	440	100	50	180	580	
Br ppm	30	ND	270	430	50	30	30	440	110	120	40	120	120	30	30	30	30	

*Errors are higher by a factor of 2 because of short measurement time at elevated temperature.

other soils and outcrops (Fe/Mn ~ 50). Because Mn^{2+} has chemical characteristics similar to Fe^{2+}, a high Fe/Mn ratio can result from the presence of oxidized Fe^{3+}-bearing minerals. Mössbauer spectra of the spherules indicate that hematite (Fe_2O_3) is the major Fe-bearing mineral (*12*). Because the high Fe/Mn ratios are present only in undisturbed hematite-rich soils (Fe/Mn ~ 80 to 120) overlain with spherules but are absent in the excavated trench (Fe/Mn ~ 50), where spherules are rare, the APXS results support the findings from other instruments (*3*) that the spherules are the carrier of hematite.

Except for Fe, S, and Br, the soils and outcrops show similar chemical compositions (Figs. 1 and 2). However, because of a difference in the Fe^{2+} and Fe^{3+} concentrations, the Mössbauer results (*12*) indicate a different mineralogy between hematite-free soils (high Fe^{2+}) and outcrops (high Fe^{3+}). On the basis of the similar Fe/Mn ratios in rocks and these soils, the difference in mineralogy can be explained by an isochemical change resulting from a change in the oxidation state of iron.

The compositional variations between soils and outcrops reflect the enrichment of S in the outcrops. However, the Mg/Si, K/Si, and P/Si ratios increase with increasing S concentrations, whereas Cr/Si decreases (Fig. 4). Overall, therefore, the chemical evidence suggests the deposition of sulfate salts such as $MgSO_4$. Hydrated Mg sulfates have been assumed (*13*) to explain low-latitude hydrogen-rich deposits on Mars. In addition, all K can be attributed to Jarosite (*12*). The enrichment of P points toward the presence of soluble phosphates.

Although more detailed studies would be necessary to unravel the origin of the outcrop rocks, with the available data we visualize the following scenario: Water, containing sulfuric (and hydrochloric) acid derived from volcanic exhalations reacted with rocky material to form brines. According to (*14*), such brines could even exist today. Olivine dissolved readily under these acidic and oxidizing conditions and Mg and Fe sulfates and also silica would have been formed. In contrast to olivine, pyroxene and feldspar dissolved to a much lesser extent. Because Cr is low in olivine, it is also low in the outcrops. Phosphates dissolved even more easily as reflected by the high P content of the outcrops (Fig. 4). Hence, we would expect high concentrations of large-ion lithophile elements such as U, Th, and the rare earth elements. Thus, in general, elements mainly occurring in soluble phases should be enriched and elements mainly contained in insoluble phases should be depleted in the outcrops relative to soil (Fig. 4). Because of evaporation, the brines gradually became richer in sulfates that eventually started to precipitate.

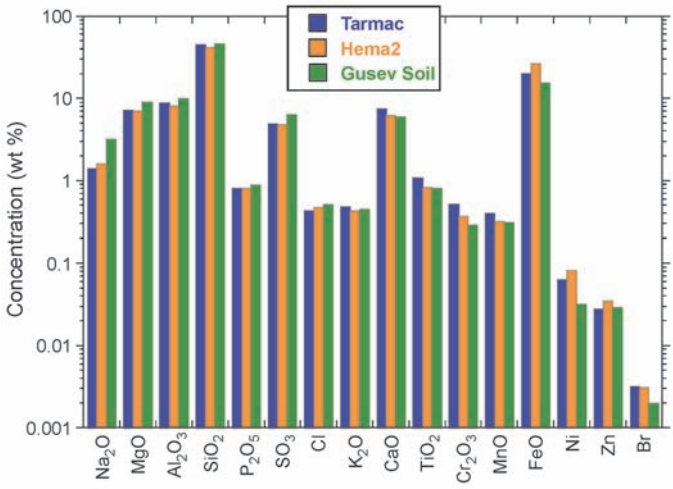

Fig. 1. Chemical composition of martian soils in Meridani Planum, compared with a Gusev crater soil (*7*).

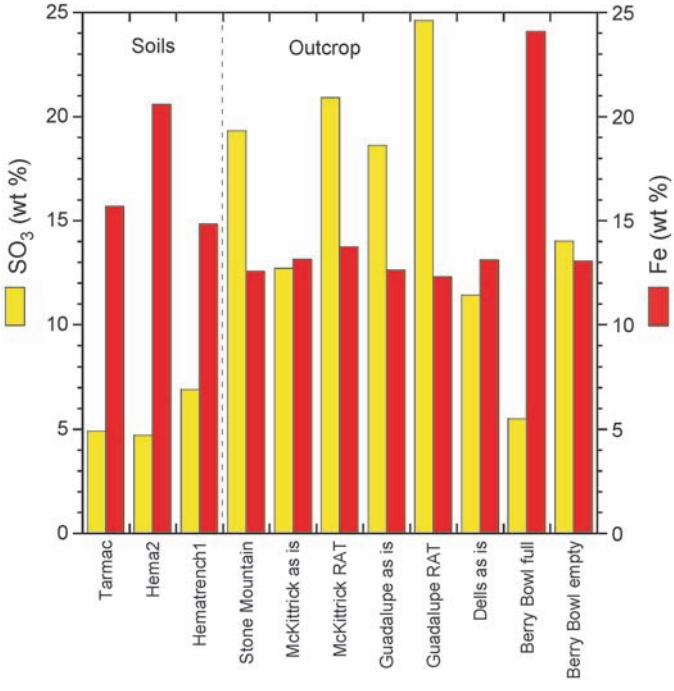

Fig. 2. Sulfate (yellow) and iron (red) concentrations in soils, spherules, and outcrops in Meridiani Planum.

Sulfur and Cl are decoupled in outcrop rocks, which can be explained by the higher solubility of chlorides in brines. The most soluble components, the rare bromides, became enriched in residual brines. Evaporitic materials were intermingled during the deposition process with possibly airborne siliciclastic materials (*3*) to produce the bulk chemistry observed by the APXS. This set of events, alternating with accumulation of fresh windblown soil, occurred in episodes over an extended period of time, explaining the large-scale multiple layering observed in these rocks.

The chemical processes described above are not limited to the small Eagle crater where Opportunity landed. A few hundred meters away from Eagle crater, in a smaller crater called Fram, the rock Pilbara was abraded with the RAT and analyzed with the APXS. It has a composition similar to the outcrop Guadalupe in Eagle crater (Table 2).

After leaving Eagle crater, Opportunity examined a nearby rock, named Bounce rock, with a textural appearance different from the outcrops in Eagle crater. Two areas on the untreated rock surface and one area that had been abraded with the RAT were analyzed by all Athena instruments (*15*). The APXS analyses show that Bounce rock has a chemical composition of basaltic rocks more evolved than Humphrey, a primitive basaltic rock typical of rocks found in Gusev crater (*7*, *16*). It is characterized by high P_2O_5 of 0.95 wt %, a S concentration of 0.2 wt %, an Fe/Mn ratio of 36 [consistent with that

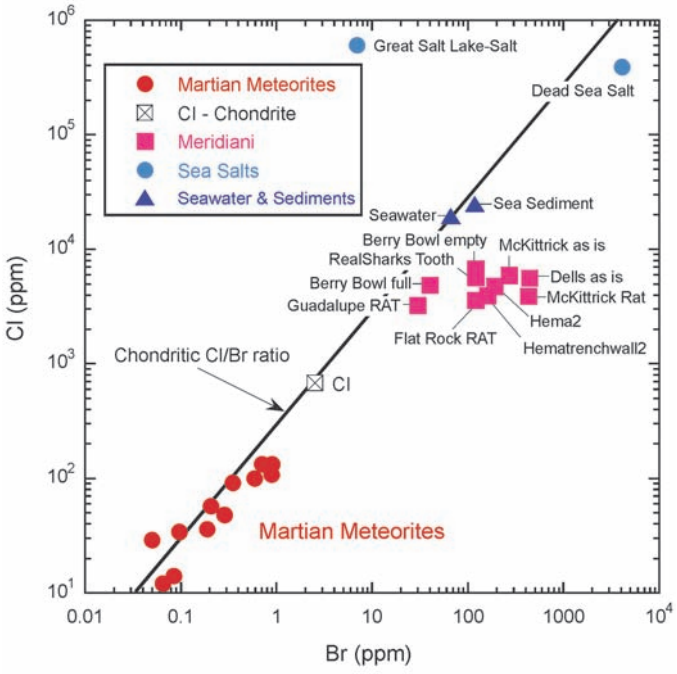

Fig. 3. Chlorine versus bromine concentrations in samples of Meridiani Planum are compared with martian meteorites (*19*), seawater, and terrestrial salts (*20*).

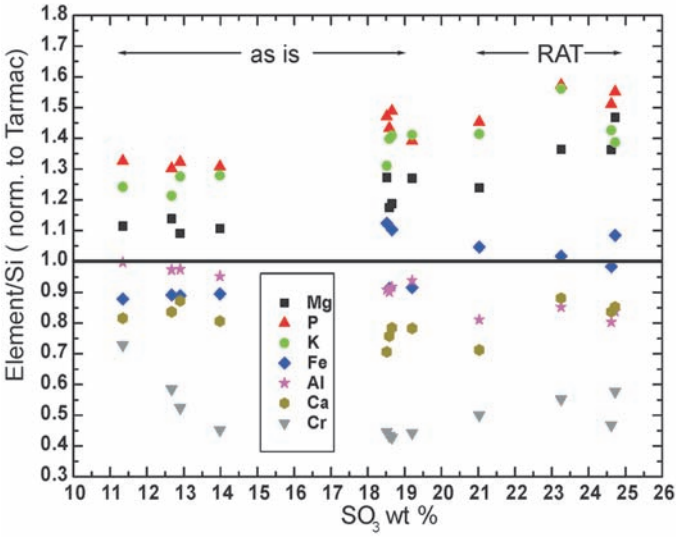

Fig. 4. Element/Si ratios in outcrops (normalized to their ratios in soil Tarmac) versus concentration of SO_3 (equivalent to the relative amount of sulfate salts in the samples). The graph shows all outcrop targets of Table 2 except Berry Bowl full.

of shergottites (*17*) (Fe/Mn = 36 to 44)], a low Mg number [molar MgO/(MgO+FeO)] of 0.42, and a high Ca/Al ratio of 1.7 (*18*). Although variable in shergottites, the Al_2O_3 concentration and Mg number of Bounce rock are identical with lithology B of the shergottite EETA79001 (*19*) within error limits.

Bounce rock, however, has a lower FeO concentration (15.6 wt %) and a higher CaO concentration (12.5 wt %) than those of shergottites. It has a calculated mineral norm that is pyroxene normative: (in wt %) magnetite 0.25, ilmenite 1.4, chromite 0.2, apatite 2.0, albite 12.7, anorthite 22.0, diopside 31.1, and hypersthene 30.5. This is the first instance in which a sample measured on Mars has a chemical composition that is close to a group of meteorites that has long been believed to have originated from Mars.

References and Notes

1. P. R. Christensen *et al.*, *J. Geophys. Res.* **105**, 9623 (2000).
2. Names have been assigned to aerographic features by the Mars Exploration Rover (MER)team for planning and operations purposes. The names are not formally recognized by the International Astronomical Union.
3. S. W. Squyres *et al.*, *Science* **306**, 1698 (2004).
4. R. Rieder *et al.*, *J. Geophys. Res.* **108**, 8066 (2003).
5. The term martian soil is used here to denote any loose unconsolidated materials that can be distinguished from rocks, bedrock, or strongly cohesive sediments. No implication of the presence or absence of organic materials or living matter is intended.
6. A martian solar day has a mean period of 24 hours 39 min 35.244 s and is referred to as a sol to distinguish this from a roughly 3% shorter solar day on Earth.
7. R. Gellert *et al.*, *Science* **305**, 829 (2004).
8. B. C. Clark *et al.*, *J. Geophys. Res.* **87**, 10059 (1982).
9. H. Wänke, J. Brückner, G. Dreibus, R. Rieder, I. Ryabchikov, *Space Sci. Rev.* **96**, 317 (2001).
10. S. P. Gorevan *et al.*, *J. Geophys. Res.* **108**, 1029, 10.1029/2003JE002061 (2003).
11. H. Palme, H. E. Suess, H. D. Zeh, in *Landolt-Börnstein, Group VI: Astronomy and Astrophysics*, K. Schaiffers, H. H. Voigt, Eds. (Springer Verlag, Heidelberg, 1981), vol. 2, pp. 257–272.
12. G. Klingelhöfer *et al.*, *Science* **306**, 1740 (2004).
13. W. C. Feldman *et al.*, *Geophys. Res. Lett.* **31**, L16702 (2004).
14. J. S. Kargel, G. M. Marion, in *Lunar Planet. Sci. XXXV*, abstr. 1965 (Lunar and Planetary Institute, Houston, TX, CD-ROM, 2004).
15. S. W. Squyres *et al.*, *J. Geophys. Res.* **108**, 8062, 10.1029/2003JE002121 (2003).
16. H. Y. McSween *et al.*, *Science* **305**, 842 (2004).
17. Shergottites are a family of meteorites that are believed to originate from Mars.
18. J. Zipfel *et al.*, *Meteorit. Planet. Sci.* **39** (suppl.), A118 (2004).
19. A. Banin, B. C. Clark, H. Wänke, in *Mars*, H. H. Kieffer, B. M. Jakosky, C. W. Snyder, M. S. Matthews, Eds. (Univ. Arizona Press, Tucson, AZ, 1992), pp. 594–625.
20. G. Dreibus, personal communication.
21. The element compositions are normalized to 100% oxides, assuming samples free of water and carbonates, S being present as SO_3 and Fe as FeO. Also, all concentration values are based on an assumed homogeneous matrix (*4*).

22. The APXS was mainly funded by the Max-Planck-Society and, in part, by the German Space Agency (DLR) (grant no. 50QM0014). G.K. and R.G. also acknowledge DLR grant 50QM0005. Funding for Athena science team members was provided by NASA contracts through Cornell and JPL.

23 August 2004; accepted 12 October 2004

REPORT

First Atmospheric Science Results from the Mars Exploration Rovers Mini-TES

Michael D. Smith,[1]* Michael J. Wolff,[2] Mark T. Lemmon,[3] Nicole Spanovich,[4] Don Banfield,[5] Charles J. Budney,[6] R. Todd Clancy,[2] Amitabha Ghosh,[1] Geoffrey A. Landis,[7] Peter Smith,[4] Barbara Whitney,[2] Philip R. Christensen,[8] Steven W. Squyres[5]

Thermal infrared spectra of the martian atmosphere taken by the Miniature Thermal Emission Spectrometer (Mini-TES) were used to determine the atmospheric temperatures in the planetary boundary layer and the column-integrated optical depth of aerosols. Mini-TES observations show the diurnal variation of the martian boundary layer thermal structure, including a near-surface superadiabatic layer during the afternoon and an inversion layer at night. Upward-looking Mini-TES observations show warm and cool parcels of air moving through the Mini-TES field of view on a time scale of 30 seconds. The retrieved dust optical depth shows a downward trend at both sites.

Spectra returned by the Mini-TES on board the Spirit and Opportunity rovers give the first view of the martian surface and atmosphere in the thermal infrared from the surface of Mars. Upward-looking observations by Mini-TES allow the temperature profile within the lowest 2 km of the planetary boundary layer (PBL) to be retrieved. The PBL is the portion of the atmosphere that directly interacts with the surface, responding to forcings such as frictional drag and surface heating. Atmospheric temperatures retrieved from orbital observations do not have sufficient vertical resolution to resolve the PBL, so the diurnal and seasonal trends of temperatures and aerosols throughout the PBL at a given location have never before been observed systematically. These observations are important because they provide a glimpse of the convective and turbulent behavior of the temperature perturbations in the PBL, and these processes control the transfer of heat, momentum, and molecular species across the surface-atmosphere interface. Retrieved PBL temperature profiles also provide valuable constraints for the validation of both global and mesoscale martian atmospheric models. Previous observations by the Viking and Pathfinder landers yielded measurements of winds and temperature only within 2 m of the surface (*1*, *2*). The Mini-TES temperature profiles contribute information from about 20 m to 2 km above the surface.

We report here on Mini-TES spectra collected during the first 100 sols (*3*) of operations by Spirit (4 January to 14 April 2004; L_s = 328° to 20°) and the first 80 sols of operations by Opportunity (25 January to 15 April 2004; L_s = 339° to 20°) (*4*). Mini-TES is a Michelson interferometer with 167 spectral channels covering the spectral range from 340 to 1997 cm^{-1} (5 to 29 μm) with a spectral resolution of 10 cm^{-1} (*5*). The nominal angular resolution is 20 mrad. A pointing mirror allows Mini-TES to view elevation angles up to 30° above the plane of the rover deck. The combination of uncertainties associated with radiometric precision of the instrument and random noise gives an expected radiance uncertainty of about 3×10^{-8} W cm^{-2} sr^{-1}/cm^{-1} (*5*), corresponding to an equivalent temperature uncertainty of 0.3 K at 15 μm for a typical atmospheric temperature of 220 K.

We acquired repeated atmospheric observations at different times of day on each sol to obtain diurnal and seasonal coverage. We typically also obtained a downward look at the surface to obtain surface temperature and near-surface atmospheric temperature immediately before or after each atmospheric observation. Observations outside the normal waking hours (~10:00 to 17:00 local time) for the rover are very expensive in terms of power, so the large majority of observations have been taken between midmorning and late afternoon. Special campaigns to coordinate atmospheric Mini-TES observations with the overflight of orbiting spacecraft were also performed.

Atmospheric temperatures were retrieved by a constrained linear inversion of observed radiance in the 15-μm CO_2 band (*6*). The retrieval is sensitive to temperatures between about 20 m and 2 km above the surface. The vertical resolution at a given height is about equal to the height above the surface. The typical elevation angle of 30° above the horizon used by Mini-TES means that atmospheric temperatures are retrieved along a slant path away from the rover, so the temperature at 2 km altitude is representative of a location 4 km away horizontally from the rover. Because there is no atmospheric pressure sensor on board the rovers, surface pressure is estimated by using the modeling results of Mars Global Circulation Models (*7*). The 15-μm CO_2 band is strong enough to produce an observable signature in downward-looking Mini-TES observations of soils (*8*) and rocks,

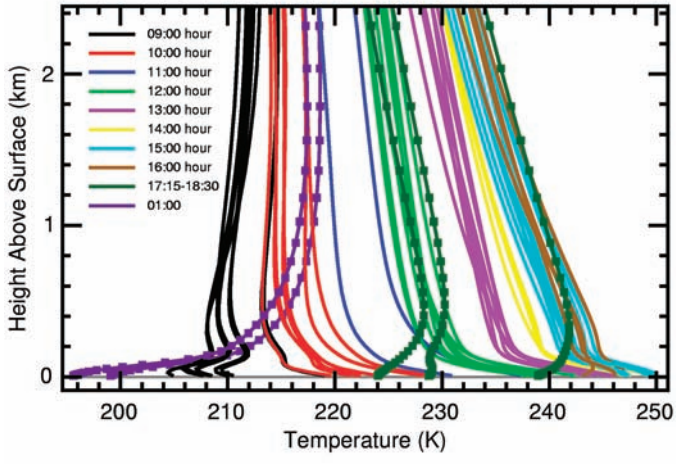

Fig. 1. Atmospheric temperature as a function of height above the surface retrieved from Spirit. Profiles without points show observations taken during nominal rover waking hours between Spirit sols 39 and 57. The three dark-green profiles with points show evening observations (from right to left) at local times of 17:15 (sol 49), 18:00 (sol 64), and 18:30 (sol 70). The two purple profiles with points show overnight observations, both near 1:00 local time (sols 45 and 55).

[1]NASA Goddard Space Flight Center, Greenbelt, MD 20771, USA. [2]Space Science Institute, Boulder, CO 80301, USA. [3]Texas A&M University, College Station, TX 77843, USA. [4]University of Arizona, Tucson, AZ 85721, USA. [5]Cornell University, Ithaca, NY 14853, USA. [6]Jet Propulsion Laboratory, Pasadena, CA 91109, USA. [7]NASA Glenn Research Center, Cleveland, OH 44135, USA. [8]Arizona State University, Tempe, AZ 85287, USA.

*To whom correspondence should be addressed. E-mail: Michael.D.Smith@nasa.gov

which typically look through 2 to 5 m of atmosphere. We model the depth of the CO_2 absorption in this geometry to give a representative near-surface temperature between the rover mast height (1.5 m) and the surface. The surface (soil) temperature is derived from the brightness temperature just outside the CO_2 absorption. In a separate step, the column-integrated water vapor abundance is retrieved using the rotation bands near 25 μm, and the column-integrated dust optical depth is retrieved using an algorithm that includes the effect of aerosol scattering (*9*). Although Mini-TES is only sensitive to atmospheric temperatures within 2 km of the surface, the absorptions caused by atmospheric dust and water vapor are not opaque, so Mini-TES spectra are sensitive to the entire column abundance of those quantities.

Uncertainty in retrieved temperatures and aerosol optical depth includes contributions from the random and systematic errors in the instrument and calibration and from systematic errors inherent in the retrieval process. Propagation of instrument errors (*5*) is straightforward and results in the relatively small uncertainty of <0.5 K in temperatures and <0.02 in optical depth. The uncertainty introduced by the assumptions inherent in the retrieval process (e.g., use of modeled surface pressure and amount of vertical smoothing used to keep retrieval stable) is more difficult to quantify. On the basis of numerical experiments and our experience with similar retrieval algorithms (*9*–*13*), we estimate the uncertainty in retrieved temperatures to be 2 K near the surface, increasing to 4 K at the upper boundary (2 km), the uncertainty in aerosol optical depth to be 0.02 or 5% (whichever is larger), and the uncertainty in water vapor abundance to be 5 precipitable micrometers (pr μm).

We retrieved 185 Mini-TES atmospheric temperature profiles using data from Spirit and 330 profiles using data from Opportunity. There is a large and systematic change in the retrieved thermal structure throughout a sol (Figs. 1 and 2). At all levels, atmospheric temperatures are minima at dawn, increase throughout the morning and early afternoon, reach maxima in midafternoon, decrease rapidly in the early evening, and then decrease more slowly throughout the night. This cycle is most dramatic in the lowest 100 m. From morning until early afternoon, atmospheric temperatures nearest the surface rapidly rise, forming a superadiabatic layer extending to more than 100 m above the surface. The lapse rate in this layer far exceeds the adiabatic value, thus creating unstable conditions. Convective motions in the thin atmosphere cannot transfer heat from the surface layer quickly enough to sustain adiabatic lapse rates, such that the superadiabatic layer persists throughout the afternoon, with resulting turbulent motions. Between 16:00 and 17:00, the superadiabatic layer collapses and is quickly replaced by a stable inversion layer. The inversion layer continues to grow in amplitude and depth throughout the night, until it dissipates after dawn the next morning. This diurnal behavior is similar to that observed by Pathfinder,

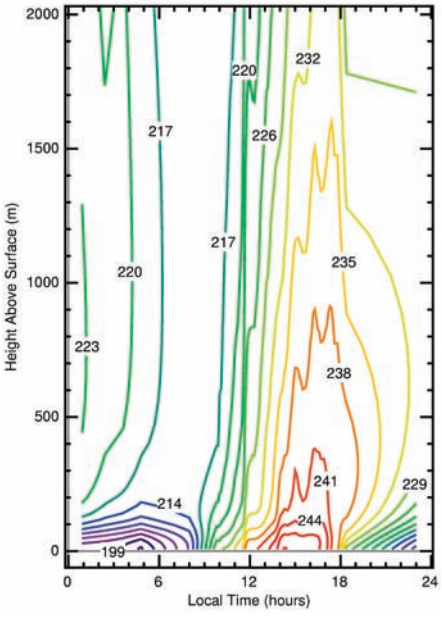

Fig. 2. The diurnal variation of the thermal structure as observed by Opportunity between sols 45 and 65 (plus overnight observations from sol 22 at 1:00, sol 33 at 3:30, and sol 40 at 4:45). The contour level increment is 3 K.

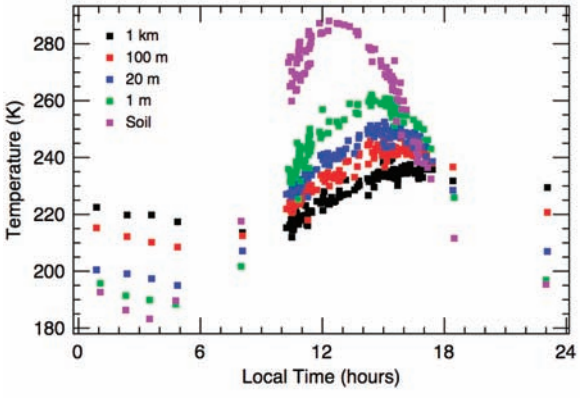

Fig. 3. Soil and atmospheric temperature as a function of time of day as observed by Opportunity between sols 45 and 65, and overnight observations from sol 22 at 1:00, sol 33 at 3:30, and sol 40 at 4:45. The surface (soil) and 1 m atmospheric temperatures were retrieved from downward-looking observations.

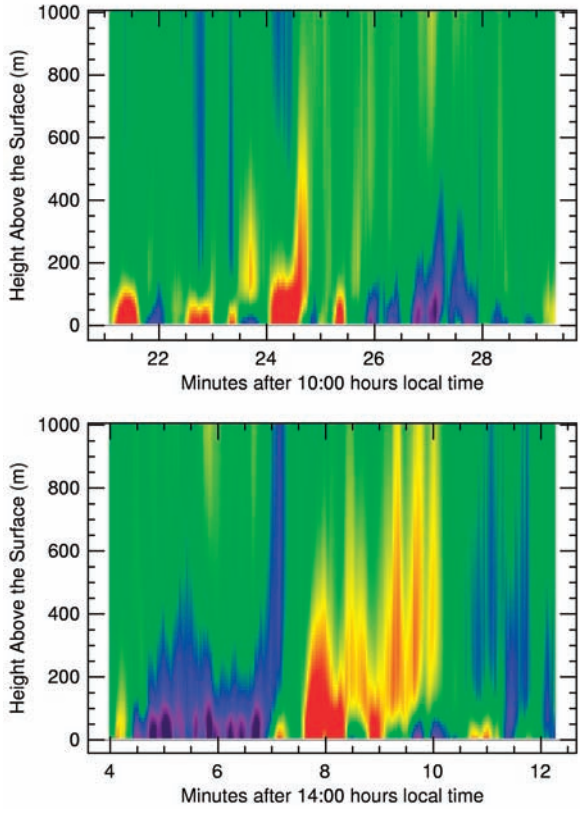

Fig. 4. Perturbations in atmospheric temperature as a function of time and height after removal of the time-mean at each height. The top panel shows data taken by Spirit on sol 12 during midmorning. The bottom panel shows data taken by Opportunity on sol 27 during midafternoon. Red and orange indicate warmer than average temperatures, green indicates near-average temperatures, and blue and purple indicate colder than average temperatures. The peak-to-peak amplitude of the fluctuations is as much as 5 K.

whose observations in the lowest 1.5 m above the surface showed superadiabatic conditions between roughly 7:30 and 16:45 and an inversion layer at night (*2*).

The surface temperature closely follows the solar input, with maximum temperatures near 12:00, while atmospheric temperatures are driven by a combination of radiation and sensible heat flux. The atmosphere at a particular height continues to warm until the soil temperature falls below the temperature at that height. This causes maximum atmospheric temperatures to lag maximum soil temperatures by several hours, with maximum atmospheric temperatures occurring progressively later at higher altitudes above the surface (Fig. 3). At 1 m above the surface, maximum temperature occurs around 14:45, whereas at 1 km the maximum temperature occurs at about 16:30.

The turbulent motions associated with convection have been captured in Mini-TES observations as large temperature fluctuations over short time scales (Fig. 4). The convective activity begins as early as 10:00 local time (Fig. 4, top panel), with peak-to-peak amplitude thermal fluctuations of up to 5 K progressing through the Mini-TES field of view on time scales of 15 to 30 s. Most of the activity is confined to the superadiabatic layer (lowest 100 to 200 m above the surface), but the largest thermal fluctuations can propagate upward with time into the neutrally stable region above to heights of at least 1 km above the surface. The amplitude and frequency of these fluctuations follows the solar heating, which is at maximum in the middle of the day. As the superadiabatic layer collapses after 16:00, the large fluctuations dissipate and do not reappear until the superadiabatic layer is reestablished the next morning. The number and amplitude of these temperature fluctuations is variable from sol to sol at the same time of day. Large-amplitude, short time scale temperature fluctuations were also observed by the Pathfinder and Viking landers during daytime hours (*1*, *2*), and the occurrence of convective vortices observed by Pathfinder follows the same diurnal dependence (*14*).

We observed seasonal changes in atmospheric conditions. Morning temperatures observed by both Spirit and Opportunity decreased at a rate of approximately 0.09 K sol^{-1}, whereas late afternoon temperatures decreased at a rate of about 0.16 K sol^{-1} (Fig. 5). A large regional dust storm in December 2003 (*15*) had not yet fully dissipated by the time Spirit and Opportunity landed in January 2004. The column-integrated 9-μm dust optical depth observed by Spirit soon after landing was 0.45 to 0.5 (Fig. 6), decreasing to 0.25 to 0.3 by sol 100. Opportunity observed a similar rate of clearing, beginning with a dust optical depth of about 0.45 after landing, and decreasing to a value of 0.35 by sol 80. The Mini-TES spectra display no detectable signature of water ice clouds during this period.

The retrieved water vapor column abundance from Spirit was 10 ± 5 pr μm, with no detectable variation in either time of sol or season. This compares favorably to the value of 12 pr μm retrieved from Mars Global Surveyor TES spectra (*12*, *13*) for this season and latitude. Although TES observations predict a similar water vapor abundance at the latitude of Meridiani Planum, retrievals from the Opportunity Mini-TES spectra show a systematically lower water vapor column abundance than Spirit by roughly a factor of two. This difference could be caused by a difference in local meteorology at the two sites that was not detected by the zonal averages used for TES analysis.

The concurrent operation of two rovers allows a direct comparison between conditions on opposite sites of the planet (*16*). In broad terms, the diurnal and seasonal variations of the thermal structure and dust optical depth were similar at the two sites (as expected, because the two rovers are at similar latitudes), but there were differences. Both the soil and atmospheric daytime temperatures observed by Opportunity were systematically higher than those observed by Spirit, likely because of the lower surface visible albedo at Meridiani Planum. The temperature difference was generally 1 K to 3 K at 1 km above the surface, increasing to 4 K to 6 K at 20 m above the surface. Nighttime atmospheric temperatures observed by Opportunity were also higher than those observed by Spirit by 5 K to 10 K.

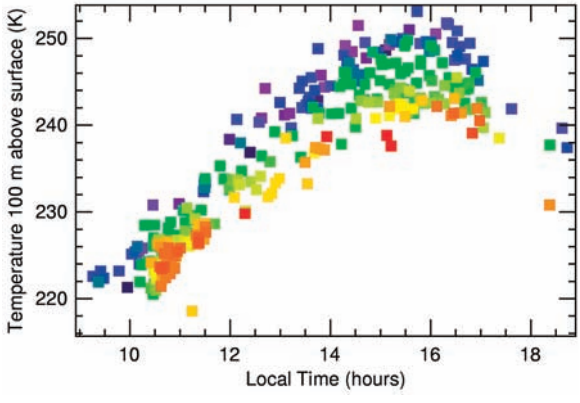

Fig. 5. Atmospheric temperature at 100 m above the surface as a function of time of day and sol number (represented by color), as observed by Opportunity. The color scale runs from purple and blue (sols 1 to 30), to green and yellow (sols 30 to 60), to orange and red (sols 60 to 80). There are insufficient observations to identify meaningful seasonal trends for overnight hours.

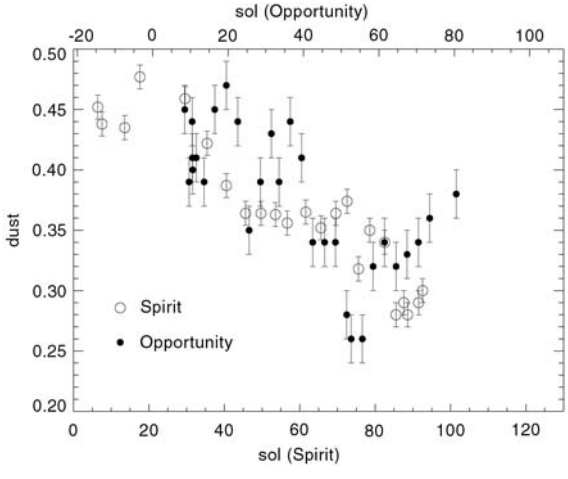

Fig. 6. Infrared (9 μm) dust optical depth for Spirit and Opportunity as a function of sol relative to the starting point of each landing. Shown here is a sampling of dust optical depth of 1 point per 3 to 4 sols. Error bars indicate 1-σ uncertainties.

References and Notes

1. S. L. Hess, R. M. Henry, C. B. Leovy, J. A. Ryan, J. E. Tillman, *J. Geophys. Res.* **82**, 4559 (1977).
2. J. T. Schofield *et al.*, *Science* **278**, 1752 (1997).
3. A martian solar day has a mean period of 24 hours 39 min 35.244 s and is referred to as a sol to distinguish this from a roughly 3% shorter solar day on Earth.
4. L_s denotes the areocentric longitude of the Sun, a measure of season on Mars. L_s values of 0°, 90°, 180°, and 270° correspond to the Northern Hemisphere spring equinox, summer solstice, autumn equinox, and winter solstice, respectively.
5. P. R. Christensen *et al.*, *J. Geophys. Res.* **108**, 8064 (2003); http://dx.doi.org/10.1029/2003JE002117.
6. M. D. Smith, B. J. Conrath, J. C. Pearl, E. A. Ustinov, *Icarus* **124**, 586 (1996).
7. Model results provided by R. M. Haberle and R. J. Wilson, personal communication, 2003. Atmospheric pressure at the surface is required by the retrieval algorithm to determine the mass of CO_2 above the rover.
8. The term martian soil is used here to denote any loose, unconsolidated materials that can be distinguished from rocks, bedrock, or strongly cohesive sediments. No implication of the presence or absence of organic materials or living matter is intended.
9. M. J. Wolff, R. T. Clancy, *J. Geophys. Res.* **108**, 5097 (2003); http://dx.doi.org/10.1029/2003JE002057.
10. M. D. Smith, J. C. Pearl, B. J. Conrath, P. R. Christensen, *J. Geophys. Res.* **105**, 9539 (2000).

11. B. J. Conrath *et al.*, *J. Geophys. Res.* **105**, 9509 (2000).
12. M. D. Smith, *J. Geophys. Res.* **107**, 5115 (2002); http://dx.doi.org/10.1029/2001JE001522.
13. M. D. Smith, *Icarus* **167**, 148 (2004).
14. J. R. Murphy, S. Nelli, *Geophys. Res. Lett.* **29**, 2103 (2002); http://dx.doi.org/10.1029/2002GL015214.
15. TES observations showed a large regional storm in mid-December 2003. The highest dust opacities during the active part of the storm were at low southern latitudes between 0° and 60°W longitude (just west of the Opportunity landing site). The dust storm began to dissipate by the last week of December 2003, and by mid-January 2004 there was little longitudinal variation in dust optical depth remaining.
16. Spirit landed in Gusev Crater near 14.5°S, 184.5°W, whereas Opportunity landed on Meridiani Planum near 2°S, 6°W.
17. This work was funded through the Mars Exploration Rovers project. We would like to thank all the scientists, engineers, and programmers who made the Mini-TES observations described here possible.

19 August 2004; accepted 12 October 2004

REPORT

Atmospheric Imaging Results from the Mars Exploration Rovers: Spirit and Opportunity

M. T. Lemmon,[1]* M. J. Wolff,[2] M. D. Smith,[3] R. T. Clancy,[2] D. Banfield,[4] G. A. Landis,[5] A. Ghosh,[3] P. H. Smith,[6] N. Spanovich,[6] B. Whitney,[2] P. Whelley,[7] R. Greeley,[7] S. Thompson,[7] J. F. Bell III,[4] S. W. Squyres[4]

A visible atmospheric optical depth of 0.9 was measured by the Spirit rover at Gusev crater and by the Opportunity rover at Meridiani Planum. Optical depth decreased by about 0.6 to 0.7% per sol through both 90-sol primary missions. The vertical distribution of atmospheric dust at Gusev crater was consistent with uniform mixing, with a measured scale height of 11.56 ± 0.62 kilometers. The dust's cross section weighted mean radius was 1.47 ± 0.21 micrometers (μm) at Gusev and 1.52 ± 0.18 μm at Meridiani. Comparison of visible optical depths with 9-μm optical depths shows a visible-to-infrared optical depth ratio of 2.0 ± 0.2 for comparison with previous monitoring of infrared optical depths.

Mars' ubiquitous airborne dust is, with CO_2, a principal driver for energy deposition in the atmosphere. The dust absorbs sunlight, especially at 400 to 600 nm, as well as thermal radiation, especially near 9 μm. The atmospheric dust loading has historically been difficult to monitor from Earth or from spacecraft orbiting Mars, because the dust in the atmosphere is similar in composition to the loose materials on the surface (*1*). The Thermal Emission Spectrometer (TES) on Mars Global Surveyor (MGS) has monitored the spatial and seasonal distribution of dust since the MGS mapping phase began in 1998 (*2*). Before the Mars Exploration Rover (MER) mission, there had been no contemporaneous surface mission to provide support for the remote dust estimates. In particular, the relation between the TES 9-μm absorption optical depth and the visible extinction optical depth has not been tested with in situ measurements.

The MER primary missions began with the landings of the rovers Spirit, at Gusev crater [14.57°S, 175.48°E (*3*)] on 4 January 2004, and Opportunity, at Meridiani Planum [1.95°S, 354.47°E (*4*)] on 25 January 2004. The seasonal extent of the primary missions was 110 sols (*5*), almost symmetric around the southern autumnal equinox [aerocentric longitude of the Sun (L_s) = 328° for Spirit sol 1; L_s = 25° for Opportunity sol 91]. During this season, TES and Viking Lander observations show decreasing optical depth with time, approaching a minimum after L_s = 60° (*2*, *6*) but before the formation of the aphelion cloud belt (*7*). The comparable Viking-measured visible optical depths fell from 1 to 2 in the wake of a global dust storm to ~0.5 to 0.6, but the full Viking record includes optical depths from 0.2 to 4 (*6*).

Both rovers are equipped with nine cameras. Pancam, which comprises a pair of mast-mounted science cameras with independent filter wheels, offers multispectral observations, including two filters designed for imaging the Sun (*8*). The solar filters, designated L8 (440 nm) and R8 (880 nm), were intended for measurements of optical depth through direct extinction of sunlight. Direct images of the Sun through the L8 filter were also used (along with time information) to update the rovers' onboard attitude data. An additional 11 filters on Pancam, sensitive to wavelengths from 430 to 1000 nm, were used for photometric observations of the sky to constrain the size and optical properties of atmospheric dust. The rovers' engineering cameras offer larger fields of view (*9*). The frequent use of the engineering cameras made them suitable for attempted serendipitous detection of dust devils and clouds. From the landing of Spirit to the end of Opportunity's 90-sol primary mission, the rovers acquired 1710 Sun images that could be used to derive atmospheric optical depth (Spirit acquired 633 L8 and 321 R8 observations from sol 2 to 110, Opportunity acquired 468 L8 and 288 R8 observations from sol 2 to 91); 17 sky surveys for deriving dust properties (9 by Spirit, 8 by Opportunity); and several other special-purpose sky images. In addition, a Miniature TES (Mini-TES) is included in the Athena payload (*10*). During rover operations, atmospheric imaging and Mini-TES observations (*11*) were operated to acquire contemporaneous constraints on the dust's visible scattering and absorption properties and on its thermal emission properties.

Temporal variation in dust loading drives changes in energy deposition in the atmosphere. To characterize the dust load and provide ground truth for orbital instruments, the atmospheric optical depth (principally dust) was measured in isolation, in coordination with other atmospheric imaging, in coordination with Mini-TES, and in coordination with MGS and Mars Express overflights. The strategy for measuring visible optical depth with MER was similar to that used by the Viking and Pathfinder Landers (*12*, *13*). Pancam was used to image the Sun through one or both of two solar filters (*14*). About one-third of the solar images were taken with the primary purpose of fine-tuning knowledge of the Rovers' attitude; a small number of images were timed to image transits of Mars' moons across the Sun (*15*, *16*) and are excluded from this analysis. Two-thirds of the images were taken specifically to measure the direct solar flux as a function of solar zenith angle.

All images were calibrated with standard procedures. Prelaunch images of a spatially uniform scene (flat-field images) through the neutral density-coated solar filters were contaminated by light scattered within the camera and had a low signal-to-noise ratio.

[1]Texas A&M University, College Station, TX 77843, USA. [2]Space Science Institute, Boulder, CO 80301, USA. [3]NASA Goddard Space Flight Center, Greenbelt, MD 20771, USA. [4]Cornell University, Ithaca, NY 14853, USA. [5]NASA Glenn Research Center, Cleveland, OH 44135, USA. [6]University of Arizona, Tucson, AZ 85721, USA. [7]Arizona State University, Tempe, AZ 85287, USA.

*To whom correspondence should be addressed. E-mail: lemmon@tamu.edu

Therefore, during Mars surface operations, several image sequences were acquired in which the Sun was allowed to drift away from the center of the frame over ~15 min (*17*). Tests validated that the R8 (880 nm) filter could be corrected with the prelaunch R5 (903 nm) flat-field image. The L8 (440 nm) filter was best matched with the L1 (719 nm, broadband) flat-field image. This is consistent with the known presence of a red leak of 750-nm light through the L8 filter, comparable in magnitude to the light the L8 filter was designed to transmit (*18*). Within each image, the center of the Sun was found to subpixel accuracy; an annulus was created around the Sun; background light, due to sky light and instrumental scattered light, was determined and subtracted from the image; and the total flux from the Sun was integrated. Because of the large flux from the Sun [typically 2000 digital numbers (DN) representing 1×10^5 electrons from each of 300 pixels] and the low background, counting statistics were a negligible source of uncertainty. Our knowledge of small-scale variations in the charge-coupled device (CCD) response contributes an uncertainty of 2%. Based on a comparison with full-resolution images, flux measurements from thumbnail images have a 3% uncertainty due to the addition of errors introduced in compression.

Potentially larger sources of uncertainty included the absolute radiometric response, at 30% uncertainty for the two solar filters, and variations in response with temperature. An algorithm, similar to the algorithm used by Pathfinder for optical depth measurements (*13*), was developed to use groups of observations taken close in time to produce a relative radiometric calibration. A grid of values for the absolute response and the temperature dependence of the response was considered. Values consistent with the laboratory calibration uncertainty (*8*) were tested. The tests found the best fitting calibration parameters (I_0 and c), in a least-squares sense, to the model

$$I_{\text{observed}} = I_0 \times (1 + c \times T) \times \exp(-\tau \times \eta)$$

where I_{observed} is the observed flux in integrated DN/s, I_0 is the modeled top-of-atmosphere flux in DN/s for a detector at 0°C, c is a temperature response coefficient, T is the temperature in °C, τ is the optical depth (which is allowed to vary on a time scale of sols), and η is the air mass for the solar elevation angle of the observation. The algorithm was applied independently to the complete data set from each rover, for each filter, for thumbnails and full-resolution images. Once the calibration parameters were set, the equation was rearranged to solve for optical depth for each individual observation. Finally, in rare cases where full-resolution images were missing, optical depth values derived from a parallel analysis of the thumbnail data set were substituted.

The principal source of uncertainty is actual temporal variation of the optical depth. Based on analysis of variations in the resulting optical depths, the uncertainty in I_0 is ±3% (due to the extrapolation from measurements mostly at 1.0 to 1.5 air masses to a parameter value at 0.0 air mass) and the uncertainty in c is $0.001°C^{-1}$. Most observations were taken at air masses from 1 to 1.5, but the calibration is strongly influenced by several sols during which images were taken at air masses of 2 to 4. For air masses near 1, typical absolute uncertainties in optical depth are ±0.04; for comparison of optical depths measured in a single filter by a single rover, typical relative uncertainties are ±0.02. Observations during the early morning, with systematically colder temperatures, were somewhat rare and had higher uncertainties, up to ±0.04, while high air mass afternoon observations had uncertainties as low as ±0.006. The uncertainties are comparable to Pathfinder values (*13*). The optical depth reported here is an average of the L8 and R8 values and should be taken as a 650- to 700-nm value.

Within the first few sols of landing, the optical depths seen by Spirit at Gusev crater were near 0.9 (Fig. 1). Rayleigh scattering by the CO_2 atmosphere contributes <0.01, so the observed optical depth is caused by atmospheric aerosols, primarily dust with a possible contribution from water ice. However, Mini-TES spectra do not show a water-ice signature (*11*), and no discrete clouds were seen during the primary missions. Spirit landed about 20 sols after a large regional dust storm on the other side of Mars (*11*). Some of the dust over Gusev crater may have been advected into the region as the distant dust storm was dispersed. Throughout the first 90 sols of the mission, the optical depth decreased following a roughly linear trend at a rate of -0.004 sol^{-1}. The trend can alternatively be described as an exponential decay, with a loss of 0.6% per sol; this results in an estimated time scale of 160 sols for dust removal if no dust lifting was occurring. On sol 91, the optical depth had fallen to near 0.57, and on sol 110 Spirit's observed optical depth was near 0.50. No diurnal variations were detected; diurnal variations comparable to those seen by the Viking Landers (*6*) are within our uncertainty of ±0.03, introduced by the systematic temperature variations between

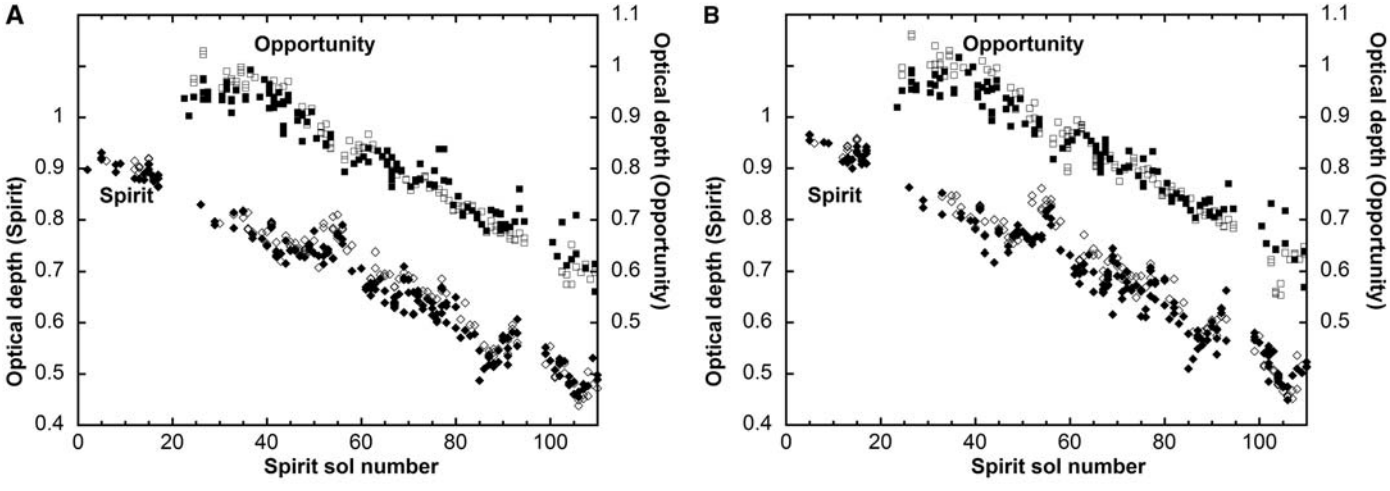

Fig. 1. Visible optical depth. Atmospheric optical depth observed with Pancam's (**A**) L8 filter (440 nm + red leak) and (**B**) R8 filter (880 nm) is shown for Spirit (diamonds) and Opportunity (squares). The closed symbols represent afternoon measurements for each sol, and the open symbols represent morning measurements for each sol. The Opportunity scale is displaced upward by 0.1 for clarity. The observations are shown as a function of Spirit sol number, defined as 1 at Spirit's landing and 20.5 at Opportunity's landing. Sol 1 corresponds to $L_s = 328°$, sol 61 to $L_s = 0°$, and sol 110 to $L_s = 24°$. The gap in data for Spirit beginning at sol 18 was due to a rover anomaly; the gap in data for both rovers beginning at about sol 95 was due to a pause in operations to allow a software upload.

morning and afternoon observations at similar air masses.

At landing, optical depths seen by Opportunity at Meridiani Planum were also near 0.9. A brief increase in optical depth to near 1.0 was followed by a roughly linear or exponential falloff to near 0.6 by the end of 90 sols. During the period of decay, the morning optical depth values decreased at a rate of –0.005 sol^{-1}, or a loss of 0.7% per sol. The optical depth decreased more slowly in the afternoon than in the morning. This was due to a combination of systematic sampling of only afternoon values early in the mission before the optical depth rose to 1, and apparently higher optical depths in the afternoons for a brief period between sols 80 and 91. The increased afternoon optical depths may indicate local dust raising during the warm part of the sol. No other trend in diurnal variations was observed.

The wavelength dependence of the optical depth is not well constrained because the relative contribution to the L8 filter of 440-nm versus 750-nm light is not well determined. Filter-level tests showed a 14% contribution from the red leak, whereas system-level tests showed a 78% contribution, but with low signal-to-noise data. The L8-derived optical depths average 3.5 ± 0.4% lower than the R8-derived values. This represents a slope of 1.4 ± 0.5% per 100 nm, considering the wavelength uncertainty. On Spirit's sol 67, the sunset was imaged through additional filters without a neutral density coating. The intensity of the solar disk and nearby sky was measured at wavelengths of 535, 602, 753, and 902 nm at solar elevations of 0.8° to 2.4° for each filter. The variation of intensity with wavelength, combined with the absolute radiometric calibration and the known solar flux (*19*), required that the optical depth increase with wavelength by 0.91 ± 0.05% per 100 nm.

Surface-based visible optical depth measurements have limited spatial and temporal sampling. The visible-to-infrared optical depth ratio is an important link between the thermal absorption that has been routinely measured and the visible scattering and absorption that control solar energy deposition. Mini-TES atmospheric observations could not be taken simultaneously with Pancam optical depth measurements. However, consideration was given to acquiring Mini-TES and Pancam observations close in time. Trends in visible optical depths can be compared to trends in 9-μm absorption optical depths measured by Mini-TES. The longer wavelength optical depth decreased from 0.48 to 0.28 at Gusev, and from 0.45 to 0.35 at Meridiani Planum (*11*). The visible optical depths are systematically 2.0 ± 0.2 times larger than the infrared optical depths, in accordance with prior models for 1.5- to 2.0-μm dust particles (*20*).

The distribution of dust with altitude controls where absorbed solar energy is deposited. A visible-light imager under an optically thick atmosphere with essentially no visible-light-absorbing gases is not well suited to determining the vertical structure of aerosols. However, low Sun observations were made with Pancam to provide constraints on the vertical structure. These observations are especially sensitive to the lowest few scale heights of the atmosphere, making them qualitatively different from limb-sounding observations that are sensitive to higher altitudes. For high solar elevations, air mass is inversely proportional to the sine of the elevation angle. At low elevations, the curvature of Mars' limb makes the vertical structure relevant (*21*). The simplest useful description of dust vertical structure is a scale-height dependence on altitude. For such a model, observations of the solar flux at elevations <10° can be used to determine an effective scale height. Spirit's sol-67 sunset observation included well-exposed images of the Sun through the solar filters at elevations of 3.6° to 4.6°, as well as the multispectral images at 0.8° to 2.4°. We combined the 880-nm and 900-nm data sets after dividing out the top-of-atmosphere solar flux in each filter. We varied the scale height (thereby varying the elevation-airmass relation) and fit the data with a single optical depth. The scale height resulting in the best fit was 11.56 ± 0.62 km, where the principal sources of uncertainty are the absolute radiometric uncertainty, the pixel-to-pixel uncertainty, and a 30-s uncertainty in the spacecraft clock. This is consistent with the atmospheric pressure scale height of 11.1 km; our data are therefore consistent with a model of the dust as being well mixed with the atmosphere in the lowest 20 to 30 km, but the data are not sensitive to the modeled small amounts of dust above 30 km. Other models with a variety of structures can also fit this simple data set, as long as they produce the same elevation-airmass profiles as the scale-height model for solar elevations of 1° to 5°.

Understanding the nature of the dust particles is important for understanding their role in the atmosphere. Pancam was used to constrain the light-scattering properties of the dust. Images of sky brightness at several visible and near-infrared wavelengths and a variety of scattering geometries were made on Spirit's sols 49 and 62, and on Opportunity's sols 27 and 33. For each rover, the earlier observation set was made near local noon, with a high Sun elevation, while the later observation set was made late in the afternoon with a low Sun elevation (Table 1). Optical depths were measured immediately before each survey of the sky. The high-Sun surveys included observations at about the same azimuth as the Sun and 180° of azimuth from the Sun, and principally observed low and intermediate scattering angles. The low-Sun survey included observations at the same elevation as the Sun at a variety of azimuths and reached scattering angles in excess of 150° (Fig. 2). Both types of surveys included surface images to allow accurate modeling of upwelling radiance and included at least filters L7, L5, L4, L2, R4,

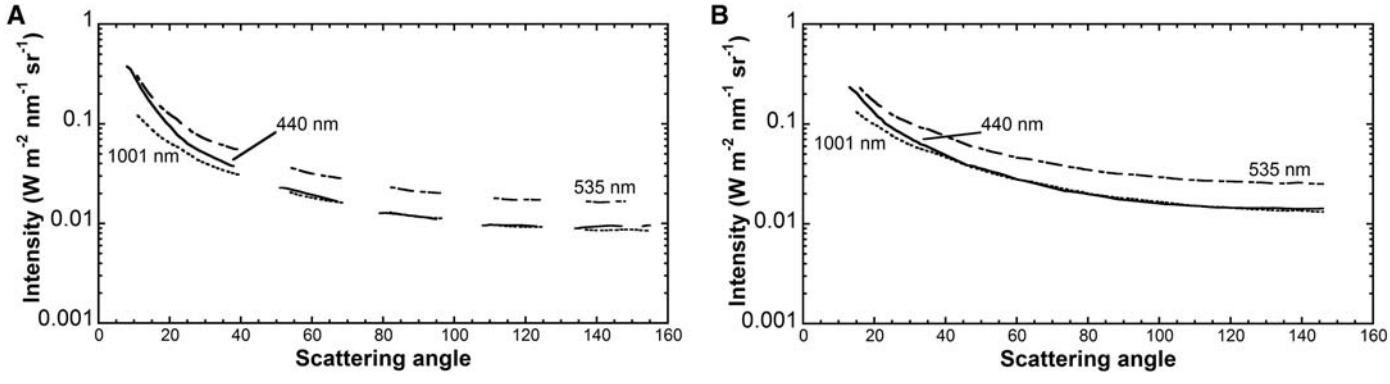

Fig. 2. Sky radiance. The sky intensity as a function of scattering angle for low-Sun sky surveys by Spirit on sol 49 (**A**) and Opportunity on sol 33 (**B**) is shown for three of the six colors observed: 440 nm (solid line), 535 nm (long-dashed line), and 1001 nm (short-dashed line). All observations between 11.5° and 12.5° elevation were averaged over 1° scattering angle intervals to obtain the intensity shown. Each discrete group represents a subset of one 128- by 128-pixel image, except that three separate images contributed the group with the lowest scattering angles.

Table 1. Sky surveys. Time, solar elevation, and sequence for the sky surveys analyzed here. The low-Sun sky survey refers to an azimuthal scan centered near 18° elevation; the high-Sun sky survey refers to an elevation scan below the Sun and in the anti-Sun direction.

Rover	Sol	Local true solar time	Solar elevation	Sequence
Spirit	49	16:52 to 17:10	12.6° to 17.0°	P2618, low Sun
Spirit	62	13:30 to 13:55	57.9° to 63.1°	P2619, high Sun
Opportunity	27	16:13 to 16:32	21.9° to 25.2°	P2618, low Sun
Opportunity	33	11:37 to 11:56	84.4° to 88.9°	P2619, high Sun

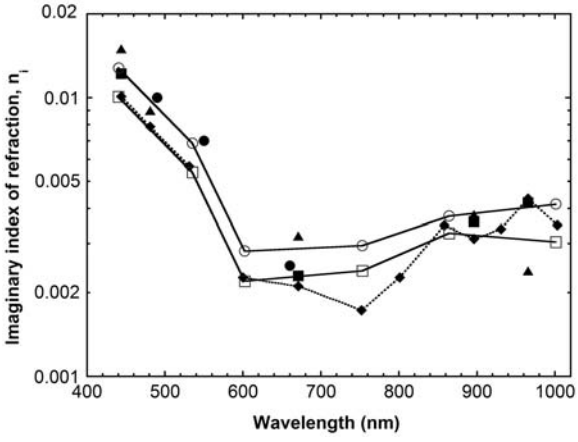

Fig. 3. Imaginary index, n_i. The value of n_i derived from the Spirit (open circles, solid line) and Opportunity (open squares, solid line) sky surveys is shown as a function of wavelength. For comparison, previously determined values of n_i of martian atmospheric dust are shown, based on Viking sky surveys (*22*) (filled circles), Pathfinder low-Sun sky surveys (*23*) (filled squares) and high-Sun sky surveys (*24*) (filled triangles), and an analysis of a single 12-filter image set (*27*) (filled triangles, dotted line).

and R7 (440, 535, 602, 753, 864, and 1001 nm, respectively). Similar sky surveys were made by the Viking and Mars Pathfinder Landers (*22–24*). We fit our model (*25*) to the shape of the radiance distribution across the sky for each wavelength. We varied a_{eff}, the cross-section weighted mean radius in our assumed gamma distribution, while holding the width of the distribution, b_{eff}, at 0.2. For each value of a_{eff} and each filter, we varied the ground reflectivity, imaginary index of absorption (n_i), and two numerical parameters (G and Θ_{min}) describing the shape of the phase function (*23*, *26*). The best fits for the observations by Spirit had $a_{\mathrm{eff}} = 1.47 \pm 0.21$ μm; for Opportunity, $a_{\mathrm{eff}} = 1.52 \pm 0.18$ μm. These values are consistent with each other and with previous measurements of the dust size distribution (*22–24*). Our values for the scattering parameters are consistent with previous observations (*22–24*, *27*). The dust absorption is relatively strong at 400 to 600 nm and has a local minimum near 600 to 750 nm (Fig. 3). The numerical parameter G varied from 80 to 400 (weakly trending down with increasing wavelength), and Θ_{min} varied from 115° to 135° (trending up with increasing wavelength). Including the systematic interdependence of these parameters, the absorption uncertainty is about 20%, the uncertainty in G is about a factor of 2, and the uncertainty in Θ_{min} is about 30°. This analysis was heavily weighted to the low-Sun surveys because of the phase angle coverage.

Before the landing at Gusev crater, there was an expectation of observing dust devils with the Athena payload. Dust-devil tracks have been identified on the floor of Gusev (*28*) and inside the landing ellipse. Spirit came to rest within one such dust-devil track, and a track was seen in Bonneville crater (*29*). The seasonal dependence of dust-devil formation (*30*) suggests that Spirit landed during "dust-devil season." Serendipitous discovery of an active dust devil was the original strategy at Gusev crater, but no dust devils were seen. Most horizon images were acquired during the morning or through red-sensitive cameras, whereas maximum surface temperatures occur in the afternoon and martian dust devils are more visible in blue light (*31*). Four systematic surveys comprised 440- and 750-nm, low-compression horizon panoramas taken to look for dust devils between 12:00 and 14:00, the most probable time of day. No dust devils were detected in any images on either rover during their primary missions. Dust devils may not have been present at the times during which the rovers imaged, or any vortices may have had an insufficient dust load ($\tau \ll 1$) to be detected (*31*).

References and Notes

1. R. Kahn *et al.*, in *Mars*, H. H. Kieffer *et al.*, Eds. (Univ. Arizona Press, Tucson, 1992), pp. 1017–1053.
2. M. D. Smith, *Icarus* **167**, 148 (2003).
3. R. E. Arvidson *et al.*, *Science* **305**, 821 (2004).
4. R. E. Arvidson *et al.*, *Science* **306**, 1730 (2004).
5. A martian solar day has a mean period of 24 hours 39 min 35.244 s and is referred to as a sol to distinguish this from a roughly 3% shorter solar day on Earth. Sol 1 was defined to begin at local solar midnight immediately before landing.
6. D. S. Colburn *et al.*, *Icarus* **79**, 159 (1989).
7. M. J. Wolff *et al.*, *J. Geophys. Res.* **104**, 9027 (1999).
8. J. F. Bell III *et al.*, *J. Geophys. Res.* **108**, 8063 (2003).
9. J. N. Maki *et al.*, *J. Geophys. Res.* **108**, 8071 (2003).
10. P. R. Christensen *et al.*, *J. Geophys. Res.* **108**, 8064 (2003).
11. M. D. Smith *et al.*, *Science* **306**, 1750 (2004).
12. J. B. Pollack *et al.*, *J. Geophys. Res.* **82**, 8064 (1977).
13. P. H. Smith, M. T. Lemmon, *J. Geophys. Res.* **104**, 8975 (1999).
14. Images were returned primarily in two formats. First, a thumbnail image was down-linked: thumbnails comprise a full-frame image, down-sampled from 1024 by 1024 pixels to 64 by 64 pixels and compressed to 1 bit per pixel. In thumbnail images, the Sun is just over 1 pixel in diameter, although the flux is typically spread over 4 or more pixels. Second, a "SUN" subframe was down-linked with lossless compression. A "SUN" subframe is 63 by 63 pixels, centered on the centroid of the solar disk. Generally, a single observation resulted in both types of images; in some cases, one product exists but the other was not down-linked. Wherever possible, observations with the lossless, full-resolution subframe were used for analysis; thumbnail observations were used only to fill in gaps in the record.
15. J. F. Bell III *et al.*, *Science* **305**, 800 (2004).
16. J. F. Bell III *et al.*, *Science* **306**, 1703 (2004).
17. The sequences used to image the Sun as it drifted across the CCD included sequences requested by the science team, but were primarily "sun-gazes" using L8 images of the Sun to update the rovers' attitude data.
18. The red leak appears as a small transmission in filter-level tests. However, in later and system-level tests with much worse signal-to-noise ratios, the red leak appeared to contribute more transmitted flux than the principal band pass. The temperature dependence of the system response through the L8 filter is similar to that of a 700- to 800-nm filter. The solar flux versus position data sets were analyzed using all of the left-eye flat fields, under the assumption that atmospheric optical depth did not change during the ~15-min experiment. The L1 flat field produced the most consistent results, although the L2 (750 nm) flat field was nearly as good. The L7 (430 nm) flat field is markedly different from the L1 or L2 flat fields.
19. W. C. Livingston, *Allen's Astrophysical Quantities*, A. Cox, Ed. (AIP Press, New York, ed. 4, 2000).
20. R. T. Clancy *et al.*, *J. Geophys. Res.* **108**, 5098 (2003).
21. The observed intensity, I, is determined by $\mathrm{d}[\ln(I)] = \kappa(s)\,\sin[\theta(s)]\,\mathrm{ds}$, where s is the path and κ is the extinction per unit distance, such that $\tau = \int \kappa\,\mathrm{dz}$, and z is altitude. For the scale-height case, $\kappa = \tau/H\,\exp(-z/H)$, where H is the scale height. The relation between z, θ, and s is purely a function of the geometry (i.e., the curvature of the limb). An arbitrary vertical profile can be ruled out by these data if it yields values of I that are out of the bounds defined by the scale-height case and its uncertainty.
22. J. B. Pollack *et al.*, *J. Geophys. Res.* **100**, 5235 (1995).
23. M. G. Tomasko *et al.*, *J. Geophys. Res.* **104**, 8987 (1999).
24. W. Markiewicz *et al.*, *J. Geophys. Res.* **104**, 9009 (1999).
25. We used the doubling and adding radiative transfer code of (*23*). Because of a 7% uncertainty in the absolute radiometric calibration, we chose to model the relative variations in intensity rather than the absolute intensity. After a best-fit model was found, a correction factor for the absolute intensity was derived. The intensity shown in Fig. 2 includes this correction factor. Intensities for the six filters (in increasing wavelength order) are multiplied by 0.97, 1.035, 0.984, 1.004, 1.021, and 0.861 for Spirit and 1.177, 1.155, 1.144, 1.109, 1.114, and 0.962 for Opportunity.
26. J. B. Pollack, J. N. Cuzzi, *J. Atmos. Sci.* **37**, 868 (1980).
27. J. R. Johnson *et al.*, *Icarus* **163**, 330 (2003).
28. R. Greeley *et al.*, *J. Geophys. Res.* **108**, 8077 (2003).
29. R. S. Greeley *et al.*, *Science* **305**, 810 (2004).
30. M. R. Balme *et al.*, *J. Geophys. Res.* **108**, 5086 (2003).
31. F. Ferri *et al.*, *J. Geophys. Res.* **108**, 5133 (2003).
32. This work was funded by NASA through the Mars Exploration Rover Project. We thank the MER engineers and scientists who enabled the observations described here.

25 August 2004; accepted 8 November 2004

The Cryptic Filtering House of an Invertebrate Larva

Bruno Pernet

The minute and diverse feeding larvae of marine invertebrates typically concentrate suspended food particles on complex arrays of cilia or setae (*1*). Here I show that the planktonic larvae of an annelid worm use a very different strategy: building large, transparent "houses" through which they filter seawater to concentrate food. This feeding mechanism is unlike any previously described in marine larvae but is strikingly similar to that of the very distantly related larvacean chordates (*2*). Cryptic and ephemeral secreted structures like these may be involved in the performance of critical functions in many marine invertebrate larvae, which would have important implications for our understanding of their ecology and evolution.

While rearing larvae of the pectinariid annelid *Pectinaria californiensis* (*3*), I noticed that they showed little forward movement despite vigorous action of their locomotory prototrochal cilia (Fig. 1, A and B). The reason for their lack of progress was revealed when opaque particles were added to the water: The particles were entrained in cilia-generated flow and trapped inside a transparent house surrounding the larva, rendering it visible (Fig. 1C and movie S1). The house is a hollow, partially flattened sphere 400 to 800 μm in maximum diameter; house diameter is positively correlated with larval body length ($R^2 = 0.81$, $P < 0.0001$, $n = 12$ larvae).

The larva occupies a hole at one pole of the house's short axis and is attached to it by the upper edge of its muscular oral hood (Fig. 1D). Prototrochal cilia propel suspended particles into the house through a gap of ~50 μm between the edge of the hole and the dorsal and lateral aspects of the larva. Observations of tethered larvae showed that particles smaller than 2 μm in diameter pass through the house wall, exiting in excurrent flow over its entire surface (movie S2), but particles larger than 6 μm are retained inside it with 100% efficiency, indicating that the pore size of the house wall is between 2 and 6 μm. The form of the occupied house depends on inflation by water pressure generated by the prototrochal cilia. Larvae abandon their houses on mechanical stimulation, and an abandoned house shrinks to a pellet about the size of its former occupant within 3 min (fig. S1). Five larvae forced to abandon their houses constructed new houses within 7 to 12 min.

Larvae first produce houses when the gut becomes functional, 3 days after fertilization, and direct observation shows that they feed while in their houses. A primary role of the house is in concentrating food particles from seawater. Particles may be concentrated by sieving or perhaps by crossflow filtration, where flow parallel to the filtration surface keeps particles in suspension while fluid is forced through its pores (*4*). The large surface area of the filter relative to that of the ciliary pump suggests that flow velocities across the filter, and the energetic costs of filtration, may be low. Many particles retained in the house are entrained in a recirculating current generated by cilia on the edges and inner surfaces of the oral hood (Fig. 1B); these are driven toward the mouth, where they are captured and ingested (Fig. 1D). Abandoned houses and particles trapped on the house's inner surface are not eaten. The house may also serve other functions unrelated to feeding, for example, as a device to allow detection of approaching predators or as a deterrent to gape-limited predators.

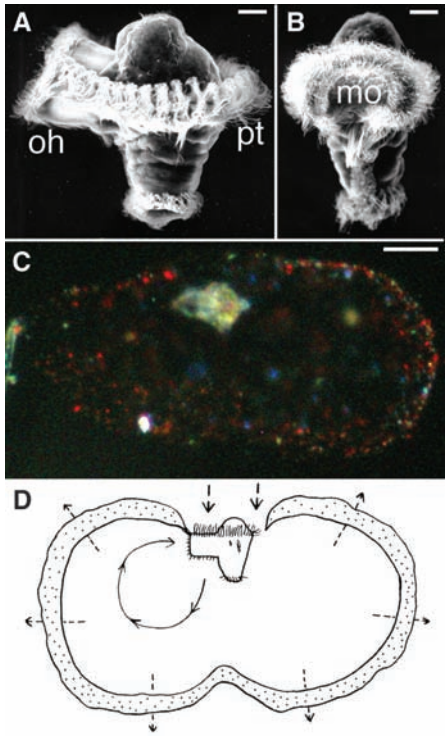

Fig. 1. Larvae of *P. californiensis* and their houses. (**A**) Scanning electron micrograph (SEM) of a larva in left-lateral view. The oral hood (oh) protrudes ventrally, and the prototrochal cilia (pt) form a ring around the larva. (**B**) SEM of a larva in ventral view, showing the mouth (mo). (**C**) A larva in its house, in left-lateral view. The inner wall of the house is labeled with carmine particles (red) and polystyrene spheres (blue). The house is tethered to a pipet visible on the left edge of the image. (**D**) A sketch of a larva in its house, in left-lateral view. The larva is attached to the house by the upper ventral edge of the hood. Flow patterns through the house are indicated by dashed arrows; a recirculating current important in feeding is indicated by a solid, arrowed line. Scale bars: (A) and (B), 25 μm; (C), 100 μm.

The houses of pectinariid larvae, like those of adult larvaceans (*2*), are so central to the lives of their inhabitants that interpretations of larval form and function made without knowledge of these external structures will often be incorrect. Filtering houses may be unique to pectinariid larvae, but the secretion of strands and sheets of transparent material has been reported in diverse marine invertebrate larvae (*1*, *5*–*7*). Though their functions are not well understood, these may act as particle traps or filters, "sea anchors" to increase shear around feeding appendages, or devices to aid in settlement to the sea floor in turbulent flow (*7*–*9*). Knowing how such structures are distributed and used is essential for an accurate understanding of the ecology and evolution of invertebrate larvae.

References and Notes

1. R. R. Strathmann, in *Reproduction of Marine Invertebrates*, A. C. Giese, J. S. Pearse, V. B. Pearse, Eds. (Blackwell Scientific, Palo Alto, CA, 1987), vol. 9, pp. 465–550.
2. P. F. Flood, D. R. Deibel, in *The Biology of Pelagic Tunicates*, Q. Bone, Ed. (Oxford Univ. Press, Oxford, 1998), pp. 105–124.
3. Materials and methods are available as supporting material on *Science* Online.
4. E. L. Brainerd, *Nature* **412**, 387 (2001).
5. P. R. G. Tranter, D. N. Nicholson, D. Kinchington, *J. Mar. Biol. Assoc. U.K.* **62**, 845 (1982).
6. W. M. Hamner, L. P. Madin, A. L. Alldredge, R. W. Gilmer, P. P. Hamner, *Limnol. Oceanogr.* **20**, 907 (1975).
7. B. Akesson, *Acta Zool.* **42**, 177 (1961).
8. R. B. Emlet, R. R. Strathmann, *Science* **228**, 1016 (1985).
9. A. Abelson, M. Denny, *Annu. Rev. Ecol. Syst.* **28**, 317 (1997).
10. I thank K. Zigler and C. Eaton for collecting adult worms, N. Ahlgren for providing *Synechococcus*, and two reviewers for helpful comments. Many colleagues offered useful advice and criticism. The director and staff of the Friday Harbor Laboratories provided laboratory space, equipment, and invaluable support.

Supporting Online Material
www.sciencemag.org/cgi/content/full/306/5702/1757/DC1
Materials and Methods
Fig. S1
Movies S1 and S2

19 August 2004; accepted 1 October 2004

Department of Biological Sciences, California State University, Long Beach, 1250 Bellflower Boulevard, Long Beach, CA 90840–3702, USA. E-mail: bpernet@csulb.edu

Detection of Methane in the Atmosphere of Mars

Vittorio Formisano,[1]* Sushil Atreya,[2] Thérèse Encrenaz,[3] Nikolai Ignatiev,[4,1] Marco Giuranna[1]

We report a detection of methane in the martian atmosphere by the Planetary Fourier Spectrometer onboard the Mars Express spacecraft. The global average methane mixing ratio is found to be 10 ± 5 parts per billion by volume (ppbv). However, the mixing ratio varies between 0 and 30 ppbv over the planet. The source of methane could be either biogenic or nonbiogenic, including past or present subsurface microorganisms, hydrothermal activity, or cometary impacts.

Methane (CH_4) is an important tracer of possible biological, internal, or atmospheric processes on Mars. The possibility of methane-producing bacteria or microorganisms on Mars has been suggested in the past (*1*, *2*). The source of methane could also be in water/rock reactions in the martian interior (*3*, *4*) or volcanic hot spots (*5*). Another possibility is external sources such as cometary impacts (*6*).

The Planetary Fourier Spectrometer (PFS) (*7*) operates in the infrared, covering a wavelength range of 1.2 to 45 μm (220 to 8190 cm^{-1}) in two spectral channels: the short wavelength (SW), from 1.2 to 5.5 μm, and the long wavelength (LW), from 5.5 to 45 μm (*8*, *9*). The spectral resolution is 1.3 cm^{-1} and the spatial resolution is ~10 km near the pericenter. Sampling is done every 1.02 cm^{-1}. Four bands of methane lie within the spectral range of the PFS, at 1300, 3000, 4400, and 6000 cm^{-1}. The 6000 cm^{-1} band is not suitable for detecting weak CH_4 signatures by the PFS because of the presence of many strong solar Fraunhofer lines and the lack of a reference solar spectrum in this region to subtract these lines. In the 4400 and 1300 cm^{-1} regions, there is some evidence of spectral signatures of minor species. However, the signal-to-noise ratio (SNR) (*10*) of the PFS is much greater in the 3000 cm^{-1} region. Therefore, we have searched for methane in this band (ν_3), centered at 3018 cm^{-1}, which is also the strongest fundamental band of methane. To increase the SNR, we first averaged data from 16 orbits obtained in January-February 2004 (*11*), covering the entire longitude range. For 16 orbits, about 100 spectra were selected in the equatorial region where a high radiance level is expected, and a total of 1680 spectra were averaged together to obtain a global spectrum (Fig. 1A). An average of 2931 spectra taken in 24 orbits during a following period in May 2004 is shown in Fig. 1B.

The electronic noise of the instrument providing a 1σ (67%) confidence level in the measurements was computed from measurements of deep space. For the SW channel of the PFS, deep space corresponds to a source of radiance intensity zero; hence it provides a measure of the instrumental noise (*10*). The noise equivalent radiance (NER) of a single spectrum at 3000 cm^{-1} is 0.01 erg/(s sr cm^2 cm^{-1}). Accordingly, the S/N ratios for our two data sets are about 1300 (Fig. 1A) and 1500 (Fig. 1B), respectively. A number of solar and water vapor lines can be identified in the spectrum. However, certain features, particularly the ones at 3006.5, 3009, and 3018 cm^{-1}, are not associated with any presently known molecules of the martian atmosphere. Figure 2, A and B, shows a comparison of the averaged data, with synthetic spectra calculated with a mean H_2O mixing ratio of 350 parts per million (ppm). With a depth of about 1% (that is, more than 10 times above the noise level), the line at 3018 cm^{-1} is significant, because it corresponds to the line position of maximum methane absorption in this wavenumber region (ν_3-Q branch). We identified this feature with methane by comparing it to a synthetic spectrum (*12*, *13*) (red curve in Fig. 2), and determined the abundance of methane in the atmosphere from the line depth. Other methane lines present in this region have been checked but are found to be less intense than the one presented here by at least a factor of 3 to 4. Many are hidden in water or solar lines. One of them, at 3028 cm^{-1}, is shown in the figures. Its behavior is similar to that of the main line at 3018 cm^{-1}; however, it is too weak for evaluating the mixing ratio, and it is also partially contaminated by water vapor lines.

At 3011 cm^{-1}, on the left side of a strong solar line, the discrepancy between the observed and synthetic spectra reflects an instrumental ("overshooting") effect that is frequently present in the PFS spectra in the red wing of single strong lines. Apart from this departure, a possible explanation for the discrepancies observed at other frequencies (3002, 3007, and 3009 cm^{-1}) is that they are due to unidentified minor molecular species. Further discrepancies can be due to (i) H_2O spectroscopic parameters or insufficient mixing ratio or (ii) surface albedo (which, in the 3000 cm^{-1} range, can be affected by mineralogic signatures of hydrated minerals). However, we believe that the identification of methane at 3018 cm^{-1} is definite, in view of the good fit of its wavenumber position.

The slope of the synthetic spectrum of the martian atmosphere (Fig. 2, A and B) indicates the presence of water ice clouds in the equatorial region of Mars. Indeed, the quality of the fits improves when such clouds are included in the synthetic spectra. In the synthetic spectra, the water ice cloud particles have an effective dimension of 1.25 μm (*14*), and optical constants from (*15*) have been used. From the direct comparison between the PFS spectra and the synthetic spectra (Fig. 2, A and B), we find that the observed line depth corresponds to a methane mixing ratio of approximately 10 parts per billion by volume (ppbv) or somewhat greater. Considering the uncertainty of the fitting with the synthetic spectrum (*10*), we derive a conservative CH_4 mixing ratio of 10 ± 5 ppbv (*16*). The synthetic calculations also show that because the individual lines are not saturated, the depth of the ν_3-Q branch should increase almost linearly with increasing mixing ratio, and this fact can be used to identify and study variations of the methane mixing ratio.

An examination of orbits with a higher air-mass factor can provide greater confidence in our analysis, because the methane line depth should increase with increasing amounts of CH_4 along the line of sight. This is possible to do because occasionally Mars Express does not point to the nadir, its normal operation mode, but at a slant angle due to its inertial attitude. This results in an increased air mass in the line of sight, which implies that the line of sight abundance of methane should also increase, whereas its mixing ratio is expected to remain unchanged. The average spectrum over 121 measurements taken during the

[1]Istituto di Fisica dello Spazio Interplanetario INAF-IFSI, Via del Fosso del Cavaliere 100, 00133 Rome, Italy. [2]Department of Atmospheric, Oceanic, and Space Sciences, University of Michigan, Ann Arbor, MI 48109–2143, USA. [3]Laboratoire d'Etudes Spatiales et d'Instrumentation en Astrophysique (LESIA), Observatoire de Paris, 5 Place Janssen, 92195 Meudon, France. [4]Space Research Institute of Russian Academy of Sciences (IKI) Profsojuznaja 84/32, 117810 Moscow, Russia.

*To whom correspondence should be addressed. E-mail: formisan@nike.ifsi.rm.cnr.it

pericenter pass of orbit 145, with an air-mass factor of 1.12, is shown in Fig. 3. Upon taking into account the air-mass factor, we obtain a methane mixing ratio of 30 ± 5 ppbv. This value is higher than the global average ratio of 10 ± 5 ppbv and indicates that the methane mixing ratio may be variable. Motivated by this possibility, we have examined several other orbits, including orbit 68, 202, and 72, for which the air-mass factors are, respectively, 1.03, 1.33, and 2.1. We discovered that orbit 72, for which the air-mass factor (2.1) was even greater than in orbit 145 (1.12), gives another extreme in CH_4. Because the number of measurements for this case (120) is close to those in orbit 145, a similar sigma value is obtained. Figure 4 gives the average PFS spectrum for orbit 72. However, there is no indication of the methane line, and the synthetic spectrum with no methane fits the data nicely. Because the synthetic spectrum fitting orbit 72 data has been computed using the same solar spectrum as we used for other fits, this indicates that the 3018 cm^{-1} line was not due to the Sun. From the four orbits 68, 145, 202, and 72, with respective air-mass factors of 1.03, 1.12, 1.33, and 2.1, methane mixing ratios of 9, 30, 30, and 0 ppbv are derived by comparing the observed methane line depth to synthetic spectra, after taking into account the air-mass factors. In the case of orbit 72, we conclude that the methane abundance is below our detectability limit: lower than 5 ppbv.

The above variation in CH_4 could represent either spatial or temporal changes or both. Because the time span of our observations (January through May 2004) is short compared to the martian year (almost 2 Earth years) and seasons (about 6 months each), the CH_4 variation mentioned above can be studied versus spatial changes. Space variations could be present because of localized sources and/or localized surface sinks. We can attempt to determine whether the spatial variations occur over a large range of longitude by dividing our original 16 orbits (or 24 orbits) into three longitudinal ranges: longitudes –55° to –170° (orbits 10, 30, 32, 41, *44*, and *202*); longitudes +52° to –55° (orbits 20, 61, 100, 103, *145*, and 148); and longitudes +52° to +190° (orbits 24, 71, *72*, and 97) (the numbers in italics represent inertial orbits) (Fig. 5). The three sets of orbits for the second group are as follows: longitudes –55° to –170° (orbits *390*, 386, 394, 397, *400*, and 401); longitudes +52° to –55° (orbits *404*, 405, *408*, *410*, 411, 426, 427, *428*, *429*, 430, and *431*); longitudes +52° to +19° (orbits *414*, *417*, 418, 420, 421, 424, and 425) (the numbers in italics represent inertial orbits). The three sets of longitudes are presented in different colors in Fig. 5.

The methane mixing ratio decreases from group 1 to group 3 (Fig. 6). The best fit is obtained for the methane mixing ratios of 25 ± 5, 15 ± 5, and 10 ± 5 ppbv, respectively, for the three longitude ranges, going from eastern longitudes to western longitudes. However, orbit 145 in group 2 has the highest mixing ratio of any individual orbit, implying that methane concentrations can be high in smaller regions within these longitudinal ranges.

Previously, an upper limit of 20 ppbv of methane was obtained by Mariner 9 (*17*), and another one of 70 ± 50 ppbv was inferred from ground-based observations (*18*). However, recently two ground-based detections of methane were reported (*19*, *20*) with a mixing ratio of 11 ± 4 ppbv (*20*), in agreement with the Mars Express PFS result for the global methane mixing ratio.

On Earth, the dominant source of methane is biogenic sources such as termites and cattle (*21*). Other sources of terrestrial methane include marshes, rice paddies, natural gas, lakes, and oceans. On Mars, methane could be derived from biogenic sources such as subsurface microorganisms (*1*) or nonbiogenic sources such as the slow release of methane stored in subsurface reservoirs, outgassing from volcanic/hydrothermal reservoirs, or the destruction of meteoritic or cometary material during infall. We estimated the global methane mixing ratio produced by each of these sources. The observed global average mixing ratio of 10 ppbv amounts to a column abundance of 2.2×10^{15} cm^{-2} CH_4 molecules at the surface of Mars. Assuming a CH_4 photochemical lifetime of $\sim 2 \times 10^{10}$ s near the surface (*5*, *23*) we estimate that a flux of $\sim 1 \times 10^5$ molecules cm^{-2} s^{-1} would be required to explain a CH_4 mixing ratio of 10 ppb on Mars (*16*). Integrated over the planet, this would amount to a methane source strength of ~4 g s^{-1}; that is, $\sim 1.26 \times 10^5$ kg $year^{-1}$ or ~126 tons $year^{-1}$.

The flux of micrometeoritic dust at Mars is estimated to be ~300 g s^{-1} or ~9000 tons $year^{-1}$ (*24*). Most of it would burn up in the atmosphere, but allowing for a generous 25% surviving to the surface (*24*), nearly 2300 tons $year^{-1}$ could reach the surface of Mars. If all of the micrometeoritic dust is assumed to be from carbonaceous chondrites, then organic materials would comprise about 3% of the flux (*25*): ~70 tons $year^{-1}$. If all of the organic materials could be converted to methane, then micrometeoritic sources of methane would be roughly comparable to that needed to explain

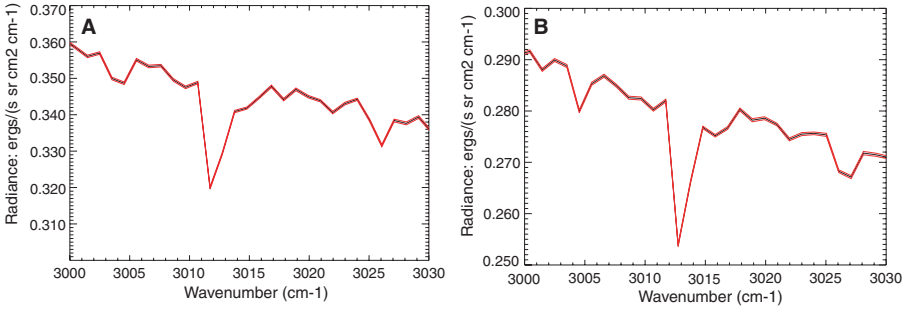

Fig. 1. (**A**) A portion of the first averaged PFS spectrum (January-February 2004, black curve), with ±1σ confidence (red lines). The SNR is about 1300. Methane is identified at 3018 cm^{-1}. There are three water lines (at 3003.5, 3022, and 3026 cm^{-1}) and two solar lines (at 3012 and 3014 cm^{-1}). The continuum slope is due to water ice clouds in the atmosphere. The small peak at the left of the main solar line is due to instrumental response function. (**B**) The second averaged PFS spectrum (May 2004) in the same frequency interval. The caption is the same as for (A). The SNR is about 1500.

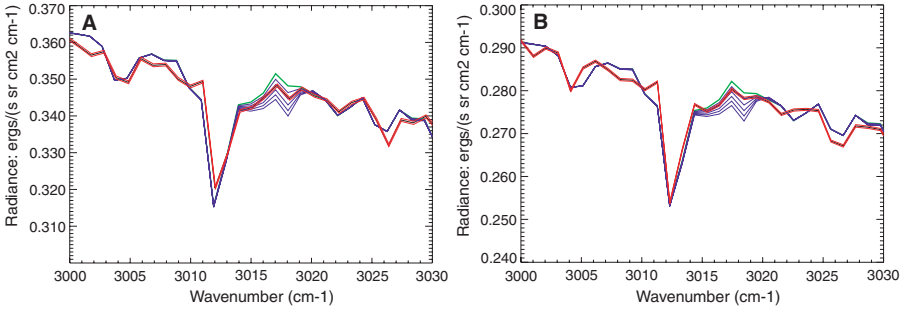

Fig. 2. (**A**) Synthetic spectra computed for 0 ppbv (green curve) and 10, 20, 30, 40, and 50 ppbv (violet curves) of methane, compared with the PFS average spectrum (black curve). The synthetic spectra have been computed for 6.7 millibars of CO_2, including 350 ppm of H_2O, along with dust and water ice clouds. The temperature profile obtained from simultaneous measurements in the thermal radiation was used. (**B**) Same as (A), with the PFS mean spectrum shown in Fig. 1B.

the 10 ppbv measured with the PFS. However, the estimated necessary micrometeoritic source of methane is much greater than what could realistically be produced, because carbonaceous chondritic material is not representative of most meteorites, which are actually depleted in carbon, and whatever organics enter the martian atmosphere would most likely not be converted to methane in the planet's oxidizing environment.

Comets are potentially the largest exogenous source of methane at Mars. From observations of eight Oort cloud comets (*26*), we conclude that the CH_4/H_2O mixing ratio lies in the 0.15 to 1.5% range, with most comets showing >0.5% and one as high as 2.3%. For our estimate, we assume a cometary CH_4 value of 1% and that most of the mass of the comet consists of water ice. Taking an average impact rate of 1.6×10^{-8} year^{-1} for the ecliptic comets at Mars (*27*) and a typical cometary radius of 1 km, the amount of methane delivered to Mars by the comets would be on the order of 1 ton year^{-1} on average; that is, less than 1% of that needed to maintain a steady-state mixing ratio of 10 ppbv of methane on Mars. Because the lifetime of methane is only a few hundred years, the "average" flux from the comets is not a very meaningful quantity, considering the above rate of one impact every 62 million years. We have therefore considered the possibility that the methane on Mars is constantly declining and that the quantity measured today may simply be a relic of a cometary impact that occurred in the past several hundred to thousands of years. We have calculated the size of that comet, with the constraint that the impactor supplied enough methane (about three times the current abundance if the impact occurred one methane lifetime ago) that 2.2×10^{15} cm^{-2} CH_4 molecules (10 ppbv) remain today on Mars. Our calculations (*28*) show that this requires an impact by a comet with a radius ranging from as small as ~130 m, which struck Mars as recently as 100 years ago, to a radius as large as ~360 m, which struck it as long ago as 2000 years. The observed variability of methane over Mars may favor a recent impact, younger than one methane lifetime, unless some localized surface sinks are present to effciently scavenge methane from the atmosphere. It is not presently known whether a single impact event of this type did actually take place, but it appears promising enough to warrant further investigation.

On the other hand, methane could have been formed by magmatic processes or stored in methane hydrates for later release to the atmosphere. Terrestrial volcanoes are not a big source of methane, and large-scale volcanism has not taken place on Mars for over 100 million years. However, small-scale outgassing of methane cannot be ruled out. A potentially larger source of methane than volcanism may come from the alteration of basalt at a temperature <150°C, a process that also results in the wet-phase conversion of original CO_2 into CH_4 in a subpermafrost aquifer. In their chemical equilibrium computer model, Wallendahl *et al*. (*3*) calculate that as much as 0.2 bar, or ~10^{15} tons, of CH_4 could have been produced if the only source of C in this region was the CO_2 initially present in the crustal pores. Methane could have been sequestered in stable methane hydrate and gradually risen to the planet's surface (*4*). The rate of release to the atmosphere is unknown, but if one assumes that leaking has been taking place at a uniform rate over time, it would amount to ~200,000 tons year^{-1}, which is much greater than the 100 tons or so per year needed to maintain a steady-state mixing ratio of 10 ppbv of CH_4 on Mars today. Even if methane from the hydrate is being released at a rate that is a factor of 1000 slower, it would still be sufficient to account for the observations. Finally, recent laboratory experiments confirm abiogenic generation of methane in mineral-catalyzed hydrothermal reactions of CO_2 and H_2O at 390°C and 400 bars (*29*),

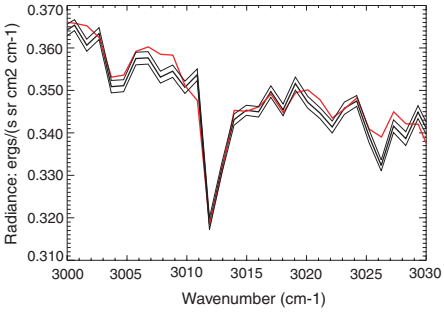

Fig. 3. Average of 121 PFS spectra (black curve) and synthetic spectra with 35 ppbv of methane (red line) for orbit 145 of Mars Express (inertial attitude). The error on the measurements is shown as ±1σ confidence lines. The water vapor mixing ratio used for the synthetic spectrum is 600 ppmv.

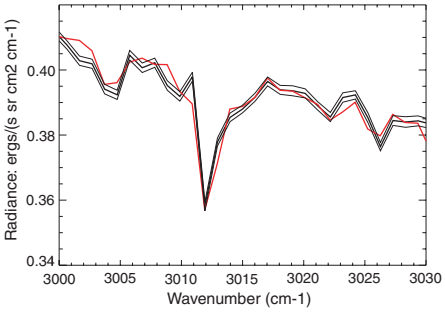

Fig. 4. Average PFS spectrum (black curve) for orbit 72 of Mars Express (inertial attitude, airmass factor 2.1). The error on the measurements is shown as ±1σ confidence lines. The PFS spectrum is an average over 120 measurements. A synthetic spectrum with 0 ppbv is shown, in good agreement with the measurements. The water mixing ratio is 400 ppb.

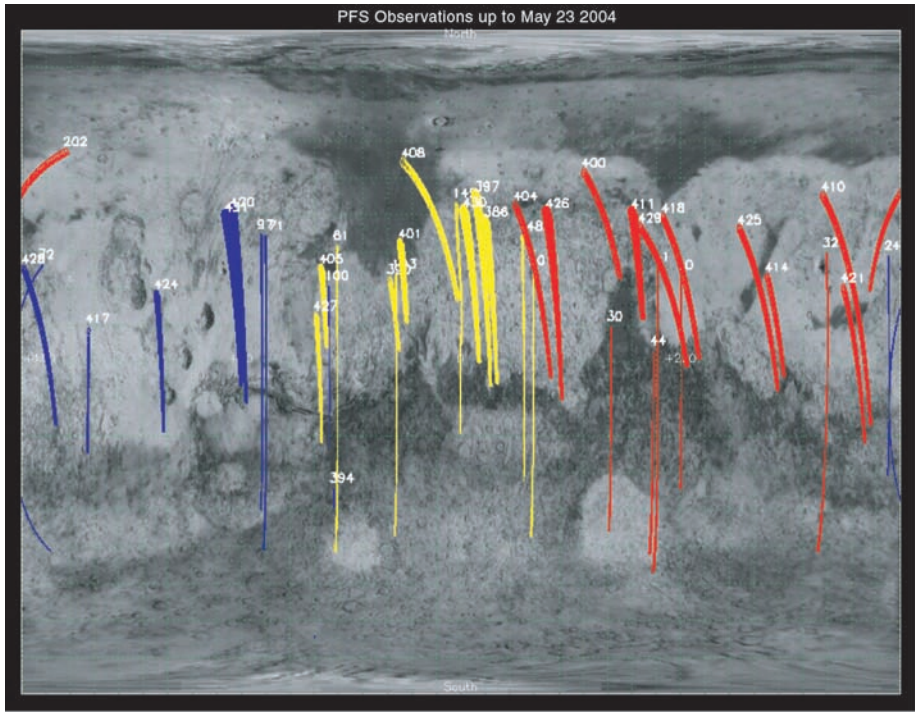

Fig. 5. Geographical distribution of the orbits considered: red (high methane mixing ratio), yellow (medium methane mixing ratio), and blue (low methane mixing ratio). Strong fluctuations occur in each of the three categories, indicating the possible presence of localized sources.

conditions that are likely to be encountered in subpermafrost aquifers or deep under the polar ice on Mars. Moreover, the catalyst used in the experiment—Fe-Cr oxide—is also believed to be present in the martian rocks.

If the source is biogenic and current, methanogens that use CO or H_2 for energy are candidate sources. Chemolithotrophic microbial ecosystems are common deep in Earth's subsurface, and they release methane as a product of metabolism, as in $4CO + 2H_2O \rightarrow CH_4 + 3CO_2$, and $4H_2 + CO_2 \rightarrow CH_4 + 2H_2O$ (*30*–*32*). There exists a distinct possibility that in the subpermafrost aquifer environment of Mars, one or several microbial colonies may exist, where microorganisms utilize CO and/or H_2 and produce methane in turn (*1*, *2*). The martian atmosphere provides a ready source of CO [~700 ppm (*33*)] and H_2 [40 to 50 ppm of H_2, based on models and observations (*34*–*37*)]. These gases are expected to diffuse through the regolith to the subsurface aquifers. Abundant H_2 may also be made available locally via the hydration of ultramafic silicates. It has been suggested that the source of methane need not be current. If microorganisms existed on Mars only in the past during its (possible) warm and wet phase and produced methane, that methane could have been stored in methane hydrates for later release, as discussed above. A comparison of the CH_4 source strength at Mars (4 g s^{-1}) with that on Earth [1.67×10^7 g s^{-1}(*38*)] indicates that if methane on Mars is microbial in origin, the microbe population must be tiny. This is because nearly all of the 1700 ppbv of CH_4 in Earth's atmosphere has its ultimate origin in living things, and the martian source pales in comparison. It is important to point out that if microorganisms are or were present on Mars, the subpermafrost region is their most likely abode, because the presence of hydrogen peroxide, intense ultraviolet (UV) radiation, and the low temperature and low pressure at the surface of Mars would render the surface hostile to life as we know it.

Finally, the relatively long lifetime of CH_4 implies that the CH_4 distribution is expected to be uniform over the planet once a steady state is reached. The observed nonuniform distribution of CH_4 is indicative of either localized source(s) or localized sink(s), or both. Diffusion of CH_4 through the regolith into the interior of Mars is a distinct possibility. The surface loss could result in a nonuniform distribution of methane on Mars only if the process is more efficient than the time it takes for methane to become uniform, which is on the order of a few weeks or faster in the martian atmosphere. If the local surface sink, such as a sink due to varying mineralogy including surface oxidants, is not as rapid, a cometary source for methane on Mars would be less viable. We want to stress that the detection of methane does not imply the presence of life on Mars, now or in the past. It is one possibility, but as shown above, other sources are at least as plausible (*39*).

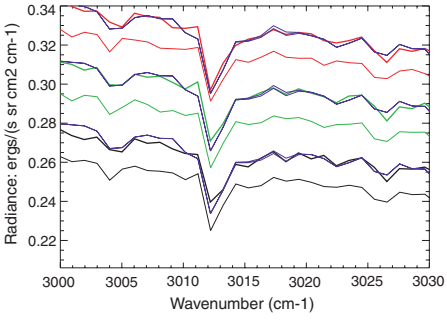

Fig. 6. Methane variation with longitude. Average PFS spectra for the January period (thick lines) and for the May period (thin lines) are shown. Curves have been vertically displaced for clarity. Corresponding SNRs range between 900 and 1040. For the 55° to 170° longitude case of January (thick black line), synthetic spectra with 20 and 30 ppbv of CH_4 are shown. The best fit result is 25 ± 5 ppbv of CH_4. Similarly, for the green curve, synthetic spectra with 10 and 20 ppbv of CH_4 are shown, and the best fit is with 15 ± 5 ppbv of CH_4. The red curve is shown with the 0 and 10 ppbv synthetic spectrum; the best fit is with slightly less than 10 ppbv of methane. The thin curves (spectra obtained in May) show the same behavior; fits are omitted for clarity.

References and Notes

1. P. J. Boston, M. V. Ivanov, C. P. McKay, *Icarus* **95**, 300 (1992).
2. B. P. Weiss, Y. L. Yung, K. H. Nealson, *Pub. Natl. Acad. Sci.* **97**, 1395 (2000).
3. A. Wallendahl, A. H. Triemann, *Lunar Planet. Sci. Conf.* **XXX**, abstract 1268 (1999).
4. M. D. Max, S. M. Clifford, *J. Geophys. Res.* **105**, 4165 (2000).
5. A. S. Wong, S. K. Atreya, Th. Encrenaz, *J. Geophys. Res.* **108**, 5026 (2003).
6. M. E. Kress, C. P. McKay, *Icarus* **168**, 475 (2004).
7. The Mars Express spacecraft was launched on 2 June 2003, attained orbit around Mars on 25 December 2003, and since February 2004 has been in a polar orbit of 87° inclination, with a pericenter altitude of ~250 km and an orbital period of 7.2 hours. The PFS is one of the seven experiments on board. The primary science objectives of the PFS are as follows: monitoring of a three-dimensional temperature field and spatial and temporal variations of H_2O and CO, characterization of aerosols and clouds, and identification of trace species. Surface temperatures and spectral information about the composition of soil and polar deposits are also obtained.
8. V. Formisano, in preparation.
9. M. Giuranna, in preparation.
10. See the discussion on the SNR and NER in the supporting online material (SOM).
11. The data cover the period from January 2004 through early February 2004 (areocentric longitude of the Sun = 330° to 350°) and the May 2004 period. This period is long compared with the average transport period in the atmosphere (less than 1 week for global dust storms), and it is short with respect to the martian year and a martian season.
12. See the discussion in the SOM on the computation of synthetic spectra.
13. N. I. Ignatiev, in preparation.
14. R. T. Clancy, M. J. Wolff, P. R. Christensen, *J. Geophys. Res.* **108**, 2-1 (2003).
15. S. G. Warren, *Appl. Opt.* **23**, 1206 (1984).
16. See SOM-1 for the definition of global average methane mixing ratio.
17. W. C. Maguire, *Icarus* **32**, 85 (1977).
18. V. A. Krasnopolsky, G. L. Bjoraker, M. J. Mumma, D. E. Jennings, *J. Geophys. Res.* **102**, 6525 (1997).
19. M. J. Mumma, R. E. Novak, M. A. DiSanti, B. P. Bonev, "A sensitive search for methane on Mars," paper presented at the American Association of Science, Division of Planetary Science Meeting, Monterey, CA, September 2003.
20. V. A. Krasnopolsky, J. P. Maillard, T. C. Owen, abstract, European Geosciences Union Meeting, Nice, France, 26 April 2004.
21. E. A. Paul, F. E. Clark, *Soil Microbiology and Biochemistry* (Academic Press, San Diego, CA, 1996).
22. The CH_4 lifetime used in the calculations (~2×10^{10} s near the surface) is taken from (*5*). It also agrees with the value for the lower atmosphere shown in figure 2 of (*39*). Because the photochemical loss of CH_4 is due to oxidation by OH and $O(^1D)$ near the surface and by solar UV above ~70 km, its lifetime can vary depending on the solar UV flux and the actual atmospheric water vapor and ozone distributions. The lifetime used in our calculations is based on average solar and martian conditions (150 ppm of H_2O at the surface), and it represents an e-folding time, or the time over which the concentration drops by a factor of exp(1) or 2.7, not by a factor of 2. For a methane lifetime that is shorter by a factor of 2, the required methane flux would be roughly twice as large.
23. A. S. Wong, S. K. Atreya, V. Formisano, Th. Encrenaz, N. Ignatiev, *Adv. Space Res.* **33**, 2236 (2004).
24. G. Flynn, *Earth Moon Planets* **72**, 469 (1996).
25. J. R. Cronin, S. Pizzarello, D. P. Cruikshank, in *Meteorites and the Early Solar System*, J. J. Kerridge, M. S. Matthews, Eds. (Univ. of Arizona Press, Tucson, AZ, 1988), pp. 819–857.
26. E. L. Gibb, M. J. Mumma, N. Dello Russo, M. A. DiSanti, K. Magee-Sauer, *Icarus* **165**, 391 (2003).
27. H. F. Levison, M. J. Duncan, K. Zahnle, M. Holman, L. Dones, *Icarus* **143**, 415 (2000).
28. See the computation in the SOM.
29. D. I. Foustouskos, W. E. Seyfried, *Science* **304**, 1002 (2004).
30. F. H. Chapelle *et al.*, *Nature* **415**, 312 (2002).
31. T. O. Stevens, J. P. McKinley, *Science* **270**, 450 (1995).
32. R. J. Parkes *et al.*, *Nature* **371**, 410 (1994).
33. E. Lellouch, G. Paubert, T. Encrenaz, *Planet. Space Sci.* **39**, 219 (1991).
34. S. K. Atreya, *J. Geophys. Res.* **99**, 13133 (1994).
35. S. K. Atreya, Z. G. Gu, *Adv. Space Res.* **16**, 57 (1995).
36. H. Nair, M. Allen, A. D. Anbar, Y. L. Yung, R. T. Clancy, *Icarus* **111**, 124 (1994).
37. V. Krasnopolsky, M. Mumma, R. G. Gladstone, *Science* **280**, 1576 (1998).
38. Y.-L. Yung, W. B. DeMore, *Photochemistry of Planetary Atmospheres* (Oxford Univ. Press, Oxford, 1999).
39. M. E. Summers, B. J. Lieb, E. Chapman, Y. L. Yung, *Geophys. Res. Lett.* **29**, 2171 (2002).

40. The PFS was built at the Istituto di Fisica dello Spazio Interplanetario of the Istituto Nazionale di Astrofisica, and the investigation is being funded by the Italian Space Agency (ASI) in the context of the Italian participation in the Mars Express mission of the European Space Agency. S.A. acknowledges support from NASA/Jet Propulsion Laboratory for participation in the Mars Express project. We are grateful to V. Cottini for a number of synthetic spectra computations and to A. Maturilli for the mapping figure.

Supporting Online Material

www.sciencemag.org/cgi/content/full/1101732/DC1
SOM Text
Figs. S1 and S2
References and Notes

21 June 2004; accepted 18 October 2004
Published online 28 October 2004;
10.1126/science.1101732
Include this information when citing this paper.

Abrupt Temperature Changes in the Western Mediterranean over the Past 250,000 Years

Belen Martrat,[1] Joan O. Grimalt,[1]* Constancia Lopez-Martinez,[1] Isabel Cacho,[1,2] Francisco J. Sierro,[3] Jose Abel Flores,[3] Rainer Zahn,[2] Miquel Canals,[2] Jason H. Curtis,[4] David A. Hodell[4]

A continuous high-resolution Western Mediterranean sea surface temperature (SST) alkenone record spanning the past 250,000 years shows that abrupt changes were more common at warming than at cooling. During marine isotope stage (MIS) 6, SST oscillated following a stadial-interstadial pattern but at lower intensities and rates of change than in the Dansgaard/Oeschger events of MIS 3. Some of the most prominent events occurred over MISs 5 and 7, after prolonged warm periods of high stability. Climate during the whole period was predominantly maintained in interglacial-interstadial conditions, whereas the duration of stadials was much shorter.

Northern Hemisphere submillennial-scale climate variations during the last glacial have been documented in Greenland ice (*1–3*), marine and continental sediments (*4–14*), and stalagmites (*15*, *16*). Some of these records also suggest that high-frequency climate variability was not restricted to this period (*6–7*, *10–14*, *16*). However, because of the lack of high-resolution marine data, very little is known about the climate history of the penultimate glacial. The deepest sections of the Greenland ice cores that cover this time interval are distorted by basal deformation (*2*, *3*). The sediments from site 977A, leg 161 of the Ocean Drilling Program (ODP), examined in this study at a time resolution of 386 ± 131 years for the past 250 thousand years (ky) may help provide better understanding of millennial scale variability over those periods.

Core ODP-977A was retrieved from the eastern subbasin of the Alboran Sea (Fig. 1). The $\delta^{18}O$ record of *Globigerina bulloides* displays a well-defined orbital modulation of glacial and interglacial marine isotope stages (MISs) (*17*, *18*) (Fig. 2, A and B). Between 80 and 11.5 thousand years ago (ka) it also shows remarkable consistency with the Dansgaard/Oeschger (D/O) cycles observed in Greenland $\delta^{18}O$ profiles (*1–3*) (Fig. 2H). Over the past 250 ky before the present, sea surface temperature (SST) derived from the $U^{k'}_{37}$ alkenone index (Fig. 2D) displays characteristic sequences of rapid warming and cooling events, here labeled as Alboran interstadials (AI-1 to AI-26 and AI-1′ to AI-15′ for the last and penultimate climate cycles, respectively) and stadials (AS-1 to AS-26 and AS-1′ to AS-15′, respectively) (*19*, *20*). Most SST changes occurred simultaneously with the variations in the $\delta^{18}O$ record of *G. bulloides*. Thus, temporal offsets due to dissimilar sedimentation processes between coccolithophores and foraminifera (*21*) appear not to be important at this site. The section between 50 and 0 ka displays SST variability similar to that in core MD95-2043, analyzed in a previous study (*8*). Parallel changes, both in terms of frequency and amplitude, have been observed during the last climate cycle from lower to higher latitudes in the Northern Hemisphere (*5*, *9*, *10*, *22*, *23*), suggesting that ODP site 977A may provide representative SST patterns on a broad regional scale.

During MIS 3, SST varied by up to 6°C within less than 1 ky after the abrupt D/O events in Greeland Ice Core Project (GRIP) (Fig. 2, D and H). Technically, abrupt climate changes occur when the climate system is forced to cross a threshold, triggering a transition into a new climate condition at a rate faster than the cause (*24*). The magnitude of the change caused by system feedbacks often appears as large as or larger than that due to the major direct climate forcings (*25*). From a more operational standpoint, paleoclimatic changes in marine systems can be compared to SST variation over the last deglaciation, i.e., an average warming of 2.6°C/ky in core ODP-977A [7.5°C in 2.9 ky (table S1)]. Thus, in the present study, abrupt SST change refers to warming or cooling episodes that happened at a rate equal to or faster than the average. Evaluation of SST during MISs 2 to 4 under this criterion shows twice as many abrupt warmings as cooling episodes (Fig. 2D). Uncertainties associated with core sampling or age modeling could lead to some variation in the absolute number of these abrupt SST changes, but the higher number of abrupt warming events is a robust feature. $\delta^{18}O$ in Greenland ice cores also shows a characteristic pattern of abrupt warming followed by gradual cooling (*1–3*).

Six SST minima in core ODP-977A [AS-2a, 2c, 5, 9, 13, and 18 (Fig. 2D)] are concurrent with the periods of massive iceberg

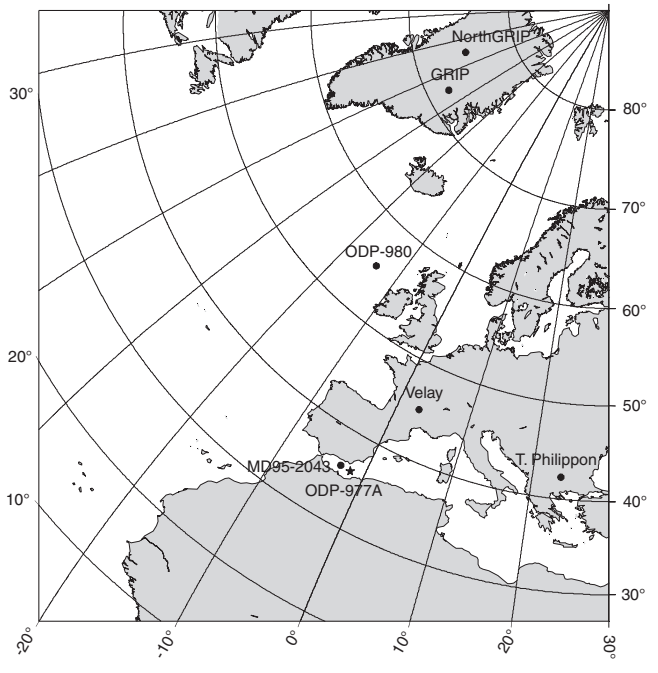

Fig. 1. Map showing the location of core ODP site 977A in the Alboran Sea. The locations of other paleoclimate sites mentioned in the text are also shown. MD95-2043 (*8*) and GRIP (*1*) were used for the age model for the past 80 ky (*17*). The Velay and the Tenaghi Philippon long pollen sequences (*13*, *14*) document the terrestrial response to climate at a time resolution of millennia. Also, the location of core ODP site 980 is indicated as an excellent archive of catastrophic iceberg discharges (*6*).

[1]Department of Environmental Chemistry Institut d'Investigacions Quimiques i Ambientals de Barcelona–Consell Superior d'Investigacions Cientifiques (CSIC), 08034-Barcelona, Spain. [2]Department of Stratigraphy, Paleontology, and Marine Geosciences, University of Barcelona, 08028-Barcelona, Spain. [3]Department of Geology, University of Salamanca, 37008-Salamanca, Spain. [4]Department of Geological Sciences, University of Florida, Gainesville, FL 32611–2120, USA.

*To whom correspondence should be addressed. E-mail: jgoqam@cid.csic.es

production and melting called Heinrich events (HEs), which lead to the deposition in the Atlantic Ocean of sediment layers dominated by detritic particles larger than 150 μm (*4*, *26*). The abrupt changes associated with HEs were also more common in increases than in decreases of SST, for example, three warmings (AS-2a ≈ H1, AS-9 ≈ H4, and AS-13 ≈ H5) and one cooling [AS-2c ≈ H2 (Fig. 2D and table S1)]. The Heinrich layers are found in the open North Atlantic (*4*, *6*) (Fig. 2G), the Nordic seas (*5*), and the western Iberian margin (*11*, *27*), but there is no evidence of transportation of ice-rafted detritus (IRD) into the Mediterranean Sea. In the Alboran Sea, the SST drops associated with HE show coeval increases in the relative proportion of the polar planktonic foraminifera *Neogloboquadrina pachyderma* (sinistral) to total foraminifera (*8*, *28*) and in the relative proportion of the tetraunsaturated C_{37} alkenone homolog, $C_{37:4}$, to total C_{37} alkenones (Fig. 2C). Increased abundance in $C_{37:4}$ is consistent with a previous study from the western Iberian margin showing that this compound indicates an influence of low-salinity water masses during such events (*29*). In this respect, the two SST drops between 25 and 20 ka in core ODP-977A, AS-2c, and AS-3 [which coincide with GS-2c and GS-3 in GRIP, respectively (Fig. 2, D and H)] can be differentiated by the $C_{37:4}$ content. Both cooling events were also observed off the west Iberian coast, and only the AS-2c was correlated with increased IRD (*29*). Thus, the AS-3 event, the lowest SST value of the whole ODP-977A record, is not related to a HE but corresponds to a well-defined $\delta^{18}O$ minimum in GRIP. The similarity between SST values in ODP-977A and GRIP points to a teleconnection between high and midlatitudes in the Northern Hemisphere that is unrelated to iceberg discharges.

Although less frequent than during MIS 2 to 4, millennial-scale variability over MIS 6 is also observed in core ODP-977A. In MIS 6 only three SST changes can be considered as abrupt, involving two warming events

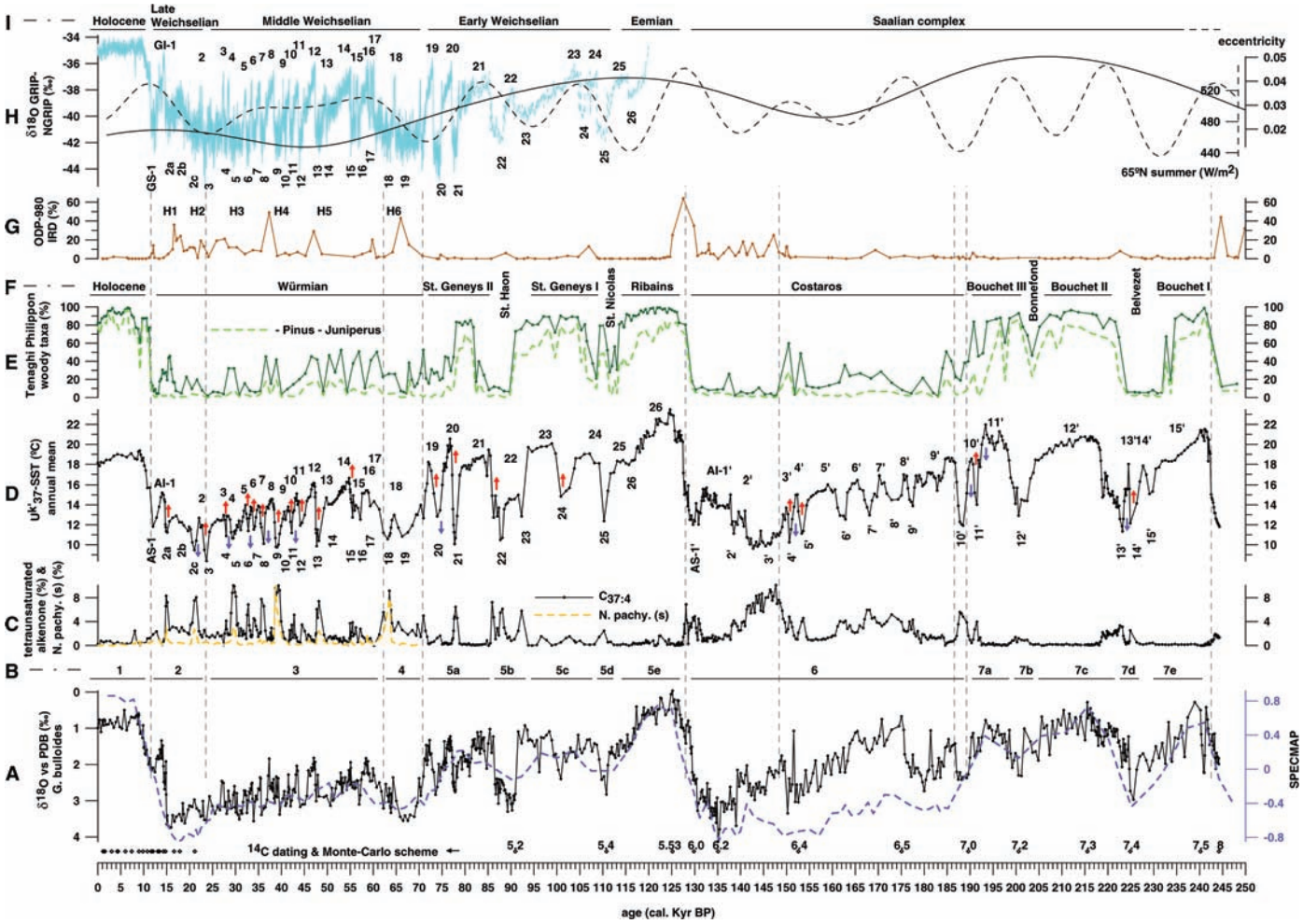

Fig. 2. Paleoenvironmental records of the last two interglacial-to-glacial cycles. (**A**) $\delta^{18}O$ of *G. bulloides* in ODP-977A (*17*) compared with the SPECMAP standard isotope curve (*18*), which is shown by the dotted line. Diamonds show some of the control points used for the age model (*17*). (**B**) Glacial (2 to 4 and 6) and interglacial (1, 5, and 7) MISs. (**C**) Relative proportion of heptatriatetraenone to total alkenones. This biomarker may be used as a tracer of cold and/or low salinity waters at the Iberian margin (*29*). The percentage of *N. pachyderma* sinistral is also plotted for reference (*28*). (**D**) SST in ODP-977A (*17*). Twenty-six interstadials (AI-1 to 26) and stadials (AS-1 to 26) have been identified over the last climate cycle. The penultimate climate cycle exhibits 15 warm (AI-1′ to 15′) and 15 cold (AS-1′ to 15′) spells that are labeled following the scheme recommended by the INTIMATE group (*20*). Abrupt changes are defined as warming (red arrows) or cooling (blue arrows) episodes that happen at a rate equal to or faster than the SST variation over the last deglaciation (2.6°C/ky) (table S1). (**E**) Tenaghi Philippon woody taxa, in addition to the temperate pollen curve shown by the dotted thick line, which excludes *Pinus* and *Juniperus* (*13*). (**F**) The Velay pollen sequence stratigraphy (*14*). (**G**) The relative proportion of detrital lithics (IRD) recorded at 55°N in the North Atlantic sediments (*6*). (**H**) The $\delta^{18}O$ in GRIP and NGRIP with the isotopically defined Greenland interstadials (GI) on the top and the subsequent Greenland stadials (GS) on the bottom (*1*, *3*). The eccentricity of the Earth's orbit and the daily insolation at 65°N during the summer solstice are also shown (*36*). (**I**) The widely used northwest European terminology.

(AI-4′ and AI-3′) and one cooling event [AS-4′, 155 to 150 ka (Fig. 2D and table S1)]. These changes registered drops in SST as severe as those coinciding with HEs during MIS 3 and were concurrent with prominent increases of up to 60% in arboreal pollen documented in the Tenaghi Philippon profile (*13*) [mainly *Pinus* and *Juniperus* (Fig. 2E)]. This sequence of events was followed by a prolonged cold episode that went along with the dominance of low-salinity surface waters as displayed by increased percentages of $C_{37:4}$ [AS-3′, 149 to 141 ka (Fig. 2, C and D)]. Toward the end of MIS 6, IRD intervals were identified in the northeast Atlantic (*6*, *30*) and the Labrador Sea (*31*). However, at the Iberian margin these events were less intense than those of the last glacial and uniquely European in origin (*11*). As discussed below, this result points to a spatial configuration in the frontal zones during the penultimate glacial that differs greatly from that of the last glacial (*32*).

One of the largest SST changes observed in the entire record occurred at the end of MIS 5 and involved an abrupt warming of 10.5°C in 1 ky and a subsequent cooling by –7.7°C in 2.8 ky [from AS-21 to AI-20 (table S1)]. This abrupt SST change was preceded by a prominent cooling (–9.4°C) after a long period of stability at warm SSTs (AI-21). Similar transitions are observed throughout MISs 5 and 7 (Fig. 2D). In four cases, these cooling transitions were abrupt (AI-20, 10′, 11′, and 13′; between –2.8 and –5.1°C/ky), whereas six abrupt warming transitions back to previous high SSTs were observed [AS-20, 21, 22, 24, 11′, and 14′; between 2.6 and 15.6°C/ky (table S1)]. The record from ODP-977A shows that major SST changes occurred within a few centuries and were often of larger magnitude than those in the glacial periods and comparable in amplitude to the glacial-to-interglacial warming. SST variability was associated with large shifts in mean annual air temperature and moisture as reflected in vegetational changes around the Mediterranean (*13*, *14*), for example, St. Nicolas, Bonnefond, and Belvezet stadials (Fig. 2, E and F). One of the most extreme events, AS-22, is coincident with one of the longest cold phases in Southern European pollen sequences, St. Haon (*13*, *14*), and in line with the maximum extension of the Barents-Kara and Scandinavian ice sheets at the Early Weichselian (*33*). This ice increase blocked the drainage of northeast European rivers owing to large proglacial lakes caused by strong regional summer cooling (*34*). During MISs 5 and 7, the iceberg discharges were drastically diminished (*6*) (Fig. 2G), which is most likely related to the scarcity of continental ice near the North Atlantic. Thus, even in the absence of large ice sheets (*6*) and major sea level fluctuations (*35*), dramatic shifts in the climate occurred, indicating that episodic abrupt change is a fundamental aspect of Pleistocene climate (*6*). High amplitude SST variability during these relatively warm and largely ice-free periods disqualifies catastrophic meltwater discharge events as a driving force of these oscillations.

An abrupt change requires a trigger, an amplifier, a source of persistence, and a globalizer (*24*). In core ODP-977A, the higher number of abrupt events during MISs 2 to 4 compared with that in MIS 6 parallel the lower amplitude of the eccentricity of the Earth's orbit and the irradiance variations at high northern latitudes in summer (*36*) in the former but not in the latter period (Fig. 2, D and H). During MIS 2 to 4, a long-term lack of seasonal contrast enhanced the role of sea or land ice and the resulting southward displacement of frontal zones (*32*), bringing about more frequent arrivals of polar climate conditions at the latitude of study. The sensitivity of climate to change was less during MIS 6. It is highly probable that changes in thermohaline circulation were influential in causing persistent SST variability over these glacial stages. In the North Atlantic, differential solar heating between high and low latitudes tends to accelerate surface waters polewards, whereas freshwater input to high latitudes, together with low-latitude evaporation, tend to restrain this flow (*37*). Data and models both suggest that, in response to small changes in the hydrological cycle, the Atlantic meridional overturning circulation and the formation of North Atlantic Deep Water (NADW) contributed to sustaining rapid climate change during the last glaciation (*5*, *37*–*39*). Ocean convection sites of NADW formation jumped between the Nordic seas and an area to the south of the Icelandic sill (*39*). Additionally, observational evidence and simulated climate conditions (*8*, *16*, *22*, *23*, *40*, *41*) point to preponderant atmospheric mechanisms interacting with the oceanic mixed layer (e.g., strength of westerly, trade, or monsoon winds or southward migration of the Intertropical Convergence Zone) for the amplification and transmission of the D/O signal observed during the last glacial.

MISs 5 and 7 show continued stability in SST for long periods, for example, 10 ky, evolving rarely although dramatically to glacial conditions and, over a period of 1 to 2 ky, moving abruptly back to warm SST. During these periods, the eccentricity of the Earth's orbit and the seasonal contrast were more pronounced than in MISs 2 to 4 and MIS 6. These conditions and the strength of the NADW formation could have buffered development of the abrupt changes sustained by hydrological instability. Predictable orbital variations led to insolation changes, which triggered less frequent but very intense oscillations. Accordingly, the last glacial inception (substage 5d) has been attributed to a connection between orbital forcing and thermohaline circulation beyond a freshwater threshold within the ocean-atmosphere-sea-ice system (*42*, *43*).

If duration may be taken as a reference for stability, the ODP-977A record shows that the climate has been predominantly in interglacial-interstadial conditions over the past 250,000 years. The repeated saw-tooth morphology of recorded oscillations calls for strong positive feedback mechanisms to accelerate warming once the threshold is reached and the flip is triggered from one condition to another. Consequently, cold stadials were periods of only limited duration, immediately followed by well-defined returns to more warmth. In this respect, the Holocene shows a stable SST trend similar to those in previous interstadial stages, tending toward progressively cooler climate conditions in accordance with the slow decrease in summer insolation in the Northern Hemisphere and the minimal eccentricity of the Earth's orbit. Within the framework of ODP-977A data, this orbital configuration suggests that the present warm period could be more prone to abrupt oscillations than MISs 5 and 7. In turn, the next bifurcation of the climate system may appear as an extremely intense cooling if the future natural climate is going to develop as an analog of some of the preceding warm periods.

References and Notes

1. W. Dansgaard *et al.*, *Nature* **364**, 218 (1993).
2. P. M. Grootes, M. Stuiver, J. W. C. White, S. J. Johnsen, J. Jouzel, *Nature* **366**, 552 (1993).
3. North Greenland Ice Core Project members, *Nature* **431**, 147 (2004).
4. G. C. Bond *et al.*, *Nature* **365**, 143 (1993).
5. T. M. Dokken, E. Jansen, *Nature* **401**, 458 (1999).
6. J. F. McManus, D. W. Oppo, J. L. Cullen, *Science* **283**, 971 (1999).
7. J. F. McManus *et al.*, *Nature* **371**, 326 (1994).
8. I. Cacho *et al.*, *Paleoceanography* **14**, 698 (1999).
9. J. P. Sachs, S. J. Lehman, *Science* **286**, 756 (1999).
10. D. Pailler, E. Bard, *Palaeogeogr. Palaeoclimatol. Palaeoecol.* **181**, 431 (2002).
11. L. de Abreu, N. J. Shackleton, J. Schonfeld, M. A. Hall, M. Chapman, *Mar. Geol.* **196**, 1 (2003).
12. J. R. M. Allen *et al.*, *Nature* **400**, 740 (1999).
13. P. C. Tzedakis, J. F. McManus, H. Hooghiemstra, D. W. Oppo, T. A. Wijmstra, *Earth Planet. Sci. Lett.* **212**, 197 (2003).
14. M. Reille, J. L. de Beaulieu, H. Svobodova, V. Andrieu-Ponel, C. Goeury, *J. Quat. Sci.* **15**, 665 (2000).
15. D. Genty *et al.*, *Nature* **421**, 833 (2003).
16. M. Bar-Matthews, A. Ayalon, M. Gilmour, A. Matthews, C. J. Hawkesworth, *Geochim. Cosmochim. Acta* **67**, 3181 (2003).
17. Materials and methods are available as supporting material on *Science* Online.
18. D. G. Martinson *et al.*, *Quat. Res.* **27**, 1 (1987).
19. In continental studies, warming stages of limited duration are referred to as interstadials, whereas short-term cooling stages are known as stadials. The differentiation between interglacials and interstadials is only a matter of intensity and duration. Over the past 250,000 years, only the marine isotope substage 5e (Eemian) is clearly of an interglacial nature. To date, there is no general agreement in considering which of the marine isotope warm units (7a, 7c, and 7e) should be classed as interglacial and which as interstadial. In this study, all warm periods are referred to as interstadials.

20. M. J. C. Walker *et al.*, *Quat. Sci. Rev.* **18**, 1143 (1999).
21. N. Ohkouchi, T. I. Eglinton, L. D. Keigwin, J. M. Hayes, *Science* **298**, 1224 (2002); published online 10 October 2002 (10.1126/science.1075287).
22. L. C. Peterson, G. H. Haug, K. A. Hughen, U. Röhl, *Science* **290**, 1947 (2000).
23. D. W. Lea, D. K. Pak, L. C. Peterson, K. A. Hughen, *Science* **301**, 1361 (2003).
24. R. B. Alley *et al.*, *Science* **299**, 2005 (2003).
25. D. Rind, *Science* **296**, 673 (2002).
26. H. Heinrich, *Quat. Res.* **29**, 143 (1988).
27. O. Cayre, Y. Lancelot, E. Vicent, M. A. Hall, *Paleoceanography* **14**, 384 (1999).
28. M. Perez-Folgado *et al.*, *Mar. Micropaleontol.* **48**, 49 (2003).
29. E. Bard, F. Rostek, J. L. Turon, S. Gendreau, *Science* **289**, 1321 (2000).
30. S. A. van Kreveld, M. Knappertsbusch, J. Ottens, G. M. Ganssen, J. E. van Hinte, *Mar. Geol.* **131**, 21 (1996).
31. R. N. Hiscott, A. E. Aksu, P. J. Mudie, D. F. Parsons, *Global Planet. Change* **28**, 227 (2001).
32. E. Calvo, J. Villanueva, J. O. Grimalt, A. Boelaert, L. D. Labeyrie, *Earth Planet. Sci. Lett.* **188**, 509 (2001).
33. J. I. Svendsen *et al.*, *Boreas* **28**, 234 (1999).
34. G. Krinner *et al.*, *Nature* **427**, 429 (2004).
35. M. Siddall *et al.*, *Nature* **423**, 853 (2003).
36. A. L. Berger, *J. Atmos. Sci.* **35**, 2362 (1978).
37. P. U. Clark, N. G. Pisias, T. F. Stocker, A. J. Weaver, *Nature* **415**, 863 (2002).
38. P. U. Clark *et al.*, *Science* **293**, 283 (2001).
39. A. Ganopolsky, S. Rahmstorf, *Nature* **409**, 153 (2001).
40. M. F. Sánchez-Goñi *et al.*, *Clim. Dyn.* **19**, 95 (2002).
41. J. C. H. Chiang, M. Biasutti, D. S. Battisti, *Paleoceanography* **18**, 41094 (2003).
42. M. Khodri *et al.*, *Nature* **410**, 570 (2001).
43. J. F. McManus, D. W. Oppo, L. D. Keigwin, J. L. Cullen, G. C. Bond, *Quat. Res.* **58**, 17 (2002).
44. We thank M. Hutterli and J. Schwander for providing the Monte Carlo wiggle-matched age scale, P. C. Tzedakis for providing data from Tenaghi Philippon, J. F. McManus for data from core ODP-980, S. J. Johnsen for the GRIP ss09sea ice-core chronology, D. Amblas for Fig. 1, B. H. Oldham for invaluable assistance in editing the text, and J. Mangerud and M. Schulz for helpful discussions. B.M. thanks, in particular, a grant from the Programa de Itinerano Integrado de Insercion Profesional program of CSIC. This work was supported by the Pole-Ocean-Pole (EVK2-2000-00089) and Coordinated European Surface Ocean Palaeoestimation (EVRI1-2001-00009) projects funded by the European Union.

Supporting Online Material
www.sciencemag.org/cgi/content/full/306/5702/1762/DC1
Materials and Methods
Table S1
References and Notes

21 June 2004; accepted 28 October 2004

Efficient Deactivation of a Model Base Pair via Excited-State Hydrogen Transfer

Thomas Schultz,[1]* Elena Samoylova,[1] Wolfgang Radloff,[1] Ingolf V. Hertel,[1] Andrzej L. Sobolewski,[2] Wolfgang Domcke[3]

We present experimental and theoretical evidence for an excited-state deactivation mechanism specific to hydrogen-bonded aromatic dimers, which may account, in part, for the photostability of the Watson-Crick base pairs in DNA. Femtosecond time-resolved mass spectroscopy of 2-aminopyridine clusters reveals an excited-state lifetime of 65 ± 10 picoseconds for the near-planar hydrogen-bonded dimer, which is significantly shorter than the lifetime of either the monomer or the 3- and 4-membered nonplanar clusters. Ab initio calculations of reaction pathways and potential-energy profiles identify the mechanism of the enhanced excited-state decay of the dimer: Conical intersections connect the locally excited $^1\pi\pi^*$ state and the electronic ground state with a $^1\pi\pi^*$ charge-transfer state that is strongly stabilized by the transfer of a proton.

An important property of DNA is its robustness with respect to damage by the harmful ultraviolet (UV) components [wavelength (λ) < 400 nm] of sunlight. The solar UV photons are ubiquitous and potent mutagens, which have accompanied the development of life for billions of years.

The $^1\pi\pi^*$ excited states of the DNA bases that are accessed by UV absorption lie approximately 5 eV above the ground state. The significant energy deposited in the molecule by UV radiation could initiate a variety of photochemical reactions. The available data (*1*) indicate that these reactive decay channels are efficiently quenched by fast radiationless decay back to the electronic ground state (termed internal conversion). These mechanisms provide DNA with a high degree of intrinsic photostability. The origin of rapid internal conversion within DNA could involve the interplay of the sugar-phosphate backbone, the hydrogen bonding of the Watson-Crick (WC) base pairs, stacking interactions, and solvation. Following a reductionistic approach, we focus here on whether isolated WC base pairs show greater photostability than do individual bases.

Several groups recently used ab initio calculations (*2–4*) and time-resolved spectroscopy (*1*) to identify specific radiationless-decay mechanisms in isolated DNA bases. However, experimental investigation of the excited-state lifetime of WC base pairs is complicated by several factors. Most importantly, the excited-state lifetimes of the monomers are already very short (*1*), and there exist several tautomeric forms of the isolated WC base pairs (*5*). Simplified mimetic models of WC base pairs allow the investigation of some of the basic photochemical reaction mechanisms without these complexities. An extensively studied reaction is double proton transfer in the mimetic model 7-azaindole dimer (*6*). Recent ab initio calculations for the guanine-cytosine (GC) base pair, however, suggest a hydrogen-atom transfer reaction involving amino groups as proton donors and ring nitrogens as proton acceptors (*7*). Near the hydrogen-transfer minimum, a conical intersection with the electronic ground state leads to rapid internal conversion. This reaction can be studied in the model compound 2-aminopyridine (2AP) dimer, which offers the relevant hydrogen bonds and reaction pathways (*8*) but otherwise lacks the complexity of the pyrimidine and purine bases. Theory predicts near-planar hydrogen-bonded structures for DNA base pairs (*7*, *9*) as well as for the 2AP dimer (*8*).

We employed pump-probe ionization spectroscopy to characterize the excited-state properties of 2AP clusters (Fig. 1A). The clusters were formed in a pulsed supersonic jet expansion of 2AP, seeded in 1 bar of helium. The size distribution [$(2AP)_n$] of the clusters was controlled by heating the 2AP sample to the 30° to 80°C range. Molecules and clusters were photoexcited by a femtosecond laser pump pulse at 293, 274, or 250 nm, then ionized by a delayed probe pulse at 200 or 800 nm, and finally mass-analyzed in a time-of-flight mass spectrometer. Clustering conditions were varied to obtain very narrow cluster size n ($n \leq 2$ molecules) or broad (n = 1 to 8) cluster distributions to diagnose cluster fragmentation effects.

In the mass spectrum with broad cluster distribution (Fig. 1B) obtained by excitation with a 274-nm pulse and three-photon ionization with an 800-nm pulse, the magnitude of the ion signal was directly proportional to the number of molecules in the excited state. Measurement of a chosen ion signal as a function of the pump-probe delay thus allowed for the characterization of the

[1]Max Born Institute Berlin, Max-Born-Straße 2a, D-10247 Berlin, Germany. [2]Institute of Physics, Polish Academy of Sciences, Aleja Lotnikow 32/46, PL-02668 Warsaw, Poland. [3]Department of Chemistry, Technical University of Munich, Lichtenbergstraße 4, D-85747 Garching, Germany.

*To whom correspondence should be addressed. E-mail: schultz@mbi-berlin.de

excited-state population decay. The time resolution of our experiments was limited by the temporal width of the laser pulses (~120 fs). The molecule indole, with an excited-state lifetime of ~17 ns (*10*), was introduced into the molecular beam to obtain an independent measure of the pump-probe beam overlap. The time-dependent signals for pump-probe delays >100 ps were normalized to the indole signal.

The ion signals for 2AP and $(2AP)_n$ (n = 2 to 4) clusters were collected using either one-photon ionization at 200 nm or three-photon ionization at 800 nm. Both techniques gave the same decay rates, although the latter (Fig. 2) offered a significantly better signal-to-noise ratio. The excited-state population of the isolated monomer relaxed with a lifetime of τ_1 = 1.5 ns, the same value estimated from the linewidth in rotationally resolved spectra (*11*). The 2AP dimer showed a reduced lifetime of τ_2 = 65 ps, clearly indicating that an additional relaxation pathway exists in the doubly hydrogen-bonded system.

The excited-state decay dynamics in clusters with $n \geq 3$ were similar to the dynamics in the isolated molecule. The absence of fast relaxation in the larger clusters is presumably due to changes in the structure of the hydrogen-bonded clusters. Structure optimizations using the Parametric Method 3 (PM3) semi-empirical method indicate that the doubly hydrogen-bonded and near-planar structure is only one of several stable structures for the 2AP trimer (Fig. 2, C1 and C2) and is completely absent in the 2AP tetramer (Fig. 2, D1 and D2). Thus, the near-planar hydrogen-bonded structure of the dimer is essential for the fast excited-state decay. A small contribution (<30%) of this 65-ps decay channel is seen also for the n = 3 cluster, leading to a bi-exponential decay. The presence of different cluster isomers, some of which may contain the near-planar dimer (Fig. 3C1), explains this bi-exponential behavior. In contrast, for yet larger clusters ($n \geq 4$), such dimer-like substructures were not identified, and no short-time decay was observable for the tetramer and the larger clusters (*12*). Within the time resolution of the present experiment (~50 fs), no faster decay component than τ_2 = 65 ps could be found for any of the clusters studied.

Cluster ions can fragment if they are vibrationally excited, because of either unfavorable Franck-Condon factors in the ionization process or absorption of an additional probe photon after ionization. As a result of fragmentation, the excited-state dynamics of larger clusters are reflected in the mass channel of a smaller fragment. Fragmentation of $n > 2$ clusters to the dimer explains why the signal of the dimer in Fig. 2B does not approach zero at long delay times. Similarly, fragmentation of the dimer to the monomer adds a contribution of the 65-ps channel to the signal of the monomer. To diagnose the effects of cluster fragmentation, we measured additional pump-probe spectra for narrow cluster distributions. When the proportion of clusters with $n > 2$ was very small, fragmentation effects were negligible and the dimer signal indeed approached zero for long delay times within our measuring interval (Fig. 3). With 250-nm excitation

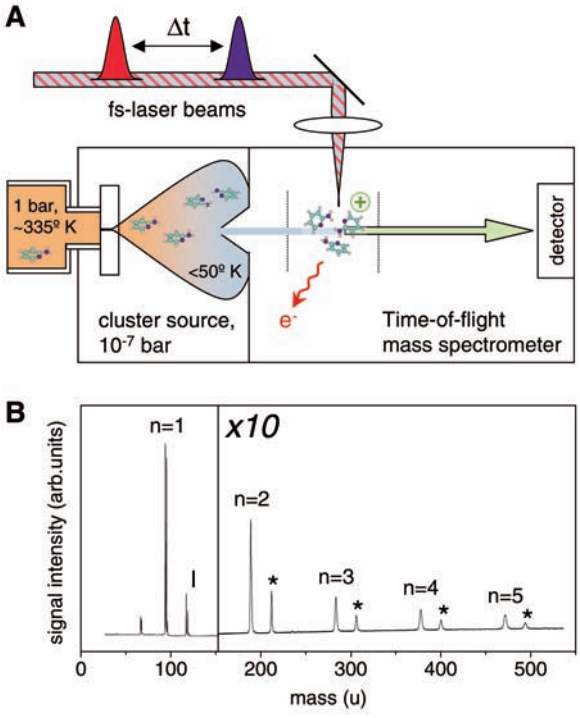

Fig. 1. (**A**) Schematic representation of the pump-probe cluster spectroscopy experiment. The clusters are formed in an adiabatic expansion of sample molecules and inert gas into a high-vacuum cluster source region. The skimmed cluster beam is crossed by femtosecond excitation and ionization pulses with a variable pump-probe time delay Δt between the two pulses. The photoionized clusters are mass-analyzed in a time-of-flight mass spectrometer. (**B**) Mass spectrum for a broad cluster distribution of 2AP and $(2AP)_n$ clusters with 274-nm excitation and 800-nm ionization. Indole (I) was added for calibration purposes and gives rise to mixed indole$(2AP)_{n-1}$ clusters which are marked with an asterisk. Arb., arbitrary.

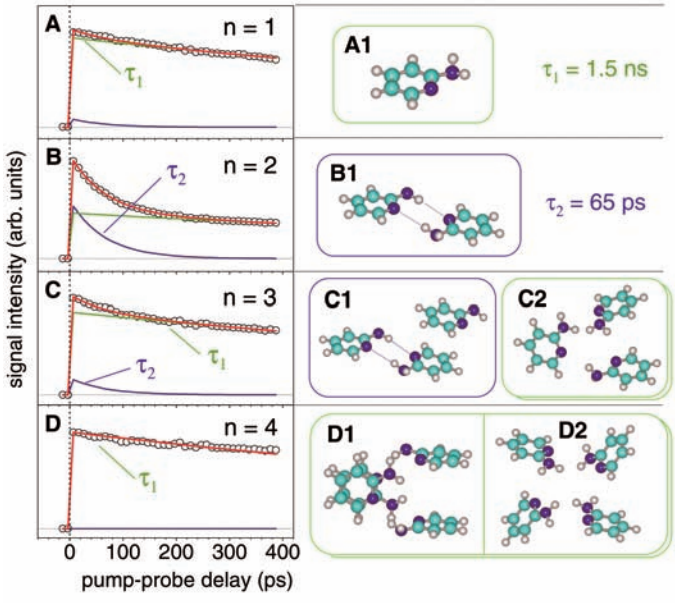

Fig. 2. (**A** to **D**) Time-dependent ion signals for $(2AP)_n$ clusters with n = 1 to 4 and (**A1** to **D2**) proposed cluster structures optimized by the PM3 semi-empirical method. The measured ion signals for 274-nm excitation and 800-nm ionization (open circles) were fitted by the sum of two exponential decays (red line). The lifetime τ_1 = 1.5 ns (green line) for the monomer corresponds to the lifetime estimated from high-resolution spectroscopy. A lifetime τ_2 = 65 ps (blue line) was fitted to the measured dynamics of the n = 2 cluster and was assigned to the near-planar, doubly hydrogen-bonded structure B1. An additional longer-lived contribution with lifetime τ_1 is due to the fragmentation of larger clusters. For the trimer, a bi-exponential decay with τ_1 = 1.5 ns and τ_2 = 65 ps was observed. The fast (τ_2) contribution was assigned to structure C1, which shows a doubly hydrogen-bonded geometry similar to that of the dimer. A large fraction of the population decays like the monomer with lifetime τ_1. This slow decay can be rationalized by several trimer geometries with disrupted hydrogen bonds (such as C2). The tetramer decays monoexponentially with lifetime τ_1, indicating complete absence of the fast decay channel. Correspondingly, optimized cluster geometries show ring (such as D1)– or star (such as D2)–shaped geometries, but no structure with doubly hydrogen-bonded 2AP pairs was identified.

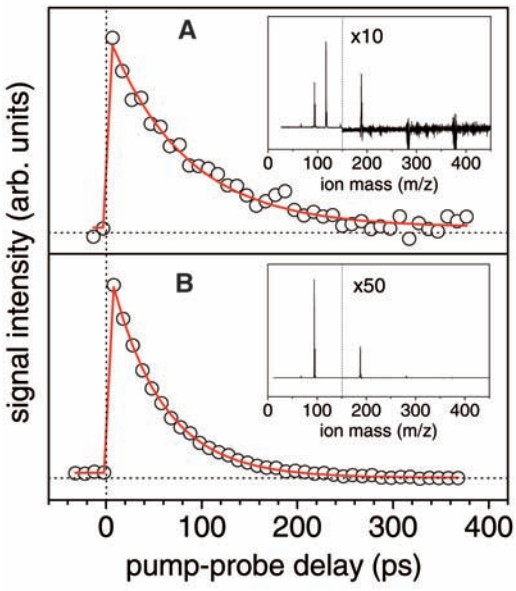

Fig. 3. Time-dependent ion signals of the 2AP dimer for narrow cluster distributions at 250-nm (**A**) and 293-nm (**B**) excitation. To remove contributions from cluster ions formed by disproportionation in the jet expansion, a background spectrum has been subtracted from the displayed mass spectra. The mass spectra show no larger ($n > 2$) clusters and we expect no fragmentation effects. The corresponding time-dependent ion signals show only single-exponential decay with $\tau_2 = 75 \pm 10$ ps at 250 nm and $\tau_2 = 55 \pm 10$ ps at 293 nm. *m*/*z*, mass/charge ratio.

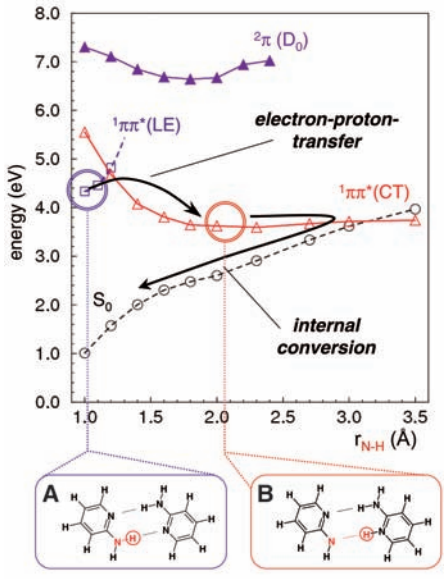

Fig. 4. Ab initio potential energies of the electronic ground state (S_0) and the locally excited [$^1\pi\pi^*$ (LE)] and charge-transfer excited [$^1\pi\pi^*$ (CT)] states of the 2AP dimer as a function of the transfer coordinate of a single proton. The equilibrium structures of the ground state and the $^1\pi\pi^*$ (CT) state are indicated by the insets (**A**) and (**B**), respectively. The excited-state potential-energy profiles have been calculated along the minimum-energy reaction path for hydrogen transfer; the energy of the S_0 state (circles) has been calculated at the $^1\pi\pi^*$ (CT)–optimized geometries. The crossings of the potential-energy functions correspond to conical intersections of the multidimensional potential-energy surfaces. Potential-energy functions of the 2AP dimer cation [$^2\pi$ (D_0)] indicate that both the $^1\pi\pi^*$ (LE) and $^1\pi\pi^*$ (CT) states can be ionized along the reaction path with the photons of the present experiment.

(vibrational excess energy of ~6450 cm^{-1} in the excited state), we saw indications of cluster fragmentation not only after ionization but also in the neutral excited-state complexes.

To obtain further information on the fast decay of the dimer, we investigated the dependence of the decay dynamics on the pump wavelength (Fig. 3). We found nearly equal time constants at 293 nm, near the origin of the S_0–S_1 transition, and at 250 nm, corresponding to 0.8 eV of vibrational energy in the excited state. Hence, we found no indication that the decay rate of the optically prepared excited state was governed by a barrier on the nuclear potential-energy surface.

We used ab initio methods to calculate the potential energy functions that account for the rapid internal conversion of the 2AP dimer. The corresponding reaction pathway is an electron-proton transfer in the excited state (Fig. 4) and was identified using the complete-active-space self-consistent-field (CASSCF) method, together with a perturbative treatment of dynamical electron correlation effects (*8*). UV absorption efficiently populates the locally excited $^1\pi\pi^*$ (LE) state of one monomer. Subsequent electron transfer from the highest π orbital of one monomer to the lowest π^* orbital of the other leads to the charge transfer $^1\pi\pi^*$ (CT) state. This state corresponds to a biradical structure in which each of the aromatic rings carries an unpaired π electron. The CT state is stabilized by the transfer of a proton along one of the hydrogen bonds (Fig. 4, A and B). The strong rise of the ground-state energy along the same reaction path results in efficient relaxation from the $^1\pi\pi^*$ (CT) state back to the ground state (S_0). These crossings of the $^1\pi\pi^*$ (LE), $^1\pi\pi^*$ (CT), and S_0 potential-energy functions (Fig. 4) indicate conical intersections (*13*) of the multidimensional potential-energy surfaces, which provide the mechanism for ultrafast internal conversion to the ground state in the near-planar hydrogen-bonded dimer.

We associate the measured lifetime of $\tau_2 = 65$ ps with the predissociation of the $^1\pi\pi^*$ (LE) state by the repulsive $^1\pi\pi^*$ (CT) state, corresponding to the transfer of a single proton. The calculated potential-energy curves of the cationic states (Fig. 4) show that the CT state has a low ionization potential similar to the LE state and can be ionized by the probe photons. The experimental data, however, do not show any evidence for ionization out of the CT state. Hence, the depopulation of the CT state via the $^1\pi\pi^*$ (CT) to S_0 conical intersection proceeds quickly compared to the population of this state via the $^1\pi\pi^*$ (LE) to $^1\pi\pi^*$ (CT) nonadiabatic coupling; therefore, no population accumulates in the CT state.

The 65-ps decay time of the $^1\pi\pi^*$ (LE) state is relatively slow for a process driven by a proton-transfer reaction coordinate. However, the equilibrium geometries of the $^1\pi\pi^*$ (LE) and $^1\pi\pi^*$ (CT) states differ in many of the other coordinates, implying that the nonadiabatic transition is slowed down by the rearrangement of these coordinates. Moreover, minimal overlap of π and π^* orbitals on different monomers leads to a small coupling matrix element of the adiabatic $^1\pi\pi^*$ (LE) and $^1\pi\pi^*$ (CT) states. These considerations can explain the relatively long excited-state lifetime, as well as the weak dependence of the decay rate on the excess energy in the $^1\pi\pi^*$ (LE) state.

The mechanism depicted in Fig. 4 may be of general relevance in multiply hydrogen-bonded chromophores, specifically WC base pairs. The lifetime of the $^1\pi\pi^*$ (LE) state should sensitively depend on the relative energy of the $^1\pi\pi^*$ (LE) and $^1\pi\pi^*$ (CT) states in the Franck-Condon zone. Recent ab initio calculations for the WC form of the GC base pair have predicted that the vertical excitation energy of the $^1\pi\pi^*$ (CT) state is close to the excitation energy of the $^1\pi\pi^*$ (LE) state of the WC pair (*7*). This property may lead to an even faster excited-state decay than that observed for the 2AP dimer. Recent experiments on the WC form of the GC base pair in a supersonic jet have revealed an extremely broad UV absorption spectrum, indicating a sub–100-fs excited-state lifetime (*14*). For other, non-WC isomers of the GC base pair, sharp spectra (corresponding to long excited-state lifetimes) were observed. These data indicate that the fast relaxation pathway is strongly dependent on the molecular structure of the clusters, similar to our observations for 2AP clusters. Direct femtosecond time-resolved studies of selected base

pair isomers are necessary to further elucidate the issue.

References and Notes

1. C. E. Crespo-Hernandez, B. Cohen, P. M. Hare, B. Kohler, *Chem. Rev.* **104**, 1977 (2004).
2. N. Ismail, L. Blancafort, M. Olivucci, B. Kohler, M. A. Robb, *J. Am. Chem. Soc.* **124**, 6818 (2002).
3. A. L. Sobolewski, W. Domcke, C. Dedonder-Lardeux, C. Jouvet, *Phys. Chem. Chem. Phys.* **4**, 1093 (2002).
4. M. Merchan, L. Serrano-Andres, *J. Am. Chem. Soc.* **125**, 8108 (2003).
5. E. Nir, C. Janzen, P. Imhof, K. Kleinermanns, M. S. de Vries, *Phys. Chem. Chem. Phys.* **4**, 732 (2002).
6. A. Douhal, S. K. Kim, A. H. Zewail, *Nature* **378**, 260 (1995).
7. A. L. Sobolewski, W. Domcke, *Phys. Chem. Chem. Phys.* **6**, 2763 (2004).
8. A. L. Sobolewski, W. Domcke, *Chem. Phys.* **294**, 73 (2003).
9. P. Jurečka, P. Hobza, *J. Am. Chem. Soc.* **125**, 15608 (2003).
10. J. W. Hager, D. R. Demmer, S. C. Wallace, *J. Phys. Chem.* **91**, 1375 (1987).
11. D. R. Borst, J. R. Roscioli, D. W. Pratt, *J. Phys. Chem. A* **106**, 4022 (2002).
12. T. Schultz *et al.*, data not shown.
13. W. Domcke, D. R. Yarkony, H. Köppel, Eds., *Conical Intersections: Electronic Structure, Dynamics and Spectroscopy* (World Scientific, Singapore, 2004).
14. M. S. de Vries, private communication.

15. We thank F. Noack for his support by providing the laser system in the Femtosecond Application Laboratory of the Max Born Institute. Financial support by the Deutsche Forschungsgemeinschaft through Sonderforschungsbereich 450 is gratefully acknowledged.

13 August 2004; accepted 1 November 2004

Interface Structure and Atomic Bonding Characteristics in Silicon Nitride Ceramics

A. Ziegler,[1,2*†] J. C. Idrobo,[3] M. K. Cinibulk,[4] C. Kisielowski,[5] N. D. Browning,[5,6] R. O. Ritchie[1,7]

Direct atomic resolution images have been obtained that illustrate how a range of rare-earth atoms bond to the interface between the intergranular phase and the matrix grains in an advanced silicon nitride ceramic. It has been found that each rare-earth atom bonds to the interface at a different location, depending on atom size, electronic configuration, and the presence of oxygen at the interface. This is the key factor to understanding the origin of the mechanical properties in these ceramics and will enable precise tailoring in the future to critically improve the materials' performance in wide-ranging applications.

Bulk silicon nitride (Si_3N_4) ceramics have been investigated extensively over the past two decades, largely because their mechanical and physical properties are relevant for many high-temperature applications, including high strength, high decomposition temperature (1900°C), good oxidation resistance, low coefficient of friction, negligible creep, good thermal shock properties, and good resistance to corrosive environments. In addition, thin silicon nitride films and coatings have been studied to understand electrical and thermal conductivity properties. All of these properties, including the processing and sintering behavior, rely on the specific crystal structure, the local chemistry, and the local bonding at the interfaces.

The widespread use of these ceramics as structural components is currently limited by their brittleness, which limits reliability. Specifically, the toughness is too low and the sensitivity to flaws and cracks correspondingly too high, resulting in poor damage tolerance. Such properties can be improved by microstructural and compositional design. Indeed, the relation between microstructure, intergranular phases, and mechanical properties in ceramics is widely acknowledged (*1*, *2*). Silicon nitride ceramic microstructures consist of elongated matrix grains that are randomly oriented, interlocked, and interspersed with a secondary phase (*3*–*8*). This intergranular phase in these materials is the key microstructural element that effectively controls most of the material's characteristics, most notably the mechanical properties, and is dependent on the local chemical composition, atomic structure, and bonding characteristics (*9*–*13*).

Previous investigations have shown empirically that the material's strength and toughness are markedly affected by the intergranular phase chemistry. An understanding of how this phase governs the macroscopic mechanical properties is limited, because the amorphous morphology of the phase and its small dimension make analysis difficult. Recent breakthroughs in scanning transmission electron microscopy (STEM) and associated chemical analysis (*14*–*18*) permit probing the local atomic structure and bonding characteristics with a resolution close to 1 Å.

We examine the immediate interface between matrix grains and the amorphous intergranular film, extracting structural and atomic bonding information. In particular, we relate the structure of the interface to the atomic size and electronic structure of the rare-earth elements in the intergranular film. The oxides of rare-earth elements are a very common type of sintering additive in Si_3N_4, because it has been shown empirically that such additions improve the mechanical properties (*12*, *13*). We investigate the interface between the intergranular phase and the Si_3N_4 matrix using high-angle annular dark-field STEM (HAADF-STEM) for imaging and electron-energy-loss spectroscopy (EELS) (*14*) for chemical analyses. Experimental EELS and incoherent high-angle ADF (Z-contrast) images (*15*) were obtained with a monochromated FEI Tecnai F20 STEM operating at 200 kV. The lens conditions in the microscope were defined for imaging and spectroscopy, with a probe size of 0.14 nm. The inner semi-angle of the ADF detector was chosen to be 74 mrad and 110 mrad. Images were acquired with an objective semi-angle of 13.5 mrad. These experimental conditions are enough to minimize the effects of strain fields on the Z-contrast image (*16*). In this experimental condition, the Z-contrast image allows the structure of the grains to be directly observed, and the image can also be used to position the electron probe for EELS (*14*).

Previous investigations of these interfaces have focused on two common additives, Y_2O_3 and La_2O_3 (*7*, *8*), showing primarily that there is Y and La segregation in the intergranular phase. Furthermore, the most recent study (*8*) uses the HAADF-STEM imaging technique described above and first-principles calculations to show that there is

[1]Materials Sciences Division, Lawrence Berkeley National Laboratory, Berkeley, CA 94720, USA. [2]Materials Science and Technology Division, Chemistry and Materials Science Directorate, Lawrence Livermore National Laboratory, Livermore, CA 94551, USA. [3]Physics Department, University of California, Davis, CA 95616, USA. [4]Materials and Manufacturing Directorate, Air Force Research Laboratory, Wright-Patterson Air Force Base, OH 45433, USA. [5]National Center for Electron Microscopy, Lawrence Berkeley National Laboratory, Berkeley, CA 94720, USA. [6]Department of Chemical Engineering and Materials Science, University of California, Davis, CA 95616, USA. [7]Department of Materials Science and Engineering, University of California, Berkeley, CA 94720, USA.

*Present address: Department of Chemical Engineering and Materials Science, University of California, Davis, CA 95616, USA.

†To whom correspondence should be addressed. E-mail: aziegler@lbl.gov

variability in this segregation at the interface between the matrix grains and the intergranular phase. However, the techniques employed did not give information about the electronic configuration or the specific atomic location for the additives at the interface. Our objective is the identification of bonding sites for a larger selection of rare-earth elements of the oxide sintering additives La_2O_3, Sm_2O_3, Er_2O_3, Yb_2O_3, and Lu_2O_3 and to extend previous investigations by analyzing their electronic configuration and determining the atomic locations of the additives at the interface with the intergranular phase. We take advantage of the "chemically sharp" interface between the intergranular phase and matrix grains caused by a miscibility gap between the Si_3N_4 crystal and any of the rare-earth atoms; that is, these atoms do not substitute for Si_3N_4 host atoms in their atomic positions nor do they sit at interstitial sites in the Si_3N_4 crystal structure.

The HAADF-STEM images in Fig. 1 depict an interface between the intergranular phase and a Si_3N_4 matrix grain for each of the five sintering additive types. The images confirm that the Si_3N_4 crystal structure ends at the interface with the intergranular phase, specifically with open hexagonal rings (*7*). The attachment of heavy atoms can be proven by the Z-contrast in the images that makes heavier atoms appear brighter. Concomitant large-area EELS measurements performed on these interfaces confirm that the heavy elements indeed segregate to the intergranular phase. Hence, the bright spots seen in the images are indeed related to the heavy atoms and their atomic positions. Accordingly, the atomic attachment at such an interface is different for each of the rare-earth elements (La, Sm, Er, Yb, and Lu) examined here. The STEM images of the sample containing La show no specific or periodic connection occurring between the Si_3N_4 matrix grain and the La atoms. The La atoms are present in the intergranular phase, as reported previously (*8*), yet they do not arrange into atomic columns that would increase contrast. Additionally, no lateral atomic ordering can be observed at this magnification. Previous investigations have shown that the La atom distribution along the intergranular phase fluctuates, with locations of high and low La atom concentration (*8*). The distance between the areas of high La concentration are rather far apart and as such cannot be associated with a particular atomic site along the interface. Concomitant theoretical calculations that attempt to determine specific atomic sites are of help; however, in agreement with the present results, a periodic atomic site for La atom attachment cannot be discerned unambiguously from the unaided STEM images.

In contrast, the images of the other four compositions containing Sm, Er, Yb, and Lu exhibit very different features. Here, the bright spots that appear at the interface in the amorphous intergranular phase are attributed to columns of Sm, Er, Yb, and Lu atoms, respectively, because of their high contrast. These images clearly show that the atomic bonding of those atoms along the Si_3N_4 prismatic plane is periodic and occurs at two very specific atomic sites, A and B (Fig. 1). Sm atoms bond in single-atom configuration to both positions. This changes with the slightly heavier, but smaller, atoms Er, Yb, and Lu, as they bond in pairs at position A with the pair axis oriented parallel to the prismatic plane. It cannot be determined to what degree the axis is also parallel to the image plane, but observing how close the bright spots are and considering the atomic size of these elements, it follows that the atom-pair axes are inclined and are seen in projection. The atom pairs of Lu, Yb, and Er appear to be separated differently: Lu, 1.43 ± 0.07 Å; Yb, 1.46 ± 0.05 Å; and Er, 1.48 ± 0.04 Å. This growing pair separation can be related to the increase of the valence shell radius from Lu to Er (Fig. 1), which may also be the cause for the occasional pair-splitting that can be observed in the images, i.e., some atom pairs are separated more than others. For Er and Yb, this results in an occasional larger atom-pair separation of 2.06 ± 0.03 Å and 2.15 ± 0.1 Å, respectively. Upon close examination of these split atom pairs, there is indication that beyond the first row of attached atoms there is a second set of rare-earth atoms, reaching even farther into the amorphous intergranular phase—possibly a partial ordering imposed by the Si_3N_4 crystal structure onto the amorphous intergranular phase. However, precise atomic positions beyond the first layer of atomic columns cannot be discerned at this point. These observations demonstrate that the bonding of the rare-earth elements to the interface is controlled by atomic size. The small atoms attach in pairs at specific and periodic sites along the interface. With increasing atom size, the pair separation increases to the point that larger atoms, as in the case of Sm, are not able to bond in pairs at position A and have to adapt a new single-atom periodic bonding configuration. Consequently, one of them has to move to position B. With a further increase in atom size, that is, La atoms, the attachment to the interface changes again, this time forfeiting all periodicity and site-specific atomic bonding. The question remains, however, why the small atoms preferably bond to position A and not B.

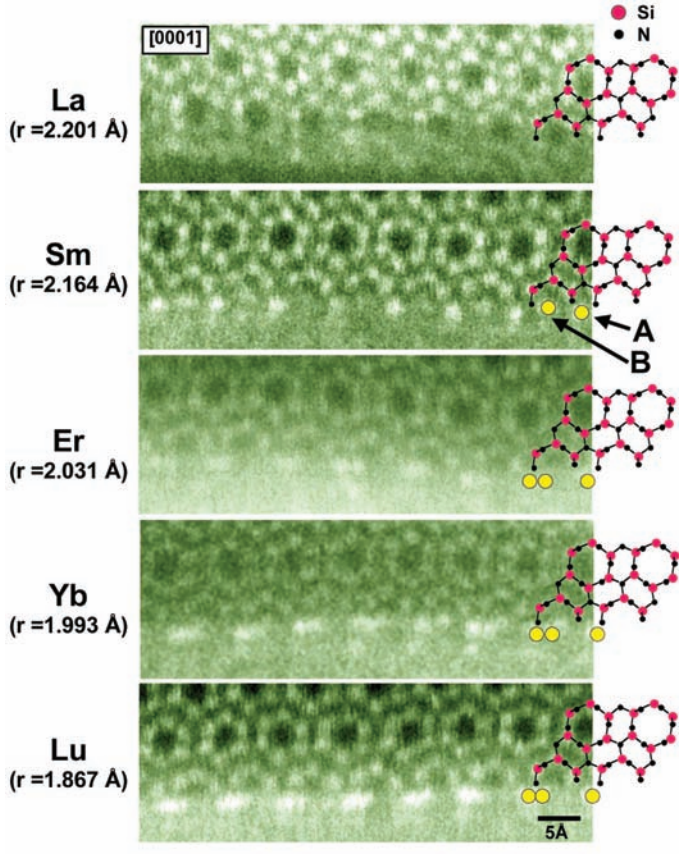

Fig. 1. In these STEM images of La-, Sm-, Er-, Yb-, and Lu-doped Si_3N_4, the matrix grain is oriented along the [0001] zone axis such that the open Si_3N_4 crystal structure is clearly visible at the atomic level and its prismatic plane faces the amorphous intergranular phase. The Si_3N_4 crystal structure ends with open hexagonal rings at the interface with the intergranular phase (*7*), which indicates that the prismatic plane may contain dangling bonds that can attract atoms from the intergranular phase. The attachment of heavy atoms in the form of atomic columns oriented normal to the image plane—here La, Sm, Er, Yb, and Lu listed with their respective valence-shell radii—is shown by the strong Z-contrast in the images that makes heavier atoms appear brighter. Two distinct atom positions, A and B, can be identified along the interface.

The initial EELS measurements, performed by area-scanning a rather large region of the intergranular films, indicated atom segregation to the interface. Attempting to identify specific atomic bonding configurations, we performed more precise EELS measurements on the Sm-containing sample with a 1.4 Å probe size, because this sample was the least electron-beam sensitive and it showed rare-earth atom attachment to positions A and B. Such a small probe size allows positioning of the electron beam over a single atom column analyzing the very local bonding characteristics (*14*). The results show the electron loss spectra for the Si L_{23} and the Sm N_{45} edges, respectively, measured on both identified atomic positions (A and B) along the interface (Fig. 2). There is no difference between the spectra at the Sm N_{45} edge, which suggests that the atomic environment and bonding characteristics are the same for the Sm atoms at both locations, that is, Sm exists in the same formal valence state in each location. The difference in the electron-loss spectra from positions A and B is at the Si L_{23} edge. A double peak (102 eV and 103.5 eV) appears in the spectrum taken from atom position A. The first peak can be identified with a Si-N bond, whereas the second peak is associated with a Si-O bond because its position in the spectrum closely coincides with measurements taken on SiO_2 (*19*). This indicates that the atomic environment around the terminating Si atoms on the Si_3N_4 prism plane that surround position A is most likely an oxygen atom. In contrast, the atomic environment of the Si atoms on the prism plane that surround position B appears to have no oxygen atoms involved, only nitrogen.

The observation that the Er, Yb, and Lu atom pairs preferably bond to position A suggests that the interaction of the rare-earth atom with the oxygen at site A plays a critical role in controlling atom attachment at the interface. Thus, a combination of both factors, that is, the difference in atomic size and the presence of oxygen, govern atom attachment and site selection along the interface. This results in different atom concentrations at the individual positions A and B. The rare-earth atom concentration is high for position A and comparably low at position B. The interaction of electronic configuration, atom size, and position of the rare-earth atoms on the prismatic plane is currently being investigated by atomic-structure calculations of this interface.

This information about the specific atomic structure and bonding characteristics in advanced ceramics has been missing for many years and should now aid the development of improved ceramics in many ways. Most important, it will assist in understanding how ceramic microstructures evolve during fabrication, especially how grain growth and microstructural evolution is affected by different sintering additives at the atomic level. Control over evolution and the ability to precisely tailor ceramic microstructures is critical in improving mechanical properties of ceramics, which invariably limits their use. From previous empirical investigations (*1*, *2*, *9*, *10*, *12*, *13*), it is known that ceramics' fracture is highly sensitive to the intergranular phase chemistry and therefore to its atomic structure and bonding characteristics. The identification of precise atom locations from the present study should also prove invaluable for atomic-structure calculations. Such computational methods (*20*–*26*) seek to calculate individual atomic bonding strengths so as to explain the particular fracture mechanisms that occur along and across the intergranular phase. However, lacking essential experimental information about the atomic structure and bonding characteristics, such calculations have been incomplete.

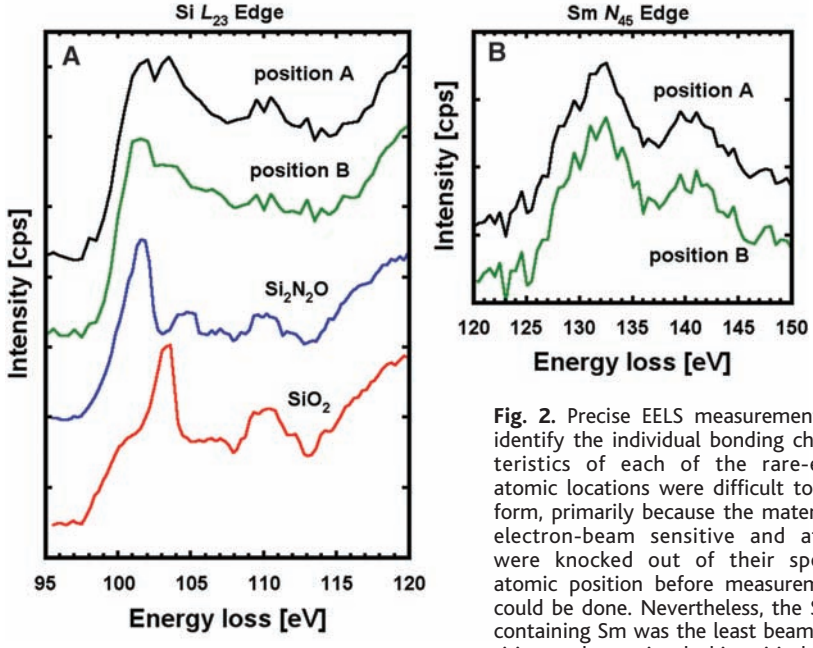

Fig. 2. Precise EELS measurements to identify the individual bonding characteristics of each of the rare-earth atomic locations were difficult to perform, primarily because the material is electron-beam sensitive and atoms were knocked out of their specific atomic position before measurements could be done. Nevertheless, the Si_3N_4 containing Sm was the least beam sensitive and permitted this critical EELS measurement. The results for (**A**) the Si L_{23} and (**B**) the Sm N_{45} edges identify the individual bonding characteristics at positions A and B. The Si L_{23} edge shows a double peak at position A but not at position B. The first peak can be identified with a Si-N bond because it coincides with measurements taken on the Si_3N_4 crystal structure. Identification of the second peak is achieved by comparing the results to reference spectra obtained from SiO_2 and Si_2N_2O. Accordingly, the peak in question can be associated with a Si-O bond. Regarding the electronic environment for the Sm atoms at positions A and B, there is no difference between the spectra at the Sm N_{45} edge.

References and Notes

1. S. Wiederhorn, *Annu. Rev. Mater. Sci.* **14**, 373 (1984).
2. P. F. Becher, S. L. Hwang, C. H. Hsueh, *Mater. Res. Soc. Bull.* **20**, 23 (1995).
3. D. R. Clarke, *J. Am. Ceram. Soc.* **70**, 15 (1987).
4. H. J. Kleebe, M. K. Cinibulk, R. M. Cannon, M. Rühle, *J. Am. Ceram. Soc.* **76**, 1969 (1993).
5. C. M. Wang, X. Pan, M. J. Hoffmann, R. M. Cannon, M. Rühle, *J. Am. Ceram. Soc.* **79**, 788 (1996).
6. I. Tanaka *et al.*, *J. Am. Ceram. Soc.* **77**, 911 (1994).
7. A. Ziegler, C. Kisielowski, M. J. Hoffmann, R. O. Ritchie, *J. Am. Ceram. Soc.* **86**, 1777 (2003).
8. N. Shibata *et al.*, *Nature* **428**, 730 (2004).
9. E. Y. Sun *et al.*, *J. Am. Ceram. Soc.* **81**, 2831 (1998).
10. F. F. Lange, B. I. Davis, M. G. Metcalf, *J. Mater. Sci.* **18**, 1497 (1983).
11. R. L. Satet, M. J. Hoffmann, *J. Eur. Ceram. Soc.* **24**, 3437 (2004).
12. M. K. Cinibulk, G. Thomas, S. M. Johnson, *J. Am. Ceram. Soc.* **75**, 2050 (1992).
13. W. A. Sanders, D. M. Mieskowski, *J. Am. Ceram. Soc.* **64**, 304 (1985).
14. N. D. Browning, M. F. Chisholm, S. J. Pennycook, *Nature* **366**, 143 (1993).
15. P. D. Nellist, S. J. Pennycook, *Ultramicroscopy* **78**, 111 (1999).
16. S. J. Pennycook, D. E. Jesson, *Phys. Rev. Lett.* **64**, 939 (1990).
17. E. M. James, N. D. Browning, *Ultramicroscopy* **78**, 125 (1999).
18. P. M. Voyles *et al.*, *Nature* **416**, 826 (2002).
19. H. Gu, R. M. Cannon, M. Rühle, *J. Mater. Res.* **13**, 376 (1998).
20. T. Nakayasu *et al.*, *J. Am. Ceram. Soc.* **81**, 565 (1998).
21. M. Yoshiya, K. Tatsumi, I. Tanaka, H. Adachi, *J. Am. Ceram. Soc.* **85**, 109 (2002).
22. L. Benco, *Surf. Sci.* **327**, 274 (1995).
23. L. Benco *et al.*, *J. Am. Ceram. Soc.* **86**, 1162 (2003).
24. I. Tanaka *et al.*, *Acta Met. Mater.* **40**, 1995 (1992).
25. W.-Y. Ching, M. Z. Huang, S. D. Mo, *J. Am. Ceram. Soc.* **83**, 780 (2000).
26. S. H. Garofalini, W. Luo, *J. Am. Ceram. Soc.* **86**, 1741 (2003).

27. The authors thank M. J. Hoffmann and R. L. Satet from IKM Karlsruhe, Germany, for providing some of the ceramic material for this investigation. This work was supported by the Director, Office of Science, Office of Basic Energy Sciences, Division of Materials Sciences and Engineering of the U.S. Department of Energy under Contract No. DE-AC03-76SF00098 and FG02-03ER-46057.

17 August 2004; accepted 27 October 2004

Coherent Atomic Motions in a Nanostructure Studied by Femtosecond X-ray Diffraction

M. Bargheer,[1] N. Zhavoronkov,[1] Y. Gritsai,[1] J. C. Woo,[2] D. S. Kim,[2] M. Woerner,[1]* T. Elsaesser[1]

Reversible structural changes of a nanostructure were measured nondestructively with subpicometer spatial and subpicosecond temporal resolution via x-ray diffraction (XRD). The spatially periodic femtosecond excitation of a gallium arsenide/aluminum gallium arsenide superlattice results in coherent lattice motions with a 3.5-picosecond period, which was directly monitored by femtosecond x-ray pulses at a 1-kilohertz repetition rate. Small changes ($\Delta R/R$ = 0.01) of weak Bragg reflexes (R = 0.005) were detected. The phase and amplitude of the oscillatory XRD signal around a new equilibrium demonstrate that displacive excitation of the zone-folded acoustic phonons is the dominant mechanism for strong excitation.

XRD can not only generate three-dimensional maps of equilibrium structures with subpicometer (pm) accuracy but can be used to follow structural changes induced by ultrashort pump pulses, which can, for example, trigger chemical reactions. The structural changes that result from these pulses can be monitored by time-delayed x-ray probe pulses.

Synchrotron sources have been used to follow structural changes in organic and protein crystals with excellent spatial resolution (*1*, *2*). The temporal resolution of approximately 150 ps (*3*, *4*), however, is not sufficient for real-time observation of intrinsic microscopic motions, such as those of chemical bonds, which occur in the femtosecond (fs) time domain. Various methods can increase the time resolution of synchrotron pulses, but this increase results in a strongly reduced flux of useful photons (*5*–*9*).

Very few experiments have been performed with such techniques. X-ray plasma sources driven by intense femtosecond optical pulses provide ultrashort bursts of incoherent hard x-rays, which allow for diffraction experiments with a 100-fs time resolution (*10*). To date, these sources have worked at a 10-Hz repetition rate and have mainly been used to investigate large atomic displacements near phase transitions that produce readily detected changes in the diffraction signal. However, these large atomic amplitudes also lead to multishot degradation and permanent damage of the samples (*10*–*16*).

We report here on nondestructive fs-XRD measurements of minute reversible structural changes in a nanostructured solid. These changes conserve the crystal volume and occur in the femtosecond time domain. We chose a GaAs/AlGaAs superlattice (SL) as a prototype sample that represents a larger class of inorganic and organic nanostructures (Fig. 1A). A femtosecond laser pulse impulsively excites electron-hole pairs in the lowest n = 1 sub-band of the GaAs quantum wells (QWs) (Fig. 1B), weakening the interatomic bonds by transferring valence band (bonding orbital) electrons into conduction band (anti-bonding orbital) states. The crystal lattice responds to such excitation with an expansion of the wells and a concomitant compression of the AlGaAs barriers, and vice versa in the next half period, triggering a coherent acoustic standing wave (Fig. 1C). The amplitude of this motion is a fraction, $S = \Delta a/a_0 = 1.5 \times 10^{-4}$, of the lattice constant a_0 = 565 pm. This displacive excitation of coherent phonons (DECP) (*17*) is a prototype for a much wider class of phase-coherent atomic motion, which is initiated in each unit cell of a (molecular) crystal. DECP is the solid-state analog of the Franck-Condon principle for electronic excitation of molecules.

The generation and detection of coherent phonons in semiconductor nanostructures have been considered in contexts such as phonon cavities (*18*) and coherent control (*19*). Weak excitation pulses have been used to drive zone-folded longitudinal acoustic phonons (ZFLAPs) in semiconductor SLs, and this process can be monitored with femtosecond optical reflectivity measurements (*20*, *21*). In contrast to bulk crystals, an SL has a mini-Brillouin zone in reciprocal space corresponding to the periodicity d_{SL} (Fig. 1A). Zone folding into this reduced scheme (Fig. 1C) transforms a former bulk acoustic phonon with wave vector $k = g_{SL}$ into an

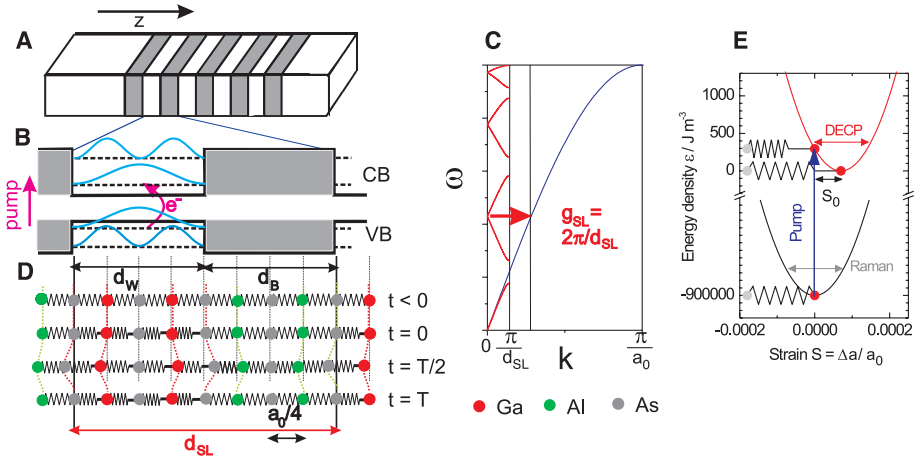

Fig. 1. (**A**) Semiconductor SL consisting of GaAs QWs (white) and AlGaAs barriers (gray). (**B**) Probability densities $|\Psi_n^{VB,CB}(z)|^2$ (blue lines) of the electronic n = 1 and n = 2 valence (VB) and conduction (CB) sub-band states in the respective SL potentials along z; that is, in the (001) direction. (**C**) Dispersion relation of longitudinal acoustic (LA) phonons in the folded Brillouin zone of the SL. The reciprocal SL vector g_{SL} indicates the experimentally excited ZFLAP. (**D**) Linear chain model for the phonon dynamics (not to scale): Atomic layers, [(001) planes] of Ga, As, or an alloy of Al and Ga atoms connected by schematic springs are in their equilibrium positions before excitation time $t < 0$. Photoexcitation at $t = 0$ results in an instantaneous stress within the QWs: compression of the springs, with the atoms still being at their initial positions (no strain). $t = T/2$, $t = T$: snapshots of the dynamically strained crystal for different phases of ZFLAP with period T. (**E**) Excitation of electrons from binding VB to anti-binding CB states corresponds to a displacement of the equilibrium position of the harmonic potential surface of the electronically excited state in the configurational coordinate drawing.

[1]Max-Born-Institut für Nichtlineare Optik und Kurzzeitspektroskopie, 12489 Berlin, Germany. [2]School of Physics, Seoul National University, Seoul 151-742, Korea.

*To whom correspondence should be addressed. E-mail: woerner@mbi-berlin.de

optical phonon of the SL at $k = 0$ (*22*). Similarly to the case of bulk optical phonons (*23*, *24*), there are controversial claims about the phonon excitation mechanism in an SL; namely, Raman excitation (*20*) versus displacive excitation (*21*). The DECP mechanism discussed above yields oscillations in the excited electronic state around a displaced equilibrium position (red arrow in Fig. 1E). In contrast, the Raman process excites phonons in the electronic ground state (gray arrow in Fig. 1E) with unchanged equilibrium. In all-optical experiments, this basic difference between the two mechanisms has to be inferred indirectly from the phases of the modulated electronic susceptibilities, where the signal strongly depends on the probe mechanism and wavelength (*20*, *21*). The use of fs-XRD remains the only method to measure the ultrafast motion of atoms directly in real time, and our experiment provides direct evidence for the displacive excitation mechanism for ZFLAPs in semiconductor SLs in the high-excitation regime. Our work shows that the oscillations of the nuclei occur around a displaced equilibrium; that is, in the excited electronic state, which is different from the situation reported for weak excitation in the same material (*20*).

The SL sample, grown by molecular beam epitaxy on a GaAs substrate, consisted of 2000 layers of electronically uncoupled 8-nm GaAs QWs and 8-nm $Al_{0.4}Ga_{0.6}As$ barriers (Fig. 1A). The tabletop setup of the laser-driven sub-ps x-ray plasma source working at a 1-kHz repetition rate is detailed in Fig. 2A. An 800-nm pump pulse with a flux of 2 mJ cm^{-2} excited electron-hole pairs via interband absorption. The pump pulse was absorbed exclusively in the QWs, and it created a spatially modulated excitation with the periodicity of the SL exactly matching the reciprocal SL vector $g_{SL} = 2\pi/d_{SL}$ (the inverse SL period $d_{SL} = 16$ nm, Fig. 1C). A time-delayed x-ray pulse was diffracted from the sample to probe the resulting lattice dynamics. Copper K_α emission was used in forward geometry, which allowed for an accurate measurement of the timing of pump and probe pulses. An x-ray charge-coupled device (CCD) camera monitored the rocking curve. The influence of intensity fluctuations of the source was removed by normalizing to reflections not affected by the pump pulse. The signal (Fig. 3A) was taken as the intensity difference between the pumped and the unpumped region in Fig. 2B.

The static rocking curve of the SL sample around the (002) reflex (Fig. 2C) consists of a zeroth-order SL peak and two ±first-order satellites (*25*), each occurring twice because the incident K_α radiation is a doublet. The central (002) peak occurs at the reciprocal lattice vector G_{002}, which was determined by the average lattice constant $a_0 = (a_W + a_B)/2$ of the entire crystal (a_W and a_B are lattice constants of the well and barrier, respectively). The spacings to the ±first order satellites are $\pm g_{SL} = \pm 2\pi/d_{SL}$, as seen in the wave vector diagram of Fig. 2D.

The intensity of the satellites depended sensitively on lattice dynamics within the SL unit cell. The pump-probe data in Fig. 3A (symbols) display a periodic intensity modulation of the −first-order peak as a function of the time delay. The oscillation period of 3.5 ps corresponds to a frequency $\nu = 0.29$ THz (Fourier transform in Fig. 3B) (*26*). In contrast, the angular position of the −first-order peak (Fig. 3C) is constant, disregarding small fluctuations on the order of $\Delta\Theta/\Theta = \Delta a/a_0 \approx 10^{-5}$. This result demonstrates both the unchanged volume of the crystal in the measured time range and the fully reversible character of the lattice excitation at the 1-kHz repetition rate. The intensity modulations (Fig. 3A) show a reflectivity change of $\Delta R_{max}/R_0 = 0.03$ for a peak with $R_0 = 0.005$, a sensitivity much higher than in earlier sub-ps diffraction experiments.

Interband excitation of the QWs by the 50-fs pump pulse at 800 nm created an electron-hole plasma in the $n = 1$ valence and conduction sub-bands. The high-excitation flux saturated the interband absorption by bandfilling; that is, transitions were blocked because the optically coupled

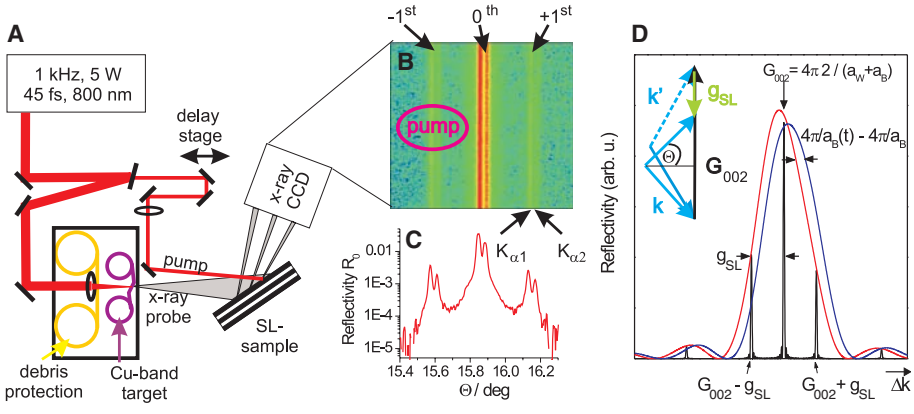

Fig. 2. (**A**) Setup for fs-XRD. The output radiation from a Ti:sapphire laser system (wavelength $\lambda = 800$ nm, 1-kHz repetition rate) with 5-mJ pulse energy and 45-fs duration is focused on a moving, 20-μm-thick Cu band to generate characteristic line emission. Together, the two Cu K_α lines at 8048 and 8027 eV provide a photon flux of 4×10^9 photons sec^{-1} sr^{-1}. The angular divergence Θ of the point source (10-μm diameter) covers the rocking curve of the (002) reflection from the –first to +first SL peak. The source-sample distance is 100 mm. An x-ray CCD camera detects the diffracted photons 200 mm after the sample. Each point in the recorded diffraction image (**B**) corresponds to a position on the sample. The ellipse indicates the region pumped by the 800-nm light. (**C**) Rocking curve obtained from vertical integration of (B). (**D**) Schematic of the (002) SL rocking curve (black line) together with that of the corresponding single SL unit cell (red envelope) as a function of $\Delta k = (4\pi/\lambda)\sin\Theta$ (Bragg's law). A compression of the barriers shifts the envelope toward the position of the blue curve, thus modulating the intensity of the satellites. (Inset) Wave vector diagram of SL x-ray diffraction.

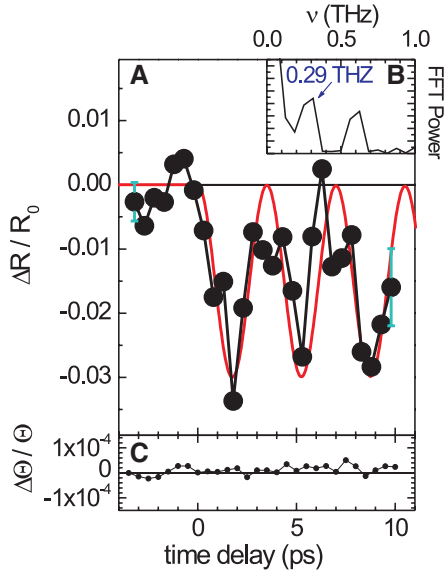

Fig. 3. (**A**) Intensity modulation of the –first-order SL peak after ultrafast excitation of electron-hole pairs in the $n = 1$ sub-bands of the semiconductor nanostructure. Plotted is the relative reflectivity change $\Delta R/R_0$ as a function of time delay between a near-infrared pump and x-ray probe pulses. The error bar on the first data point indicates the error from the photon statistics for an acquisition time of 8 min. The error bar on the right is the average standard deviation of four independent measurements. The solid red line represents the result from a simulation, showing a cosine-like oscillation with a period of 3.5 ps of the ZFLAP. (**B**) Fourier transform of the time-resolved data in (A). (**C**) Angular position ΔΘ of the –first-order peak.

valence and conduction band states were populated. For a quasi-equilibrium distribution of electron-hole pairs, we estimated a saturation carrier density $N_{ex} \approx 4 \times 10^{18}$ cm^{-3}, corresponding to 3×10^{12} cm^{-2} per QW, at which point the interband transitions around 800 nm became blocked. For our pump flux of 2 mJ cm^{-2} $\cong 8 \times 10^{15}$ photons cm^{-2}, interband absorption was saturated throughout the SL and resulted in an excitation pattern with the spatial periodicity of the SL.

Such optical excitation of electron-hole pairs was instantaneous with respect to the lattice motions observed in the experiment. The weakening of interatomic bonds by transferring valence band (bonding orbital) electrons into conduction band (anti-bonding orbital) states created an instantaneous stress that impulsively induced coherent lattice motions that gave rise to the modulation of the −first Bragg peak (Fig. 3A). The spatial periodicity d_{SL} of the excitation (*21*) (that is, the stress profile) selectively drove the coherent ZFLAPs by matching the wave vector $k = g_{SL}$ shown in Fig. 1C. The corresponding strain, however, did not affect the size of the SL unit cell, which is clear from the time-independent angular position of the Bragg peak (Fig. 3C).

We now discuss how the small atomic amplitudes $\Delta a/a$ are translated into relatively large reflectivity modulations $\Delta R/R_0$ (Fig. 3A) of the selected satellite of the (002) reflex (Fig. 2D). Because the GaAs wells have a negligible (002) structure factor (quasi-forbidden because $Z_{Ga} = 31 \approx Z_{As} = 33$), the $\Delta R/R_0$ of any (002) reflex (*27*) is exclusively caused by the AlGaAs barriers ($Z_{Al} = 13$). A compression of the barriers shifts the envelope [Fig. 2D; the red line is the calculated rocking curve for a single SL unit cell before excitation, $a_B{}^0 = a_B(t < 0)$] toward the position of the blue envelope [the same for $a_B(t) < a_B{}^0$], thereby modulating the intensity of the satellite peak strictly fixed at its initial Bragg angle. Thus, $\Delta R/R_0$ is directly proportional to the time-dependent change of the barrier lattice constant $a_B(t)$. Because dynamic x-ray diffraction theory (*28*) predicts $\Delta R/R_0 = 200 \times \Delta a_B/a_B$, the experimentally measured negative $\Delta R/R_0 = 0.03$ implies a barrier compression of $S = \Delta a_B/a_B = 1.5 \times 10^{-4}$.

We now show that the DECP mechanism is in full quantitative agreement with our experimental results. Using the hydrostatic deformation potential $A = 10$ eV (*29*) ($\Delta E_{gap} = AS$), we estimated an instantaneous stress in the QWs of $P = N_{ex} A \approx 5$ MPa. From $P = d\varepsilon/dS$, we constructed the displaced harmonic oscillator in the configurational coordinate diagram shown in Fig. 1E. The electron-phonon interaction displaces the equilibrium position of the harmonic potential surface of the electronically excited crystal relative to its ground state (no electron-hole pairs). From the elastic constant $C = 120$ kJ cm^{-3} of the harmonic potentials $\varepsilon = 1/2\ CS^2$, we calculated $S_0 = 7 \times 10^{-5}$ (Fig. 1E).

Using this impulsively excited stress with the spatial pattern of ρ_{ex} (Fig. 4B), we simulated the phonon dynamics within a linear chain model (*22*) schematically explained in Fig. 1D. The calculated strain pattern (the lattice plane distances) is shown in Fig. 4C. In Fig. 4D, we show absolute amplitudes of the selected atomic motions color-coded in Fig. 4A. The model predicts oscillations of interface atomic layers with a period of 3.5 ps and an amplitude of $a_B = 0.6$ pm.

Inserting the lattice distortion simulated in the linear chain model, we calculated the time-dependent rocking curve using standard dynamical theory of x-ray diffraction (*28*). The result is plotted as the red line in Fig. 3A together with the experimental data. We find a very good agreement for both phase and absolute amplitude of $\Delta R_{max}/R_0$. More precisely, $\Delta R(t)/R_0 \approx \Delta R_{max}/2R_0 \times [\cos(2\pi\nu t) - 1]$ is an oscillation with the amplitude $\Delta R_{max}/2R_0$ around an equilibrium position displaced by the same amount. This constitutes direct experimental proof of the displacive excitation mechanism (Fig. 1E) under conditions of strong excitation, in contrast to the results for weak excitation (*20*).

We have demonstrated that spatially modulated excitation allows for mode-selective excitation of coherent atomic motions. The use of SLs with thinner layers can reduce the oscillation period of the zone-folded phonons to hundreds of femtoseconds. The proposal to use phonons as efficient "ultrafast Bragg switches" (30) can thus be extended by tailoring suitable nanostructures. The results presented here benchmark a new limit of versatility and sensitivity of fs-XRD with high repetition-rate laser-plasma sources. The broad range of applications to diverse systems from superconductors to molecular crystals sets a future direction for ultrafast x-ray research.

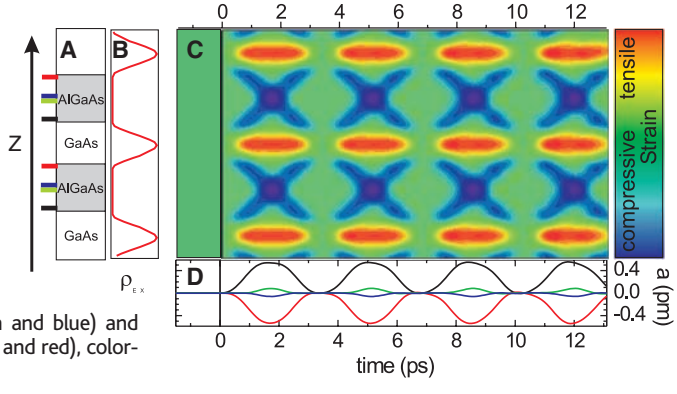

Fig. 4. Simulation of the phonon dynamics using a linear chain model. (**A**) Schematic of SL. (**B**) Impulsively excited spatial electron-hole density (initial condition). (**C**) Contour plot of the transient strain in the SL as a function of time and *z*. (**D**) Transient amplitudes *a* of the central atoms in the wells (green and blue) and the interface atoms (black and red), color-coded in (A).

References and Notes

1. E. Collet *et al.*, *Science* **300**, 612 (2003).
2. F. Schotte *et al.*, *Science* **300**, 1944 (2003).
3. M. F. DeCamp *et al.*, *Nature* **413**, 825 (2001).
4. D. A. Reis *et al.*, *Phys. Rev. Lett.* **86**, 3072 (2001).
5. R. W. Schoenlein *et al.*, *Science* **274**, 236 (1996).
6. R. W. Schoenlein *et al.*, *Science* **287**, 2237 (2000).
7. Z. Chang *et al.*, *Appl. Phys. Lett.* **69**, 133 (1996).
8. J. Larsson *et al.*, *Opt. Lett.* **22**, 1012 (1997).
9. A. M. Lindenberg *et al.*, *Phys. Rev. Lett.* **84**, 111 (2000).
10. K. Sokolowski-Tinten *et al.*, *Phys. Rev. Lett.* **87**, 225701 (2001).
11. K. Sokolowski-Tinten *et al.*, *Nature* **422**, 287 (2003).
12. A. Cavallieri *et al.*, *Phys. Rev. Lett.* **85**, 586 (2000).
13. C. Rose-Petruck *et al.*, *Nature* **398**, 310 (1999).
14. C. Rischel *et al.*, *Nature* **390**, 490 (1997).
15. C. W. Siders *et al.*, *Science* **286**, 1340 (1999).
16. A. Rousse *et al.*, *Nature* **410**, 65 (2001).
17. H. J. Zeiger *et al.*, *Phys. Rev. B* **45**, 768 (1992).
18. M. Trigo, A. Bruchhausen, A. Fainstein, B. Jusserand, V. Thierry-Mieg, *Phys. Rev. Lett.* **89**, 227402 (2002).
19. Ü. Özgür, C. W. Lee, H. O. Everitt, *Phys. Rev. Lett.* **86**, 5604 (2001).
20. A. Bartels, T. Dekorsy, H. Kurz, K. Köhler, *Phys. Rev. Lett.* **82**, 1044 (1999).
21. C. K. Sun, J. C. Liang, X. Y. Yu, *Phys. Rev. Lett.* **84**, 179 (2000).
22. C. Colvard *et al.*, *Phys. Rev. B* **31**, 2080 (1985).
23. K. J. Yee, Y. S. Lim, T. Dekorsy, D. S. Kim, *Phys. Rev. Lett.* **86**, 1630 (2001).
24. T. E. Stevens, J. Kuhl, R. Merlin, *Phys. Rev. B* **65**, 144304 (2002).
25. L. Tapfer, K. Ploog, *Phys. Rev. B* **33**, 5565 (1986).
26. The Fourier spectrum (Fig. 3 B) shows an additional frequency component around 0.6 THz, corresponding to the zone-folded phonon with $k = 2g_{SL}$.
27. A. Krost, G. Bauer, J. Woitok, *Optical Characterization of Epitaxial Semiconductor Layers*, G. Bauer, W. Richter, Eds. (Springer, Berlin, 1996), pp. 287–391.
28. S. M. Durbin, G. C. Follis, *Phys. Rev. B* **51**, 10127 (1995).
29. A. R. Goñi, K. Strössner, K. Syassen, M. Cardona, *Phys. Rev. B* **36**, 1581 (1987).
30. P. H. Bucksbaum, R. Merlin, *Solid State Commun.* **111**, 535 (1999).

31. This work was sponsored by the Deutsche Forschungsgemeinschaft via Schwerpunktprogramm SPP 1134 and by the Bundesministerium für Bildung und Forschung, project 13N7923. We acknowledge D. H. Woo, K. G. Yee, and S. B. Choi for the sample growth. This work in Korea was supported by the Korean Science and Engineering Foundation, the Ministry of Science and Technology, and the Korean Research Foundation (2003-015-C00185).

1 September 2004; accepted 22 October 2004

Hematotoxicity in Workers Exposed to Low Levels of Benzene

Qing Lan,[1]* Luoping Zhang,[2]* Guilan Li,[3] Roel Vermeulen,[1] Rona S. Weinberg,[4] Mustafa Dosemeci,[1] Stephen M. Rappaport,[5] Min Shen,[1] Blanche P. Alter,[1] Yongji Wu,[6] William Kopp,[7] Suramya Waidyanatha,[5] Charles Rabkin,[1] Weihong Guo,[2] Stephen Chanock,[1,8] Richard B. Hayes,[1] Martha Linet,[1] Sungkyoon Kim,[5] Songnian Yin,[3] Nathaniel Rothman,[1]† Martyn T. Smith[2]†‡

Benzene is known to have toxic effects on the blood and bone marrow, but its impact at levels below the U.S. occupational standard of 1 part per million (ppm) remains uncertain. In a study of 250 workers exposed to benzene, white blood cell and platelet counts were significantly lower than in 140 controls, even for exposure below 1 ppm in air. Progenitor cell colony formation significantly declined with increasing benzene exposure and was more sensitive to the effects of benzene than was the number of mature blood cells. Two genetic variants in key metabolizing enzymes, myeloperoxidase and NAD(P)H:quinone oxidoreductase, influenced susceptibility to benzene hematotoxicity. Thus, hematotoxicity from exposure to benzene occurred at air levels of 1 ppm or less and may be particularly evident among genetically susceptible subpopulations.

Benzene causes toxicity to the hematopoietic system (hematotoxicity) and leukemia (*1*). Exposure to benzene occurs worldwide to workers in the oil, shipping, automobile repair, shoe manufacture, and other industries and to the general public from cigarette smoke, gasoline, and automobile emissions (*2*). In addition to ongoing concern about health effects at or below the current U.S. occupational standard of 1 ppm, high environmental exposures in cities (*3*) have led to regulatory consideration of the risks posed by benzene as an air pollutant.

Limitations in previous occupational studies evaluating hematotoxicity at low levels of benzene exposure led us to perform a large cross-sectional study with detailed exposure assessment that measured lymphocyte subsets and colony formation from progenitor cells in addition to the standard blood-count analyses reported in most previous investigations. Because benzene is thought to lower blood cell counts via metabolite effects on hematopoietic progenitor cells (*4*), we also evaluated the influence of genetic variants in cytochrome P4502E1 (CYP2E1) and myeloperoxidase (MPO), which metabolize benzene to toxic quinones and free radicals (*5*), and NAD(P)H:quinone oxidoreductase (NQO1), which protects against this toxicity (*6*, *7*).

We compared 250 benzene-exposed shoe workers with 140 unexposed age- and sex-matched controls who worked in three clothes-manufacturing factories in the same region near Tianjin, China. Subjects were young (mean ± SD: 29.9 ± 8.4 years), about two-thirds were female (table S1), and shoe workers had been employed an average of 6.1 ± 2.9 years. For each subject, individual benzene and toluene exposure was monitored repeatedly up to 16 months before phlebotomy, and postshift urine samples were collected from each subject (*8*, *9*). Subjects were categorized into four groups by mean benzene levels measured during the month before phlebotomy [controls, <1 ppm, 1 to <10 ppm, and ≥10 ppm (Table 1)], and more than 100 of the exposed workers had exposures below 1 ppm.

All types of white blood cells (WBCs) measured in the Complete Blood Count and platelets (*9*) were significantly decreased in workers exposed to <1 ppm benzene compared to controls (Table 1). Lymphocyte subset analysis showed significantly decreased $CD4^+$–T cells, $CD4^+/CD8^+$ ratio, and B cells. Hemoglobin concentrations were decreased only among workers exposed to ≥10 ppm. Tests for a linear trend using benzene air level as a continuous variable were significant for platelets and all WBC measures except monocytes and $CD8^+$–T cells (Table 1). Adjustment for a range of potential confounders had a negligible effect on the strength of the associations (*9*).

We then restricted the linear-trend analyses to workers exposed to <10 ppm benzene, excluding controls and higher exposed workers, and found that inverse associations remained for total WBCs (P = 0.013), granulocytes (P = 0.02), lymphocytes

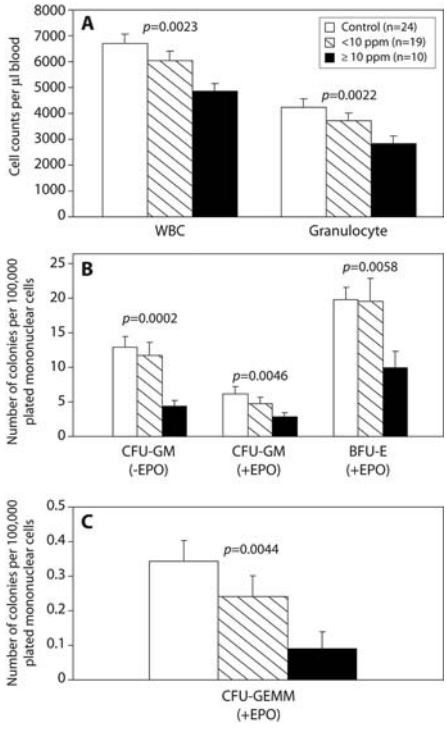

Fig. 1. Effect of benzene exposure on (**A**) white blood cell (WBC) and granulocyte counts; (**B**) colonies from the colony-forming unit–granulocyte-macrophage (CFU-GM) and burst-forming unit–erythroid (BFU-E); and (**C**) colonies from the colony-forming unit–granulocyte, erythroid, macrophage, megakaryocyte (CFU-GEMM). Erythropoietin (EPO) was added to half of the cultures (*9*). Trends with benzene were tested by linear regression (WBC, granulocytes), negative binomial regression (CFU-GM, BFU-E), and unconditional logistic regression [CFU-GEMM, categorizing subjects into 0 or more than 0 colonies (92%, 74%, and 40% of subjects had >0 colonies among controls, <10 ppm, and ≥10 ppm, respectively)]. Models were adjusted for age and sex, and additionally for smoking, alcohol, recent infections, and body mass index (BMI) if significant (*9*). Strong, inverse trends between benzene and all cell types were present (P_{trend} shown). There was a greater proportional decrease in colonies in workers exposed to ≥10 ppm versus controls for CFU-GM, BFU-E, and CFU-GEMM compared to the decline in WBCs (P < 0.011, 0.048, and 0.0078, respectively) and for CFU-GM and -GEMM compared to the decline in granulocytes (P = 0.026 and 0.0094, respectively) (*9*).

[1]Division of Cancer Epidemiology and Genetics, National Cancer Institute (NCI), National Institutes of Health (NIH), Department of Health and Human Services (DHHS), Bethesda, MD 20892, USA. [2]School of Public Health, University of California, Berkeley, CA 94720, USA. [3]Chinese Center for Disease Control and Prevention, Beijing, China. [4]New York Blood Center, Clinical Services, White Plains, NY 10605, USA. [5]School of Public Health, University of North Carolina, Chapel Hill, NC 27599, USA. [6]Peking Union Medical College, Beijing, China. [7]SAIC-Frederick, Inc., Frederick, MD 21702, USA. [8]Center for Cancer Research, NCI, NIH, DHHS, Bethesda, MD 20892, USA.

*These authors contributed equally to this work.
†These authors co-supervised this work.
‡To whom correspondence should be addressed. E-mail: martynts@berkeley.edu

(P = 0.045), B cells (P = 0.018), and platelets (P = 0.0016). To address the influence of past benzene exposure on these cell types, we examined workers exposed to mean benzene <1 ppm over the previous year (n = 60), and a subset who also had <40-ppm-years lifetime cumulative benzene exposure (n = 50), and found that the above cell types were decreased compared to controls ($P < 0.05$). Finally, to exclude the effect of other potential exposures on these associations, we identified a group of workers exposed to <1 ppm benzene with negligible exposure to other solvents (n = 30) (fig. S1) (*9*) and found decreased levels of WBCs, granulocytes, lymphocytes, and B cells compared to controls ($P < 0.05$). These findings, based on differentiated blood cell counts, provide evidence of hematotoxicity in workers exposed to benzene at or below 1 ppm.

Because benzene affected nearly all blood cell types, toxicity to progenitor cells was suspected. A fraction of hematopoietic progenitor cells circulate in the bloodstream in dynamic equilibrium with the bone marrow and can be cultured in colony-forming assays to measure their proliferative potential (*10*). Using peripheral blood from 29 benzene-exposed workers and 24 matched controls, we examined the dose-dependent effects of benzene on different types of progenitor cell colony formation (CFU-GM, BFU-E, CFU-GEMM) (*9*). Highly significant dose-dependent decreases in colony formation from progenitor cells were observed (Fig. 1). Further, benzene caused a greater proportional decrease in colony formation than in levels of differentiated WBCs and granulocytes (compare Fig. 1, B and C, to Fig. 1A), suggesting that early progenitor cells are more sensitive than are mature cells to the hematotoxic effects of benzene. This greater sensitivity of early progenitor cells is in agreement with previous findings in human cell cultures and mice (*11*, *12*).

Genetic variation in enzymes responsible for activating and detoxifying benzene has been shown to confer susceptibility to benzene poisoning in highly exposed workers (*6*, *13*, *14*). We examined four nonsynonymous single-nucleotide polymorphisms (SNPs), with probable functional significance, in the *CYP2E1*, *MPO*, and *NQO1* genes (*9*). Two genotypes significantly influenced WBC counts in benzene-exposed workers, *MPO* –463GG (rs2333227) (P = 0.04) and *NQO1* 465CT (rs4986998) (P = 0.014) (table S2). In exposed subjects who carry either one (n = 191) or both of the "at risk" genotypes (n = 11), there was a strong gene-dosage effect (P_{trend} = 0.004) (table S3), which was also present among those exposed to <1 ppm (P_{trend} = 0.003). Compared to a mean ± SD WBC count of 5980 ± 1420 cells/μl among subjects with neither "at risk" genotype, the WBC count was 5480 ± 1120 cells/μl among subjects with either "at risk" genotype (P = 0.006) and 4900 ± 1240 cells/μl (P = 0.039) for both genotypes, in subjects exposed to <1 ppm. Neither genotype was associated with WBC count in controls, either separately (table S2) or in combination (P_{trend} = 0.94) (table S3), and the trends in exposed workers and controls were significantly different from each other (test for interaction, P = 0.03). Subjects with the *MPO* –463GG genotype have normal expression and had a greater decrease in WBC counts from benzene exposure compared to individuals with the GA or AA genotypes (the latter two being associated with reduced expression) (*15*). The functional significance of the *NQO1* 465C>T SNP is less clear, but it may increase alternative splicing and lower expression, thereby enhancing benzene hematotoxicity, as we observed. The other two SNPs [*CYP2E1* –1053C>T (rs2031920) and *NQO1* 609C>T (rs1800566)] were not significantly related to WBCs (table S2).

There have been numerous studies of benzene-induced hematotoxicity (www.epa.gov/iris/toxreviews/0276-tr.pdf), but few have been able to study effects at low levels of exposure. Ward *et al*. (*16*) found no evidence of a threshold for hematotoxic effects of benzene and suggested that exposure to <5 ppm benzene could result in hematologic suppression. Occupational exposure decreased WBCs in petrochemical workers exposed to <10 ppm benzene (*17*), and Qu *et al*. reported that WBCs and other cell types were decreased in workers exposed to <5 ppm benzene (*18*). In contrast, Collins *et al*. (*19*, *20*) and Tsai *et al*. (*21*) did not detect decreased blood cell counts based

Table 1. Peripheral blood cell counts in relation to benzene exposure level. There are up to 418 observations on 390 unique subjects (140 controls and 250 benzene-exposed workers). Data were obtained from 28 exposed subjects in both years (2000 and 2001) and are treated as independent observations in the summary data shown, distributing into benzene category on the basis of exposure level in the year that the blood sample was collected. Statistical analyses were adjusted for repeated measures by generalized estimating equations (*22*). Models were adjusted for age, sex, current smoking, current alcohol drinking, BMI, recent infections, and, where appropriate, ln toluene air level (which can competitively inhibit benzene's metabolism) (*9*). Data shown here are from all subjects except one benzene-exposed subject with data for only $CD4^+/CD8^+$ ratio; two benzene-exposed subjects and one control with no benzene urine data; and two controls with no BMI data.

Subject category (n)*	Controls (140)	<1 ppm (109)	1 to <10 ppm (110)	≥10 ppm (31)	P for <1 ppm vs. controls†	P_{trend}, all subjects‡§
			Benzene exposure			
Benzene air level (ppm)‖	<0.04	0.57 (0.24)	2.85 (2.11)	28.73 (20.74)		
Benzene urine (μg/liter)¶	0.382 (1.24)	13.4 (18.3)	86.0(130)	847(1250)		
			Peripheral blood cell counts#			
White blood cells (WBC)**	6480 (1710)	5540 (1220)	5660 (1500)	4770 (892)	<0.0001	<0.0001
Granulocytes	4110 (1410)	3360 (948)	3480 (1170)	2790 (750)	<0.0001	<0.0001
Lymphocytes††	2130 (577)	1960 (541)	1960 (533)	1800 (392)	0.018	0.0014
$CD4^+$–T cells	742 (262)	635 (187)	623 (177)	576 (188)	0.003	0.019
$CD8^+$–T cells	553 (208)	543 (212)	564 (229)	549 (160)	0.75	0.97
$CD4^+/CD8^+$ ratio	1.46 (0.58)	1.26 (0.41)	1.22 (0.45)	1.09 (0.35)	0.015	0.024
B cells	218 (94)	186 (95)	170 (75)	140 (101)	0.003	0.0002
NK cells	586 (318)	558 (299)	566 (271)	415 (188)	0.56	0.0044
Monocytes	241 (92)	217 (97)	224 (93)	179 (74)	0.018	0.28
Platelets	230 (59.7) × 10^3	214 (48.8) × 10^3	200 (53.4) × 10^3	172 (44.8) × 10^3	0.023	0.0002
Hemoglobin (g/dl)	14.5 (1.6)	14.7 (1.5)	14.5 (1.7)	13.6 (1.6)	0.12	0.29

*The 28 subjects studied in both the first (2000) and second (2001) year of the study are categorized based on the exposure assessment in 2000. †Controls versus exposed <1 ppm, by linear regression on ln of each endpoint. ‡P_{trend} using ln air benzene as a continuous variable. All statistically significant endpoints were inversely associated with benzene exposure. §Comparison of subjects ≥10 ppm versus controls for endpoints without statistically significant trends: $CD8^+$–T cells, P = 0.31; monocytes, P = 0.0006; hemoglobin $P < 0.0001$. ‖Benzene air level is the arithmetic mean (±SD) of an average of two measurements per subject collected during the month before phlebotomy (*9*). This time period was chosen because granulocytes have relatively short half-lives in peripheral blood. ¶Urinary benzene (mean ± SD) and mean individual air levels of benzene were strongly correlated (Spearman r = 0.88, $P < 0.0001$). #Unadjusted mean (±SD) cells/μl blood. **Supplementary analyses are shown in the SOM Text. ††Absolute count.

on routine monitoring of workers exposed to low levels of benzene.

The present study showed that total WBCs, granulocytes, lymphocytes, B cells, and platelets significantly declined with increasing benzene exposure and were lower in workers exposed to benzene at air levels of 1 ppm or less compared to controls. Our findings are particularly robust because we carried out extensive exposure assessment over a 16-month period (*8*) and linked individual air-monitoring data to the endpoints measured. Further, we showed that benzene exposure decreased colony formation from myeloid progenitor cells, and that these progenitors were more sensitive to benzene toxicity than were mature WBCs. Finally, genetic variation in *MPO* and *NQO1* conferred susceptibility to benzene-induced lowering of WBC counts. Although confirmation of these findings in other studies is needed, these data provide evidence that benzene causes hematologic effects at or below 1 ppm, particularly among susceptible subpopulations.

References and Notes

1. M. Aksoy, *Environ. Health Perspect.* **82**, 193 (1989).
2. G. L. Gist, J. R. Burg, *Toxicol. Ind. Health* **13**, 661 (1997).
3. V. Simon *et al.*, *Sci. Total Environ.* **334–335**, 177 (2004).
4. B. I. Yoon *et al.*, *Exp. Hematol.* **29**, 278 (2001).
5. D. Ross, *Eur. J. Haematol. Suppl.* **60**, 111 (1996).
6. N. Rothman *et al.*, *Cancer Res.* **57**, 2839 (1997).
7. A. K. Bauer *et al.*, *Cancer Res.* **63**, 929 (2003).
8. R. Vermeulen *et al.*, *Ann. Occup. Hyg.* **48**, 105 (2004).
9. Materials and methods are available as supporting material on *Science* Online.
10. L. Kreja, K. M. Greulich, T. M. Fliedner, B. Heinze, *Int. J. Radiat. Biol.* **75**, 1241 (1999).
11. M. T. Smith *et al.*, *Carcinogenesis* **21**, 1485 (2000).
12. D. J. Abernethy, E. V. Kleymenova, J. Rose, L. Recio, B. Faiola, *Toxicol. Sci.* **79**, 82 (2004).
13. J. Wan *et al.*, *Environ. Health Perspect.* **110**, 1213 (2002).
14. J. N. Xu *et al.*, *Zhonghua Lao Dong Wei Sheng Zhi Ye Bing Za Zhi* **21**, 86 (2003).
15. C. C. Winterbourn, M. C. Vissers, A. J. Kettle, *Curr. Opin. Hematol.* **7**, 53 (2000).
16. E. Ward *et al.*, *Am. J. Ind. Med.* **29**, 247 (1996).
17. B. Zhang, *Zhonghua Yu Fang Yi Xue Za Zhi* **30**, 164 (1996).
18. Q. Qu *et al.*, *Am. J. Ind. Med.* **42**, 275 (2002).
19. J. J. Collins *et al.*, *J. Occup. Med.* **33**, 619 (1991).
20. J. J. Collins, B. K. Ireland, P. A. Easterday, R. S. Nair, J. Braun, *J. Occup. Environ. Med.* **39**, 232 (1997).
21. S. P. Tsai *et al.*, *Regul. Toxicol. Pharmacol.* **40**, 67 (2004).
22. S. L. Zeger, K. Y. Liang, *Biometrics* **42**, 121 (1986).

23. We thank the participants for taking part in this study. Supported by NIH grants RO1ES06721, P42ES04705, and P30ES01896 (M.T.S.), P42ES05948 and P30ES10126 (S.M.R.), and NIH contract N01-CO-12400 with SAIC-Frederick, Inc. M.T.S. has received consulting and expert testimony fees from law firms representing both plantiffs and defendants in cases involving exposure to benzene. G.L. has received funds from the American Petroleum Institute for consulting on benzene-related health research.

Supporting Online Material

www.sciencemag.org/cgi/content/full/306/5702/1774/DC1
Materials and Methods
SOM Text
Fig. S1
Tables S1 to S3.
References

7 July 2004; accepted 5 October 2004

A Survey Method for Characterizing Daily Life Experience: The Day Reconstruction Method

Daniel Kahneman,[1] Alan B. Krueger,[1,2] David A. Schkade,[3]* Norbert Schwarz,[4] Arthur A. Stone[5]

The Day Reconstruction Method (DRM) assesses how people spend their time and how they experience the various activities and settings of their lives, combining features of time-budget measurement and experience sampling. Participants systematically reconstruct their activities and experiences of the preceding day with procedures designed to reduce recall biases. The DRM's utility is shown by documenting close correspondences between the DRM reports of 909 employed women and established results from experience sampling. An analysis of the hedonic treadmill shows the DRM's potential for well-being research.

How do people experience the settings and activities of their lives? How do they use their time? These questions are usefully considered together, but there is no generally accepted method for collecting the relevant data. Quantitative information about time use and the frequency and intensity of stress, enjoyment, and other affective states is potentially useful to medical researchers for assessing the burden of different illnesses (*1*) and the health consequences of stress (*2*); to epidemiologists interested in social and environmental stressors (*3*); to economists and policy researchers for evaluating policies and for valuing nonmarket activities (*4*, *5*); and to anyone who wishes to measure the well-being of society. In particular, economic models that define well-being by the temporal integral of momentary experienced utility (*6–8*) require detailed measures of the quality and duration of people's experiences in daily life.

Information about the allocation of time in the daily life of the population is a component of national statistics in several countries. With rare exceptions (*4*, *9*), time-budget studies have not included measures of the satisfaction people derive from their activities. Similarly, questions about time-use and about the subjective experience of specific situations are rarely included in surveys of subjective well-being. Instead, these studies usually rely on global reports of happiness or satisfaction with life in general, or with domains such as work and family (*10*, *11*).

The development of the experience sampling method (ESM) (*12*) and of ecological momentary assessment, which encompasses all momentary phenomena including physiological events (*13*), marked a notable advance in the measurement of the quality of people's lives. Participants in ESM studies are prompted to record where they are, what they are doing, and how they feel several times throughout the day. This technique provides a rich description of a sample of moments in respondents' lives, while avoiding the distortions that affect the delayed recall and evaluation of experiences (*14*). However, experience sampling is expensive, involves high levels of participant burden, and provides little information about uncommon or brief events, which are rarely sampled.

We present a new hybrid approach, the DRM, which combines a time-use study with a technique for recovering affective experiences. DRM respondents first revive memories of the previous day by constructing a diary consisting of a sequence of episodes. Then they describe each episode by answering questions about the situation and about the feelings that they experienced, as in experience sampling. The goal is to provide an accurate picture of the experience associated with activities (e.g., commuting) and circumstances (e.g., a job with time pres-

[1]Woodrow Wilson School and Department of Psychology, [2]Woodrow Wilson School and Economics Department, Princeton University, Princeton, NJ 08540, USA. [3]Rady School of Management, University of California, San Diego, La Jolla, CA 92093–0093, USA. [4]Institute of Social Research and Department of Psychology, University of Michigan, Ann Arbor, MI 48106–1248, USA. [5]Department of Psychiatry and Behavioral Science, Stony Brook University, Stony Brook, NY 11794–8790, USA.

*To whom correspondence should be addressed. E-mail: schkade@ucsd.edu

sure). Evoking the context of the previous day is intended to elicit specific and recent memories, thereby reducing errors and biases of recall (*14*, *15*). Experience sampling is the gold standard to which DRM results must be compared; the DRM is intended to reproduce the information that would be collected by probing experiences in real time. The new method is more efficient than ESM: It imposes less respondent burden; does not disrupt normal activities; and provides an assessment of contiguous episodes over a full day, rather than a sampling of moments. Finally, the DRM provides time-budget information, which is not collected effectively in experience sampling.

We demonstrate the method with a convenience sample of 1018 employed women, focusing on the subset of 909 who had worked on the reference day. The questionnaire and methodological details are available online (*16*). Completion times for the self-administered instrument ranged from 45 to 75 min. The ethnic composition of the sample was 49% white (non-Hispanic), 24% African American, 22% Hispanic, and 5% other. Average age was 38 years. Average household income was $54,700.

Respondents first answered demographic and general satisfaction questions. Next, they were asked to construct a short diary of the previous day: "Think of your day as a continuous series of scenes or episodes in a film. Give each episode a brief name that will help you remember it (for example, 'commuting to work', or 'at lunch with B'…). Write down the approximate times at which each episode began and ended. The episodes people identify usually last between 15 minutes and 2 hours. Indications of the end of an episode might be going to a different location, ending one activity and starting another, or a change in the people you are interacting with." Respondents were not required to turn in their diary. The average number of episodes was 14.1 (SD = 4.8), and average episode duration was 61 min. Next, respondents answered structured questions about each episode: When it occurred (start and end times); what they were doing (by checking one or more of 16 activities); where they were; with whom they were interacting; and how they felt, using 12 affect descriptors, listed in Table 1. The affect scales ranged from 0 (not at all) to 6 (very much). Finally, respondents answered questions about their jobs and other personal details.

To show the results of the DRM, Table 1 presents affect ratings of situations, grouped by activity (e.g., eating or working) or by interaction partner. The values shown are average ratings of particular experiences. They differ in interesting and predictable ways from generic enjoyment ratings of the same activities. Juster (*4*) and Flood (*9*), for example, observed that interactions with one's children topped the list of enjoyable activities, followed by going on trips, being with friends, and working at one's job. Grocery shopping and cleaning the house were rated lowest among 28 activities. In Table 1, taking care of one's children ranks just above the least enjoyable activities of working, housework, and commuting. The contrasting results likely reflect the difference between belief-based generic judgments ("I enjoy my kids") and specific episodic reports ("but they were a pain last night"). The task of judging a category of events evokes instances that are prototypical but not necessarily typical, and discourages reports of socially inappropriate affect (*14*). These deficiencies are attenuated when respondents describe specific episodes, as they do in the DRM.

Table 1 shows a large difference between positive and negative affect. Negative affect is relatively infrequent and mild, and the total absence of positive affect is rare. In

Table 1. Mean affect by situation. Positive affect is the average of happy, warm/friendly, enjoying myself. Negative affect is the average of frustrated/annoyed, depressed/blue, hassled/pushed around, angry/hostile, worried/anxious, criticized/put down. For each situation, the table shows the mean ratings on affect descriptors, the average amount of time all respondents spent in the situation, and the proportion of respondents reporting at least one episode of that type. Episodes for which the respondent reported multiple activities or interaction partners were included in each of the corresponding computations.

	Mean affect rating					Mean hours/day	Proportion of sample reporting
	Positive	Negative	Competent	Impatient	Tired		
Activities							
Intimate relations	5.10	0.36	4.57	0.74	3.09	0.2	0.11
Socializing	4.59	0.57	4.32	1.20	2.33	2.3	0.65
Relaxing	4.42	0.51	4.05	0.84	3.44	2.2	0.77
Pray/worship/meditate	4.35	0.59	4.45	1.04	2.95	0.4	0.23
Eating	4.34	0.59	4.12	0.95	2.55	2.2	0.94
Exercising	4.31	0.50	4.26	1.58	2.42	0.2	0.16
Watching TV	4.19	0.58	3.95	1.02	3.54	2.2	0.75
Shopping	3.95	0.74	4.26	2.08	2.66	0.4	0.30
Preparing food	3.93	0.69	4.20	1.54	3.11	1.1	0.62
On the phone	3.92	0.85	4.35	1.92	2.92	2.5	0.61
Napping	3.87	0.60	3.26	0.91	4.30	0.9	0.43
Taking care of my children	3.86	0.91	4.19	1.95	3.56	1.1	0.36
Computer/e-mail/Internet	3.81	0.80	4.57	1.93	2.62	1.9	0.47
Housework	3.73	0.77	4.23	2.11	3.40	1.1	0.49
Working	3.62	0.97	4.45	2.70	2.42	6.9	1.00
Commuting	3.45	0.89	4.09	2.60	2.75	1.6	0.87
Interaction partners							
Friends	4.36	0.67	4.37	1.61	2.59	2.6	0.65
Relatives	4.17	0.80	4.17	1.70	3.06	1.0	0.38
Spouse/SO	4.11	0.79	4.10	1.53	3.46	2.7	0.62
Children	4.04	0.75	4.13	1.65	3.40	2.3	0.53
Clients/customers	3.79	0.95	4.65	2.59	2.33	4.5	0.74
Co-workers	3.76	0.92	4.43	2.44	2.35	5.7	0.93
Boss	3.52	1.09	4.48	2.82	2.44	2.4	0.52
Alone	3.41	0.69	3.76	1.73	3.12	3.4	0.90
Duration-weighted mean	3.89	0.84	4.31	2.09	2.90		
% time > 0	97%	66%	90%	59%	76%		

both respects, the DRM replicates results obtained with experience sampling (*12*, *13*).

We also compared the diurnal rhythm of tiredness and affect to the corresponding patterns exhibited in experience sampling data (*17*) (Fig. 1). Despite demographic differences between the samples, the diurnal cycles of affect and tiredness produced by both methods are remarkably similar. This is especially impressive for tiredness because the V-shaped diurnal pattern differs from the naïve expectation that tiredness increases steadily throughout the day. Negative affect was most pronounced in the morning and then fell for most of the day. These results suggest that participants were generally successful in recovering their actual experience. The diurnal pattern of tiredness is also similar to the diurnal pattern of on-the-job work accidents (*18*).

Figure 2A displays the diurnal pattern of tiredness for participants who reported that they slept a nightly average of 6 hours or less, or 7 hours or more, in the last month. Each group exhibits the V-shape pattern and, quite plausibly, those who slept less are more tired at each hour of the day. Figure 2B shows the diurnal pattern of tiredness for three age groups. The V-shape pattern is particularly pronounced for the young (under 30), who start off their day much more tired than their older counterparts, but then converge to roughly the same level of tiredness by midday. It is extremely unlikely that DRM participants produced these patterns by consulting general beliefs about how tired or cheerful they are at various times of the day. Furthermore, the plausibility of the results suggests that respondents used the scales in a similar way, lending credence to interpersonal comparisons of reported affective experience.

In well-being research, the standard deviation of individual differences is normally the metric used to express the size of group differences. Because the DRM supports both between-subjects comparisons (e.g., different age groups) and within-subject comparisons (e.g., different situations or times of day), it provides an additional metric that facilitates the interpretation of results. Exploiting the broad consensus that exists on the relative enjoyment value of many activities and situations, we constructed a scale of enjoyment demarcated by types of familiar situations. We first chose two activities near the extremes of low and high enjoyment: commuting to work (mean = 2.86) and relaxing with friends (mean = 4.92). We then identified five other activities with mean enjoyment ratings spaced approximately evenly within that range. The selected activities satisfied two conditions: (i) There was no significant difference in the overall average of enjoyment ratings between individuals who engaged in the activity and others who did not; and (ii) there was broad agreement between the rankings of the activities in the DRM results and in generic judgments of their enjoyment value (*19*, *20*). Using this scale, we display the effects of selected work circumstances and individual differences on reported enjoyment, at work and at home (Fig. 3).

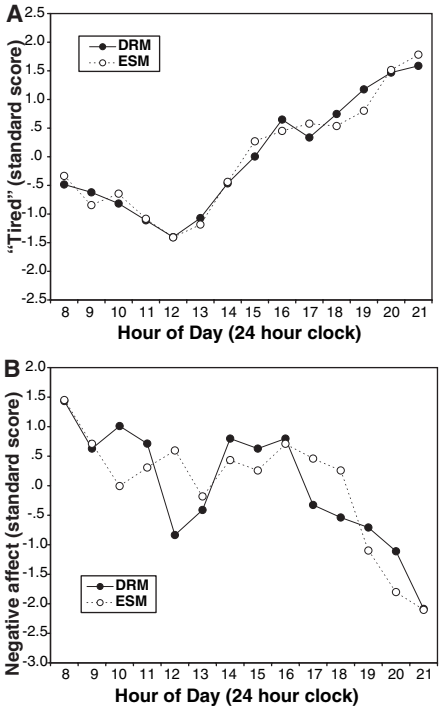

Fig. 1. Comparison of diurnal patterns of tiredness (**A**) and negative affect (**B**) for DRM and ESM studies. Points are standard scores computed across hourly averages within each sample.

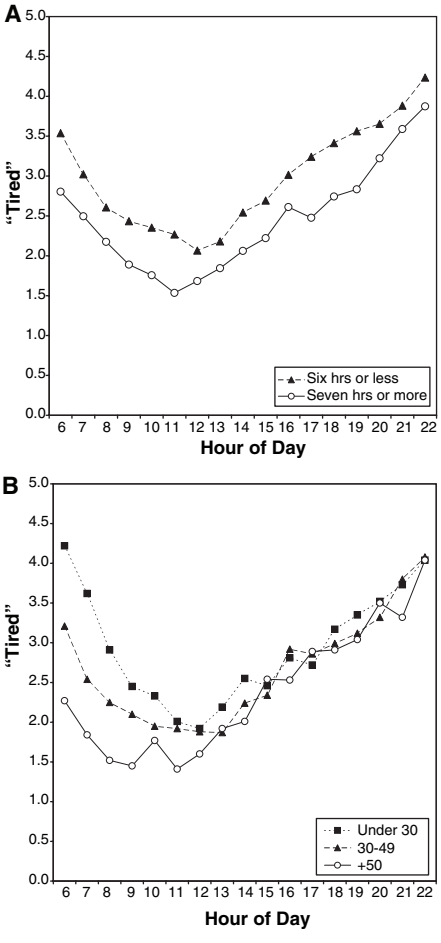

Fig. 2. Comparison of diurnal patterns of tiredness by average hours of sleep per night (**A**) and by age (**B**) for the DRM sample. Points are hourly averages within each subsample.

Line A shows the enjoyment of work episodes reported by respondents who do (n = 200; mean = 2.88) or do not (n = 179; mean = 3.96) report time pressure at work. The difference is about as large as the difference in enjoyment between "commuting to work" (mean = 2.86) and "shopping with your spouse/significant other" (SO) (mean = 3.90). Time pressure at work is unrelated to enjoyment in home situations (line B). Controlling for other job features (*21*) does not change these results, suggesting that time pressure is a particularly important determinant of enjoyment at work (*22*). Whereas the effect of time pressure is 52% as large as the enjoyment difference between commuting to work and relaxing with friends, being "at risk of being laid off" (line C) or having a job that requires "specialized education or training" (line D) exhibited a much smaller effect.

A similar analysis can be applied to personal characteristics. For example, differences in reported sleep quality are associated with a very large difference in reported enjoyment during episodes at home (line E). The effect is 56% of the entire scale range. Controlling for other personal features slightly reduces this effect (*23*). Differences in temperament and personality have similarly large effects (*24*), whereas the influence of other individual characteristics is much smaller. Substantial differences in household income have a modest influence on enjoyment (line G, 19%), which shrinks to marginal statistical significance under controls. The effect of religion is similar (line F, 19%), but shrinks less after controls, and the difference in enjoyment between divorced and married women (which slightly favors the divorced) is still smaller (line H).

We conclude that positive affect and enjoyment are strongly influenced by aspects of temperament and character (e.g., depression and sleep quality) and by features of the current situation. In contrast, general circumstances (e.g., income and education) have little impact on the enjoyment of a regular day.

These findings parallel the observation that life circumstances have surprisingly

little influence on global reports of life satisfaction. For example, large increases of real income in the developed world over the past 50 years have yielded no change in reported life satisfaction (*25*). The observation that improved life circumstances quickly cease to provide increased satisfaction has been called the hedonic treadmill (*26*). Our data allow us to compare the impact of life circumstances on affective experience and on global life satisfaction (*27*). We considered three hypotheses. The hedonic treadmill hypothesis holds that life satisfaction and affective experience are equally susceptible to adaptation. The aspiration treadmill hypothesis holds that treadmill effects observed in satisfaction judgments are due mainly to changing standards (*28*). Thus, the rich may experience more pleasure than the poor, but they also require more pleasure to be equally satisfied. Accordingly, real differences in enjoyment are not reflected in satisfaction. Finally, the focusing hypothesis predicts that the effects of life circumstances on reported satisfaction, though small, actually overstate the effects on experience (*29*). The task of evaluating one's life, in part, evokes a comparison of one's objective circumstances to conventional standards, reminding the rich that they are rich and the divorced that they are divorced. Because these circumstances are most likely to come to the mind of the newly rich or recently divorced, their influence on satisfaction judgments declines over time, producing adaptation. The relative impact of life circumstances on actual affective experience is even smaller, because thoughts of one's circumstances are much more likely to come to mind when answering questions about one's life than in the routine course of experience. Affective experience as assessed by the DRM is less dependent on comparison standards than is evaluative judgment as assessed by global satisfaction questions.

To our surprise, the test favored the focusing hypothesis over the alternatives. Life satisfaction is moderately correlated (r = 0.38) with daily "net affect" (the difference between positive and negative affect). The correlations of objective circumstances with life satisfaction are low, replicating the original treadmill puzzle, but their impact on affective experience is even smaller. For example, log(household income) correlates more with life satisfaction (r = 0.20) than with net affect (r = 0.05; $P < 0.001$ for the difference). The corresponding values for the married/divorced distinction are 0.10 and –0.08 ($P < 0.001$), where married women report slightly higher satisfaction and divorced women report slightly more positive affect. In contrast, personal characteristics related to temperament and personality correlate at least as strongly with affect as with life satisfaction. Reported sleep quality (r = 0.30 versus 0.28 for life satisfaction, nonsignificant) and an indicator of depression ("trouble maintaining enthusiasm"; r = 0.44 versus 0.28 for life satisfaction; $P < 0.01$) are illustrative examples.

Similarly, long-term job circumstances tend to have more impact on job satisfaction than on the affective experience of the working day. For example, the report of "excellent benefits" correlates 0.18 with job satisfaction and 0.10 with affect at work (difference $P < 0.05$). The corresponding correlations for "my job requires specialized training" are 0.20 and 0.09, respectively ($P < 0.01$). The few job characteristics that influence affect more than job satisfaction are features of the immediate work situation, including time pressure (r = –0.28 for job satisfaction versus –0.19 for affect at work; $P < 0.01$) and "opportunity to talk with coworkers" (r = 0.10 for job satisfaction versus 0.02 for affect at work; $P < 0.05$).

These findings suggest a possible resolution of the treadmill puzzle. Three distinct patterns can be identified in the affect results: (i) Personal characteristics, such as mild depression or poor sleep, have a pervasive influence on affect. Such characteristics are correlated at least as highly with affect as with satisfaction. (ii) Local features of the current situation, such as the partners in interactions or the level of time pressure in the work situation, exert a powerful influence on affect. (iii) Life circumstances have relatively small effects on affective experience, unless they are locally salient, as in the case of time pressure at work, or when the individual is intensely preoccupied with a topic, as is most likely to happen for a limited time after a marked change of circumstances. Thus, time pressure is always relevant for affect at work, but job security is affectively important mainly when one thinks about it. Life circumstances are also likely to become salient when people are questioned about their well-being and implicitly encouraged to evaluate how (un)fortunate they are. As a result, circumstances often have more impact on life satisfaction than on affective experience, in accord with the focusing hypothesis.

The present analysis does not suggest that circumstances are irrelevant to well-being. On the contrary, the observation of large variations in affective state during the course of a normal day highlights the importance of optimizing the allocation of time across situations and activities, subject to time and income constraints (*30*, *31*).

The goal of this report was to introduce a new tool for the study of well-being and to illustrate its potential uses. The following features define a generic DRM study: (i) the elicitation of a detailed description of the previous day in the respondent's life; (ii) the goal of approximating the results of continuous, real-time experience measurement; (iii) procedures designed to support accurate retrieval of specific episodes; (iv) structured elicitation of the objective circumstances of episodes; and (v) multidimensional description of the affect experienced in each episode.

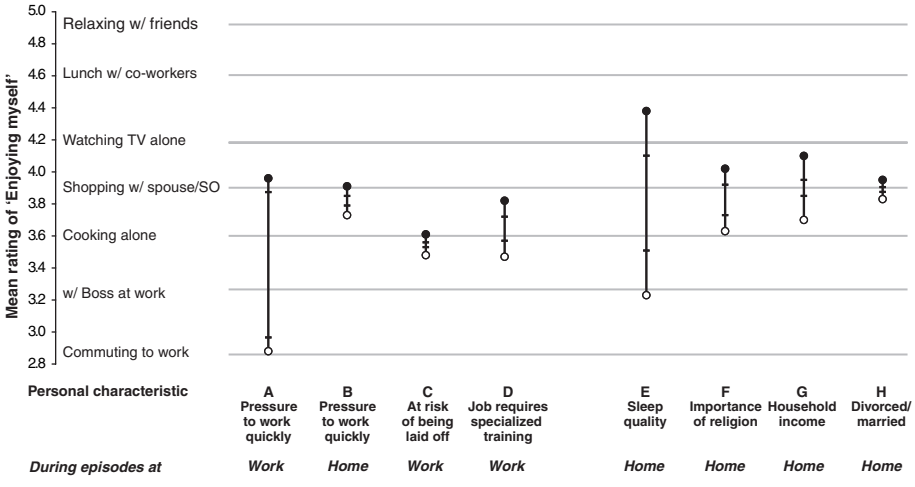

Fig. 3. Range of mean enjoyment ratings for lowest and highest levels of selected person and job characteristics. Open circles represent the mean for the most enjoyable category of the characteristic, and closed circles for the least enjoyable. Horizontal hash marks show results after controlling for other job features [for (A) to (D)] or for other personal features [for (E) to (H)]. (**A**) Constant pressure to work quickly (definitely yes/definitely not) work episodes. (**B**) Constant pressure to work quickly (definitely yes/definitely not) home episodes. (**C**) At risk of being laid off (definitely yes or definitely not) work episodes. (**D**) Requires specialized education/training (definitely yes or definitely not) work episodes. (**E**) Sleep quality (very bad or very good) home episodes. (**F**) Importance of religion (not at all or very important) home episodes. (**G**) Household income (less than $30,000 or more than $90,000) home episodes. (**H**) Marital status (divorced or married) home episodes.

Many variations of the method are possible. The activity and affect descriptors used to describe episodes should fit the particular topic of investigation. Interactive questionnaires offer further opportunities to tailor the affect terms to the respective episode; for example, when the individual identifies an episode as an interaction with customers rather than with family members, different descriptors could be presented. Other variations could make the method more practical for adoption in conventional surveys. Our preliminary work suggests that much of the benefit of the DRM in producing accurate emotional recall could be retained if respondents are asked to retrieve specific recent episodes of a designated type (e.g., "the last occasion on which you went out to dinner"). When samples are large and interviewing time is scarce, the allocation of different situations to subgroups of respondents makes it possible to achieve comprehensive coverage of situations while minimizing respondent burden. In conjunction with time-use data obtained from other sources, affect profiles of the main activities in which people engage could be integrated to produce a duration-weighted assessment of the experience of the population and of subgroups. The DRM or its variants could also contribute to the development of an accounting system for the well-being of society, a potentially important tool for social policy (*32*, *33*).

References and Notes

1. M. Bergner, M. L. Rothman, *Annu. Rev. Public Health* **8**, 191 (1987).
2. S. Cohen, W. Doyle, R. Turner, C. Alper, D. Skoner, *Psychol. Sci.* **14**, 389 (2003).
3. M. Marmot, *The Status Syndrome* (Bloomsbury, London, 2004).
4. F. T. Juster, in *Time, Goods, and Well-Being*, F. Juster, F. Stafford, Eds. (Institute for Social Research, Ann Arbor, MI, 1985), pp. 397–414.
5. P. van de Ven, B. Kazemier, S. Keuning, *Measuring Well-Being with an Integrated System of Economic and Social Accounts* (Department of National Accounts, Voorburg, Netherlands, 1999).
6. F. Y. Edgeworth, *Mathematical Psychics: An Essay on the Application of Mathematics to the Moral Sciences* (C. K. Paul, London, 1881).
7. D. Kahneman, P. Wakker, R. Sarin, *Q. J. Econ.* **112**, 375 (1997).
8. G. Dow, J. F. Juster, in *Time, Goods, and Well-Being*, F. Juster, F. Stafford, Eds. (Institute for Social Research, Ann Arbor, 1985), pp. 397–413.
9. L. Flood, *Household, Market, and Nonmarket Activities; Procedures and Codes for the 1993 Time-Use Survey* (Uppsala Univ. Dept. Economics, Uppsala, Sweden, 1997), vol. VI.
10. A. Campbell, *The Sense of Well-Being in America* (McGraw-Hill, New York, 1981).
11. F. M. Andrews, S. B. Whithey, *Social Indicators of Well-Being: Americans' Perceptions of Life Quality* (Plenum, New York, 1976).
12. M. Csikszentmihalyi, R. E. Larsen, *J. Nerv. Ment. Dis.* **175**, 526 (1987).
13. A. A. Stone, S. S. Shiffman, M. W. DeVries, in *Well-Being: The Foundations of Hedonic Psychology*, D. Kahneman, E. Diener, N. Schwarz, Eds. (Russell-Sage, New York, 1999), pp. 61–84.
14. M. D. Robinson, G. L. Clore, *Psychol. Bull.* **128**, 934 (2002).
15. R. Belli, *Memory* **6**, 383 (1998).
16. Materials and methods are available as supporting material on *Science* Online.
17. A. A. Stone *et al.*, *J. Pers. Soc. Psychol.* **74**, 1670 (1998). Respondents with high levels of job stress were recruited in New York (n = 88 men, 91 women; average age 40.0 years; 89% white; 58% married; 50% had some college). Situations and affect descriptors were similar to the DRM study.
18. K. N. Fortson, *Monthly Labor Rev.* **127**, 18 (2004).
19. We conducted an auxiliary random-digit-dial phone survey of 69 women, who ranked the activities from most to least enjoyable. Kendall's W coefficient of concordance among the ranks was 0.47, slightly higher than the concordance of economists' rankings of journals (*20*).
20. K. Axarloglou, V. Theoharakis, *J. Euro. Econ. Assoc.* **1**, 1402 (2003).
21. Thirty-nine job features (e.g., tenure and job level) were entered into a regression to predict duration-weighted enjoyment at work (*16*).
22. N. K. Semmer, S. Grebner, A. Elfering, in *Research in Occupational Stress and Well-being*, P. Perrewé, D. Ganster, Eds. (JAI, Amsterdam, 2004), vol. 3, pp. 207–263.
23. Twenty personal features (e.g., age and marital status) predicted duration-weighted enjoyment at work (*16*).
24. We computed enjoyment at home for respondents who reported "no problem at all" in keeping up "enough enthusiasm to get things done" during the last month and for respondents who reported "somewhat of a problem." The difference between the groups spanned 46% of the enjoyment scale.
25. R. A. Easterlin, *J. Econ. Behav. Org.* **27**, 35 (1995).
26. P. Brickman, D. T. Campbell, in *Adaptation-Level Theory*, M. Appley, Ed. (Academic Press, New York, 1971), pp. 215–231.
27. The first question in the survey was "How satisfied are you with your life as a whole these days? Are you very satisfied, satisfied, not very satisfied, or not at all satisfied?".
28. D. Kahneman, in *Choices, Values and Frames*, D. Kahneman, A. Tversky, Eds. (Cambridge Univ. Press, New York, 2000), chap. 38.
29. D. A. Schkade, D. Kahneman, *Psychol. Sci.* **9**, 340 (1998).
30. S. Lyubomirsky, K. M. Sheldon, D. Schkade, *Rev. Gen. Psychol.*, in press.
31. G. Becker, *Econ. J.* **75**, 493 (1965).
32. D. Kahneman, A. B. Krueger, D. A. Schkade, N. Schwarz, A. A. Stone, *Am. Econ. Rev.* **94**, 429 (2004).
33. E. Diener, M. Seligman, *Psychol. Sci. Pub. Int.* **5**, 1 (2004).

34. This research was supported by the William and Flora Hewlett Foundation, and also by the Woodrow Wilson School of Public and International Affairs at Princeton, the NSF, and the National Institute on Aging. Order of authorship is alphabetical. D.K. is affiliated with the Gallup Organization. A.A.S. holds equity in and is the Associate Chair of the Scientific Advisory Board of invivodata, Inc., a company that markets an electronic patient diary system.

Supporting Online Material

www.sciencemag.org/cgi/content/full/306/5702/1776/DC1
Materials and Methods

2 August 2004; accepted 30 September 2004

Conditional Use of Sex and Parthenogenesis for Worker and Queen Production in Ants

Morgan Pearcy,[1] Serge Aron,[1]* Claudie Doums,[2] Laurent Keller[3]

The near-ubiquity of sexual reproduction in animal species has long been considered a paradox because sexually reproducing individuals transmit only half of their genome to their progeny. Here, we show that the ant *Cataglyphis cursor* circumvents this cost by using alternative modes of reproduction for the production of reproductive and nonreproductive offspring. New queens are almost exclusively produced by parthenogenesis, whereas workers are produced by normal sexual reproduction. By selectively using sex for somatic growth and parthenogenesis for germline production, *C. cursor* has taken advantage of the ant caste system to benefit from the advantages of both sexual and asexual reproduction.

The main advantage of asexual reproduction is that it confers a twofold advantage over sexuality by allowing, generation by generation, the transmission of twice the number of genes to offspring (*1*, *2*). However, asexual reproduction is also associated with both short-term and long-term disadvantages, including a lower genetic diversity of offspring and a reduced rate of adaptive evolution of species (*3*, *4*). The nature and the degree of the cost associated with asexual reproduction is expected to vary across taxa, depending on the biology of the species and the type of environment in which they live (*1*–*3*).

In ants, as in other Hymenoptera, females are usually produced by sexual reproduction and are diploid, whereas males develop from unfertilized eggs and are haploid (*3*). The diploid fertilized eggs can develop into either new queens (gynes) or workers, with the developmental switch generally under environmental control (*5*). In the Cape honey bee and five ant species, however, unmated workers may reproduce by thelytokous parthenogenesis (*6*–*11*); that is, they may produce female

[1]Behavioural and Evolutionary Ecology, CP 160/12, Université Libre de Bruxelles, av. F. D. Roosevelt 50, B-1050 Brussels, Belgium. [2]Fonctionnement et Evolution des Systèmes Ecologiques, Université Paris VI, 7 quai St. Bernard, 75252 Paris Cedex 05, France. [3]Department of Ecology and Evolution, Bâtiment de Biologie, CH-1015 Lausanne, Switzerland.

*To whom correspondence should be addressed. E-mail: saron@ulb.ac.be

offspring from unfertilized eggs. While conducting a population genetic study of one of these species, the ant *Cataglyphis cursor*, we discovered that not only unmated workers but also mated queens can use thelytokous parthenogenesis. Pedigree analyses indicated that queens use automictic parthenogenesis with central fusion where two of the four products of meiosis merge. Unlike workers, queens use this mode of reproduction specifically to produce new queens.

Cataglyphis cursor is a common ant in the dry forests of Europe. Colonies usually contain a single queen and up to 3000 workers. Only few colonies produce gynes, and the number of gynes produced per colony is small. This is because *C. cursor* has an unusual mating system whereby gynes mate near the parental nest before leaving the colony with adult workers to initiate new colonies 3.2 to 11.3 m away (*12*). Previous studies also indicate that *C. cursor* workers can produce both gynes and workers parthenogenetically in colonies that have lost the mother queen (*7*).

We collected 38 large colonies in Southern France and genotyped 532 workers at four highly polymorphic microsatellite loci (expected heterozygosities, 0.833 to 0.944) (*13*). The genotypes indicated that 35 of these colonies contained a single reproductive queen (monogyny), whereas three colonies contained offspring from at least two queens. Analysis of lab-raised worker progeny (n = 437 freshly eclosed workers) from 12 queens showed that they had mated with an average of 5.6 ± 1.3 males (range, 4 to 8).

A detailed analysis of the 35 monogynous colonies showed that most of the workers in these colonies could only have been produced by sexual reproduction. Overall, 476 of the 489 workers (97.3%) genotyped in the 35 colonies harbored, at one or several loci, alleles that were not present in the mother queen and came from one of the queen's mates. It is impossible to determine whether the 13 workers harboring only alleles identical to those of their mother were fathered by a male that had no allele distinct from those of the queen or whether they had been parthenogenetically produced. Because the four microsatellite loci were highly polymorphic, the probability of mating with a male harboring no diagnostic allele at any of the four loci was low, ranging from 0.0001 to 0.013 across colonies according to the queen's genotype. Thus, of the 476 workers, only one was expected to have no diagnostic alleles if they were all sexually produced. Hence, it is likely that some or all of the 13 workers with no diagnostic paternal allele may indeed have been asexually produced (the estimated proportion of asexually produced workers is 2.5% when corrected for the probability of nondetection of paternal alleles).

A total of 56 gynes were produced by 10 of the 35 monogynous colonies. In contrast to workers, most of these gynes (54 of 56) had alleles at the four loci that could all be attributed to the queen (Fig. 1A), hence these gynes had been produced by parthenogenesis. The alternative explanation, that these 54 gynes had been fathered by a male having no diagnostic alleles, can be ruled out. Queens and males came from the same gene pool, as indicated by a lack of significant difference in allele frequencies for the four loci (Fisher exact test, all $P > 0.05$) and the workers' *Fis* value (an index of observed versus expected homozygosity), which was not significantly different from zero (*Fis* = 0.011 ± 0.015, n = 35 colonies; two-tailed t test, $t = 0.691$, $P = 0.494$). This, together with the high allelic diversity, resulted in a very high probability to detect a male's genetic contribution. However, none of the gynes produced in nine of the 10 colonies had any diagnostic allele, even though the likelihood of such a matched mating was lower than 0.013 in each of the nine colonies (range, 0.0001 to 0.013). Overall, the probability that all the fathers of the gynes produced in the nine colonies had no diagnostic alleles was $P < 10^{-28}$. Indeed, the genotypes of workers in these nine colonies confirmed that all or most of the males that mated with the queens had diagnostic alleles at one or more loci (Fig. 1B). The outcome of the vast majority of gynes being produced by parthenogenesis was that the relatedness between queens and gynes was very high (r = 0.864 ± 0.046, n = 56 gynes) and significantly greater ($P < 0.001$) than the theoretical value of 0.50 expected under sexual reproduction.

Most of the 54 parthenogenetic gynes were neither genetically identical to each other within a colony nor genetically identical to their mother queen. The discrepancies resulted from gynes being homozygous at some loci where the mother queen was heterozygous. In all cases, the gynes were homozygous for one of the two maternal alleles. This is the expected pattern under automictic parthenogenesis with central fusion. Because two of the four products of meiosis merge, the offspring have the same genotype as their mother for the loci that did not cross over, whereas the offspring is homozygous for one of the two maternal alleles if crossing-over did occur (*14*, *15*). The frequency of transition from heterozygosity is expected to vary across loci depending on their distance to the centromere (*15*). Consistent with this prediction, the frequency of transition from heterozygosity to homozygosity varied significantly across the four loci, presumably reflecting differences in the distance between each locus and the centromere (Table 1; $\chi^2 = 25.53$, $P < 0.0001$).

The expected outcome of automictic parthenogenesis is a gradual increase in homo-

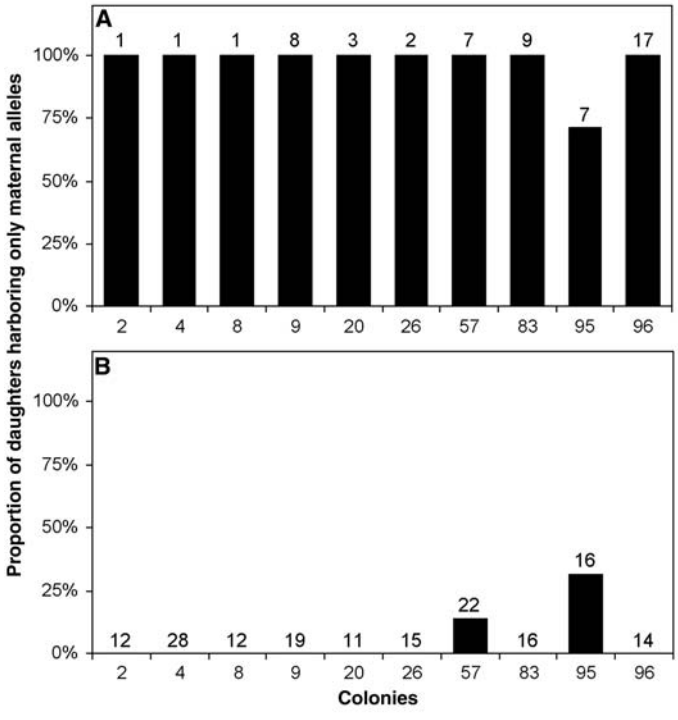

Fig. 1. Respective proportion of gynes (**A**) and workers (**B**) harboring maternal alleles only, and therefore interpreted as parthenogenetic daughters, in each of 10 colonies (colony numbers are laboratory designations). The sample size for each colony is indicated above the bars.

Table 1. Proportion of gynes homozygous for a given locus when the mother was heterozygous at that locus. The sample size for each locus is indicated.

Locus	Sample size	Percentage of gynes homozygous
Ccur11	53	5.7
Ccur46	47	46.8
Ccur58	47	34.0
Ccur63b	41	17.1

zygosity over time (*16*). Indeed, the overall level of homozygosity was significantly higher in gynes than in workers (Fig. 2; Fisher's exact test on the number of homozygous versus heterozygous loci in gynes and workers: $P < 0.0001$). Accordingly, F statistics revealed a significant excess of homozygosity in gynes ($F = 0.396 \pm 0.12$, $P < 0.001$) and queens ($F = 0.255 \pm 0.051$, $P < 0.001$) but not in workers from the same colonies ($F = 0.002 \pm 0.016$, $P = 0.45$). By increasing the levels of homozygosity, parthenogenesis should result in reduced queen survival and fitness, much like inbreeding does. However, the fitness effect might be limited for ant queens because they stay in the protected environment of the nest, except during colony founding. Even at this stage, the intensity of this cost should vary according to the mode of colony founding, with selection against more homozygous queens being higher in species where queens start a new colony on their own and lower in species, such as *C. cursor*, where queens do not go through a stage of independent colony founding (*12*).

In addition, two processes appear to counteract the process of genetic homogenization induced by automictic parthenogenesis. The first is the occasional production of gynes by sexual reproduction. The overall production of such gynes was 3.6% (2 of 56) in the 10 colonies studied. The second process is the occasional queen production by worker parthenogenesis. Because workers are usually produced by sexual reproduction, their contribution to gyne production will contribute to the maintenance of heterozygosity in gynes and queens, just as under queen sexual reproduction.

Although *C. cursor* queens do not require mating to produce diploid offspring, they have retained sexual reproduction to produce workers, which suggests that sexual reproduction has important benefits for colony function. The observed mating frequencies in this species lie on the high end of the continuum of mating frequencies reported in ants (*17*). A possible explanation is that genetic input from an increased number of mates compensates for the negative effect of high queen homozygosity on colony genetic diversity. Parthenogenetic production of workers at the level observed for gynes would lower colony genetic diversity, which could lead to reduced defense against parasites, less efficient division of labor, and a decreased range of environmental conditions that a colony can tolerate (*18–20*). These costs are akin to those thought to lead to the instability of parthenogenetic reproduction in nonsocial organisms (*2*). Multiple mating lowered the overall relatedness of nestmate workers to $r = 0.42$ ($SE_{jackknife} = 0.02$, $n = 35$), a value well within the range of values reported in other ants (*21*). Thus, the high queen mating frequency may cancel out reduced genetic diversity at the colony level stemming from the relatively high queen homozygosity.

Using alternative modes of reproduction for the queen and worker castes may also enhance cooperation within the social group by aligning the interests of queens and workers. Parthenogenetic production of gynes by queens reduces conflict with workers because, just like queens, workers are significantly more closely related ($t = 2.31$, df = 43, $P = 0.03$) to the parthenogenetic gynes ($r = 0.59$, $SE_{jackknife} = 0.07$, $n = 10$) than they would be to sexually produced gynes or to gynes produced parthenogenetically by other workers (these two values are identical to the relatedness between workers, $r = 0.42$). As a result, workers should police the reproduction of other workers (*22*). The almost complete lack of worker-produced gynes in colonies containing a queen is consistent with this idea.

Conditional use of parthenogenesis for queen production might also occur in other ants, yet it may remain unnoticed because it primarily occurs in dependent-founding species where it is most difficult to detect. In ants there is a strong association between the mode of colony founding and the number of queens, with dependent colony founding being almost exclusively restricted to species with high numbers of queens per nest (*23*, *24*). The likelihood of detecting parthenogenesis with genetic markers is low in such species because it is very difficult to determine the maternity of female offspring. As a result, only a handful of studies in highly polygynous ants are sufficiently detailed to have enabled the detection of parthenogenesis.

This study shows that by taking advantage of the social caste system, *C. cursor* colonies can benefit from the advantages of both sexual and asexual reproduction. By using alternative modes of reproduction for the queen and worker castes, queens can increase the transmission rate of their genes to their reproductive female offspring while maintaining genetic diversity and social cohesion in the worker population. These findings, together with those of other recent genetic studies (*25–29*), indicate greater flexibility of the ant reproductive and social systems, thus providing an ideal ground to test various evolutionary predictions.

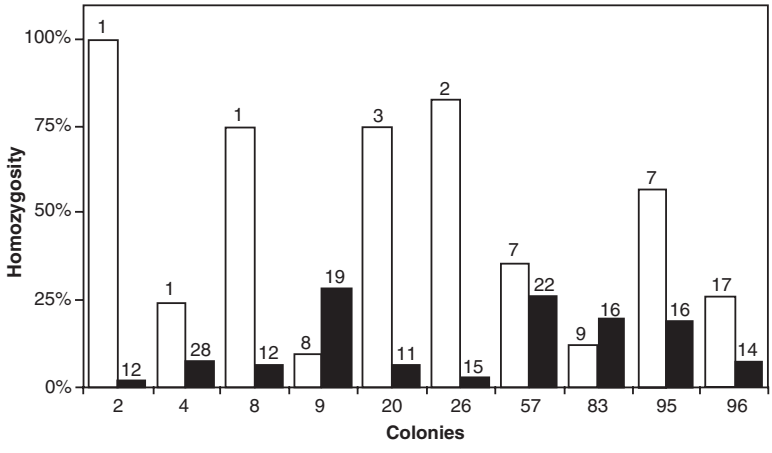

Fig. 2. Overall homozygosity detected in gynes (white) and workers (black) at all four loci, for each of 10 colonies. The sample size for each colony is indicated above the bars.

References and Notes

1. G. C. Williams, *Sex and Evolution* (Princeton Univ. Press, Princeton, NJ, 1975).
2. J. Maynard Smith, *The Evolution of Sex* (Cambridge Univ. Press, Cambridge, 1978).
3. G. Bell, *The Masterpiece of Nature: The Evolution and Genetics of Sexuality* (Univ. of California Press, Berkeley, CA, 1982).
4. S. A. West, C. M. Lively, A. F. Read, *J. Evol. Biol.* **12**, 1003 (1999).
5. E. O. Wilson, *The Insect Societies* (Harvard Univ. Press, Cambridge, MA, 1971).
6. S. Verma, F. Ruttner, *Apidologie (Celle)* **14**, 41 (1983).
7. H. Cagniant, *Insect. Soc.* **26**, 51 (1979).
8. T. Itow *et al.*, *Insect. Soc.* **31**, 87 (1984).
9. K. Tsuji, K. Yamauchi, *Insect. Soc.* **42**, 333 (1995).
10. J. B. Heinze, B. Hölldobler, *Naturwissenschaften* **82**, 40 (1995).
11. D. A. T. Grasso, T. Wenseleers, A. Mori, F. Le Moli, J. Billen, *Ethol. Ecol. Evol.* **12**, 309 (2000).
12. A. Lenoir, L. Quérard, N. Pondicq, F. Berton, *Psyche (Stuttgart)* **95**, 21 (1988).
13. See supporting data on *Science* Online.
14. E. Suomalainen, A. Saura, J. Lokki, *Cytology and Evolution in Parthenogenesis* (CRC Press, Boca Raton, FL, 1987).
15. E. Baudry *et al.*, *Genetics*, in press.
16. J.-C. Simon, F. Delmotte, C. Rispe, T. Crease, *Biol. J. Linn. Soc.* **79**, 151 (2003).
17. J. E. Strassmann, *Insect. Soc.* **48**, 1 (2001).
18. P. W. Sherman, T. D. Seeley, H. K. Reeve, *Am. Nat.* **131**, 602 (1988).
19. R. H. Crozier, R. E. Page, *Behav. Ecol. Sociobiol.* **18**, 105 (1985).
20. B. J. Cole, D. C. Wiernasz, *Science* **285**, 891 (1999).
21. R. H. Crozier, P. Pamilo, *Evolution of Social Insect Colonies: Sex Allocation and Kin Selection* (Oxford Univ. Press, Oxford, 1996).
22. F. L. W. Ratnieks, *Am. Nat.* **132**, 217 (1988).
23. L. Keller, *Ethol. Ecol. Evol.* **3**, 307 (1991).
24. A. F. G. Bourke, N. R. Franks, *Social Evolution in Ants* (Princeton Univ. Press, Princeton, NJ, 1995).
25. S. Helms Cahan *et al.*, *Proc. R. Soc. London Ser. B.* **269**, 1871 (2002).

26. G. E. Julian, J. H. Fewell, J. Gadau, R. A. Johnson, D. Larrabee, *Proc. Natl. Acad. Sci. U.S.A.* **99**, 8157 (2002).
27. V. P. Volny, D. M. Gordon, *Proc. Natl. Acad. Sci. U.S.A.* **99**, 6108 (2002).
28. S. Helms Cahan, L. Keller, *Nature* **424**, 306 (2003).
29. A. Hartmann, J. Wantia, J. A. Torres, J. Heinze, *Proc. Natl. Acad. Sci. U.S.A.* **100**, 12836 (2003).
30. We thank L. Beukeboom, M. Chapuisat, P. Christe, R. Hammond, S. H. Cahan, J. M. Pasteels, K. Parker, and I. Sanders for their comments on the manuscript. Supported by a doctoral grant from Fonds pour la Recherche dans l'Industrie et l'Agriculture (M.P.) and grants from the Belgian Fond National de la Recherche Scientifique (S.A.), the French Ministry of Research "Action concertée incitative jeunes chercheurs 2001" (C.D.), and the Swiss National Science Foundation (L.K.).

Supporting Online Material
www.sciencemag.org/cgi/content/full/306/5702/1780/DC1
Materials and Methods
References

21 September 2004; accepted 5 October 2004

Status and Trends of Amphibian Declines and Extinctions Worldwide

Simon N. Stuart,[1]* Janice S. Chanson,[1] Neil A. Cox,[1] Bruce E. Young,[2] Ana S. L. Rodrigues,[3] Debra L. Fischman,[3] Robert W. Waller[3]

The first global assessment of amphibians provides new context for the well-publicized phenomenon of amphibian declines. Amphibians are more threatened and are declining more rapidly than either birds or mammals. Although many declines are due to habitat loss and overutilization, other, unidentified processes threaten 48% of rapidly declining species and are driving species most quickly to extinction. Declines are nonrandom in terms of species' ecological preferences, geographic ranges, and taxonomic associations and are most prevalent among Neotropical montane, stream-associated species. The lack of conservation remedies for these poorly understood declines means that hundreds of amphibian species now face extinction.

Scientists first became concerned about widespread amphibian population declines when they met in 1989 at the First World Congress of Herpetology. Historical data indicate that declines began as early as the 1970s in the western United States (*1*, *2*), Puerto Rico (*3*), and northeastern Australia (*4*). Subsequent reports revealed the severity of the declines. At one site in Costa Rica, 40% of the amphibian fauna disappeared over a short period in the late 1980s (*5*). Sudden disappearances of montane species were noted simultaneously in Costa Rica, Ecuador, and Venezuela (*5–8*). In some regions, many declines took place in seemingly pristine habitats (*1–8*). These reports were initially received with some skepticism because amphibian populations often fluctuate widely (*9*), but tests of probabilistic null models showed that the declines were far more widespread and severe than would be expected under normal conditions of demographic variation (*5*). This finding, in addition to many further reports of declines in the 1990s (*8*, *10–13*), was pivotal in convincing most herpetologists that amphibian declines are nonrandom unidirectional events.

The lack of a comprehensive picture of the extent and severity of amphibian declines prompted us to conduct the IUCN–The World Conservation Union Global Amphibian Assessment (GAA) to gather data on the distribution, abundance, population trends, habitat associations, and threats for all 5743 described species of amphibians (*14*, *15*). From this information, we used the IUCN Red List Criteria (*16*) to determine the level of threat to every species. The raw GAA data are publicly available (*14*). The results demonstrate that amphibians are far more threatened than either birds (*17*) or mammals (*18*), with 1856 species (32.5%) being globally threatened [that is, listed in the IUCN Red List Categories (*16*) of Vulnerable, Endangered, or Critically Endangered], as compared with 12% of birds (1211 species) (*17*) and 23% of mammals (1130 species) (*18*). At least 2468 amphibian species (43.2%) are experiencing some form of population decrease, whereas only 28 (0.5%) are increasing and 1552 (27.2%) are stable; 1661 (29.1%) species have an unknown trend.

Many amphibian species are on the brink of extinction, with 427 species (7.4%) listed as Critically Endangered (CR) (the IUCN category of highest threat), as compared with 179 birds (1.8%) (*17*) and 184 mammals (3.8%) (*18*). The level of threat to amphibians is undoubtedly underestimated because 1294 species (22.5%) are too poorly known to assess [Data Deficient (DD)], as compared with only 78 birds (0.8%) (*17*) and 256 mammals (5.3%) (*18*). A significant proportion of DD amphibians is likely to be globally threatened. Analysis of trends in population and habitat availability indicates

Table 1. Habitat preferences and biogeographic affinities of rapidly declining and enigmatic-decline amphibians in relation to all amphibian species (*15*). Rapidly declining species are those that now qualify for listing in a IUCN Red List Category of higher threat than they would have had in 1980. Enigmatic-decline species are rapidly declining species that have shown dramatic declines, even where suitable habitat remains, for reasons that are not fully explained.

Habitat preferences	Total number of species (%)	Number of rapidly declining species (%)	Number of enigmatic-decline species (%)
Forest	4699 (81.8)	365 (82.6)	187 (90.3)***↑
Savanna	487 (8.5)	7 (1.6)***↓	0 (0.0)***↓
Shrubland	814 (14.2)	47 (10.6)*↓	14 (6.8)***↓
Grassland	953 (16.6)	81 (18.3)	39 (18.8)
Flowing water	2650 (46.1)	277 (62.7)***↑	164 (79.2)***↑
Marshes/swamps	760 (13.2)	43 (9.7)*↓	14 (6.8)**↓
Still water bodies	2030 (35.3)	107 (24.2)***↓	28 (13.5)***↓
Artificial terrestrial habitats	1304 (22.7)	40 (9.0)***↓	22 (10.6)***↓
Tropical lowland habitats	3392 (59.1)	212 (48.0)**↓	79 (38.2)***↓
Tropical montane habitats	2714 (47.3)	251 (56.8)***↑	155 (74.9)***↑
Biogeographic realms			
Afrotropical	951 (16.6)	28 (6.3)***↓	1 (0.5)***↓
Australasian/Oceanic	561 (9.8)	36 (8.1)	23 (11.1)
Australia and New Zealand	219 (3.8)	32 (7.2)***↑	23 (11.1)***↑
Indomalayan	938 (16.3)	59 (13.3)	1 (0.5)***↓
Nearctic	331 (5.8)	24 (5.4)	9 (4.3)
Neotropical	2,825 (49.2)	279 (63.1)***↑	174 (84.1)***↑
Palearctic	451 (7.9)	34 (7.7)	2 (1.0)***↓

*$P < 0.05$, **$P < 0.01$, ***$P < 0.001$ (*27*). ↑Significantly higher than average; ↓significantly lower than average.

[1]IUCN Species Survival Commission/Conservation International Center for Applied Biodiversity Science Biodiversity Assessment Unit, 1919 M Street N.W., Washington, DC 20036, USA. [2]NatureServe, Apartado 75-5655, Monteverde, Puntarenas, Costa Rica. [3]Center for Applied Biodiversity Science, Conservation International, 1919 M Street N.W., Suite 600, Washington, DC 20036, USA.

*To whom correspondence should be addressed. E-mail: s.stuart@conservation.org

a deterioration in the status of amphibians since 1980 (*15*), when 1772 species (31.0%) would have been globally threatened, including 231 species (4.0%) in the CR category. Thus, in 1980, the percentage of CR amphibians would have been similar to that of mammals today, but the number of CR amphibians has almost doubled since then.

Only 34 species of amphibian are reported to have become extinct since 1500, compared with 129 birds (*17*) and 74 mammals (*18*), but there is strong evidence that this situation is worsening, because nine of these extinctions have taken place since 1980 [compared with five birds (*17*) and no mammals (*18*)]. Of greater concern is the number of species that can no longer be found ("Possibly Extinct," not formally "Extinct" until exhaustive surveys to establish their disappearance are completed). The GAA lists 122 such species, and it appears that up to 113 of these have almost or completely disappeared since 1980. Proving extinction beyond reasonable doubt is often very difficult, because many of these declines have been very rapid and have happened only recently, and a few species that were thought to be extinct have been rediscovered in recent years (*19*). The GAA estimates that between 9 and 122 amphibian species have therefore become extinct since 1980, and extensive fieldwork is needed to produce a more precise number.

There are 435 species that qualify for listing in IUCN categories of higher threat than they would have in 1980 (*15*). We define these as "rapidly declining" species, and divide them into three groups based on the causes of their decline (*15*): "overexploited"—declining because of heavy extraction (50 species); "reduced-habitat"—suffering significant habitat loss (183 species); and "enigmatic-decline"—declining, even where suitable habitat remains, for reasons that are not fully understood, although disease and climate change are emerging as the most commonly cited causes (207 species) (*3*, *7*, *13*, *20–24*). Five species fall into both the overexploited and enigmatic-decline groupings. Overexploited and reduced-habitat species are widely recorded in many taxonomic groups, such as birds and mammals (*17*, *18*), and are the traditional focus of conservation efforts. However, enigmatic-decline species have never previously been recorded at a level comparable to that currently observed in amphibians. The percentage of enigmatic-decline species increases with increasing extinction risk, from 9.7% of the rapidly declining species in the IUCN Category Near Threatened, to 25.0% in Vulnerable, 47.3% in Endangered, 57.1% in Critically Endangered, and 92.4% in Critically Endangered (Possibly Extinct). This observation suggests that the factors causing "enigmatic" declines are driving species toward extinction particularly rapidly.

The geographic distribution of rapidly declining species is nonrandom (Table 1) (*15*). Neotropical species are much more affected than, for example, those in the Afrotropical and Indomalayan realms. Species from the Australasian-Oceanic realm show average numbers of rapidly declining species, but if Australia and New Zealand are considered as a separate group, they have significantly more enigmatic-decline species than the average for amphibians as a whole. The geographic distribution of rapidly declining species (Fig. 1) shows that overexploited species are concentrated in East and Southeast Asia; reduced-habitat species occur more widely, but especially in Southeast Asia, West Africa, and the Caribbean; and enigmatic-decline species are restricted mostly to South America, Mesoamerica, Puerto Rico, and Australia. There is remarkably little geographic overlap between concentrations of species in the three groupings.

Enigmatic-decline species present the greatest challenge for conservation, because there are currently no known techniques for ensuring their survival in the wild. Such declines have taken place even within well-protected areas, such as Yosemite National Park (California) (*1*), Monteverde Cloud Forest Preserve (Costa Rica) (*5*, *6*), and Eungella National Park (Australia) (*14*). Enigmatic-decline species are positively associated with streams at high elevations in the tropics and negatively associated with still water and low elevations (Table 1). Several studies indicate that the virulence of the fungal disease chytridiomycosis, one of the most commonly cited causes of enigmatic declines (*22–24*), is greater at higher elevations and among streamside species (*3*, *7*, *25*). Most enigmatic declines have been recorded from the Americas south to Ecuador and Brazil, Australia, and New Zealand, but they are spreading, for instance to Peru, Chile, Dominica, Spain, and Tanzania (*14*, *26*, *27*). It is likely that the GAA underestimates the number and geographical extent of enigmatic declines, particularly in the tropics, where amphibians have been insufficiently monitored. Indeed, these declines tend to be very rapid, and few of them have actually been observed taking place. More commonly, researchers return to a site to find that several species have disappeared since the last visit. For instance, scientists only recently documented disappearances of frogs in southern Mexico, although some of

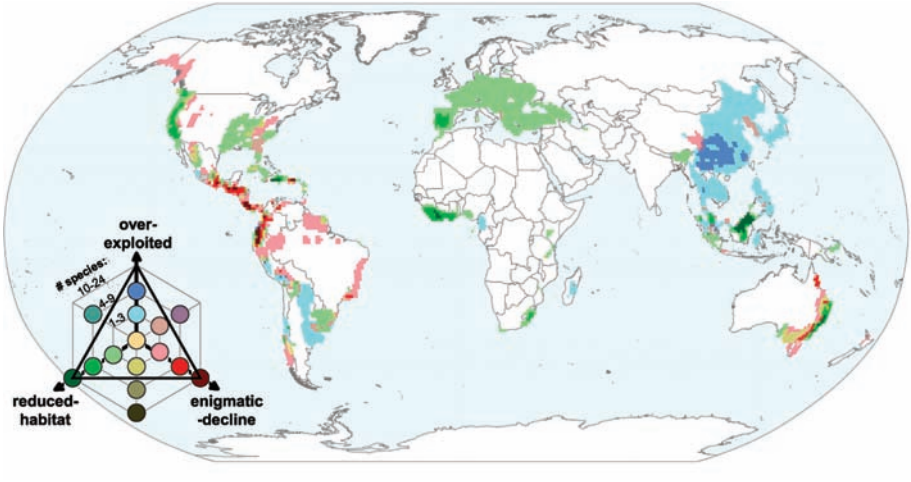

Fig. 1. Geographical pattern of the dominant causes of rapid decline (*15*) in amphibian species: overexploited (shades of blue); reduced-habitat (shades of green); and enigmatic-decline (shades of red). Where two threat types overlap in the same 1° cell, the color referring to the threat type with the larger number of rapidly declining species in that cell is indicated on the map. Intermediate colors are shown in cases of equal numbers of species experiencing two types of decline in the same cell, as shown in the key. Darker colors correspond to larger numbers of rapidly declining species of any type (not just of the dominant type in the cell in question).

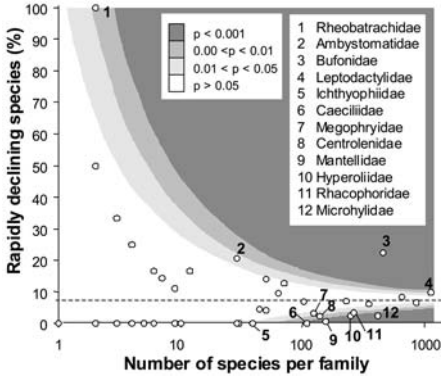

Fig. 2. Percentage of rapidly declining species (*15*) per amphibian family in relation to the average across all amphibians. The horizontal dashed line represents the overall mean percentage of rapidly declining species (7.6%).

these declines probably took place in the early 1980s (*28*). Accordingly, well-sampled countries tend to have a higher incidence of enigmatic declines: for example, 12.9% in Costa Rica, compared to 6.0% in the entire geographic region where most enigmatic declines have taken place. It is also possible that some species are not experiencing enigmatic declines yet but are susceptible to doing so, particularly if these are the results of factors such as the spread of a contagious disease (*13*, *22*–*24*) or increasing severity in environmental conditions due to climate change (*20*, *21*).

Rapid amphibian declines exhibit important taxonomic as well as regional patterns. Four amphibian families have significantly more rapidly declining species than the average for all amphibians: Rheobatrachidae (gastric-brooding frogs), Leptodactylidae (typical Neotropical frogs), Bufonidae (true toads), and the Ambystomatidae (mole salamanders) (Fig. 2) (*15*). Both known species of Rheobatrachidae are now extinct. Eight families have significantly fewer than the average percentage of rapidly declining species (Fig. 2), but for the two caecilian families, Caeciliidae and Ichthyophidae, this result might be an artifact caused by the large percentages of DD species (61 and 82%, respectively). The analysis depicted in Fig. 2 compares the percentage of rapidly declining species per family with the average for amphibians as a whole. However, taxa such as birds and mammals have few rapidly declining species, suggesting that rapid declines are usually rare occurrences. From this perspective, most amphibian families have significantly more rapidly declining species than should be expected.

Four families contribute overwhelmingly to the total number of rapidly declining species: Bufonidae, Leptodactylidae, Hylidae (treefrogs), and Ranidae (true frogs) (Fig. 3). The three kinds of decline vary in their importance to each family. Overexploitation is much more important in the Ranidae than in the other large families, reflecting the extensive harvest of these species for human consumption, especially in Asia. Declines caused by habitat loss are important in most families, and enigmatic declines have had a particularly major impact in the Bufonidae (*29*). Some very small families, such as Rheobatrachidae, Rhinodermatidae (Darwin's frogs), and Cryptobranchidae (giant salamanders) also have high proportions of rapidly declining species.

The wide variation between families in the number and proportion of rapidly declining species is confounded by the nonrandom geographic pattern of declines (Table 1 and Fig. 1). Families that are endemic to regions where enigmatic declines have taken place tend to be more susceptible to serious declines. If enigmatic declines spread to other regions, especially in Africa and Asia, then it is likely that some other families will prove to be susceptible to declining rapidly (*29*).

The findings of the GAA confirm earlier suspicions that rapid and poorly explained declines in amphibian populations are taking place in addition to the typical causes of biodiversity loss, including habitat loss and overexploitation (which are also serious for amphibians) (*5*, *10*). Most extinction rate models are based on predicted habitat loss, either as a result of direct human activity (*30*, *31*) or climate change (*32*). Because these models do not take account of enigmatic declines of the type affecting amphibian species, they underestimate the current extinction rate in amphibians. For a species facing an enigmatic decline, the only conservation option currently available is captive breeding, but many of the species affected are hard to maintain in ex situ conditions. Unless these declines are quickly understood and reversed, hundreds of species of amphibian can be expected to become extinct over the next few decades.

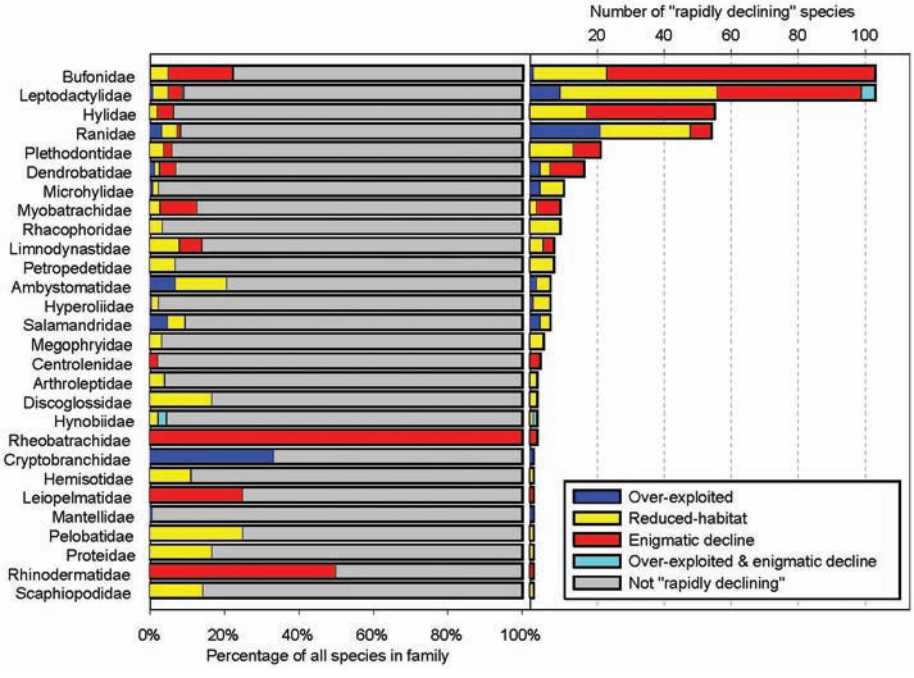

Fig. 3. Percentages and numbers of rapidly declining species (*15*) in amphibian families (with at least one rapidly declining species), broken into groups reflecting the dominant cause of rapid decline: overexploitation; habitat loss; or enigmatic decline.

References and Notes

1. C. Kagarise Sherman, M. L. Morton, *J. Herpetol.* **27**, 186 (1993).
2. C. A. Drost, G. M. Fellers, *Conserv. Biol.* **10**, 415 (1996).
3. P. A. Burrowes, R. L. Joglar, D. E. Green, *Herpetologica* **60**, 141 (2004).
4. G. V. Czechura, G. Ingram, *Mem. Queensland Mus.* **29**, 361 (1990).
5. J. A. Pounds, M. P. L. Fogden, J. M. Savage, G. C. Gorman, *Conserv. Biol.* **11**, 1307 (1997).
6. J. A. Pounds, M. L. Crump, *Conserv. Biol.* **8**, 72 (1994).
7. S. R. Ron, W. E. Duellman, L. A. Coloma, M. R. Bustamante, *J. Herpetol.* **37**, 116 (2003).
8. B. E. Young *et al.*, *Conserv. Biol.* **15**, 1213 (2001).
9. J. H. Pechmann, H. M. Wilbur, *Herpetologica* **50**, 65 (1994).
10. J. E. Houlahan, C. S. Findlay, B. R. Schmidt, A. H. Meyer, S. L. Kuzmin, *Nature* **404**, 752 (2000).
11. K. R. Lips, *Conserv. Biol.* **12**, 106 (1998).
12. J. D. Lynch, T. Grant, *Rev. Acad. Colomb. Ciencias* **22**, 149 (1998).
13. W. F. Laurance, K. R. McDonald, R. Speare, *Conserv. Biol.* **10**, 406 (1996).
14. IUCN Species Survival Commission, Conservation International Center for Applied Biodiversity Science, NatureServe, *IUCN Global Amphibian Assessment* (http://www.globalamphibians.org) (2004).
15. Methods are available as supporting online materials on *Science* Online.
16. IUCN–The World Conservation Union, *IUCN Red List Categories and Criteria* (IUCN, Gland, Switzerland, 2001).
17. BirdLife International, *State of the World's Birds: Indicators for our Changing World* (BirdLife International, Cambridge, 2004).
18. IUCN–The World Conservation Union, *2003 IUCN Red List of Threatened Species* (http://www.redlist.org) (2003).
19. J. Manzanilla, E. La Marca, *Mem. Fund. La Salle Ciencias Nat.* **62**, 5 (2004).
20. J. A. Pounds, *Nature* **410**, 639 (2001).
21. J. A. Pounds, R. Puschendorf, *Nature* **427**, 107 (2004).
22. L. Berger *et al.*, *Proc. Natl. Acad. Sci. U.S.A.* **95**, 9031 (1998).
23. K. R. Lips, *Conserv. Biol.* **13**, 117 (1999).
24. P. Daszak, A. A. Cunningham, A. D. Hyatt, *Div. Distrib.* **9**, 141 (2003).
25. K. R. Lips, J. D. Reeve, L. R. Witters, *Conserv. Biol.* **17**, 1078 (2003).
26. C. Magin, *Oryx* **37**, 406 (2003).
27. J. Bosch, I. Martínez-Solano, M. García-París, *Biol. Conserv.* **97**, 331 (2001).
28. K. R. Lips, J. R. Mendelson III, A. Muñoz-Alonso, L. Canseco-Márquez, D. G. Mulcahy, *Biol. Conserv.* **119**, 555 (2004).
29. Further information is available as supporting online material on *Science* Online.
30. S. L. Pimm, G. J. Russell, J. L. Gittleman, T. M. Brooks, *Science* **269**, 347 (1995).
31. S. L. Pimm, P. Raven, *Nature* **403**, 843 (2000).

32. C. D. Thomas *et al.*, *Nature* **427**, 145 (2004).
33. We thank the Moore Family Foundation, the Gordon and Betty Moore Foundation, Conservation International, the MAVA Foundation, the U.S. Department of State, the Regina Bauer Frankenberg Foundation for Animal Welfare, NSF (grants DEB-0130273 and INT-0322375), the Critical Ecosystem Partnership Fund, George Meyer, Ben Hammett, and the Disney Foundation for financial support of the IUCN GAA. We are grateful to the more than 500 herpetologists who generously gave of their time and knowledge to compile the GAA data. R. Akçakaya, T. Brooks, D. Church, M. Denil, D. Frost, C. Gascon, G. da Fonseca, M. Foster, C. Hilton-Taylor, M. Hoffmann, T. Lacher, P. Langhammer, G. Mace, L. Manler, L. Master, A. Mitchell, R. Mittermeier, D. Wake, and F. Xie provided extensive help and advice on the implementation of the GAA. The majority of the distribution maps used for U.S. species were adapted from the United States Amphibian Atlas Database, which was assembled at Ball State University by P. Nanjappa, L. Blackburn, and M. Lannoo, and which was supported in part by grants and/or matching funds from the National Fish and Wildlife Foundation, United States Fish and Wildlife Service, and Disney Wildlife Conservation Fund.

Supporting Online Material
www.sciencemag.org/cgi/content/full/1103538/DC1
Materials and Methods
Fig. S1
Tables S1 to S7
Appendix S1
References

2 August 2004; accepted 4 October 2004
Published online 14 October 2004;
10.1126/science.1103538
Include this information when citing this paper.

Lysosomal Glycosphingolipid Recognition by NKT Cells

Dapeng Zhou,[1]* Jochen Mattner,[1] Carlos Cantu III,[2] Nicolas Schrantz,[2] Ning Yin,[3] Ying Gao,[3] Yuval Sagiv,[1] Kelly Hudspeth,[1] Yun-Ping Wu,[4] Tadashi Yamashita,[4] Susann Teneberg,[5] Dacheng Wang,[6] Richard L. Proia,[4] Steven B Levery,[7] Paul B. Savage,[3] Luc Teyton,[2] Albert Bendelac[1]*

NKT cells represent a distinct lineage of T cells that coexpress a conserved αβ T cell receptor (TCR) and natural killer (NK) receptors. Although the TCR of NKT cells is characteristically autoreactive to CD1d, a lipid-presenting molecule, endogenous ligands for these cells have not been identified. We show that a lysosomal glycosphingolipid of previously unknown function, isoglobotrihexosylceramide (iGb3), is recognized both by mouse and human NKT cells. Impaired generation of lysosomal iGb3 in mice lacking β-hexosaminidase b results in severe NKT cell deficiency, suggesting that this lipid also mediates development of NKT cells in the mouse. We suggest that expression of iGb3 in peripheral tissues may be involved in controlling NKT cell responses to infections and malignancy and in autoimmunity.

As with protein-derived antigens, lipids, glycolipids, and lipopeptides (either of microbial or self origin) can be recognized by TCRαβ-expressing T lymphocytes (*1*). Of these, NKT cells represent an unusual population that recognizes lipids presented by the MHC class I–like CD1d protein and displays characteristics of innate rather than adaptive lymphocytes (*2*). The TCR of NKT cells is limited mainly to a single invariant α chain (mouse Vα14-Jα18 and the homologous human Vα24-Jα18) combined with variable mouse Vβ8 and human Vβ11 TCR β. These cells express a phenotype of effector or memory lymphocytes before encounter with any foreign antigen and display a panoply of inhibitory receptors also expressed on NK cells. Such features suggest that they may respond to conserved endogenous ligands, as well as foreign microbial antigens (*3*).

Mouse (m) Vα14 and human (h) Vα24 NKT cells appear to regulate a number of conditions in vivo, including malignancy and infection, as well as autoimmune diseases, through the rapid secretion of T helper 1 (T_H1) and T_H2 cytokines and chemokines (*4*). Without knowledge of the natural antigens recognized by these cells, it has been difficult to explore the mechanisms that govern their recruitment, activation, and development. Previous work has established the requirement for lysosomal trafficking of CD1d molecules (*5*) and the role of lysosomal proteases in presenting endogenous lipid antigens (*6*); the essential function of lysosomal lipid transfer proteins, known as sphingolipid activator proteins, or saposins, is now also established (*7–9*). These findings, and the recent report that a β-glucosylceramide synthase mutant cell line was defective in Vα14 NKT cell stimulation (*10*), have indicated that the natural ligands of NKT cells might be lysosomal glycosphingolipids.

We found that mice genetically deficient in the lysosomal glycosphingolipid degrading enzyme β-hexosaminidase b subunit ($Hexb^{-/-}$) (*11–13*) exhibited a severe reduction in the number of Vα14 NKT cells (Fig. 1, A and B). Thus, staining for NKT cells in these mice using tetramers of CD1d complexed with the artificial lipid αGalCer (CD1d-αGalCer) was reduced by 95% on average. All subsets of NKT cells, including the earliest $CD44^{low}NK1.1^{-}$ precursor and the CD4 and $CD4^{-}8^{-}$ cells, were equally affected as early as these cells could be detected in young 2.5-week-old mice [fig. S1 and (*14*)]. In contrast, the development of classical, naïve, and memory CD4 and CD8 T cells, as well as B cells, γδ T cells, and NK cells were not affected by Hexb deficiency [Fig. 1D and (*14*)].

Although CD1d surface expression was unaltered in $Hexb^{-/-}$ mice (Fig. 1C), thymocytes from these animals failed to elicit a response from a $Vα14^{+}$ NKT cell hybridoma (DN32.D3) (Fig. 2A). In contrast, they normally stimulated a $Vα14^{-}$, CD1d-reactive NKT hybridoma (TCB11) (Fig. 2A). Presentation of the ligand of DN32.D3, but not that of TCB11, is dependent on lysosomal function (*7*); these results suggested defects in presentation of lysosomal ligands. To rule out general, nonspecific lysosomal defects, resulting, for example, from lysosomal lipid storage in these mutant mice, we tested the lysosomal functions of $Hexb^{-/-}$ cells using a panel of diglycosylated αGalCer derivatives that require lysosomal processing before recognition by Vα14 NKT cells (*15*). The presentation of *N*-acetylgalactosamine (GalNAc) β1,4 Gal αCer by cells deficient in β-hexosaminidase b was selectively defective (Fig. 2B, upper panel), as expected from the specificity of this enzyme (*11–13*). In contrast, α-galactosidase A (αGalA)–deficient cells were selectively defective in processing Gal α1,4 Gal αCer and Gal α1,2 Gal αCer (Fig. 2B, lower panels), as expected from the specificity of αGalA (*15*). In contrast to these specific processing defects, control cells expressing a truncated form of CD1d missing the cytoplasmic endosomal targeting [CD1-TD "knock-in" (*5*)] were impaired in the presenta-

[1]University of Chicago, Department of Pathology, Chicago, IL 60637, USA. [2]The Scripps Research Institute, Department of Immunology, La Jolla, CA 92037, USA. [3]Brigham Young University, Department of Chemistry and Biochemistry, Provo, UT 84602–5700, USA. [4]Genetics of Development and Disease Branch, National Institute of Diabetes and Digestive and Kidney Diseases, NIH, Bethesda, MD 20892, USA. [5]Institute of Medical Biochemistry, Göteborg University, SE 405 30 Göteborg, Sweden. [6]Institute of Biophysics, Chinese Academy of Sciences, Beijing 100101, China. [7]Department of Chemistry, University of New Hampshire, Durham, NH 03824–3598, USA.

*To whom correspondence should be addressed. E-mail: dzhou@midway.uchicago.edu (D.Z.) and abendela@bsd.uchicago.edu (A.B.)

tion of all the diglycosylated αGalCer precursors we tested (Fig. 2B). Thus, Hexb$^{-/-}$ cells had a highly specific defect in the generation of the lysosomal ligands of Vα14 NKT cells.

Therefore, one of the natural products of the Hexb-dependent enzymes (β-hexosaminidase A and B) may be the ligand of mVα14 NKT cells. In mammalian cells, these two enzymes remove β-linked GalNAc residues found on glycosphingolipids of the ganglio-series (GalNAc β1,4 Gal) and the globo- and isoglobo-series (GalNAc β1,3 Gal), as well as GlcNAc residues of the lacto-series (GlcNAc β1,3 Gal) (*16*). Mice lacking ganglio-series glycolipids as a result of genetic deficiency of the key enzymes responsible for their synthesis, GM2 synthase and GM3 synthase (*17*, *18*), displayed no apparent defect in NKT cell development (Fig. 1B). Focusing on the other three series, we chemically synthesized globotrihexosylceramide Gb3 (Gal α1,4 Gal β1,4 Glc β 1,1 Cer) and isoglobotrihexosylceramide iGb3 (Gal α1,3 Gal β1,4 Glc β 1,1 Cer) (fig. S3), and purified the lacto-series glycolipid Gal α1,3 Gal β1,4 GlcNAc β 1,3 Gal β1,4 Glc β 1,1 Cer (*19*) to test their ability to stimulate NKT cells. Of these, only iGb3 displayed stimulatory activity [Fig. 3 and (*14*)]. Thus, iGb3 selectively expanded human Vα24 NKT cells in 4-day cultures of fresh peripheral blood mononuclear cells (PBMCs) (Fig. 3B) and stimulated strong T_H1 [as measured by interferon-γ (IFN-γ)] and T_H2 [as measured by interleukin 4 (IL-4)] cytokine secretion by a polyclonal human Vα24 NKT line (Fig. 3C). Fluorescence-activated cell sorting (FACS) analysis for intracellular IFN-γ revealed that about 50% of the cells stimulated by αGalCer responded to iGb3 [fig. S2A (*20*)], although this is likely an underestimate, because iGb3 elicited less IFN-γ per cell. Both of two NKT cell subclones tested, one with a CD4$^+$ and the other a CD4$^-$8$^-$ phenotype, also responded to iGb3 (*14*). iGb3 derived from other sources, including natural iGb3 purified from cat intestine (*19*) and iGb3 produced in vitro by action of iGb3 synthase on lactosylceramide and uridine diphosphate (UDP)–galactose, (fig. S3) were as stimulatory as synthetic iGb3 (Fig. 3C, right panel; fig. S3). iGb3 presented by CD1d-expressing bone marrow–derived dendritic cells stimulated the mVα14 NKT cell hybridoma DN32.D3 (Fig. 3D) and all the other mVα14 hybridomas tested, whether they used TCR Vβ8, Vβ7, or Vβ2, although responses were not elicited from any of the non-Vα14 hybridomas (fig. S2B). No response was observed with CD1d$^{-/-}$ dendritic cells (*14*).

In the lysosome, β-hexosaminidase removes the terminal GalNAc of iGb4 to produce iGb3, with α-galactosidase A subsequently transforming iGb3 into lactosylceramide (LacCer) by removal of the terminal Gal (see Fig. 3A). iGb4 presented by bone marrow–derived dendritic cells was stimulatory for mouse (Fig. 3D, right panel) and human NKT cells (*14*), whereas LacCer was not (Fig. 3C). However, Hexb$^{-/-}$ cells presented iGb3 but failed to present iGb4, which indicated directly that processing of iGb4 into iGb3 is necessary for NKT cell recognition (Fig. 3D). Trafficking of CD1d to lysosomal compartments was essential to present these antigens, as shown using cytoplasmic tail–truncated CD1d (CD1-TD)–expressing antigen-presenting cells (APCs) (Fig. 3D), and the absence of lysosomal saposins impaired iGb3 presentation (Fig. 3E). These results are consistent with previous reports showing that NKT cell development and function required CD1d trafficking to lysosomal compartments (*5*), as well as the lipid transfer function of saposins (*7*).

In a cell-free assay (*7*, *21*), loading of iGb3 and iGb4 onto CD1d required saposin B (Fig. 3F, left panel). Attempts to stain NKT cells directly with CD1d/iGb3 tetramers were unsuccessful, perhaps because of a low affinity for TCR and our inability to achieve 100% loading with iGb3 even in the presence of saposins (see Fig. 3F). Nevertheless, we found that CD1d/iGb3, but not CD1d/iGb4, complexes could significantly

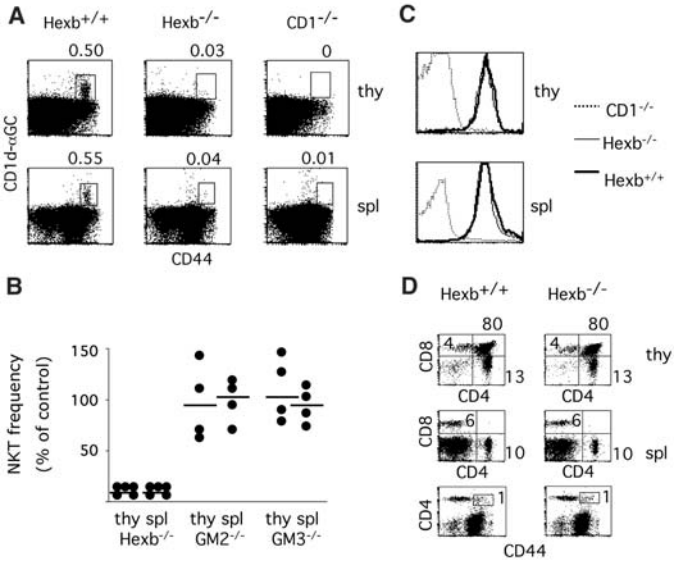

Fig. 1. Deficient thymic selection of Vα14 NKT cells in Hexb$^{-/-}$ mice. (**A**) Lymphocytes from thymus and spleen of Hexb$^{+/+}$ and Hexb$^{-/-}$ littermates, and CD1d$^{-/-}$ mice were stained with CD1d-αGalCer tetramers and anti-CD44. Representative FACS profiles are shown with percentages indicated in the upper quadrants. Absolute numbers of lymphocytes in the thymus and the spleen of mutant and wild-type mice were similar. The NKT cell defect was also observed in the liver (*14*). (**B**) Summary of experiments where the frequency of thymic (thy) and splenic (spl) NKT cells in individual mutant mouse is represented as a percentage of control wild-type littermate. GM2$^{-/-}$ and GM3$^{-/-}$ mice are lacking GM2 synthase and GM3 synthase, respectively. (**C**) FACS analysis of CD1d in thymocytes and splenocytes. (**D**). CD4/CD8 and CD4/CD44 profiles of thymocytes and splenocytes.

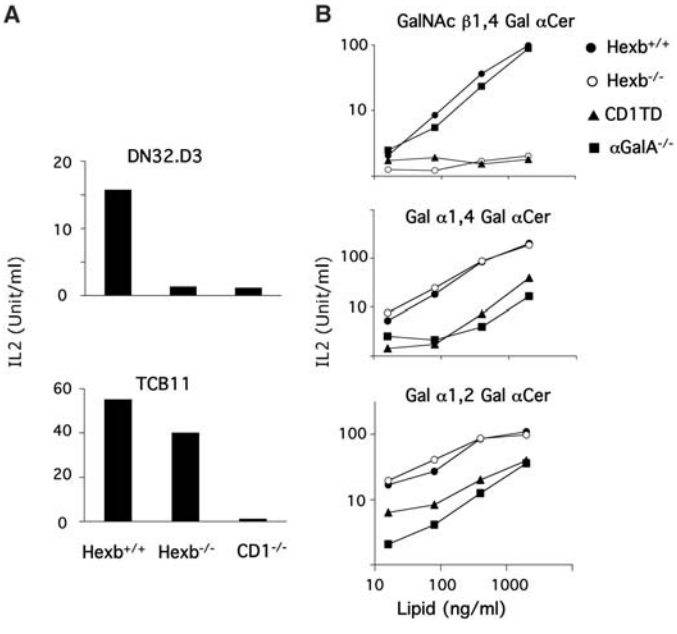

Fig. 2. Specific antigen presentation defects in Hexb$^{-/-}$ mice. (**A**) Autoreactive responses of Vα14$^+$ DN32.D3 and Vα14$^-$ TCB11 hybridomas stimulated by CD1d-expressing thymocytes from Hexb$^{-/-}$ and Hexb$^{+/+}$ littermates. CD1$^{-/-}$ thymocytes served as negative control. (**B**) Spleen cells from Hexb$^{-/-}$ and Hexb$^{+/+}$ littermates, αGalA$^{-/-}$, and CD1-TD knock-in mice were pulsed with various diglycosylated variants of αGalCer, as indicated, before stimulation of Vα14$^+$ DN32.D3 hybridoma. The data are representative of two separate experiments.

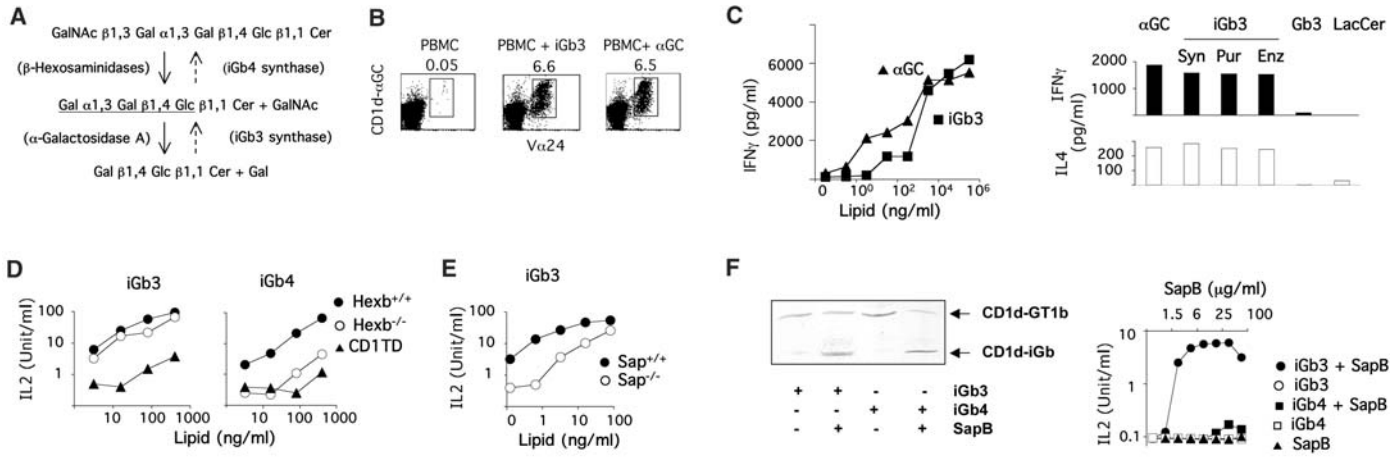

Fig. 3. iGb3 is the ligand of mVα14 and hVα24 NKT cells. (**A**) A schematic of synthesis (dotted arrows, right) in the Golgi, and degradation (continuous arrows, left) in the lysosome, of iGb3. From top to bottom, iGb4, iGb3, and LacCer. (**B**) Frequency of hVα24 NKT PBL, doubly-stained by antibody against Vα24 and CD1d-αGalCer tetramers, in PBMCs cultured for 4 days in the presence of 100 ng/ml αGalCer, iGb3, or medium alone, as indicated. Similar results were found in six out of six healthy human subjects. (**C**) (Left) IFN-γ production by a human Vα24 NKT line stimulated with different concentrations of iGb3 and αGalCer in the presence of irradiated PBMCs as CD1d-expressing APCs. Similar results were obtained with two out of two additional cloned CD4 and DN Vα24 NKT lines. (Right) IFN-γ and IL-4 production by the human Vα24 NKT line in response to irradiated PBMCs and 100 ng/ml of iGb3 of synthetic, purified, and enzymatic origin, versus 100 ng/ml of αGalCer, Gb3, or LacCer, as indicated. Similar results were obtained with two out of two additional CD4 and CD4$^-$CD8$^-$ hVα24 NKT clones. (**D**) Stimulation of mouse Vα14$^+$ DN32.D3 by iGb3 and iGb4 presented by bone marrow–derived dendritic cells from Hexb$^{-/-}$, Hexb$^{+/+}$, and CD1-TD mice as indicated. (**E**) Stimulation of mouse DN32.D3 by iGb3 with bone marrow–derived dendritic cells from saposin-deficient (Sap$^{-/-}$) and -sufficient (Sap$^{+/+}$) littermates, as indicated. (**F**) (Left) In vitro loading of iGb3 and iGb4 onto recombinant CD1d in the presence of saposin B, visualized by isoelectrofocusing. Electromobility shift indicates partial replacement of GT1b by iGb3 and iGb4, as indicated. (Right) Stimulation of DN32.D3 by iGb3 and iGb4 loaded on plate-bound CD1d in the presence of saposin B, as indicated.

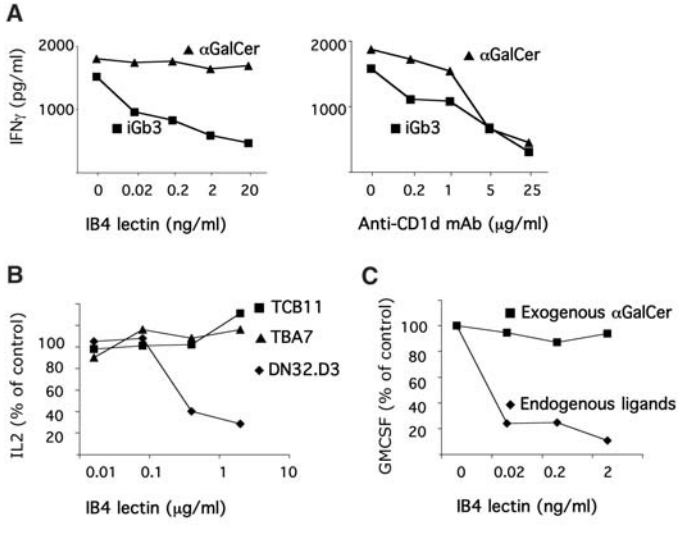

Fig. 4. Blocking CD1d/iGb3 stimulation by the lectin IB4. (**A**) IB4 inhibited the stimulation of the human Vα24 NKT line by iGb3 but not αGalCer pulsed PBMC (left). In contrast, anti-human CD1d mAb 51 inhibited stimulation by both iGb3 and αGalCer (right). (**B**) IB4 specifically inhibited the CD1d-autoreactive response of Vα14$^+$ DN32.D3 but not that of non-Vα14 hybridomas TCB11 and TBA7 to RBL.CD1d. Results expressed as a percentage of control without lectin and representative of four separate experiments. (**C**) IB4 inhibited the CD1d-autoreactive response of the hVα24 NKT line to PBMC-derived dendritic cells alone (endogenous ligands), measured by enzyme-linked immunosorbent assay (ELISA) as granulocyte/macrophage colony-stimulating factor (GMCSF) released in the supernatant. The control response to PBMC-derived dendritic cells plus exogenous αGalCer was not altered. Results are expressed as a percentage of control without lectin (i.e., 939 pg/ml for exogenous ligand and 294 pg/ml for endogenous ligand) and are representative of three separate experiments.

stimulate Vα14 NKT cells (Fig. 3F, right panel). These results reveal that, whereas both iGb3 and iGb4 can bind CD1d, only iGb3 is a major antigen of the Vα14 NKT cell and that removal of the distal GalNAc residue of its precursor iGb4 by lysosomal β-hexosaminidase is required for TCR recognition in vivo.

The almost-complete block in Vα14 NKT cell development in Hexb$^{-/-}$ mice and the inability of Hexb$^{-/-}$ thymocytes to stimulate Vα14 NKT hybridomas suggested that iGb3 might alone represent the principal natural ligand of NKT cells. To test this further, the *Griffonia simplicifolia*–derived isolectin B4 (IB4), a lectin that binds the terminal Gal α1,3 Gal of iGb3 (*22*), was used to inhibit NKT cell stimulation. IB4 impaired hVα24 NKT cell stimulation by exogenously added iGb3, but not by αGalCer (Fig. 4A, left panel), whereas a monoclonal antibody (mAb) against CD1d blocked stimulation by both glycolipids (Fig. 4A, right panel). These results are consistent with specific recognition by IB4 of the terminal carbohydrates of iGb3, even when bound to CD1d. This binding property of IB4 was next exploited to test whether these terminal Gal α1,3 Gal residues contribute significantly to the natural stimulation of mVα14 and hVα24 NKT cells. IB4 prevented the autoreactive stimulation of the Vα14$^+$ DN32.D3 hybridoma by rat basophilic leukemia (RBL) cells transfected to express mouse CD1d (Fig. 4B). In contrast, stimulation of two control (non-Vα14) CD1d autoreactive hybridomas was unaffected (Fig. 4B). Furthermore, IB4 also blocked natural recognition of CD1d-expressing PBMC-derived dendritic cells by the human Vα24 NKT line but failed to block recognition of exogenously added αGalCer (Fig. 4C). Blockade of iGb3 recognition by IB4 in humans consistently required lower amounts of lectin (by a factor of ~1000) than for mouse and rat cells, possibly because mice and rats, but not humans, express abundant levels of an additional ligand recognized by IB4, the Gal α1,3 Gal epitope expressed on glycoproteins (*23*), which would compete for binding.

Because of their role in regulating a range of disease states, the nature of ligands recognized by mVα14/hVα24 NKT cells has been the subject of intense research and speculation (*24*–*26*). Our findings suggest that a single glycosphingolipid, the isoglobo-side iGb3, may represent the principal endogenous ligand of mVα14 and hVα24 NKT cells, at least under conditions not associated with disease. It should be noted, however, that glycosphingolipids of the isoglobo-series have not been purified and characterized in all mammalian species yet. In particular, while they have been biochemically demonstrated in rat (*22*), dog, and cat (*27*), they have not been reported in mouse and human. Both mouse and human, however, have the iGb3 synthase gene, which we showed to be expressed and functional in mouse (fig. S3, A to C). Furthermore, the Hexb requirement for natural ligand expression in mouse and the blockade of its recognition by IB4 in mouse and human suggest that this natural ligand must have a sequence of carbohydrates identical or highly similar to that of iGb3, i.e., a [Gal α1,3 Gal] exposed on removal of a hexosamine in the lysosome. In humans, natural antibodies against [Gal α1,3 Gal] epitopes have been reported (*23*), raising the possibility that they might interfere with iGb3 or that iGb3 might be low or absent. We have shown that these natural antibodies against Gal do not recognize iGb3 [fig. S4 and (*27*, *28*)]. Thus, despite the current lack of direct biochemical evidence for the presence of iGb3 in mouse and human, the combined data suggest that iGb3 or a close structural analog is the principal self antigen of NKT cells. Our results, however, do not rule out the existence of additional endogenous ligands. For example, the few residual Vα14 NKT cells found in $Hexb^{-/-}$ mice might recognize other ligands. It is also possible that alternative endogenous ligands are expressed in some disease conditions or in particular cell types not examined here. Direct biochemical studies will be required to elucidate these issues.

The lack of NKT cell precursors in the thymus of $Hexb^{-/-}$ mice suggests that iGb3 is also the ligand involved in their thymic development. Although this hypothesis remains to be confirmed, it is consistent with the model that the unusual effector memory phenotype imparted to the thymocyte precursors of NKT cells is a consequence of their thymic stimulation by agonist ligands, i.e., antigens that also stimulate the mature NKT cell (*29*, *30*). Our findings should allow a further dissection of the mechanisms underlying the development of these autoreactive, regulatory lymphocytes.

It is possible that lysosomal expression of iGb3 is dysregulated in diseases regulated by NKT cells, such as type I diabetes and cancer (*4*, *31*) or microbial infection (*32*). Additional ligands, such as the mycobacterial glycolipid phosphatidylinositolmannoside (*33*), may also elicit NKT cell responses. Thus, the discovery of natural endogenous and microbial NKT cell ligands, as well as the synthesis of pharmacologic agonists or inhibitors, may lead to novel approaches to manipulating NKT cells for the prevention and treatment of diseases.

References and Notes

1. M. Brigl, M. B. Brenner, *Annu. Rev. Immunol.* **22**, 817 (2004).
2. A. Bendelac, M. N. Rivera, S.-H. Park, J. H. Roark, *Annu. Rev. Immunol.* **15**, 535 (1997).
3. A. Bendelac, M. Bonneville, J. F. Kearney, *Nature Rev. Immunol.* **1**, 177 (2001).
4. M. J. Smyth, D. I. Godfrey, *Nature Immunol.* **1**, 459 (2000).
5. Y. H. Chiu *et al.*, *Nature Immunol.* **3**, 55 (2002).
6. K. Honey *et al.*, *Nature Immunol.* **3**, 1069 (2002).
7. D. Zhou *et al.*, *Science* **303**, 523 (2004).
8. S. J. Kang, P. Cresswell, *Nature Immunol.* **5**, 175 (2004).
9. F. Winau *et al.*, *Nature Immunol.* **5**, 169 (2004).
10. A. K. Stanic *et al.*, *Proc. Natl. Acad. Sci. U.S.A.* **100**, 1849 (2003).
11. K. Sandhoff, T. Kolter, *Philos. Trans. R. Soc. London Ser. B* **358**, 847 (2003).
12. R. L. Proia, *Philos. Trans. R. Soc. London Ser. B* **358**, 879 (2003).
13. K. Sango *et al.*, *Nature Genet.* **14**, 348 (1996).
14. D. Zhou *et al.*, unpublished observations.
15. T. I. Prigozy *et al.*, *Science* **291**, 664 (2001).
16. E. Conzelmann, K. Sandhoff, *Adv. Exp. Med. Biol.* **125**, 295 (1980).
17. T. Yamashita *et al.*, *Proc. Natl. Acad. Sci. U.S.A.* **100**, 3445 (2003).
18. K. A. Sheikh *et al.*, *Proc. Natl. Acad. Sci. U.S.A.* **96**, 7532 (1999).
19. S. Teneberg, J. Angstrom, A. Ljungh, *Glycobiology* **14**, 187 (2004).
20. Materials and methods and figs. S1 to S4 are available as supporting online material on *Science* Online.
21. C. Cantu, K. Benlagha, P. B. Savage, A. Bendelac, L. Teyton, *J. Immunol.* **170**, 4673 (2003).
22. J. J. Keusch, S. M. Manzella, K. A. Nyame, R. D. Cummings, J. U. Baenziger, *J. Biol. Chem.* **275**, 25308 (2000).
23. U. Galili, L. Wang, D. C. LaTemple, M. Z. Radic, *Subcell. Biochem.* **32**, 79 (1999).
24. T. Kawano *et al.*, *Science* **278**, 1626 (1997).
25. J. E. Gumperz *et al.*, *Immunity* **12**, 211 (2000).
26. D. Y. Wu, N. H. Segal, S. Sidobre, M. Kronenberg, P. B. Chapman, *J. Exp. Med.* **198**, 173 (2003).
27. S. Teneberg *et al.*, *Glycobiology* **6**, 599 (1996).
28. H. Xu *et al.*, *Transplantation* **73**, 1549 (2002).
29. K. A. Hogquist *et al.*, *Cell* **76**, 17 (1994).
30. A. Bendelac, *Nature Immunol.* **5**, 557 (2004).
31. L. Beaudoin, V. Laloux, J. Novak, B. Lucas, A. Lehuen, *Immunity* **17**, 725 (2002).
32. M. Brigl, L. Bry, S. C. Kent, J. E. Gumperz, M. B. Brenner, *Nature Immunol.* **4**, 1230 (2003).
33. K. Fischer *et al.*, *Proc. Natl. Acad. Sci. U.S.A.* **101**, 10685 (2004).

34. This work was supported by CRI fellowships (D.Z. and Y.S.) and NIH grants (P01 AI053725 to A.B., L.T., and P.B.S. and R01 AI38339 and AI50847 to A.B.). S.T. is supported by Swedish Medical Research Council (no. 12628) and the Swedish Cancer Foundation. S.B.L. is supported by the New Hampshire Biological Research Infrastructure Network-Center for structural biology (NIH P20RR16459). We thank C. Borowski, A. Chong, U. Galili, K. Hayakawa, T. Henion, F.-F. Hsu, B. Jabri, P. Matzinger, and B. Meresse for advice and help with reagents, and C. Bowers for mouse care.

Supporting Online Material
www.sciencemag.org/cgi/content/full/1103440/DC1
Materials and Methods
Figs. S1 to S4
References and Notes

30 July 2004; accepted 22 October 2004
Published online 11 November 2004;
10.1126/science/1103440
Include this information when citing this paper.

Crystal Structure of a Photolyase Bound to a CPD-Like DNA Lesion After in Situ Repair

Alexandra Mees,[1] Tobias Klar,[2] Petra Gnau,[2] Ulrich Hennecke,[1] Andre P. M. Eker,[3] Thomas Carell,[1]* Lars-Oliver Essen[2]*

DNA photolyases use light energy to repair DNA that comprises ultraviolet-induced lesions such as the *cis-syn* cyclobutane pyrimidine dimers (CPDs). Here we report the crystal structure of a DNA photolyase bound to duplex DNA that is bent by 50° and comprises a synthetic CPD lesion. This CPD lesion is flipped into the active site and split there into two thymines by synchrotron radiation at 100 K. Although photolyases catalyze blue light–driven CPD cleavage only above 200 K, this structure apparently mimics a structural substate during light-driven DNA repair in which back-flipping of the thymines into duplex DNA has not yet taken place.

Life under the sun is endangered by ultraviolet (UV) radiation that causes the formation of genotoxic photoproducts in DNA (*1*). Major UV-induced lesions include *cis-syn* cyclobutane pyrimidine dimers (CPDs) formed by a [2+2] cycloaddition of two adjacent pyrimidine bases, usually thymine. The importance of efficient repair systems for UV lesions is highlighted by hereditary diseases such as xeroderma pigmentosum. In prokaryotes, plants, and many animals, DNA photolyases (EC no. 4.1.99.3) are mainly responsible for the repair of CPD lesions by catalyzing the cleavage of the cyclobutane ring, using blue or near-UV light [absorbance (λ) of 360 to 500 nm] as the energy source (*2*, *3*).

Despite three crystal structures of DNA photolyases (*4*–*6*) and the high affinity of photolyases toward DNA strands with *cis-syn* CPD lesions [dissociation constant $K_D \sim 10^{-9}$ M (*2*)], it has proved difficult to obtain structural information on a substrate complex with CPD-comprising DNA. Thus, questions remain concerning the mechanism of CPD lesion recognition and binding. A long-standing hypothesis, supported by biochemical data (*7*, *8*), computer modeling (*6*, *9*, *10*), and nuclear magnetic resonance (NMR) spectroscopy (*11*), states that photolyases flip the damaged dinucleotide out of the DNA double helix into their active site. After substrate binding, photon absorption by an antenna pigment (deazaflavin or methenyltetrahydrofolate) triggers transfer of the excitation energy to the catalytic flavin adenine dinucleotide, reduced state ($FADH^-$) cofactor (Fig. 1A). The excited cofactor then transmits an electron to the CPD lesion to induce splitting of the cyclobutane ring. The resulting radical anion then transfers back the excess electron to the FADH cofactor (semiquinone), closing the catalytic cycle within 0.5 to 2 ns after initial photon absorption (*2*).

To elucidate the recognition mode of CPD lesions, we crystallized a complex between the *Anacystis nidulans* DNA photolyase (*4*, *12*) and a 14-nucleotide oligomer DNA duplex with a CPD analog in the central position (*13*). The synthetic CPD analog has the same *cis-syn* stereochemistry as natural CPD lesions and is efficiently photoreactivated by DNA photolyases (*14*); however, it contains a formacetal linkage instead of the intradimer phosphate. The latter was highly useful in preparing the CPD lesion analog in quantities sufficient for crystallization studies. After data collection at a synchrotron beamline, structure solution, and refinement to 1.8 Å resolution (R_{factor}/R_{free}: 0.206/0.226), the crystals, which comprise four photolyase/DNA complexes per asymmetric unit, revealed the DNA photolyase in two different states (fig. S1A): In two complexes, duplex DNA is bound to the enzyme (complexes A and B), whereas the other two complexes (C and D) show only short stretches of single-stranded DNA (*13*). Unless otherwise stated, the following structural analysis concerns complex A. Despite the extensive structural distortion of the duplex DNA upon binding to the DNA photolyase, the protein itself undergoes only minor changes, with a root mean square deviation (RMSD) of 0.583 Å for 473 C_α-positions as compared to the uncomplexed enzyme. Marked differences are found only along the protein-DNA interface, which buries about 1216 $Å^2$ of molecular surface, rather little compared to other DNA repair enzymes (Fig. 1B).

Outside the site of lesion recognition, the DNA adopts a B-type conformation (Figs. 1B and 2A) and makes numerous interactions with the protein via its phosphodeoxyribose backbone, as expected for a sequence-independent DNA repair enzyme. The overall orientation of the DNA strand that contains the CPD is consistent with models derived from both biochemical (*8*) and NMR spectroscopic data (*11*). The thymine dimer is specifically recognized in the active site by being completely flipped out of the duplex DNA (Fig. 2A). The complementary adenines stack with their outside neighbors but do not stack on top of each other because of a large intrahelical bend at the CPD site. Previous studies showed that a single CPD lesion induces bending of regular B-DNA by 20 to 30° (*15*, *16*). In the complex with DNA photolyase, the DNA bending was increased to about 50° (Fig. 2B). The photolyase/DNA complex differs significantly from a complex with the DNA-repair enzyme T4 endonuclease V (*17*), which also recognizes CPD lesions. Instead of the thymine dimer, the endonuclease flips the adenine opposite the 5′-T of the CPD lesion into its active site, thus causing the DNA to bend in the opposite direction from that in the photolyase/DNA complex (Fig. 2A).

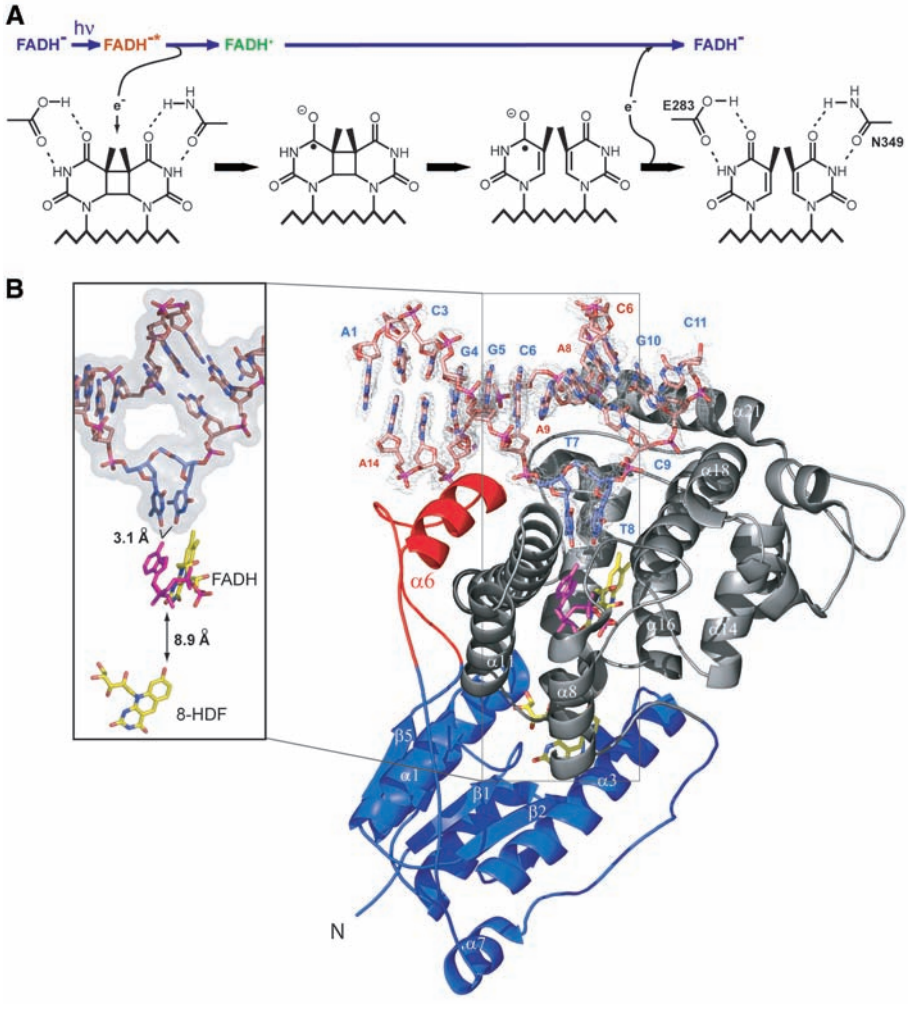

Fig. 1. (**A**) Mechanism of blue light–mediated repair of CPD lesions by DNA photolyases. Asterisks indicate an excited state of the flavin cofactor, *hv* indicates a blue-light or near-UV photon. (**B**) Ribbon model of complex A with the CPD-DNA in sticks representation and the $2F_{obs}$-F_{calc} electron density (contouring level, 1σ) that defines the duplex DNA (blue labels, CPD strand; red labels, counterstrand). The thymine dimer is highlighted in blue; the protruding α6 helix (red) contacts DNA along the minor groove. Apart from the adenine moiety of FAD (flavin adenine dinucleotide, purple), the cofactors are colored in yellow. Nomenclature and definition of secondary structure elements are given in (*4*).

[1]Department of Chemistry and Biochemistry, Butenandt-Straße 5-13, Ludwig Maximilians University, D-81377 Munich, Germany. [2]Department of Chemistry, Philipps University, Hans-Meerwein-Straße, D-35032 Marburg, Germany. [3]Department of Cell Biology and Genetics, Medisch Genetisch Centrum, Erasmus University Medical Centre, Post Office Box 1738, 3000 DR Rotterdam, Netherlands.

*To whom correspondence should be addressed. E-mail: essen@chemie.uni-marburg.de (L.-O.E.) and thomas.carell@cup.uni-muenchen.de (T.C.)

The disruption of the two base pairs at the CPD lesion site and partial unwinding of the duplex DNA created a large hole of about 10 by 10 Å. This was partly occupied by a nonregular ridge comprising residues G397 to F406 (*18*) of the photolyase. Here, the only specific interactions between the photolyase and DNA involved van-der-Waals contacts between P402 and the adenines opposite the CPD lesion and a hydrogen bond between the amide of L403 and the phosphate group between the two adenines (Fig. 3). The conformation of this ridge differs between the complexed and uncomplexed photolyase molecules (fig. S1). In the complex, the ridge G397-F406 is displaced by about 4.0 Å with the biggest movement found at its tip for D399 (10 Å) and in a large swiveling motion of the side chain of R404.

Salt bridges and hydrogen bonds are extensively formed between the photolyase and the phosphates P^{-1}, P^{+1}, P^{+2}, and P^{+3} (Fig. 3). Although the synthetic CPD lesion comprises a formacetal group instead of the intradimer phosphate P^0, major interactions with the missing P^0 phosphate are unlikely, because there are no residues close to the flipped thymine dimer that could interact with P^0. This observation agrees with biochemical footprinting data (*19*, *20*). Like several other DNA binding proteins, DNA photolyases use the dipole moment of helices for electrostatic stabilization of the protein-DNA complex. For example, the N terminus of helix α6 is directed toward the minor groove around the P^{-1} phosphate (Fig. 1B). An analogous interaction may be postulated between the P^{+2} phosphate and helix α18, which moves by ~0.6 Å upon DNA binding.

Negative F_{obs}-F_{calc} difference electron density at the postulated cyclobutane ring revealed that the C5-C5 and C6-C6 bonds of the synthesized CPD lesion were broken. Thus, the active site harbors a repaired thymine dinucleotide (Fig. 4, B and C). To exclude adventitious DNA repair during crystallization or crystal handling, single crystals were analyzed by capillary electrophoresis (CE) for the presence of the synthetic CPD lesion. We found that the cyclobutane ring was still intact after 12 months of crystallization, showing that neither crystal growth nor harvest, both performed under strict red light conditions, induce repair (fig. S2). Likewise, the CE analysis of crystals only briefly exposed (~2 s) to synchrotron irradiation showed intact CPD lesions. However, for crystals exposed for a complete data collection run (overall exposure time, 600 to 1000 s), we observed mainly decomposition products of the DNA strands in the CE runs. Unlike blue light–catalyzed cycloreversions of CPD lesions by photolyases, which proceed only above 200 K (*21*), the observed cleavage of the CPD lesion by prolonged synchrotron exposure occurred at the data collection temperature of 100 K. Although the repair of CPDs by radiolytically produced electrons has been reported even at 77 K (*22*), it has

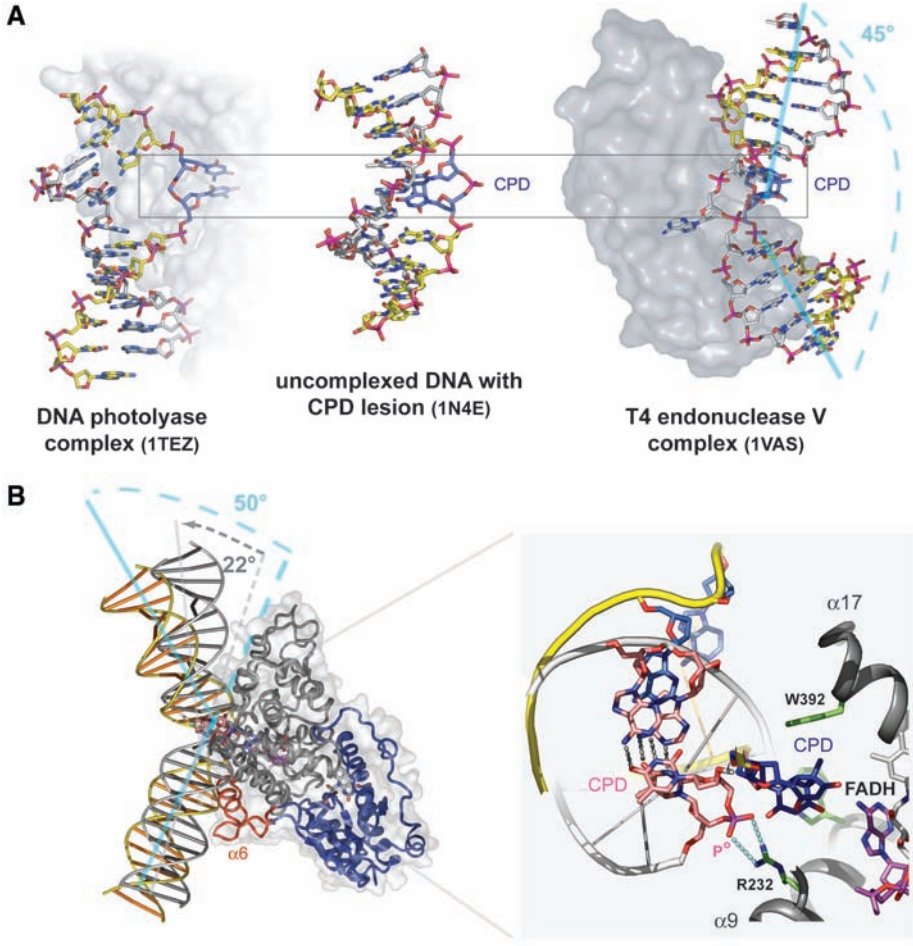

Fig. 2. (**A**) CPD-comprising DNA duplexes bound to DNA photolyase, to T4 endonuclease V (*17*), or in the uncomplexed state (*16*). Accession numbers are in parentheses. (**B**) The overall bend of modeled duplex B-DNA with an internal CPD lesion (*13*) increased from about 22° (gray) to 50° on binding to DNA photolyase (yellow). The inset shows the expected structural changes around the thymine dimer in the modeled states before and after base flipping. R232 might assist in the recognition of CPD-comprising DNA before base flipping by forming a salt bridge with the P^0 phosphate. The flip-out of the thymine dimer into the active site pocket by ~13 Å is accompanied by large structural changes in the CPD-comprising DNA strand.

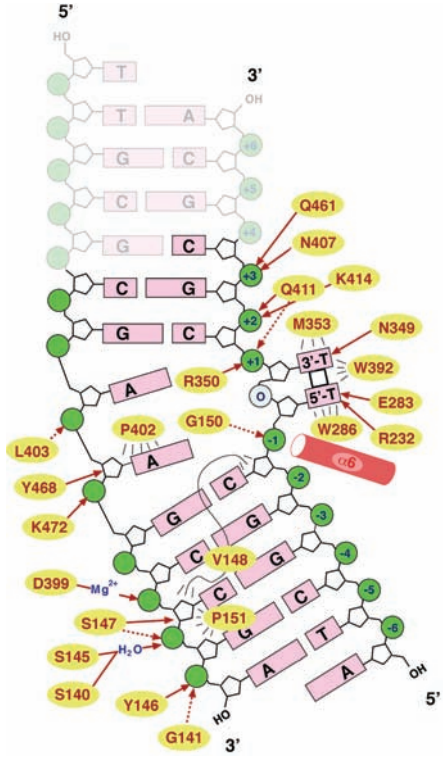

Fig. 3. Schematic diagram showing the interactions between duplex DNA and the enzyme. Nucleotides not defined by electron density are shown faded. Dashed arrows indicate interactions with the protein backbone; solid arrows, with side chains. Numbering of the phosphate groups starts from the intradimer formacetal group (0). Interactions between the enzyme and the complementary strand may stabilize the bending of duplex DNA, because there are no major differences in the affinities toward CPD-comprising single- and double-stranded DNA (*2*).

not been observed in other structures of DNA strands containing CPD lesions, either uncomplexed (*16*) or complexed to T4 endonuclease V (*17*) or an archaeal Y-type polymerase (*23*). The vulnerability of the CPD lesion in our crystals could be caused either by the unusual flip of the CPD lesion out of the DNA helix or by true catalysis in the active site that mimics blue light–mediated CPD cleavage. The latter is supported by the observation that a second photochemical reaction of photolyases, the reduction of the catalytic flavin cofactor from an inactive, oxidized state to $FADH^-$, is likewise triggered in the *A. nidulans* enzyme by high brilliance synchrotron radiation (*24*). In our structure, flavin reduction by radiation-generated electrons was sustained by the 9° "butterfly bend" along the N5-N10 axis of the isoalloxazine ring (Fig. 4A). CPD photolyases have high quantum yields for photochemical dimer splitting (~0.9); thus, it is likely that the geometry of the active site allows particularly efficient unidirectional electron transfer and dimer splitting.

As might be expected for the structure of a cryotrapped reaction product, the thymine dinucleotide differs structurally only slightly from a hypothetical CPD lesion within the active site (Fig. 4B). The pyrimidine rings of the 5′-T and 3′-T improve their stacking by decreasing the tilt angle between the base planes from 56° (*16*) to 16° after cleavage. The rotational offset of –26° perpendicular to the base planes of the thymine dinucleotide mimics quite well the CB^+ pucker of the cyclobutane ring that was found in the crystal structure of a CPD lesion within duplex DNA [C6*-C5*-C5-C6 dihedral: –24° (*16*)] and in theoretical calculations (*25*, *26*). The interactions that we observed between the thymine dinucleotide and the active site are likely preserved before cleavage of a bound CPD lesion. An L-shaped wedge comprising the conserved tryptophans W286 and W392 shielded the cyclobutane ring during the reaction course by making van-der-Waals interactions with the ring plane of the 5′-T and the edge of the thymine dinucleotide. The C4 carbonyl groups of the 5′-T and the 3′-T formed hydrogen bonds with the adenine N6 amino group of the $FADH^-$ cofactor (Fig. 4, C and D). In addition, the two thymines formed hydrogen bonds via their C4-carbonyl and N3-imide groups to the side chains of E283 and N349, although these residues are apparently free to flip their side chain for an alternative hydrogen-bonding pattern with cytosine-comprising CPD lesions. Nevertheless, the hydrogen bonds between the 3′-T and N349 and between the 5′-T and E283 might be important for catalysis. Protonated E283 could stabilize the radical anion of the CPD formed after electron transfer from $FADH^-$ (Fig. 1A). A mutation of this residue to alanine in the yeast photolyase did not affect substrate binding, but diminished the quantum yield for the CPD cleavage reaction by 60% (*8*).

A still unresolved issue of the photolyase mechanism is the nature of the electron transfer pathway used in blue light–driven electron transfer from $FADH^-$ to the CPD lesion. Compared to other flavoproteins, the $FADH^-$ cofactor of photolyases adopts a unique U-shaped conformation and might hence facilitate indirect electron transfer through its adenine moiety toward the CPD lesion. Quantum chemical calculations corroborated such an electron transfer pathway from the electron-donating π-system of the isoalloxazine via the 1′-CH and 2′-OH groups of the ribityl group and the adenine moiety (*27*, *28*). Our structure firmly supports this pathway, because the adenine ring bridges the electron donating isoalloxazine ring and the thymine dinucleotide via two hydrogen bonds (Fig. 4, C and D). Nevertheless, a direct electron transfer pathway cannot be excluded, because the C4-carbonyl of the 3′-T almost contacts the C8-methyl group of the isoalloxazine (4.3 Å), and the center of the electron-donating isoalloxazine ring system of $FADH^-$ is only 7 Å away from the 3′-T. Further experimental and theoretical data are needed to clarify which of the two pathways is operational.

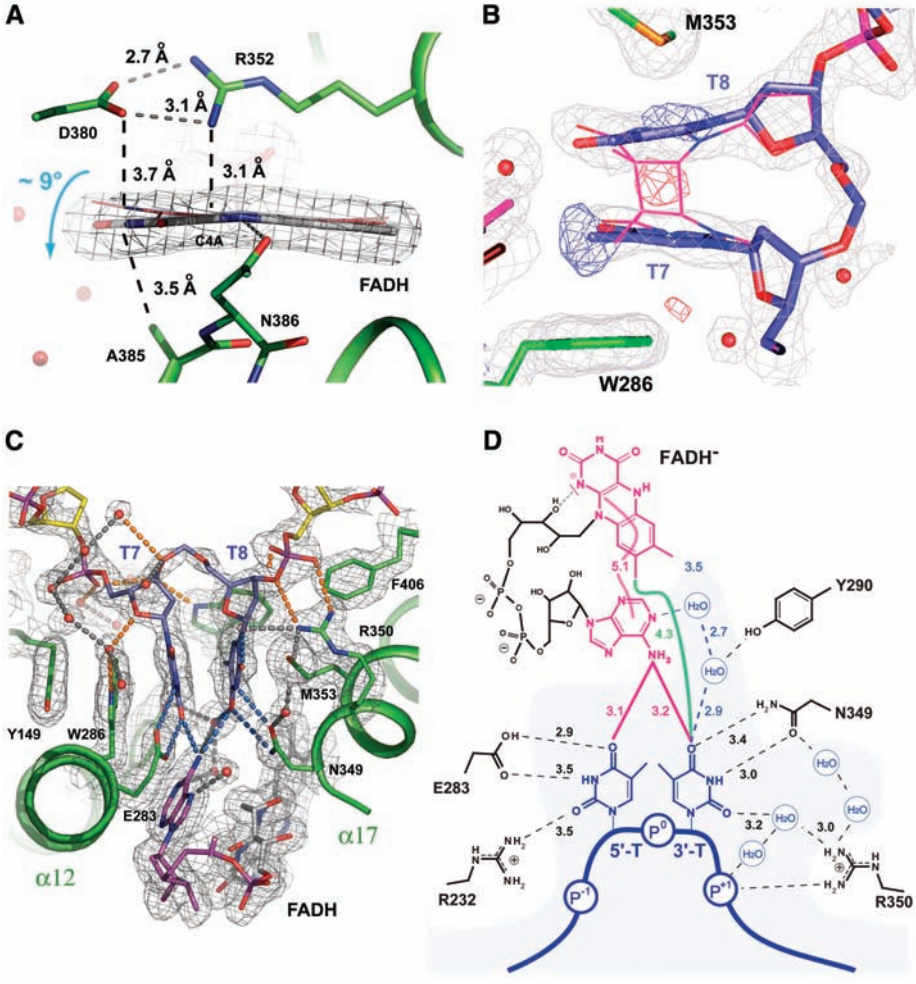

Fig. 4. Synchrotron-induced structural changes inside the DNA/DNA photolyase complex and recognition of the CPD lesion. (**A**) The bent isoalloxazine moiety of the catalytic flavin is shown with $2F_{obs}$-F_{calc} electron density contoured at 1σ. For comparison, the flavin cofactor of noncomplexed DNA photolyase (accession no. 1QNF) is shown as light red wireframe. (**B**) With the intact CPD lesion (pink) being modeled in the active site, F_{obs}-F_{calc} difference electron density around the C5 and C6 atoms of the cyclobutane ring (red, –3σ; blue, +3σ) indicated the cleavage of the CPD group. For comparison, the cleaved CPD lesion (blue) is shown with its $2F_{obs}$-F_{calc} density (gray, 1σ). (**C**) Hydrogen bonds with the thymine dimer are shown as blue dashed bonds, others in orange. (**D**) Diagram of the interactions between the CPD lesion and active site residues; distances are given in Å. Possible electron transfer routes are indicated either via the adenine moiety of FADH (purple) or between the isoalloxazine and the 3′-T (green).

References and Notes

1. R. P. Sinha, D. P. Hader, *Photochem. Photobiol. Sci.* **1**, 225 (2002).
2. A. Sancar, *Chem. Rev.* **103**, 2203 (2003).
3. T. Carell, L. T. Burgdorf, L. M. Kundu, M. Cichon, *Curr. Opin. Chem. Biol.* **5**, 491 (2001).
4. T. Tamada *et al.*, *Nature. Struct. Biol.* **4**, 887 (1997).
5. H. Komori *et al.*, *Proc. Natl. Acad. Sci. U.S.A.* **98**, 13560 (2001).

6. H.-W. Park, S.-T. Kim, A. Sancar, J. Deisenhofer, *Science* **268**, 1866 (1995).
7. K. S. Christine, A. W. MacFarlane IV, K. Yank, R. J. Stanley, *J. Biol. Chem.* **277**, 38339 (2002).
8. B. J. Vande Berg, G. B. Sancar, *J. Biol. Chem.* **273**, 20276 (1998).
9. D. B. Sanders, O. Wiest, *J. Am. Chem. Soc.* **121**, 5127 (1999).
10. J. Antony, D. M. Medvedev, A. A. Stuchebrukhov, *J. Am. Chem. Soc.* **122**, 1057 (2000).
11. T. Torizawa *et al.*, *J. Biol. Chem.* **279**, 32950 (2004).
12. K. Miki *et al.*, *J. Mol. Biol.* **233**, 167 (1993).
13. Materials and methods are available as supporting material on *Science* Online.
14. J. Butenandt *et al.*, *Chem. Eur. J.* **6**, 62 (2000).
15. I. Husain, J. Griffith, A. Sancar, *Proc. Natl. Acad. Sci. U.S.A.* **85**, 2558 (1988).
16. H. Park *et al.*, *Proc. Natl. Acad. Sci. U.S.A.* **99**, 15965 (2002).
17. D. G. Vassylyev *et al.*, *Cell* **83**, 773 (1995).
18. Single-letter abbreviations for the amino acid residues are as follows: A, Ala; C, Cys; D, Asp; E, Glu; F, Phe; G, Gly; H, His; I, Ile; K, Lys; L, Leu; M, Met; N, Asn; P, Pro; Q, Gln; R, Arg; S, Ser; T, Thr; V, Val; W, Trp; and Y, Tyr.
19. I. Husain, G. B. Sancar, S. R. Holbrook, A. Sancar, *J. Biol. Chem.* **262**, 13188 (1987).
20. A. Kiener, I. Husain, A. Sancar, C. Walsh, *J. Biol. Chem.* **264**, 13880 (1989).
21. T. Langenbacher *et al.*, *J. Am. Chem. Soc.* **119**, 10532 (1997).
22. A. Pezeshk, I. D. Podmore, P. F. Heelis, M. C. R. Symons, *J. Phys. Chem.* **100**, 19714 (1996).
23. H. Ling, F. Boudscoq, B. S. Plosky, R. Woodgate, W. Yang, *Nature* **424**, 1083 (2003).
24. R. Kort, H. Komori, S. Adachi, K. Miki, A. P. M. Eker, *Acta Crystallogr.* **D60**, 1205 (2004).
25. J. Rak, A. A. Voityuk, M.-E. Michel-Beyerle, N. Rösch, *J. Phys. Chem. A* **103**, 3569 (1999).
26. J. Hahn, M. E. Michel-Beyerle, N. Rösch, *J. Phys. Chem. B* **103**, 2001 (1999).
27. S. Weber, K. Möbius, G. Richter, C. W. M. Kay, *J. Am. Chem. Soc.* **123**, 3790 (2001).
28. D. Medvedev, A. A. Stuchebrokhov, *J. Theor. Biol.* **210**, 237 (2001).

29. We thank A. Yasui for provision of the *A. nidulans* photolyase expression construct; J. Bosch for help with data collection; C. Schulze-Briese for support at synchrotron beamline X06SA, Swiss Light Source, Villingen, Switzerland, and P. Tucker at beamline BW7A, European Molecular Biology Laboratory, Hamburg, Germany; and J. H. J. Hoeijmakers for his continuing interest. Supported by the Deutsche Forschungsgemeinschaft, Volkswagen Foundation, Fonds der chemischen Industrie, and the Boehringer Ingelheim Fonds. Coordinates and structure factors of the photolyase/CPD-DNA complex are deposited in the Research Collaboratory for Structural Bioinformatics protein data bank (accession no. 1TEZ).

Supporting Online Material
www.sciencemag.org/cgi/content/full/306/5702/1789/DC1
Materials and Methods
Figs. S1 and S2
Table S1
References and Notes

17 June 2004; accepted 18 October 2004

Human Prion Protein with Valine 129 Prevents Expression of Variant CJD Phenotype

Jonathan D. F. Wadsworth, Emmanuel A. Asante, Melanie Desbruslais, Jacqueline M. Linehan, Susan Joiner, Ian Gowland, Julie Welch, Lisa Stone, Sarah E. Lloyd, Andrew F. Hill,* Sebastian Brandner, John Collinge†

Variant Creutzfeldt-Jakob disease (vCJD) is a unique and highly distinctive clinicopathological and molecular phenotype of human prion disease associated with infection with bovine spongiform encephalopathy (BSE)–like prions. Here, we found that generation of this phenotype in transgenic mice required expression of human prion protein (PrP) with methionine 129. Expression of human PrP with valine 129 resulted in a distinct phenotype and, remarkably, persistence of a barrier to transmission of BSE-derived prions on subpassage. Polymorphic residue 129 of human PrP dictated propagation of distinct prion strains after BSE prion infection. Thus, primary and secondary human infection with BSE-derived prions may result in sporadic CJD-like or novel phenotypes in addition to vCJD, depending on the genotype of the prion source and the recipient.

Distinct prion strains are associated with biochemically distinct forms of disease-related prion protein (PrP^{Sc}). Four PrP^{Sc} types have been observed in brain tissue from patients with distinct Creutzfeldt-Jakob disease (CJD) phenotypes: types 1 to 3 in classical (sporadic or iatrogenic) CJD and type 4 in vCJD (*1*–*3*). Polymorphism at residue 129 of human PrP (where either methionine or valine can be encoded) powerfully affects genetic susceptibility to human prion diseases (*4*–*7*) and appears to critically influence the propagation of these human PrP^{Sc} types. So far, types 1 and 4 PrP^{Sc} have been found only in humans homozygous for Met^{129}; type 3 PrP^{Sc} is seen almost exclusively in individuals with at least one valine allele; and type 2 PrP^{Sc} has been commonly observed in all codon 129 genotypes (*1*–*3*). BSE and vCJD prion infection in transgenic mice expressing human PrP, but not mouse PrP (*1*, *8*–*10*), indicates that codon 129 polymorphism determines the ability of human PrP to form type 4 PrP^{Sc} and to generate the neuropathological phenotype of vCJD.

Challenge of transgenic mice expressing human PrP Met^{129} (129MM Tg35 and 129MM Tg45 mice) with BSE and vCJD prions (*11*) resulted in faithful propagation of type 4 PrP^{Sc} (*10*) (Figs. 1 and 2) accompanied by the key neuropathological hallmark of vCJD, the presence of abundant florid PrP plaques (*10*). However, transgenic mice expressing human PrP Val^{129} (129VV Tg152 mice) responded quite differently. Although these 129VV Tg152 mice lack a transmission barrier to classical forms of CJD, regardless of the codon 129 genotype of the inoculum (*1*, *8*, *9*), the primary challenge with vCJD prions was characterized by a substantial transmission barrier to infection (only ~50% of inoculated mice were infected, compared with 100% of 129MM Tg35 and 129MM Tg45 mice) (Fig. 1; table S1). In addition, rather than type 4 PrP^{Sc}, vCJD-inoculated 129VV Tg152 mice propagated type 5 PrP^{Sc} (*9*), which shares the same predominance of the diglycosylated glycoform seen in type 4 PrP^{Sc} but is distinguished by proteinase K digestion products of greater molecular mass (Fig. 2A), which closely resemble those seen in human type 2 PrP^{Sc} (*9*). Type 5 PrP^{Sc} is associated with very weak diffuse PrP deposition in the brain (*9*), which contrasts markedly with the florid PrP plaques associated with the propagation of type 4 PrP^{Sc} in humans (*12*) or transgenic mice (*10*). Similar diffuse deposition of PrP is also observed in clinically affected BSE-inoculated 129VV Tg152 mice; however, type 5 PrP^{Sc} is undetectable in brain homogenate (*9*).

To further evaluate the molecular and neuropathological phenotype of vCJD- or BSE-inoculated 129VV Tg152 mice, we performed a second passage in the same breed of mice. Primary transmission of prions from one species to another is associated with a species or transmission barrier that is largely or completely abrogated on second and subsequent passage in the second species as the prions adapt to the new host. Second passage then resembles within-species transmission with a high (typically 100%) attack rate and much shortened and more consistent incubation period. It was remarkable, however, that such adaptation did not occur on second passage of BSE or vCJD prions in

Medical Research Council (MRC) Prion Unit and Department of Neurodegenerative Disease, Institute of Neurology, University College London, Queen Square, London WC1N 3BG, UK.

*Present address: Department of Biochemistry and Molecular Biology and Department of Pathology, University of Melbourne, Parkville, Victoria 3010, Australia.

†To whom correspondence should be addressed. E-mail: j.collinge@prion.ucl.ac.uk

129VV Tg152 mice. Brain inocula derived from four clinically affected BSE-inoculated 129VV Tg152 mice failed to transmit clinical disease or asymptomatic prion infection to additional 129VV Tg152 mice (Figs. 1 and 3; table S2). However, two of these inocula produced clinical prion disease (Fig. 3; table S2) with abundant PrP^{Sc} accumulation (fig. S1) on inoculation of wild-type FVB mice with incubation periods that are not compatible with persistence of the original BSE inoculum [supporting online material (SOM) text]. The prion strain generated in BSE-inoculated 129VV Tg152 mice was thus infectious in wild-type FVB mice, but not in additional 129VV Tg152 mice.

Valine 129 is unique to human PrP, and the failure of BSE prions to adapt in 129VV Tg152 mice on second passage contrasts sharply with the marked adaptation of BSE prions in FVB mice (Fig. 3; table S2) or in other murine (*13*) or primate (*14*) hosts that encode methionine at the corresponding position of PrP. BSE prions also efficiently adapt on second passage in 129MM Tg35 transgenic mice. Primary transmission of BSE prions in 129MM Tg35 mice resulted in bifurcation of propagated strain type and produced either type 2 or 4 PrP^{Sc} (Figs. 1 and 2) and neuropathology consistent with human sporadic CJD or vCJD, respectively (*10*). These distinct molecular and neuropathological phenotypes consistently "breed true" with very high efficiency on second passage in additional 129MM Tg35 transgenic mice (*15*). These findings contrast sharply with the complete lack of prion transmission on second passage of the same BSE inocula in 129VV Tg152 mice, supporting the interpretation that human PrP Val^{129} severely restricts propagation of the BSE prion strain.

This conclusion was further reinforced by study of the parameters of second passage of vCJD prions. As seen with second passage of BSE prions, clinical disease was observed only in FVB, and not in 129VV Tg152, recipients. Brain inocula from clinically affected, type 5 PrP^{Sc} positive, primary vCJD-inoculated 129VV Tg152 mice produced clinical prion disease (Fig. 3; table S2) and PrP^{Sc} accumulation (fig. S1) on subpassage in FVB mice, but produced only subclinical infection (with PrP^{Sc} accumulation) in 7 out of 11 inoculated 129VV Tg152 mice (Figs. 1 and 3). Notably, in four of these, high-sensitivity methods (*16*) were required to detect PrP^{Sc} in brain homogenate (table S2). Type 5 PrP^{Sc} was faithfully propagated on second passage in 129VV Tg152 mice (Fig. 2A). In the three mice containing the highest levels of type 5 PrP^{Sc}, extensive spongiosis was also observed (Fig. 4), and in one of these, in contrast to the pathology seen on first passage, numerous PrP plaques were seen (Fig. 4). Type 4 PrP^{Sc} is invariably associated with prominent florid plaques in the cortex of human vCJD brain (*12*) and in vCJD- or BSE-prion inoculated 129MM Tg35 and Tg45 transgenic mice (*10*), whereas plaques associated with type 5 PrP^{Sc} were restricted to the corpus callosum and had a nonflorid morphology (Fig. 4). The lack of adaptation of vCJD prions on second passage in 129VV Tg152 mice contrasted sharply with the behavior of

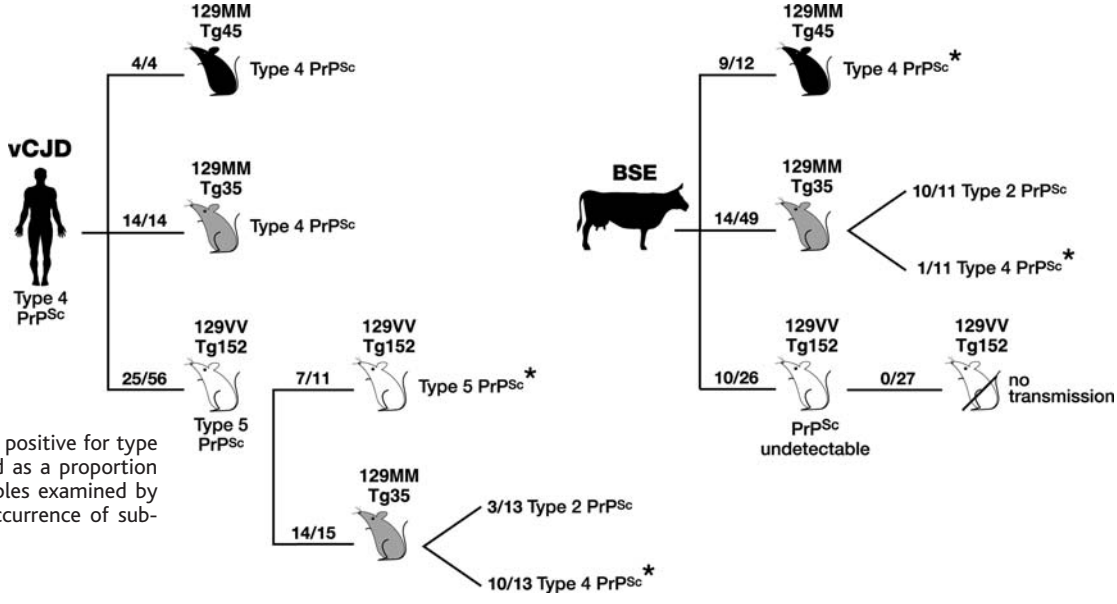

Fig. 1. Summary of transmissions of vCJD and BSE prions to transgenic mice. The total number of prion-affected mice (both clinical and subclinical) is reported for each inoculated group: 129MM Tg45 mice (black), 129MM Tg35 mice (gray), 129VV Tg152 mice (white). Animals were scored by clinical signs, immunoblotting, and/or immunohistochemistry. Primary transmission data have been published previously (*9*, *10*). In transmissions that result in bifurcation of propagated PrP^{Sc} type, the number of samples positive for type 2 or type 4 PrP^{Sc} is reported as a proportion of the total number of samples examined by immunoblotting. (⋆), The occurrence of subclinical prion infection only.

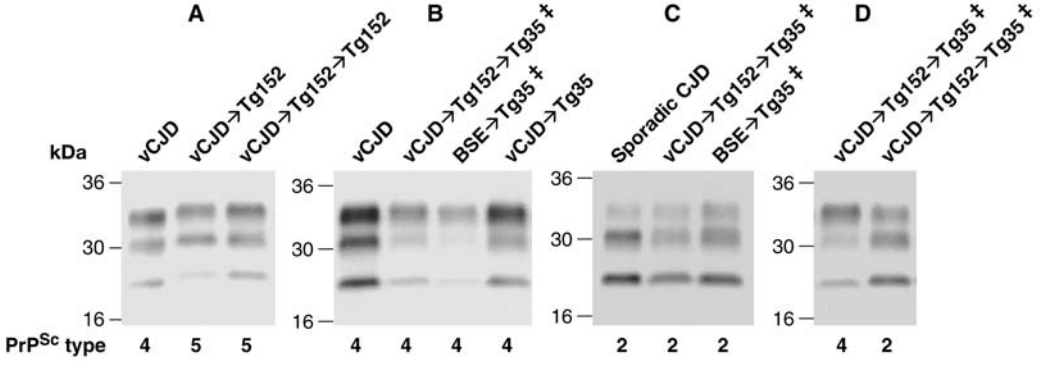

Fig. 2. Molecular strain typing of vCJD and BSE prion transmissions in transgenic mice. (**A** to **D**) Immunoblots of proteinase K–treated brain homogenates from variant and sporadic CJD (*PRNP* 129 MM genotype) and transgenic mice were analyzed by enhanced chemiluminescence with either monoclonal antibody 3F4 against PrP (A) or biotinylated monoclonal antibody ICSM 35 against PrP (B to D). The identity of the brain sample is designated above each lane with the type of PrP^{Sc} present in the sample designated below.
‡Transmissions that result in the propagation of either type 2 or type 4 PrP^{Sc}.

vCJD prions in wild-type FVB mice, where typical adaptation was observed on second passage with 100% clinical prion disease with abundant PrP^{Sc} accumulation (fig. S1) at markedly reduced incubation periods (Fig. 3; table S2).

Both BSE and vCJD prions failed to propagate efficiently on either primary or, remarkably, second passage, in 129VV Tg152 mice in sharp contrast to 129MM Tg mice or wild-type animals, and where detectable, infection was associated with a distinct PrP^{Sc} type and pathological phenotype. Thus, human PrP Val^{129} appears not to be a compatible substrate for propagation of the prion strain seen in vCJD. This interpretation was supported by the transmission properties of 129VV Tg152–passaged vCJD prions in 129MM Tg35 mice. Here, 14 out of 15 129MM Tg35 mice inoculated with isolates containing type 5 PrP^{Sc} showed PrP^{Sc} accumulation (Fig. 1; table S3), typically to much higher levels than seen in 129VV Tg152 mice receiving the same inocula. However, the PrP^{Sc} seen was not of the type 5 pattern but instead these transmissions mirrored the behavior of BSE prions in 129MM Tg35 mice (*10*), where, instead, either type 4 or type 2 PrP^{Sc} were seen (Figs. 1 and 2, B to D). Thus human PrP^{Sc} types 4 and 5 are restricted to propagating in mice expressing human PrP Met^{129} or Val^{129}, respectively.

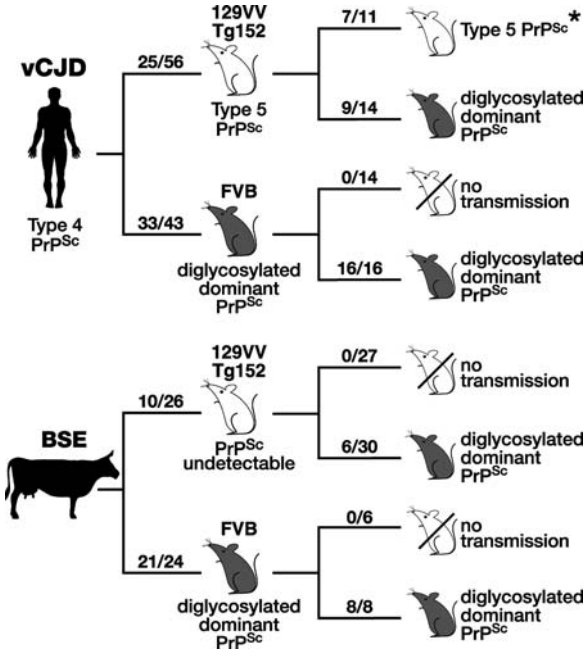

Fig. 3. Summary of transmissions of vCJD and BSE prions to transgenic and wild-type FVB mice. The total number of prion-affected mice (both clinical and subclinical) is reported for each inoculated group: 129VV Tg152 mice (white), wild-type FVB mice (gray). Animals were scored by clinical signs, immunoblotting, and/or immunohistochemistry. Data are derived from tables S1 and S2. (★), The occurrence of subclinical prion infection only.

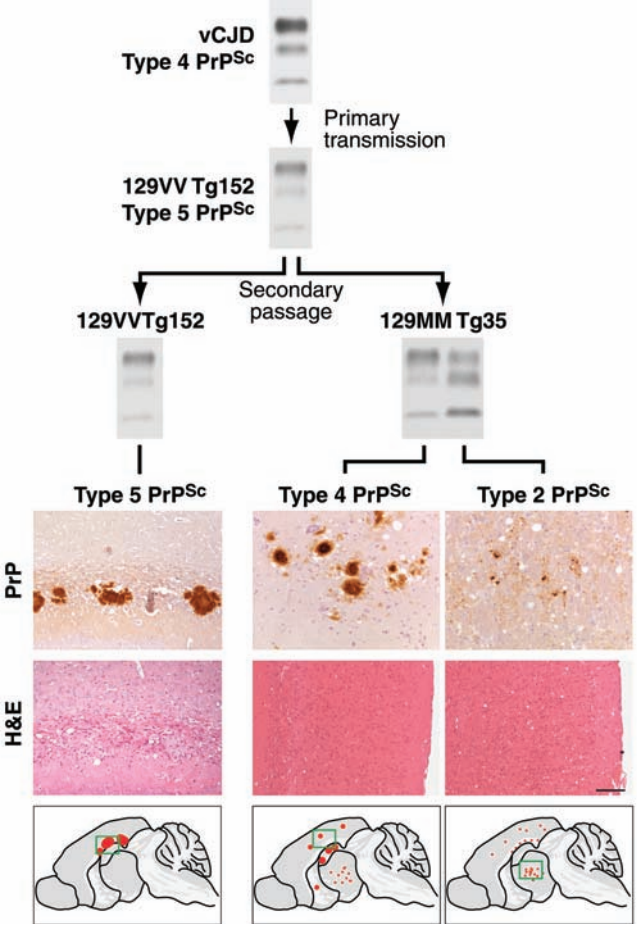

Fig. 4. Neuropathological analysis of transgenic mouse brain. Primary transmission of vCJD prions in 129VV Tg152 mice produces type 5 PrP^{Sc} that is maintained after secondary passage in 129VV Tg152 mice but induces propagation of either type 2 or type 4 PrP^{Sc} after passage in 129MM Tg35 mice. Immunohistochemistry (PrP) shows abnormal PrP immunoreactivity, including PrP-positive plaques, stained with monoclonal antibody 3F4 against PrP. Sections stained with hematoxylin-and-eosin (H&E) show spongiform neurodegeneration (left, corpus callosum; middle and right, parietal cortex). Scale bar, 100 μm. Lower panels show the regional distribution of abnormal PrP deposition. Green boxes in the sketches denote the area from which PrP-stained sections are derived.

Neuropathologically, type 4 PrP^{Sc} was associated with relatively little spongiosis and abundant florid plaques (Fig. 4) typical of vCJD in humans (*12*), whereas type 2 PrP^{Sc} was associated with much higher levels of vacuolation in many areas of the brain, accompanied by generally diffuse PrP deposition and occasional small, non-florid plaques (Fig. 4) that closely resembled human sporadic CJD with type 2 PrP^{Sc} *PRNP* (human prion protein gene) 129MM (*3*). Clinical prion disease was observed in all 129MM Tg35 mice propagating type 2 PrP^{Sc}, whereas mice propagating type 4 PrP^{Sc} were subclinically infected (table S3).

In conclusion, we have demonstrated that BSE and vCJD prion infection in transgenic mice can result in the propagation of distinct molecular and neuropathological phenotypes dependent on host PrP residue 129 and possibly other, as yet unidentified, disease modifying loci (*10*). These data predict a critical role for *PRNP* codon 129 in governing the thermodynamic permissibility of human PrP^{Sc} conformation that can be interpreted within a conformational selection model of prion transmission barriers (*17–19*) (SOM text) and suggest that there is no overlapping preferred conformation for Val^{129} and Met^{129} human PrP that can be generated as a result of exposure to the vCJD/BSE prion strain. Biophysical measurements suggest that this powerful effect of residue 129 on prion strain selection is likely to be mediated by means of its effect on the conformation of PrP^{Sc} or its precursors or on the kinetics of their formation, as it has no measurable effect on the folding, dynamics, or stability of the normal cellular prion protein PrP^{C} (*20*).

Although caution must be exercised in extrapolating from animal models, even

where, as here, faithful recapitulation of molecular and pathological phenotypes is possible, our findings argue that primary human BSE prion infection, as well as secondary infection with vCJD prions by iatrogenic routes, may not be restricted to a single disease phenotype. These data, together with the recent recognition of probable iatrogenic transmission of vCJD prions to recipients of blood (*21*, *22*), including a *PRNP* codon 129 Met/Val heterozygous individual (*22*), reiterate the need to stratify all human prion disease patients by PrP^{Sc} type. This surveillance will facilitate rapid recognition of novel PrP^{Sc} types and of any change in relative frequencies of particular PrP^{Sc} subtypes in relation to either BSE exposure patterns or iatrogenic sources of vCJD prions.

References and Notes

1. J. Collinge, K. C. L. Sidle, J. Meads, J. Ironside, A. F. Hill, *Nature* **383**, 685 (1996).
2. J. D. F. Wadsworth *et al.*, *Nature Cell Biol.* **1**, 55 (1999).
3. A. F. Hill *et al.*, *Brain* **126**, 1333 (2003).
4. J. Collinge, M. S. Palmer, A. J. Dryden, *Lancet* **337**, 1441 (1991).
5. M. S. Palmer, A. J. Dryden, J. T. Hughes, J. Collinge, *Nature* **352**, 340 (1991).
6. H. S. Lee *et al.*, *J. Infect. Dis.* **183**, 192 (2001).
7. S. Mead *et al.*, *Science* **300**, 640 (2003).
8. J. Collinge *et al.*, *Nature* **378**, 779 (1995).
9. A. F. Hill *et al.*, *Nature* **389**, 448 (1997).
10. E. A. Asante *et al.*, *EMBO J.* **21**, 6358 (2002).
11. Materials and methods are available as supporting material on *Science* Online.
12. R. G. Will *et al.*, *Lancet* **347**, 921 (1996).
13. M. Bruce *et al.*, *Philos. Trans. R. Soc. London Ser. B.* **343**, 405 (1994).
14. C. I. Lasmezas *et al.*, *Proc. Natl. Acad. Sci. U.S.A.* **98**, 4142 (2001).
15. E. A. Asante, J. D. F. Wadsworth, J. Collinge, unpublished observations. These data will be reported in full elsewhere.
16. J. D. F. Wadsworth *et al.*, *Lancet* **358**, 171 (2001).
17. J. Collinge, *Lancet* **354**, 317 (1999).
18. J. Collinge, *Annu. Rev. Neurosci.* **24**, 519 (2001).
19. A. F. Hill, J. Collinge, *Trends Microbiol.* **11**, 578 (2003).
20. L. L. Hosszu *et al.*, *J. Biol. Chem.* **279**, 28515 (2004).
21. C. A. Llewelyn *et al.*, *Lancet* **363**, 417 (2004).
22. A. H. Peden, M. W. Head, D. L. Ritchie, J. E. Bell, J. W. Ironside, *Lancet* **364**, 527 (2004).

23. We thank C. Brown and his team for animal care, R. Young for preparation of figures, and K. Fox and S. Cooper for technical assistance. We especially thank all patients and their families for generously consenting to use of human tissues in this research, and the UK neuropathologists who have kindly helped in providing these tissues. We thank R. Bradley, D. Matthews, S. A. C. Hawkins and colleagues at the UK Veterinary Laboratories Agency for providing BSE tissues. This work was funded by the UK Medical Research Council and European Commission. One of the routine antibodies used in this work (ICSM 35) is marketed by D-Gen Ltd., an academic spin-off company. J.C. is a director of D-Gen and J.C., J.D.F.W., and A.F.H. are shareholders and consultants of D-Gen.

Supporting Online Material
www.sciencemag.org/cgi/content/full/1103932/DC1
Materials and Methods
SOM Text
Fig. S1
Tables S1 to S3
References and Notes

11 August 2004; accepted 21 October 2004
Published online 11 November 2004;
10.1126/science.1103932
Include this information when citing this paper.

Rescue of Dystrophic Muscle Through U7 snRNA–Mediated Exon Skipping

Aurélie Goyenvalle,[1] Adeline Vulin,[1] Françoise Fougerousse,[1] France Leturcq,[2] Jean-Claude Kaplan,[2] Luis Garcia,[1] Olivier Danos[1]*

Most mutations in the dystrophin gene create a frameshift or a stop in the mRNA and are associated with severe Duchenne muscular dystrophy. Exon skipping that naturally occurs at low frequency sometimes eliminates the mutation and leads to the production of a rescued protein. We have achieved persistent exon skipping that removes the mutated exon on the dystrophin messenger mRNA of the *mdx* mouse, by a single administration of an AAV vector expressing antisense sequences linked to a modified U7 small nuclear RNA. We report the sustained production of functional dystrophin at physiological levels in entire groups of muscles and the correction of the muscular dystrophy.

Duchenne muscular dystrophy (DMD) is an X-linked recessive disorder caused by mutations in a gene that encodes dystrophin, a large cytoskeletal protein that complexes with other partners at the sarcolemma and is essential for membrane integrity of the muscle fiber. The dystrophin gene spans about 2.5 Mb and encodes a major 14-kb mRNA transcript processed from 79 exons. Full-length dystrophin (427 kD) is composed of several domains consisting of an actin-binding site at the N terminus; a central rod domain of 24 spectrin-like repeats; and a cysteine-rich domain, which binds other

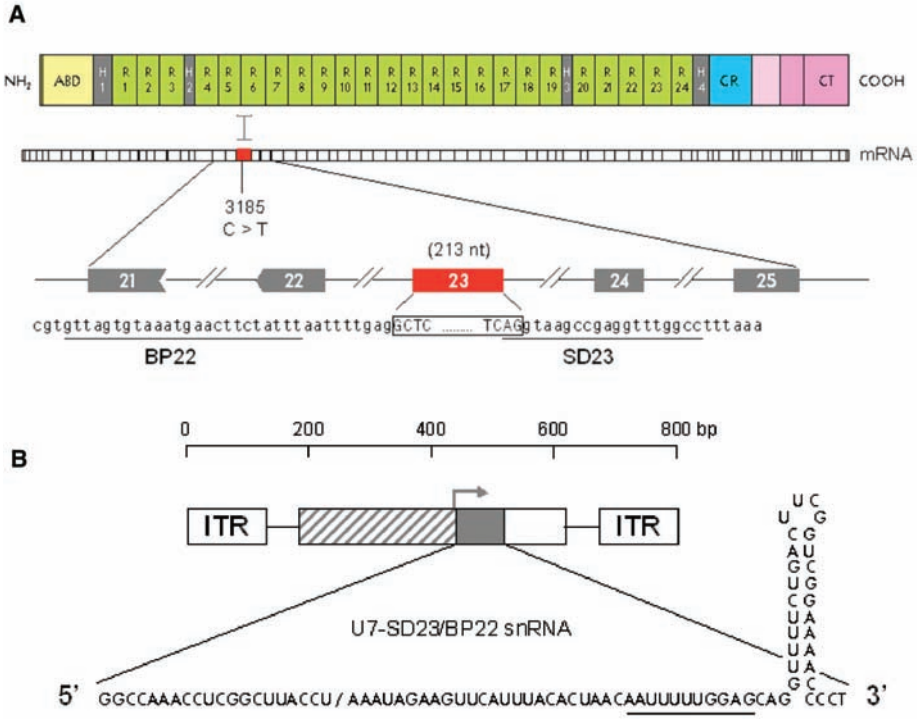

Fig. 1. (**A**) (Top) Dystrophin includes an actin-binding domain (ABD) at the N terminus, a central rod domain that contains 24 spectrin-like repeats (R) and four hinge segments (H), a β-dystroglycan binding, a cysteine-rich domain (CR), and a C-terminal domain (CT). (Middle) Position of exon 23 partly encoding repeats R5 and R6 in which a C to T mutation creates a stop codon in the *mdx* mouse. (Bottom) Target sequences for exon skipping at the branch point (BP22) upstream of exon 23 and at the downstream donor splice site (SD23). (**B**) Structure of the AAV(U7-SD23/BP22) vector. The U7-SD23/BP22 cassette includes the U7-promoter (position –267 to +1, hatched box), the U7SmOPT snRNA (gray box and sequence below) and downstream sequences down to position 116 (open box). It is shown between two AAV2 inverted terminal repeats (ITRs).

members of the sarcolemmal complex, near the C terminus. As a consequence of the modular structure of dystrophin, internally truncated proteins missing some of the repeats can be fully functional or at least partly active as seen in patients with mild (Becker) forms of DMD (*1*). About 70% of mutations in the dystrophin gene result in the absence of protein and are associated with a severe Duchenne phenotype, because they create a disruption of the translational frame of the mRNA. It is noteworthy that exon skipping that naturally occurs during dystrophin mRNA processing can restore the reading frame and give rise to rare "revertant" fibers that contain shortened proteins (*2*, *3*). Strategies for dystrophin rescue in the DMD muscle have been evaluated with the use of antisense oligonucleotides that cause the skipping of selected exons [reviewed in (*4*)]. In the *mdx* mouse, which carries a nonsense mutation in exon 23 of the dystrophin gene (*5*), although the local injection of 2′-*O*-methyl antisense oligoribonucleotides resulted in rescue of the protein, the effect remained localized and started to vanish after 4 weeks (*6*). Our goal here was to achieve a stable long-term expression of antisense sequences that would generate sustained therapeutic levels of rescued dystrophin in entire groups of muscles.

The activity of antisense sequences that can interfere with the mRNA maturation process is considerably enhanced when these are linked to small nuclear RNAs (snRNAs), because it allows for their proper subcellular localization and facilitates their inclusion into mRNA processing machines such as the spliceosome (*7*, *8*). U7, a nonspliceosomal snRNA normally involved in the processing of the histone mRNA 3′ end, can be engineered to bind the appropriate Sm proteins, redirected to the spliceosome, and used to deliver antisense sequences (*9*). The stable expression of modified U7 snRNAs (U7SmOPT) transfected into cells can result in a sustained and sequence-specific modification of the targeted mRNA structure (*10*, *11*). A number of antisense sequences have been used to skip the nonsense mutation containing exon 23 on the *mdx* dystrophin mRNA (Fig. 1A) (*12*). From these, we selected a 24-nucleotide sequence located across the splicing branching point in intron 22 (BP22) (*13*), and a 20-nucleotide sequence in intron 23 that corresponds to the U1 binding region at the donor site (SD23) (*14*) for the construction of a "double-target" U7SmOPT gene according to Suter *et al*. (*10*) (Fig. 1).

The modified U7 gene, along with its natural promoter and 3′ elements, was introduced into an AAV-2–based vector that was packaged into an AAV-1 capsid for high-efficiency gene transfer into the skeletal muscle (*15*). Adult *mdx* mice (n = 37) were injected in the tibialis anterior (TA) muscle with single vector doses of 0.2 to 1 × 10^{12} viral genomes (vg), and the results were analyzed at different time points between 2 and 13 weeks. One of the experimental group was also injected into the extensor digitorum longus (EDL) muscle with 0.4 to 2 × 10^{11} vg (table S1). In comparison with the endogenous U7 snRNA, the U7-SD23/BP22 snRNA was robustly expressed in the injected TA muscles after 2 weeks (Fig. 2A). The presence of the modified U7 snRNA was associated with the appearance in these samples of dystrophin transcripts lacking exon 23, as detected by reverse transcription polymerase chain reaction (RT-PCR) and analyzed by DNA sequencing (Fig. 2, B and C). The 688-bp product amplified from the skipped mRNA represented ~15% of the PCR products 2 weeks after injection and became the major species at 4, 6, and 13 weeks (Fig. 2B). This slow accumulation of skipped transcripts was not the result of a progressive transgene expression during the first weeks after AAV-mediated gene transfer (*16*), because the levels of modified U7 were already maximal at 2 weeks. Rather, it suggests a limited availability of the pre-mRNA and/or a slow turnover of the processed dystrophin mRNA in the muscle fiber.

Consistent with the generation of skipped transcripts, the dystrophin protein was readily detected both by Western blot on muscle extracts (Fig. 2D) and by immunofluorescence on tissue sections (Fig. 3). The levels of dystrophin mirrored those of the rescued mRNA (3% of normal at 2 weeks and 50 to 80% thereafter). The skipping procedure generated immunoreactive protein species with the expected mobility around 426 kD, without evidence for multiply deleted by-products. (Note: The expected 8-kD difference between wild-type and rescued proteins could not be resolved on this gel.) Virtually all fibers in the injected muscle stained positive from 4 weeks post injection onwards, and the protein was typically localized at the periphery of fibers (Fig. 3, D and E). The histology of the corrected muscles was essentially normal, with fibers displaying a "healthy" polygonal shape. Small-caliber

[1]Généthon & CNRS UMR 8115, 1, rue de l'Internationale, Evry, France. [2]Laboratoire de Biochimie et de Génétique Moléculaire, Hôpital et Institut Cochin, 123 boulevard de Port-Royal, Paris, France.

*To whom correspondence should be addressed. E-mail: danos@genethon.fr

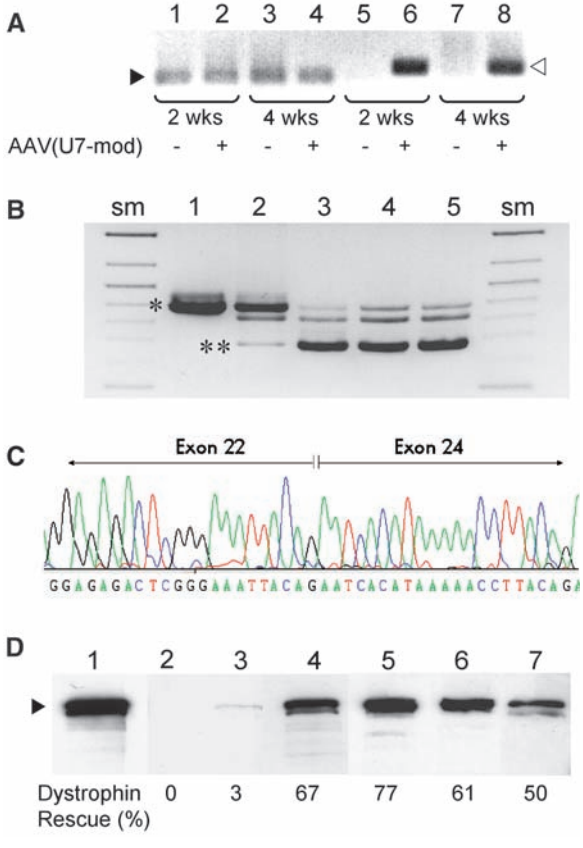

Fig. 2. (**A**) Detection of native and modified U7 snRNAs in *mdx* muscles. Total RNA from treated muscles (lanes 2, 4, 6, and 8) or contralateral untreated muscles (lanes 1, 3, 5, and 7) was analyzed by RT-PCR at 2 weeks (lanes 1, 2, 5, and 6) and 4 weeks (lanes 3, 4, 7, and 8). The 60- and 80-bp products corresponding to endogenous and newly expressed U7 snRNA, respectively, are shown by arrowheads. (**B**) Detection of exon 23–skipped dystrophin mRNA. RNA samples were analyzed at 0, 2, 4, 6, and 13 weeks by nested RT-PCR with primers in exons 20 and 26. The 901-bp band corresponding to the normal mRNA (*) is the only species detected at day 0 (lane 1), and it is progressively replaced by a 688-bp fragment (**) that corresponds to the exon 23–skipped mRNA (lanes 2 to 5). (**C**) DNA sequence of the 688-bp band. (**D**) Western blot of total protein extracted from injected *mdx* muscles stained with the NCL-DYS1 monoclonal antibody. Arrows indicate the full-length 427-kD dystrophin, as detected in normal C57BL6 sample (lane 1). Lanes 2 to 7 correspond to uninjected control and samples at 2, 4, 6, 8, and 13 weeks, respectively. Each lane was loaded with 40 μg of total protein. The same profile was obtained by using the NCL-DYS2 monoclonal antibody (*18*).

fibers indicative of previous regeneration activity were more abundant in the treated muscles. CD11b-positive monocytes/macrophages that massively infiltrate the dystrophic *mdx* muscle lesions (*17*) were completely absent after dystrophin rescue, which indicated that the process of necrosis and regeneration had been arrested. Moreover, no $CD4^+$ or $CD8^+$ cells were detected, consistent with an absence of immune response against the rescued dystrophin (see SOM).

A group of five *mdx* animals received the AAV-U7-SD23/BP22 vector by intra-arterial perfusion of the lower limb. This resulted, after 1 month, in the efficient rescue of dystrophin in >80% of the fibers in most muscles of the perfused leg, including tibialis anterior and extensor digitorum longus muscles (Fig. 3F), gastrocnemius, soleus, plantaris, and biceps femoris muscles (*18*). Along with the rescued dystrophin, the components of its associated glycoprotein complex, including α- and β-sarcoglycans and β-dystroglycan, were expressed at the periphery of the fibers in treated animals (Fig. 4). This indicates that the dystrophin produced from the skipped mRNA contains the C-terminal β-dystroglycan binding domain essential for membrane anchoring of the complex (*19*).

The contractile and mechanical properties of treated muscles were studied by measuring resistance to tetanic contractions accompanied by forced lengthening (Fig. 5A). For this assay, animals that had been injected in the EDL were analyzed after 6 weeks. Muscles from *mdx* animals were unable to sustain repeated elongations and lost 65% of their maximum force over five eccentric contractions. In contrast, treated muscles, displaying >70% of fibers with rescued dystrophin, were essentially normal by this criterion. One representative example where the treated muscle displayed 17% force drop compared with 15% for the wild type is shown in Fig. 5A. Exercise-induced damage was also evaluated by submitting TA-injected animals to extensive downhill running on a treadmill, followed by an intravenous injection of Evans blue, a cell-impermeable dye. Muscle lesions revealed by dye entry into the fibers in all untreated contralateral legs (Fig. 5B) were absent from muscles of the legs injected with AAV-U7-SD23/BP22 (Fig. 5C).

The accumulating data on AAV-mediated gene transfer into the skeletal muscle in rodent, canine, and primates, including human subjects, indicate that U7-mediated rescue may be permanent (*20*–*23*). The levels and stability of exon skipping that we report are significantly higher than those obtained using other U7-based constructs in myoblast cultures (*8*, *13*) or oligonucleotides injected in vivo (*6*, *14*, *24*, *25*). This may be, in part, related to the particular combination of target sequences that we have chosen and to the high efficiency of AAV-1–mediated gene transfer into mature skeletal muscle. It is possible, too, that the muscle fiber provides an especially favorable environment for U7-mediated targeting of antisense sequences. In this respect, it will be important to explore the potential of the AAV-U7 system

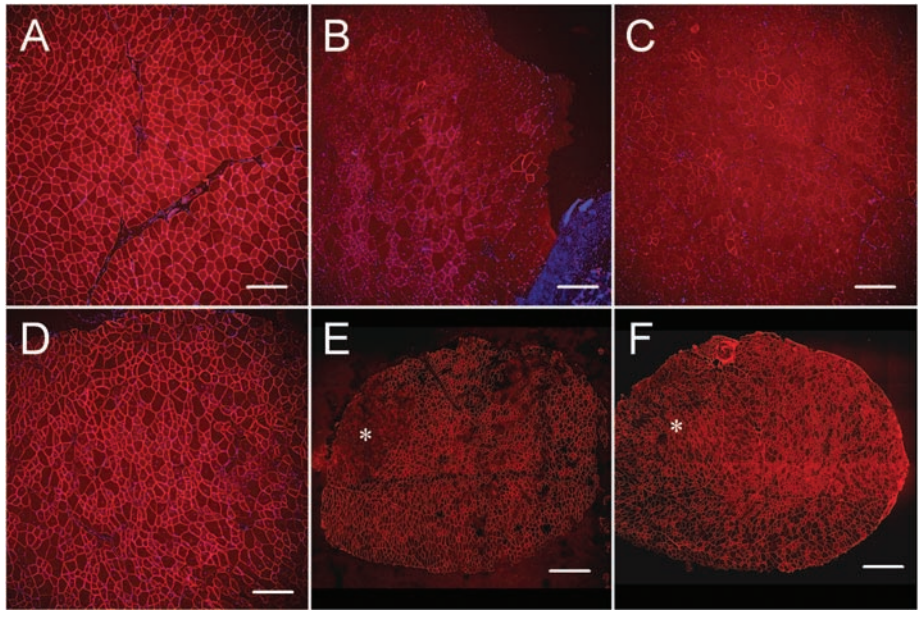

Fig. 3. Dystrophin rescue in *mdx* mice after administration of AAV(U7-SD23/BP22). NCL-DYS2 immunostaining of whole transverse sections from the hind limb anterior compartment (tibialis anterior and extensor digitorum longus* muscles) from normal C57BL6 (**A**), untreated *mdx* (**B**), *mdx* 2, 4, and 13 weeks after intramuscular injection (**C** to **E**), and *mdx* 4 weeks after intra-arterial vector delivery (**F**). Scale bars (A to D), 0.5 mm; (E and F), 1 mm.

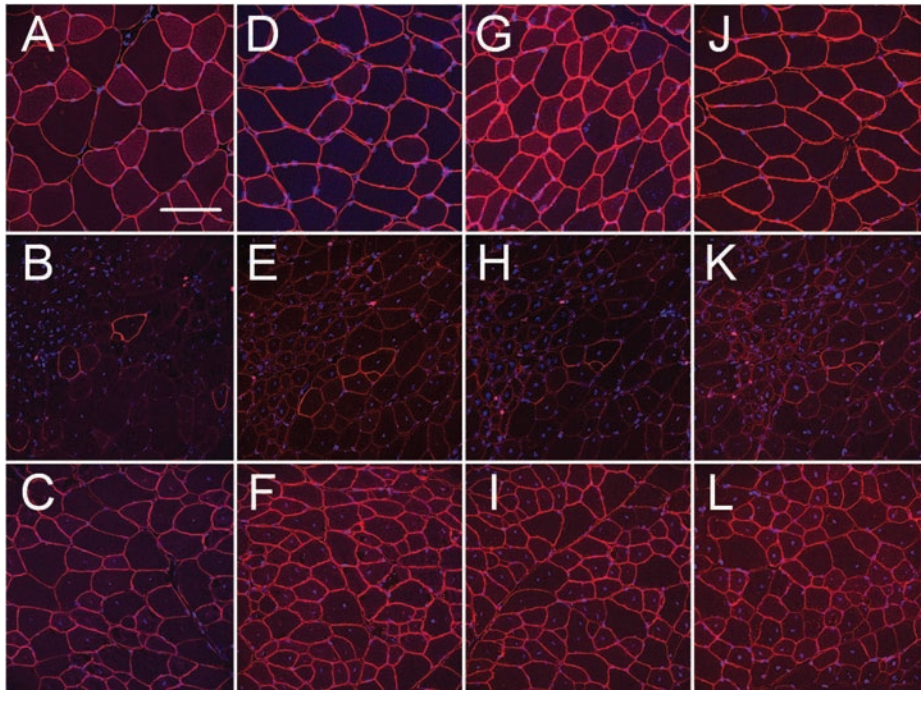

Fig. 4. Restoration of the dystrophin-associated protein complex in treated *mdx* muscles. Left, middle, and right columns show sections from TA muscles of C57BL6, untreated *mdx*, and *mdx*, respectively, 4 weeks after treatment. Sections were immunostained for (**A** to **C**) dystrophin, (**D** to **F**) α-sarcoglycan, (**G** to **I**) β-sarcoglycan, and (**J** to **L**) β-dystroglycan. The same cluster of revertant fibers displaying dystrophin, as well as the associated protein complex, is shown on the serial sections from untreated *mdx*.

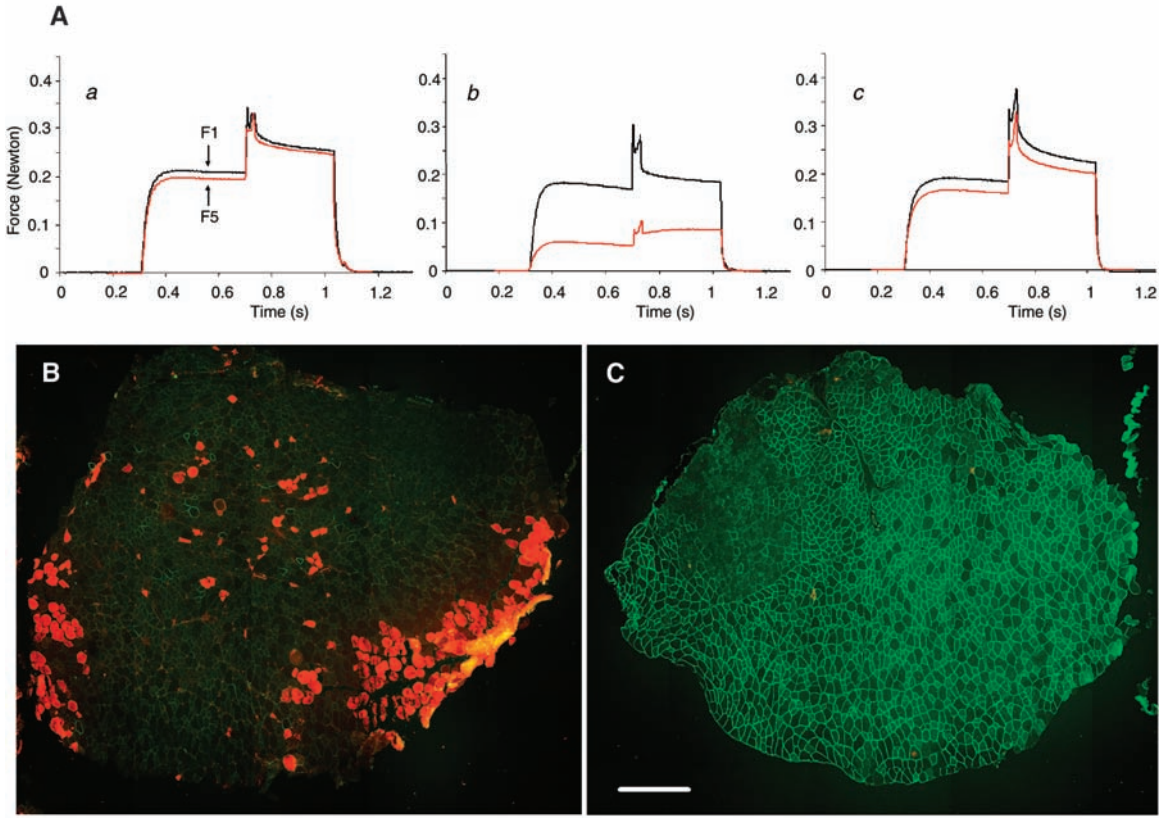

Fig. 5. Dystrophin rescue in AAV(U7-SD23/BP22)–treated *mdx* muscle restores normal susceptibility to exercise-induced damage. (**A**) Superimposed traces of tension produced by EDL muscles during five tetanic contractions with forced lengthening. F_1 is the isometric force developed just before lengthening in the first tetanus, and F_5 that of the fifth one. In the experiment shown, the force drop was 15% for C57BL6 muscle (a), 65% in *mdx* (b), and 17% in 6 week treated *mdx* (c). (**B** and **C**) Double staining of dystrophin and Evans blue detection of exercise-damaged muscle fibers in TA muscles of untreated (B) and treated (C) legs from the same *mdx* animal, 60 days after vector administration. Damaged fibers incorporate Evans blue, whose fluorescence is collected in the red channel, and dystrophin is revealed with NCL-DYS2 (green).

for modifying or inactivating various mRNA targets in the muscle, in comparison with current small interfering RNA tools (*26*).

AAV vectors can be safely and efficiently administered through the vascular route, resulting in the permanent modification of multiple muscle groups (*27*). Our study now defines a pathway for the development of effective therapies based on exon skipping for DMD and other neuromuscular diseases (*28*, *29*). DMD is uniquely suited to therapeutic exon skipping, given the modular and repetitive nature of some dystrophin domains. Among DMD patients registered in our database (Hôpital Cochin), 43% could benefit from skipping of a single exon, and this proportion might be increased if skipping of multiple exons can be accomplished (*4*). In most cases, an attenuated Becker-like phenotype would be obtained, but a fully functional rescued protein can be predicted for selected genotypes.

References and Notes

1. F. Muntoni, S. Torelli, A. Ferlini, *Lancet Neurol.* **2**, 731 (2003).
2. L. V. Nicholson, *Neuromuscul. Disord.* **3**, 525 (1993).
3. Q. L. Lu *et al.*, *J. Cell Biol.* **148**, 985 (2000).
4. A. Aartsma-Rus *et al.*, *Am. J. Hum. Genet.* **74**, 83 (2004).
5. P. Sicinski *et al.*, *Science* **244**, 1578 (1989).
6. Q. L. Lu *et al.*, *Nature Med.* **9**, 1009 (2003).
7. Y. Zhuang, A. M. Weiner, *Cell* **46**, 827 (1986).
8. F. G. De Angelis *et al.*, *Proc. Natl. Acad. Sci. U.S.A.* **99**, 9456 (2002).
9. L. Gorman, D. Suter, V. Emerick, D. Schumperli, R. Kole, *Proc. Natl. Acad. Sci. U.S.A.* **95**, 4929 (1998).
10. D. Suter *et al.*, *Hum. Mol. Genet.* **8**, 2415 (1999).
11. M. M. Vacek *et al.*, *Blood* **101**, 104 (2003).
12. M. G. Dunckley, M. Manoharan, P. Villiet, I. C. Eperon, G. Dickson, *Hum. Mol. Genet.* **7**, 1083 (1998).
13. C. Brun *et al.*, *Cell. Mol. Life Sci.* **60**, 557 (2003).
14. C. J. Mann, K. Honeyman, G. McClorey, S. Fletcher, S. D. Wilton, *J. Gene Med.* **4**, 644 (2002).
15. H. Chao *et al.*, *Mol. Ther.* **2**, 619 (2000).
16. N. Vincent-Lacaze *et al.*, *J. Virol.* **73**, 1949 (1999).
17. E. P. Parrish *et al.*, *Gene Ther.* **3**, 13 (1996).
18. A. Goyenvalle *et al.*, unpublished observations.
19. D. Jung, B. Yang, J. Meyer, J. S. Chamberlain, K. P. Campbell, *J. Biol. Chem.* **270**, 27305 (1995).
20. R. O. Snyder *et al.*, *Hum. Gene Ther.* **8**, 1891 (1997).
21. R. W. Herzog *et al.*, *Nature Med.* **5**, 56 (1999).
22. P. Chenuaud *et al.*, *Mol. Ther.* **9**, 410 (2004).
23. C. S. Manno *et al.*, *Blood* **101**, 2963 (2003).
24. B. L. Gebski, C. J. Mann, S. Fletcher, S. D. Wilton, *Hum. Mol. Genet.* **12**, 1801 (2003).
25. K. E. Wells, S. Fletcher, C. J. Mann, S. D. Wilton, D. J. Wells, *FEBS Lett.* **552**, 145 (2003).
26. S. Liu *et al.*, *Nucleic Acids Res.* **32**, 3752 (2004).
27. P. Gregorevic *et al.*, *Nature Med.* **10**, 828 (2004).
28. V. Allamand *et al.*, *Hum. Mol. Genet.* **6**, 747 (1997).
29. S. R. Lim, K. J. Hertel, *J. Biol. Chem.* **276**, 45476 (2001).

30. We thank T. Partridge for review of the manuscript and P. Gonin, C. Peccate, and the Généthon in vivo evaluation and vector cores for assistance. This work was supported by the Association Française contre les Myopathies and the Fondation pour la Recherche Medicale.

Supporting Online Material

www.sciencemag.org/cgi/content/full/1104297/DC1
Materials and Methods
Fig. S1
Table S1
References and Notes

20 August 2004; accepted 15 October 2004
Published online 4 November 2004;
10.1126/science.1104297
Include this information when citing this paper.

New Products

http://science.labvelocity.com

Multiwell Insert System

The BD Falcon 96-Well Insert System is a cell culture insert platform suitable for both manual and robotic screening of compounds in cell-based assays. The system has been tested for its ability to produce a differentiated monolayer of Caco-2, LLC-PK1, and MDCK cells, making it suitable for in vitro bioavailability and permeability studies. This automation-compatible platform is composed of a 1.0-μm pore size PET (polyethylene terephthalate) membrane-based 96-Multiwell Insert plate, a media feeder tray, and a lid. To analyze individual samples, the user simply transfers the 96-well insert plate into the BD Falcon 96-Square Well, Angled-Bottom Plate, or a BD Gentest Enhanced Recovery Plate.

BD Biosciences For more information 800-343-2035 www.bdbiosciences.com

PCR Master Mix

The TAQurate Real-Time PCR Master Mix is designed for routine and high-throughput real-time polymerase chain reaction (PCR) applications. Simply add your primers and template to the master mix, mix thoroughly, and begin your PCR thermal cycler. The mix contains SYBR Green I Dye for the detection and quantification of real-time PCR products, the TAQurate Real-Time PCR Enzyme blend for highly specific and reliable amplification of even difficult templates, and the patented PCR Enhancer (with betaine) for high amplification efficiencies and fewer nonspecific PCR products.

Epicentre For more information 800-284-8474 www.epicentre.com

Gene Knockdown

The X-tremeGENE siRNA Transfection Reagent can be used to perform knockdown experiments with small interfering RNA (siRNA) and co-transfection experiments using siRNA and DNA. This easy-to-use reagent requires no media changes and demonstrates minimal cytotoxicity.

Roche Applied Science For more information 800-428-5433 www.roche-applied-science.com

Nuclear Receptor Study

Active Motif's Nuclear Receptor product line provides flexibility for research in this area. Researchers can measure DNA-binding activity using TransAM enzyme-linked immunosorbent assays (ELISAs), compare agonist/antagonist effects using Nuclear Receptor ELISAs, perform traditional electrophoretic mobility shift assays with Gelshift Kits, and perform protein immunoblots with confidence using highly characterized antibodies coupled with recombinant protein or cellular extract positive controls.

Active Motif For more information 877-222-9543 www.activemotif.com

High-Speed Two-Megapixel Camera

The TM-2016-15 is a 2.1-megapixel camera with a one-inch progressive scan charge-coupled device. Featuring 1920 × 1080 resolution, it includes 8-bit digital or optional 10-bit linear output, arranged in a 2K × 1K, 16:9 aspect ratio, and is suited to applications requiring a wide field of view. The TM-2016-15's progressive scan provides full vertical and horizontal resolution at up to 15 frames per second. Two-row binning can be used to achieve 30 frames per second. It features full asynchronous reset with electronic shutter up to 1/10,000 seconds or pulse-width exposure control. The asynchronous reset trigger function allows time image capture and processing.

Pulnix For more information 408-747-0300 www.jaipulnix.com

Sample Preparation for Biomarker Discovery

A sample preparation method for the detection and identification of biomarkers combines Millipore's ultrafiltration (UF) and microvolume solid-phase extraction (SPE) technologies to reduce sample complexity, improve isolation of lower molecular weight proteins, and enhance analysis by mass spectrometry (MS). Complex biological samples, such as serum, plasma, and urine, present a significant challenge for analysis due to high salt and lipid content, as well as an abundant number of proteins. As a result, the reduction of sample complexity is an essential first step. Filter devices with UF membranes are used to efficiently remove larger molecular weight proteins from the samples. Microvolume SPE devices are then used to desalt and concentrate the ultrafiltrate and spot the proteins onto a matrix-assisted laser desorption ionization target for MS analysis. The protocol provides fast, reproducible fractionation of 1 to 96 samples simultaneously.

Millipore For more information 800-MILLIPORE www.millipore.com

For more information visit GetInfo, *Science*'s new online product index at *http://science.labvelocity.com*

From the pages of GetInfo, you can:
- Quickly find and request free information on products and services found in the pages of *Science*.
- Ask vendors to contact you with more information.
- Link directly to vendors' Web sites.

Literature

A new brochure describes the Model HT-24 high-throughput centrifugal evaporator. The HT-24 allows chemists to evaporate two different solvents simultaneously, significantly speeding drying in busy high-performance liquid chromatography (HPLC) and central purification laboratories. Up to 96 shallow-well microplates can be dried down at the same time, and capacity for 16 × 100-mm fraction collector tubes is 576 tubes per run. Compact in design and offering a high capacity for a wide range of sample formats including microplaes, tubes, vials, fraction collector racks, and hybrid HPLC blocks, the HT-24 offers the versatility and productivity to assist chemists in high-throughput drug discovery and purification.

Genevac For more information +44 1473 240000 www.genevac.co.uk

Newly offered instrumentation, apparatus, and laboratory materials of interest to researchers in all disciplines in academic, industrial, and government organizations are featured in this space. Emphasis is given to purpose, chief characteristics, and availability of products and materials. Endorsement by *Science* or AAAS of any products or materials mentioned is not implied. Additional information may be obtained from the manufacturer or supplier by visiting www.science.labvelocity.com on the Web, where you can request that the information be sent to you by e-mail, fax, mail, or telephone.

Published by AAAS